Data-driven situational awareness and decision making for smart grid operation

Edited by
Lipeng Zhu, Yuchen Zhang, Yue Song, Xinran Zhang
and Xue Lyu

Published in
Frontiers in Energy Research

About Frontiers

Frontiers is more than just an open access publisher of scholarly articles: it is a pioneering approach to the world of academia, radically improving the way scholarly research is managed. The grand vision of Frontiers is a world where all people have an equal opportunity to seek, share and generate knowledge. Frontiers provides immediate and permanent online open access to all its publications, but this alone is not enough to realize our grand goals.

Frontiers journal series

The Frontiers journal series is a multi-tier and interdisciplinary set of open-access, online journals, promising a paradigm shift from the current review, selection and dissemination processes in academic publishing. All Frontiers journals are driven by researchers for researchers; therefore, they constitute a service to the scholarly community. At the same time, the *Frontiers journal series* operates on a revolutionary invention, the tiered publishing system, initially addressing specific communities of scholars, and gradually climbing up to broader public understanding, thus serving the interests of the lay society, too.

Dedication to quality

Each Frontiers article is a landmark of the highest quality, thanks to genuinely collaborative interactions between authors and review editors, who include some of the world's best academicians. Research must be certified by peers before entering a stream of knowledge that may eventually reach the public - and shape society; therefore, Frontiers only applies the most rigorous and unbiased reviews. Frontiers revolutionizes research publishing by freely delivering the most outstanding research, evaluated with no bias from both the academic and social point of view. By applying the most advanced information technologies, Frontiers is catapulting scholarly publishing into a new generation.

What are Frontiers Research Topics?

Frontiers Research Topics are very popular trademarks of the *Frontiers journals series*: they are collections of at least ten articles, all centered on a particular subject. With their unique mix of varied contributions from Original Research to Review Articles, Frontiers Research Topics unify the most influential researchers, the latest key findings and historical advances in a hot research area.

Find out more on how to host your own Frontiers Research Topic or contribute to one as an author by contacting the Frontiers editorial office: frontiersin.org/about/contact

Data-driven situational awareness and decision making for smart grid operation

Topic editors

Lipeng Zhu — Hunan University, China

Yuchen Zhang — University of New South Wales, Australia

Yue Song — The University of Hong Kong, Hong Kong, SAR China

Xinran Zhang — Beihang University, China

Xue Lyu — Pacific Northwest National Laboratory (DOE), United States

Citation

Zhu, L., Zhang, Y., Song, Y., Zhang, X., Lyu, X., eds. (2023). *Data-driven situational awareness and decision making for smart grid operation*. Lausanne: Frontiers Media SA. doi: 10.3389/978-2-8325-3471-7

Table of
contents

Editorial: Data-driven situational awareness and decision making for smart grid operation

Lipeng Zhu[1], Yue Song[2], Xinran Zhang[3]*, Yuchen Zhang[4] and Xue Lyu[5]

[1]College of Electrical and Information Engineering, Hunan University, Changsha, China, [2]School of Electronic and Information Engineering, Tongji University, Shanghai, China, [3]School of Automation Science and Electrical Engineering, Beihang University, Beijing, China, [4]School of Electrical Engineering and Telecommunications, The University of New South Wales, Kensington, NSW, Australia, [5]Electricity Infrastructure and Buildings Division, Pacific Northwest National Laboratory, Richland, WA, United States

Editorial on the Research Topic
Data-driven situational awareness and decision making for smart grid operation

1 Introduction

Recent advancements in information and communication technologies have greatly helped strengthen the capability of modern smart grids in online situational awareness and decision making against potentially risky/insecure conditions. In particular, the extensive configuration of various advanced sensing devices has enabled the Research Topic of massive operational information to improve the observability of the grids. With huge volumes of operational information available, emerging computational intelligence and machine learning technologies can be leveraged to augment the intelligence level of system-wide situational awareness and decision making, thereby making the grids smarter than ever before.

Considering the need for addressing challenges related to the above new trend, we thus launched this Research Topic to provide a worldwide platform that collects innovative works reporting recent advances in data-driven intelligent situational awareness and decision making for smart grid operation. After an extensive call-for-paper and peer-review process of more than 1 year, we have accepted 16 papers in total for publication. All the accepted papers have been categorized into two groups according to their subjects: 1) system dynamics awareness, control, and protection; and 2) system optimized dispatch, operation, and restoration. Specific highlights of each paper are summarized in the following.

2 Part I: system dynamics awareness, control, and protection

In the article "*Online correction of transient voltage security region boundary based on load parameter variations in power systems*", Zhang et al. proposed a data-driven transient

voltage security region (TVSR) estimation approach with the impact of composite load model and distributed photovoltaic (PV) power parameters. The relationship between TVSR boundary and load-leading parameters combination scenarios is further mined through the CatBoost learning framework. A more accurate TVSR boundary can be provided by this approach.

In the article "*Stator single-line-to-ground fault protection for powerformers based on HSGC and CNN*", Liu et al. proposed a novel single-line-to-ground fault protection framework with a convolutional neural network (CNN) and the hub-and-spoke grid data converting algorithm (HSGC). HSGC is applied to convert one-dimensional time series to two-dimensional grid-structured ones, and the CNN is trained to extract the features for fault identification. The scheme can accurately detect faulty powerformers.

In the article "*Improved unscented Kalman filter based interval dynamic state estimation of active distribution network considering uncertainty of photovoltaic and load*", Wu et al. proposed an interval dynamic state estimation (IDSE) approach for the interval state estimation of active distribution networks (ADNs) to handle the increasing penetration of distributed PV generations. Through the unscented Kalman filter method, the proposed approach is able to track the dynamic status of an ADN accurately.

In the article "*Deep learning model-transformer based wind power forecasting approach*", Huang et al. proposed a deep learning-based model transformer for wind power forecasting to address the uncertainty and fluctuation of large-scale penetrated wind power. By training a neural network architecture based on the attention mechanism, the wind power forecasting approach can provide more accurate results with better efficiency than other deep learning methods.

In the article "*A neural network-based adaptive power-sharing strategy for hybrid frame inverters in a microgrid*", Deng et al. proposed a novel microgrid framework with hybrid parallel-connected inverters, including capacitive-coupling inverters (CCIs) and inductive-coupling inverters (ICIs). An adaptive power sharing approach was further proposed to reduce power loss. Rapid and accurate power sharing can be achieved through a neural network-based control layer. Case studies and experimental results verified the efficacy of the proposed approach.

In the article "*Online prediction and control of post-fault transient stability based on PMU measurements and multi-task learning*", Liu et al. proposed an integrated approach for online transient stability prediction and real-time emergency control, in which the gated recurrent unit (GRU) based predictor is applied in post-disturbance transient stability prediction. The case study results show that the GRU-based predictor can provide accurate prediction results, and the control scheme can keep the synchronism of the power system.

In the article "*Enhancing transient stability of power systems using a resistive superconducting fault current limiter*", Alashqar et al. proposed a resistive superconduction fault current limiter (SFCL) to enhance the stability of interconnected power systems to address the weakness of existing approaches. The case study results show that the proposed approach is able to keep the stable operation of the power system without tuning power system stabilizers.

In the article "*Virtual inertia based hierarchical control scheme for distributed generations considering communication delay*", Zhou et al. proposed a virtual inertia-based hierarchical control scheme in which the impact of communication delay caused by distributed generations is considered. The proposed approach is validated to be effective through case studies with time delay considered.

3 Part II: system optimized dispatch, operation, and restoration

In the article "*Data-driven reliability evaluation of the integrated energy system considering optimal service restoration*", Dai et al. proposed a data-driven reliability improvement and evaluation method for integrated energy systems (IES) combining a three-state reliability model and an optimal service restoration model (OSR). The reliability model considers the transitional process and partial failure mode using the historical measurement data, while the OSR model determines the best repairment moment for minimizing the load curtailment.

In the article "*Robust dispatching model of active distribution network considering PV time-varying spatial correlation*", Ma et al. proposed a robust ADN dispatch model considering the dynamic spatial correlation and uncertainty of PV. The PV spatial correlation is described by a dynamic conditional correlation generalized autoregressive conditional heteroskedasticity model. The PV uncertainty is modeled by a time-varying ellipsoidal uncertainty set. A mixed integer robust program is constructed to realize the robust optimal dispatch.

In the article "*Adaptive robust economic dispatch and real-time control of distribution system considering controllable inverter air-conditioner clusters*", Chen and Liu proposed an adaptive robust economic dispatch (ARED) model and a real-time decentralized control strategy for distribution systems that utilize the adjustable capabilities of controllable inverter air-conditioner (IAC) clusters. The ARED model is solved by the constraint generation algorithm. The real-time control of IAC clusters is used to hedge against stochastic renewable fluctuation after every round of ARED decisions.

In the article "*Coordination of network reconfiguration and mobile energy storage system fleets to facilitate active distribution network restoration under forecast uncertainty*", Xu et al. proposed a coordinated network reconfiguration and mobile energy storage system (MESS) fleets dispatch model considering the renewable and load uncertainty to increase the ADN resilience after natural disasters. This framework consists of the uncertainty description by an ellipsoidal uncertainty set and a robust restoration model incorporating the MESS and network reconfiguration in the form of mixed-integer linear programming.

In the article "*Hosting capacity of distributed generation based on holomorphic embedding method in distribution networks*", Xie et al. proposed a DG hosting capacity assessment method based on a directional holomorphic embedding method that describes the voltage constraint region and judges DG hosting capacity under a single scenario. The cumulative distribution curve is statistically obtained using the Monte Carlo method, which represents the relationship between the level of voltage violation risk and DG hosting capacity.

In the article "*Transactive energy system: Concept, configuration, and mechanism*", Zhou et al. introduced the basic concept of a transactive energy system (TES). The TES configuration is described

from the perspectives of its physics, information, transaction, and regulation. The TES mechanism allows participants to conduct various transactions with any other party to the extent that regulatory policy permits. Finally, some challenges to the development of TESs are discussed.

In the article "*Accommodation capacity evaluation of renewable energy in power systems considering peak and frequency regulation*", Yu et al. proposed an evaluation method of renewable energy accommodation capacity (REAC) based on a source-network-storage interaction model. The deep peak regulation and frequency response of thermal power units are explicitly modeled and incorporated in the REAC evaluation.

In the article "*A data-driven hybrid interval reactive power optimization based on the security limits method and improved particle swarm optimization*", Chen et al. proposed a data-driven hybrid approach based on the security limits method (SLM) and the improved particle swarm optimization (IPSO) to solve the reactive power optimization with interval uncertainty. The historical data is processed to obtain the boundary of the optimal uncertainty set. In the optimization model, the continuous and discrete variables are alternately solved via SLM and IPSO.

4 Summary

The past few years have witnessed significant progress in the field of data-driven smart grid situational awareness and decision making. By soliciting the above research efforts, we have formed a paper Research Topic to report the state of the art in this field from two major aspects. Nonetheless, the high potential of data-driven technologies has not been thoroughly unlocked, especially the advancing artificial intelligence methods that could be sufficiently leveraged to systematically mine and discover knowledge from massive complicated operational scenarios of complex power grids. We hope this Research Topic can also play a crucial role in enlightening more related innovations and findings in both industry and academia.

Author contributions

LZ: Writing–original draft, Writing–review and editing. YS: Writing–original draft, Writing–review and editing. XZ: Writing–original draft, Writing–review and editing. YZ: Writing–review and editing. XL: Writing–review and editing.

Funding

Conflict of interest

The authors declare that the research was conducted in the absence of any commercial or financial relationships that could be construed as a potential conflict of interest.

Publisher's note

Data-Driven Reliability Evaluation of the Integrated Energy System Considering Optimal Service Restoration

Pan Dai[1], Li Yang[1], Yang Zeng[2]*, Ming Niu[2], Chao Zhu[1], Zhesheng Hu[1] and Yuheng Zhao[2]

[1]Institute of Economics and Technology, State Grid Zhejiang Electric Power Co., Ltd., Hangzhou, China, [2]College of Electrical Engineering, Zhejiang University, Hangzhou, China

The demand for environmental protection and energy utilization transformation has promoted the rapid development of integrated energy systems (IES). Reliability evaluation is a fundamental element in designing IES as it could instruct the planning and operation of IES. This study proposes a novel data-driven reliability improvement and evaluation method considering the three-state reliability model and an optimal service restoration model (OSR). First, a multi-energy flow model is introduced and linearized in order to reduce the computing complexity. Next, a three-state reliability model is developed, considering the transitional process and partial failure mode. Furthermore, an optimal service restoration model is established to determine the best repairment moment for minimizing the load curtailment, and a data-driven reliability evaluation method is developed that integrates OSR and models the stochastic state transition process using the historical measurement data of the smart meters. Finally, the proposed reliability evaluation method is tested on a test IES, and the numerical results validate its effectiveness in evaluating the reliability of IES and improving the overall reliability.

Keywords: integrated energy system, partial failure model, repairment scheduling decision, optimal service restoration, data-driven reliability evaluation

1 INTRODUCTION

Concerns over environmental pollution and fossil fuel depletion have been urging us to explore more efficient and low-carbon energy utilization methods (Xu et al., 2020; Zhang et al., 2020; Li P. et al., 2021). The integrated energy system (IES) has received increasing attention (Zhang G. et al., 2021) as it has the merits of improved energy utilization efficiency and low carbon emissions. The IES couples different forms of energy such as electricity, gas, and heat in a synthetic manner and, thus, achieves mutual complementarity and support as well as coordinated optimization of multiple energy scheduling (Zhang Y. et al., 2021). However, the complex composition and structure of the IES also increase the operational complexity remarkably, which exerts significant influence on the energy supplying reliability of IES and poses a great challenge to the widespread application of IES (Li J. et al., 2021). Therefore, it is imperative to investigate advanced reliability evaluation and improvement methods for IES.

The reliability assessment for convention power systems has been extensively investigated(Li, 2014). However, only a few efforts have been devoted to research on IES reliability

evaluation and improvement. Basically, establishing the reliability model of system components is the key step for analyzing system operation status and assessing system overall reliability. Zhang et al. (2018) and Yan et al. (2021) used a typical two-state model of components to describe the reliability of IES components and obtain the failure rate of the components based on the statistical results. Bao et al. (2019) developed a multi-state model for gas source, compressor, and gas storage to evaluate the reliability of a natural gas system based on universal generating function. Wang et al. (2013) proposed a state space method based on the probabilistic analysis of the Markov model, which uses a two-state model to analyze the sub-system of different components and then further derives the reliability model of the whole component. In the work of Fu et al. (2018), a data-driven model was established to estimate the probability of incident of an insufficient natural gas supply arising from the uncertainty of weather as well as the impact on the reliability of IES. To sum up, although aforementioned research works have made great progress in the reliability modeling of multi-energy system, they fail to account for the actual operating characteristics, transitional process and heterogeneity of various components.

The reliability evaluation outcome heavily relies on the actual applied evaluation method. Thus, developing an appropriate reliability assessment method could benefit the stakeholders by improving the evaluation accuracy. Up to now, several methods have been proposed by researchers (Shariatkhah et al., 2015; Ansari et al., 2020; Cao et al., 2021; Chi et al., 2021). To name a few, H. Wang. et al. (Cao et al., 2021) proposed a reliability assessment framework combining IES dynamic optimal energy flow and Monte Carlo simulation to identify the overall risk of the multi-energy system. In the work of Shariatkhah et al. (2015), a sequential Monte Carlo method incorporating Markov chains is proposed to assess the energy supply reliability of IES. Chi et al. (2021) evaluated the probability distribution of each functional state of the IES based on machine learning methods and statistical methods. In the work of Ansari et al. (2020), a data-driven method via mixture models and importance sampling is proposed to construct time-dependent probability distributions of wind-integrated systems. However, the aforementioned studies mainly focus on improving the reliability evaluation efficiency without considering the potential attempts like repair scheduling to enhance the overall system reliability and fail to take into account the impact of optimization of system operation on the reliability outcome.

Generally, the influence of component failure can be mitigated by the network reconfiguration and repair scheduling optimization and thus the overall reliability can be improved. In the work of Sultana et al. (2016), a comparative analysis of reliability improvement and power loss reduction of distribution networks was conducted using different network reconfiguration technologies. Basically, the network can be reconfigured and some of the affected load can be transferred without being disturbed. However, the network reconfiguration can only maintain partial load supply and cannot fully alleviate the impact of the failure. In contrast, the system service restoration optimization can be adopted to quickly schedule the repair crews and restore the damaged components in order to minimize the

impact of the failure. In the work of Lei et al. (2019), a method of disaster recovery logistics is proposed to optimize service restoration of the distribution network with the scheduling of repair crews and mobile power sources. In the work of Li et al. (2022), a multi-level collaborative optimization model is proposed to integrate the repair unit scheduling and the distribution network restoration. Inspired by these works, the network reconfiguration and service restoration are integrated in the reliability assessment method to improve the overall reliability.

To sum up, most existing works have not considered the influence of partial failure mode and optimization of system operation on the IES reliability outcome. To fill this research gap, this paper proposes an advanced data-driven reliability evaluation and improvement method for IES considering partial failure mode and optimal service restoration. Firstly, a three-state reliability model has been developed for IES to describe the component state transition. Secondly, the influence of the repairment scheduling decision of damaged components is analyzed and an optimal service restoration model is established. Finally, a data-driven reliability evaluation method incorporating the optimal service restoration has been developed. The contributions of this paper are three-fold as follows.

1) A novel three-state reliability model is proposed, including the full-up state, full-down state, derated state and the state transition limits, which can better describe the actual operating states of the components.

2) An optimal service restoration model is established considering the three-state models and repair scheduling decisions. Using the proposed model, the best repairment moment can be autonomously determined so as to minimize the overall load curtailment.

3) By integrating with the optimal service restoration model, a data-driven reliability evaluation method is proposed. Consequently, the overall reliability is enhanced and the accuracy of the evaluation outcome is improved.

The remainder of the paper is organized as follows. **Section 1** introduces the energy flow model of IES. **Section 2** develops a three-state reliability model for IES components and analyzes the influence of the repair scheduling decision. **Section 3** proposes an optimal service restoration model and reliability evaluation method for IES. **Section 4** implements the simulations and discusses the numerical results. Finally, **Section 5** concludes this paper.

2 ENERGY FLOW MODEL OF THE INTEGRATED ENERGY SYSTEM

IES integrates the electric power distribution network (DN), natural gas network (NGN), and heat network (HN) through the energy hub. The structure of the heat network is much more complex than the natural gas network and electric power distribution network. Hence, we did not consider the detailed heat network structure for simplicity and concentrated on the main purpose of our research. The structure of IES is illustrated in

$$V_{\Pi_i} - V_i = r_i P_i + x_i Q_i \quad \forall i \in N_b. \quad (1c)$$

Eqs. 1a, **1b** describe the active and reactive power balance at each bus, where p_i and q_i are the active and reactive power injection at bus i, P_i and Q_i are the active and reactive power on branch i. **Eq. 1a** shows the voltage drop on branch i, where V_i is the voltage magnitude of bus i, r_i and x_i are the resistance and reactance of branch i.

2.2 Natural Gas Network Model

Natural gas transmission and consumption in steady-state can be described by the energy balance equation as **Eq. 2** based on the law of conservation of mass Abeysekera et al. (2016).

$$A_g f + L_g = 0, \quad (2)$$

where A_g is the NGN node-pipe incidence matrix (Osiadacz, 1987); f is the vector of pipeline flow of NGN; and L_g is the vector of nodal gas load.

As is known, the natural gas pipeline flow rate f_{mn} is related to the pressure difference between two terminal ends m and n (Abeysekera et al., 2016). Low and medium pressure natural gas networks can be represented by the well-known Lacey's equation (Abeysekera et al., 2016) as follows:

$$|f_{mn}|f_{mn} = 32.7184 \times 10^{-8} \frac{(\pi_m - \pi_n) D^5}{f_r LS} \quad \forall mn \in N_p, \quad (3)$$

where f_{mn} is the gas flow rate of the pipeline mn. When f_{mn} is positive, the gas flow is from node m to node n; otherwise, it is from node n to node m. π_m and π_n are the air pressure at nodes m and n, respectively; D is the diameter of the pipeline; f_r is the friction coefficient of the pipeline wall; L is the length of the pipeline; S is the specific gravity of the gas; N_p is the set of NGN pipelines. Note that for a given natural gas network, the parameters D, f_r, S, and N_p are known.

It can be observed from **Eq. 3** that the Lacey **formula 3** is nonlinear. To reduce computational complexity, it is linearized

2.1 Electric Power Distribution Network Model

Electric power is delivered through the DN to the end-use customers. Generally, the DN is operated in a radial manner (Zeng et al., 2016) and thus can be represented by a directed tree $G = (N_d, N_b)$, where $N_d = 0, 1, \ldots, N$ denotes the set of buses, and N_b denotes the set of branches. Note that each bus I except the substation bus indexed by 0 has a unique parent bus labeled as Π_i. Each bus i may have several child buses, and the set of child buses of bus i is labeled as C_i. Since each bus except bus 0 has a unique incoming branch, the incoming branch can be labeled with the index of the corresponding bus. Specifically, the branch pointing from a parent bus Π_i to bus i is labeled as i for consistency. Therefore, the set of branches can be expressed as $N_b = 1, \ldots, N$ (Li et al., 2019).

To model the power flow in DN, the linear DistFlow model (Yeh et al., 2012) is adopted as (1) by neglecting the line loss and assuming a relatively flat voltage profile. The applicability of the linear DistFlow model has been validated through its wide applications in resolving practical operational issues in DN, such as voltage violations (Zhu and Liu, 2015) and line overloading (Haque et al., 2020).

$$P_i - \sum_{j \in C_i} P_j = -p_i \quad \forall i \in N_d, \quad (1a)$$

$$Q_i - \sum_{j \in C_i} Q_j = -q_i \quad \forall i \in N_d, \quad (1b)$$

FIGURE 1 | Multi-energy flow diagram of IES.

using the piece-wise linearization technique (Correa-Posada and Sanchez-Martin, 2014). The nonlinear term $|f_{mn}|f_{mn}$ in **Eq. 3** is generalized as $h(x) = |x|x$ and f_{mn} is denoted by a general notation x. Since the gas flow rate f_{mn} is constrained by the pipeline transmission capacity, without loss of generality, x is defined within the interval $[A, B]$, where A and B are associated with the transmission capacity. The operating interval $[A, B]$ is divided into $Z-1$ segments and the value of $h(x)$ at each segment is represented by the line segment between $h(X_z)$ and $h(X_{z+1})$ as illustrated in **Figure 2**, where X_z and X_{z+1} are the two terminal points of the z-th segment. Hence, the piece-wise linearized approximation of $h(x)$ can be represented by the following equations:

$$h(x) \approx h(X_1) + \sum_{z=1}^{Z-1} \left[h(X_{z+1}) - h(X_z) \right] \delta_z, \qquad (4a)$$

$$x = X_1 + \sum_{z=1}^{Z-1} \left(X_{z+1} - X_z \right) \delta_z, \qquad (4b)$$

$$\delta_{z+1} \le \sigma_z \le \delta_z \qquad z \in \{1, \ldots, Z-2\}, \qquad (4c)$$

$$0 \le \delta_z \le 1 \qquad z \in \{1, \ldots, Z-1\}, \qquad (4d)$$

where δ_z is a continuous variable that represents the portion of the z-th segment; σ_z is an auxiliary binary variable that indicates whether x lies on the right-side of the z-th segment. Specifically, if $X_z < x \le X_{z+1}$, then $\sigma_t = 1$ for all $t \le z$ and $\sigma_t = 0$ for all $t > z$.

2.3 Energy Hub Model

The EH interconnects different energy systems and thus could provide a certain degree of flexibility for the coordination of multi-energy systems (Lei et al., 2018). In this paper, two types of EH structures are used to model the energy conversion within the multi-energy system, which is demonstrated in **Figure 3**. Type-A EH consists of a distribution transformer (DT), CHP, and GB, and
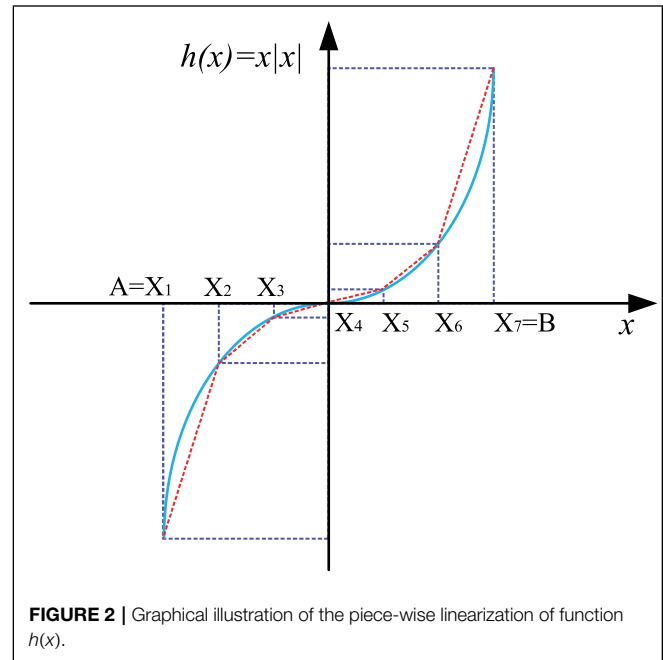
FIGURE 2 | Graphical illustration of the piece-wise linearization of function $h(x)$.

type-B EH is composed of DT, CHP, and EB. For both types of EH, the input energy consists of electricity and gas, while the output energy consists of electricity and heat. The energy conversion in EHs can be described by the following equation:

$$\begin{bmatrix} L^{ehe} \\ L^{ehh} \end{bmatrix} = \begin{bmatrix} (1-\nu_e)\eta^{DT} & (1-\nu_g)\eta_{ge}^{CHP} \\ \nu_e\eta^{EB} & (1-\nu_g)\eta_{gh}^{CHP} + \nu_g\eta^{GB} \end{bmatrix} \begin{bmatrix} P^{ehe} \\ P^{ehg} \end{bmatrix}, \qquad (5)$$

where the superscripts $ehe, ehg,$ and ehh denote electricity, natural gas, and heat, respectively; P and L are input and output vectors, respectively; $P^{ehg} = F^{ehg} GHV$ is the natural gas flow injected into EH, and GHV is the natural gas high calorific value; η_{ge}^{CHP} and η_{gh}^{CHP} are the efficiencies of CHP for converting natural gas energy into electric energy and heat energy, respectively; η^{DT} is the efficiency of the distribution transformer; η^{GB} and
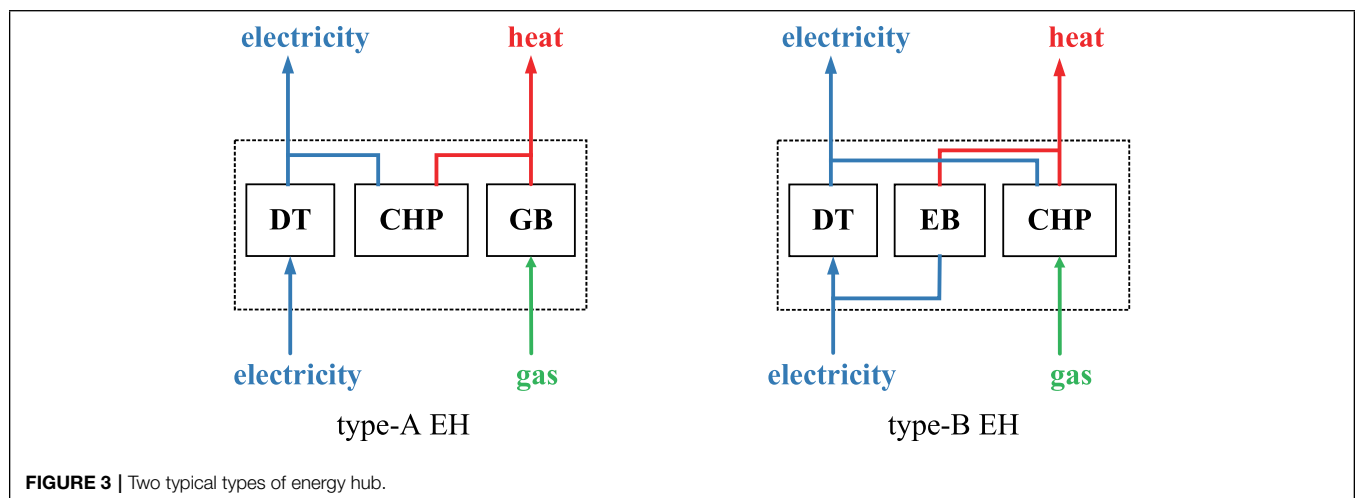
FIGURE 3 | Two typical types of energy hub.

η^{EB} are the efficiency of the gas fired boiler and electrical boiler, respectively; v_g and v_e represent the proportion of natural gas feeding into GB and the proportion of electric energy feeding into EB, respectively. The values of v_g and v_e lie between 0 and 1. For type-A EH, $v_e = 0$, and for type-B EH, $v_g = 0$.

It can be observed from **Eq. 5** that the **formula 5** is nonlinear. To reduce computational complexity, the auxiliary variables are introduced to replace the nonlinear term with an independent variable. Specifically, we introduce P^{DT}, P^{EB}, P^{CHP}_{ge}, P^{CHP}_{gh} and P^{GB} to represent $(1-v_e)\eta^{DT}P^{ehe}$, $v_e\eta^{EB}P^{ehe}$, $(1-v_g)\eta^{CHP}_{ge}P^{ehg}$, $(1-v_g)\eta^{CHP}_{gh}P^{ehg}$ and $v_g\eta^{GB}P^{ehg}$, respectively. Therefore, **formula 5** can be reformulated as the following linearized equations:

$$L^{ehe} = P^{DT} + P^{CHP}_{ge}, \tag{6a}$$

$$L^{ehh} = P^{EB} + P^{CHP}_{gh} + P^{GB}, \tag{6b}$$

$$P^{ehe} = P^{DT}/\eta^{DT} + P^{EB}/\eta^{EB}, \tag{6c}$$

$$P^{ehg} = P^{CHP}_{ge}/\eta^{CHP}_{ge} + P^{GB}/\eta^{GB}, \tag{6d}$$

where P^{DT} is the active power output of the distribution transformer; P^{CHP}_{ge} and P^{CHP}_{gh} are the active power output of CHP for converting natural gas energy into electric energy and heat energy, respectively; P^{EB} and P^{GB} are the active power output of the gas fired boiler and electrical boiler, respectively. Furthermore, P^{CHP}_{gh} is equal to $(\eta^{CHP}_{gh}/\eta^{CHP}_{ge})P^{CHP}_{ge}$.

3 RELIABILITY MODEL OF THE INTEGRATED ENERGY SYSTEM

As the IES integrates DN and NGN, its reliability level is influenced jointly by the operating state of DN and NGN as well as the healthy state of the coupling equipment like EHs. Since the failure of the coupling equipment could threaten the reliable operation of both the electric power network and the natural gas network, more efforts should be devoted to the investigation of the impact of the coupling equipment on the overall reliability of the entire IES.

3.1 Reliability Model of the System

Conventionally, the states of all components are represented by the two-state model in evaluating the reliability of the whole system. However, it fails to account for the actual operating characteristics, transitional processes, and heterogeneity of various components.

Generally, it is sufficient to use the two-state model to represent most components. For instance, DN branches and NGN pipelines are either in a full-up state or in a full-down state. For some coupling equipment and energy sources, the derated state, aks. partial failure mode, is commonly observed in practice, and thus it is necessary to take the derated state into account as it could exert a great influence on the overall reliability assessment.

The partial failure mode could last for a long period and could eventually lead to the full-down state if not repaired, thereby causing significant economic losses. The partial failure mode could also be restored to the full-up state after repair. Therefore, this paper proposes a novel three-state model that integrates full-up state, full-down state, and derated state as illustrated in **Figure 4**.

As previously discussed, the states of DN branches and NGN pipelines can be described by the two-state mode as **Eq. 7a**, and the states of other components like substation, natural gas source and coupling devices including DT, CHP, GB, EB are represented by the three-state model as **Eq. 7b**.

$$u_{d,t} = \begin{cases} 1 & \text{if } full - up \\ 0 & \text{if } full - down \end{cases} \tag{7a}$$

$$u_{m,t} = \begin{cases} 1 & \text{if } full - up \\ \xi & \text{if } derated \\ 0 & \text{if } full - down \end{cases} \tag{7b}$$

where $u_{d,t}$ denotes the state of the component d at time t described by the two-state model, $u_{m,t}$ denotes the state of the component m at time t described by the three-state model, and ξ represents the ratio of the actual available capacity of the component m in derated state to rated capacity in full-up state. ξ can be any value between 0 and 1.

3.2 Influence of Repair Scheduling Decision

After a component damage event, the system operator needs to perform the damage assessment before mobilizing the repair crew to repair the damaged components. The reliability assessment is highly related to the repairment scheduling decision (Arif et al., 2018).

To mitigate the impact of damaged components, the system operator should determine the repair schedule decision by either mobilizing the repair crew to immediately repair the damaged components or delaying the repair for a certain period. If the damaged component is in a full-down state, the repair should be immediately performed so as to minimize load curtailment. If the damaged component is in a derated state, the system operator will invoke the optimal service restoration process (which is introduced in the following section) to determine the best moment for the repair taking into account the system operating condition and load predication profiles in order to achieve the minimal load curtailment.

The initial state of the component m is denoted by $u_{m,0}$ and is known to the system operator. It is assumed that if $u_{m,0} = 1$, then the state of the component m is maintained as healthy for the entire assessment horizon, e.g., one week. Thus, the initial state of the component decides whether it needs to be repaired or not, which can be represented as follows:

$$\alpha_m = \begin{cases} 1 & \text{if } u_{m,t} = 0 \text{ or } \xi \\ 0 & \text{if } u_{m,t} = 1 \end{cases} \tag{8a}$$

$$\beta_m = \begin{cases} 1 & \text{if } u_{m,t} = \xi \\ 0 & \text{if } u_{m,t} = 0 \text{ or } 1 \end{cases} \tag{8b}$$

FIGURE 4 | State space diagram of the component.
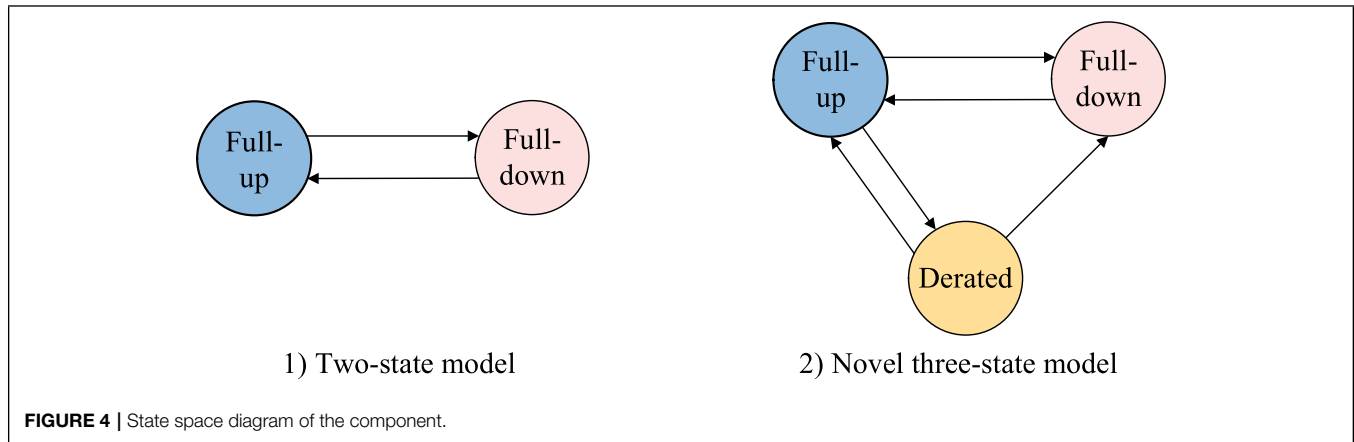
where α_m is the indicator that indicates whether the component m needs to be repaired or not. Specifically, if initially the component m is in a full-down or derated state, then it needs to be repaired and α_m is set as 1. β_m is the indicator indicating whether the repair of damaged component m could be delayed or not. If the damaged component is in a derated state, then it does not need to be repaired immediately.

Let T denote the reliability assessment horizon for the IES, which is divided into T time intervals with the duration of each time interval being 1 h. Two binary variables $y_{m,t}$ and $d_{m,t}$ are introduced to indicate the repair start time interval and completion time interval. Particularly, $y_{m,t_1} = 1$ and $d_{m,t_2} = 1$ represent the repair of the damaged component m is started at time interval t_1 and is completed at time interval t_2, respectively. For example, if the repairment of the component m starts at $t = 1$ and is restored at $t = 3$, then $y_m = \{0, 1, 0, 0, \dots, 0\}$, $d_m = \{0, 0, 0, 1, \dots, 0\}$; if the component m does not need to be repaired, then $y_m = d_m = \{0, 0, 0, 0, \dots, 0\}$. Constraint **Eq. 9b** is enforced to guarantee only one of the $y_{m,t}$ and $d_{m,t}$ will be set as 1 over the entire horizon if the component m is damaged.

$$y_{m,t} \ , \ d_{m,t} \in \{0, 1\} \qquad \forall m \in N_m, \qquad (9a)$$

$$\sum_{t=1}^{T} y_{m,t} = \sum_{t=1}^{T} d_{m,t} = \alpha_m \qquad \forall m \in N_m, \qquad (9b)$$

where N_m is a set of the coupling equipment and energy sources in IES. With the binary variables $y_{m,t}$ and $d_{m,t}$, the repair start time and completion time can be represented by $\Sigma_t t y_{m,t}$ and $\Sigma_t t d_{m,t}$, respectively.

It is required that the derated component should be repaired before reaching the maximum allowed operating time $T_{df,m}$ as described by **Eq. 10a** since otherwise the derated component may further be damaged to the full-down state. **Eqs. 10b, 10c** illustrate the relationship between the repair start time interval $\Sigma_t t y_{m,t}$ and the completion time interval $\Sigma_t t d_{m,t}$. Specifically, if the component m is in a full-down state, its repairment completion time interval is equal to the round up of the repairment start time interval plus the required repairment time $T_{fn,m}$; if the component m is in a derated state, its repairment completion time interval is equal

to the round up of the repairment start time plus the required repairment time $T_{dn,m}$.

$$\sum_{t=1}^{T} t y_{m,t} \le T_{df,m} \beta_m \qquad \forall m \in N_m, \qquad (10a)$$

$$\sum_{t=1}^{T} t d_{m,t} \ge \sum_{t=1}^{T} t y_{m,t} + T_{fn,m}\alpha_m + \left(T_{dn,m} - T_{fn,m}\right)\beta_m \qquad \forall m \in N_m, \qquad (10b)$$

$$\sum_{t=1}^{T} t d_{m,t} \le \sum_{t=1}^{T} t y_{m,t} + T_{fn,m}\alpha_m + \left(T_{dn,m} - T_{fn,m}\right)\beta_m + 1 - \epsilon \qquad \forall m \in N_m, \qquad (10c)$$

where ϵ is a very small number.

The component state $u_{m,t}$ can also be viewed as the availability of the component m. In particular, when $u_{m,t} = 0$ either in full-down state or during the repairment, component m is unavailable at time interval t; when $u_{m,t} = 1$ either the initial state is full-up or it has been repaired, component m is fully available at time interval t; when $u_{m,t}$ is equal to other value between 0 and 1, component m is partially available. For instance, if $u_{m,t} = 0.5$, only half of the rated capacity of the component m can be used. To derive the logical relationship between $u_{m,t}$ and $d_{m,t}$, we further introduce an auxiliary binary variable $\chi_{m,t}$ which indicates the repairment state and can be represented by **Eq. 11a**. Then, $u_{m,t}$ can be expressed as a function of $\chi_{m,t}$, $d_{m,\tau}$ and $u_{m,0}$ as **Eq. 11b**.

$$\chi_{m,t} = \sum_{\tau=1}^{t} \left(y_{m,\tau} - d_{m,\tau}\right) \qquad \forall m \in N_m, \qquad (11a)$$

$$u_{m,t} = u_{m,0}\left(1 - \chi_{m,t}\right) + \left(1 - u_{m,0}\right)\sum_{\tau=1}^{t} d_{m,\tau} \qquad \forall m \in N_m. \qquad (11b)$$

The following three examples with different initial states are used to illustrate the influence of the repairment scheduling decision on the state/availability of each component m represented by **Eq. 11b**. Suppose the required repair times $T_{fn,m}$

and $T_{dn,m}$ are 3h and 2h, respectively, and the maximum allowed operating time $T_{df,m}$ for the derated state is 3h. If initially the component m is in full-up state, it will be maintained in a full-up state for the entire assessment horizon $t = \{0, 1, 2, 3, 4, 5\}$. Hence, it does not need to be repaired. Consequently, we have $y_m = \{0, 0, 0, 0, 0, 0\}$ and $d_m = \{0, 0, 0, 0, 0, 0, 0\}$. Then, according to (11a) and (11b), we have $\chi_m = \{0, 0, 0, 0, 0, 0\}$ and $u_m = \{1, 1, 1, 1, 1, 1, 1\}$ as illustrated by **Figure 5A**.

If initially the component m is in full-down state, the repair should be started immediately at time $t = 0$ and is completed at time $t = 3$ so as to minimize the load curtailment. After that, it will return to the full-up state for the remainder of the assessment horizon. Consequently, we have $y_m = \{1, 0, 0, 0, 0, 0\}$ and $d_m = \{0, 0, 0, 1, 0, 0, 0\}$. Then, according to **Eqs 11a**, **11b**, we have $\chi_m = \{1, 1, 1, 0, 0, 0\}$ and $u_m = \{0, 0, 0, 1, 1, 1, 1\}$ as illustrated by **Figure 5B**.

If initially the component m is in a derated state (for instance, $u_{m,0} = 0.5$), the optimal service restoration process will be invoked (which is introduced in the following section) to determine the best moment of repairment in order to achieve the minimal load curtailment. The component m will remain in the derated operating state until the repairment start time, i.e., $t = 1$ in this example. When the repairment of the component m is completed (i.e., $t = 3$ in this example), it will return to the full-up state for the remainder of the assessment horizon. Hence, we have $y_m = \{0, 1, 0, 0, 0, 0\}$ and $d_m = \{0, 0, 0, 1, 0, 0\}$. Then, according to (11a) and **Eq. 11b**, we have $\chi_m = \{0, 1, 1, 0, 0, 0\}$ and $u_m = \{0.5, 0, 0, 1, 1, 1, 1\}$ as illustrated by **Figure 5C**.

4 RELIABILITY IMPROVEMENT AND EVALUATION WITH OPTIMAL SERVICE RESTORATION

4.1 Optimal Service Restoration Model

In order to improve the IES overall reliability, a novel optimal service restoration (OSR) model is proposed, considering the multi-state mode of various equipment. The optimal repair scheduling decision in **Section 2.2** is obtained by solving the OSR model to mitigate the adverse impact caused by the failure of IES components.

4.1.1 Objective Function

The objective of the OSR model is to minimize the overall load curtailment cost, including electric load curtailment cost in DN, natural gas load curtailment cost in NGN, as well as electric load curtailment cost and thermal load curtailment cost in EHs, which is formulated as follows:

$$\min f = \sum_{t=1}^{T} \left[\sum_{i=0}^{N_d} \lambda_{e,i} \Delta P_{i,t}^D + \sum_{n=1}^{N_n} \lambda_{g,n} \Delta F_{n,t}^D + \sum_{k=1}^{N_{eh}} \left(\lambda_{e,k} \Delta L_{k,t}^{ehe} + \lambda_{h,k} \Delta L_{k,t}^{ehh} \right) \right], \tag{12}$$

where the first term is the electric load curtailment cost in DN, the second term is the natural gas load curtailment cost in NGN, and the last two terms are the electric load curtailment cost and

thermal load curtailment cost in EHs, respectively; $\Delta P_{i,t}^D$, $\Delta F_{n,t}^D$, $\Delta L_{k,t}^{ehe}$, $\Delta L_{k,t}^{ehh}$ are the electric load curtailment of DN bus i at time t, the natural gas load curtailment of NGN node n at time t, the electric load curtailment of EH k at time t, and the thermal load curtailment of EH k at time t, respectively; $\lambda_{e,i}$, $\lambda_{g,n}$, $\lambda_{e,k}$, and $\lambda_{h,k}$ are the corresponding unit curtailment costs; N_n and N_{eh} are the total numbers of NGN nodes and EHs, respectively.

4.1.2 Network Reconfiguration

When the IES is inflicted with damage, the networks can be reconfigured such that the fault can be isolated and the load in the unfaulted region can be transferred and supplied by other power sources. As a result, the load curtailment can be reduced and the overall reliability can be enhanced.

Practically, not every DN branch and NGN pipeline is switchable. In fact, several buses/nodes are interconnected by the non-switchable branches/pipelines. Hence, these buses/nodes can be clustered as a bus/node block, and the bus/node blocks are interconnected by the switchable branches/pipelines. Therefore, to reduce the computational complexity, a virtual power/gas flow model is adopted, taking into account the bus/node blocks (Arif et al., 2019). To this end, the virtual load is introduced for each DN bus block and NGN node block, which is essentially a binary variable indicating the energization status of the DN bus block and NGN node block. In DN, each bus block can only be energized by the black-start power sources, e.g., substation and CHP, through a connected energization path. Thus, for an isolated network without black-start power sources, all internal nodes are de-energized and all internal loads are un-served. Likewise, each NGN node block can only be energized by the natural gas sources through a connected energization path. The proposed virtual power/gas flow model is introduced as follows:

$$g_{i,t} + \sum_{(i,k) \in L^R} v_{ik,t} = X_{i,t} + \sum_{(k,j) \in L^R} v_{kj,t} \qquad \forall i, t, \tag{13a}$$

$$g_{I,t} = 0 \qquad \forall i \in \Omega_B \backslash \{\Omega_{NS}\}, \tag{13b}$$

$$-u_{ik,t} M \leq v_{ik,t} \leq u_{ik,t} M \qquad \forall (i,k) \in L^R, t. \tag{13c}$$

Constraint **Eq. 13a** represents the virtual power flow balance for each DN bus block/NGN node block, where $g_{i,t}$ is the output of a power/gas source in block I at time t, $v_{ik,t}$ is the virtual power/gas flow transferred from block i to block k, L^R is the set of the switchable branches/pipelines, and $X_{i,t}$ is the energization status associated with the virtual load of block i. Constraint **Eq. 13b** requires the outputs of the non-black-start power/gas sources to be 0, where Ω_B is the set of the energy sources, Ω_{NS} is the set of the black-start power sources in DN, and is the set of the natural gas sources in NGN. Constraint **Eq. 13c** imposes the capacity limits on the switchable branches/pipelines, where $u_{ik,t}$ is the availability of the switchable branch/pipeline connecting blocks i and k, M is a very large number. If the virtual load can be served by the energy sources, then $X_i = 1$ (i.e., block i is energized); otherwise, $X_i = 0$ (i.e., block i de-energized).

FIGURE 5 | Illustration of the relationship between y_m, f_m and χ_m, u_m when $u_{m,0}$ is different values, **(A)** is $u_{m,0} = 1$, **(B)** is $u_{m,0} = 0$, **(C)** is $u_{m,0} = 0.5$.
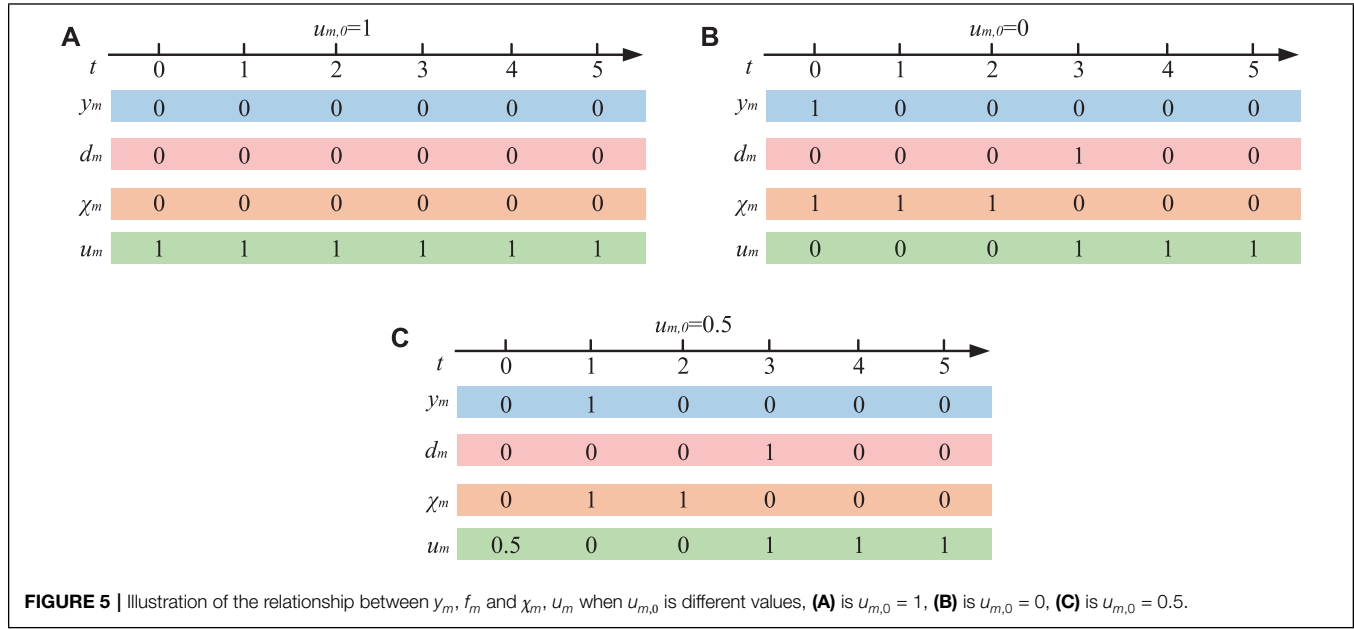
4.1.3 Nodal Power Balance

The nodal power balance, gas balance, and EH load balance equation can be formulated as follows:

$$p_{i,t} = P_{i,t}^{TS} + P_{i,t}^{wt} + P_{i,t}^{pv} - P_{i,t}^{ehe} - \Delta P_{i,t}^{wt} - \Delta P_{i,t}^{pv} - \left(P_{i,t}^D - \Delta P_{i,t}^D\right)$$
$$\forall i \in N_d, \quad (14a)$$

$$q_{i,t} = Q_{i,t}^{TS} + Q_{i,t}^{wt} + Q_{i,t}^{pv} + Q_{i,t}^C - \left(Q_{i,t}^D - \Delta P_{i,t}^D\left(Q_{i,t}^D/P_{i,t}^D\right)\right)$$
$$\forall i \in N_d, \quad (14b)$$

$$f_{n,t} = F_{n,t}^{GS} - F_{n,t}^{ehg} - \left(F_{n,t}^D - \Delta F_{n,t}^D\right) \qquad \forall n \in N_n, \quad (14c)$$

$$L_{k,t}^{ehe} = P_{k,t}^{DT} + P_{ge,k,t}^{CHP} + \Delta L_{k,t}^{ehe} \qquad \forall k \in N_{eh}, \quad (14d)$$

$$L_{k,t}^{ehh} = P_{k,t}^{EB} + P_{gh,k,t}^{CHP} + P_{k,t}^{GB} + \Delta L_{k,t}^{ehh} \qquad \forall k \in N_{eh}. \quad (14e)$$

Constraint **Eq. 14a** shows the composition of the nodal active power injection, where $P_{i,t}^{TS}$, $P_{i,t}^{wt}$, $P_{i,t}^{pv}$, $P_{i,t}^{ehe}$, $P_{i,t}^D$ are the active power of subtation, WT, PV, EH and load at bus i at time t, respectively; $\Delta P_{i,t}^{wt}$, $\Delta P_{i,t}^{pv}$ are the amount of curtailed wind power and solar power at bus i at time t, respectively. Constraint **Eq. 14b** illustrates the composition of the nodal reactive power injection, where $Q_{i,t}^{TS}$, $Q_{i,t}^{wt}$, $Q_{i,t}^{pv}$, $Q_{i,t}^C$, $Q_{i,t}^D$ are the reactive power of subtation, WT, PV, compensation devices and load at bus i at time t, respectively. Note that the nodal reactive power load is curtailed proportionally to the nodal active power curtailment. Constraint **Eq. 14c** reveals that the nodal net gas injection $f_{n,t}$ at node i is equal to the gas injection $F_{n,t}^{GS}$ by the gas source minus the gas consumption $F_{n,t}^{ehg}$ by the EH and nodal gas load $\left(F_{n,t}^D - \Delta F_{n,t}^D\right)$, where $F_{n,t}^D$ is the required nodal gas load and $\Delta F_{n,t}^D$ is the curtailednodal gas load. Constraints **Eqs 14d**, **14e** are

the electric power balance and thermal energy balance in EHs, respectively.

4.1.4 Operational Security Constraints

Three categories of operational security constraints are considered as follows:

1. Operational limits for load curtailment
2. Operational limits for various devices include WT, PV, CHP, DT, GB, and EB
3. Network operational security constraints, including bus voltage limits, node gas pressure limits, branch flow limits, and pipeline flow limits

The abovementioned three categories of constraints can be generalized as the following two mathematical inequalities.

$$\Delta L^{\min} \leq \Delta L \leq \Delta L^{\max}, \quad (15a)$$

$$u_{w,t} W^{\min} \leq W \leq u_{w,t} W^{\max}, \quad (15b)$$

where $\Delta L = [\Delta P_{I,t}^D, \Delta F_{n,t}^D, \Delta L_{k,t}^{ehe}, \Delta L_{k,t}^{ehh}]^T$; $\Delta L^{\max}$ and $\Delta L^{\min}$ denote the upper and lower limits of ΔL, respectively. $W = [P_{i,t}^{TS}, P_{i,t}^{wt}, P_{i,t}^{pv}, \Delta P_{i,t}^{wt}, \Delta P_{i,t}^{pv}, Q_{i,t}^{TS}, Q_{i,t}^{wt}, Q_{i,t}^{pv}, Q_{i,t}^C, F_{n,t}^{GS}, P_{ge,k,t}^{CHP}, P_{gh,k,t}^{CHP}, P_{k,t}^{DT}, P_{k,t}^{GB}, P_{k,t}^{EB}, V_{i,t}, \pi_{n,t}, Tl_{i,t}, Pl_{n,t}]^T$. $u_{w,t}$ denotes the state of the component z at time t. $W^{\max}$ and $W^{\min}$ denote the upper and lower limits of W, respectively. Here, $P_{ge,k,t}^{CHP}$, $P_{gh,k,t}^{CHP}$ are the active power output of the heat production and electricity production of CHP, respectively; $P_{k,t}^{DT}$, $P_{k,t}^{GB}$, $P_{k,t}^{EB}$ are the active power output of DT, GB, EB in EH, respectively. $V_{i,t}$, $\pi_{n,t}$ are bus voltage in DN and node pressure in NGN, respectively. $Tl_{i,t}$, $Pl_{n,t}$ are the capacity of branches in DN and pipelines in NGN, respectively. For example, the bus voltage $V_{i,t}$ in DN should be within the scope of the up limit $V^{\max}$ and down limit $V^{\min}$ when it is energized. When it is not energized, it is 0.

4.2 Data-Driven Reliability Evaluation Process

Based on the proposed optimal service restoration model, we developed a data-driven reliability evaluation method for the IES that integrates OSR and models the stochastic state transition process using the historical measurement data of the smart meters, whose flowchart is demonstrated in **Figure 6**.

The proposed reliability evaluation of the IES consists of eight steps illustrated as follows:

Step(**B1**). We select the reliability assessment horizon *T*, which is greater than the maximum restoration time of each component.

Step(**B2**). We enter IES component data and obtain the load, WT, and PV prediction data for the entire horizon *T*.

Step(**B3**). The historical measurement data of the smart meters is used to model the state transition probability of each component. Then, we use the Monte Carlo simulation method to get the initial state of the IES components according to the state transition probability distribution.

Step(**B4**). We analyze DN and NSN topology.

Step(**B5**). We solve the optimal service restoration model.

Step(**B6**). We check if all scenarios are considered. If so, we move to *Step*(**B7**); otherwise, we go back to *Step*(**B3**).

Step(**B7**). We calculate reliability evaluation indices. The IES reliability evaluation indices used in the paper mainly include the expected electricity not supply *EENS*, the expected gas not supply *EGNS*, and the expected heat not supply *EHNS*. Their calculation formulas are presented as follows:

$$EENS = \sum_{X \in E} P(X) \sum_{t=1}^{T} \left[\sum_{i=1}^{N_d} \Delta P_{i,t}^{D} + \sum_{k=1}^{N_{eh}} \Delta L_{k,t}^{ehe} \right], \qquad (16a)$$

$$EGNS = \sum_{X \in G} P(X) \sum_{t=1}^{T} \sum_{n=1}^{N_n} \Delta F_{n,t}^{D}, \qquad (16b)$$

$$EHNS = \sum_{X \in H} P(X) \sum_{t=1}^{T} \sum_{k=1}^{N_{eh}} \Delta L_{k,t}^{ehh}, \qquad (16c)$$

where $P(X)$ is the probability of the scenario X.

Step(**B8**) Output results.

5 NUMERICAL RESULTS

In order to verify the effectiveness of the proposed optimal service restoration model and the proposed reliability evaluation method, case studies on a test IES are carried out on the platform of MATLAB using CPLEX as the MILP solver.

5.1 Test System Specification

The test IES is composed of the modified IEEE 33-node distribution network (Group, 2010), the 11-node natural gas network (Abeysekera et al., 2016) and two EHs, as demonstrated by **Figure 7**, where EH1 is a type-A EH and EH2 is a type-B EH.

The base voltage of the IEEE 33-node DN is 12.66k*V,* and the voltages in the case studies are expressed in per-unit value.

The parameter of the derated state ξ is assumed to be 0.5. The upper and lower limits for the nodal voltage magnitude are 0.95 and 1.05, respectively. The maximum and minimum values of nodal pressure in NGN are $75mbar$ and $22.5mbar$, respectively. The capacity of the pipeline is $1600m^3/h$. The parameters related to the coupling equipment and energy sources in IES are shown in **Table 1**, and the required repair times for the damaged coupling equipment and energy sources are summarized in **Table 2**. The assessment horizon of 1 week is considered and the weekly profiles of electric load, gas load, and thermal load are demonstrated in **Figure 8**, where the peak electric load of DN and NGN can be found in (Group, 2010) and (Abeysekera et al., 2016), respectively. In addition, the peak electric load and heat load in EH are 600kW and 600kW, respectively. Besides, the unit cost for electric load curtailment, gas load curtailment, and thermal load curtailment are assumed as 10\$, 98\$ and 10\$, respectively.

5.2 Effectiveness of the Proposed Three-State Model

In this subsection, the effectiveness of the proposed novel three-state model considering partial failure mode is verified.

Table 3 lists the load curtailments in IES due to the damages occurring to the coupling equipment and energy sources using two different reliability models. As shown in the table, the load curtailment from the two-state model without considering the derated state is much greater than the load curtailment from the proposed three-state model considering the partial failure mode, which validates the effectiveness of the proposed three-state model. The reason is that when a component is in a derated state, it can still be operated for a certain period so that the repair can be delayed to the moment when the net load is relatively low. Therefore, the proposed three-state model outperforms the conventional two-state model, as the proposed three-state model can describe the states of components more accurately.

5.3 Effectiveness of the Optimal Service Restoration Model

To demonstrate the merits of the proposed optimal service restoration (OSR) model, its performance is compared with a benchmark approach without considering OSR, denoted as NOSR, for the damages that occurred to different types of components.

Table 4 summarizes the load curtailments in IES due to the derated or full-down states of the coupling equipment and energy sources using the proposed OSR model and the benchmark approach to NOSR. As shown in the table, when the coupling equipment and energy sources are in a full-down state, the amount of load curtailments with the OSR model is the same as that with NOSR. The reason is that when a component is in a full-down state, it should be repaired immediately in order to minimize the load curtailment. When the coupling equipment and energy sources are in derated state, the amount of load curtailments with OSR model is reduced substantially compared to the load curtailments with NOSR since the repairment of
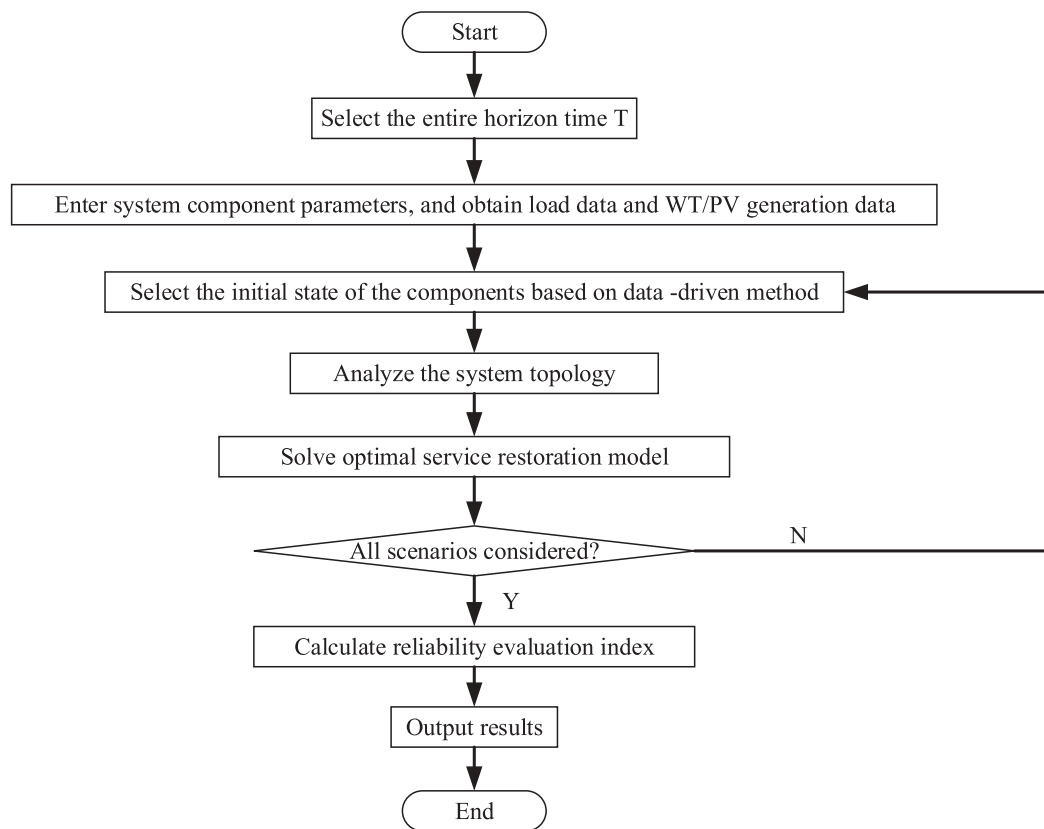
FIGURE 6 | Reliability evaluation flowchart of IES.
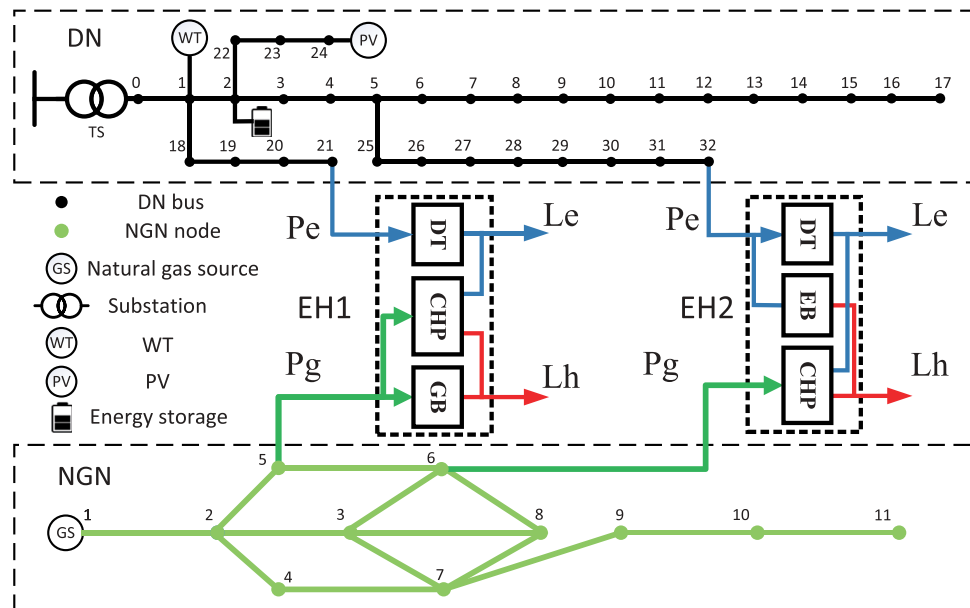
FIGURE 7 | Topology of the test IES.

TABLE 1 | Parameters of IES components.

η_{ge}^{CHP}	η_{gh}^{CHP}	η^{DT}	η^{GB}	η^{EB}	P_{CHP}^{max}	P_{CHP}^{min}	P_{DT}^{max}	P_{DT}^{min}	P_{GB}^{max}	P_{GB}^{min}	P_{EB}^{max}	P_{EB}^{min}
0.3	0.4	0.99	0.8	0.6	1,000	0	600	−600	400	0	500	0

TABLE 2 | Reliability parameters of IES components.

Components	$T_{dn,m}(h)$	$T_{fn,m}(h)$	$T_{df,m}(h)$
CHP	30	36	16
DT	18	25	10
GB	18	21	16
EB	18	21	16
Substation	54	64	24
Natural gas source	32	40	16
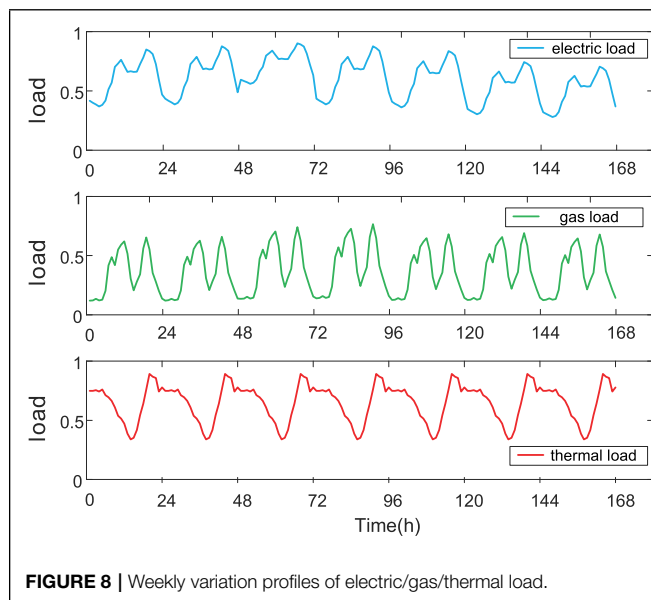
FIGURE 8 | Weekly variation profiles of electric/gas/thermal load.

FIGURE 9 | Load curtailment due to the derated EH equipment using different methods.

the derated component is delayed to the best moment in term of overall load curtailment using the proposed OSR model. Therefore, the proposed OSR model is effective in reducing load curtailment caused by the damage of the key components in IES.

Figure 9 depicts the load curtailment due to the derated coupling equipment using the proposed OSR method and the NOSR method. It can be observed from the figure that when the coupling equipment is derated, it mainly leads to electric load curtailment and thermal load curtailment within the EH and has little effect on DN and NGN. Besides, the proposed OSR model could significantly lower the overall load curtailment caused by the partial failure of CHP, DT, GB, and EB. **Figure 10** shows the load curtailment due to the derated state of the energy sources in IES using the proposed OSR method and

the NOSR method. We can see from the figure that when the energy sources are partially damaged, it leads to a large amount of load curtailment in IES and its impact on EH is also considerable. When the substation is partially damaged, it mainly affects the distribution network load and EH electric load supply, and when the natural gas source is partially damaged, it mainly influences the natural gas load and EH thermal load supply. When the OSR method is applied, the load curtailment is substantially lessened. Therefore, the proposed OSR method is more favorable than the benchmark approach NOSR in reducing the load curtailment due to the partial failure of key components.

Table 5 lists the reliability evaluation indices of the test IES with and without the optimal service restoration model considering the fault scenarios of coupling equipment and energy sources. In each scenario, only one fault is occurred to the aforementioned components, either the full-down failure of derated partial failure. We did not consider the possibility of multiple faults occurring simultaneously on different components as the probability of this scenario is relatively low.

From **Table 5**, it can be seen that the reliability index *EGNS* is larger than *EENS*, and *EENS* is greater than *EHNS*. Because in the test system, there is only one natural gas source. When the natural gas source fails down, all gas loads are curtailed, which leads to the high value of *EGNS*. In contrast,

TABLE 3 | Performance comparision between the two-state model and the proposed three-state model.

Components	Load curtailment with the two-state model (kWh)	Load curtailment with the three-state model (kWh)
CHP1	4,860.40	3,906.46
CHP2	13,965.19	10,765.98
DT1	3,815.14	3,417.71
DT2	4,505.76	4,034.88
GB	1,330.09	1,035.73
EB	1,313.40	1,019.04
Substation	143,395.14	110,982.63
Natual gas source	282,533.93	204,924.09

TABLE 4 | Comparison of overal load curtailment under different methods.

Method	Load curtailment with OSR (kWh)		Load curtailment with NOSR (kWh)	
Components	Derated	Full-down	Derated	Full-down
CHP1	2,274.10	3,255.38	3,906.46	3,255.38
CHP2	7,357.99	9,260.69	10,765.98	9,260.69
DT1	2,332.83	3,123.54	3,417.71	3,123.54
DT2	2,406.28	3,733.11	4,034.88	3,733.11
GB	498.39	810.27	1,035.73	810.27
EB	498.39	793.59	1,019.04	793.59
Substation	72,768.29	96,308.96	110,982.63	96,308.96
Natural gas source	153,344.05	203,249.82	204,924.09	203,249.82

FIGURE 10 | Load curtailment due to the derated energy sources using different methods.
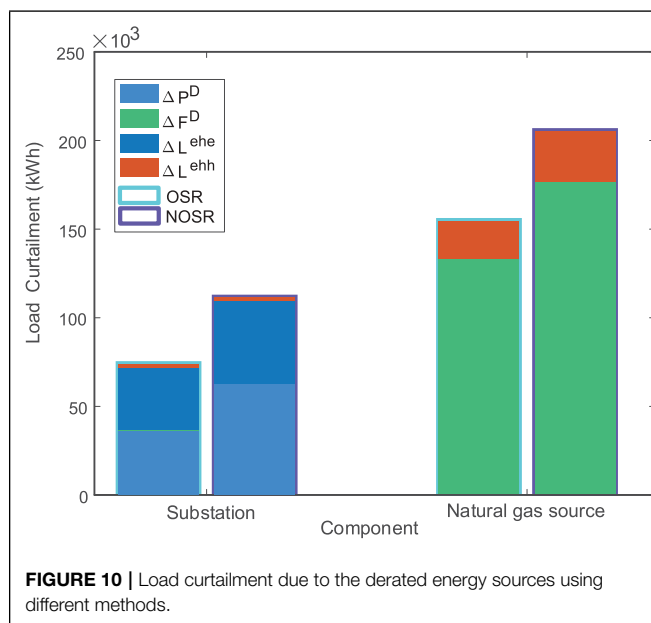
TABLE 5 | Reliability evaluation indices using different methods.

Method	EENS (kWh/week)	EGNS (kWh/week)	EHNS (kWh/week)
OSR	7,291.23	12,947.51	3,178.58
NOSR	8,972.91	14,796.88	3,756.12

the electric loads are served by the substation, PV, WT, and CHP. Thus, even if the substation is out of work, some electric loads can still be served by other power sources. The overall thermal load level is much smaller than the electric load level and gas load level, which results in a lower value of *EHNS*. Besides, all reliability assessment indices *EENS*, *EGNS*, and *EHNS* are substantially lowered when the OSR model is adopted, which further verifies the effectiveness of the proposed optimal service restoration model in improving the overall reliability of IES.

6 CONCLUSION

This paper develops a novel reliability improvement and evaluation method by integrating the three-state reliability model and the optimal service restoration model. First, the multi-energy flow model is introduced and linearized to reduce computational complexity. Then, a three-state model is proposed, taking into account the partial failure mode of the IES components based on the conventional two-state model. Furthermore, an innovative optimal service restoration model is developed to determine the best repairment moment for minimizing the overall load curtailment, and a data-driven reliability assessment method is presented by incorporating the optimal service restoration model. Finally, the effectiveness of the proposed method is validated by the numerical results of a test IES.

DATA AVAILABILITY STATEMENT

The original contributions presented in the study are included in the article/Supplementary Material; further inquiries can be directed to the corresponding author.

AUTHOR CONTRIBUTIONS

FUNDING

REFERENCES

Abeysekera, M., Wu, J., Jenkins, N., and Rees, M. (2016). Steady State Analysis of Gas Networks with Distributed Injection of Alternative Gas. *Appl. Energy* 164, 991–1002. doi:10.1016/j.apenergy.2015.05.099

Arif, A., Ma, S., Wang, Z., Wang, J., Ryan, S. M., and Chen, C. (2018). Optimizing Service Restoration in Distribution Systems with Uncertain Repair Time and Demand. *IEEE Trans. Power Syst.* 33, 6828–6838. doi:10.1109/tpwrs.2018.2855102

Arif, A., Wang, Z., Chen, C., and Wang, J. (2019). Repair and Resource Scheduling in Unbalanced Distribution Systems Using Neighborhood Search. *IEEE Trans. Smart Grid* 11, 673–685.

Aslam Ansari, O., Gong, Y., Liu, W., and Yung Chung, C. (2020). Data-driven Operation Risk Assessment of Wind-Integrated Power Systems via Mixture Models and Importance Sampling. *J. Mod. Power Syst. Clean Energy* 8, 437–445. doi:10.35833/mpce.2019.000163

Bao, M., Ding, Y., Singh, C., and Shao, C. (2019). A Multi-State Model for Reliability Assessment of Integrated Gas and Power Systems Utilizing Universal Generating Function Techniques. *IEEE Trans. Smart Grid* 10, 6271–6283. doi:10.1109/tsg.2019.2900796

Cao, M., Shao, C., Hu, B., Xie, K., Li, W., Peng, L., et al. (2021). Reliability Assessment of Integrated Energy Systems Considering Emergency Dispatch Based on Dynamic Optimal Energy Flow. *IEEE Trans. Sustain. Energy* 13, 290–301.

Chi, L., Su, H., Zio, E., Qadrdan, M., Li, X., Zhang, L., et al. (2021). Data-driven Reliability Assessment Method of Integrated Energy Systems Based on Probabilistic Deep Learning and Gaussian Mixture Model-Hidden Markov Model. *Renew. Energy* 174, 952–970. doi:10.1016/j.renene.2021.04.102

Correa-Posada, C. M., and Sanchez-Martin, P. (2014). Integrated Power and Natural Gas Model for Energy Adequacy in Short-Term Operation. *IEEE Trans. Power Syst.* 30, 3347–3355.

Fu, X., Li, G., Zhang, X., and Qiao, Z. (2018). Failure Probability Estimation of the Gas Supply Using a Data-Driven Model in an Integrated Energy System. *Appl. Energy* 232, 704–714. doi:10.1016/j.apenergy.2018.09.097

Group, D. T. F. W. (2010). *Distribution Test Feeders*.

Haque, N., Tomar, A., Nguyen, P., and Pemen, G. (2020). Dynamic Tariff for Day-Ahead Congestion Management in Agent-Based Lv Distribution Networks. *Energies* 13, 318. doi:10.3390/en13020318

Lei, S., Chen, C., Li, Y., and Hou, Y. (2019). Resilient Disaster Recovery Logistics of Distribution Systems: Co-optimize Service Restoration with Repair Crew and Mobile Power Source Dispatch. *IEEE Trans. Smart Grid* 10, 6187–6202. doi:10.1109/TSG.2019.2899353

Lei, Y., Hou, K., Wang, Y., Jia, H., Zhang, P., Mu, Y., et al. (2018). A New Reliability Assessment Approach for Integrated Energy Systems: Using Hierarchical Decoupling Optimization Framework and Impact-Increment Based State Enumeration Method. *Appl. Energy* 210, 1237–1250. doi:10.1016/j.apenergy.2017.08.099

Li, J., Khodayar, M. E., and Feizi, M. R. (2022). Hybrid Modeling Based Co-optimization of Crew Dispatch and Distribution System Restoration Considering Multiple Uncertainties. *IEEE Syst. J.* 16, 1278–1288. doi:10.1109/JSYST.2020.3048817

Li, J., Khodayar, M. E., Wang, J., and Zhou, B. (2021a). Data-driven Distributionally Robust Co-optimization of P2p Energy Trading and Network Operation for Interconnected Microgrids. *IEEE Trans. Smart Grid* 12, 5172–5184. doi:10.1109/tsg.2021.3095509

Li, J., Xu, Z., Zhao, J., and Zhang, C. (2019). Distributed Online Voltage Control in Active Distribution Networks Considering Pv Curtailment. *IEEE Trans. Ind. Inf.* 15, 5519–5530. doi:10.1109/tii.2019.2903888

Li, P., Zhang, F., Ma, X., Yao, S., Zhong, Z., Yang, P., et al. (2021b). Multi-time Scale Economic Optimization Dispatch of the Park Integrated Energy System. *Front. Energy Res.* 533. doi:10.3389/fenrg.2021.743619

Li, W. (2014). *Risk Assessment of Power Systems: Models, Methods, and Applications*. John Wiley & Sons.

Osiadacz, A. (1987). *Simulation and Analysis of Gas Networks*.

Shariatkhah, M.-H., Haghifam, M.-R., Parsa-Moghaddam, M., and Siano, P. (2015). Modeling the Reliability of Multi-Carrier Energy Systems Considering Dynamic Behavior of Thermal Loads. *Energy Build.* 103, 375–383. doi:10.1016/j.enbuild.2015.06.001

Sultana, B., Mustafa, M. W., Sultana, U., and Bhatti, A. R. (2016). Review on Reliability Improvement and Power Loss Reduction in Distribution System via Network Reconfiguration. *Renew. Sustain. Energy Rev.* 66, 297–310. doi:10.1016/j.rser.2016.08.011

Wang, J.-J., Fu, C., Yang, K., Zhang, X.-T., Shi, G.-h., and Zhai, J. (2013). Reliability and Availability Analysis of Redundant Bchp (Building Cooling, Heating and Power) System. *Energy* 61, 531–540. doi:10.1016/j.energy.2013.09.018

Xu, X., Jia, Y., Xu, Y., Xu, Z., Chai, S., and Lai, C. S. (2020). A Multi-Agent Reinforcement Learning-Based Data-Driven Method for Home Energy Management. *IEEE Trans. Smart Grid* 11, 3201–3211. doi:10.1109/tsg.2020.2971427

Yan, C., Bie, Z., Liu, S., Urgun, D., Singh, C., and Xie, L. (2021). A Reliability Model for Integrated Energy System Considering Multi-Energy Correlation. *J. Mod. Power Syst. Clean Energy* 9, 811–825. doi:10.35833/mpce.2020.000301

Yeh, H.-G., Gayme, D. F., and Low, S. H. (2012). Adaptive Var Control for Distribution Circuits with Photovoltaic Generators. *IEEE Trans. Power Syst.* 27, 1656–1663. doi:10.1109/tpwrs.2012.2183151

Zeng, Q., Fang, J., Li, J., and Chen, Z. (2016). Steady-state Analysis of the Integrated Natural Gas and Electric Power System with Bi-directional Energy Conversion. *Appl. Energy* 184, 1483–1492. doi:10.1016/j.apenergy.2016.05.060

Zhang, G., Xie, P., Huang, S., Chen, Z., Du, M., Tang, N., et al. (2021a). Modeling and Optimization of Integrated Energy System for Renewable Power Penetration Considering Carbon and Pollutant Reduction Systems. *Front. Energy Res.*, 818. doi:10.3389/fenrg.2021.767277

Zhang, S., Gu, W., Yao, S., Lu, S., Zhou, S., and Wu, Z. (2020). Partitional Decoupling Method for Fast Calculation of Energy Flow in a Large-Scale Heat and Electricity Integrated Energy System. *IEEE Trans. Sustain. Energy* 12, 501–513.

Zhang, S., Wen, M., Wen, M., Cheng, H., Hu, X., and Xu, G. (2018). Reliability Evaluation of Electricity-Heat Integrated Energy System with Heat Pump. *Csee Jpes* 4, 425–433. doi:10.17775/cseejpes.2018.00320

Zhang, Y., Shan, Q., Teng, F., and Li, T. (2021b). Distributed Economic Optimal Scheduling Scheme for Ship-Integrated Energy System Based on Load Prediction Algorithm. *Front. Energy Res.* 443. doi:10.3389/fenrg.2021.720374

Zhu, H., and Liu, H. J. (2015). Fast Local Voltage Control under Limited Reactive Power: Optimality and Stability Analysis. *IEEE Trans. Power Syst.* 31, 3794–3803.

Conflict of Interest: PD, LY, CZ, and ZH were employed by State Grid Zhejiang Electric Power Co., Ltd.

The remaining authors declare that the research was conducted in the absence of any commercial or financial relationships that could be construed as a potential conflict of interest.

Stator single-line-to-ground fault protection for powerformers based on HSGC and CNN

Xiaohan Liu[1], Yuanyuan Wang[1]*, Xiaomin Luo[1], Chengjun Cao[1], Wei Li[2], Buming Wang[3], Jiabao Wang[3] and Yin Wang[1]

[1]School of Electrical and Information Engineering, Changsha University of Science and Technology, Changsha, Hunan, China, [2]China Electric Power Research Institute (CEPRI), Beijing, China, [3]Xiangtan Electric Co., Ltd. Hualian, Xiangtan, Hunan, China

It is necessary for powerformers running in parallel to identify which powerformer occurs at the stator single-line-to-ground (SLG) fault. Some state-of-the-art fusion discriminations are used to identify stator SLG fault, but these methods extract fault features artificially, and application conditions are limited. Convolutional neural network (CNN) has shown superior automatic feature extraction ability in various fields, but it cannot directly extract features from one-dimensional time series vectors collected by powerformers. Therefore, this article proposed a novel SLG fault protection scheme based on the hub-and-spoke grid data converting algorithm (HSGC) and CNN. First, Pearson product-moment correlation coefficients (PCCs) are used to calculate the correlations of one-dimensional time series vectors, establish a correspondence between them and the distance of two-dimensional grid cells, and then convert one-dimensional time series vectors to two-dimensional grid-structured data by HSGC. Second, the trained CNN automatically extracts the features of two-dimensional grid-structured data. Finally, the faulty powerformer can be identified based on the output of CNN. The proposed protection scheme is verified through the simulation of ATP-EMTP and Python. The results show that the scheme can accurately detect a faulty Powerformer under different conditions where neutral point is high-resistance or reactance grounding, even if fault resistance is 8,000 Ω.

KEYWORDS

powerformer, single-phase-to-ground fault protection, HSGC, CNN, PCCs

1 Introduction

High-voltage equipment used in power generation is continuously being developed in order to reduce production costs, improve efficiency, and, more recently, minimize environmental impact (Tzelepis et al., 2020; Zhou et al., 2022). Over the past decades, a series of changes have taken place in high-voltage apparatus. One of them is the powerformer (Leijon, 1998), a new type of generator developed by ABB with a stator winding made up of cross-linked polyethylene (XLPE) cable (Shi et al., 2021). The cross section of the XLPE cable is a circular winding, which can avoid uneven electric field distribution along the conductor surface caused by the shape of rectangular stator bars of the conventional generator (Wang et al., 2020a), allowing the output voltage at the terminal of powerformer to exceed about 30–35 kV and reach theoretical levels of 400 kV. Thus, it can be directly connected to the power transmission systems, which leads to lower power losses.

The stator SLG fault is the most potential harm, and it is the most frequent fault that generators will experience (Xue et al., 2022; Huang and Jia, 2017). Especially for powerformers, because of the XLPE cable with greater capacitance to ground, the fault current is greater and the damage to the powerformer is greater after the stator SLG fault occurs. Meanwhile, the stator SLG fault is very likely to develop into a more severe inter-turn fault and phase-to-phase fault, leading to the damage of stator core and stator winding of powerformers and seriously affecting the safe and stable operation of the power grid. To avoid such consequences, reliable detection and isolation of stator SLG fault have become essential for powerformers.

For a group of generators running in parallel, if an SLG fault occurs on a generator, it is necessary to selectively detect the faulty generator. Several selective protection methods for detecting stator SLG fault of powerformers have been proposed. Wang et al. (2013a) proposed using the direction and the magnitude of leakage current as identification criteria to detect the SLG fault and combining the fundamental component and the third-harmonic component of leakage current to realize 100% coverage of fault detection. However, the protection criteria were analyzed separately, and the reliability was low. To address this problem, some protection methods based on fault feature fusion have been proposed in the study by Wang et al. (2013b). Wang et al. (2013c) proposed a stator SLG fault protection scheme based on a fuzzy clustering algorithm and hierarchical clustering algorithm, which synthesizes several fault features to calculate cluster centers and then compares the distance between the detected pattern and two cluster centers to identify the faulty powerformer. Also, Fang et al. (2020) further proposed a stator SLG fault protection scheme for powerformers based on multi-dimensional information fusion. They used the discriminant analysis method to synthesize four fault features and discriminated the faulty powerformer by comparing the Manhattan distance

between fault features. Even though these methods extracted fault features artificially, their application conditions were limited.

CNN is a successful algorithm of deep learning that has been widely used in multiple fields, especially in digital image processing, face recognition, audio retrieval, and other fields (Abdalla et al., 2019; Liu et al., 2019; Rajeev et al., 2019; Klompenburg et al., 2020; Roneel et al., 2021). CNN solves the dilemma that other algorithms need to artificially extract features. Also, it finds the optimal weight parameters matrix by error back propagation along with local connections and weight sharing based on correlation between data (Zhang et al., 2019), which can automatically extract abstract and valuable features from the data to complete specific tasks (Hao et al., 2022; Huang et al., 2021). Applying CNN to powerformer protection has the potential to achieve good results.

Considering that "the simpler the information, the more reliable the relay protection result", the simplest case of the data collected by powerformer's protection method is a one-dimensional time series vector, and there is a strong correlation between the data. CNN can only process multi-dimensional data (Liu et al., 2020) and cannot process one-dimensional time series data collected by powerformer. In order to accurately identify, which Powerformer has stator SLG fault in parallel operation, and use CNN with powerful automatic feature extraction capability to process one-dimensional time series vectors, this article proposes a data dimension transformation method based on HSGC and then uses CNN to implement powerformer stator SLG fault protection. Section 2 introduces the main modules and the framework of the proposed protection scheme. Section 3 explains the physical model of powerformer, sample set acquisition, fundamental theories of HSGC, and the protection principle. Section 4 shows the results of the ATP-EMTP and Python simulation and compares between the proposed protection scheme and other protection schemes.

2 General protection scheme

Basically, the protection scheme proposed in this article is divided into the following three modules: the fault detector module, the signal processor module, and the fault classifier module. A general protection scheme is shown in Figure 1.

2.1 Fault detector module

The zero-sequence voltage can be measured by the voltage transformer connected to the terminal of Powerformer. The effects of zero-sequence fundamental and third-harmonic voltages are eliminated by setting the reliable pickup of the overvoltage relay, which is the sum of zero-sequence fundamental voltage and zero-sequence harmonic voltage
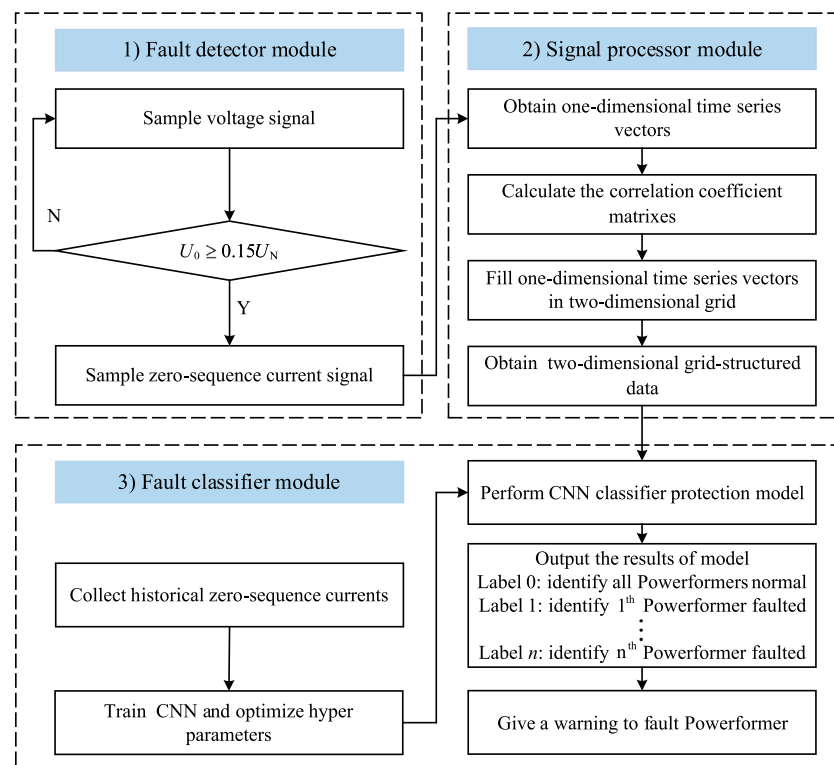
FIGURE 1
General protection scheme.

(15% phase voltage). When the zero-sequence voltage is detected to be greater than or equal to the pickup, the protection is activated, and then the zero-sequence currents can be measured by the current transformer connected to the terminal of Powerformer; conversely, it returns.

2.2 Signal processor module

First, if the fault detector protection is activated, the one-dimensional time series vectors, which consist of zero-sequence currents, are input to the signal processor module. Second, one-dimensional time series vectors are converted into two-dimensional grid-structured data by HSGC. Concretely, in order to reflect the correlation information of the one-dimensional time series vectors, the correlation coefficient matrixes of the one-dimensional time series vectors are calculated using PCCs. According to the correlation coefficient matrixes and the spatial neighborhood correlation of grid cells, the one-dimensional time series vectors are converted into two-dimensional grid-structured data. Finally, the two-dimensional grid-structured data was used as input to the fault classifier module.

2.3 Fault classifier module

In the fault classifier module, the historical zero-sequence currents of each powerformer are collected under normal or fault conditions when n powerformers are running in parallel. The collected zero-sequence currents are divided into $n+1$ classifications. The zero-sequence currents are classified into one class when all powerformers are in a normal state, and the zero-sequence currents are classified into class n when the stator SLG fault occurs on the nth powerformer. After converting these zero-sequence currents into two-dimensional grid-structured data separately, they are fed into the CNN classifier protection model to train it and optimize hyper-parameters. After training, the CNN classifier protection model can be used to identify the classification of two-dimensional grid-structured data and then accurately identify the faulty powerformer. If the stator SLG fault occurs on one of the powerformers running in parallel, this module starts and gives an alarm according to the output of the CNN classifier, so that maintenance personnel can take actions to reduce the loss caused by the fault. If the powerformers are all running normally, the results can be recorded and used as a reference for subsequent research.

FIGURE 2
Equivalent phase-to-ground capacitance of each phase winding of powerformer.

FIGURE 3
Schematic diagram of data dimension conversion algorithm.
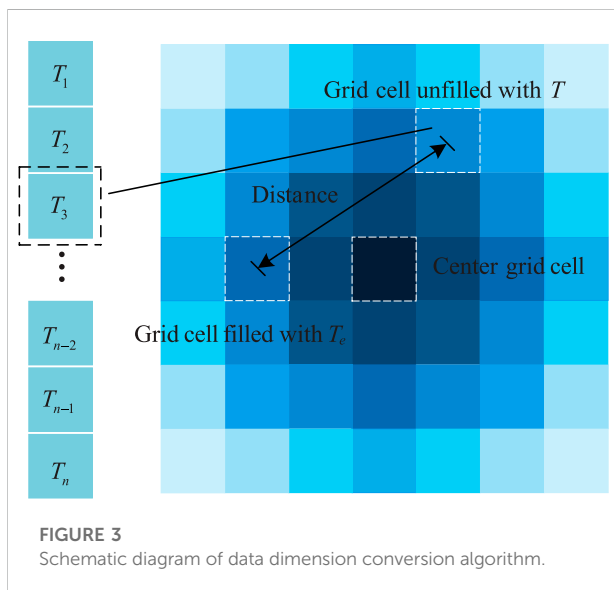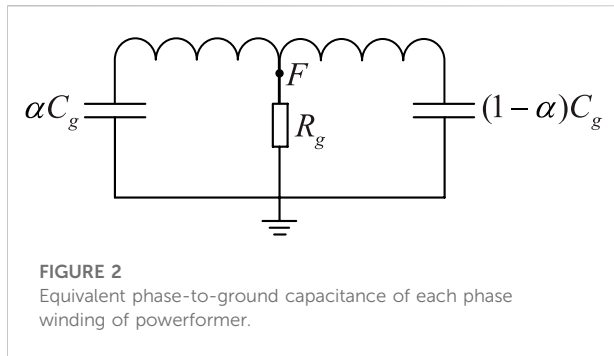
3 Protection principle

3.1 Powerformer equivalent model and sample set acquisition

Establish an equivalent model for Powerformer. Since the Powerformer winding uses graded insulation (there are no linear relations between the ground capacitance of stator winding and turns) (Lin et al., 2018), the Powerformer cannot simply apply the equivalent model of conventional generators. When the stator SLG fault occurs on the Powerformer, this article equates the total ground capacitance C_g of one phase of the stator winding into two parts: one portion αC_g of the total ground capacitance from the neutral point to the fault location of the winding, while the rest $(1-\alpha)C_g$ of the total ground capacitance from the fault location to the powerformer terminal winding (Wang et al., 2020b; Tian et al., 2007). Then, the terminal voltage and the established equivalent capacitance are used to calculate the zero-sequence capacitance current when the powerformer is

at fault. The equivalent phase-to-ground capacitance of each phase winding of the powerformer is shown in Figure 2.

After the stator SLG fault occurs on the Powerformer, the zero-sequence current of powerformers operating in parallel is measured. Also, the samples of zero-sequence currents measured from each Powerformer compose a one-dimensional time series vector.

The original data matrix T consists of one-dimensional time series vectors, which can be defined as follows:

$$T = \begin{bmatrix} t_{11} \ t_{12} \cdots t_{1n} \\ t_{21} \ t_{22} \cdots t_{2n} \\ \vdots \ \ \vdots \ \ \vdots \ \ \vdots \\ t_{m1} \ t_{m2} \cdots t_{mn} \end{bmatrix}, \qquad (1)$$

where n represents the number of powerformers operating in parallel, and m represents the number of zero-sequence current samples from each powerformer. Define each row of the original data matrix T as a one-dimensional vector T_i with n quantities.

3.2 Hub-and-spoke grid data converting algorithm

In order to take advantage of CNN, it is necessary to convert one-dimensional time series vectors into two-dimensional grid-structured data that can be directly processed by CNN. This section introduces the HSGC proposed in this article, which can increase the dimensionality of one-dimensional time series vectors.

The relative positions and distances between two-dimensional grid cells can be used to describe the spatial neighborhood relations between grid cells, that is, the correlation between two-dimensional grid cells. The correlation is strongest for neighborhood grid cells and weakest for grid cells at diagonal vertices. Correspondingly, one-dimensional time series vectors also have strong correlations. Therefore, the correlation between two-dimensional grid cells can be used to reflect the correlation between one-dimensional vectors.

Based on the above mentioned correlation, in order to increase the dimension of one-dimensional time series vectors, this article first determines a one-dimensional vector to fill the center cell of the two-dimensional grid and then radially fills the remaining one-dimensional vectors into the unfilled two-dimensional grid cells one by one. Specifically, in order to fill the one-dimensional vector with the strongest correlation into the geometrical center cell of the two-dimensional grid, the two-dimensional grid should be a square with $b \times b$ cells (b is odd, $b > 1$, and $b \times b = m$) because the square has one and only one center grid cell, which meets the requirements of this article. The number of zero-sequence current samples should be consistent with the number of cells of the two-dimensional grid so that each one-dimensional vector T_i can be mapped to the cell of the two-dimensional grid one by one, and the spatial

FIGURE 4
CNN classifier flow chart.

FIGURE 5
Simulation model of a parallel system with three powerformers.
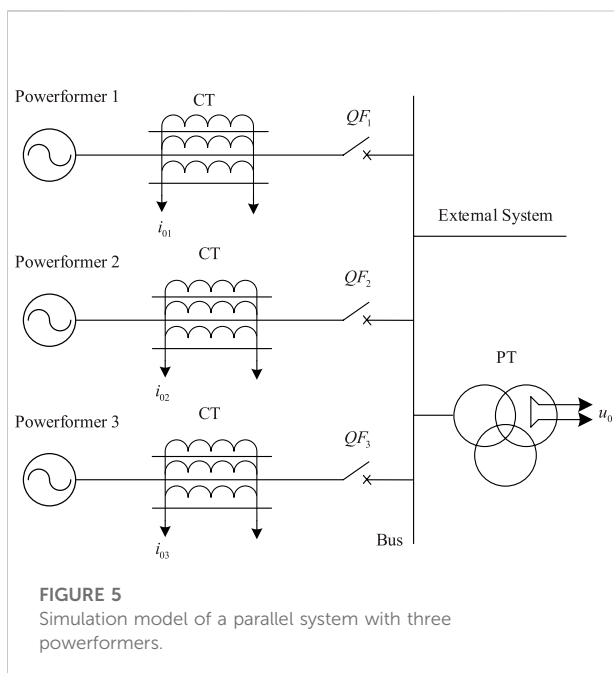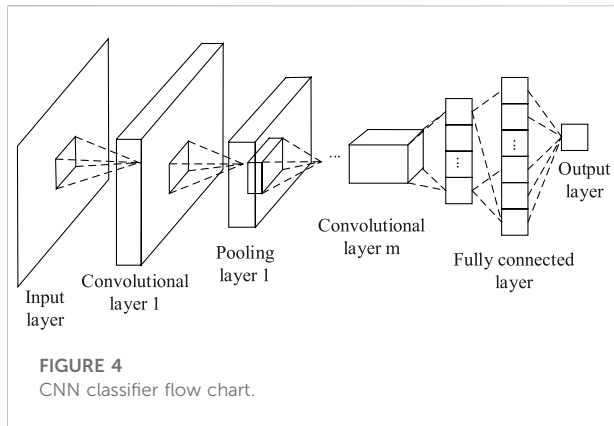
neighborhood relations of the grid cells can well reflect the implicit correlation information of the one-dimensional vectors.

3.2.1 Center grid cell selection strategy

The grid cell at the geometrical center of the square two-dimensional grid has the strongest overall correlation. Since the one-dimensional vector T_i is mapped to the grid cell one by one, the one-dimensional vector with the strongest overall correlation is selected and then filled into the center grid cell. The PCCs of the one-dimensional vectors are applied to describe the correlation between them. The equation is as follows:

$$Corr\left(T_i, T_j\right) = \frac{Cov\left(T_i, T_j\right)}{\sigma_i \sigma_j}, \qquad (2)$$

where $Corr\ (T_i, T_j)$ represents the variances of the one-dimensional vectors T_i and T_j, σ_i and σ_j represent the

standard deviation of the one-dimensional vectors T_i and T_j, respectively. The PCCs between m one-dimensional vectors are calculated by (2) to build an $m \times m$ correlation coefficient matrix. The sum of each row of the matrix is defined to represent the overall correlation of the corresponding one-dimensional vector. The greater the sum of PCCs of a one-dimensional vector, the stronger its overall correlation.

3.2.2 Rest cells' selection strategy

The rest of the grid cells are filled radially outward from the center grid cell. The filling order is based on the correlation of one-dimensional data, that is, the spatial neighborhood relation of the two-dimensional grid. Based on the relative distance between the unfilled grid cell and all filled grid cells, we select the one-dimensional vector with the largest score and fill it into the corresponding grid cell each time. The specific score rule is shown in Eq. 3.

3.2.3 Score rule

When filling the one-dimensional vectors into the rest of the grid cells, the average of the PCCs weighted by the relative distance is defined as the score rule for the rest cells' selection strategy.

The set of one-dimensional vectors filled into the grid is **Q**, the set of the rest of one-dimensional vectors unfilled into the grid is **P**, and the unfilled grid cell is defined as A; let A_e be the grid cell filled with the one-dimensional vector T_e. For any one-dimensional vectors $T \in \textbf{\textit{P}}$, $|\textbf{\textit{Q}}| = n$, the scoring equation is as follows:

$$score\left(T\right) = \frac{1}{n}\sum_{e=1}^{n}\frac{Corr\left(T, T_e\right)}{Dist\left(A, A_e\right)}, \qquad (3)$$

where $Dist\ (A, A_e)$ is the length of the connection of the geometrical center between grid cells A and A_e (the relative linear distance between them).

The $score(T)$ of the rest of the one-dimensional vectors is calculated by Eq. 3, and the one-dimensional vector with the largest $score(T)$ is selected to fill the grid cell A.

Figure 3 shows the schematic diagram of the HSGC, in which the depth of the grid cell filling color represents the priority of the filling order. The darker color of the grid cell is filled first.

3.3 Powerformer protection principle

The basic idea of identifying faulty Powerformer with the help of CNN is to perform hierarchical processing on image data, which is two-dimensional grid-structured data in this article, to extract features autonomously, to fuse features at the high level of the network, and to complete the classification task of stator SLG fault in Powerformer. Specifically, in order to identify the faulty Powerformer, the two-dimensional data converted from one-dimensional vectors are used as the input of CNN, and then the

FIGURE 6
Zero-sequence voltage and zero-sequence current of powerformers when the SLG fault occurs at 0.055 s.
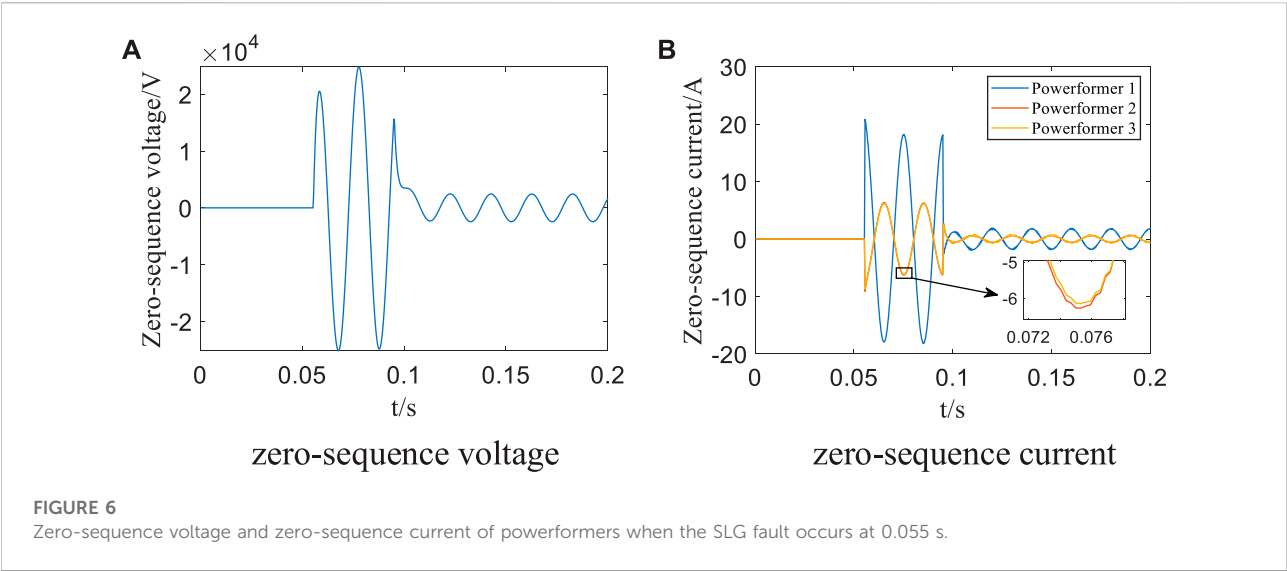
TABLE 1 Zero-sequence currents of powerformer 1 under different fault conditions.

Neutral grounding method	R_g	α	Zero-sequence current samples of powerformer 1
High-resistance grounding	5	0%	[-0.60788917; 0.30851999; -0.27880605; 0.10633977; -0.12194124; 0.02240053; -0.04838275; -0.00232426; -0.01602729]
	100	25%	[55.93843142; 35.60664558; 23.96540705; 18.69411469; 13.92200724; 11.99219259; 8.835983276; 7.47810173; 4.878698071]
	500	50%	[27.02622859; 25.18531545; 22.91681035; 21.36199188; 19.14410273; 17.6465613; 15.43405787; 13.83491516; 11.644967]
	……	……	……
	7,750	75%	[2.749214808; 2.802613576; 2.765174866; 2.755957286; 2.648429235; 2.581607183; 2.420020103; 2.295909882; 2.094366391]
	8,000	100%	[3.552270253; 3.621972402; 3.574234009; 3.562864939; 3.424406687; 3.338462194; 3.130012194; 2.969912052; 2.709702412]
Reactance grounding	5	0%	[-0.59140396; 0.33029556; -0.27327219; 0.10557429; -0.13298098; 0.00188382; -0.07752037; -0.04104487; -0.06283362]
	100	25%	[55.63127136; 34.33812141; 21.76983643; 16.41232427; 12.39474996; 11.85453606; 10.50195313; 11.17452272; 10.70542415]
	500	50%	[27.03229459; 25.12030411; 22.68122482; 20.95497386; 18.6288414; 17.1318175; 15.05434736; 13.73387051; 11.96792761]
	……	……	……
	7,750	75%	[3.16090711; 3.228677114; 3.187924703; 3.17470932; 3.043077469; 2.952977498; 2.749420484; 2.584888776; 2.328799963]
	8,000	100%	[3.559144338; 3.639770508; 3.597915649; 3.586538951; 3.44129626; 3.342091242; 3.114433606; 2.929886659; 2.641470591]

CNN autonomously extracts key information and features from it through multiple convolutions and pooling operations (Ren et al., 2020). These key information and features are fed into a fully connected layer. Also, the overall information can be obtained after fusing key information and features at the fully connected layer. The output layer outputs the classification labels of powerformers based on the overall information. Finally, the faulty powerformer is determined corresponding to the classification label, and the classification task of CNN is completed.

Define $Y \in R^{(b \times b \times n)}$ and $Y_0 \in Y, Y_1 \in Y, \ldots \ldots, Y_n \in Y$, where Y is the sample set of two-dimensional grid-structured

FIGURE 7
Variation of zero-sequence currents with time under different fault conditions.
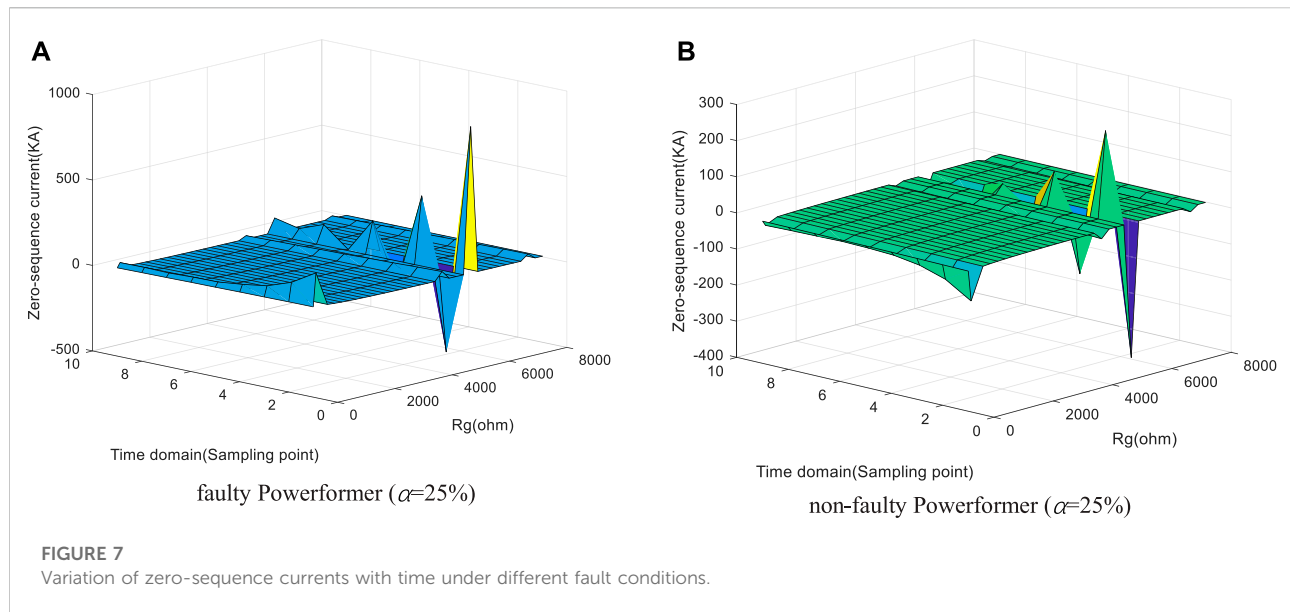
TABLE 2 Correlation coefficient matrix of samples.

	T_1	T_2	T_3		T_8	T_9
T_1	1	0.99999	0.99999	…….	0.99995	0.99992
T_2	0.99999	1	0.99999	…	0.99996	0.99993
T_3	0.99999	0.99999	1	…	0.99997	0.99994
T_4	0.99999	0.99999	0.99999	…	0.99997	0.99995
T_5	0.99999	0.99999	0.99999	…	0.99998	0.99996
T_6	0.99998	0.99998	0.99999	…	0.99999	0.99998
T_7	0.99997	0.9997	0.99999	…	0.99998	0.99998
T_8	0.99995	0.99996	0.99997	…	1	0.99999
T_9	0.99992	0.99993	0.99994	…	0.99999	1

data, Y_0 is the sample set when all powerformers are in a normal situation, Y_1 is the sample set when powerformer 1 occurs at the stator SLG fault, and Y_n is the sample set when Powerformer n occurs at the stator SLG fault. The key information and features of the sample y are extracted by convolution operation of convolution kernel k and sample y. The convolution operation equation is as follows:

$$Cov(x,k) = \sum_{t=1}^{p} x(t)k(t), \tag{4}$$

where x is the receptive field of sample y (Zhang et al., 2022), and the size of both the convolution kernel k and the receptive field x is p.

The pooling layer applies subsampling to extract key information and features and ensure the invariance of them (Chang and Shen, 2021). After multiple convolutions and pooling operations, the key information and features are used as input to the fully connected layer to obtain overall information, which is used to obtain the probability distribution [g0, g1,.....,, gn-1, gn] that the sample belongs to each class (g0 is the probability of all powerformers being in a normal state, and gn is the probability of nth powerformer being in a fault state). The protection criterion is as follows:

$$\begin{cases} g_0 = \max\{g_0, g_1, ..., g_n\}, \ y \in Y_0 \\ g_1 = \max\{g_0, g_1, ..., g_n\}, \ y \in Y_1 \\ \qquad\qquad\qquad \vdots \\ g_n = \max\{g_0, g_1, ..., g_n\}, \ y \in Y_n, \end{cases} \tag{5}$$

If $g_0 = \max\{g_0, g_1, ..., g_n\}$, all powerformers are in normal situation, and the output label is 0; if $g_1 = \max\{g_0, g_1, ..., g_n\}$, it means the stator SLG fault occurs on the Powerformer 1, and the output label is 1; …….; if $g_n = \max\{g_0, g_1, ..., g_n\}$, it means the stator SLG fault occurs on the Powerformer n, and the output label is n. The CNN classifier flow chart is shown in Figure 4.

4 Simulation verification and analysis

4.1 Simulation model

To test the reliability of the powerformer protection method, a simulation model of the stator SLG fault of powerformer was established by ATP-EMTP. A parallel system with three powerformers is taken as an example (fault started at 0.055 s). The model is shown in Figure 5. Specifically, the related parameters of the model are as follows:

FIGURE 8
Validation accuracy and cost of the CNN classifier protection model.

4.2 Simulation analysis

This section presents the experimental results which are performed on the parallel system with three powerformers. To increase the diversity of samples and to evaluate the efficiency of fault detection, the fault conditions, including the transition resistance, fault location, and neutral grounding method of the powerformers, were tested. The obtained data are then fed into a Python code which executes the protection scheme proposed by this article according to the block diagram in Figure 1.

Table 1 shows the one-dimensional time series vectors under different fault conditions (only partial data of Powerformer 1 is listed). In this simulation, a two-dimensional grid has nine cells ($b = 3$ and $m = b{\times}b = 9$). So, the one-dimensional time series vectors are composed of the first nine current sampling samples after the stator SLG fault occurs. A total of 3,813 one-dimensional time series vectors, which are the zero-sequence current samples, are obtained as the sample set. Specifically, 960 one-dimensional time series vectors are obtained from cases where all powerformers are in a normal situation, and 2,853 one-dimensional time series vectors are obtained from cases where a stator SLG fault occurs on one of the powerformers running in parallel under different fault conditions.

Figure 7 shows the variation of zero-sequence currents with time under different fault conditions. It has been found from the figure that the amplitude of zero-sequence currents of the powerformer changes smoothly under most fault conditions, while it changes drastically only in few cases. Also, the zero-sequence currents of faulty and non-faulty powerformers have similar trends over time in most cases. CNN is used to avoid the dilemma of artificial feature extraction and automatically extract features from zero-sequence currents.

Table 2 shows some data from the correlation coefficient matrix of one sample. Since the zero-sequence currents of the parallel system with three powerformers are sampled nine times at equal time intervals, nine one-dimensional vectors with three components (each representing a powerformer) can be obtained. The PCCs between each of the nine one-dimensional vectors are calculated to obtain 1,271 correlation coefficient matrixes of the sample set. According to the correlation coefficient matrixes of the sample set and the selection strategy of HSGC, the one-dimensional vectors of the sample set are converted to obtain 1,271 × 3 × 3 two-dimensional grids. Each cell in the two-dimensional grid is mapped to the one-dimensional vector one to one, and the spatial adjacent relationship between the grid cells can reflect the correlation information between the one-dimensional vectors well. At the same time, two-dimensional grid-structured data can be used as input to the CNN classifier protection model.

Figure 8 shows the validation accuracy and cost of the CNN model; 90% of the two-dimensional grid-structured data is used as the training set, and the remaining 10% is used as the test set.

the rated voltage U_N of powerformers 1–3 is 150 kV; the rated frequency f_N is 50Hz; the winding ground capacitances C_{g1}, C_{g2}, and C_{g3} per phase is 0.555, 0.5574, and 0.555 μF, respectively; the ground capacitance C_t per phase of the external system is 0.15 μF; the inception angle is 0º; the inductance L_n is 1,838 mH, the equivalent resistance R_n is 57 Ω; the neutral grounding resistance R_l is 1,900 Ω; the set of fault resistance R_g is 5, 100, 500, 750, 1,000 Ω, ..., 7,500, 7750, 8,000 Ω; the stator SLG fault occurs when 0, 25, 50, 75, and 100% (α) of the stator winding are grounded.

Figure 6 shows the zero-sequence voltage and zero-sequence current of powerformers when the SLG fault occurs at 0.055 s. When the Powerformer operating in parallel occurs at a stator SLG fault, zero-sequence voltage and zero-sequence current components will be measured by the fault detector module. If $U_0 \geq 0.15U_N$, the protection is activated.

TABLE 3 Simulation results under different fault conditions.

Sample number	Probability distribution	Label	Result of classification
13	[1, 0, 0, 0]	0	True
72	[0, 1, 0, 0]	1	True
117	[0, 0, 0, 1]	3	True
183	[1, 0, 0, 0]	0	True
277	[0, 0, 1, 0]	2	True
324	[0, 0, 0, 1]	3	True
372	[0, 0, 1, 0]	2	True
429	[0, 1, 0, 0]	1	True

TABLE 4 Comparison results between the proposed schemes.

Fault condition	Protection scheme	Measurement data		Result
Reactance grounding powerformer 2 (50%–10%)	Fuzzy clustering algorithm	Distance from fault cluster left d_{1g} = 2.576	Distance from non-fault cluster left d_{2g} = 2.9471	$d_{1g} < d_{2g}$ (true)
	Multi-dimensional fusion	None		Unable to identify
	Scheme of this article	Probability distribution [0, 0, 1, 0]		Label = 2 (true)
High-resistance grounding powerformer 1 (5–50%)	Fuzzy clustering algorithm	Distance from fault cluster left d_{1g} = 4.0314	Distance from non-fault cluster left d_{2g} = 3.8326	$d_{1g} > d_{2g}$ (fault)
	Multi-dimensional fusion	Faulty Manhattan distance D_{1f} = 0.442	Sound Manhattan distance D_{1s} = 4.624	$D_{1f} < D_{1s}$ (true)
	Scheme of this article	Probability distribution [0, 1, 0, 0]		Label = 1 (true)

By inputting the training set into the CNN classifier protection model, it can be found that the model has high validation accuracy, low cost, and stable results.

Table 3 shows the results of feeding the test set into the trained CNN classifier protection model (due to the one-hot algorithm, the probability is only zero and one). Label 0 represents all powerformers that are in a normal situation; Label 1 represents the 1st Powerformer that occurs at the stator SLG fault; Label 2 represents the 2nd Powerformer that occurs at the stator SLG fault; Label 3 represents the 3rd Powerformer that occurs at the stator SLG fault. The simulation results show that the faulty powerformer can be accurately identified by the protection scheme based on the HSGC and CNN proposed in this article.

4.3 Comparative analysis of algorithms

A comparison between the proposed protection scheme and the other existing protection schemes of multi-dimensional

fusion (Fang et al., 2020) and a protection scheme based on a fuzzy clustering algorithm (Wang et al., 2016) is conducted. The comparison results are shown in Table 4. The protection scheme of multi-dimensional fusion is not applicable when the neutral point is grounded by an arc suppression coil due to the compensation effect of the arc suppression coil on capacitance current; the fuzzy clustering algorithm experiences misclassification under the fault condition of powerformer 1 (5–50%) due to the influence of the initial clustering center selection caused by artificial feature extraction.

In contrast, the protection proposed in this article converts the one-dimensional time series vectors into two-dimensional grid-structured data, which can be processed directly by CNN. The protection scheme avoids the artificial selection of features. Meanwhile, since local connectivity and weight sharing of CNN are based on the correlation between input data, the protection scheme uses the spatial adjacent correlation between two-dimensional grid cells to retain the correlation information between one-dimensional vectors. CNN is used to automatically extract the features of one-dimensional time

series vectors to discriminate whether the powerformer occurs at the stator SLG fault.

The simulation results show that the protection scheme proposed in this article is not affected by the system operation mode, and it can accurately identify the faulty Powerformer when the abovementioned two comparison methods cannot correctly identify the fault. The protection scheme based on HSGC and CNN can better realize the protection of parallel operation of powerformers with high accuracy, low cost, and stable results.

5 Conclusion

Some state-of-the-art fusion discriminations are used to identify which powerformer occurs at a stator SLG fault when they are operating in parallel, but these methods extract fault features artificially, and the application conditions are limited. A novel protection scheme based on HSGC and CNN has been developed in order to overcome these problems. Its specific advantages are as follows:

1) The protection model has superior automatic feature extraction capability and takes correlation information between one-dimensional data into account. The protection scheme has high validation accuracy, low cost, and stable results, which improves the reliability of stator SLG fault protection for powerformer.
2) Using the deep learning capabilities, strong generalization ability, and robustness of CNN, abstract and valuable features are automatically extracted from the zero-sequence current data to accurately identify which powerformer occurs at the stator SLG fault.
3) The protection model has a strong adaptive ability. There is no need to set the threshold, which can realize protection without a threshold. Also, the scheme is not easily affected by fault resistance, fault location, and neutral grounding mode. The protection scheme can be used to identify the faulty powerformer under different fault conditions.

Data availability statement

The raw data supporting the conclusion of this article will be made available by the authors, without undue reservation.

Author contributions

XL carried out the simulation and drafted the manuscript. YW designed the project and revised the manuscript. XL participated in the design of the study and performed the statistical analysis. YW and WL participated in its design and coordination. CC, BW, and JW revised the manuscript. All authors have read and approved the final manuscript.

Funding

Conflict of interest

Authors BW and JW were employed by Xiangtan Electric Co., Ltd.

The remaining authors declare that the research was conducted in the absence of any commercial or financial relationships that could be construed as a potential conflict of interest.

Publisher's note

All claims expressed in this article are solely those of the authors and do not necessarily represent those of their affiliated organizations, or those of the publisher, the editors, and the reviewers. Any product that may be evaluated in this article, or claim that may be made by its manufacturer, is not guaranteed or endorsed by the publisher.

References

Abdalla, Y., Tariq Iqbal, M., and Shehata, M. (2019). Convolutional neural network for copy-move forgery detection[J]. *Symmetry* 11 (10). doi:10.3390/sym11101280

Chang, M., and Shen, Y. X. (2021). Fault diagnosis strategy of a wind power bearing based on an improved convolutional neural network[J]. *Power Syst. Prot. Control* 49 (06), 131–137. doi:10.19783/j.cnki.pspc.200585

Fang, T., Zhou, Y., and Liao, W. P. (2020). A new discrimination of stator single-phase grounding fault based on multi-dimensional fusion for Powerformer[J]. *J. Phys. Conf. Ser.* 1633 (1), 1–7. doi:10.1088/1742-6596/1633/1/012113

Hao, H., Zhenhua, Z. H., Ziyi, Z. Y., Xu, X. X. Y., and Xu, Y. C. (2022). Insulator fouling monitoring based on acoustic signal and one-dimensional convolutional neural network. *Front. Energy Res.* 10, 906107. doi:10.3389/FENRG.2022.906107

Huang, S. F., and Jia, W. C. (2017). A new fault location method for stator single-phase ground fault in large turbine generator[J]. *Power Syst. Prot. Control* 45 (9), 35–40. doi:10.7667/PSPC161504

Huang, X. H., Li, Y. Y., and Chai, Y. (2021). Intelligent fault diagnosis method of wind turbines planetary gearboxes based on a multi-scale dense fusion network[J]. *Front. Energy Res.* 9, 747622. doi:10.3389/FENRG.2021.747622

Klompenburg, T. V., Kassahun, A., and Catal, C. (2020). Crop yield prediction using machine learning: A systematic literature review[J]. *Comput. Electron. Agric.*, 177. doi:10.1016/j.compag.2020.105709

Leijon, M. (1998). Powerformer TM-aradically new rotating machine[J]. *ABB Rev.* 2 (2), 21–26.

Lin, C., Wang, Y. Y., and Zeng, X. J. (2018). Stator single phase ground Fault protection of powerformers based on grading insulation[J]. *Proc. CSEE* 38 (23), 7052–7060+7139. doi:10.13334/j.0258-8013.pcsee.180189

Liu, C. Y., Wang, Q., and Bi, X. J. (2020). Research on rain removal method for single image based on multi-channel and multi-scale CNN[J]. *J. Electronics&Information Technol.* 42 (09), 2285–2292. doi:10.11999/JEIT190755

Liu, J. H., Chen, K. X., and Ma, J. (2019). Classification of three-phase voltage dips based on CNN and random forest[J]. *Power Syst. Prot. Control* 47 (20), 112–118. doi:10.19783/j.cnki.pspc.181337

Rajeev, R., Vishal M, P., HyperFace, C. R., and [J] (2019). A deep multi-task learning framework for face detection, landmark localization, pose estimation, and gender recognition. *IEEE Trans. pattern analysis Mach. Intell.* 41 (1). doi:10.1109/TPAMI.2017.2781233

Ren, H. Y., Hou Z, J., Bharat, V., Wang, H., and Pavel, E. (2020). Power system event classification and localization using a convolutional neural network[J]. *Front. Energy Res.* 8, 607826. doi:10.3389/FENRG.2020.607826

Roneel, S. V., Hao, X., and Shlomo, B. (2021). Benchmarking audio signal representation techniques for classification with convolutional neural networks [J]. *Sensors* 21 (10). doi:10.3390/s21103434

Shi, J. F., Ge, B. J., and Lv, Y. L. (2021). Analysis of excitation loss fault of cable winding asynchronous high-voltage generator[J]. *Electr. Mach. Control* 25 (03), 46–55+66. doi:10.15938/j.emc.2021.03.006

Tian, Q., Lin, X. N., and Liu, L. (2007). A novel self-adaptive compensated differential protection design suitable for the generator with considerable winding distributed capacitance. *IEEE Trans. Power Deliv.* 22 (2), 836–842. doi:10.1109/tpwrd.2007.893590

Tzelepis, D., Psaras, V., Tsotsopoulou, E., Mirsaeidi, S., Dysko, A., Hong, Q., et al. (2020). Voltage and current measuring technologies for high voltage direct current supergrids: A Technology review identifying the options for protection, fault location and automation applications. *IEEE Access* 8, 203398–203428. doi:10.1109/access.2020.3035905

Wang, Y. Y., Guo, Y. S., Zeng, X. J., Chen, J., Kong, Y., and Sun, S. (2020). Stator single-line-to-ground Fault protection for bus-connected powerformers based on

S-transform and bagging ensemble learning. *IEEE Access* 8, 88322–88332. doi:10.1109/access.2020.2993692

Wang, Y. Y., Huang, X. C., and Zeng, X. J. (2020). Studies on stator single-line-to-ground faults protection for a Powerformer considering the winding electromotive force distribution[J]. *Int. J. Electr. Power Energy Syst.* 119©, 321–328. doi:10.1016/j.ijepes.2020.105940

Wang, Y. Y., Zeng, X. J., Dong, J. B. Z. Y., Li, Z. W., and Huang, Y. (2013). Studies on the stator single-phase-to-ground Fault protection for a high-voltage cable-wound generator. *IEEE Trans. Energy Convers.* 28 (2), 344–352. doi:10.1109/tec.2013.2240303

Wang, Y. Y., Zeng, X. J., and Huang, Z. Y. (2013). Novel protection scheme of stator single-phase-to-ground fault for powerformers. *Int. J. Electr. Power & Energy Syst.* 53 (1), 321–328. doi:10.1016/j.ijepes.2013.05.010

Wang, Y. Y., Zeng, X. J., Xu, Z. Y. Y., Yuan, J., and Huang, Y. (2013). Stator single-phase-to-ground Fault protection for bus-connected powerformers based on hierarchical clustering algorithm. *IEEE Trans. Energy Convers.* 28 (4), 991–998. doi:10.1109/tec.2013.2281491

Wang, Y. Y., Zhou, J. M., Wei, G., Dong, Z., and Chen, H. (2016). Stator winding single-phase grounding faults protective scheme based on discriminant analysis for Powerformers with selectivity. *Int. J. Electr. Power & Energy Syst.* 77 (1), 145–150. doi:10.1016/j.ijepes.2015.11.037

Xue, L., Sun, G. H., and Wang, X. H. (2022). Novel location method for stator single-phase grounding fault of large non-salient pole generator[J]. *Electr. Power Autom. Equip.* 42 (1), 221–224. doi:10.16081/j.epae.202109023

Zhang, D. H., Zhang, X. W., Sun, H., and He, J. H. (2022). Fault diagnosis for AC/DC transmission system based on convolutional neural network[J]. *Automation Electr. Power Syst.* 46 (05), 132–145. doi:10.7500/AEPS20210201006

Zhang, Q., Wang, J. P., and Li, W. T. (2019). Insulator state detection of CNN based on feedback mechanism[J]. *Trans. China Electrotech. Soc.* 34 (16), 3311–3321. doi:10.19595/j.cnki.1000-6753.tces.180962

Zhou, H. Y., Yao, W., Ai, X. M., and Li, D. H. (2022). Comprehensive review of commutation failure in HVDC transmission systems[J]. *Electr. Power Syst. Res.*, 205. doi:10.1016/j.epsr.2021.107768

Nomenclature

Variables C_g total ground capacitance of one phase of the stator winding

α location of the stator winding grounded

T_i ith one-dimensional vectors of the original data matrix T

n number of powerformers operating in parallel

m number of zero-sequence current samples

σ_i standard deviation of the one-dimensional vector T_i

A_e grid cell filled in the one-dimensional vector T_e

p size of the convolution kernel and receptive field

g_0 probability of all powerformers being in a normal state

g_n probability of nth powerformer being in a fault state

u result of the output of CNN

R_g ground fault resistance.

Sets

Q set of one-dimensional vectors filled into the grid

P set of one-dimensional vectors unfilled into the grid

Y set of the two-dimensional grid-structured data samples.

A neural network-based adaptive power-sharing strategy for hybrid frame inverters in a microgrid

Wenyang Deng, Yongjun Zhang, Yuan Tang*, Qinhao Li and Yingqi Yi

School of Electric Power, South China University of Technology, Guangzhou, China

The capacitive-coupling inverter (CCI) is more cost-effective in reactive power conditioning and enhanced reactive power regulation ability when compared with the inductive-coupling inverter (ICI). As power conditioning capability is vital for a microgrid (MG) system, a new MG frame with hybrid parallel-connected ICIs and CCIs was proposed in this paper. With lower DC-link voltage for the CCI, an adaptive power sharing method was proposed for reducing total rated power and losses. A power-sharing control layer based on a back-propagation neural network that guarantees rapid and accurate sharing ratio computation was investigated as well. The results of simulations and experiments were used to verify the effectiveness of the proposed method.

KEYWORDS

microgrid, capacitive-coupling inverter, unequal power sharing, power capacity, BPNN

1 Introduction

Distributed generation (DG), which offers distinct advantages, including lower transmission losses, greater power control flexibility, high energy efficiency and lower pollution dissipation, is playing an important role in the development of next-generation power grids (Deng et al., 2021; Liu et al., 2019a). A microgrid (MG) is a self-sufficient energy system based on DG that serves a discrete geographic footprint, such as a college campus, business center or neighborhood. Ensuring a stable point-of-common-coupling (PCC) voltage in a MG is vital, and requires that the DG unit have a wide reactive power control capability to cope with load fluctuations through its inverter interface (Ahmed et al., 2021; Murty and Kumar, 2022).

With large active power transfer capacity, the inductive-coupling inverter (ICI) is used in most DG applications (Zhang et al., 2019). However, the reactive power compensation capability of the ICI relies on a DC-link voltage that is higher than the PCC voltage, resulting in high conversion losses and increased operational breakdown risks (Deng et al., 2020). The reactive power compensation capacity of ICI is also limited by the output capacity of the DG system (Ziyi et al., 2023); therefore, additional reactive compensation

FIGURE 1
Architecture of the proposed parallel-connected ICI-CCI structure.
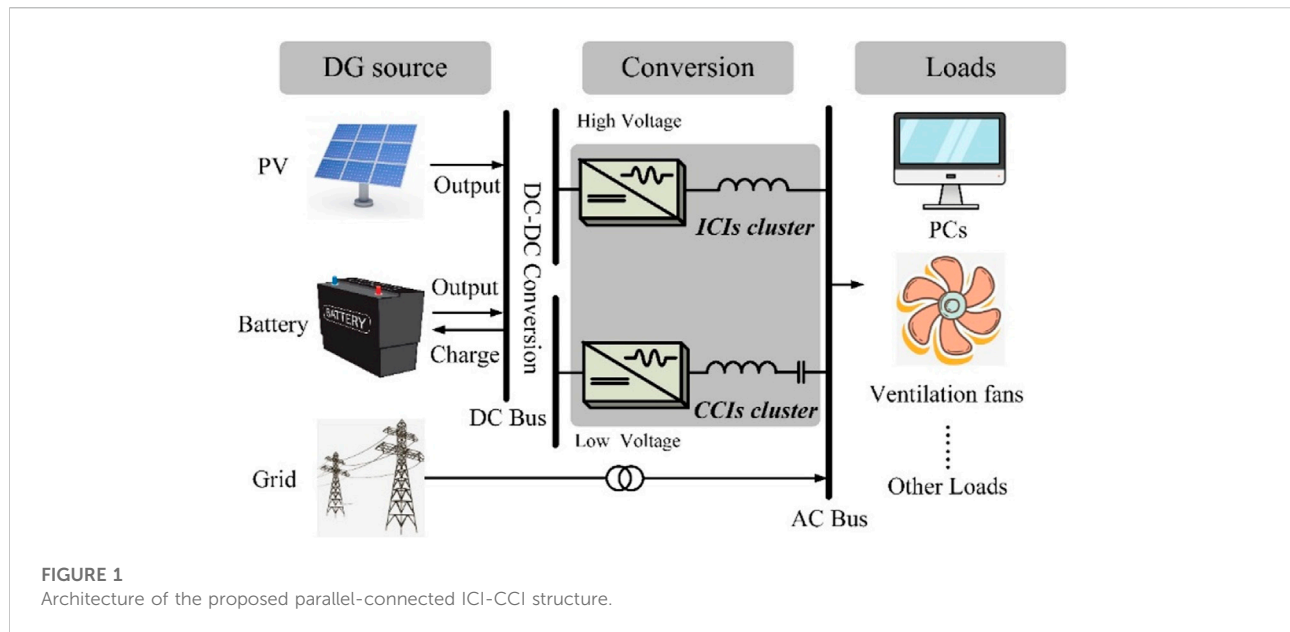
TABLE 1 Comparison of different inverters.

	P output	Q compensation	DC requirement
CCI	The coupling impedance is large, and the active output range is narrow at the same DC voltage.	At the same DC voltage, the reactive power compensation range for inductive loads is wide.	When the DC voltage is lower than the double bus voltage, the active output and reactive power compensation for inductive loads can be realized.
ICI	The coupling impedance is small, and the active output range is wider at the same DC voltage.	At the same DC voltage, the reactive power compensation range for inductive loads is narrow.	When the DC voltage is lower than the double bus voltage, reactive power compensation for inductive loads cannot be realized.

devices, such as the static VAR compensator (SVC), are necessary for an ICI-based MG system, leading to increased investment cost.

In order to have enhanced reactive power compensation capability with reduced conversion loss and cost, as well as increased control flexibility and operational stability, a capacitive-coupling inverter (CCI) has been proposed by researchers (Pang et al., 2022). It was first presented in the form of a reactive power compensator and then, was studied as a standalone generation unit (Fujita and Akagi, 1991; Deng et al., 2019; Gong et al., 2021). Because the capacitor was series-connected, the CCI had a better reactive power control capability with a lower DC-link voltage than the ICI (Sou et al., 2022). To fully utilize the power regulation capabilities of both ICI and CCI, and keep the conversion loss and equipment cost low, a new hybrid consisting of parallel-connected ICIs and CCIs was proposed in this paper (Figure 1). A comparison of CCI and ICI is presented in Table 1.

For the proposed MG system, coordinative operation of the inverters is required to regulate the DG output according to changes in load demand (Yazdani et al., 2020). Power-sharing control plays a pivotal role in the inverter's coordinative operation, and this was investigated by (Mousazadeh Mousavi et al., 2018; Qi et al., 2020). Droop control is simple and widely used since it can regulate inverters locally and achieve power sharing automatically. However, the controller characteristics were easily affected by mismatched feeder impedance, unbalanced loads, and other factors (Mousazadeh Mousavi et al., 2018; Liu et al., 2019b; Razi et al., 2020). For this reason, modified droop control strategies were proposed. To compensate for differences in feeder impedance, a virtual-impedance was devised (Mousazadeh Mousavi et al., 2018)-(Razi et al., 2020). Using specifically designed parameters, the virtual-impedance could also tune the resistive and capacitive feeder impedances and maintain satisfactory power-sharing (Liu et al., 2019b)- (He et al., 2019). Furthermore, by revising the control algorithm, droop control could be enhanced to compensate for inaccurate power-sharing (Lao et al., 2019).

The modified controllers are only for the ICI, and are inappropriate for the proposed MG system. This is first because of the differences in DC-link voltage, which means that the power transfer range was not the same for the CCI and ICI, and the

FIGURE 2
Equivalent circuit of hybrid connected inverters in a microgrid system.
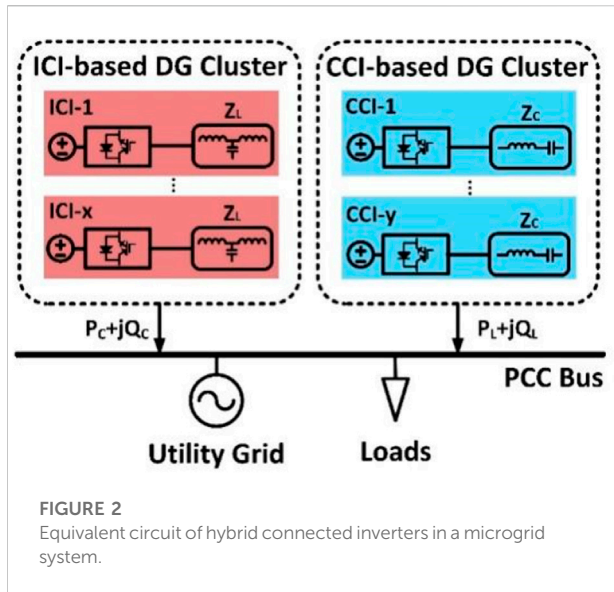
targeted power may surpass the control range of the CCI or the ICI with conventional equal power-sharing control. Secondly, the equal power-sharing ratio was not optimized for inverter total power reduction. For these reasons, a neural network (NN)-based adaptive power sharing scheme was proposed in order to calculate the optimal power-sharing ratio and maintain minimum power capacity. The main contributions of this work include:

- Proposal of a new hybrid system of parallel-connected ICIs and CCIs for better power control flexibility of a microgrid.
- Investigation of the effect of power-sharing ratio on the inverters' power capacity reduction and its arithmetic computation methods.
- Proposal of a power-sharing controller based on an artificial neural network (NN), to achieve fast, accurate, adaptive power-sharing.
- The principles underlying the NN model applied to the proposed method were studied and evaluated.

This paper is organized as follows. Section 2 introduces the power delivery characteristics of ICIs and CCIs. In Section 3, power flow equations are provided and we investigate how different power sharing ratios affect the proposed MG system's performance. Section 4 presents the power-ratio restraints and computations based on minimum system cost. A power sharing controller based on an artificial neural network model is also presented in this section. The results of simulations and experiments are given in Section 5 to verify the effectiveness of the proposed control method. The conclusions and implications for adoption are presented in Section 6.

2 Hybrid connected inverters in the MG

2.1 Modelling of the hybrid connected inverters

The equivalent circuit of the hybrid connected inverters is shown in Figure 2. ICI-based and CCI-based DG units are coupled to the power grid with different DC sources. The general power flow from the DG unit to the power grid can be expressed as:

$$
\begin{cases}
P = \dfrac{VV_{pcc}}{Z}\cos(\theta - \delta) - \dfrac{V_{pcc}^2}{Z}\cos\theta \\[3mm]
Q = \dfrac{VV_{pcc}}{Z}\sin(\theta - \delta) - \dfrac{V_{pcc}^2}{Z}\sin\theta
\end{cases}
\tag{1}
$$

where V_{pcc} and V are the magnitudes of the voltage of the power grid and inverter, and δ is the phase difference between the voltage of the inverter and the power grid. Z and θ are the magnitude and phase angle of the coupled impedance. With different coupling structures for ICI and CCI, Z and θ are also different as shown in Eqs 2, 3:

$$
\begin{cases}
Z_L = \omega L \\
\theta_L = 90°
\end{cases}
\tag{2}
$$

$$
\begin{cases}
|Z_C| = \dfrac{1}{\omega C_C} = \dfrac{1}{\omega C} - \omega L_C \\[2mm]
\theta_C = -90°
\end{cases}
\tag{3}
$$

To generalize the power flow, a power base is defined as:

$$
\begin{cases}
S_{base-L} = \dfrac{V_{pcc}^2}{Z_L} \\[3mm]
S_{base-C} = \dfrac{V_{pcc}^2}{|Z_C|}
\end{cases}
\tag{4}
$$

By standardizing all ICIs as one ICI unit and all CCIs as one CCI unit, the power output of the inverters in Figure 2 can be expressed as:

$$
\begin{bmatrix} P_L \\ Q_L \\ P_C \\ Q_C \end{bmatrix}
=
\begin{bmatrix}
\dfrac{\sin\delta}{V_{pcc}}S_{base-L} & 0 \\[2mm]
\dfrac{\cos\delta}{V_{pcc}}S_{base-L} & 0 \\[2mm]
0 & \dfrac{\sin\delta}{V_{pcc}}S_{base-C} \\[2mm]
0 & -\dfrac{\cos\delta}{V_{pcc}}S_{base-C}
\end{bmatrix}
\begin{bmatrix} V_L \\ V_C \end{bmatrix}
+
\begin{bmatrix} 0 \\ -S_{base-L} \\ 0 \\ S_{base-C} \end{bmatrix}
\tag{5}
$$
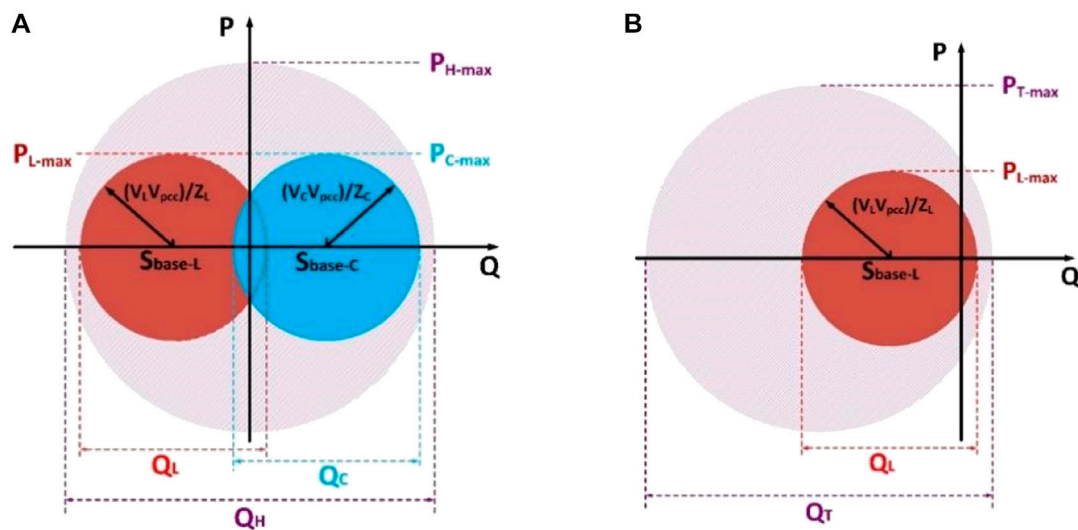
FIGURE 3
Possible power range boundaries with different structures (when the equivalent coupling impedance and the DC voltage of CCI and ICI are the same). **(A)** Hybrid-connected ICI and CCI. **(B)** Parallel-connected ICIs.

2.2 Power control range

Usually, there are three factors that affect the power control range of the inverter: the property of the coupling impedance (inductive or capacitive), the output voltage, and the equivalent value of the coupling impedance. The following discussion focuses on these three aspects in describing the advantages of the proposed MG system. Since the output voltage is proportional to the DC-link voltage, these two voltages are not distinguished in the following discussion.

The main difference between ICI and CCI is the property of the coupling impedance, which leads to different power delivery characteristics. Assuming the direction of active power injection and reactive power compensation is positive, the power base and the DC-link voltage of the ICI and CCI are the same, and the last term is $> \sqrt{2}V_{pcc}$. Thus, the power range boundary of the ICI and CCI can be illustrated as a circle, in which the points are at the power base and the radii of ICI and CCI are $V_L V_{pcc}/Z_L$ and $V_C V_{pcc}/Z_C$, where V_L and V_C are the output voltage of the ICI and CCI, respectively. Figure 3A depicts the positions of the power range circles of the ICI and CCI, and the total power range of the hybrid connected CCI and ICI. The total power ranges of the traditional parallel-connected ICIs are shown in Figure 3B.

In Figure 3, $P_{L-\max}$ and $P_{C-\max}$ are the maximum active power transfer boundaries of ICI and CCI, respectively; Q_L and

Q_C indicate the reactive power compensation range of these two inverters, respectively; $P_{H-\max}$ and $P_{H-\max}$ are the maximum active power transfer boundaries of the proposed hybrid connected system, respectively; and Q_H is the power compensation range of a parallel-connected ICI system.

According to Figure 3, it can be found, that with the proposed system, the active power transfer range of the two MG systems is the same, and the reactive power compensation range of the proposed system is much larger than the traditional one.

The output voltage of the inverter will also affect the power transfer. Figure 4 shows the power range with the variation of the output voltage of ICI and CCI.

The CCI achieved a wide range of reactive power compensation with lower output voltage, and the DC-link voltage requirement of CCI could be effectively reduced, which increased the adaptiveness and flexibility of the MG system in reactive power compensation (Figure 4).

The equivalent value concept of the coupling impedance can be replaced by the power base. Practically, the power base of the CCI is usually set equal to the nominal load demand of the MG. In this paper, the CCI's power base is set as a reference like the following:

$$S_{base} = S_{base-C}$$

The ratio of the ICI power base to the reference power base was set as:

FIGURE 4
Variation in output voltage with power delivery of ICI and CCI.
(A) ICI. **(B)** CCI.

TABLE 3 Power reference coefficients in the case studies.

Case	Power reference coefficients
1	$\begin{cases} r_p = 1.8 \\ r_q = 0.35 \end{cases}$
2	$\begin{cases} r_p = 1.4 \\ r_q = 1 \end{cases}$
3	$\begin{cases} r_p = 0.7 \\ r_q = 0.35 \end{cases}$
4	$\begin{cases} r_p = 0.7 \\ r_q = 1.6 \end{cases}$
5	$\begin{cases} r_p = 0.3 \\ r_q = 1 \end{cases}$

3 Power-sharing for the proposed MG system

3.1 Power sharing ratio

The power-sharing ratio was defined for the proposed MG system. The power reference of the hybrid-connected ICI and CCI can be described as:

$$P_L = m^\star P_{out} \tag{7}$$
$$Q_L = n^\star Q_{out}$$
$$P_C = (1 - m)^\star P_{out}$$
$$Q_C = (1 - n)^\star Q_{out}$$

where P_{out} and Q_{out} represent the total power injected into the PCC, P_L and Q_L are the power references of the ICI, and P_C and Q_C are the power references of the CCI.

To normalize the power demands, power reference coefficients are defined as:

$$\begin{bmatrix} P_{out} \\ Q_{out} \end{bmatrix} = \lambda S_{base} \begin{bmatrix} r_p \\ r_q \end{bmatrix} \tag{8}$$

The power capacity of ICI and CCI can be deduced as:

$$\begin{cases} S_L = V_L i_L \\ S_C = V_C i_C \end{cases} \tag{9}$$

where i_L and i_C are the output currents from ICI and CCI, respectively. They are expressed as:

TABLE 2 Power boundary of the hybrid MG system.

Inverter	Boundary
ICI	$0 \leq P_L \leq \lambda V_L / V_{pcc} S_{base}$
	$\lambda(V_L/V_{pcc} - 1)S_{base} \leq Q_L \leq \lambda(V_L/V_{pcc} + 1)S_{base}$
CCI	$0 \leq P_C \leq V_C / V_{pcc} S_{base}$
	$(1 - V_C/V_{pcc})S_{base} \leq Q_C \leq (V_C/V_{pcc} + 1)S_{base}$

$$\lambda = \frac{S_{base-L}}{S_{base}} \tag{6}$$

If the battery charging in a MG is not considered, the power range boundaries of the proposed MG system can be deduced (Table 2).

To sum up, we believe that the proposed hybrid of ICIs and CCIs connected to a MG system is able to achieve a wider reactive power compensation range. Since the CCI is able to work under a lower DC-link voltage, an optimal power sharing method could reduce the total power capacity compared with a traditional microgrid using ICIs only.

$$\begin{cases} i_L = \dfrac{\sqrt{P_L^2 + Q_L^2}}{V_{pcc}} = \dfrac{\sqrt{(mP_{out})^2 + (nQ_{out})^2}}{V_{pcc}} \\[4ex] i_C = \dfrac{\sqrt{P_C^2 + Q_C^2}}{V_{pcc}} = \dfrac{\sqrt{[(1-m)P_{out}]^2 + [(1-n)Q_{out}]^2}}{V_{pcc}} \end{cases} \tag{10}$$

FIGURE 5
Locations of power references in the case study.
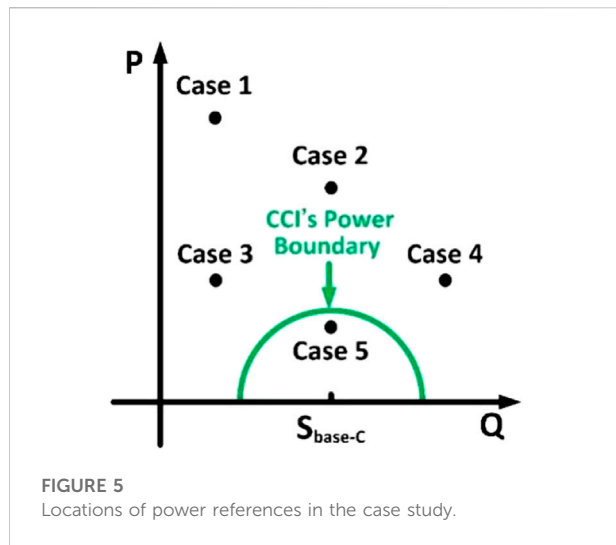
According to Eq. 9 and Eq. 10, the power capacity of an inverter changes with the power ratio for a given set of active and reactive power references. A detailed discussion will be provided hereinafter.

3.2 Effect of power sharing ratio on power capacity

To better evaluate the effect of power sharing ratio on power capacity, a case study is essential.

Assuming that the power base of the ICI was 1/8 times that of the CCI and the ratio of DC-link voltage to PCC voltage for the ICI was 1.5 and for the CCI, 0.7, six cases with random power reference coefficients are listed in Table 3.

The positions of the case studies in terms of the power delivery range of the CCI are shown in Figure 5. As shown in the figure, the active power reference in case 1 was much larger than the reactive power reference. In cases 2, 3, and 4, there was little difference between the active and reactive power references, which were uniformly distributed outside the CCI's power output range. The power references in case 5 both fell within CCI's power range. To keep the proposed system always working within the minimum power capacity, after receiving the power demand signals, the current from the CCI should be as large as possible because of the lower DC-link voltage, and to keep minimum power capacity the current from the CCI must obey the relationship:

$$\frac{i_C}{i_L} \leq \frac{V_L}{V_C}$$

By substituting the power reference coefficients into (Eq. 11), we noted that the current from the ICI varied according to the different power-sharing ratios (Figure 6). Thus, the power sharing ratios significantly affected the output current.

According to Figure 6, the lowest point is always located at (0, 0) in the x-y plane, which means the ICI should never output any current on mathematical calculation. However, due to the limitation of voltage and the power base, a single CCI may not always satisfy the power demands. Therefore, to find the

FIGURE 6
Total power capacity varies with different power ratios.

FIGURE 7
Graph of current vectors in different cases.

correct power sharing ratio to meet the power demands and reduce the ICI current to the lowest possible, a power sharing ratio calculation method is proposed in the next part.

4 Adaptive power sharing method

From the above discussion, we concluded that the power sharing ratio critically affected the total power capacity. Thus, determining the optimal power sharing ratio for the lowest power capacity in the proposed MG is important. In this section, we investigated the power sharing ratio calculation for the unequal power sharing method.

4.1 Power sharing ratio restraints

Power capacity is seriously restricted by the inverter's output voltage and PCC voltage. Eq. 11 described the relationship between voltage and power, as well as power references as:

$$\begin{cases} \sqrt{\left(1 + \dfrac{Q_L}{\lambda S_{base}}\right)^2 + \left(\dfrac{P_L}{\lambda S_{base}}\right)^2} \leq \dfrac{V_{DC-L}}{\sqrt{2}\, V_{pcc}} \\[4mm] \sqrt{\left(1 - \dfrac{Q_C}{S_{base}}\right)^2 + \left(\dfrac{P_C}{S_{base}}\right)^2} \leq \dfrac{V_{DC-C}}{\sqrt{2}\, V_{pcc}} \end{cases} \quad (11)$$

The power sharing ratio boundary is also obtained as:

$$\begin{cases} \sqrt{\left(1 + n r_q\right)^2 + \left(m r_p\right)^2} \leq \dfrac{V_{DC-L}}{\sqrt{2}\, V_{pcc}} \\[4mm] \sqrt{\left[1 - (1-n)r_q\right]^2 + \left[(1-m)r_p\right]^2} \leq \dfrac{V_{DC-C}}{\sqrt{2}\, V_{pcc}} \end{cases} \quad (12)$$

4.2 Power sharing ratio calculation

In the hybrid MG system, the output current of the ICI should be as small as possible because of its higher DC-link voltage. This calculation is expressed as:

$$S_L + S_C < S_{equal} \quad (13)$$

Since only the CCI is active in case 5, power sharing is not available. The current vector graphs for power-sharing are illustrated in Figure 7 for cases 1–4.

In the figure, i_{L-e} is the output current from the ICI under equal power sharing, and it can be obtained as:

$$i_{L-e} = \frac{\sqrt{r_p^2 + r_q^2}}{2V_L} S_{base} \tag{14}$$

For this case study, the number of ICIs under equal power sharing was assumed to be 2.

In Figure 7, i_{p-ref}, i_{q-ref} are the active and reactive power vectors in the reference current, respectively. They can be obtained as:

$$\begin{cases} i_{p-ref} = \dfrac{r_p}{V_{pcc}} S_{base} \\ i_{q-ref} = \dfrac{r_q}{V_{pcc}} S_{base} \end{cases} \tag{15}$$

where i_{qC} is the reactive power vector current when the CCI compensates for the reactive power equal with the power base as:

$$i_{qC} = \frac{S_{base}}{V_{pcc}} \tag{16}$$

The radius of the circle of the CCI's power range can be described as:

$$r_c = \left| \frac{V_C}{V_{pcc}^2} * S_{base} \right| \tag{17}$$

The initial point and the location of the power reference are marked as α_1 and α_3, respectively. Their positions on the coordinate are:

$$\begin{cases} \overrightarrow{\alpha_1} = 0 + j0 \\ \overrightarrow{\alpha_3} = i_{q-ref} + j i_{p-ref} \end{cases} \tag{18}$$

and i_C and i_L can be calculated as:

$$\begin{cases} i_L = \overrightarrow{\alpha_3} - \overrightarrow{\alpha_2} \\ i_C = \overrightarrow{\alpha_2} - \overrightarrow{\alpha_1} \end{cases} \tag{19}$$

Assuming the acute angle between r_c and the horizon axis is β, the point α_2 gives the maximum current from the CCI with a given power reference. It has three positions:

1. When $r_q > 1$, the current is:

$$\vec{\alpha}_2 = \left(r_c \sqrt{\frac{1}{1 + tan^2 \beta}} + i_{qC} \right) + j \left(r_c \sqrt{1 - \frac{1}{1 + tan^2 \beta}} \right) \tag{20}$$

The power-sharing ratio is:

$$\begin{cases} m = \dfrac{\left(i_{p-ref} - r_c \sqrt{1 - \dfrac{1}{1 + tan^2 \beta}} \right) V_L}{r_p S_{base}} \\ n = \dfrac{\left[i_{q-ref} - \left(r_c \sqrt{\dfrac{1}{1 + tan^2 \beta}} + i_{qC} \right) \right] V_L}{r_q S_{base}} \end{cases} \tag{21}$$

and:

$$tan \beta = \frac{i_{p-ref}}{i_{q-ref} - i_{qC}} \tag{22}$$

2. When $r_q < 1$, the current is:

$$\vec{\alpha}_2 = \left(i_{qC} - r_c \sqrt{\frac{1}{1 + tan^2 \beta}} \right) + j \left(r_c \sqrt{1 - \frac{1}{1 + tan^2 \beta}} \right) \tag{23}$$

The power-sharing ratio is:

$$\begin{cases} m = \dfrac{\left(i_{p-ref} - r_c \sqrt{1 - \dfrac{1}{1 + tan^2 \beta}} \right) V_L}{r_p S_{base}} \\ n = \dfrac{\left[i_{q-ref} - \left(i_{qC} - r_c \sqrt{\dfrac{1}{1 + tan^2 \beta}} \right) \right] V_L}{r_q S_{base}} \end{cases} \tag{24}$$

and:

$$tan \beta = \frac{i_{qC} - i_{q-ref}}{i_{p-ref}} \tag{25}$$

3, When $r_q = 1$, $\beta = 90°$, and r_p is larger than the maximum active power transfer of CCI, the current is:

$$i_{qC} = i_{q-ref} \tag{26}$$

the expression for α_2 is:

$$\vec{\alpha}_2 = i_{qC} + j i_{p-ref} \tag{27}$$

and the power-sharing ratio is:

$$\begin{cases} m = \dfrac{\left(i_{p-ref} - 8 \dfrac{V_L}{V_{pcc}^2} S_{base} \right) V_L}{r_p S_{base}} \\ n = 0 \end{cases} \tag{28}$$

- If the power references satisfy:

$$\sqrt{(1 - r_q)^2 + r_p^2} \leq \frac{V_C}{V_{pcc}} \tag{29}$$

the power-sharing ratio is:

$$\begin{cases} m = 0 \\ n = 0 \end{cases} \tag{30}$$

TABLE 4 Summary and comparison of power capacities of different systems.

Case	Total power capacity (S/S$_{base-C}$)			
	ICIs equal sharing	ICI and CCI		
		Adaptive sharing	m	n
1	2.7546	1.9812	1	−0.16
2	3.4181	1.5463	0.69	0
3	2.9984	0.7913	0.87	−0.18
4	3.1026	1.0675	0.51	−0.94
5	1.3254	1.0189	0	0

4.3 Effectiveness of the adaptive power sharing method

According to Eqs 14–30, the power sharing ratios can be obtained for cases 1–4. The power sharing ratio in case 5 is determined as (0, 0). Thus, the corresponding power ratios under the proposed method and the conventional method were calculated and are summarized in Table 4. As the comparison shows, the proposed power sharing method for the hybrid MG system can effectively reduce the power capacity.

5 Realization of the NN-based power sharing controller

In the last section, a complete power sharing calculation process is provided. It can be seen that the calculation process is complicated and includes some complex forms of computation, such as trigonometric functions and square roots. It could be difficult for the controller chip to compute when the load demands vary rapidly. To solve this problem, an NN-based power sharing model is proposed in this work.

5.1 Training and evaluation of the NN model

The architecture of an NN model is based on neurons and can be divided into three main parts: the input layer, the hidden layer, and the output layer (Wang et al., 2020). The input layer receives signals from the outside world. The hidden layer is the intermediate layer connecting the input layer and the output layer, and constitutes the core of the NN as being composed of many neurons. The output layer returns the results of the mathematical operations on the input (Liu et al., 2021).
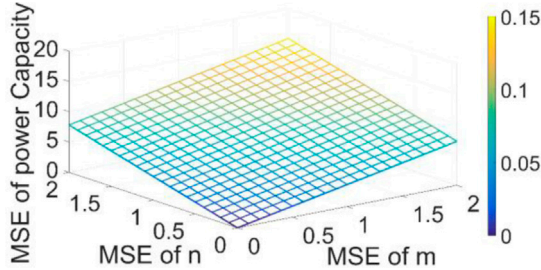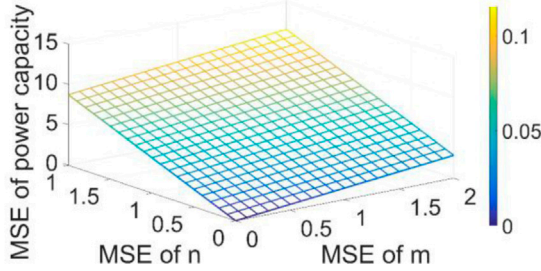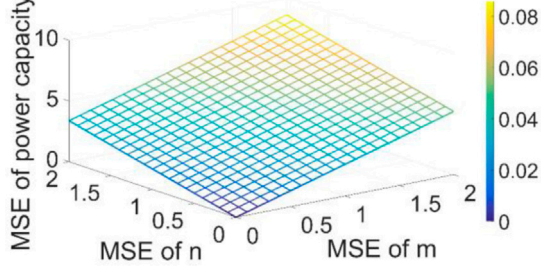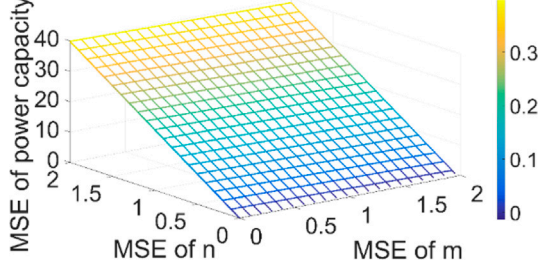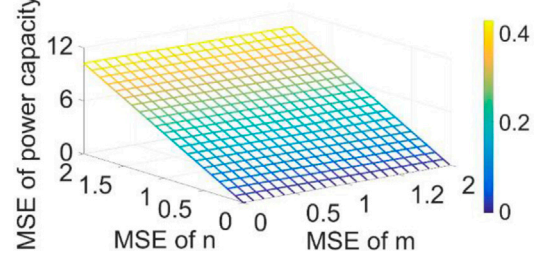
As a representative of a NN the application areas of a back-propagation neural network (BPNN) include function

FIGURE 8
Principal process diagram of the BP neural network algorithm.
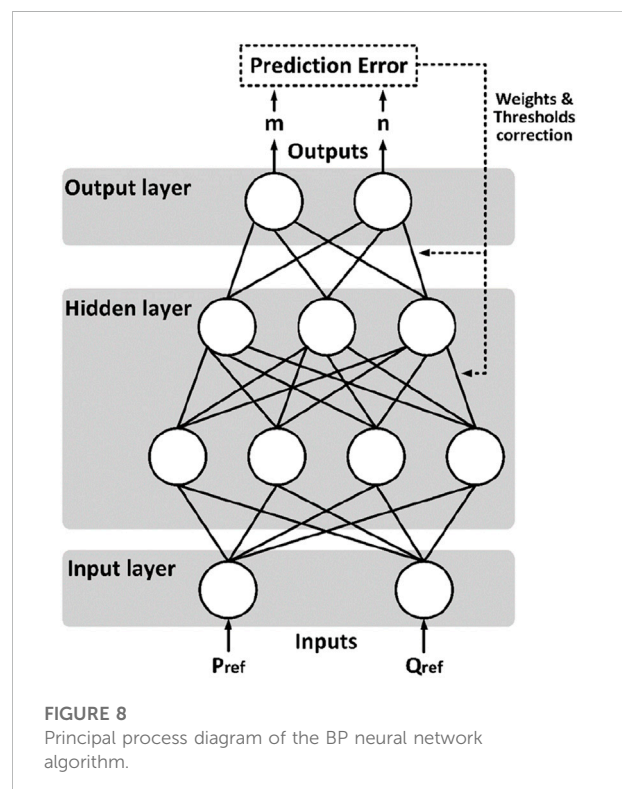
approximation, regression analysis, numerical prediction, and classification and data processing (Chen et al., 2020). The BPNN calculates the final network error based on the forward operation of the input data, transmits the error in the opposite direction, and contains a mechanism for adjusting the weights and thresholds of the corresponding layers according to certain rules when crossing different layers. After a large number of data samples are trained, an algorithmic model that can accomplish complex nonlinear mapping is finally constructed. For such networks, the input layer is responsible for feeding data into the neural network. The hidden layer fits and optimizes the parameters to the

TABLE 5 Partial equation calculation results.

Case	MSE
1	
2	
3	
4	
5	

FIGURE 9
Training results of the proposed BPNN.
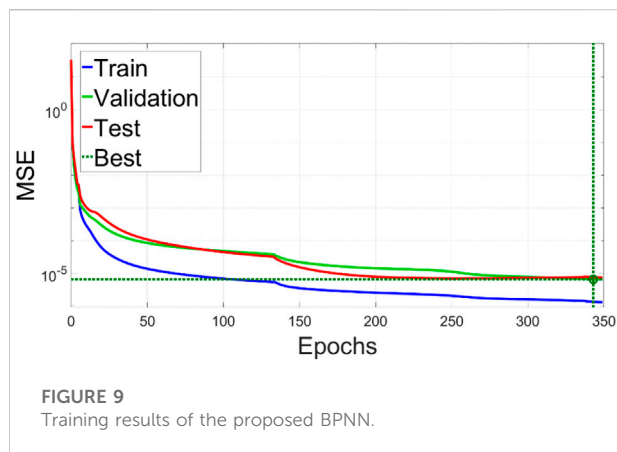
neural network by model training. These include weights and biases as well as the selection of various parameters and activation functions. The output layer is responsible for outputting the computational results from the neural network (Wang et al., 2022). The principal algorithm process of the BPNN model in this paper is illustrated in Figure 8.

The BPNN model can be expressed mathematically as $f\left(\sum_i X_i W_i + b_i\right)$, where f is the activation function, which introduces non-linear factors to a linear model, thus solving problems that are difficult to solve with a linear model. X_i represents the output data, W_i is the weight between the connected input data and the hidden layer, while b_i is the bias vector. During the training process, the accuracy of the NN

model is improved by continuously changing the values of the parameters W_i and b_i.

A loss function was set to examine the difference between the predicted value and the known answer, and also to evaluate the accuracy of the trained NN model. With enough training sessions, the loss function will be stable in the vicinity of a very small value, which can be regarded as the prediction error of the NN model (Huang et al., 2021). In this paper, the sigmoid function was chosen as the activation function and the mean square error (MSE) as the loss function to describe the prediction error.

5.2 Effect of the prediction error

For a BPNN, the number of neurons, hidden layers, as well as training sessions, have a high positive correlation with the final MSE. However, an excessive number of neurons and hidden layers will increase the computational power required of the chip in the power sharing controller. In addition, an increase in the amount of training data will also increase the difficulty of BPNN training (Huang et al., 2021). Therefore, it is essential to choose the proper numbers of neurons and hidden layers, and also the amount of training data. The selection principle is based on experience, as well as the required prediction error of the BPNN.

To evaluate the impact on the total power capacity due to the prediction error, a partial derivative equation is presented. Assuming that the prediction error of the total power capacity is defined as:
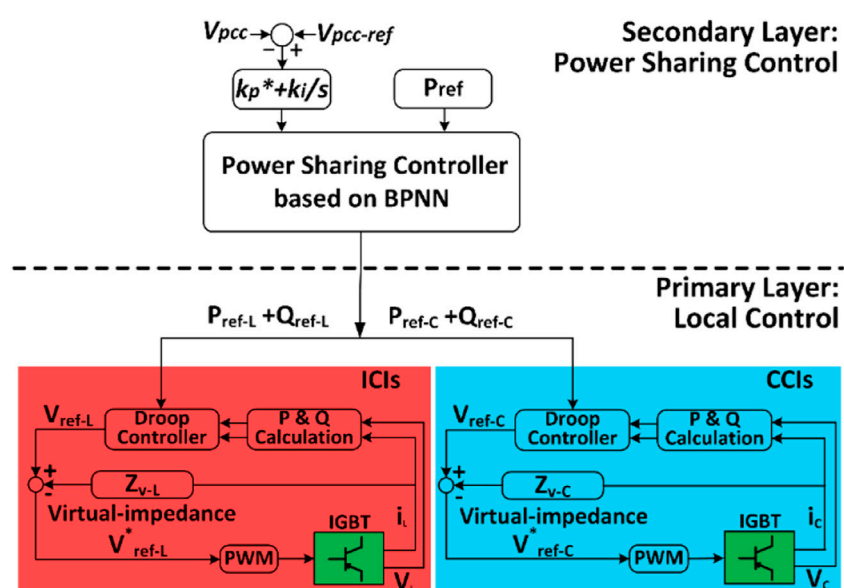
FIGURE 10
Control block diagram of the proposed control method.

TABLE 6 Summary and comparison of power capacities of different systems.

System	
V_{PCC}	$110\,V/50\,Hz$
ICI	
V_{DC-L}	$170\,V$
L_i	$4\,mH$
S_{base-L}	$9680\,Var$
Active power transfer	$1.1S_{base-L}$
Reactive power compensation	$0.1S_{base-L}$
CCI	
V_{DC-C}	$80\,V$
L_c	$2\,mH$
C_c	$340\,\mu F$
S_{base-C}	$1210\,Var$
Active power transfer	$0.5S_{base-C}$
Reactive power compensation range	$(0.5 \sim 1.5)S_{base-C}$

$$\Delta s = \frac{\partial S}{\partial m}\Delta m + \frac{\partial S}{\partial n}\Delta n \tag{31}$$

there are:

$$\frac{\partial S}{\partial m} = \frac{\partial S_L}{\partial m} + \frac{\partial S_C}{\partial m} \tag{32}$$

$$\frac{\partial S_L}{\partial m} = \frac{1}{2}\frac{2mr_p^2}{\sqrt{(1+nr_q)^2 + (mr_p)^2}}\sqrt{(nr_q)^2 + (mr_p)^2}\,S_{base-L}$$
$$+ \sqrt{(1+nr_q)^2 + (mr_p)^2}\,\frac{2mr_p}{\sqrt{(nr_q)^2 + (mr_p)^2}}\frac{1}{2}S_{base-L} \tag{33}$$

$$\frac{\partial S_C}{\partial m} = (m-1)r_p^2 S_{base-C}$$
$$\times \left[\frac{\sqrt{[(1-m)r_p]^2 + [(1-n)r_q]^2}}{\sqrt{[1-(1-n)r_q]^2 + [(1-m)r_p]^2}} + \frac{\sqrt{[1-(1-n)r_q]^2 + [(1-m)r_p]^2}}{\sqrt{[(1-m)r_p]^2 + [(1-n)r_q]^2}}\right] \tag{34}$$

and:

$$\frac{\partial S}{\partial n} = \frac{\partial S_L}{\partial n} + \frac{\partial S_C}{\partial n} \tag{35}$$

$$\frac{\partial S_L}{\partial n} = (1+nr_q)r_q S_{base-C}$$
$$\times \left[\frac{\sqrt{(mr_p)^2 + (nr_q)^2}}{\sqrt{(1+nr_q)^2 + (mr_p)^2}} + \frac{\sqrt{(1+nr_q)^2 + (mr_p)^2}}{\sqrt{(mr_p)^2 + (nr_q)^2}}\right] \tag{36}$$
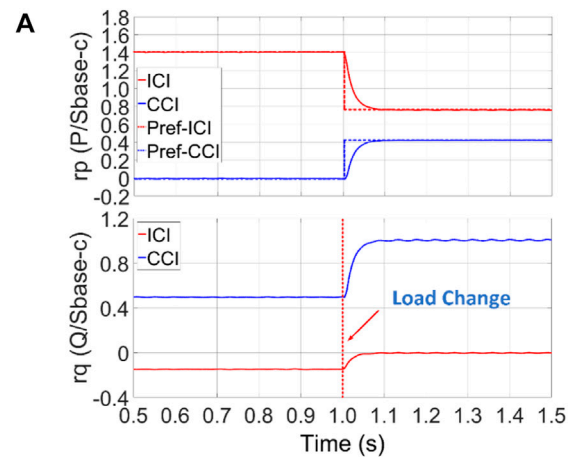
FIGURE 11
Simulation results with the proposed adaptive power sharing in **(A)** cases 1 and 2, **(B)** cases 3 and 4, and **(C)** cases 4 and 5.
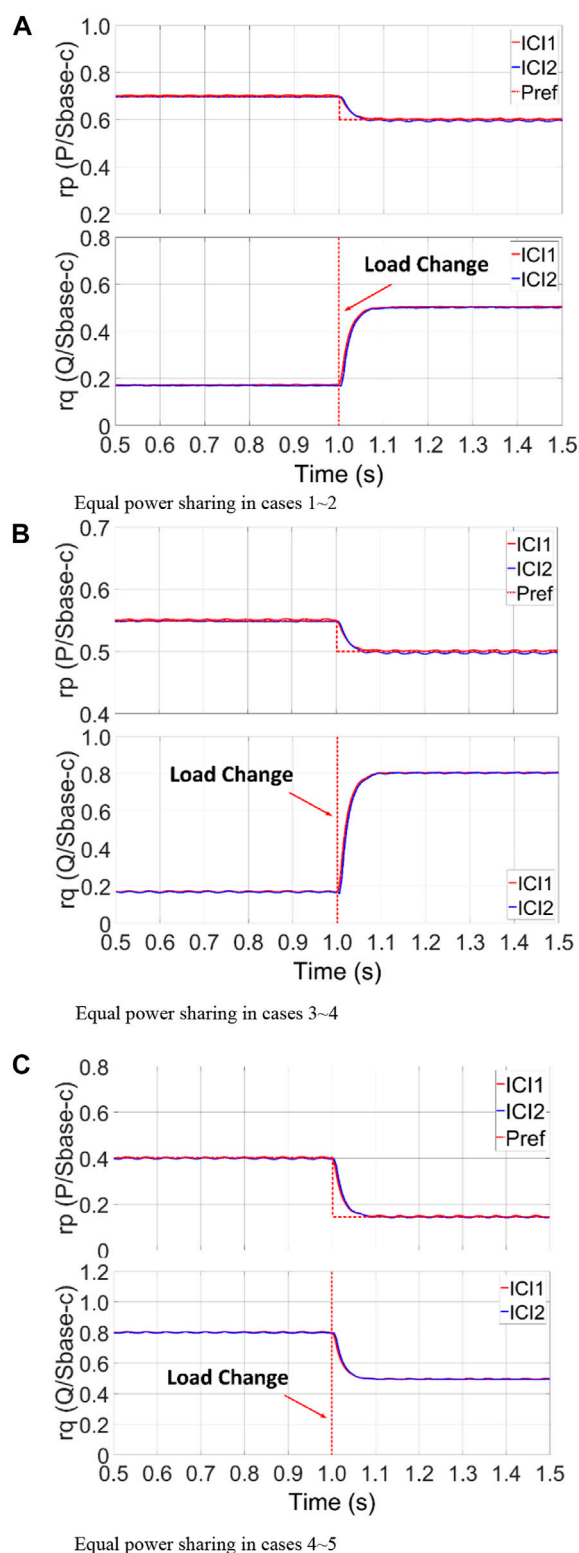
FIGURE 12
Simulation results in the equal power sharing in **(A)** cases 1 and 2, **(B)** cases 3 and 4, and **(C)** cases 4 and 5.
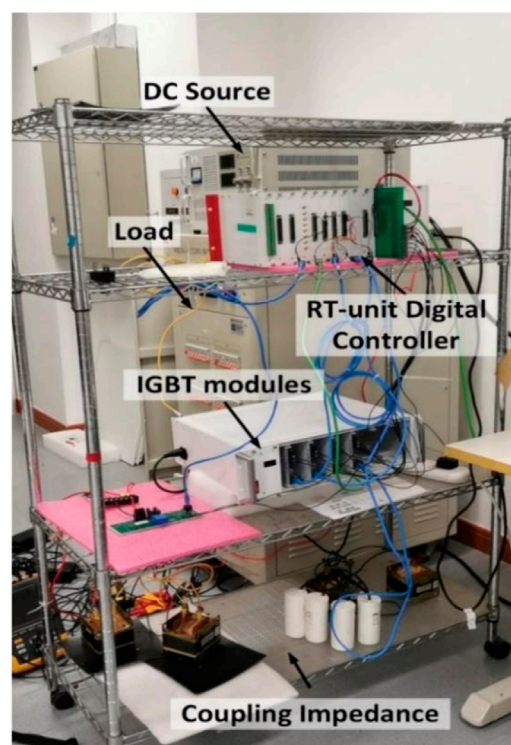
FIGURE 13
Experimental platform.

$$\frac{\partial S_C}{\partial n} = \left[1 - (1-n)r_q\right]r_q S_{base-C}$$

$$\times \left[\frac{\sqrt{\left[(1-m)r_p\right]^2 + \left[(1-n)r_q\right]^2}}{\sqrt{\left[1-(1-n)r_q\right]^2 + \left[(1-m)r_p\right]^2}} + \frac{\sqrt{\left[1-(1-n)r_q\right]^2 + \left[(1-m)r_p\right]^2}}{\sqrt{\left[(1-m)r_p\right]^2 + \left[(1-n)r_q\right]^2}}\right]$$

(37)

The results from inserting the parameters from cases 1 to 5 into (Eq. 26) are summarized in Table 5.

As in Table 4, the degrees of impact of *m* and *n* on the total power capacity are not the same. As the reactive power sharing ratio will more critically affect the prediction error, a larger active power demand will increase the effect of the reactive power sharing ratio error on the power capacity. A smaller reactive power output will reduce the influence of the active power sharing ratio on the power capacity.

Assuming that the total power capacity bias should not exceed 5%, the prediction errors of the active and reactive power sharing ratio must be smaller than 0.5%, which means that the MSE of the BPNN cannot be larger than 0.005 to keep the total power bias within a satisfactory range.

The BPNN model includes two hidden layers, and a total of 15 neurons were proposed. The size of the training set was 380 groups of power references and sharing ratios. Like the

Power transfer of cases 1~2

Power transfer of cases 3~4

Power transfer of cases 4~5

FIGURE 14
Power transfer waveforms under the proposed power sharing. **(A)** Power transfer of cases 1 and 2. **(B)** Power transfer of cases 3 and 4. **(C)** Power transfer of cases 4 and 5.

Power transfer of cases 1~2

Power transfer of cases 3~4

Power transfer of cases 4~5

FIGURE 15
Power transfer waveforms under equal power sharing. **(A)** Power transfer of cases 1 and 2. **(B)** Power transfer of cases 3 and 4. **(C)** Power transfer of cases 4 and 5.

training results shown in Figure 9, after training, the MSE of the BPNN model reached a value on the order of 10^{-5}, which is satisfactory for generating power sharing ratios.

The control block diagram of the proposed power sharing method for the hybrid ICI and CCI system microgrid is presented in Figure 10. As the figure shows, the power demands will be sent to the secondary power sharing layer with a well-trained BPNN model and generate an optimal power sharing ratio, which can reduce the total power capacity requirement of the hybrid MG system to the minimum value. The power sharing ratio then will be used to calculate the actual power references for the local inverters. Virtual-impedance loops are employed in the local control layers to eliminate the tracking errors by droop control.

6 Simulations and experimental verification

The proposed power sharing method aims to keep the hybrid MG system working with the lowest power capacity and to ensure accurate power transfer. Since the power capacity cannot be obtained by the results of the test, therefore, in this section, all tests will follow the case study strictly, and the results will verify the accuracy of power transfer under the proposed power sharing method.

6.1 Simulation results

Simulation tests were conducted in Matlab/Simulink, to verify the effectiveness of the proposed power sharing strategy. Test cases are listed in Table 3, and the control block diagram is given in Figure 10. Simulation parameters are listed in Table 6. All tests were performed with ICIs under equal power sharing and using the proposed adaptive power sharing model. The simulation results with the proposed MG system and adaptive power sharing method are illustrated in Figure 11 and the results of equal power sharing with the ICIs in the MG system are shown in Figure 12. Power references for each inverter were calculated based on the total power references and power sharing ratio; the references were varied by 1.5 s in each case. Based on the results, the power sharing algorithm proved effective and the output power tracked the reference smoothly and accurately.

6.2 Experiment verification

To verify the power control effectiveness of the proposed method on the hardware level, a prototype was implemented in the lab (Figure 13). The configuration of the testing system was the same as the simulation. The parallel-connected inverters were controlled by a DSP-based controller. All tests followed the simulation settings. The power transfer waveforms under the different cases are shown in Figure 14.

Similarly, the conventional equal power sharing method was also tested on parallel-connected ICIs. The power transfer waveforms are provided in Figure 15.

7 Conclusion

The CCIs and ICIs have advantages in active and reactive power transfer, respectively. To enhance the reactive power compensation capacity, lower the total power capacity, and reduce transmission losses in a MG system, a hybrid of ICIs and CCIs grid-tied to the MG system was proposed. With its different power characteristics, the conventional equal-sharing method was not suitable for the proposed system. In order to keep the MG system operating continually at minimum power capacity, a power-sharing ratio calculation method for adaptive power sharing was proposed. Simulations and experimental results proved that the hybrid MG system can work well with the proposed control strategy.

Data availability statement

The original contributions presented in the study are included in the article/Supplementary Material; further inquiries can be directed to the corresponding author.

Author contributions

WD and YT provided the ideas and theory of the paper, QL and YY helped to implement the experimental platform, and YZ supervised the research work.

Funding

Conflict of interest

The authors declare that the research was conducted in the absence of any commercial or financial relationships that could be construed as a potential conflict of interest.

Publisher's note

All claims expressed in this article are solely those of the authors and do not necessarily represent those of their affiliated organizations, or those of the publisher, the editors and the reviewers. Any product that may be evaluated in this article, or claim that may be made by its manufacturer, is not guaranteed or endorsed by the publisher.

References

Ahmed, K., Seyedmahmoudian, M., Mekhilef, S., Mubarak, N. M., and Stojcevski, A. (2021). A review on primary and secondary controls of inverter-interfaced microgrid. *J. Mod. Power Syst. Clean Energy* 9 (5), 969–985. doi:10.35833/mpce.2020.000068

Chen, L., Zhang, F., and Sun, L. (2020). Research on the calibration of binocular camera based on BP neural network optimized by improved genetic simulated annealing algorithm. *IEEE Access* 8, 103815–103832. doi:10.1109/access.2020.2992652

Deng, W., Dai, N., Lao, K. -W., and Guerrero, J. M. (2020). A virtual-impedance droop control for accurate active power control and reactive power sharing using capacitive-coupling inverters. *IEEE Trans. Ind. Appl.* 56 (6), 6722–6733. doi:10.1109/tia.2020.3012934Nov.-Dec.

Deng, W., Dai, N. Y., Lao, K., and Guerrero, J. M. "An enhanced power decoupling control for grid-connected capacitive-coupling inverters," in 2019 IEEE Energy Conversion Congress and Exposition (ECCE), Baltimore, MD, USA, September, 2019, 1466–1473.

Deng, W., Li, Q., Zhang, Y., Yi, Y., and Huang, G. "An unequal power sharing strategy for capacitive- and inductive-coupling inverters in microgrid," in 2021 IEEE Energy Conversion Congress and Exposition (ECCE), Vancouver, BC, Canada, October, 2021, 3444–3451.

Fujita, H., and Akagi, H. (1991). A practical approach to harmonic compensation in power systems—series connection of passive and active filters. *IEEE Trans. Ind. Appl.* 27 (6), 1020–1025. doi:10.1109/28.108451Nov.-Dec.

Gong, C., Sou, W.-K., and Lam, C.-S. (2021). Design and analysis of vector proportional–integral current controller for LC-coupling hybrid active power filter with minimum DC-link voltage. *IEEE Trans. Power Electron.* 36 (8), 9041–9056. doi:10.1109/tpel.2021.3049834Aug

He, J., Du, L., Liang, B., Li, Y., and Wang, C. (2019). A coupled virtual impedance for parallel ac/dc converter-based power electronics system. *IEEE Trans. Smart Grid* 10 (3), 3387–3400. doi:10.1109/tsg.2018.2825383

Huang, A., Cao, Z., Wang, C., Wen, J., Lu, F., and Xu, L. (2021). An FPGA-based on-chip neural network for TDLAS tomography in dynamic flames. *IEEE Trans. Instrum. Meas.* 70, 1–11. doi:10.1109/tim.2021.3115210Art no. 4506911

Lao, K., Deng, W., Sheng, J., and Dai, N. (2019). PQ-coupling strategy for droop control in grid-connected capacitive-coupled inverter. *IEEE Access* 7, 31663–31671. doi:10.1109/access.2019.2902314

Liu, B., Liu, Z., Liu, J., An, R., Zheng, H., and Shi, Y. (2019). An adaptive virtual impedance control scheme based on small-AC-signal injection for unbalanced and harmonic power sharing in islanded microgrids. *IEEE Trans. Power Electron.* 34 (12), 12333–12355. doi:10.1109/tpel.2019.2905588Dec

Liu, J., Huang, J., Sun, R., Yu, H., and Xiao, R. (2021). Data fusion for multi-source sensors using GA-PSO-BP neural network. *IEEE Trans. Intell. Transp. Syst.* 22 (10), 6583–6598. doi:10.1109/tits.2020.3010296Oct

Liu, P., Cai, Z., Xie, P., Li, X., and Zhang, Y. (2019). A decomposition coordination planning method for flexible generation resources in isolated microgrids. *IEEE Access* 7, 76720–76730. doi:10.1109/access.2019.2922756

Mousazadeh Mousavi, S. Y., Jalilian, A., Savaghebi, M., and Guerrero, J. M. (2018). Autonomous control of current- and voltage-controlled DG interface inverters for reactive power sharing and harmonics compensation in islanded microgrids. *IEEE Trans. Power Electron.* 33 (11), 9375–9386. doi:10.1109/tpel.2018.2792780Nov

Murty, V., and Kumar, A. (2022). Multi-objective energy management in microgrids with hybrid energy sources and battery energy storage systems. *Prot. Control Mod. Power Syst.* 5 (6), 1–20.

Pang, Y., Xiang, Z., Bai, Z., Wang, L., Wong, C. K., Lam, C. S., et al. (2022). A fusion topology of higher efficiency and lower capacity hybrid parallel multi-converters for power quality compensation. *IEEE Trans. Power Electron.* 37 (5), 5957–5969. doi:10.1109/tpel.2021.3131747

Qi, Y., Tang, Y., Potti, K. R. R., and Rajashekara, K. (2020). Robust power sharing control for parallel three-phase inverters against voltage measurement errors. *IEEE Trans. Power Electron.* 35 (12), 13590–13601. doi:10.1109/tpel.2020.2993290Dec

Razi, R., Iman-Eini, H., and Hamzeh, M. (2020). An impedance-power droop method for accurate power sharing in islanded resistive microgrids. *IEEE J. Emerg. Sel. Top. Power Electron.* 8 (4), 3763–3771. doi:10.1109/jestpe.2019.2926319Dec

Sou, W.-K., Chao, C.-W., Gong, C., Lam, C.-S., and Wong, C.-K. (2022). Analysis design and implementation of multi-quasi-proportional-resonant controller for thyristor-controlled LC-coupling hybrid active power filter (TCLC-HAPF). *IEEE Trans. Ind. Electron.* 69 (1), 29–40. doi:10.1109/tie.2021.3050393

Wang, S., Zhu, H., Wu, M., and Zhang, W. (2020). Active disturbance rejection decoupling control for three-degree-of- freedom six-Pole active magnetic bearing based on BP neural network. *IEEE Trans. Appl. Supercond.* 30 (4), 1–5. doi:10.1109/tasc.2020.2990794Art no. 3603505

Wang, W., Zhu, Q., Wang, Z., Zhao, X., and Yang, Y. (2022). Research on indoor positioning algorithm based on SAGA-BP neural network. *IEEE Sens. J.* 22 (4), 3736–3744. doi:10.1109/jsen.2021.312088215 Feb.15

Yazdani, S., Ferdowsi, M., Davari, M., and Shamsi, P. (2020). Advanced current-limiting and power-sharing control in a PV-based grid-forming inverter under unbalanced grid conditions. *IEEE J. Emerg. Sel. Top. Power Electron.* 8 (2), 1084–1096. doi:10.1109/jestpe.2019.2959006

Zhang, J., Li, L., Dorrell, D. G., Norambuena, M., and Rodriguez, J. (2019). Predictive voltage control of direct matrix converters with improved output voltage for renewable distributed generation. *IEEE J. Emerg. Sel. Top. Power Electron.* 7 (1), 296–308. doi:10.1109/jestpe.2018.2874275

Ziyi, B., Pang, Y., Xiang, Z., Wong, C. K., Wang, L., Lam, C. S., et al. (2023). A capacitive-coupling winding tap injection DSTATCOM integrated with distribution transformer for balance and unbalance operations. *IEEE Trans. Ind. Electron.* 70, 1081–1093. doi:10.1109/tie.2022.3156042

Coordination of network reconfiguration and mobile energy storage system fleets to facilitate active distribution network restoration under forecast uncertainty

Yundai Xu[1], Min Zhao[2], Han Wu[1]*, Sheng Xiang[1] and Yue Yuan[1]

[1]College of Energy and Electrical Engineering, Hohai University, Nanjing, China, [2]State Grid Shanghai Pudong Electric Power Supply Company, Shanghai, China

The active distribution network (ADN) shows great potential for use in network restoration services, given its ability to actively control the network topology, distributed generation (DG) outputs, and demand response (DR) resources. However, its utility may be limited due to the geographical dispersion of DG and DR resources when applied to natural disasters such as windstorms, earthquakes, and floods. In addition, the increasing use of renewable energy creates fluctuations and uncertainties, hindering ADNs from realizing reliable energy scheduling during disasters. Mobile energy storage system (MESS) fleets can be used to economically provide flexible emergency power supply for network restoration services. MESSs can also hedge against load and DG output forecast risks. This article proposes a novel coordinated network reconfiguration and MESS fleets dispatching model considering the uncertainty in DG output and load forecasts to increase the resilience of the ADN after disasters. The MESS traveling strategy is modeled by an extended transit delay model. Then, a novel deterministic network restoration model incorporating the MESS, stationary energy storage system, DG, DR, and network reconfiguration is proposed and programmed using mixed-integer linear programming. Then, an ellipsoidal uncertainty set is employed to describe the uncertainty of load and DG output forecasts, and a robust network restoration model is proposed based on the deterministic one. The proposed deterministic and robust network restoration models are verified on a 59-bus rural distribution system in China.

1 Introduction

Recently, extreme weather disasters have posed unprecedented challenges to power grids, especially distribution networks. For example, in the event of a bus failure owing to an earthquake, the distribution network cannot restore the network without load shedding. Therefore, the demand for flexible and resilient distribution network technology is rising to prevent blackouts and irreparable economic and social impacts.

Compared to traditional distribution networks, active distribution networks (ADNs) are able to achieve higher reliability and resilience *via* advanced active distribution network management (ADNM) schemes (Kabirifar et al., 2019). In an ADN, faults can be actively isolated *via* transforming the status of the switches and network topology (Chen et al., 2016). Furthermore, with the interconnection of high-penetration distribution generation (DG), the ADN can temporarily recover the power supply of essential blackout areas (Han et al., 2019).

Recently, several studies have been conducted to improve network resilience. Salimi et al. (2020) introduced the information gap decision theory to assist distribution system operators (DNO) when extreme events occur. Esfahani et al. (2020) presented a resilience-oriented operation scheduling model for ADN against windstorms. Gholami et al. (2016) utilized a microgrid (MG) to mitigate the load shedding of contingencies, and the dynamic network reconfiguration showed great potential for load recovery. Many studies have highlighted the use of energy storage for restoring loads. Energy storage can provide stable and critical power when a disaster occurs. However, stationary energy storage in the literature relies on the integrity of the power grid, which may be unreliable when extreme events occur.

Mobile energy storage system (MESS) fleets provide a flexible and inexpensive option in terms of mobility and flexibility (Wang et al., 2022). The MESS is a utility-scale storage bank (e.g., lithium-ion batteries) that is fully controlled by the utility. When a severe fault occurs, the DNO can schedule MESSs to move between different positions for service restoration (Abdeltawab and Mohamed, 2017). Compared with aggregated electric vehicles (EVs) owned by residents or third parties, the MESS is more reliable and more accessible to schedule, which is critical for network restoration. Kim and Dvorkin (2019) proposed an investment model that includes a joint allocation and operation strategy for an MESS with microgrids. Huang et al. (2020) used an MESS to mitigate voltage violations. Prabawa and Choi (2020) provided a multiagent framework for coordinating switches, distributed generators, and static/mobile energy storage systems for network restoration. Mirzaei et al. (2020) employed MESSs in a railway system. Dabbaghjamanesh et al. (2021) considered the idea of MESSs for coastal distribution grids and used mobile marine microgrids to maximize the distribution grid resiliency. Abdeltawab and Mohamed (2017) proposed a day-ahead energy management system (EMS) for the MESS, which aims to minimize the cost of importing electricity from the grid. Jiang et al. (2021) proposed a two-step optimal allocation model to obtain the optimal allocation (location and size) of a stationary energy storage system (SESS) and an MESS to improve network resilience.

Nevertheless, the uncertainty that comes from the real world sets tremendous obstacles to restoration tasks (Peng et al., 2020). In the real world, fluctuating DG outputs, time-varying load demands, and estimation errors of loads are the three significant sources of uncertainty in ADN restoration. Regarding the corresponding uncertainty risks, poor restoration performance may result in uncertain conditions when using a deterministic model, even leading to failures under some restoration strategies because of the violation of security constraints. Sekhavatmanesh and Cherkaoui (2020) proposed a new formulation for the reconfiguration problem with a limited number of reconfiguration steps according to DG start-up requirements. Yao et al. (2020) proposed a rolling optimization framework of MESS to fulfill service restoration with both uncertainties from the traffic system and load forecasting. Liu et al. (2021) considered the uncertain temporal-spatial distribution of traffic flows, along with traffic congestion and its impacts, in MESS scheduling. However, the study by Yao et al. (2020) and Liu et al. (2021) did not consider the uncertainty of the DG output, thus, did not provide a robust and reliable restoration scheme.

In this context, this study aims to bridge the gap in the coordination of MESSs, DG outputs, microgrids, and ADNM strategies (i.e., network reconfiguration, SVC adjustment, and demand response), considering the uncertainty from both the DG output and load demand forecast. The operation of MESSs, DGs, and distribution networks is formulated as a two-stage robust optimization problem, where the uncertainties of the load demands and DG outputs are depicted using ellipsoidal uncertainty sets. In the first stage, the vehicle scheduling problem of MESSs is modeled and optimized to harness the flexibility and mobility of the MESSs. Meanwhile, the network configuration is activated to isolate the faults and determine the scale of each microgrid. In the second stage, the actual charging/discharging behaviors of the MESSs and stationary ESSs, the output of the DGs, and responsible load demands are adjusted in accordance with the realized uncertain factors. The major contributions of this study are summarized as follows:

1) A novel network restoration model, which coordinates MESSs, SESSs, network restoration, DG dispatch, and demand response (DR) resources in blackout areas, is proposed to recover the power supply.
2) Furthermore, a robust variant of the proposed coordinated network restoration model is developed. In this robust
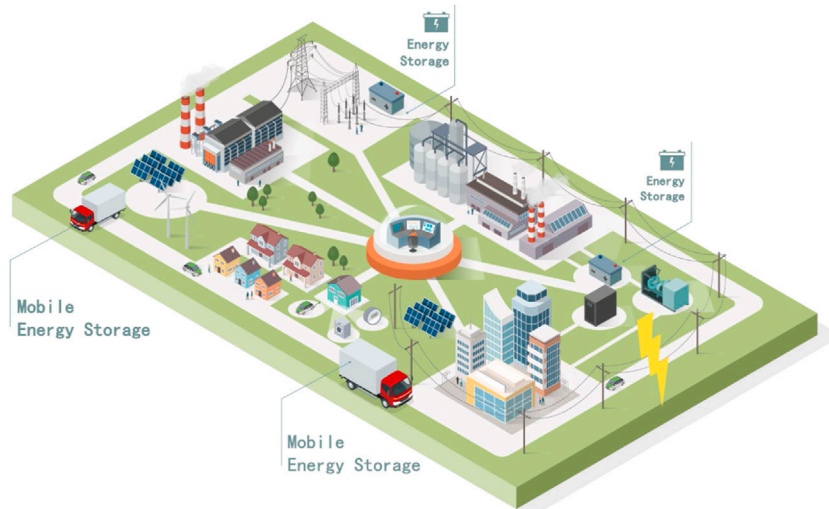
FIGURE 1
Schematic of the post-event network restoration scheme with the MESS.

model, the uncertainty of load and DG output forecast is considered.

The rest of this article is organized as follows: Section 2 introduces the traveling model of MESS fleets; Section 3 presents the formulation of the deterministic and robust network restoration problem, both of them consider DG, DR, SESS, and network reconfiguration; Section 4 displays the case study results from a real 59-bus distribution network system located in Jiangsu, China; at last, the conclusions are presented in Section 5.

2 Traveling model of MESS fleets

Compared with the traditional SESS, which can restore loads only at fixed places, the MESS can travel among MGs to transport energy after major blackouts. See Figure 1 for an example. However, the operation of the MESS is limited by the traffic condition, state of charge (SOC) of the energy storage system carried by the MESS, and travel time between the MG. A detailed traffic and MESS model should be developed to better facilitate the mobility of the MESS. This section introduces the transit delay model (TDM) to briefly represent MESS travel, including the traffic distance matrix and traveling time matrix. Second, the MESS traveling model was laid out, including the parking and traveling states and charging and discharging models.

2.1 Transit delay model of MESS

Because MESSs deliver electrical energy through transportation systems, the traffic model is crucial to the

MESS-based restoration service. Here, the transit delay model, which describes the commute time between two stations, is employed to formulate the traveling time.

For a set of nodes Ψ_N in the distribution system, the distance between each node is defined by the distance matrix $\mathbf{D}$ with zero diagonal elements, where each element d_{ij} denotes the distance between two nodes (i, j). Because there may be one-way streets in the transportation system, d_{ij} may not be equal to d_{ji}.

$$\mathbf{D} = \begin{bmatrix} 0 & \cdots & d_{1N} \\ \vdots & \ddots & \vdots \\ d_{N1} & \cdots & 0 \end{bmatrix}. \tag{1}$$

The traveling time τ_{ij} is also critical to MESS scheduling. The traffic time consists of three parts: commute time d_{ij}/V_{avg}, traffic congestion time tc_{ij}, and installation time t_{ins}.

$$\tau_{ij} = \text{round}\left(\frac{tc_{ij} + d_{ij}/V_{\text{avg}} + t_{\text{ins}}}{T_s}\right) \tag{2}$$

where the function $round$ () rounds the object toward the nearest integer; V_{avg} denotes the average truck speed; and t_{ins} denotes the MESS installation time. Although the MESS operates in plug-and-play mode, connecting the MESS to the grid at the node takes a finite time. T_s denotes the sample time in minutes.

2.2 Operation constraints of the MESS

The MESS carries energy storage to travel from where energy is sufficient to where electricity is urgently needed. Because the MESS works on both transportation and power

systems, the geographical position and energy should be carefully modeled.

2.2.1 MESS position constraints

The initial and final state of the MESS is formulated as follows:

$$z_{m,i=station_{m,i}^{ini},t_0} = 1, \forall m \in \Psi_{MESS}, \forall i \in \Psi_N, \tag{3}$$

$$\omega_{m,t_0} = 0, \forall m \in \Psi_{MESS}, \tag{4}$$

$$\omega_{m,t_{end}} = 0, \forall m \in \Psi_{MESS}, \tag{5}$$

where $z_{m,i,t}$ is a binary variable that indicates the position of the MESS in each time period. If the MESS m is at node i at time t, $z_{m,i,t}$ equals one; otherwise, $z_{m,i,t}$ equals zero; $station_{m,i}^{ini}$ denotes the initial place i of MESS m; and $\omega_{m,t}$ is a binary variable that denotes the traveling state of the MESS. If $\omega_{m,t} = 1$, the MESS m is moving at time t. Eqs 3, 4 indicate that the MESS is parked at $station_{m,i}^{ini}$ before MESS scheduling. Eq. 5 indicates that the MESS should stop moving when time is out. Eq. 5 prevents unnecessary travel during service restoration.

One MESS truck can only be deployed at one node i at time t; that is,

$$\sum_{i \in \Psi_N} z_{m,i,t} = 1 - \omega_{m,t}, \forall m \in \Psi_{MESS}, \forall t \in \Psi_T. \tag{6}$$

2.2.2 MESS traveling constraints

Several logical constraints should be satisfied when the MESS travels in the distribution network.

$$\begin{cases} st_{m,t}^{MESS} - sp_{m,t}^{MESS} = \omega_{m,t}^{MESS} - \omega_{m,t-1}^{MESS} \\ \forall m \in \Psi_{MESS}, \forall t \in \Psi_T \end{cases}, \tag{7}$$

$$st_{m,t}^{MESS} + sp_{m,t}^{MESS} \leq 1, \forall m \in \Psi_{MESS}, \forall t \in \Psi_T, \tag{8}$$

$$\sum_{t'=t}^{t+\tau_{ij}} z_{m,t'} \leq 1, \forall m \in \Psi_{MESS}, \forall t \in \Psi_T, \tag{9}$$

$$\sum_{t'=t}^{t+\tau_{ij}} st_{m,t}^{MESS} \leq 1, \forall m \in \Psi_{MESS}, \forall t \in \Psi_T, \tag{10}$$

$$\sum_{t \in T} st_{m,t}^{MESS} \leq \overline{Travel}, \forall m \in \Psi_{MESS}. \tag{11}$$

Eq. 7 defines the binary start and stop state indicators $st_{m,t}^{MESS}$ and $sp_{m,t}^{MESS}$, when MESS m starts to travel at time t, $st_{m,t}^{MESS}$ equals one. Eq. 8 is a logic constraint that implies that the start and stop state indications $st_{m,t}^{MESS}$ and $sp_{m,t}^{MESS}$ cannot equal one at the same time. Eqs 9, 10 denote the traveling time of the MESS from the perspective of position and traveling state, respectively. Eq. 11 implies that the travel frequency of the MESS should not exceed a predefined maximum value, $\overline{Travel}$.

2.2.3 MESS power output constraints

The battery carried by truck follows similar operation constraints as SESSs, but only charges/discharges when the truck stops at parking lots.

$$\begin{cases} -(1 - \omega_{m,t})\overline{P_m^{MESS}} \leq P_{m,t}^{MESS} \leq (1 - \omega_{m,t})\overline{P_m^{MESS}} \\ \forall m \in \Psi_{MESS}, \forall t \in \Psi_T \end{cases}, \tag{12}$$

$$P_{i,t}^{MatN} = \sum_m z_{m,i,t} \cdot P_{m,t}^{MESS}, \forall i \in \Psi_N, \forall t \in \Psi_T, \tag{13}$$

$$Q_{i,t}^{MatN} \leq P_{i,t}^{MatN} \tan \delta, \forall i \in \Psi_N, \forall t \in \Psi_T, \tag{14}$$

$$SOC_{m,0}^{MESS} = SOC_{m,set}^{MESS}, \forall m \in \Psi_{MESS}, \forall t \in \Psi_T, \tag{15}$$

$$\begin{cases} SOC_{m,t}^{MESS} = SOC_{m,t-1}^{MESS} + P_{m,t}^{MESS} / (\eta_m^{MESS} E_m^{MESS} \Delta t) \\ \forall m \in \Psi_{MESS}, \forall t \in \Psi_T \end{cases}, \tag{16}$$

$$\underline{SOC_m^{MESS}} \leq SOC_{m,t}^{MESS} \leq \overline{SOC_m^{MESS}}, \forall m \in \Psi_{MESS}, \forall t \in \Psi_T, \tag{17}$$

where η_m^{MESS} denotes charging and discharging efficiency of MESS m; E_m^{MESS} denotes the capacity of MESS m; δ denotes the maximum power factor of the MESS system, here we set $\delta = 0.8$ to make sure the MESS can support the local voltage while providing enough active power.

Constraint (Eq. 12) denotes the operational logic of the MESS, which means that the MESS is not permitted to charge or discharge when moving. Furthermore, (Eq. 12) limits the maximum charging and discharging powers of the MESS. Eq. 13 summarizes the total MESS power output at node i at time t. Eq. 14 denotes the reactive power output of MESS. In this study, the maximum power factor of MESS is set to 0.9. Eq. 15 sets the primary SOC of the energy storage. Eq. 16 defines the SOC of MESS at time t. Eq. 17 restrains the maximum and minimum SOC to obviate over-charging and over-discharging.

Eq. 13 contains a product term of a binary variable and a continuous variable, which is nonlinear and computationally expensive. Thus, Eq. 13 is linearized using the "Big-M" method, as follows:

$$\begin{cases} -\sum_m z_{m,i,t} \cdot \overline{P_m^{MESS}} \leq P_{i,t}^{MatN} \leq \sum_m z_{m,i,t} \cdot \overline{P_m^{MESS}} \\ \forall i \in \Psi_N, \forall t \in \Psi_T \end{cases}, \tag{18}$$

$$\begin{cases} \sum_m (1 - z_{m,i,t}) \cdot \overline{P_m^{MESS}} \leq \sum_m P_{m,t}^{MESS} - P_{i,t}^{MatN} \leq \sum_m (1 - z_{m,i,t}) \cdot \overline{P_m^{MESS}} \\ \forall i \in \Psi_N, \forall t \in \Psi_T \end{cases}, \tag{19}$$

where Eqs 18, 19 are the linear variants of Eq. 13.

Compared with existing articles, our model considers the reactive power output of MESS, which provides vital voltage support for the network. It also limits the parking times of the MESS, improving the utilization of energy storage.

3 Mathematical formulation of the coordinated network restoration model

The post-event recovery of ADN with MESS intends to achieve an optimal recovery scheme, including network reconfiguration decisions, SESS operation strategy, SVC dispatch, DG control, DR resources dispatch, and the most crucial coordination scheme with the MESS.

3.1 Deterministic network restoration model

When catastrophic failure or significant disturbances occur, ADN can automatically divide the isolated islands so that more loads will be restored to the power supply under the action of high-penetration DG and the cutting-edge ADNM system. Therefore, this section presents the coordinated network restoration model, including distributed SESS, DR resources, SVC, and microgrid, the concrete mathematical expressions are as follows.

3.1.1 Objective function

$$\max \sum_{j \in \Psi_N} b_j P_{j,t}^L. \qquad (20)$$

To cover as much important load as possible, the restoration model takes the sum of the forecasted power of each bus as the objective function and maximizes it.

3.1.2 DG power output constraints

In the network restoration progress, the renewable energy-based DG can be used to support active power temporally. In this model, it is natural to assume that all DGs are operated in maximum power point tracking mode to supply more renewable energy. Furthermore, we assume that all DGs are equipped with low-voltage ride-through devices to maintain the power supply in the restoration progress. Because the inverter is connected to the photovoltaic panel, it is supposed that the reactive power output can be continuously adjusted within the set scope. In line with the photovoltaic grid-connected standard, the variation scope of the power factor is set as [−0.95, 0.95] (Wang et al., 2016).

$$P_{i,t}^{DG} \le \eta_{i,t}^{DG} S_i^{DG}, \forall i \in \Psi_{DG}, \forall t \in \Psi_T, \qquad (21)$$

$$-P_{i,t}^{DG} \tan \underline{\phi} \le Q_{i,t}^{DG} \le P_{i,t}^{DG} \tan \bar{\phi}, \forall i \in \Psi_{DG}, \forall t \in \Psi_T, \qquad (22)$$

$$\left(P_{i,t}^{DG}\right)^2 + \left(Q_{i,t}^{DG}\right)^2 \le \left(S_i^{DG}\right)^2, \forall i \in \Psi_{DG}, \forall t \in \Psi_T. \qquad (23)$$

Constraints in Eqs 21, 22 present the active power and reactive power output limits of each DG at time *t*. The constraint in Eq. 23 denotes the capacity of each DG system.

Eq. 23 is a quadratic constraint, which will increase the calculation time. In order to solve the sub-problem, this article uses a cyclic linearization method to linearize the constraint (Eq. 23). In the cyclic linearization method, two square constraints are employed to approximate the quadratic constraint, see Figure 2. In Figure 2, the blue circle represents the value of S_i^{DG}, while $P_{i,t}^{DG}$ and $Q_{i,t}^{DG}$ can only take values in this circle according to constraint Eq. 23. The idea of the cyclic linearization method is to use two squares, see Figure 2, to approximate the circle constraint. According to (Kabirifar
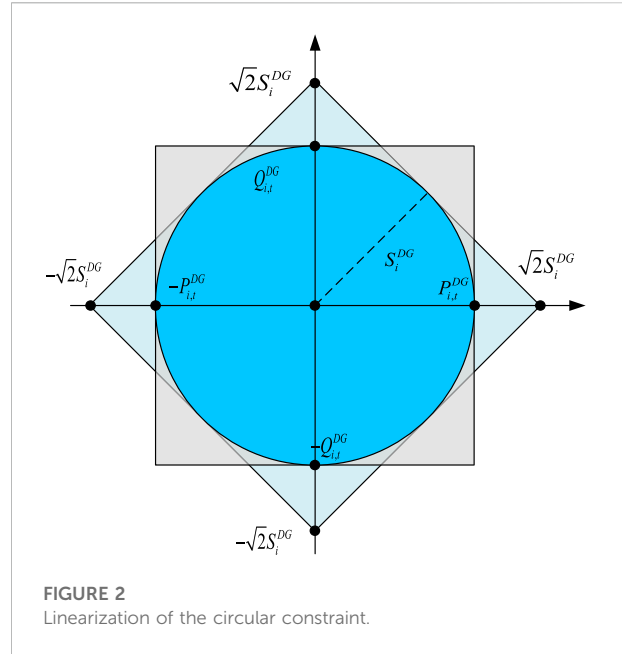
FIGURE 2
Linearization of the circular constraint.

et al., 2019), this approximation is sufficiently accurate in engineering applications.

$$\begin{cases} -S_i^{DG} \le P_{i,t}^{DG} \le S_i^{DG} \\ -S_i^{DG} \le Q_{i,t}^{DG} \le S_i^{DG} \\ -\sqrt{2}S_i^{DG} \le P_{i,t}^{DG} + Q_{i,t}^{DG} \le \sqrt{2}S_i^{DG} \\ -\sqrt{2}S_i^{DG} \le P_{i,t}^{DG} - Q_{i,t}^{DG} \le S_i^{DG} \\ \forall i \in \Psi_{DG}, \forall t \in \Psi_T \end{cases}. \qquad (24)$$

3.1.3 Reactive power output constraints of SVC

As a flexible reactive power supply in ADN, SVC can adjust swiftly according to the reactive power requirement in the process of restoration, which plays the role of reactive power support.

$$\underline{Q_i^{SVC}} \le Q_{i,t}^{SVC} \le \overline{Q_i^{SVC}}, \forall i \in \Psi_{SVC}, \forall t \in \Psi_T, \qquad (25)$$

where $\underline{Q_i^{SVC}}$, and $\overline{Q_i^{SVC}}$ represent the lower and upper thresholds of SVC reactive power output, respectively.

3.1.4 SESS power output constraints

The SESS provides local support to the load demand in faulty areas. The SESS has multiple functions. First, it is the energy supply unit of the important load of the microgrid. Second, it can smooth the fluctuation of DG output and transmit high-quality power to loads.

$$u_{i,t}^{char} + u_{i,t}^{dis} \le 1, \forall i \in \Psi_{ESS}, \forall t \in \Psi_T, \qquad (26)$$

$$u_{i,t}^{char} \underline{P_i^{char}} \le P_{i,t}^{char} \le u_{i,t}^{char} \overline{P_i^{char}}, \forall i \in \Psi_{ESS}, \forall t \in \Psi_T, \qquad (27)$$

$$u_{i,t}^{dis} \underline{P_i^{dis}} \le P_{i,t}^{dis} \le u_{i,t}^{dis} \overline{P_i^{dis}}, \forall i \in \Psi_{ESS}, \forall t \in \Psi_T, \qquad (28)$$

$$SOC_{i,0} = SOC_{i,set}, \forall i \in \Psi_{ESS}, \forall t \in \Psi_T, \quad (29)$$

$$\begin{cases} SOC_{i,t} = SOC_{i,t-1} + \dfrac{\left(P_{i,t}^{char}/\eta_i^{char}\Delta t - P_{i,t}^{dis}/\eta_i^{dis}\Delta t\right)}{E_i^{nomal}}, \\ \forall i \in \Psi_{ESS}, \forall t \in \Psi_T \end{cases} \quad (30)$$

$$\underline{SOC_i} \leq SOC_{i,t} \leq \overline{SOC_i}, \forall i \in \Psi_{ESS}, \forall t \in \Psi_T. \quad (31)$$

The constraint in Eq. 26 is the mutually exclusive constraint of ESS, indicating that ESS cannot charge and discharge simultaneously. Eqs 27, 28 are the upper and lower bounds of charge and discharge of SESS. Eq. 29 sets the primary SOC of the SESS. Eq. 30 defines the SOC at time t. Eq. 31 restrains the maximum and minimum SOC.

3.1.5 Power flow constraints

In this article, the DistFlow equation is used to model the radial grid, and the specific model is as follows:

$$\begin{cases} \sum_{k\in\pi(i)} P_{ki,t} - \sum_{j\in\gamma(i)} P_{ij,t} = P_{i,t}^{DG} - P_{i,t}^L + r_{ij}I_{ij,t}^2, \\ \forall i \in \Psi_N, \forall ij \in \Psi_E, \forall t \in \Psi_T \end{cases} \quad (32)$$

$$\begin{cases} \sum_{k\in\pi(i)} Q_{ki,t} - \sum_{j\in\gamma(i)} Q_{ij,t} = Q_{i,t}^{DG} + Q_{i,t}^{SVC} - P_{i,t}^L\tan\varphi + x_{ij}I_{ij}^2, \\ \forall i \in \Psi_N, \forall ij \in \Psi_E, \forall t \in \Psi_T \end{cases} \quad (33)$$

$$\begin{cases} V_{i,t}^2 - V_{j,t}^2 = 2\left(P_{ij,t}r_{ij} + Q_{ij,t}x_{ij}\right) - \left(r_{ij}^2 + x_{ij}^2\right)I_{ij,t}^2, \\ \forall i \in \Psi_N, \forall ij \in \Psi_E, \forall t \in \Psi_T \end{cases} \quad (34)$$

where $I_{ij,t}^2 = (P_{ij,t}^2 + Q_{ij,t}^2)/V_{i,t}^2$.

In Eqs 32, 33, $r_{ij}I_{ij,t}^2$ is a nonlinear term, which can be ignored since the energy loss is relevantly small. In addition, since ADN has a relatively flat voltage profile (i.e., $V_i \approx 1, i \in \Psi_N$). The left term in Eq. 34 can be approximated by $V_{i,t}^2 - V_{j,t}^2 \approx 2(V_{i,t} - V_{j,t})$, with a minor approximation error [approximately 0.25% (1%) if there is a 5% (10%) deviation in the voltage amplitude approximation]. Taking these two simplifications into consideration, Eqs 32–34 can be simplified to

$$\begin{cases} \sum_{k\in\pi(i)} P_{ki,t} - \sum_{j\in\gamma(i)} P_{ij,t} = P_{i,t}^{DG} - P_{i,t}^L, \\ \forall i \in \Psi_N, \forall ij \in \Psi_E, \forall t \in \Psi_T \end{cases} \quad (35)$$

$$\begin{cases} \sum_{k\in\pi(i)} Q_{ki,t} - \sum_{j\in\gamma(i)} Q_{ij,t} = Q_{i,t}^{DG} + Q_{i,t}^{SVC} - P_{i,t}^L\tan\varphi, \\ \forall i \in \Psi_N, \forall ij \in \Psi_E, \forall t \in \Psi_T \end{cases} \quad (36)$$

$$\begin{cases} V_{i,t} - V_{j,t} = P_{ij,t}r_{ij} + Q_{ij,t}x_{ij}. \\ \forall i \in \Psi_N, \forall ij \in \Psi_E, \forall t \in \Psi_T \end{cases} \quad (37)$$

Furthermore, to consider the network reconfiguration and bus failure in the recovery, we use the Big-M method to build a variation of Eqs 35–37.

$$\begin{cases} -M(1 - b_i) \leq P_{i,t}^{DG} - P_{i,t}^L - \sum_{k\in\pi(i)} P_{ki,t} + \sum_{j\in\gamma(i)} P_{ij,t} \\ \leq M(1 - b_i), \forall i \in \Psi_N, \forall ij \in \Psi_E, \forall t \in \Psi_T \end{cases}, \quad (38)$$

$$\begin{cases} -M(1 - b_i) \leq Q_{i,t}^{DG} + Q_{i,t}^{SVC} - P_{i,t}^L\tan\varphi - \sum_{k\in\pi(i)} Q_{ki,t} + \sum_{j\in\gamma(i)} Q_{ij,t}, \\ \leq M(1 - b_i), \forall i \in \Psi_N, \forall ij \in \Psi_E, \forall t \in \Psi_T \end{cases} \quad (39)$$

$$\begin{cases} -M(1 - c_{ij}) \leq V_{i,t} - V_{j,t} - P_{ij,t}r_{ij} - Q_{ij,t}x_{ij} \\ \leq M(1 - c_{ij}), \forall i \in \Psi_N, \forall ij \in \Psi_E, \forall t \in \Psi_T \end{cases}. \quad (40)$$

Eqs 38, 39 are the active and reactive power flow equations, respectively, where b_j is the 0–1 variable, indicating whether connected with the grid, and M denotes a large constant. Eq. 40 uses the linearized DistFlow formulation to display the bus voltage drop, c_{ij} is the 0–1 variable, which represents the status of the line ij.

3.1.6 Network security constraints

The line capacity and bus voltage constraints are considered to make the microgrid and ADN operate normally after restoration.

$$P_{ij,t}^2 + Q_{ij,t}^2 \leq S_{ij}^{\max 2} \cdot c_{ij}, \forall ij \in \Psi_E, \forall t \in \Psi_T, \quad (41)$$

$$\underline{V_i} \leq V_{i,t} \leq \bar{V}_i, \forall i \in \Psi_N, \forall t \in \Psi_T. \quad (42)$$

Eqs 41, 42 constrain the line capacity and bus voltage, respectively. The quadratic form in Eq. 41 can also be approximated using the circular linearization method as follows:

$$\begin{cases} -S_{ij}^{\max} \cdot c_{ij} \leq P_{ij,t} \leq S_{ij}^{\max} \cdot c_{ij} \\ -S_{ij}^{\max} \cdot c_{ij} \leq Q_{ij,t} \leq S_{ij}^{\max} \cdot c_{ij} \\ -\sqrt{2}S_{ij}^{\max} \cdot c_{ij} \leq P_{ij,t} + Q_{ij,t} \leq \sqrt{2}S_{ij}^{\max} \cdot c_{ij} \\ -\sqrt{2}S_{ij}^{\max} \cdot c_{ij} \leq P_{ij,t} - Q_{ij,t} \leq \sqrt{2}S_{ij}^{\max} \cdot c_{ij} \\ \forall ij \in \Psi_E, \forall t \in \Psi_T \end{cases}. \quad (43)$$

3.1.7 Demand response constraints

DR can change load demand through a series of incentive measures, which are widely used in ADN. When the power grid is attacked, DR can alleviate the power supply pressure to a certain extent. To display the role of DR in the restoration plan, this article presents an interruptible load modeling scheme, which is the most typical and effective.

$$P_{i,t}^{DR} \leq q_{i,t}^{DR}u_{i,t}^{DR}, \forall i \in \Psi_{DR}, \forall t \in \Psi_T, \quad (44)$$

$$st_{i,t}^{DR} - sp_{i,t}^{DR} = u_{i,t}^{DR} - u_{i,t-1}^{DR}, \forall i \in \Psi_{DR}, \forall t \in \Psi_T, \quad (45)$$

$$st_{i,t}^{DR} + sp_{i,t}^{DR} \leq 1, \forall i \in \Psi_{DR}, \forall t \in \Psi_T, \quad (46)$$

$$\sum_{t'=t}^{t+TLC_{\min}^{DR}-1} u_{i,t'}^{DR} \geq TLC_{\min}^{DR}st_{i,t}^{DR}, \forall i \in \Psi_{DR}, \forall t \in \Psi_T, \quad (47)$$

$$\sum_{t'=t}^{t+TLC_{\max}^{DR}-1} sp_{i,t'}^{DR} \geq st_{i,t}^{DR}, \forall i \in \Psi_{DR}, \forall t \in \Psi_T, \quad (48)$$

$$\sum_{t \in T} st_{i,t}^{DR} \le \mathrm{Num}^{DR}, \forall i \in \Psi_{DR}, \tag{49}$$

where $q_{i,t}^{DR}$ denotes the maximum load capacity that can be interrupted at bus i in time interval t; $st_{i,t}^{DR}$, $sp_{i,t}^{DR}$, and $u_{i,t}^{DR}$ are 0–1 variables that represent the start, stop, and interrupt states of loads, respectively; $TLC_{\min}^{DR}$ and $TLC_{\max}^{DR}$ denote the lower and upper limits of interruptible time; and Num^{DR} represents the maximum number of interruptible loads.

3.1.8 Topology constraints

The abovementioned model should be convenient for coordination and protection based on effectively reducing the short-circuit current. Hence, ADN needs to meet a series of topology constraints during operation. This study uses a virtual network (Lavorato et al., 2012; Ding et al., 2017) to formulate the reconfiguration model, and the radial topology constraint can be equally replaced by the connectivity constraint and the branch number constraint.

In the linearized DistFlow model, a virtual network with the same topology as ADN is added to represent the connectivity constraint. Among them, the power source nodes are regarded as "source" nodes, and the load nodes are considered as "sink" nodes. In this study, we assume that both buses and power lines can be attacked. Therefore, we are supposed to verify whether the bus is in the restored grid.

$$\sum_{k \in \pi(i)} F_{ki} - \sum_{j \in \gamma(i)} F_{ij} = -b_i, \forall i \in \Psi_N \setminus \{\Psi_{DG} \cup \Psi_{Sub}\}, \tag{50}$$

$$\sum_{k \in \pi(i)} F_{ki} - \sum_{j \in \gamma(i)} F_{ij} = H_i, \forall i \in \Psi_{DG} \cup \Psi_{Sub}, \tag{51}$$

$$b_i \le H_i \le M \cdot b_i, \forall i \in \Psi_{DG} \cup \Psi_{Sub}, \tag{52}$$

$$-M \cdot c_{ij} \le F_{ij} \le M \cdot c_{ij}, \forall ij \in \Psi_E, \tag{53}$$

$$\sum_{ij \in \Psi_E} c_{ij} = \sum_{i \in \Psi_N} b_i - n^{MG}, \forall ij \in \Psi_E, \tag{54}$$

where $\pi(i)$ is the node set that contains the nodes flows to node i; $\gamma(i)$ is the node set that contains the node flows from node i.

Eqs 50, 51 make sure that the "sink" nodes must connect to at least one "source" node. Eq. 52 connects the fictitious network and the real distribution network.

The branch number constraints are shown in Eqs 55–58, where $|\cdot|$ represents the cardinality of the set, n^{MG} represents the number of microgrids, and if n^{MG} equals one, there are no microgrids in ADN. Eqs 57, 58 make sure that the lines connected to the disconnected bus should be cut off.

$$\sum_{i \in \Psi_N} b_i \le |\Psi_N|, \tag{55}$$

$$n^{MG} \ge 1, \tag{56}$$

$$c_{i,j} \le b_i, \forall ij \in \Psi_E, \tag{57}$$

$$c_{i,j} \le b_j, \forall ij \in \Psi_E. \tag{58}$$

The proposed restoration model can control the connections of each bus. In addition, we define variable b_i to show whether bus i is powered by the microgrid. It can also obtain the optimal number of microgrids through the value of the variable n^{MG}.

By comparing Eqs 2–22 and Eqs 24–31 and Eq. 38, the deterministic grid reconfiguration model in this study is a mixed-integer linear programming model.

3.2 DG and load forecast uncertainty

A qualified network restoration scheme should handle the uncertainty of DG output and load forecast. Thus, we introduce a predefined ellipsoidal uncertainty set to describe uncertainty.

The load demand and DG output forecast value can be represented by a combination of its mean value and forecast error as follows:

$$P_{i,t}^L = \overline{P_{i,t}^L} + \Delta P_{i,t}^L, \tag{59}$$

$$\eta_{i,t}^{DG} = \overline{P_{i,t}^{DG}} + \Delta P_{i,t}^{DG}, \tag{60}$$

where $\overline{P_{i,t}^L}$, $\overline{P_{i,t}^{DG}}$, $\Delta P_{i,t}^L$, and $\Delta P_{i,t}^{DG}$ are the predicted active power and forecast error of the load demand and DG outputs, respectively.

The following ellipsoidal uncertainty set describes the boundary of the forecast error as follows:

$$\Omega_N = \left\{ \Delta P_{i,t}^L : \Delta P_{i,t}^L \Theta_{L,i}^{-1} \Delta P_{i,t}^L \le C_{conf}^L \right\}, \forall i \in \Psi_N, \forall t \in \Psi_T, \tag{61}$$

$$\Omega_{DG} = \left\{ \Delta P_{i,t}^{DG} : \Delta P_{i,t}^{DG} \Theta_{DG,i}^{-1} \Delta P_{i,t}^{DG} \le C_{conf}^{DG} \right\}, \forall i \in \Psi_{DG}, \forall t \in \Psi_T, \tag{62}$$

where Ω_N and Ω_{DG} denote the ellipsoidal uncertain set of the load forecast error and DG forecast error, respectively; Θ_i^{-1} and Φ_i^{-1} denote the covariance matrices of the load forecast error and DG forecast error, respectively; C_{conf}^L and C_{conf}^{DG} are the uncertainty budgets. By adjusting the uncertainty budget, the DNO can control the conservativeness of the entire network restoration model to adapt to various disasters.

In this study, we assumed the system error of the forecasted load and forecasted DG output is zero and is subject to multivariate normal distributions. Therefore, the uncertainty budget can be determined by the chi-square distribution using the relation

$$C_{conf}^L = \chi_{1-\alpha}^2 (|\Psi_T|), \tag{63}$$

$$C_{conf}^{DG} = \chi_{1-\alpha}^2 (|\Psi_T|), \tag{64}$$

where $\chi_{1-\alpha}^2 (|\Psi_T|)$ represents the $(1 - \alpha)$ quantile of the chi-square distribution with $|\Psi_T|$ degrees of freedom. $|\Psi_T|$ is the cardinal number of set Ψ_T.

The ellipsoidal uncertainty can be normalized to a sphere by defining $\Xi_{L,i} = \Theta_{L,i}^{1/2}$, $\Xi_{DG,i} = \Theta_{DG,i}^{1/2}$, and using ζ_L and ζ_{DG} to

denote the radial uncertainty. Then, the uncertainty sets Ω_N and Ω_{DG} can be rewritten as follows:

$$\Omega_N = \left\{ \Delta P_{i,t}^L = \sqrt{C_{conf}^L} \, \Xi_{L,i} \zeta_L, \|\zeta_L\| \le 1 \right\}, \tag{65}$$

$$\Omega_{DG} = \left\{ \Delta P_{i,t}^{DG} = \sqrt{C_{conf}^{DG}} \, \Xi_{DG,i} \zeta_{DG}, \|\zeta_{DG}\| \le 1 \right\}. \tag{66}$$

3.3 Robust optimization formulation

In this section, the original deterministic network restoration model in Section 3.1 is reformatted to a robust optimization model to consider the uncertainty in the network restoration problem.

The robust optimization model can be understood using the "max–min" framework. In the outer layer, the uncertainty is fixed, aiming to maximize the total load in the "worst" scenario. In the inner layer, the uncertainty parameters are regarded as variables, and the aim is to find the "worst" scenario against the outer layer and minimize the total restored loads. The objective function under the "max–min" framework is as follows:

$$\max \min_{\Delta P_{i,t}^{DG}, \Delta P_{i,t}^L} \sum_t \sum_{i \in N} b_i \cdot P_{i,t}^L. \tag{67}$$

The constraint should also be modified to accommodate the robust optimization model. First, the load demand and DG output in constraints Eq. 23 and Eqs 40, 41 are modified using Eqs 61, 62.

$$P_{i,t}^{DG} \le \left(\overline{P_{i,t}^{DG}} + \Delta P_{i,t}^{DG} \right) \cdot S_i^{DG}, \forall i \in \Psi_{DG}, \forall t \in \Psi_T, \tag{68}$$

$$\begin{cases} -M(1 - b_i) \le P_{i,t}^{DG} - \overline{P_{i,t}^L} - \Delta P_{i,t}^L - \sum_{k \in \pi(i)} P_{ki,t} + \sum_{j \in \gamma(i)} P_{ij,t} \\ \le M(1 - b_i), \forall i \in \Psi_N, \forall ij \in \Psi_E, \forall t \in \Psi_T \end{cases}, \tag{69}$$

$$\begin{cases} -M(1 - b_i) \le Q_{i,t}^{DG} + Q_{i,t}^{SVC} - \left(\overline{P_{i,t}^L} + \Delta P_{i,t}^L \right) \tan \varphi \\ - \sum_{k \in \pi(i)} Q_{ki,t} + \sum_{j \in \gamma(i)} Q_{ij,t} \le M(1 - b_i) \\ \forall i \in \Psi_N, \forall ij \in \Psi_E, \forall t \in \Psi_T \end{cases}. \tag{70}$$

Taking the ellipsoidal uncertainty set into the account, Eqs 68–70 can be further transformed into a set of second-order cone robust counterparts as follows:

$$P_{i,t}^{DG} \le \left(\overline{P_{i,t}^{DG}} + \left\| \sqrt{C_{conf}^{DG}} \Xi_{DG,i} \zeta_{DG} \right\| \right) S_i^{DG}, \forall i \in \Psi_{DG}, \forall t \in \Psi_T, \tag{71}$$

$$\begin{cases} -M(1 - b_i) \le P_{i,t}^{DG} - \overline{P_{i,t}^L} - \left\| \sqrt{C_{conf}^L} \Xi_{L,i} \zeta_L \right\| - \sum_{k \in \pi(i)} P_{ki,t} + \sum_{j \in \gamma(i)} P_{ij,t} \\ \le M(1 - b_i), \forall i \in \Psi_N, \forall ij \in \Psi_E, \forall t \in \Psi_T \end{cases}, \tag{72}$$

$$\begin{cases} -M(1 - b_i) \le Q_{i,t}^{DG} + Q_{i,t}^{SVC} - \sum_{k \in \pi(i)} Q_{ki,t} + \sum_{j \in \gamma(i)} Q_{ij,t} \\ - \left(\overline{P_{i,t}^L} + \left\| \sqrt{C_{conf}^L} \Xi_{L,i} \zeta_L \right\| \right) \tan \varphi \le M(1 - b_i) \\ \forall i \in \Psi_N, \forall ij \in \Psi_E, \forall t \in \Psi_T \end{cases}. \tag{73}$$

The robust coordinated network restoration model, represented by Eqs 2–22, Eqs 27–33, Eqs 71–73, and Eqs 44–58), is formulated using mixed-integer second-order cone programming (MISOCP). However, both the proposed deterministic and robust network restoration models contain numerous binary variables, resulting in high computational costs. Most commercial optimization solvers, such as CPLEX, can solve the proposed model at only a small scale. For practical use, a faster algorithm is required to solve the proposed model.

4 Case study

The proposed models were tested on a 59-bus rural distribution system in Jiangsu, China. The structure of the 59-bus rural distribution system is shown in Figure 3. There are five PV locations in the testing system, each with a 1.5 MW capacity. Two 300 kVar SVCs were set at Nodes 18 and 42. Two ESS are located at bus 16 and bus 38, with one MWh capacity and 0.5 MW maximum charging and discharging power, and 0.9 charging/discharging efficiency. The total load demand of the system is 3.85 MW and 0.97 MVar. There are three types of loads: residential, industrial, and commercial loads. The location of each load is shown in Figure 3. The flexible load, which actively reacts to the DNO, is located at buses four, 16, 22, and 30. Their load curves are consistent with the load on the bus. The maximum scheduling frequency is set to two, and the maximum hour for load scheduling is set to 20 min each time. Referring to the Chinese standard, an example is analyzed with 5 min as an interval and the total restoration time is 2 h. The voltage amplitude of the substation bus is set to 10.5 kV, the base power of the distribution system is set to 50 MW, the base power of the SESS is set to 1 MW, and the voltage scope of all nodes is set to [0.93, 1.07] p. u. In this article, the load is divided into residential, commercial and industrial loads. In the restoration period, the curves of load and forecasted PV output are shown in Figure 4. The covariance of the forecast error is assumed to be one, and there is no correlation between time and space.

The distance between each bus is shown in Figure 5. The maximum distance in Figure 5 is between bus 20 and bus 50, approximately 10,500 m, while the mean distance is approximately 4,110 m. Assume the traveling speed of the MESS truck is 60 km/h (1,000 m/min), the maximum traveling time should be 10 min, and the mean traveling speed should be 4.1 min, accordingly. The MESS installation time is set to 3 min, and the sample time Ts is set to 5 min to consist of the time slot of the load and DG curves.

In the following text, we assume that two faults occur between buses 2 and 24, and between buses 1 and 10. The deterministic and robust models were tested successively to demonstrate their performances.
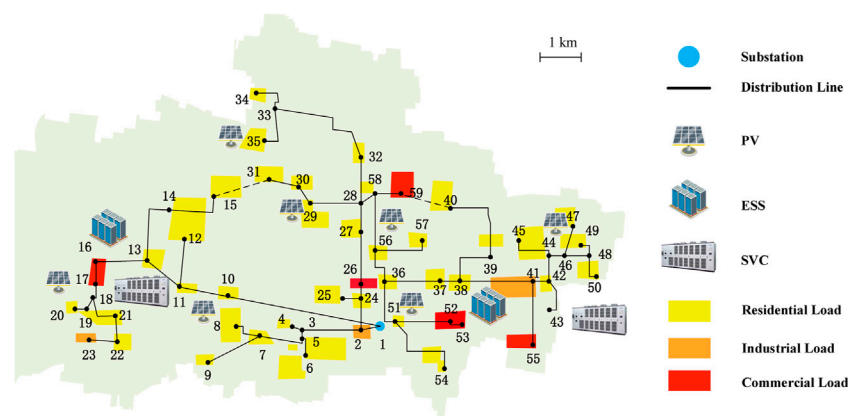
FIGURE 3
Testing the proposed model on the 59-bus rural distribution network.
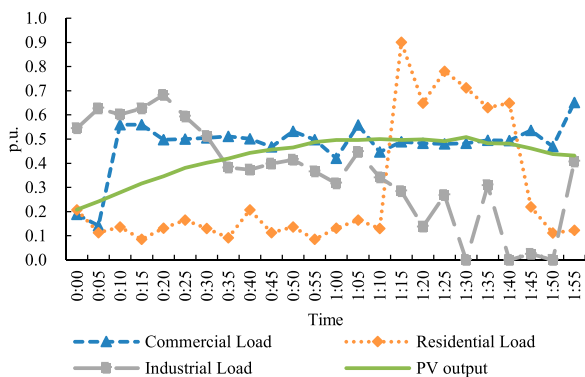
FIGURE 4
Forecasted load and PV output curves.
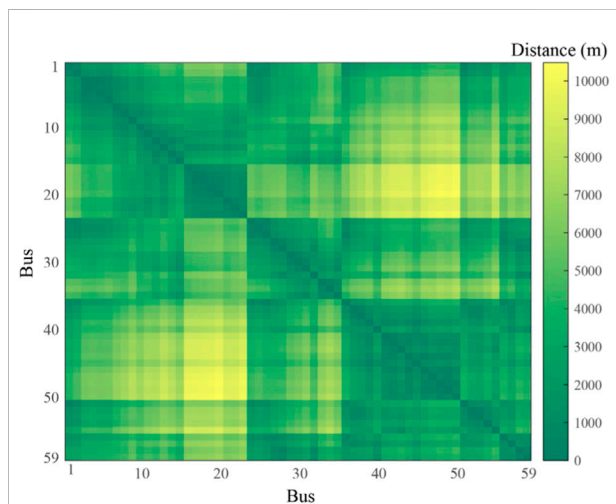
FIGURE 5
Distance matrix of the 59 buses.

4.1 Computational result of the deterministic model

We shall first look at the simulation results without considering the uncertainty of DG outputs, that is, the deterministic dispatching model is used to help network restoration. Specifically, the deterministic dispatching model with and without MESS is compared to show the effectiveness of MESS in improving network reliability.

4.1.1 Case A: No MESS connected

Case A is a benchmark in which no MESS is connected to ADN. In this case, only the ADNM schemes were employed, and two SESS located at buses 16 and 38 were used to help with network restoration.

Figure 6 illustrates the network operation status in Case A. In Figure 6, the black dashed line denotes the microgrids divided by

the network reconfiguration scheme and the red dashed line denotes the disconnected lines. As shown in Figure 6, the entire network was divided into two microgrids, while only 45 buses and 43 lines were connected to the grid.

Figure 7 illustrates the restored load, PV output, and SOC of the SESS in Case A. As shown in Figure 7, the total restored load was 29.031 MWh, and the PV output energy was 21.227 MWh. Based on the SOC curve in Figure 6, the SESS was not fully used in network restoration. In particular, SESS1, located on bus 16, received 1 hour of charging from the PV. Meanwhile, SESS2, located at bus 38, was frequently charging and discharging to maintain a regional energy balance. The proposed model thus can be used for network restoration even if the ADNM scheme is implemented.
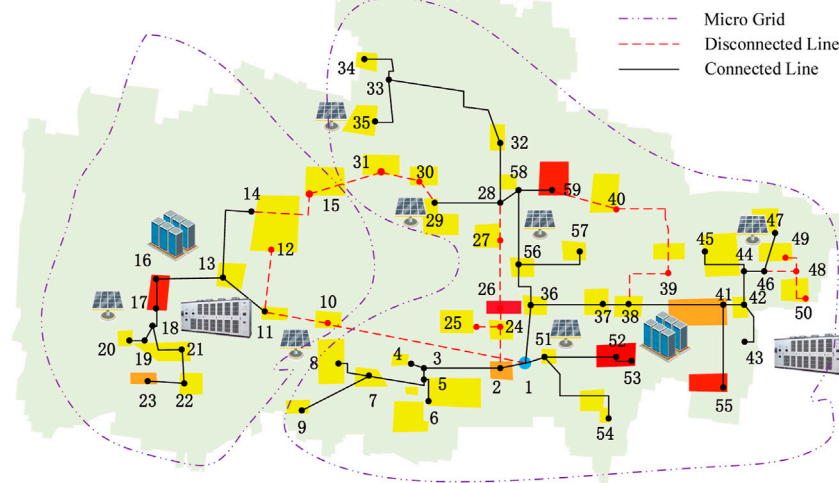
FIGURE 6
Island partition result of Case A.
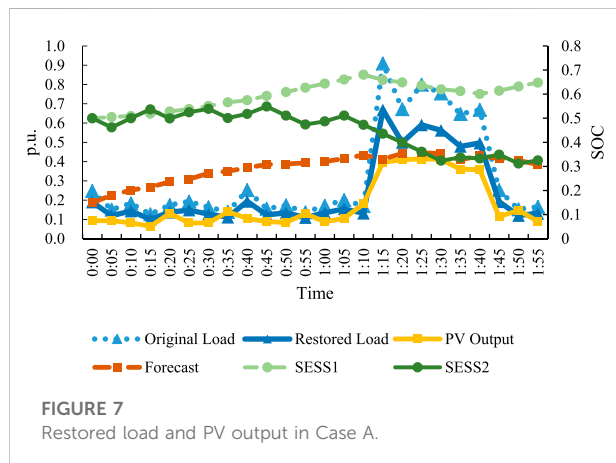
FIGURE 7
Restored load and PV output in Case A.

4.1.2 Case B: MESS connected

In Case B, the MESS was employed in the AND. The MESS had a capacity of 0.5 MWh and a 0.5 MW power limit. The initial allocation of the MESS is at bus one. The initial SOC of the MESS was set to 0.8.

Figure 8 illustrates the network operation status of Case B. Unlike the result in Case A, the integrity of the distribution network was preserved, and no microgrid was divided from the original network. In Case B, 47 buses and 46 lines were connected to the grid.

Figure 9 illustrates the restored load, PV output, and SOC of the SESS in Case B. As shown in Figure 9, the total restored load was 30.39 MWh, and the PV output energy was 20.221 MWh. It is easy to find that with the assistance of

MESS, the restored load in the ADN has been significantly improved. Figure 9 shows the SOC curve of the MESS. Combined with Figures 8, 10, we can see that the MESS travels among nodes one, 46, 59, and 38 at the 1st, 2nd, 16th, and 24th time periods.

Based on the abovementioned analysis, the cooperative work of MESS and network reconfiguration can greatly improve the fault recovery of the distribution network. However, problems such as the uncertainty of PV in actual scenarios inevitably lead to a certain degree of error in the analysis of the entire system. Therefore, the introduction of uncertainty analysis transforms the problem into a robust optimization problem.

4.2 Computational result of the robust model

First, we consider the case of an uncertainty budget of 10 percent (denoted as RO10), in which the system provides a lower degree of consideration for possible uncertainties. The island partition and the MESS moving track are shown in Figure 11. The restored load, PV output, and SOC of the SESS, as shown in Figure 12. Figure 13 shows the SOC of MESS.

In RO10, the network is divided into two parts: 40 nodes and 38 lines in the system are connected to the microgrid. As shown in Figure 12, the total restored load was 25.891 MWh, and the PV output energy was 15.780 MWh. Figure 13 shows the SOC curve of the MESS. Combined with Figures 11, 12, we can see that the
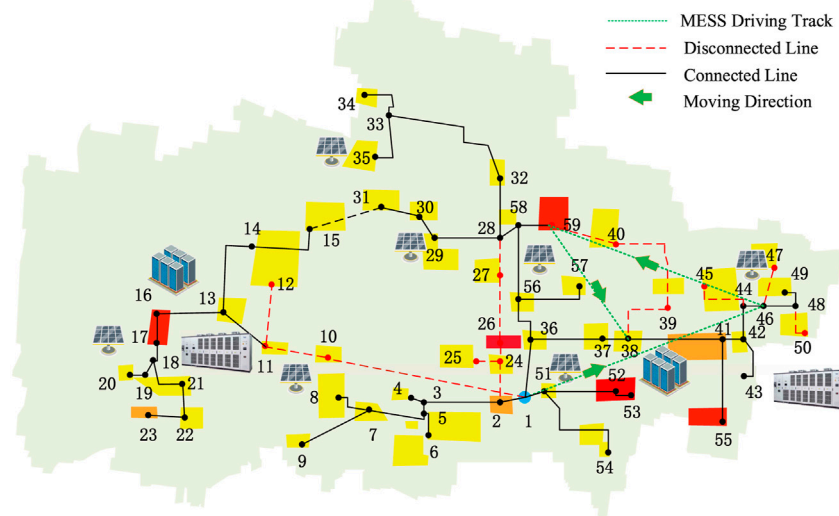
FIGURE 8
Island partition and MESS allocation result of Case B.
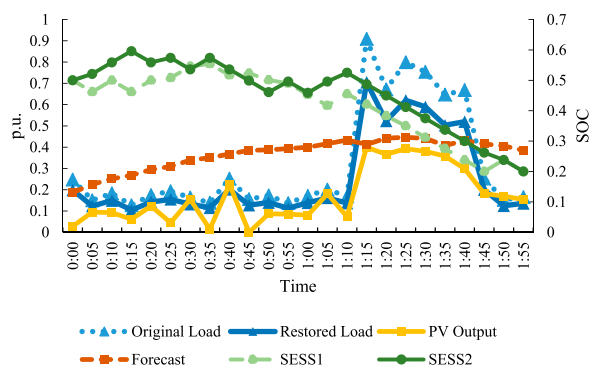
FIGURE 9
Restored load, PV output, and SOC of the SESS in Case B.
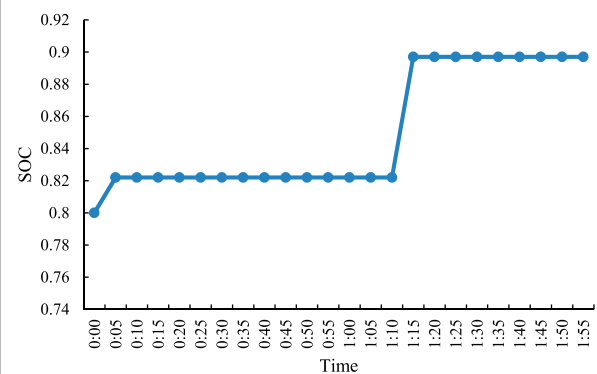
FIGURE 10
SOC result of the MESS in Case B.

MESS travels among nodes 1, 28, and 9 at the 1st, 16th, and 24th time periods.

Compare with the above figs, we can see that the restored load and PV outputs have a significant drop if the uncertainty is considered. Compared with the deterministic model result in Case B, the number of unconnected nodes and unconnected lines also declines greatly. The charging and discharging of MESS were also slightly gentler than those in Case B.

As we can see in RO10, a slight uncertainty can dramatically change the network restoration results. If the uncertainty budget of the system is further increased to 90% (denoted as RO90), a more conservative restoration result can be obtained. The network status at RO90 is shown in

Figure 14; the load, PV, and SOC curves are shown in Figure 15.

It can be seen from Figure 14 that the network is divided into two microgrids; only nine nodes and seven lines of the whole system are connected to the network. Only 5.420 MWh load and 2.00 MWh PV were restored in RO90, even if the SESS is fully used. This is because the PV output is heavily limited under the most conservative condition.

However, considering the uncertainty of the random output of renewable energy also decreases the load-restoration rate. From the results of the robust optimization model, it is not difficult to find that with an increase in the uncertainty budget, the conservatism of the calculation results will also increase, and
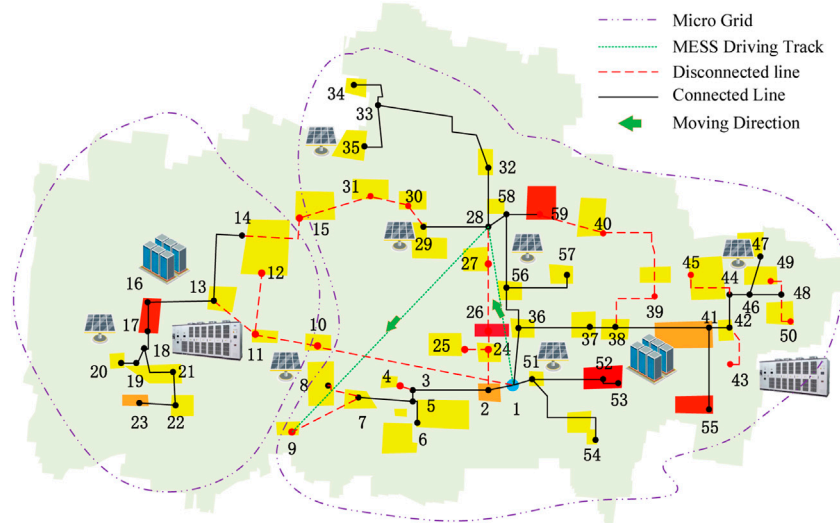
FIGURE 11
Island partition and MESS allocation result of RO10.
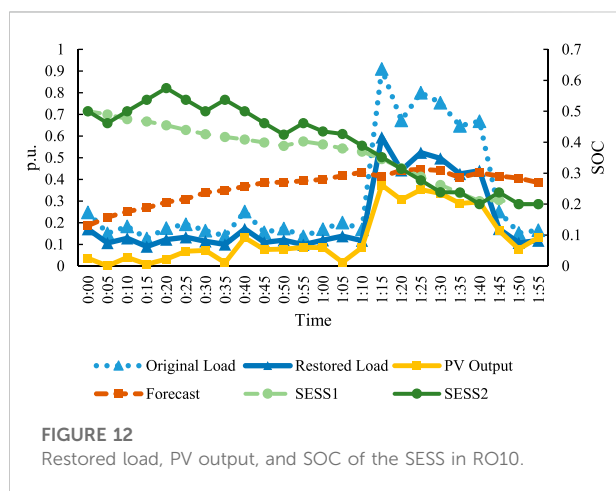
FIGURE 12
Restored load, PV output, and SOC of the SESS in RO10.
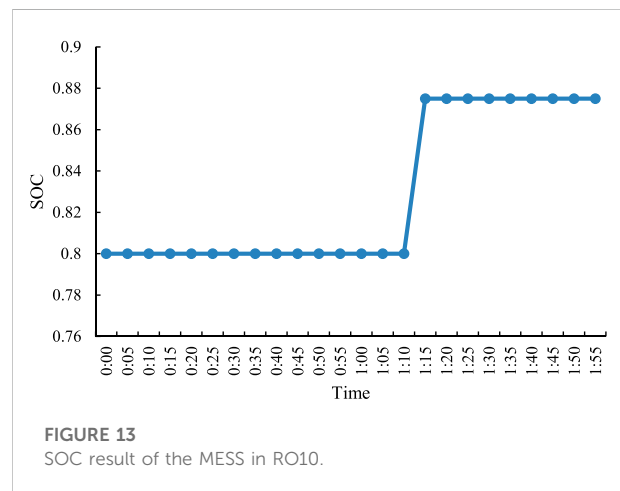
FIGURE 13
SOC result of the MESS in RO10.

the system must sacrifice the economy and part of the load to deal with possible extremely bad conditions. During the actual operation of the distribution network, decision makers can choose different uncertainty budgets according to the actual needs of the system.

4.3 Computational performance

All algorithms were executed on an HP Z840 workstation with Intel(R) Xeon(R) E5-2650v4 CPUs running at 2.20 GHz and 16 GB RAM. The proposed models were programmed and solved using the general algebraic modeling system (GAMS) software

and the commercial solver CPLEX 20.1. The CPU times for the proposed models are presented in Figure 16.

As shown in Figure 16, the deterministic model without MESS (Case A) exhibits the best computational performance. When MESS was considered (Case B), the computational time increased significantly. This is because the MESS model contains a large number of binary variables, which require much more time to tackle. The uncertainty set in the robust model reduces the feasible region, which results in a significant reduction in computational time. Furthermore, the computational time generally decreases with an increase in the conservative levels. For a post-event dispatch, the 30% conservative level is recommended to reach a balance between computational burden and robustness.
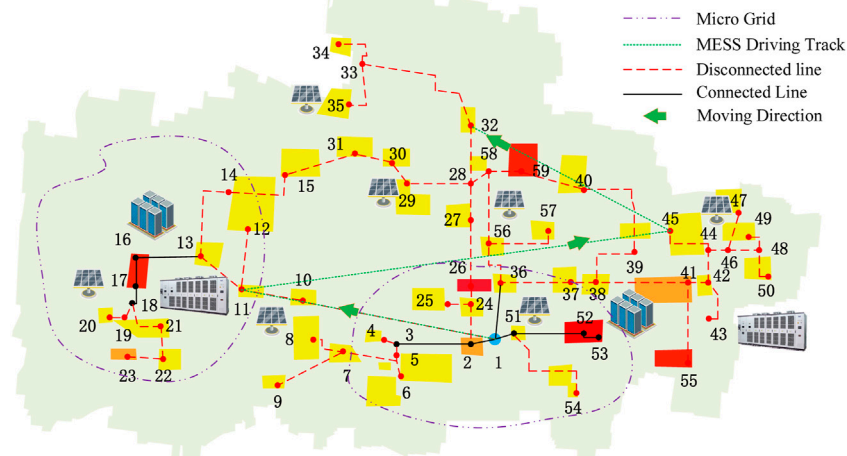
FIGURE 14
Island partition and MESS allocation result of RO90.
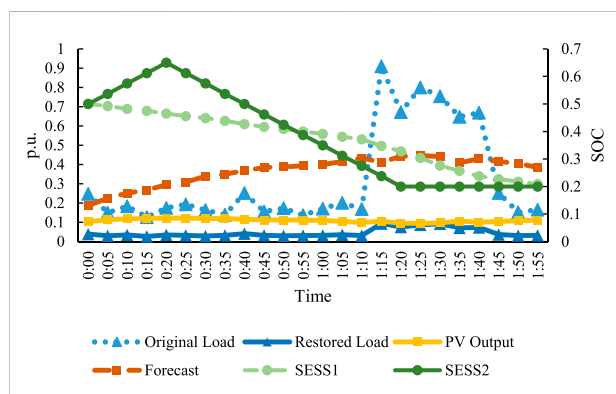
FIGURE 15
Restored load, PV output, and SOC of the SESS in RO90.
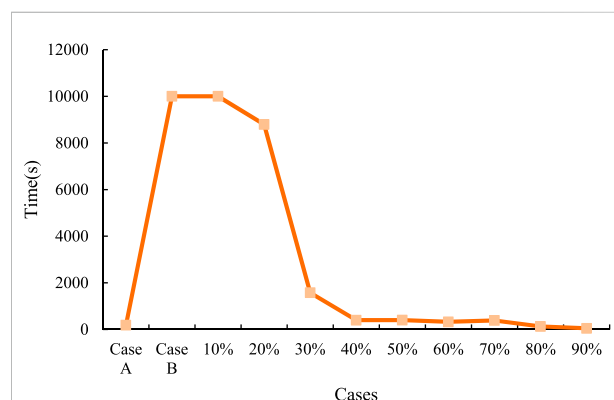
FIGURE 16
Computational time for each case.

5 Conclusion

This article proposed an MESS and ADNM coordinate dispatching model to optimize the restoration load after disasters. The ability of the MESS to move between different locations was exploited to enhance power grid resilience after natural disasters. The proposed optimization is a robust MISOCP employing binary recourse decisions, which account for the relocation of the MESS under DG and load forecast uncertainty. Results of numerical experiments reveal that the coordination of the MESS and ADNM can facilitate network restoration after natural disasters. (Chen et al., 2016).

Data availability statement

The datasets presented in this study can be found in online repositories. The names of the repository/repositories and accession number(s) can be found in the article/supplementary material.

Author contributions

YX: analysis and writing. MZ: conceptualization and review. HW: methodology, software, review, and editing. SX: methodology, analysis, and writing. YY: supervision, review, and editing.

Conflict of interest

Author MZ was employed by the State Grid Shanghai Pudong Electric Power Supply Company.

The remaining authors declare that the research was conducted in the absence of any commercial or financial relationships that could be construed as a potential conflict of interest.

Publisher's note

All claims expressed in this article are solely those of the authors and do not necessarily represent those of their affiliated organizations, or those of the publisher, the editors, and the reviewers. Any product that may be evaluated in this article, or claim that may be made by its manufacturer, is not guaranteed or endorsed by the publisher.

References

Abdeltawab, H. H., and Mohamed, Y. A. I. (2017). Mobile energy storage scheduling and operation in active distribution systems. *IEEE Trans. Ind. Electron.* 64 (9), 6828–6840. doi:10.1109/TIE.2017.2682779

Chen, X., Wu, W., and Zhang, B. (2016). Robust restoration method for active distribution networks. *IEEE Trans. Power Syst.* 31 (5), 4005–4015. doi:10.1109/TPWRS.2015.2503426

Dabbaghjamanesh, M., Senemmar, S., and Zhang, J. (2021). Resilient distribution networks considering mobile marine microgrids: A synergistic network approach. *IEEE Trans. Ind. Inf.* 17 (8), 5742–5750. doi:10.1109/TII.2020.2999326

Ding, T., Lin, Y., Li, G., and Bie, Z. (2017). A new model for resilient distribution systems by microgrids formation. *IEEE Trans. Power Syst.* 32 (5), 4145–4147. doi:10.1109/TPWRS.2017.2650779

Esfahani, M., Amjady, N., Bagheri, B., and Hatziargyriou, N. D. (2020). Robust resiliency-oriented operation of active distribution networks considering windstorms. *IEEE Trans. Power Syst.* 35 (5), 3481–3493. doi:10.1109/TPWRS.2020.2977405

Gholami, A., Shekari, T., Aminifar, F., and Shahidehpour, M. (2016). Microgrid scheduling with uncertainty: The quest for resilience. *IEEE Trans. Smart Grid* 7 (6), 2849–2858. doi:10.1109/TSG.2016.2598802

Han, C., Song, S., Yoo, Y., Lee, J., Jang, G., and Yoon, M. (2019). Optimal operation of soft-open points for high penetrated distributed generations on distribution networks. 2019 10th Int. Conf. Power Electron. ECCE Asia (ICPE 2019 - ECCE Asia), Busan, Korea, May 2019, 806–812. doi:10.23919/ICPE2019-ECCEAsia42246.2019.8796910

Huang, D., Chen, B., Huang, T., Fang, X., Zhang, H., and Cao, J. (2020). Open capacity enhancement model of medium voltage distribution network with mobile energy storage system. *IEEE Access* 8, 205061–205070. doi:10.1109/ACCESS.2020.3026417

Jiang, X., Chen, J., Zhang, W., Wu, Q., Zhang, Y., and Liu, J. (2021). Two-step optimal allocation of stationary and mobile energy storage systems in resilient distribution networks. *J. Mod. Power Syst. Clean Energy* 9 (4), 788–799. doi:10.35833/MPCE.2020.000910

Kabirifar, M., Fotuhi-Firuzabad, M., Moeini-Aghtaie, M., and Pourghaderia, N. (2019). Joint distributed generation and active distribution network expansion planning considering active management of network. 2019 27th Iran. Conf. Electr. Eng. (ICEE), Yazd, Iran, May 2019, 702–708. doi:10.1109/IranianCEE.2019.8786665

Kim, J., and Dvorkin, Y. (2019). Enhancing distribution system resilience with mobile energy storage and microgrids. *IEEE Trans. Smart Grid* 10 (5), 4996–5006. doi:10.1109/TSG.2018.2872521

Lavorato, M., Franco, J. F., Rider, M. J., and Romero, R. (2012). Imposing radiality constraints in distribution system optimization problems. *IEEE Trans. Power Syst.* 27 (1), 172–180. doi:10.1109/tpwrs.2011.2161349

Liu, X., Soh, C. B., Zhao, T., and Wang, P. (2021). Stochastic scheduling of mobile energy storage in coupled distribution and transportation networks for conversion capacity enhancement. *IEEE Trans. Smart Grid* 12 (1), 117–130. doi:10.1109/TSG.2020.3015338

Mirzaei, M. A., Hemmati, M., Zare, K., Mohammadi-Ivatloo, B., Abapour, M., Marzband, M., et al. (2020). Two-stage robust-stochastic electricity market clearing considering mobile energy storage in rail transportation. *IEEE Access* 8, 121780–121794. doi:10.1109/ACCESS.2020.3005294

Peng, H., Wei, N., Li, S., Wang, X., Li, H., and Hu, Y. (2020)., Continuous power flow for hybrid AC/DC microgrid considering uncertainty of intermittent DG output. *IET.Conf. Proc.*, 16th IET Int. Conf. AC D.C. Power Transm, ACDC. London, England: Institution of Engineering and Technology (IET) 2020 (1), 251–258. July 2-3, 2020. doi:10.1049/icp.2020.0108

Prabawa, P., and Choi, D. (2020). Multi-agent framework for service restoration in distribution systems with distributed generators and static/mobile energy storage systems. *IEEE Access* 8, 51736–51752. doi:10.1109/ACCESS.2020.2980544

Salimi, M., Nasr, M. A., Hosseinian, S. H., Gharehpetian, G. B., and Shahidehpour, M. (2020). Information gap decision theory-based active distribution system planning for resilience enhancement. *IEEE Trans. Smart Grid* 11 (5), 4390–4402. doi:10.1109/TSG.2020.2992642

Sekhavatmanesh, H., and Cherkaoui, R. (2020). A multi-step reconfiguration model for active distribution network restoration integrating DG start-up sequences. *IEEE Trans. Sustain. Energy* 11 (4), 2879–2888. doi:10.1109/TSTE.2020.2980890

Wang, S., Chen, S., Ge, L., and Wu, L. (2016). Distributed generation hosting capacity evaluation for distribution systems considering the robust optimal operation of OLTC and SVC. *IEEE Trans. Sustain. Energy* 7 (3), 1111–1123. doi:10.1109/TSTE.2016.2529627

Wang, W., Xiong, X., He, Y., Hu, J., and Chen, H. (2022). Scheduling of separable mobile energy storage systems with mobile generators and fuel tankers to boost distribution system resilience. *IEEE Trans. Smart Grid* 13 (1), 443–457. doi:10.1109/TSG.2021.3114303

Yao, S., Wang, P., Liu, X., Zhang, H., and Zhao, T. (2020). Rolling optimization of mobile energy storage fleets for resilient service restoration. *IEEE Trans. Smart Grid* 11 (2), 1030–1043. doi:10.1109/TSG.2019.2930012

Nomenclature

Indices and sets

Ψ_N Set of all buses

Ψ_E Set of all branches

Ψ_T Set of time intervals

Ψ_{DG} Set of DG buses

Ψ_{SVC} Set of SVC buses

Ψ_{MESS} Set of mobile energy storage fleets

Scalars and parameters

M A large constant in the Big-M method

r_{ij}, x_{ij} Resistance and reactance of branch ij

$S_{ij}^{\max}$, $S_i^{DG,\max}$ Capacity of branch ij and DG at bus i

$station_{m,i}^{ini}$ Initial parking station i of MESS m

$\overline{SOC_{i,t}}$ $\underline{SOC_{i,t}}$ Maximum and minimum state of charge of stationary energy storage i

$\overline{SOC_i^{MESF}}$, $\underline{SOC_i^{MESF}}$ Maximum and minimum state of charge of mobile energy storage i

$\overline{Travel}$ Maximum traveling frequency of MESS

$P_{i,t}^{DG}$, $Q_{i,t}^{DG}$ Forecasted active and reactive DG output at bus i at time t

$P_{i,t}^L$, $Q_{i,t}^L$ Forecasted load demand of bus i at time t

$\Delta P_{i,t}^{DG}$, $\Delta P_{i,t}^L$ DG and load forecast error of DG/bus i at time t

$\underline{Q_i^{SVC}}$, $\overline{Q_i^{SVC}}$ Minimum/maximum reactive power of SVC i

$\overline{V_i}$, $\underline{V_i}$ Maximum/minimum voltage magnitude at bus i

Ω_{DG}, Ω_L Budget level of DG/load forecast uncertainty

Variables

b_i, c_{ij} Binary status of bus i and branch ij: 0 for disconnected and 1 for connected

$u_{i,t}^{char}$, $u_{i,t}^{dis}$ Binary status of charging or discharging of stationary energy storage i at time t

n^{MG} Number of microgrids, integer variable

H_i Power supplied by bus i in fictitious network

F_{ij} Power flow in fictitious network associated to branch ij

$P_{i,t}^{DG}$, $Q_{i,t}^{DG}$ Active/reactive power output of DG unit at bus i at time t

$P_{ij,t}$, $Q_{ij,t}$ Active/reactive power in line ij at time t

$P_{i,t}$, $Q_{i,t}$ Active/reactive power injection of bus i at time t

$Q_{i,t}^{SVC}$ Reactive power output of SVC i at time t

$SOC_{i,t}^{MESF}$ State of charge of mobile energy storage i at time t

$SOC_{i,t}$ State of charge of energy storage system i at time t

$st_{m,t}^{MESS}$, $sp_{m,t}^{MESS}$ Start and stop traveling indictors, respectively, of MESS fleets m at time t

$st_{i,t}^{DR}$, $sp_{i,t}^{DR}$ Start and stop demand response indictors, respectively, of load at node i at time t

$V_{i,t}$ Voltage magnitude of bus i at time t

$U_{i,t}$ Squared voltage magnitude of bus i at time t

$u_{i,t}^{DR}$ Demand response scheduling indictor of load at node i at time t

$\omega_{m,t}$ Traveling state of MESS m at each time period t

$z_{m,i,t}$ Position indictor of MESS m at each time period t at bus i

Hosting capacity of distributed generation based on holomorphic embedding method in distribution networks

Jiarui Xie, Fei Tang*, Junfeng Qi, Xinang Li, Zhiyuan Lin, Zhuo Liu and Yuhan Guo

School of Electrical Engineering and Automation, Wuhan University, Wuhan, China

Considering the voltage rise problem caused by integrating large-scale distributed generation into the distribution networks, a distributed generation hosting capacity assessment method based on the improved holomorphic embedding method is proposed. First, the relationship between distributed generator penetration and voltage at the access point is explored and voltage violation is used as a constraint to solve the hosting capacity. Secondly, a self-defined directional holomorphic embedding method is proposed based on the classical model, further, the safety region under voltage constraints is derived. The intersection of the bus trajectory with the boundary of the voltage constraint region is used as the criterion for judging the maximum hosting capacity of distributed generation under a single access scenario. Then, a sufficient number of distributed generation access scenarios are generated using Monte Carlo, and the proposed criterion is used to solve the hosting capacity under each scenario. The cumulative distribution curve is obtained by statistically solving admission capacity data, which can represent the relationship between the level of voltage violation risk and the hosting capacity of distributed generation. The validity and correctness of the proposed method are verified on the IEEE 22-bus distribution network.

1 Introduction

Under the severe form of global energy transformation and global fossil energy depletion, distributed generation (DG) is widely connected to the distribution network due to its high utilization efficiency and low negative environmental impact. With the increasing penetration rate of DG, the radial single-way distribution network will be

Abbreviations: DG, distributed generation; HEM, holomorphic embedding method; EIMM, embedded impedance mode margin; PDF, probability density function; CDF, cumulative distribution function; PF, power factor; HC, hosting capacity.

transformed into a complex network with dense distribution and user interconnection. This change will inevitably have a negative impact on the line loss, power quality, and operational stability of the distribution network, voltage violation is particularly evident among them. (Dong et al., 2019). Therefore, analyzing and evaluating the DG hosting capacity of distribution networks considering voltage violation is of great practical significance.

At present, domestic and foreign scholars are rich in technical research on DG access to distribution networks (Keane et al., 2013; Mahmud et al., 2014), and also pay more attention to the voltage violation problem (Shayani et al., 2011; Yuan et al., 2020) caused by DG access to distribution networks, and start to try different new methods for research and solution. The holomorphic embedding method (HEM) (Trias 2012) is a power flow calculation method proposed by Antonio Trias, a Spanish scholar, in 2012, which is different from the conventional iterative idea. The characteristics of this method can be summarized as three points: 1) non-iterative, the solution process is a recursive process rather than iterative, avoiding the situation that the power flow does not converge due to the convergence of the algorithm; 2) unique initial values, unlike the conventional iterative method that requires setting appropriate initial values, a set of holomorphic embedding equations has definite and unique initial values; 3) deterministic, when the power flow solution exists, the correct solution can be obtained, and when the power flow has no solution, a clear signal of voltage collapse can be given.

Recently, the HEM has been gradually attached to scholars and applied to the field of power system voltage stability analysis (Singh and Tiwari, 2020; Gao et al., 2021; Lai et al., 2022). The calculation of voltage collapse points using HEM has a significant advantage over the continuous power flow since the method requires only one calculation to obtain the results (Yang, 2015; Du et al., 2021). The visualized *Sigma* index (Trias 2014) based on the HEM is proposed to determine the margin of buses from the instability boundary. Still, the imaginary part of the bus voltage is strongly correlated with the position of *Sigma*, so it cannot determine the margin by relying on the distance of the *Sigma* index to the boundary. Further, the concept of *Sigma* trajectory (Lai et al., 2021; Liu et al., 2022) is proposed, which determines the weak voltage buses in the order in which the *Sigma* trajectory touches the boundary, and the method achieves this purpose accurately. All the above studies adopt the scalable holomorphic embedding model, which is only applicable to the scenario where the system load and the active output of the generator are scaled in the same proportion, so it is not easy to be applied to the analysis of distributed generation hosting capacity.

The research methods for DG hosting capacity are mainly divided into analytical methods, intelligent optimization methods, and stochastic scenario simulation methods (Dong et al., 2019). The analytical method can generally be translated into solving optimal power flow problem, usually using methods such as second-order cone programming (Xing et al., 2016) to convert some of the

nonlinear constraints into linear constraints to speed up the solution of DG hosting capacity. The intelligent optimization algorithm (Sun et al., 2015; Rabiee and Seyed, 2017; Zhou et al., 2017) is more convenient for obtaining the optimal global solution, so it is mostly used for solving more complex multi-objective optimization models. The rapid solution process is the advantage of the analytical method and the intelligent optimization algorithm. However, the results obtained characterize the optimal configuration of the model and are often more optimistic than the actual distribution network's hosting capacity (Jin et al., 2022). The stochastic scenario simulation method (Zhao et al., 2015; Liu et al., 2022) refers to the calculation and statistics of the hosting capacity of the randomly generated DG access scenarios under certain constraints, which can be more accurate in terms of the actual hosting capacity. Yet, it is computationally laborious, as follows: 1) a sufficient number of scenarios need to be calculated to ensure the credibility of the results; 2) when calculating the hosting capacity of a specific scenario, multiple cycles of judgment are required, which is time-consuming.

In summary, this paper constructs an analysis process based on the HEM for the DG hosting capacity of the distribution network, which can balance the assessment accuracy and computational complexity. The specific steps are as follows: first, the relationship between DG penetration rate and voltage at the access point is analyzed, and it is clear that voltage violation is the critical factor limiting DG access to the distribution network. Then, to address the limitations of the existing HEM, the traditional model is improved into a self-defined directional holomorphic embedding model so that it can be used for DG hosting capacity analysis. A voltage constrained region based on the *Sigma* index is derived, and the bus *Sigma* trajectory intersecting with the region boundary is used as the criterion for the maximum DG hosting capacity, which can realize the solution process of a single access scenario view. At the same time, the embedded impedance mode margin index is proposed to quantify the static voltage stability of buses, and the weak buses of the system are removed according to this index to narrow the range of DG alternative sets, which can reduce the computational effort brought by the random scenario simulation method. Finally, Monte Carlo is used to simulating mutually independent DG access scenarios in the alternative set, and the proposed criterion is used to solve the DG hosting capacity under each scenario. The cumulative distribution function based on the voltage violation risk is statistically obtained, which reflects the relationship between the voltage violation risk and DG hosting capacity.

The rest of this paper is organized as follows: Section 2 analyzes the mechanism of voltage rise at the access point due to DG access. Section 3 describes the improved HEM and the criterion for determining the maximum DG hosting capacity based on the voltage constraint region. Section 4 describes the DG hosting capacity calculation process, considering the risk of voltage violation. Section 5 simulates the IEEE 22-bus distribution network system and analyzes the effects of the

FIGURE 1
DG access distribution network diagram.

FIGURE 2
Access point voltage vector diagram.
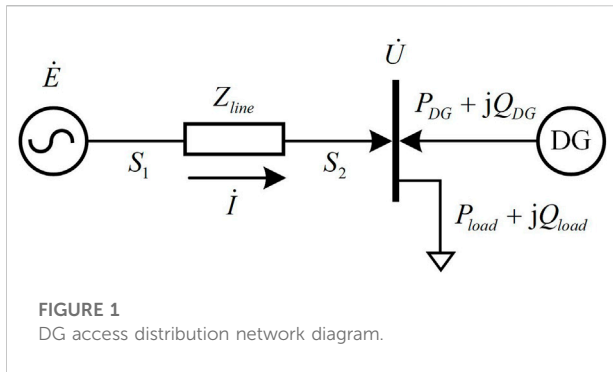
number of DG accesses and power factor on the hosting capacity. Finally, Section 6 summarizes the main conclusions.

2 Effect of DG access on voltage

The low-voltage distribution network typically has a radial structure, and when DG is connected to the distribution network, its operation will directly affect the voltage at the access point. Figure 1 is a simplified topology diagram of DG connection to the distribution network, where E is the generator voltage, U is the voltage at the DG connection point, I is the line current, $P_{\text{load}} + jQ_{\text{load}}$ is the load, $P_{\text{DG}} + jQ_{\text{DG}}$ is the DG injected power, S_1 is the generator output power, S_2 is the total power at the DG connection point, and Z_{line} is the line impedance. Write the voltage balance equation for this topology column, as shown in Equation 1:

$$\dot{U} = \dot{E} - \dot{I}Z_{line} = \dot{E} - \left(\frac{S_1}{\dot{E}}\right)^* Z_{line}. \tag{1}$$

Since the losses of the distribution network mainly come from the distribution transformers, where the line losses account for a relatively small percentage (Ding et al., 2000), compared to the load power and the DG injection power can be neglected, this paper makes $S_1 = S_2$ and the load has the same reactive power/active power λ as DG.

$$
\begin{aligned}
\dot{U} &= \dot{E} - \frac{(P_{load} - P_{DG}) - j(Q_{load} - Q_{DG})}{\dot{E}^*}Z_{line} \\
&= \dot{E} - \frac{(P_{load} - P_{DG})(1 - j\lambda)}{\dot{E}^*}Z_{line}
\end{aligned}. \tag{2}
$$

From Equation 2, it can be seen that as the DG injected power gradually increases, the current amplitude of the line will gradually decrease to zero and then increase in reverse. As shown in Figure 2, with the increase of DG penetration, the line current decreases from I_1 to I_2 and then increases to I_3 in the reverse direction, and the voltage amplitude of DG connection
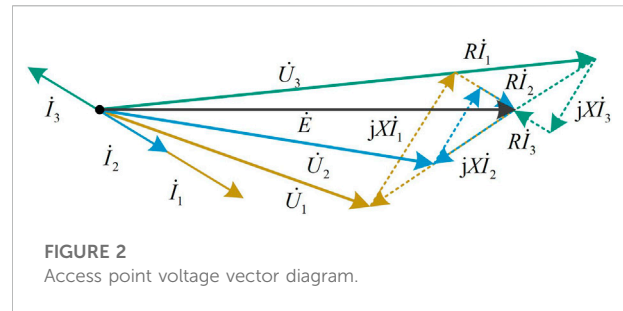
point corresponding to different currents is $U_1 < U_2 < U_3$. Even the voltage at the access point is higher than the generator voltage under the action of reverse current.

As such, the above analysis determines that DGs access to the distribution networks lead to a voltage rise at the connection point, and the voltage amplitude positively correlates with the DG penetration rate. This phenomenon may lead to voltage violation at the connection point, so voltage violation will be a crucial factor limiting DG hosting capacity.

3 Self-defined directional HEM and voltage constraint region

3.1 Definition and properties of holomorphic functions

A function $f(z) = u\ (x,y) + iv\ (x,y)$ is claimed to be holomorphic in region D if $f(z)$ is differentiable at every point in the region **D**. Another equivalent condition for a function to satisfy holomorphic in region **D** is the existence of continuous partial derivatives of $u = u\ (x,y)$ and $v = v\ (x,y)$ at every point in the region **D** and the satisfaction of the *Cauchy-Riemann* condition, As shown in Equation 3:

$$\frac{\partial u}{\partial x} = \frac{\partial v}{\partial y}, \frac{\partial u}{\partial y} = -\frac{\partial v}{\partial x}. \tag{3}$$

An essential property of the holomorphic function is that $f(z)$ can be expanded into a power series in some domain at any point in **D**, as shown in Equation 4:

$$f(z) = \sum_{n=0}^{\infty} f[n]z^n, z \subset \mathbf{D}. \tag{4}$$

3.2 Self-defined directional holomorphic embedding model

For the conventional HEM, it is correct only for a particular operating state of the network and cannot scale the network

generator output and load level. For the scalable HEM, all generator active power outputs and load levels can only be scaled in proportion to the embedding factor s. However, for non-global scaling scenarios (i.e., some buses are scaled and some buses are fixed) neither of the above two models is applicable. In this section, the holomorphic embedding model is improved so that the scaling direction of the improved model can be self-defined. This creates the conditions for using the HEM to analyze DG hosting capacity issues.

$$
\begin{cases}
\sum_{k=1}^{N} Y_{ik} V_k(s) = \dfrac{S_i^* + s\Delta S_i^*}{V_i^*(s^*)}, i \in \text{PQ} \\
V_i(s) = V_i^{sp}, i \in \text{slack} \\
\sum_{k=1}^{N} Y_{ik} V_k(s) = \dfrac{\left(P_{gi} - P_{li} + jQ_{gi}(s) - jQ_{li}\right)^* + s\left(\Delta P_{gi} - \Delta P_{li} - j\Delta Q_{li}\right)^*}{V_i^*(s^*)}, i \in \text{PV} \\
V_i(s)^* V_i^*(s^*) = |V_i^{sp}|^2, i \in \text{PV}
\end{cases}
\tag{5}
$$

The set of holomorphic embedding equations in the self-defined direction is shown in Equation 5, where Y_{ik} is the element at (i,k) in the bus derivative matrix, $S_i=P_{li}+jQ_{li}$ is the load complex power at bus i, V_i^{sp} is the voltage set at the slack and PV buses, P_{gi} is the active power emitted by the generator at bus i, P_{li} is the load active power at bus i, and Q_{li} is the load reactive power at bus i. ΔS_i is the scaling unit for load at PQ bus i. ΔP_{gi}, ΔP_{li} and ΔQ_{li} are the generator active power scaling unit, load active power scaling unit, and load reactive power scaling unit at PV bus, respectively. All the above power scaling units can be self-defined.

$V_i(s)$, and $Q_{gi}(s)$ are holomorphic functions of voltage and reactive power concerning the embedding factor s, which can be uniquely expanded to the Maclaurin series, as shown in Equation 6:

$$
\begin{cases}
V(s) = \sum_{n=0}^{\infty} V[n](s)^n \\
Q(s) = \sum_{n=0}^{\infty} Q[n](s)^n
\end{cases}
,
\tag{6}
$$

Where $V[n]$ and $Q[n]$ are both coefficients of the series, the voltage in the Cartesian axes is represented by a complex number, so the voltage coefficient $V[n]$ is complex number, and the generator's reactive power output is real number, so the reactive power coefficient $Q[n]$ is real number. The analytical expressions for the voltage and reactive power output concerning the embedding factor s are obtained by bringing the two functions into the power flow equations to solve the coefficients.

3.3 Model recursion process and solution

For simplicity of expression, define the inverse function of voltage $W_i(s)$. The inverse function satisfies the requirements of Equation 7.

$$
V_i(s)W_i(s) = 1.
\tag{7}
$$

Expanding the voltage function and the voltage inverse function in Equation 7 into the series form:

$$
\begin{aligned}
(V_i[0] &+ V_i[1]s + \cdots + V_i[n]s^n) \bullet (W_i[0] + W_i[1]s + \cdots \\
&+ W_i[n]s^n) \\
&= 1.
\end{aligned}
\tag{8}
$$

Rectifying Equation 8 to obtain the recursive equation:

$$
\begin{cases}
V_i[0]W_i[n] + V_i[n]W_i[0] = 1, n = 0 \\
V_i[0]W_i[n] + V_i[n]W_i[0] = -\sum_{\tau=1}^{n-1} W_i[\tau]V_i[n-\tau], n \geq 1
\end{cases}
.
\tag{9}
$$

The recursive equation for the PQ bus is shown in Equation 10:

$$
\sum_{k=1}^{N} Y_{ik} V_k[n] - S_i^* W_i^*[n] = \Delta S_i^* W_i^*[n-1], n \geq 1.
\tag{10}
$$

The recursive equation for the slack bus is represented by Equation 11:

$$
\begin{cases}
V_i[n] = V_i^{sp}, n = 0 \\
V_i[n] = 0, n \geq 1
\end{cases}
.
\tag{11}
$$

For the PV bus, the recursive equation can be expressed as Equation 12:

$$
\begin{aligned}
\sum_{k=1}^{N} &Y_{ik} V_k[n] - \left(P_i + jQ_{li}\right)W_i^*[n] + jQ_{gi}[n]W_i^*[0] + jQ_{gi}[0]W_i^*[n] \\
&= \left(\Delta P_i + j\Delta Q_{li}\right)W_i^*[n-1] - j\left(\sum_{\tau=1}^{n-1} Q_{gi}[\tau]W_i^*[n-\tau]\right), n \geq 1
\end{aligned}
,
\tag{12}
$$

where $P_i = P_{gi} - P_{li}$ and $\Delta P_i = \Delta P_{gi} - \Delta P_{li}$.

$$
\begin{cases}
V_i[0]V_i^*[n] + V_i[n]V_i^*[0] = |V_i^{sp}|^2, n = 0 \\
\Re(V_i[0])\Re(V_i^*[n]) + \Im(V_i[n])\Im(V_i^*[0]) = -\dfrac{1}{2}\sum_{\tau=1}^{n-1} V_i[\tau]V_i^*[n-\tau], n \geq 1
\end{cases}
,
\tag{13}
$$

where $\Re$ denotes taking the real part and $\Im$ denotes taking the imaginary part.

The real and imaginary parts of Equations 9–13 are separated and written in the form of matrices. The left-hand side coefficient matrix is known and the right-hand side matrix can be solved recursively. Furthermore, $V_i[n]$, $W_i[n]$, and $Q_{gi}[n]$ can be obtained by solving the set of linear equations.

The germ (Du et al., 2021) of self-defined directional HEM does not have the same meaning as the germ of the scalable HEM. The physical meaning of the germ of the scalable model represents the system state with no load and no generator, but the germ of the self-defined directional model represents the state with rated load and generator output. The germ $V_i[0]$, $W_i[0]$,

FIGURE 3
Simplified diagram of two bus system.

FIGURE 4
System instability boundary and voltage constraint region.
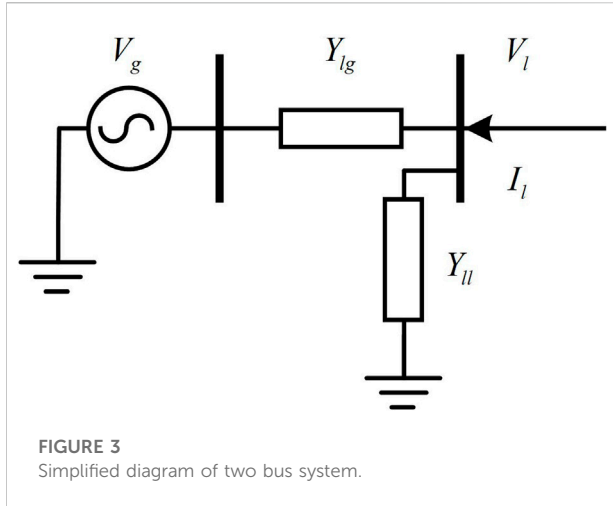
and Q_{gi} [0] of the improved model can be derived from the traditional power flow methods or the conventional HEM.

3.4 Voltage constrained region based on HEM

Write the current balance equation for the two-bus system in Figure 3, as shown in Equation 14:

$$Y_{lg}\left(V_g - V_l\right) + Y_{ll}V_l = I_l, \tag{14}$$

$$V_l = \frac{Y_{lg}}{Y_{lg} + Y_{ll}}V_g + \frac{I_l}{Y_{lg} + Y_{ll}} = V_{eq} + \frac{I_l}{Y_L}, \tag{15}$$

Where $V_{eq} = Y_{lg}V_g/(Y_{lg} + Y_{ll})$, $Y_L = Y_{lg} + Y_{ll}$.

Furthermore, the bus voltage is normalized and expressed by Equation 16:

$$U = 1 + \frac{S_l^*}{Y_L V_l^* V_{eq}\frac{V_{eq}^*}{V_{eq}^*}} = 1 + \frac{\sigma}{U^*}, \tag{16}$$

Where: $U = V_l/V_{eq}$, defined as the normalized voltage, $S_l = V_l I_l^*$ is the load power. $\sigma = S_l^*/(Y_L|V_{eq}|^2)$, defined as the *Sigma* index, which is a complex index that can reflect the system's static voltage stability margin.

Next, separating the imaginary and real parts of Equation 16 can be obtained as Equation 17:

$$\begin{cases} |U|^2 = \Re(U) + \Re(\sigma) \\ \Im(U) = \Im(\sigma) \end{cases}. \tag{17}$$

After squaring the upper and lower equations of Equation 24 and adding them together, it equals:

$$F\left(|U|^2\right) = |U|^4 - [1 + 2\Re(\sigma)]|U|^2 + |\sigma|^2. \tag{18}$$

From Equation 18, $F\left(|U|^2\right)$ is a parabola with an opening upward and the coordinate of the vertex d is $(\Re(\sigma)+0.5, \Im(\sigma)$
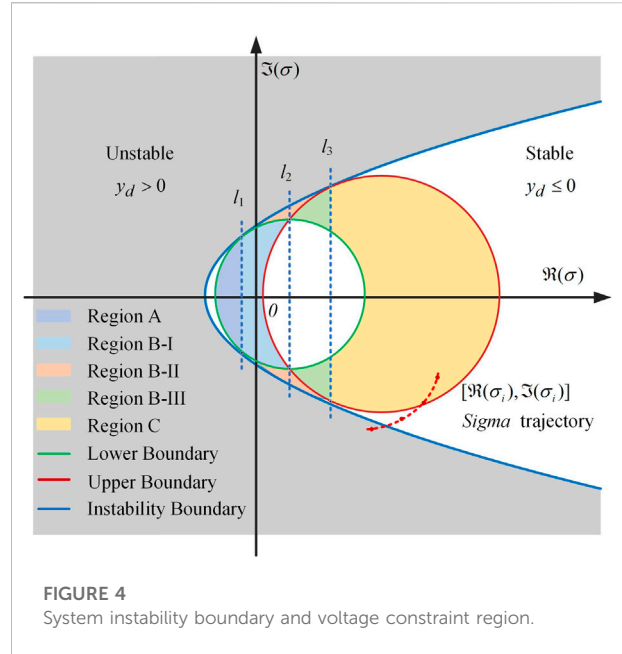
$^2 - \Re(\sigma) - 0.25)$. If the equation is solvable, it must satisfy that the vertex vertical coordinate is less than or equal to zero (i.e., $y_d = \Im(\sigma)^2 - \Re(\sigma) - 0.25 \le 0$). Therefore, the boundary that makes the equation solvable can be drawn on the *Sigma* plane, defined as the system's instability boundary, as shown by the blue parabola in Figure 4. If the *Sigma* index of the bus is always inside the parabola means that the system is stable; if it is on the parabola, the system is in a state of critical instability; if it is outside the parabola means that the system is unstable.

Further, if the solution of the equation is required to be a fixed value R, it means:
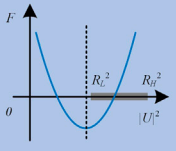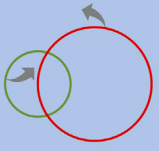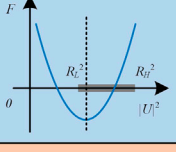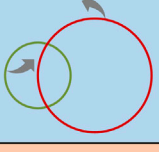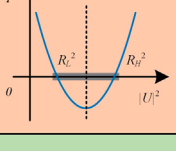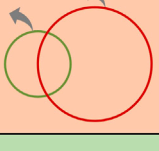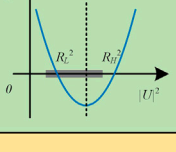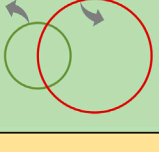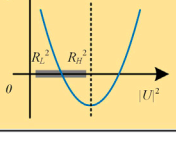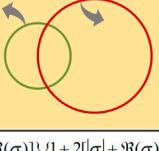
$$|U|^2 = \frac{[1 + 2\Re(\sigma)]}{2} \pm \frac{1}{2}\sqrt{\{1 - 2[|\sigma| - \Re(\sigma)\}\{1 + 2[|\sigma| + \Re(\sigma)]\}}$$
$$= R^2. \tag{19}$$

Simplify and organize equation (19) to obtain equation (20):

$$[\Re(\sigma) - R^2]^2 + \Im(\sigma)^2 = R^2. \tag{20}$$

It can be observed that Equation 20 is a circle with a center of $(R^2, 0)$ and a radius of R. The bus normalized voltages' amplitudes corresponding to the circle trajectory points are all equal to R.

If the restriction on the solution of the equation is weakened to allow the amplitude of the normalized bus voltage to vary in some range, $R_L^2 \le |U|^2 \le R_H^2$. Then the voltage amplitude is satisfied when the bus *Sigma* index varies within the colored region (including region A, region B-I, region B-II, region B-III, and region C) in Figure 4, where the colored region is defined as the voltage constraint region.

Symmetric axis position	Location of high and low voltage solutions		Corresponding regions	
	Mathematical expression	Image expression	Mathematical expression	Image expression
$\dfrac{1+2\Re(\sigma)}{2} < R_L^2$	$\begin{cases} \dfrac{[1+2\Re(\sigma)]}{2} + \dfrac{1}{2}\sqrt{\Delta} > R_L^2 \\ \dfrac{[1+2\Re(\sigma)]}{2} + \dfrac{1}{2}\sqrt{\Delta} < R_H^2 \end{cases}$		$\begin{cases} [\Re(\sigma)-R_L^2]^2 + \Im(\sigma) < R_L^2 \\ [\Re(\sigma)-R_H^2]^2 + \Im(\sigma) > R_H^2 \end{cases}$	
$R_L^2 \le \dfrac{1+2\Re(\sigma)}{2} \le R_H^2$	$\begin{cases} \dfrac{[1+2\Re(\sigma)]}{2} - \dfrac{1}{2}\sqrt{\Delta} \le R_L^2 \\ \dfrac{[1+2\Re(\sigma)]}{2} + \dfrac{1}{2}\sqrt{\Delta} \le R_H^2 \end{cases}$		$\begin{cases} [\Re(\sigma)-R_L^2]^2 + \Im(\sigma) \le R_L^2 \\ [\Re(\sigma)-R_H^2]^2 + \Im(\sigma) \ge R_H^2 \end{cases}$	
	$\begin{cases} \dfrac{[1+2\Re(\sigma)]}{2} - \dfrac{1}{2}\sqrt{\Delta} \ge R_L^2 \\ \dfrac{[1+2\Re(\sigma)]}{2} + \dfrac{1}{2}\sqrt{\Delta} \le R_H^2 \end{cases}$		$\begin{cases} [\Re(\sigma)-R_L^2]^2 + \Im(\sigma) \ge R_L^2 \\ [\Re(\sigma)-R_H^2]^2 + \Im(\sigma) \ge R_H^2 \end{cases}$	
	$\begin{cases} \dfrac{[1+2\Re(\sigma)]}{2} - \dfrac{1}{2}\sqrt{\Delta} \ge R_L^2 \\ \dfrac{[1+2\Re(\sigma)]}{2} + \dfrac{1}{2}\sqrt{\Delta} \ge R_H^2 \end{cases}$		$\begin{cases} [\Re(\sigma)-R_L^2]^2 + \Im(\sigma) \ge R_L^2 \\ [\Re(\sigma)-R_H^2]^2 + \Im(\sigma) \le R_H^2 \end{cases}$	
$\dfrac{1+2\Re(\sigma)}{2} > R_H^2$	$\begin{cases} \dfrac{[1+2\Re(\sigma)]}{2} - \dfrac{1}{2}\sqrt{\Delta} > R_L^2 \\ \dfrac{[1+2\Re(\sigma)]}{2} - \dfrac{1}{2}\sqrt{\Delta} < R_H^2 \end{cases}$		$\begin{cases} [\Re(\sigma)-R_L^2]^2 + \Im(\sigma) > R_L^2 \\ [\Re(\sigma)-R_H^2]^2 + \Im(\sigma) < R_H^2 \end{cases}$	

Note: $\Delta = \{1-2[|\sigma|-\Re(\sigma)]\}\{1+2[|\sigma|+\Re(\sigma)]\}$

FIGURE 5
Voltage constraint region partitioning proof.

We illustrate Figure 4 with some details. It is not difficult to prove that both the upper and lower boundary circle trajectories are tangent to the instability boundary, and the horizontal coordinates of Qureshi et al., 2020, Ballanti and Ochoa, 2015, Navarro and Navarro, 2017 Chen et al., 2017 Abad et al., 2018 Kulmala et al., 2017 Torquato et al., 2018 the intersection point with the boundary of the lower boundary are R_L^2-0.5, and the horizontal coordinates of the intersection point with the boundary of the upper boundary are R_H^2-0.5, which exactly correspond to the conditions of Scenario 1 and Scenario 3, and the regional divider l_1: $\Re(\sigma) = R_L^2-0.5$, l_3: $\Re(\sigma) = R_H^2-0.5$. In addition, the upper boundary circle and the lower boundary circle have two intersection points with the transverse coordinates of 0.5 $(R_L^2+R_H^2-1)$, at which time the symmetry axis of $F(|U|^2)$ is located at the midpoint of R_L^2 and R_H^2, and the low voltage solution is exactly equal to R_L^2 and the high voltage

solution is exactly equal to R_H^2. The detailed partitioning of the constraint region and the proof process are shown in Figure 5.

In the evaluation of the admittance capacity, we need to continuously input DG power into the network and observe when the system crosses the voltage limit. The *Sigma* index is a description of a certain state of the system, but we need to continuously obtain the *Sigma* indexes of different states of the system, and the curve they connect to form is called the *Sigma* trajectory $\sigma_i(s)$. The way $\sigma_i(s)$ is embedded and solved is shown below.

Solving the *Sigma* index with HEM requires performing the embedding factor *s* into the *Sigma* index and the normalized voltage of Equation 16:

$$U(s) = 1 + \frac{\sigma(s)}{U^*(s^*)}. \tag{21}$$

From the properties of holomorphic functions, it follows that the *Sigma* function can be expressed in power series form as:

$$\sigma(s) = \sum_{n=0}^{\infty} \sigma[n](s)^n. \tag{22}$$

Based on the equality of the power series coefficients on both sides of the equation, it is deduced that:

$$\begin{cases} \sigma[0] = U[0]U^*[0] - U^*[0] \\ \sigma[n] = \sum_{\tau=0}^{n} U[\tau]U^*[n-\tau] - U^*[n] \end{cases}. \tag{23}$$

All coefficients of the series $\sigma[n]$ can be calculated according to Equation 23, which means that the condition for plotting the *Sigma* trajectory is available. In this paper, the intersection of the bus *Sigma* trajectory with the boundary of the voltage constraint region is used as the criterion for determining the maximum hosting capacity of DG. When the *Sigma* Shayani and Oliveira, 2011 Yang, 2015 Liu et al., 2020 Wang et al., 2016 Qureshi et al., 2021 Tang and Chang, 2018 Varma and Singh, 2020trajectory intersects the boundary of the set voltage constraint region for the first time means that the system has voltage violation, by recording the embedding factor s at this point, we can calculate the DG hosting capacity for the current access scenario.

4 DG hosting capacity calculation method

When using the stochastic scenario simulation method for DG hosting capacity analysis, a specified number of access locations (n) in the DG alternative set (m) need to be selected for the hosting capacity operation, and a total of C_m^n access scenarios are generated. If the locations unsuitable for accessing DGs can be removed in advance to reduce the number of DG alternative locations (m), the number of DG access schemes generated can be significantly reduced, and ultimately the overall computation can be reduced. Therefore, this paper proposes the embedded impedance mode margin index (EIMM) to judge each bus's static voltage stability margin, which is used to eliminate weak buses and reduce the number of DG alternative positions.

4.1 Derivation and solution of EIMM index

From the circuit principle, it is clear that for a linear circuit containing a constant voltage source, internal resistance, and load resistance, the maximum transmitted power can be obtained when the load resistance is equal to the internal resistance of the power source. Research (Li et al., 2014) extends the above conclusions on maximum power transfer strictly to non-analytic complex variable systems. The necessary condition for obtaining the maximum value of active power at the load bus in a non-analytic complex power system is that the system dynamic equivalent impedance amplitude is equal to the load static equivalent impedance.

The integrated dynamic impedance is defined as the slope of the voltage concerning the current curve, but since the bus voltage is not a complex analytic function of the load current in a non-analytic complex system (Li et al., 2014), finding the dynamic equivalent impedance of the system requires the injected power as a covariate and then the derivative of the complex function, as shown in Equation 24:

$$-\frac{\frac{dV}{ds}}{\frac{dI}{ds}} = -\frac{dV}{dI} = Z_{THEV}. \tag{24}$$

From the maximum transmission power theorem, it can be obtained that if the system satisfies the maximum power transmission condition, the load bus is in a critical state of static voltage stability. From this, the embedded impedance mode margin index can be defined as follows:

$$\mu(s) = \frac{|Z_{LD}(s)| - |Z_{THEV}(s)|}{|Z_{LD}(s)|}, \tag{25}$$

where different values of s represent different system states, and $s = 1$ represents the rated state system.

$\mu(s)$ represents the system's distance from the maximum transmission power condition. The value of $\mu(s)$ ranges from 0 to 1, and the larger the value, the more stable the current system state is. $\mu(s) = 0$ means the system is at the static voltage stability boundary, and $\mu(s) < 0$ means the system is destabilized. After bringing in different s-values according to the demand, the EIMM index of the bus with load can be acquired, and the ranking of the strength of the static voltage stability of the system buses in different operating states can be obtained.

To obtain the expression for $Z_{iTHEV}(s)$, the analytical expression for the bus voltage $V_i(s)$ is first derived concerning the embedding factor s as follows:

$$dV_i/ds = V_i[1] + 2V_i[2]s + \cdots + nV_i[n]s^{n-1}. \tag{26}$$

The relationship between voltage and current is shown in Equation 27 below:

$$\boldsymbol{I} = \boldsymbol{Y}\boldsymbol{V}, \tag{27}$$

where $\boldsymbol{I} = [I_1, I_2, \cdots, I_n]$ and $\boldsymbol{V} = [V_1, V_2, \cdots, V_n]$.

The analytic expression of the current concerning the embedding factor s is equal to:

$$I_i(s) = \sum_{k=1}^{N} Y_{ik} V_k(s). \tag{28}$$

The analytic expression of the current $I_i(s)$ is derived concerning the embedding factor s:
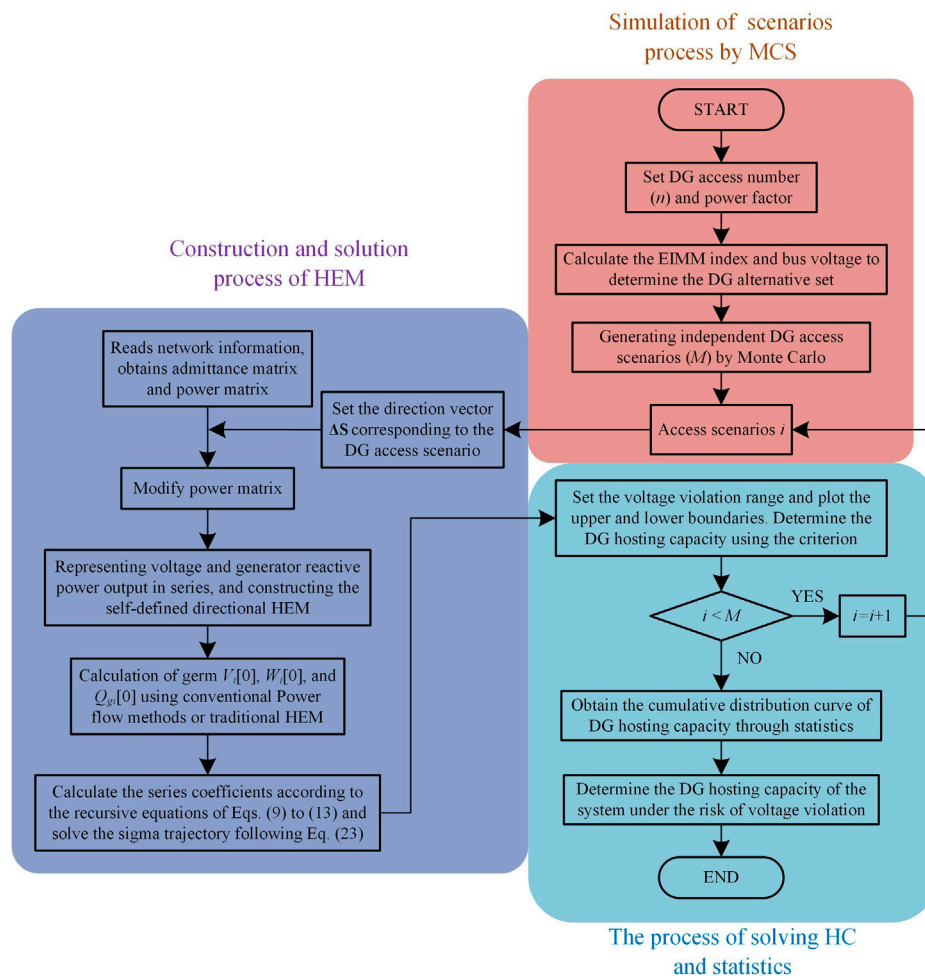
FIGURE 6
Flow chart of DG hosting capacity assessment of distribution network.

$$dI_i(s)/ds = \sum_{k=1}^{N} Y_{ik}(dV_k(s)/ds). \qquad (29)$$

The integrated dynamic equivalent impedance at bus i is equal to:

$$Z_{iTHEV}(s) = -\frac{dV_i(s)/ds}{dI_i(s)/ds}$$

$$= -\frac{V_i[1] + 2V_i[2]s + \cdots + nV_i[n]s^{n-1}}{\sum_{k=1}^{N} Y_{ik}(V_i[1] + 2V_i[2]s + \cdots + nV_i[n]s^{n-1})}. \qquad (30)$$

The static equivalent impedance of the load at bus i is expressed as follows:

$$Z_{iLD}(s) = \frac{V_i(s)}{I_i(s)}. \qquad (31)$$

The embedded impedance mode margin $\mu_i(s)$ of each bus is obtained by bringing Equation 30 and Equation 31 into Equation 25.

4.2 DG hosting capacity considering voltage violation risk

This paper applies the stochastic scenario simulation method to solve the DG hosting capacity under the risk of voltage violation. The flow chart is shown in Figure 6 and the specific steps are described as follows:

1) The bus strength is evaluated using the EIMM index, and the buses with poor static voltage stability and high voltage amplitude are eliminated, so that the remaining buses are considered as an alternative set for DG access;
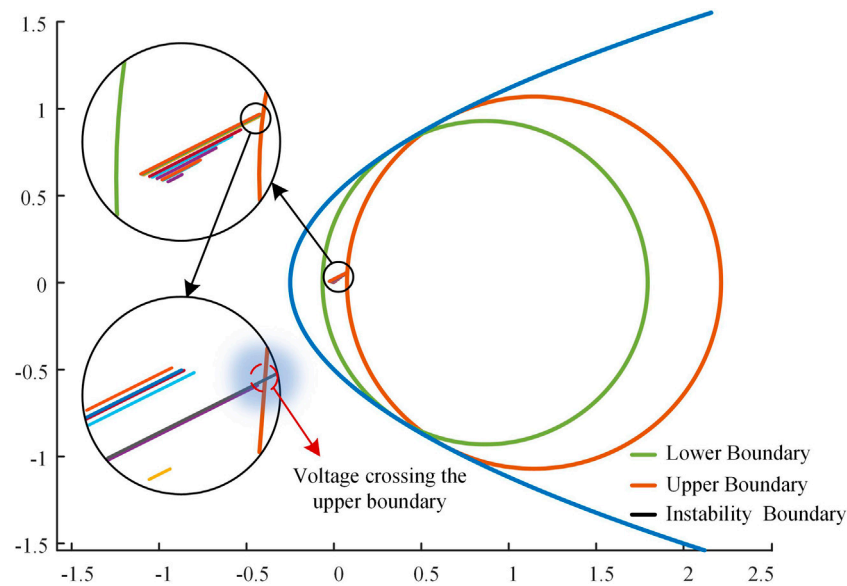
FIGURE 7
Bus sigma index crossing boundary diagram.

2) Generating a certain number of DG access scenarios using Monte Carlo simulations, with variance coefficients set in advance as stopping conditions for the simulations;

3) Determine the number of connected distributed generation n and the power factor, denoted as DG_1, DG_2, . . . , DG_n;

4) Set the initial access total active power of the DGs, distribute the DGs' access power (ΔP_1, ΔP_2, . . . ,ΔP_n) based on the load active power ratio at the DGs' access site, and set the associated reactive power (ΔQ_1, ΔQ_2, . . . ,ΔQ_n) following the power factor. The scaling unit for DGs is the above $\Delta S_i = \Delta P_i + j\Delta Q_i$;

5) Solving the self-defined directional holomorphic embedding model and calculating the *Sigma* index $\sigma_i(s)$ for each bus;

6) Set the upper and lower boundaries of the bus voltage amplitude, gradually increase the embedding factor s and plot the trajectory of each bus in the *Sigma* plane. If there is a bus trajectory intersecting with the upper and lower boundary circles (as shown in Figure 7), record the corresponding s value at this time and calculate the hosting capacity of the system under this DG access scenario;

7) Statistical acquisition of probability distribution curves as well as cumulative distribution curves of DG hosting capacity after the Monte Carlo simulation has been stopped;

8) Determine the acceptable level of voltage violation risk and obtain the DG hosting capacity of the distribution network considering the risk according to the cumulative distribution curve.

5 Example analysis

This paper uses the 22-bus distribution network system (Raju et al., 2012) for simulation. The parameters are set according to the simulation requirements in Section 4.2 as follows:

1) Calculate each bus's EIMM index and initial state voltage, as shown in Table 1. Eliminate the buses with poor static voltage stability (the weakest four buses are eliminated in this paper); (2) eliminate the buses with higher voltage (the initial voltage offset of this system is relatively small, so the buses are not eliminated). The remaining 17 buses (excluding slack bus) are all used as DG access alternative sets;

2) Set the Monte Carlo simulation stopping condition to a variance coefficient of $\beta < 0.005$;

3) Set the number of different DG accesses n = [2, 4, 6, 8, 10, 12, 14], and set different power factors PF = [0.95 (leading), 1.0, 0.95 (lagging)]

4) Set the initial access total active power of DGs to 1 MW and calculate the power scaling unit ΔS_i corresponding to each DG;

5) Since the allowable deviation of the three-phase supply voltage at 10 kV and below is ± 7% of the rated voltage, the bus voltage amplitude range is set to (0.93,1.07);

6) Set the acceptable voltage violation risk to 10%.

The probability distribution curves and cumulative distribution curves for different DG access numbers when the DG power factor is equal to 1 are given in Figure 8. It can be seen

TABLE 1 Bus static voltage stability and voltage amplitude.

Bus number	Initial state EIMM index	Bus number	Voltage amplitude
22	0.9711	2	0.9969
21	0.9713	3	0.9969
20	0.9713	4	0.9926
19	0.9715	5	0.9925
18	0.9726	6	0.9919

FIGURE 8
PDF and CDF of DG hosting capacity at PF = 1.
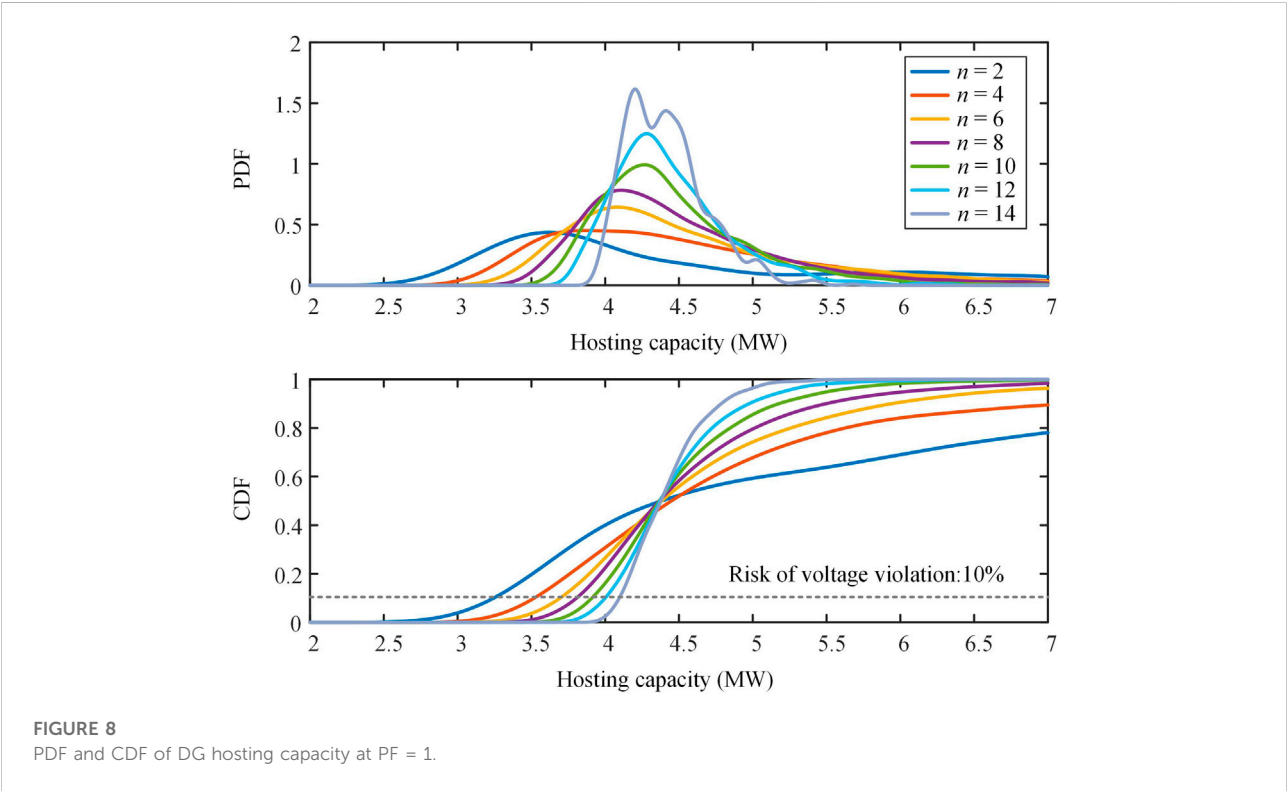
that as the number of DG accesses n increases, the probability distribution curve shifts to the right as a whole, implying that the DG hosting capacity also increases; in the cumulative distribution diagram, the horizontal coordinates of the intersection of each curve with the dashed line represent the DG hosting capacity of the distribution network at different access numbers. When n = 2, the access active power P_{min} = 3.24MW, and when n = 14, the access active power P_{max} = 4.1 MW. The reason for this "the more decentralized the access, the stronger the capacity" is that more access locations can better match the load of the access points locally, which can reduce the probability of backflow caused by excessive power injection at individual buses, thus reducing the risk of over-voltage at the buses.

Figure 9 shows the system hosting capacity corresponding to the three DG power factors. As shown in the figure, when the DG operates at the leading power factor, the system hosting capacity

increases with the increase in power factor. This is because when DG penetration is low, the reactive power emitted is used to balance the reactive load at the access point. As the penetration rate of DG continues to rise, the redundant reactive power generated by DG starts to be injected into the grid after the load reactive power is fully balanced, which will cause the system bus voltage to rise rapidly and cause the voltage to exceed the upper boundary. Therefore, the smaller the percentage of reactive power emitted by DG, the smaller the probability of voltage crossing the upper boundary at the access point, and the higher the hosting capacity of the system.

When the power factor of DG changes from leading to lagging, the system's hosting capacity will continue to improve. The main reason is that the absorption of reactive power by DG reduces the voltage level at the access point, which to a certain extent slows down the rising trend of
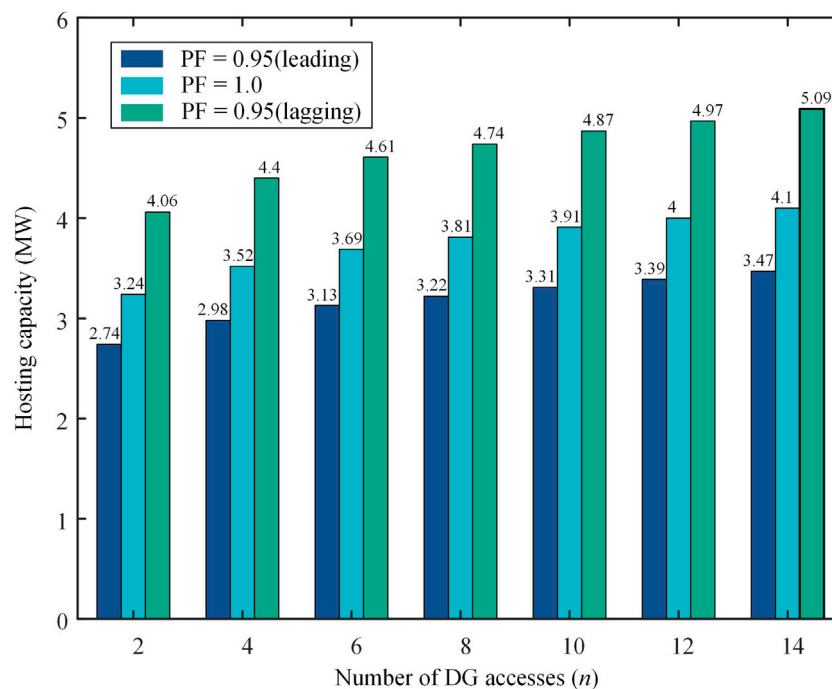
FIGURE 9
DG hosting capacity at different power factors and access numbers.

voltage caused by active power injection and delays the timing of voltage crossing the upper boundary at the access point, thus improving the hosting capacity of the system. When the lagging power factor equals 0.95 and $n = 14$, the maximum DG admitted active power $P_{\max} = 5.09$ MW for this distribution network. Therefore, DG appropriately absorbs reactive power for regulating the voltage at the access point, which is conducive to enhancing the hosting capacity of the system. However, excessive absorption of reactive power may cause the bus voltage to cross the lower boundary, reducing the system's hosting capacity.

6 Conclusion

This paper combines an improved holomorphic embedding method with the stochastic scenario simulation method for evaluating the DG hosting capacity of distribution networks. It can accurately evaluate the hosting capacity while considering the computational efficiency. The main conclusions are as follows:

1) Improvement obtains the self-defined directional HEM, and the methodology for solving it is provided. The voltage constraint region based on *Sigma* index is derived from this, and the bus *Sigma* trajectory intersecting the voltage constraint region is used as the criterion for deciding of the maximum value of DG

hosting capacity. Compared with the traditional methods, using the HEM does not require multiple iterations and only needs to solve the model once to obtain the results, which can effectively improve the efficiency of a single solution;

2) The embedded impedance mode margin index is proposed for quantifying the static voltage stability of buses to reduce the number of DG alternative buses, which effectively reduces the computational effort introduced by using the stochastic scenario simulation method;

3) The influencing factors of DG hosting capacity of distribution network are explored. The simulation found that the more DG access locations, the higher the ability of the distribution network to accept DG; the lagging power factor is more favorable to improving the ability of the distribution network to accept DG compared to the leading power factor.

For the IEEE 22-bus distribution system, the maximum DG hosting capacity of the system is 5.09 MW at the acceptable voltage violation risk level of 10%.

Data availability statement

The original contributions presented in the study are included in the article/Supplementary Material, further inquiries can be directed to the corresponding author.

Author contributions

JX was responsible for article construction article ideas, manuscript writing, simulation experiments, and data analysis. FT was responsible for review and supervision. JQ and XL were responsible for organizing data and drawing figures. ZnL, ZoL, and YG were responsible for checking for errors and polishing the manuscript. All authors contributed to read, and approved the submitted version.

Funding

Conflict of interest

The authors declare that the research was conducted in the absence of any commercial or financial relationships that could be construed as a potential conflict of interest.

Publisher's note

All claims expressed in this article are solely those of the authors and do not necessarily represent those of their affiliated organizations, or those of the publisher, the editors and the reviewers. Any product that may be evaluated in this article, or claim that may be made by its manufacturer, is not guaranteed or endorsed by the publisher.

References

Abad, M. S. S., Ma, J., Zhang, D., Ahmadyar, A. S., and Marzooghi, H. (2018). Probabilistic assessment of hosting capacity in radial distribution systems. *IEEE Trans. Sustain. Energy* 9, 1935–1947. doi:10.1109/TSTE.2018.2819201

Ballanti, A., and Ochoa, L. F., 2015. On the integrated PV hosting capacity of MV and LV distribution networks. Proceedings of the 2015 IEEE PES Innovative Smart Grid Technologies Latin America (ISGT LATAM), 05-07 October 2015, Montevideo, Uruguay. 366–370. doi:10.1109/ISGT-LA.2015.7381183

Chen, X., Wu, W., Zhang, B., and Lin, C. (2017). data-driven dg capacity assessment method for active distribution networks. *IEEE Trans. Power Syst.* 32, 3946–3957. doi:10.1109/TPWRS.2016.2633299

Ding, X. H., Lou, Y. F., Liu, W., and Shi, L. Z. (2000). A new practical method for calculating line loss of distribution network: improved iteration method. *Power Syst. Technol.* 01, 39–42. doi:10.13335/j.1000-3673.pst.2000.01.012

Dong, Y. C., Wang, S. X., and Yan, B. K. (2019). Review on evaluation methods and improvement techniques of DG hosting capacity in distribution Network. *Power Syst. Technol.* 43, 2258–2266. doi:10.13335/j.1000-3673.pst.2019.0428

Du, N. C., Tang, F., Liao, Q. F., Gao, X., Li, Y., and Wei, X. Q. (2021). Static voltage stability based on holomorphic embedding method. *Smart Powe* 49, 8–15.

Gao, H., Chen, J., Diao, R., and Zhang, J. (2021). A HEM-based sensitivity analysis method for fast voltage stability assessment in distribution power network. *IEEE Access* 9, 13344–13353. doi:10.1109/ACCESS.2021.3051843

Jin, F., Liu, J. L., Liu, X. L., Wen, G. Q., Dong, Y. C., Wang, S. X., et al. (2022). Uncertainty analysis of DG hosting capacity in distribution network based on voltage sensitivity. *Electr. Power Autom. Equip.* 42, 183–189. doi:10.16081/j.epae.202204076

Keane, A., Ochoa, L. F., Borges, C. L. T., Ault, G. W., Alarcon-Rodriguez, A. D., Currie, R. A. F., et al. (2013). state-of-the-art techniques and challenges ahead for distributed generation planning and optimization. *IEEE Trans. Power Syst.* 28, 1493–1502. doi:10.1109/TPWRS.2012.2214406

Kulmala, A., Repo, S., and Pylvänäinen, P. (2017). Generation curtailment as a means to increase the wind power hosting capacity of a real regional distribution network. *24th Int. Conf. Electr. Distribution* 2017, 1782–1786. doi:10.1049/oap-cired.2017.0925

Lai, Q. P., Liu, C. X., and Sun, K. (2022). Formulation and visualization of bus voltage-var safety regions for a power system. *IEEE Trans. Power Syst.* 37, 3153–3156. doi:10.1109/TPWRS.2022.3156444

Lai, Q. P., Liu, C. X., and Sun, K. (2021). Vulnerability assessment for voltage stability based on solvability regions of decoupled power flow equations. *Appl. Energy* 304, 117738–122619. doi:10.1016/j.apenergy.2021.117738

Li, S. H., Cao, Y. J., and Liu, G. Y. (2014). Optimal allocation method of dynamic var compensator based on the impedance modulus margin index. *Proc. CSEE* 34, 3791–3798. doi:10.13334/j.0258-8013.pcsee.2014.22.026

Liu, C. X., Lai, Q. P., Yao, L. Z., Xu, J., and Sun, Y. Z. (2022). Power system decoupling model based on holomorphic embedding method:weak bus identification. *Proc. CSEE* 42, 1736–1748. doi:10.13334/j.0258-8013.pcsee.202241

Liu, D. C., Wang, C. X., Tang, F., and Zhou, Y. (2020). Probabilistic assessment of hybrid wind-PV hosting capacity in distribution systems. *Sustainability* 12, 2183–2202. doi:10.3390/su12062183

Mahmud, M. A., Hossain, M. J., and Pota, H. R. (2014). Voltage variation on distribution networks with distributed generation: worst case scenario. *IEEE Syst. J.* 8, 1096–1103. doi:10.1109/JSYST.2013.2265176

Navarro, B. B., and Navarro, M. M., 2017. A comprehensive solar PV hosting capacity in MV and LV radial distribution networks. Proceedings of the 2017 IEEE PES Innovative Smart Grid Technologies Conference Europe (ISGT-Europe), 26-29 September 2017, Turin, Italy. 1–6. doi:10.1109/ISGTEurope.2017.8260210

Qureshi, M. U., Kumar, A., GrijalvaDeboever, S., J., Deboever, J., Peppanen, M., and Rylander, M., 2021 Fast hosting capacity analysis for thermal loading constraint using sensitivity-based decomposition method. Proceedings of the 2020 52nd North American Power Symposium (NAPS), June 3 2021, China. 1–5. doi:10.1109/NAPS50074.2021.9449771

Qureshi, M. U., Kumar, A., Grijalva, S., Deboever, J., Peppanen, J., and Rylander, M., 2020. Fast hosting capacity analysis considering over-voltage criteria and impact of regulating devices. Proceedings of the 2020 IEEE/PES Transmission and Distribution Conference and Exposition (T&D), 12-15 October 2020, Chicago, IL, USA. 1–5. doi:10.1109/TD39804.2020.9300035

Rabiee, A., and Mohseni-Bonab, M. (2017). Maximizing hosting capacity of renewable energy sources in distribution networks: A multi-objective and scenario-based approach. *Energy* 120, 417–430. doi:10.1016/j.energy.2016.11.095

Ramalinga Raju, M. R., Ramachandra Murthy, K. V. S. R., and Ravindra, K. (2012). Direct search algorithm for capacitive compensation in radial distribution systems. *Int. J. Electr. Power & Energy Syst.* 42, 24–30. doi:10.1016/j.ijepes.2012.03.006

Shayani, R., and de Oliveira, M. (2011). Photovoltaic generation penetration limits in radial distribution systems. *IEEE Trans. Power Syst.* 26, 1625–1631. doi:10.1109/TPWRS.2010.2077656

Singh, P., and Tiwari, R. (2020). Extended holomorphic embedded load-flow method and voltage stability assessment of power systems. *Electr. Power Syst. Res.* 185, 106381–107796. doi:10.1016/j.epsr.2020.106381

Sun, Q., Wang, X., Luo, F. Z., Yin, Q., Ni, Y. T., and Li, J. (2015). Capacity of distribution network on acceptance of distributed photovoltaic system based on cuckoos search algorithm. *Proc. CSU-EPSA.* 27, 1–6.

Tang, N. C., and Chang, G. W., 2018. A stochastic approach for determining PV hosting capacity of a distribution feeder considering voltage quality constraints. Proceedings of the 2018 18th International Conference on Harmonics and Quality of Power (ICHQP), 13-16 May 2018, Ljubljana, Slovenia. 1–5. doi:10.1109/ICHQP.2018.8378864

Torquato, R., Salles, D., Oriente Pereira, C. O., Meira, P. C. M., and Freitas, W. (2018). A comprehensive assessment of pv hosting capacity on low-voltage distribution systems. *IEEE Trans. Power Deliv.* 33, 1002–1012. doi:10.1109/TPWRD.2018.2798707

Trias, A. (2014). *Sigma algebraic approximants as a diagnostic tool in power networks.* Savannah, DC: U.S. PatentSeverna Park.

Trias, A. (2012). The holomorphic embedding load flow method. *IEEE Power Energy Soc. General Meet.*, 1–8. doi:10.1109/PESGM.2012.6344759

Varma, R. K., and Singh, V., 2020. Review of studies and operational experiences of pv hosting capacity improvement by smart inverters. Proceedings of the 2020 IEEE Electric Power and Energy Conference (EPEC), 09-10 November 2020, Edmonton, AB, Canada. 1–6. doi:10.1109/EPEC48502.2020.9320116

Wang, S., Chen, S., Ge, L., and Wu, L. (2016). Distributed generation hosting capacity evaluation for distribution systems considering the robust optimal operation of OLTC and SVC. *IEEE Trans. Sustain. Energy* 7, 1111–1123. doi:10.1109/TSTE.2016.2529627

Xing, H. J., Cheng, H. Z., Zeng, P. L., and Zhang, Y. (2016). IDG accommodation based on second-order cone programming. *Electr. Power Autom. Equip.* 36, 74–80. doi:10.16081/j.issn.1006-6047.2016.06.011

Yang, F. (2015). *Solving for the low-voltage/large-angle power-flow solutions by using the holomorphic embedding method.* [Tucson]: Arizona State University. [dissertation].

Yuan, Z. Y., Lei, J. Y., Zhou, C. C., Bai, H., Shi, Y. S., and Tao, S. Y. (2020). Research on maximum allowable capacity of dispersed wind farm in distribution network considering network structure. *South. Power Syst. Technol.* 14, 73–79. doi:10.13648/j.cnki.issn1674-0629.2020.09.010

Zhao, B., Wei, L. K., Xu, Z. C., Zhou, J. H., and Ge, X. H. (2015). Photovoltaic accommodation capacity determination of actual feeder based on stochastic scenarios analysis with storage system considered. *Automation Electr. Power Syst.* 39, 34–40.

Zhou, L. X., Zhang, D., Li, C. B., Li, H., and Huo, W. W. (2017). Access capacity analysis considering correlation of distributed photovoltaic power and load. *Automation Electr. Power Syst.* 41, 56–61.

Robust dispatching model of active distribution network considering PV time-varying spatial correlation

Xin Ma[1], Han Wu[2]* and Yue Yuan[1]

[1]College of Energy and Electrical Engineering, Hohai University, Nanjing, China, [2]Smart Grid Research Institute, Nanjing Institute of Technology, Nanjing, China

With a high proportion of photovoltaic (PV) connected to the active distribution network (ADN), the correlation and uncertainty of the PV output will significantly affect the grid dispatching operation. Therefore, this paper proposes a novel robust ADN dispatching model, which considers the dynamic spatial correlation and power uncertainty of PV. First, the dynamic spatial correlation of PV output is innovatively modeled by dynamic conditional correlation (DCC) generalized autoregressive conditional heteroskedasticity (DCC-GARCH) model. DCC can accurately represent and forecast the spatial correlation of the PV output and reflect its time-varying characteristics. Second, a time-varying ellipsoidal uncertainty set constructed using the DCC, is introduced to bound the uncertainty of the PV outputs. Subsequently, the original mixed integer linear programming (MILP) model is transformed into the mixed integer robust programming (MIRP) model to realize robust optimal ADN dispatching. Finally, a numerical example is provided to demonstrate the effectiveness of the proposed method.

1 Introduction

As a clean and sustainable renewable energy source, photovoltaic (PV) generation has become one of the world's fastest-growing energy sources, progressively becoming the primary source of electricity in power system (Calcabrini et al., 2019). However, owing to the correlation and uncertainty of PV output, the high proportion of PV in the active distribution network (ADN) significantly influences ADN operation and increases the complexity of dispatching (Yu et al., 2015; Haque and Wolfs, 2016). Thus, a reasonable consideration of the correlation and uncertainty of PV outputs in the ADN dispatching model can help enhance PV consumption and promote the balanced development of the ADN.

First, the modeling of PV-output spatial correlation is considered. According to earlier research, there is a spatial correlation between the PV output attributed to locational considerations, micrometeorological circumstances (Ding and Mather,

TABLE 1 Advantages and disadvantages of methods for constructing spatial correlation of PV output.

Method	Advantages	Disadvantages
Correlation-coefficient matrices (including Pearson coefficient, rank correlation coefficient, …)	• Can capture the nonlinear properties of multidimensional PVs	• Cannot precisely quantify the correlation in extreme cases • Can only obtain the average over the time from data and cannot measure the PV spatial correlation at each moment
Covariance Matrix	• Easy to calculate • Can be applied to multi-dimensional PV output	• A static model that cannot account for the joint nonlinear distribution of variables
Copula Function	• Can efficiently design a multi-variate correlation model	• Only helpful for panel data • A probability distribution model that disregards the autocorrelation of PV output series across time
Deep Learning Networks	• Can accurately explain the complicated relationship among various variables	• A significant quantity of computation • A low level of efficiency

2017). Currently, common methods to establish a PV-output spatial-correlation model mainly include correlation coefficient matrices, covariance matrix, Copula function, and deep neural network. In (Wu et al., 2021), the Pearson correlation coefficient matrix was used to calculate the spatial correlation of the two PVs, from which empirical distributions of spatial correlation coefficients and distances were obtained. In (Luo et al., 2020), the Kendall rank correlation coefficient, which can measure the correlation of nonlinear variables, was used as the parameter of the Frank-Copula function. Various correlation coefficient matrices were used to evaluate and compare the numerical values of PV-output spatial correlation. In (Wu et al., 2022), a covariance-based spatiotemporal correlation model was proposed to quantify and exploit the PV output spatial correlation. In (Pan et al., 2019), a variety of Copula functions were selected to obtain an appropriate PV spatial correlation expression. In (Zamee and Won, 2020), Spearman rank-order correlation and an artificial neural network (ANN) were combined to characterize PV output. Each method has its own advantages and disadvantages, as listed in Table 1. Overall, neither the numerical expression nor the model establishment of PV-output spatial correlation can measure or represent the state of spatial correlation at each moment; that is, they cannot reflect the time-varying characteristics of PV-output spatial correlation. Furthermore, there is a lack of prediction models for multidimensional PV output spatial correlations in existing studies.

Second, the modeling of PV-output uncertainty in the optimal dispatching problem of an ADN is investigated. Stochastic optimization (SO) and robust optimization (RO) are the two primary forms of modeling optimization methodologies for PV-output uncertainty (Aharon and Laurent El, 2009). For instance, in (Liu et al., 2019), a day-ahead economic scheduling method based on chance-constrained programming was proposed considering the uncertainty of PV output. In (Vilaça Gomes et al., 2019), a

new approach was formulated to model the uncertainty of the wind-sun-hydrothermal system by generating several representative scenarios. However, SO requires estimating the probability distribution of variables from historical data, which is prone to large errors in actual situations. In addition, considering the accurate representation of uncertainty, many scenarios may need to be considered, which will increase the computational complexity. Conversely, RO does not need to know the specific probability distribution, but given the values ranges of variables, that is, the uncertainty set (El-Meligy et al., 2022). In (Xu et al., 2020; Choi et al., 2022), the box uncertainty sets were used to restrict the upper and lower bounds of variables, which tend to be over-conservative. (Ji et al., 2019). and (Aghamohamadi et al., 2021) used the polyhedral uncertainty sets, which have a linear structure and can easily control the uncertain budget, to describe the uncertainties of PV outputs. However, it is difficult to depict the correlation between these parameters using box or polyhedral uncertainty sets. Significantly, the ellipsoidal uncertainty sets can effectively describe multi-type sets to facilitate data input and indicate the correlation between uncertain multi-variables (Chassein and Goerigk, 2016; Golestaneh et al., 2018). Considering the dynamic spatial correlation between multiple PV outputs, it is better to use an ellipsoidal uncertainty set to characterize the PV-output uncertainty in the robust optimization dispatching model of ADN.

Based on the above discussions, this study establishes a robust dispatching model for an ADN that fully considers the spatial correlation and uncertainty of PV output. In this model, the dynamic conditional correlation (DCC) generalized autoregressive conditional heteroskedasticity (DCC-GARCH) model is introduced to construct and predict multidimensional dynamic correlation coefficient models of PV outputs, representing temporal changes in spatial correlation. After modeling the dynamic spatial correlation, a time-varying ellipsoidal uncertainty set is introduced to bound the uncertainty of PV outputs. In addition, to build a highly
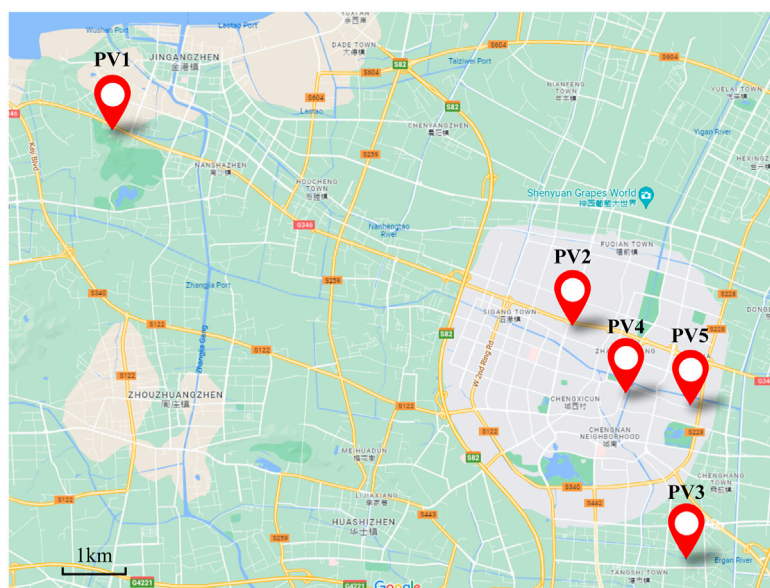
FIGURE 1
Location of five PV stations.

reasonable and widely applicable ADN dispatching model, the coordination optimization of active and reactive power is considered, and a variety of methods are adopted to linearize the nonlinear constraints for an easy solution. Finally, the effectiveness and rationality of the proposed methodologies are demonstrated considering a rural ADN in China as an example. The major contributions of this study are as follows:

1) To characterize the time-varying characteristics of PV-output spatial correlation, the DCC-GARCH model is proposed in this study to establish a dynamic model of the correlation. The model also allows for intraday short-term forecasting of DCC, which can measure the spatial correlation.

2) To address the uncertainty problem of PV output in the optimization dispatching of an ADN, a time-varying ellipsoidal uncertain set based on the DCC-GARCH model is proposed to improve the robustness of photovoltaic output modeling. By introducing the uncertainty set, the MILP model for ADN optimal dispatching can be transformed into mixed integer robust optimization (MIRP).

The remainder of this paper is organized as follows. Section 2 describes the dynamic spatial correlation and proposes a time-varying spatial correlation model for the PV outputs. Section 3 explains the time-varying ellipsoidal uncertainty set of the PV outputs and constructs a robust dispatch model of ADN. In Section 4, the numerical results for a rural ADN in China are presented to verify the effectiveness of the proposed model. Finally, the conclusions are presented in Section 5.

2 Multidimensional dynamic spatial correlation model of PV output based on DCC-GARCH

2.1 Dynamic changes of PV output spatial correlation

Owing to the influence of micro-meteorology, PV power stations in the same area show different output variations. Relevant research has shown that there is a high correlation between the outputs of these PV stations, which is known as spatial correlation. The five PV stations in Zhangjiagang, Suzhou is taken as an example, which are shown in Figure 1. The PV output data in 2018 is used to draw Figure 2, which has been standardized by the installed capacity. And the sampling interval is 5 min.

Figure 2 displays the scatter plots of the power distribution of PVs at various time scales and dimensions, as well as the accompanying confidence intervals. As shown in Figure 2, the confidence ellipses of the same PVs at different times are considerably different, which implies that the spatial correlation of the same PVs varies over the time. In Figures 2A–C, the time scale is a month. The confidence ellipse for January is longer and thinner than those for March and May, resulting in a stronger spatial correlation. Figures 2D–F reflects the changes of three-dimensional (3D) confidence ellipses of PV1, PV2, and PV3 outputs across three consecutive days from April 6th to April 8th. On April 8th, the ellipsoid is the most elongated and has the shape of a prolate ellipsoid. Thus, the
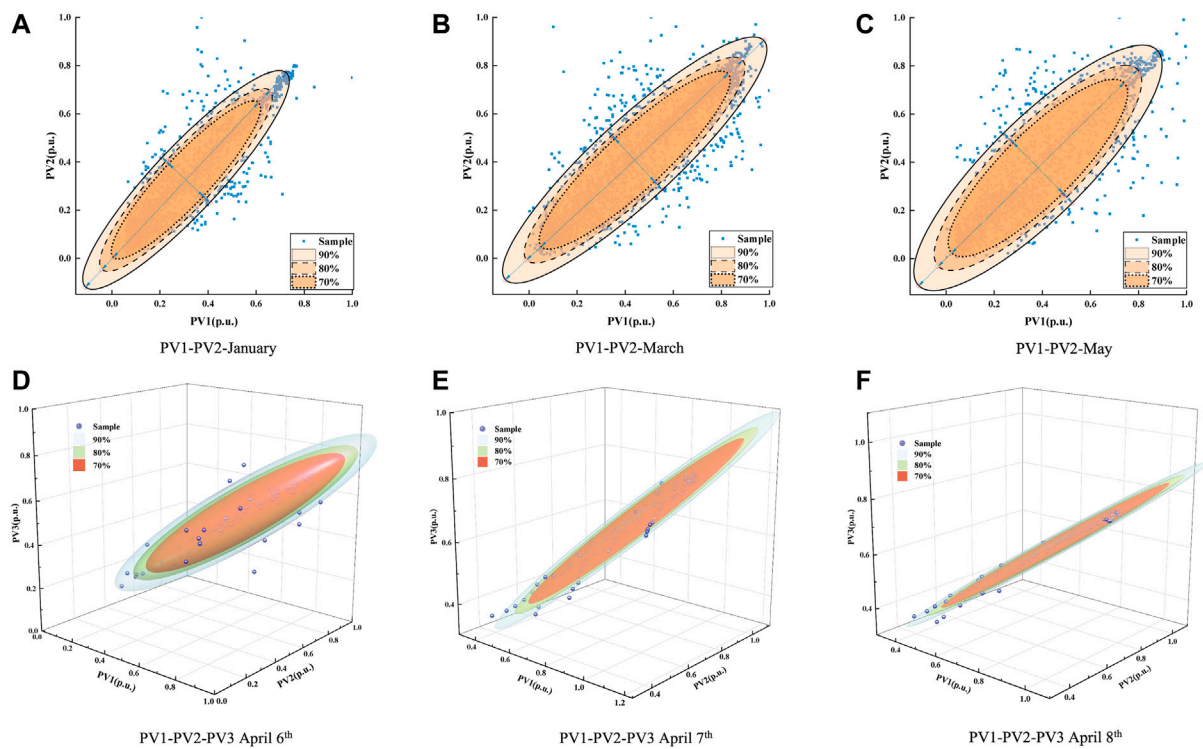
FIGURE 2
Power distribution and confidence interval of PV1-PV2 and PV1-PV2-PV3 at partial time. **(A)** PV1-PV2-January, **(B)** PV1-PV2-March, **(C)** PV1-PV2-May, **(D)** PV1-PV2-PV3 April 6th, **(E)** PV1-PV2-PV3 April 7th, and **(F)** PV1-PV2-PV3 April 8th.

spatial correlation among the three PV stations is the strongest for the 3 days. In addition, on comparing Figures 2D–F with Figures 2A–C, it can be observed that the smaller the time scale is, the more noticeable is the fluctuation of spatial correlation of PV output.

Figure 2 illustrates that the spatial correlation of PV output has a significant time-varying feature, with the smaller time scale indicating a larger variation. However, most existing studies have built static models of spatial correlation and do not predict the spatial correlation itself. Based on this, a dynamic spatial-correlation model based on the DCC-GARCH model is proposed in this paper to realize the numerical characterization and prediction of spatial correlation with time-varying properties.

2.2 Dynamic spatial-correlation model and prediction based on DCC-GARCH

Suppose that the output time-series of k PV stations is $\boldsymbol{P}_t^{PV} = [P_{1,t}^{PV}, \ldots P_{i,t}^{PV}, \ldots P_{K,t}^{PV}]^T$, where $P_{i,t}^{PV}$ denotes the output

time series of the ith PV station. Defining the mean of $P_{i,t}^{PV}$ as $\bar{P}_{i,t}^{PV}$, the mean equation of each series is represented by the ARMA model, and the DCC-GARCH model of PV output spatial correlation is expressed as

$$\bar{P}_{i,t}^{PV} = c_i + \sum_{a=1}^{p_{arma}} \varphi_{i,a} \bar{P}_{i,t-a}^{PV} + \sum_{b=1}^{q_{arma}} \theta_{i,b} e_{i,t-b}^{PV} \tag{1}$$

$$h_{i,t}^{PV} = \omega_i + \sum_{x=1}^{p} \lambda_{i,x} \left(e_{i,t-x}^{PV}\right)^2 + \sum_{y=1}^{q} \delta_{i,y} \left(h_{i,t-y}^{PV}\right) \tag{2}$$

$$\boldsymbol{P}_t^{PV} = \begin{bmatrix} P_{1,t}^{PV} \\ \cdots \\ P_{i,t}^{PV} \\ \cdots \\ P_{i,t}^{PV} \end{bmatrix} = \bar{\boldsymbol{P}}_t^{PV} + \boldsymbol{e}_t^{PV} \tag{3}$$

$$\boldsymbol{H}_t^{PV} = \boldsymbol{D}_t^{PV} \boldsymbol{R}_t^{PV} \boldsymbol{D}_t^{PV} \tag{4}$$

$$\boldsymbol{D}_t^{PV} = diag\left(\sqrt{h_{1,t}^{PV}}, \cdots, \sqrt{h_{i,t}^{PV}}, \cdots, \sqrt{h_{k,t}^{PV}}\right) \tag{5}$$

$$\boldsymbol{R}_t^{PV} = \begin{bmatrix} \rho_{11} & \rho_{12} & \cdots & \rho_{1k} \\ \rho_{21} & \rho_{22} & \cdots & \rho_{2k} \\ \cdots & \cdots & \cdots & \cdots \\ \rho_{k1} & \rho_{k2} & \cdots & \rho_{kk} \end{bmatrix} = \boldsymbol{Q}_t^{'-1} \boldsymbol{Q}_t \boldsymbol{Q}_t^{*-1} \tag{6}$$

$$\boldsymbol{Q}_t = \begin{bmatrix} q_{11} & q_{12} & \cdots & q_{1k} \\ q_{21} & q_{22} & \cdots & q_{2k} \\ \cdots & \cdots & \cdots & \cdots \\ q_{2k} & \cdots & \cdots & q_{kk} \end{bmatrix}$$

$$= \left(1 - \sum_{m=1}^{M} \alpha_m - \sum_{n=1}^{N} \beta_n \right) \bar{\boldsymbol{Q}} + \sum_{m=1}^{M} \alpha_m \boldsymbol{\xi}_{t-m} \boldsymbol{\xi}'_{t-} + {}_m\sum_{n=1}^{N} \beta_n \boldsymbol{Q}_{t-n} \quad (7)$$

$$\bar{\boldsymbol{Q}} = T^{-1} \sum_{t=1}^{T} \boldsymbol{\xi}_t \boldsymbol{\xi}'_t \quad (8)$$

Equations 1, 2 establish the ARMA-GARCH model for the output of each PV station. Equation 1 is the mean equation using the ARMA model, and Equation 2 refers to the variance equation of the GARCH model, where the residual term $\{e_{i,t}^{PV}\}$ is subject to $N(0, \sqrt{h_{i,t}^{PV}})$. c_i, w_i, φ_a, θ_b, λ_x and δ_y are constant coefficients. p_{arma} and q_{arma} are the orders of ARMA, and p and $\underline{q}$ are the lag orders of the GARCH. Eq. 3 is the variance equation, which can be calculated using the GARCH model. To ensure that the variance is positive, the parameters must satisfy $\omega_i > 0$, $\lambda_{i,x} > 0$, $\delta_{j,y} > 0$, and $(\sum_{x=1}^{p} \lambda_{i,x} + \sum_{y=1}^{q} \delta_{i,y}) < 1$.

Equations 3–8 build the DCC-GARCH model. In Eq. 3, $e_{i,t}^{PV}$ denotes the residual term, which is subject to $N(0, H_t^{PV})$. The covariance matrix H_t^{PV} of P_t^{PV} can be decomposed into a DCC matrix R_t^{PV} and two standard-deviation matrices D_t^{PV}, as shown in Equation 4. Eq. 6 defines R_t^{PV} which is disintegrated into matrices $\boldsymbol{Q}_t^*$ and $\boldsymbol{Q}_t$. $\boldsymbol{Q}_t^*$ refers to a diagonal matrix whose elements are the square roots of the diagonal values of $\boldsymbol{Q}_t$. In Eq. 8, $\boldsymbol{\xi}_t$ refers to a residual vector after standardization that satisfies $\boldsymbol{\xi}_t$ $(D_t^{PV})^{-1} \boldsymbol{e}_t^w$. $\bar{\boldsymbol{Q}}$ is an unconditional variance matrix of $\boldsymbol{e}_t^w$, satisfying Eq. 8.

The DCC (1,1)-GARCH (1,1) model is more frequently. In the simplified model, Eqs 2, 7 are simplified to Eqs 9, 10, respectively. The DCC can then be written as Eq. 11.

$$h_{i,t}^{PV} = \omega_i + \lambda_i \left(e_{i,t-1}^{PV}\right)^2 + \delta_i \left(h_{i,t-1}^{PV}\right) \quad (9)$$

$$\boldsymbol{Q}_t = (1 - \alpha - \beta)\bar{\boldsymbol{Q}} + \alpha \boldsymbol{\xi}_{t-1} \boldsymbol{\xi}'_{t-} + \beta \boldsymbol{Q}_{t-1} \quad (10)$$

$$\rho_{ij,t} = \frac{q_{ij,t}}{\sqrt{q_{ii,t} q_{jj,t}}}$$

$$= \frac{(1-\alpha-\beta)\bar{q}_{ij} + \alpha\xi_{i,t-1}\xi_{j,t-1} + \beta q_{ij,t-1}}{\sqrt{\left((1-\alpha-\beta)\bar{q}_{ii} + \alpha\xi_{i,t-1}^2 + \beta q_{ii,t-1}\right)\left((1-\alpha-\beta)\bar{q}_{jj} + \alpha\xi_{j,t-1}^2 + \beta q_{jj,t-1}\right)}} \quad (11)$$

where ω_i, λ_i, and δ_i are the parameters to be estimated in GARCH (1,1) and should be positive. α and β are positive parameters in DCC (1,1) and satisfy $\alpha + \beta < 1$.

Consider the covariance matrix of r-step ahead prediction is

$$\boldsymbol{Q}_{t+r} = (1 - \alpha - \beta)\bar{\boldsymbol{Q}} + \alpha \boldsymbol{\xi}_{t+r-1} \boldsymbol{\xi}'_{t+r-1} + \beta \boldsymbol{Q}_{t+r-1} \quad (12)$$

where $E_t[\boldsymbol{\xi}_{t+r-1}\boldsymbol{\xi}_{t+r-1}] = E_t[\boldsymbol{R}_{t+r}^{PV}]$, $\boldsymbol{R}_{t+r}^{PV} = \boldsymbol{Q}_{t+r}^{*-1} \boldsymbol{Q}_{t+r} \boldsymbol{Q}_{t+r}^{*-1}$. Because of the nonlinearity, the prediction cannot be directly solved forward to provide a convenient method for prediction. Hence, an efficient method is proposed to generate the r-step ahead prediction of Q by approximating that $\bar{\boldsymbol{Q}} \approx \bar{\boldsymbol{R}}$ and that $E_t[\boldsymbol{Q}_{t+1}^{PV}] = E_t[\boldsymbol{R}_{t+1}^{PV}]$ (Engle and Sheppard, 2001). Using this

approximation, the DCC matrix $\boldsymbol{R}PV\ t$ can be predicted using the following relationship

$$E_t[\boldsymbol{R}_{t+r}^{PV}] = E_t[\boldsymbol{Q}_{t+r}]$$
$$= \sum_{i=0}^{r-2} (1 - \alpha - \beta)\bar{\boldsymbol{R}}(\alpha + \beta)^i + (\alpha + \beta)^{r-1} \boldsymbol{R}_{t+1} \quad (13)$$

So far, a dynamic spatial correlation model of PV output can be obtained. In addition to accurately describing the PV output, the model can also assess, compute, and predict the DCC of different PV outputs. In this study, the relative value $\boldsymbol{R}_t^{PV}$ is used to characterize the DCC. The absolute value $\boldsymbol{Q}_t$, which denotes the covariance matrix, is used to denote the time-varying ellipsoidal uncertainty set and solve the optimal dispatching model. $\boldsymbol{R}_t^{PV}$ and $\boldsymbol{Q}_t$ are interconnected using Eq. 11.

3 Robust dispatching model for ADN considering the dynamic PV spatial correlation

In contrast to the transmission network, the resistance and reactance values of the ADN lines are close to each other, and the coupling between active and reactive power is strong (Sun et al., 2022). It is not sufficient to establish a unilateral active- or reactive-power dispatching model based on the traditional active- and reactive-power decoupling theory. The reactive-power resources about the high proportion of PV will affect the network loss and voltage quality (Antoniadou-Plytaria et al., 2017; Hu et al., 2022). Active power optimization can reduce generation costs, and reactive power regulation can reduce network losses, together achieving the goal of minimizing operating costs. Therefore, first, this section establishes the active- and reactive-power coordination dispatching model of the ADN. Thereafter, to facilitate the solution, the nonlinear constraints are linearized to form the MILP model. Finally, considering the uncertainty of PV output, a time-varying ellipsoid uncertainty set is proposed to construct a robust dispatching model of ADN.

3.1 Objective function

Because economy is a significant evaluation indicator for ADN, the lowest operating cost of ADN is chosen as the objective function in this paper. The operational expense consists of the cost of purchasing electricity from the grid, the dispatching cost of curtailable loads, and the lifespan-loss cost of the energy storage system (ESS), which is expressed as:

$$Min\ F = \sum_{t=1}^{T} \left(F^{buy}(t) + F^{CL}(t)\right) + F^{Ess} \quad (14)$$

$$F^{buy}(t) = \sum_i m^{buy}(t) P_{i,t}^{Load} \Delta t \qquad (15)$$

$$F^{CL}(t) = \sum_i m_i^{CL} P_{i,t}^{CL} \Delta t \qquad (16)$$

$$F^{Ess} = (\pi^{rep} - \pi^{res}) DP^{cy} \qquad (17)$$

where $F^{buy}(t)$ and $F^{CL}(t)$ denote the cost of electricity purchase and dispatching cost of the curtailable load at time t, respectively, and F^{Ess} denotes the lifespan-loss cost of energy storage. In Eq. 15, $m^{buy}(t)$ denotes the unit cost of electricity purchased from the upper grid. In Eq. 16, m_i^{CL} denotes the demand-side response compensation cost. In Eq. 17, π^{rep} and π^{res} denote the replacement cost and residual value of the ESS, respectively, and DP^{cy} denotes the cycle degradation percentage of the ESS.

3.2 Constraints

The normal operation of the ADN must satisfy power flow constraints. To achieve reasonably coordinated dispatching within the system, it is also necessary to consider the operating constraints of each device. In this study, we consider the demand-side response constraints and the operating constraints of an ESS, on-load tap changer (OLTC), capacitor bank (CB), static var generator (SVG), and distributed generation (DG), as well as the impact of ESS lifespan losses on operational costs.

3.2.1 Power flow constraints

The injected and outflow powers at each node must be equal for the ADN. Therefore, the branch flow model can be expressed as

$$\begin{cases} P_{ij,t} = \left(u_{i,t}^2 - u_{i,t}u_{j,t}\cos\theta_{ij,t}\right)g_{ij} - u_{i,t}u_{j,t}b_{ij}\sin\theta_{ij,t} \\ Q_{ij,t} = -\left(u_{i,t}^2 - u_{i,t}u_{j,t}\cos\theta_{ij,t}\right)b_{ij} - u_{i,t}u_{j,t}g_{ij}\sin\theta_{ij,t} \end{cases} \quad i,j \in B^{Node}, t \in T$$

$$(18)$$

$$\begin{cases} P_{i,t} = \sum_{(i,j)} P_{ij,t} + \left(\sum_{j=1}^N G_{ij}\right)v_{i,t}^2 = P_{i,t}^{PV} + P_{i,t}^{Essdis} - P_{i,t}^{Esschar} \\ \qquad -\left(P_{i,t}^{Load} - P_{i,t}^{CL}\right) \\ Q_{i,t} = \sum_{(i,j)} Q_{ij,t} + \left(\sum_{j=1}^N -B_{ij}\right)v_{i,t}^2 = Q_{i,t}^{PV} + Q_{i,t}^{Ess} + Q_{i,t}^{CB} + Q_{i,t}^{SVG} \\ \qquad -\left(Q_{i,t}^{Load} - P_{i,t}^{CL}\tan\phi\right) \end{cases} \quad (19)$$

$$P_{ij,t}^2 + Q_{ij,t}^2 \le S_{ij,\max}^2 \qquad (20)$$

Eq. 18 gives the branch power flow equations, where $\theta_{ij,t}$ is the difference in the voltage phase angle between nodes i and j. g_{ij} and b_{ij} are the electric conductance and susceptance of branch ij, respectively. Eq. 19 shows the node power-balance equation, where G_{ij} and B_{ij} are the conductance and susceptance of the node to the ground, respectively. ϕ is the power-factor angle of the load being reduced. Eq. 20 constraints the capacity of branch ij.

3.2.2 OLTC operation constraints

OLTC can regulate the voltage by adjusting the position of the tap, which is an important component for maintaining voltage stability. A virtual node m can be added to the branches that contain OLTC to separate the transformer branch into an ideal transformer section and a lossy section.

The voltage of the ideal transformer on the secondary side can be expressed as

$$u_{m,t} = \left(\delta_{ij,t}\right)^2 u_{j,t}, i, m, j \in B^{OLTC} \qquad (21)$$

where $\delta_{ij,t}$ represents the turn ratio of the transformer branch at time t, which can be defined as a linear combination of the following constraints.

$$\delta_{ij,t} = \delta_{ij}^{min} + T_{ij,t}\Delta\delta_{ij} \qquad (22)$$

$$\Delta\delta_{ij} = \left(\delta_{ij}^{max} - \delta_{ij}^{min}\right)\big/K_{ij} \qquad (23)$$

$$0 \le T_{ij,t} \le K_{ij} \qquad (24)$$

where δ_{ij}^{min} and δ_{ij}^{max} are the minimum and maximum OLTC turn ratio, respectively. T_{ij} denotes the actual tap position, which is a non-negative integer variable. $\Delta\delta_{ij}$ is the change in turn ratio of each tap. K_{ij} denotes the maximum number of OLTC tap positions.

3.2.3 ESS operation constraints

$$u_{i,t}^{char} + u_{i,t}^{dis} \le 1, \forall i \in B^{ESS}, \forall t \in T \qquad (25)$$

$$\begin{cases} u_{i,t}^{char}\underline{P_i^{Esschar}} \le P_{i,t}^{Esschar} \le u_{i,t}^{char}\overline{P_i^{Esschar}} \\ u_{i,t}^{dis}\underline{P_i^{Essdis}} \le P_{i,t}^{Essdis} \le u_{i,t}^{dis}\overline{P_i^{Essdis}} \end{cases} \qquad (26)$$

$$\begin{cases} SOC_{i,0} = SOC_{i,set} \\ SOC_{i,t} = SOC_{i,t-1} + \left(P_{i,t}^{Esschar}\big/\eta_i^{char}\Delta t \right. \\ \qquad \left. -P_{i,t}^{Essdis}\big/\eta_i^{dis}\Delta t\right)\big/E_i^{nomal} \quad \forall i \in B^{ESS}, \forall t \in T \\ \underline{SOC_i} \le SOC_{i,t} \le \overline{SOC_i} \\ SOC_{i,end} = SOC_{i,0} \end{cases} \quad (27)$$

Constraints (25) and (26) limits the active power of the ESS at node i at time t. Constraint (27) limits the state of charge (SOC) at node i at time t. In constraint (27), E_i^{nomal} is the rated capacity of the ith ESS. η_i^{char} and η_i^{dis} denote the charging and discharging efficiencies, respectively. To ensure that the ESS has the same operational performance in each scheduling cycle, it is assumed that the initial value of the SOC in this cycle is the same as the initial value of the SOC in the following cycle.

3.2.4 ESS cycle life loss constraints

The ESS loss cost accounts for a significant portion of the ADN operational cost. Because the ESS lifespan-loss might

influence economic efficiency during operation, cyclic-life loss constraints for the ESS are constructed in this paper using the method proposed in the literature (Wang et al., 2016).

Assuming that the charging and discharging procedures have the same impact on the cycle lifespan degradation, a full charging and discharging cycle is divided into two distinct processes. The daily degradation is the sum of the degradations during each time interval, as shown in (28). For each period, the cycle lifespan degradation can be calculated by deducting the two regular degradations.

$$DP^{cy} = \sum_t \deg_t^{cy} \tag{28}$$

$$\deg_t^{cy} = 0.5 \left| \deg_t - \deg_{t-1} \right| \tag{29}$$

where $\deg_t$ denotes the cycle loss percentage corresponding to the SOC at time t, which can be obtained from the degradation-SOC curve, as shown in Wang et al. (2016).

Given that all the absolute values in Eq. 29 are less than 1, the nonlinear function can be converted into a linear inequality constraint by adding two binary variables d_1 and d_2. The functions are as follows:

$$\begin{cases} 0 \le \deg_t^{cy} - 0.5 \left(\deg_t - \deg_{t-1} \right) \le 2d_2 \\ 0 \le \deg_t^{cy} - 0.5 \left(\deg_{t-1} - \deg_t \right) \le 2d_1 \\ d_1 + d_2 = 1 \end{cases} \tag{30}$$

3.2.5 CB and SVG constraints

Reactive-power-compensation components in an ADN typically fall into one of two types: the discrete component CB and the continuous component SVG. The constraints of the CB are as follows:

$$\begin{cases} y_{i,t}^{CB} Q_i^{CB,step} = Q_{i,t}^{CB} \\ 0 \le y_{i,t}^{CB} \le \overline{Y_i^{CB}} \quad \forall t \in T, \forall i \in B^{CB} \\ y_{i,t}^{CB} \in int \end{cases} \tag{31}$$

$$\begin{cases} \sum_{t \in T} \delta_{i,t}^{CB} \le N_i^{CB,max} \\ -\delta_{i,t}^{CB} \overline{Y_i^{CB}} \le y_{i,t}^{CB} \le \delta_{i,t}^{CB} \overline{Y_i^{CB}} \end{cases} \quad \forall t \in T, \forall i \in B^{CB} \tag{32}$$

Constraint (32) constrains the number of operations, where where $N_i^{CB,max}$ is the upper limits of the operating quantity during each dispatching. $\delta_{i,t}^{CB}$ denotes the change in CB compensation capacity at adjacent moments.

SVG is a continuous reactive power compensation device that can effectively respond to the sudden changes in voltage or overvoltage caused by DG fluctuations in an ADN. The constraints of an SVG are as shown in Constraint (33):

$$Q_i^{SVG,min} \le Q_{i,t}^{SVG} \le Q_i^{SVG,max} \quad \forall t \in T, \forall i \in B^{SVG} \tag{33}$$

where $Q_i^{SVG,min}$ and $Q_i^{SVG,max}$ denote the lower and upper limits of SVG-compensated reactive power, respectively.

3.2.6 PV-output constraints

$$\begin{cases} 0 \le P_{i,t}^{PV} \le \overline{P_{i,t}^{PV}} \\ -P_{i,t}^{PV} \tan \underline{\phi} \le Q_{i,t}^{PV} \le P_{i,t}^{PV} \tan \bar{\phi} \end{cases} \quad \forall t \in T, \forall i \in B^{PV} \tag{34}$$

$$\left(P_{i,t}^{PV} \right)^2 + \left(Q_{i,t}^{PV} \right)^2 \le S_i^{PV} \quad \forall t \in T, \forall i \in B^{PV} \tag{35}$$

The PV output constraints are presented in Constraints (34) and (35). Constraint (34) denotes the maximum PV active power at time t, whereas $\bar{\phi}$ and $\underline{\phi}$ are the maximum and minimum power factor angles, respectively. The maximum PV apparent power is limited by Constraint (35) to ensure system economy and safety.

3.2.7 Demand-response constraints

Demand response (DR) is crucial for ADN dispatch and optimization. It can reduce the uneven tide distribution caused by DG uncertainty. By tracking DG generation, DR can provide some regulation capability for the ADN. In this study, the main DR we considered is the curtailable load with the following constraints:

$$P_{i,t}^{CL} \le q_{i,t}^{CL} u_{i,t}^{CL} \quad \forall i \in B^{CL}, \forall t \in T \tag{36}$$

$$y_{i,t}^{CL} - z_{i,t}^{CL} = u_{i,t}^{CL} - u_{i,t-1}^{CL} \quad \forall i \in B^{CL}, \forall t \in T \tag{37}$$

$$y_{i,t}^{CL} + z_{i,t}^{CL} \le 1 \quad \forall i \in B^{CL}, \forall t \in T \tag{38}$$

$$\sum_{t'=t}^{t+TCL_{min}^{CL}-1} u_{i,t'}^{CL} \ge TCL_{min}^{CL} y_{i,t}^{CL} \quad \forall i \in B^{CL}, \forall t \in T \tag{39}$$

$$\sum_{t'=t}^{t+TCL_{max}^{CL}-1} z_{i,t'}^{CL} \ge y_{i,t}^{CL} \quad \forall i \in B^{CL}, \forall t \in T \tag{40}$$

$$\sum_{t \in T} y_{i,t}^{CL} \le Num^{CL} \quad \forall i \in B^{CL} \tag{41}$$

where $q_{i,t}^{CL}$ is the maximum reduction per unit time for each curtailable load. $u_{i,t}^{CL}$ denotes the condition of load reduction, and $y_{i,t}^{CL}$ and $z_{i,t}^{CL}$ denote that load reduction starts or stops, respectively, whereas all of them are binary variables. *TCL_{min}^{CL} and TCL_{max}^{CL} are the minimum and maximum load-reduction times.* Num^{CL} *is the maximum quantity of loads that participates in the DR throughout the day.*

3.3 Model linearization

3.3.1 Successive linear approximation of power flow

Despite the high computational accuracy of AC power flow, its non-convex nonlinear properties render it unsuitable for

integration into complex distribution network optimization issues. Consequently, this study linearizes the power flow equation to improve the solution efficiency while maintaining appropriate computational accuracy. It then creates a linearized optimization model for an ADN.

Constraint (18) is nonlinear because of the product of a trigonometric function with the voltage. Suppose that an initial point $(v_{i,j,k}, \theta_{i,j,k})$ is provided. The first-order Taylor series expansion of the sine and cosine functions is expressed as:

$$\begin{cases} \sin \theta_{ij,t} \approx s^1_{ij,t,k} \theta^1_{ij,t,k} + s^0_{ij,t,k} \\ \cos \theta_{ij,t} \approx c^1_{ij,t,k} \theta^1_{ij,t,k} + c^0_{ij,t,k} \end{cases} \tag{42}$$

where,

$$\begin{cases} s^1_{ij,t,k} = \cos \theta_{ij,t,k}, s^0_{ij,t,k} = \sin \theta_{ij,t,k} - \theta_{ij,t,k} \cos \theta_{ij,t,k} \\ c^1_{ij,t,k} = -\sin \theta_{ij,t,k}, c^0_{ij,t,k} = \cos \theta_{ij,t,k} + \theta_{ij,t,k} \sin \theta_{ij,t,k} \end{cases} \tag{43}$$

The power flow equation is formulated by incorporating (42) and (43) into Equation 18.

$$\begin{cases} P_{ij,t} = v^2_{i,t} g_{ij} - v_{i,t} v_{j,t} \left(g_{ij} c^0_{ij,t,k} + b_{ij} s^0_{ij,t,k} \right) \\ \qquad - v_{i,t} v_{j,t} \theta_{ij,t} \left(g_{ij} c^1_{ij,t,k} + b_{ij} s^1_{ij,t,k} \right) \\ Q_{ij,t} = -v^2_{i,t} b_{ij} + v_{i,t} v_{j,t} \left(-g_{ij} s^0_{ij,t,k} + b_{ij} c^0_{ij,t,k} \right) \\ \qquad - v_{i,t} v_{j,t} \theta_{ij,t} \left(g_{ij} s^1_{ij,t,k} - b_{ij} c^1_{ij,t,k} \right) \end{cases} \tag{44}$$

With $v^2_{i,t}$ as an integral variable, the nonlinear terms in the equation are $v_{i,t} v_{j,t}$ and $v_{i,t} v_{j,t} \theta_{ij,t}$. To decompose these two terms, we use the first-order Taylor expansion for $\theta_{ij,t}$ near the initial value, as shown in (45).

$$v_{i,t} v_{j,t} \theta_{ij,t} \approx v_{i,t,k} v_{j,t,k} \theta_{ij,t} + \left(v_{i,t} v_{j,t} - v_{i,t,k} v_{j,t,k} \right) \theta_{ij,t,k} \tag{45}$$

The $v_{i,t} v_{j,t}$ can be uncoupled as (46). Subsequently, the first-order Taylor expansion can be used to further approximate the linearization of $v^2_{ij,t}$, as shown in (47).

$$v_{i,t} v_{j,t} = \frac{1}{2} \left[v^2_{i,t} + v^2_{j,t} - \left(v_{i,t} - v_{j,t} \right)^2 \right] = \frac{v^2_{i,t} + v^2_{j,t}}{2} - \frac{v^2_{ij,t}}{2}$$
$$= \frac{U_{i,t} + U_{j,t}}{2} - \frac{v^2_{ij,t}}{2} \tag{46}$$

$$v^2_{ij,t} \approx 2v_{ij,t,k} v_{ij,t} - v^2_{ij,t,k} \approx 2v_{ij,t,k} v_{ij,t} \frac{v_{i,t} + v_{j,t}}{v_{i,t,k} + v_{j,t,k}} - v^2_{ij,t,k}$$

$$= 2 \frac{v_{i,t,k} - v_{j,t,k}}{v_{i,t,k} + v_{j,t,k}} \left(v^2_{i,t} - v^2_{j,t} \right) - v^2_{ij,t,k}$$

$$= 2 \frac{v_{i,t,k} - v_{j,t,k}}{v_{i,t,k} + v_{j,t,k}} \left(U_{i,t} - U_{j,t} \right) - v^2_{ij,t,k} \tag{47}$$

$$= v^s_{ij,t,L}$$

The linearized power flow constraints can be obtained by substituting (45)–(47) into (44), as follows:

$$\begin{cases} P^k_{ij,t} = g_{ij} U_{i,t} - g^{P,k}_{ij} \dfrac{U_{i,t} + U_{j,t}}{2} - b^{P,k}_{ij} \left(\theta_{ij,t} - \theta_{ij,t,k} \right) \\ \qquad + g^{P,k}_{ij} \dfrac{v^s_{ij,t,L}}{2} \\ Q_{ij,t} = -b_{ij} U_{i,t} + b^{Q,k}_{ij} \dfrac{U_{i,t} + U_{j,t}}{2} - g^{Q,k}_{ij} \left(\theta_{ij,t} - \theta_{ij,t,k} \right) \\ \qquad - b^{Q,k}_{ij} \dfrac{v^s_{ij,t,L}}{2} \end{cases} \tag{48}$$

where

$$\begin{cases} g^{P,k}_{ij} = \left(g_{ij} c^0_{ij,k} + b_{ij} s^0_{ij,k} \right) + \left(g_{ij} c^1_{ij,k} + b_{ij} s^1_{ij,k} \right) \theta_{ij,t,k} \\ b^{P,k}_{ij} = \left(g_{ij} c^1_{ij,k} + b_{ij} s^1_{ij,k} \right) v_{i,t,k} v_{j,t,k} \\ b^{Q,k}_{ij} = \left(-g_{ij} s^0_{ij,k} + b_{ij} c^0_{ij,k} \right) - \left(g_{ij} s^1_{ij,k} - b_{ij} c^1_{ij,k} \right) \theta_{ij,t,k} \\ g^{Q,k}_{ij,k} = \left(g_{ij} s^1_{ij,k} - b_{ij} c^1_{ij,k} \right) v_{i,t,k} v_{j,t,k} \end{cases} \tag{49}$$

In Yang et al. (2016) and Yang et al. (2017), it has been demonstrated by the examination of numerous instances that successive linear approximation of power flow has high accuracy. Its efficiency has a sizable advantage over heuristic methods owing to the rapid development of commercial linear-programming tools. Furthermore, compared with the second-order cone relaxation, the successive linear approximation, which is based on the Taylor series, has unrestricted objects and superior scalability.

3.3.2 Linearization of line capacity and DG capacity

Constraints (20), (35) are elliptical nonlinear constraints on capacity. Linearization can be realized using a linear approximation with multiple rectangular constraints.

The line capacity constraint is transformed into (50). The capacity constrained of DG inverter is transformed into (51).

$$\begin{cases} -S_{ij,\max} \le P_{ij,t} \le S_{ij,\max} \\ -S_{ij,\max} \le Q_{ij,t} \le S_{ij,\max} \\ -\sqrt{2} S_{ij,\max} \le P_{ij,t} + Q_{ij,t} \le \sqrt{2} S_{ij,\max} \\ -\sqrt{2} S_{ij,\max} \le P_{ij,t} - Q_{ij,t} \le \sqrt{2} S_{ij,\max} \end{cases} \tag{50}$$

$$\begin{cases} -S^{DG}_{i,t} \le P^{DG}_{i,t} \le S^{DG}_{i,t} \\ -S^{DG}_{i,t} \le Q^{DG}_{i,t} \le S^{DG}_{i,t} \\ -\sqrt{2} S^{DG}_{i,t} \le P^{DG}_{i,t} + Q^{DG}_{i,t} \le \sqrt{2} S^{DG}_{i,t} \\ -\sqrt{2} S^{DG}_{i,t} \le P^{DG}_{i,t} - Q^{DG}_{i,t} \le \sqrt{2} S^{DG}_{i,t} \end{cases} \quad \forall t \in T, \forall i \in B^{DG} \tag{51}$$

3.3.3 Linearization of ESS cycle lifespan loss constraints

The constraints of the ESS cycle lifespan loss are non-convex and nonlinear and have integer variables. Through the second type of special-order sets (SOS2), the degradation-SOC curve can be linearized and is expressed as:

$$SoC_t = \sum_m \Delta_{t,m} SoC_{t,m} \tag{52}$$

$$\deg_t = \sum_m \Delta_{t,m} \deg_{t,m} \tag{53}$$

$$\sum_m \Delta_{t,m} = 1 \qquad (54)$$

$$\sum_m \delta_{t,m} = 1 \qquad (55)$$

$$\Delta_{t,m} \le \delta_{t,m} + \delta_{t,m-1} \qquad (56)$$

where m is the number of SOC-curve segments of the ESS. $\Delta_{t,m}$ and $\delta_{t,m}$ are the SOS2 variables at time t.

3.4.4 Linearization of OLTC operating constraints

There are integer variables in the OLTC constraints. To avoid the dimensional disaster caused by the non-deterministic polynomial (NP) problem, the OLTC constraints are linearized using following procedure:

Suppose $\lambda_{ij,t,n}$ is a binary variable,

$$T_{ij,t} = \sum_{n=0}^{N_{ij}} 2^n \lambda_{ij,t,n} \qquad (57)$$

where

$$\min_{N_{ij}} \sum_{n=0}^{N_{ij}} 2^n, s.t. \sum_{n=0}^{N_{ij}} 2^n \ge K_{ij} \qquad (58)$$

While defining $m_{ij,t} = \delta_{ij,t} U_{j,t}$, $h_{ij,t} = \lambda_{ij,t,n} U_{j,t}$, and $g_{ij,t,n} = \lambda_{ij,t,n} m_{ij,t}$, Eqs 59, 60 can be respectively obtained by multiplying both sides of Equation 22 by $U_{j,t}$ and $m_{ij,t}$.

$$m_{ij,t} = \delta_{ij}^{\ \min} U_{j,t} + \Delta\delta_{ij} \sum_{n=0}^{N_{ij}} 2^n h_{ij,t} \qquad (59)$$

$$\delta_{ij,t} m_{ij,t} = \delta_{ij}^{\ \min} m_{ij,t} + \Delta\delta_{ij} \sum_{n=0}^{N_{ij}} 2^n g_{ij,t,n} \qquad (60)$$

Using the Big-M method, two equivalences can be achieved by introducing a large number M:

$$h_{ij,t} = \lambda_{ij,t,n} U_{j,t} \Rightarrow \begin{cases} 0 \le U_{j,t} - h_{ij,t} \le (1 - \lambda_{ij,t,n})M \\ 0 \le h_{ij,t} \le \lambda_{ij,t,n} M \end{cases} \qquad (61)$$

$$g_{ij,t,n} = \lambda_{ij,t,n} m_{ij,t} \Rightarrow \begin{cases} 0 \le m_{ij,t} - g_{ij,t,n} \le (1 - \lambda_{ij,t,n})M \\ 0 \le g_{ij,t,n} \le \lambda_{ij,t,n} M \end{cases} \qquad (62)$$

Thus far, OLTC operation constraints have been linearized, converting the model to a mixed integer model. Additionally, daily modifications of the OLTC must be restricted, as shown in (63).

$$\begin{cases} \delta_{ij,t,up} + \delta_{ij,t,do} \le 1 \\ \sum_{n=0}^{N_{ij}} 2^n \lambda_{ij,t,n} - \sum_{n=0}^{N_{ij}} 2^n \lambda_{ij,t-1,n} \ge \delta_{ij,t,up} - \delta_{ij,t,do} K_{ij} \\ \sum_{n=0}^{N_{ij}} 2^n \lambda_{ij,t,n} - \sum_{n=0}^{N_{ij}} 2^n \lambda_{ij,t-1,n} \le \delta_{ij,t,up} - \delta_{ij,t,do} \\ \sum_{t \in T} \delta_{ij,t,up} + \delta_{ij,t,do} \le N_j^{\ \max} \end{cases} \qquad (63)$$

where $\delta_{ij,t,up}$ and $\delta_{ij,t,do}$ are binary variables that define the increasing and decreasing of OLTC ratio at time t. N_j^{max} is the maximum time of changes during operation.

3.4 Time-varying ellipsoidal uncertainty set of PVs

It is vital to describe the uncertainty set for many optimizations dispatching problems based on robust optimization. Among the different ways to contribute to uncertainty sets, the box uncertainty set is over conservative, and the polyhedral uncertainty set cannot express the correlation between uncertain parameters. Therefore, a more flexible ellipsoidal uncertainty set is adopted to describe the uncertainty of PV output. The specific ellipsoidal uncertainty set is as follows

$$\Psi^\alpha: \left(X_t^{PV} - \bar{X}_t^{PV}\right)^T \Sigma^{-1} \left(X_t^{PV} - \bar{X}_t^{PV}\right) \le \Gamma^\alpha \qquad (64)$$

where X_t^{PV} denotes a multivariate PV-output variable of dimension k at time t that can be forecasted by historical PV output data, and $\bar{X}_t^{PV}$ is the mean value of X_t^{PV}; Σ is the predicted covariance matrix, which is obtained from the historical data; Γ^α, which is usually called the uncertainty budget, denotes the coverage rate of observations.

In this study, the ARMA model is used to obtain the PV output predicted value $\bar{X}_t^{PV}$ of dimension k at every time t. The covariance matrix Q_t predicted using DCC-GARCH is regarded as Σ, which changes over time and represents the spatial correlation of different PVs. The uncertainty budget, which controls the robustness of the optimization model, is chosen by different confidence levels of the PV output data.

$$\Psi^\alpha: \left(X_t^{PV} - \bar{X}_t^{PV}\right)^T Q_t^{-1} \left(X_t^{PV} - \bar{X}_t^{PV}\right) \le \Gamma^\alpha \qquad (65)$$

3.5 Solution method

Through the modeling process of Sections 3.1–Sections 3.2, we obtained the active and reactive power coordination dispatching model of the ADN. After the linearization process of the constraints mentioned in Section 3.3, the model proposed in this study is transformed into a mixed integer linear programmed (MILP) optimization model.

Considering the uncertainty of PV output, the time-varying ellipsoidal uncertainty set was developed in Section 3.4. Introducing this set, a robust constraint, into the MILP model, we can obtain a mixed integer robust programmed (MIRP) optimization model that can be computed using solvers. The detailed flowchart of modeling process in this study is presented as Figure 3.
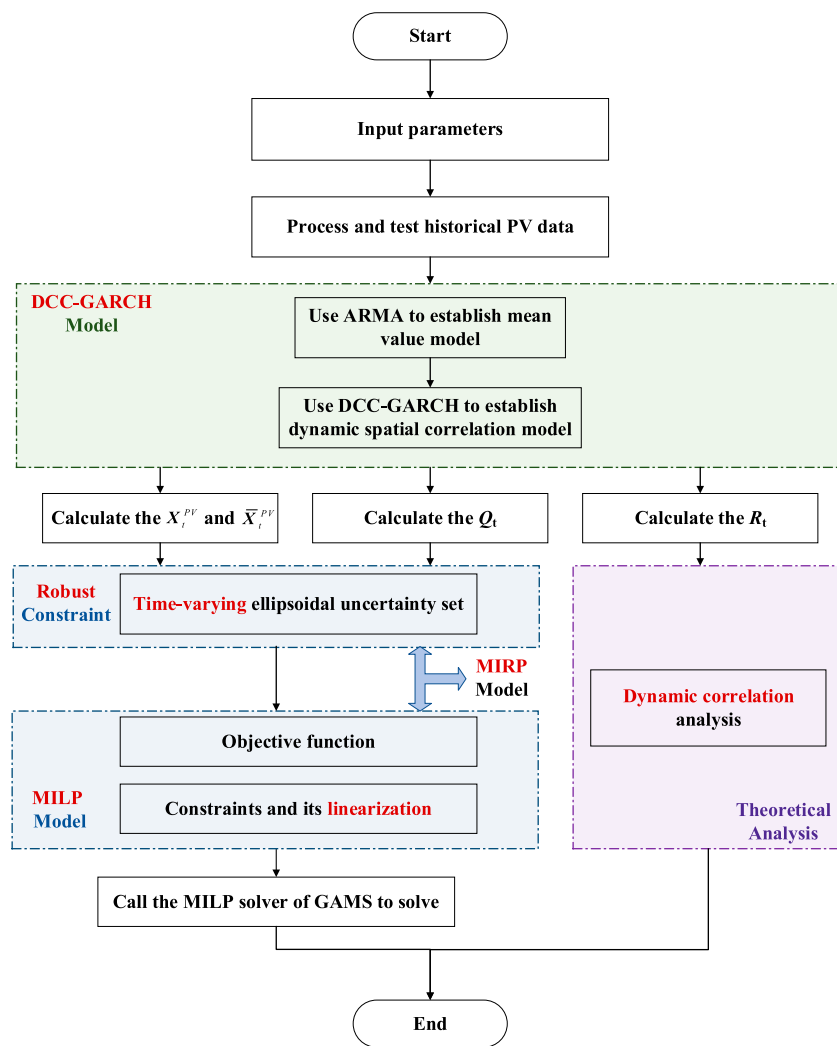
FIGURE 3
Flowchart of the robust dispatching model of ADN considering PV time-varying spatial correlation

4 Case studies

4.1 Dynamic spatial correlation model and prediction based on DCC-GARCH

First, the dynamic spatial correlation model of PV output is analyzed, and the data are from the output of PV system in Figure 1 in Suzhou, China. The data of March 1–24 in 2018, during which the weather was sunny, were selected for modeling and prediction. The interval was set to 20 min from 8:00 to 16:00, which can display the changes in the spatial correlation between PVs. After the Augmented Dickey-Fuller (ADF) test, normality, and Lagrange multiplier (LM) test, the results indicate that the historical PV data can be modeled using ARMA and DCC-GARCH, with the ARMA model of PV output being shown in

TABLE 2 Parameters of five-dimensional DCC-GARCH model.

	ω	λ	δ	α	β
PV1	0.002628	0.7385	0.2535		
PV2	0.001509	0.7150	0.1840		
PV3	0.002897	0.8221	0.1477	0.1273	0.8468
PV4	0.002967	0.7325	0.2240		
PV5	0.002138	0.7442	0.2538		

Supplementary Table S1. The parameters of the five-dimensional DCC-GARCH model being shown in Table 2.

The standardized residual series were re-evaluated after the model was constructed. The results indicated no correlation

FIGURE 4
DCC diagrams of PV output. **(A)** DCC12, DCC13, **(B)** DCC14, DCC15, **(C)** DCC23, DCC24, **(D)** DCC25, DCC34, and **(E)** DCC35, DCC45.
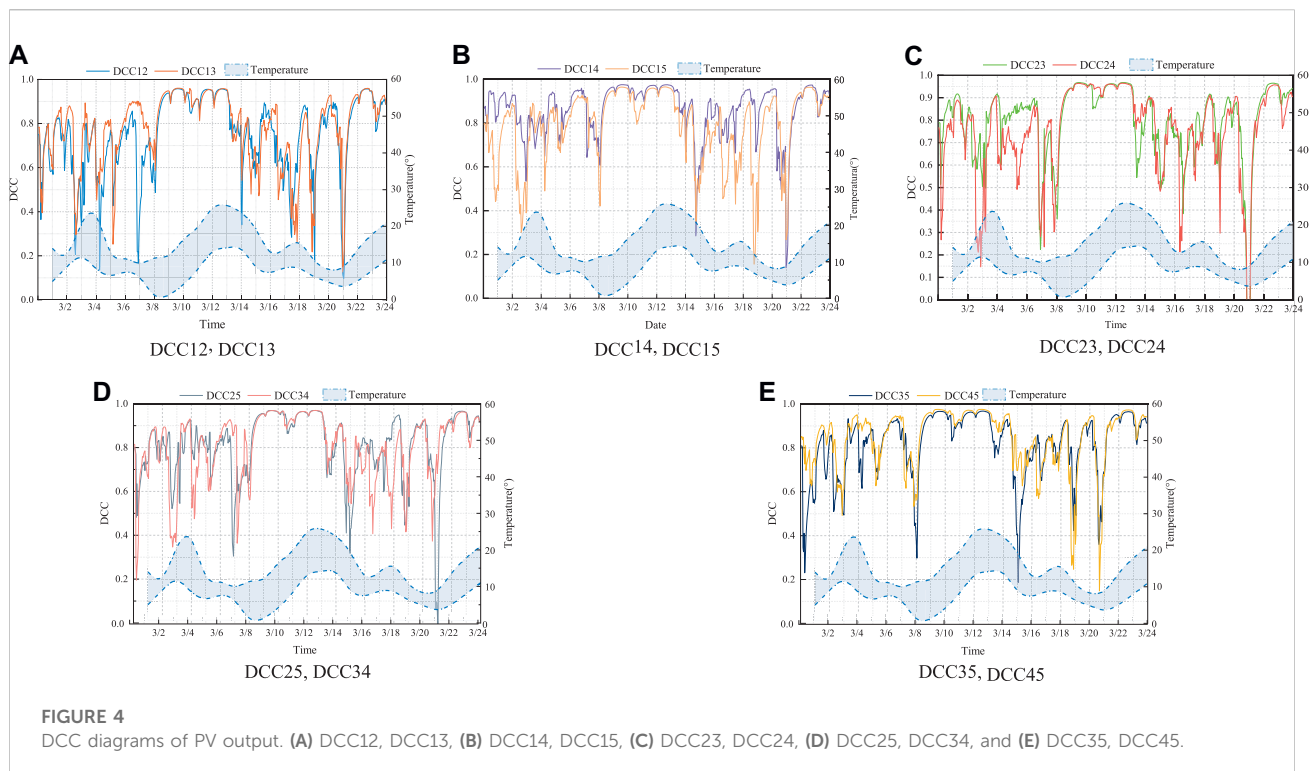
TABLE 3 The average DCC of different PVs.

	Average		Average
DCC12	0.747911	DCC24	0.804797
DCC13	0.756521	DCC25	0.810146
DCC14	0.777482	DCC34	0.811955
DCC15	0.788915	DCC35	0.844137
DCC23	0.793603	DCC45	0.858636

between variables, proving that the model had successfully eliminated the autocorrelation and heteroscedasticity of the data itself. As shown in Table 2, α and β are positive. The sum of α and β (0.974) is less than 1, which indicates that the model is stable, and there is a valid dynamic correlation between the five PVs. Parameter α indicates the influence of the current residual on the time series volatility at the next moment, and a higher α indicates that the time series is more sensitive to the recent residual. Parameter $\alpha + \beta$ indicates the disappearance speed of current fluctuations in the future, namely, the duration of the spatial correlation of PV output. The higher the value $\alpha + \beta$ is, the longer is the correlation duration. From Table 2, the result of fitting β is larger than α, indicating that the current dynamic heteroscedasticity of each series arises mainly from the residual of the previous period. The sum of $\alpha + \beta$ is close to 1, which implies that the spatial correlation has strong continuity.

The DCC matrix $\boldsymbol{R}_t$ of the PV output was calculated using the DCC-GARCH model, with the DCC curve between two pairs under 20 min time resolution being drawn as shown in Figure 4 below.

According to the comparison between Figure 1 and Table 3, it can be observed that distance is one of the factors that affect DCC. The closer the PVs are, the higher is the DCC value. Otherwise, owing to the dynamic change of DCC, the spatial correlation between the two PVs shows different magnitude relationships at different times. This phenomenon is mainly related to temperature and weather.

Comparing Figure 4 with the weather conditions shown in Supplementary Table S2, the maximum and minimum temperatures varied significantly from March 9 to 13. However, the temperature difference remained largely the same owing to five consecutive days of partly cloudy weather. Therefore, the DCC was mainly above 0.9, indicating a high spatial correlation among the PVs during this period. Additionally, the DCC varied dramatically owing to the more pronounced temperature difference fluctuations on March 1–7 and March 5–21. On these days, the weather in the location was cloudy and rainy.

Therefore, the following conclusions can be drawn: When the temperature difference fluctuates more steadily, the DCC changes smoothly, and the DCC is more prominent when the weather is fine. When the temperature difference fluctuates sharply, usually accompanied by inclement weather, the

FIGURE 5
Comparison of DCC predicted value and actual value. **(A)** PV1-PV2, PV1-PV3, **(B)** PV1-PV4, PV1-PV5, **(C)** PV2-PV3, PV2-PV4, **(D)** PV2-PV5, PV3-PV4, and **(E)** PV3-PV5, PV4-PV5.
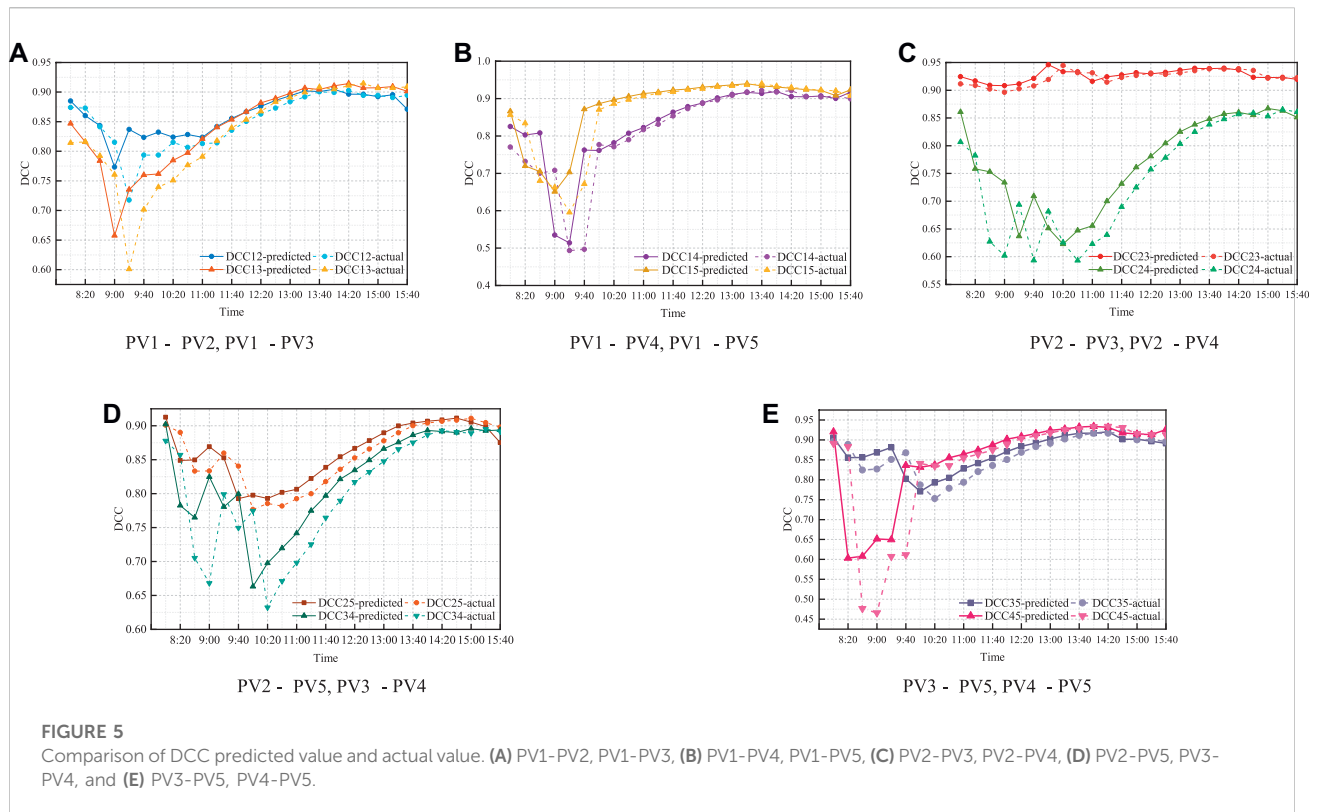
change in solar radiation causes a considerable change in the PV output, which in turn causes a variation in the DCC.

Data from March 1 to 24 were used as the test set, and the forecast step was set to 24. The DCC-GARCH model was used for the rolling forecast to obtain the DCC from 8:00 to 16:00 on March 25 (with an interval of 20 min). The predicted values of the DCC are compared with the actual values in Figure 5, and the mean square error (MSE) is shown in Supplementary Table S3. It can be observed that the errors are within the acceptable range, and the prediction results are accurate. However, in most instances, the prediction values are more prominent than the actual values because of the rapid variation in cloud cover.

4.2 Case description

Robust ADN dispatching is verified in the next section. The grid structure is abstracted from a rural distribution network in Anhui, China, as shown in Figure 6. There are five PV stations (different from Figure 1), one ESS, one SVG, and three CBs. The case uses 24 h as the dispatch period and 60 min as the dispatch interval. The capacities of the PV stations were set to 3MW, 2.4MW, 2MW, 2.4MW, and 4 MW. The parameters of the ESS are as follows: The ESS capacity is 1MW; the initial charge state $SOC_{i,0}$ is 0.5; η_i^{char} and η_i^{dis}, the efficiency of charging and discharging, are set to 88% and 90%,

FIGURE 6
A typical rural distribution system.
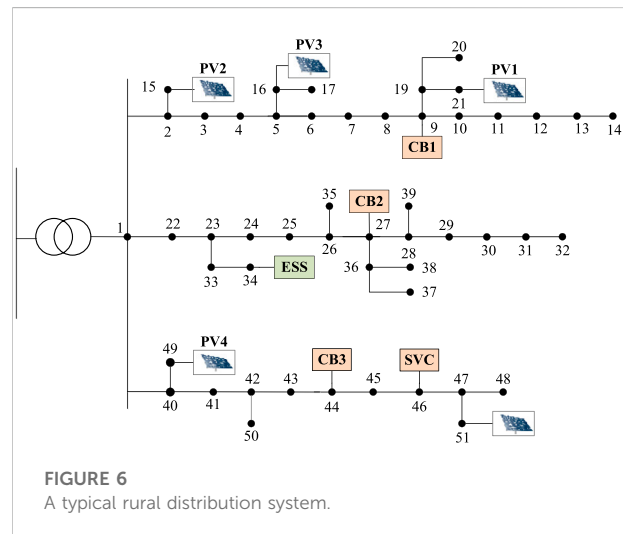
respectively; and the depth of discharge is 90%. For the OLTC (at node one), the maximum number of OLTC tap positions K_{ij} was set to 16. d_{ij}^{min} and d_{ij}^{max} were set to 0.857 and 1.048, respectively. For the DR, the compensation cost value was set to 100 yuan/MWh. Additionally, the electricity price purchased from the power grid adopts a peak-to-valley sales tariff. The load in the system includes residential and agricultural loads.
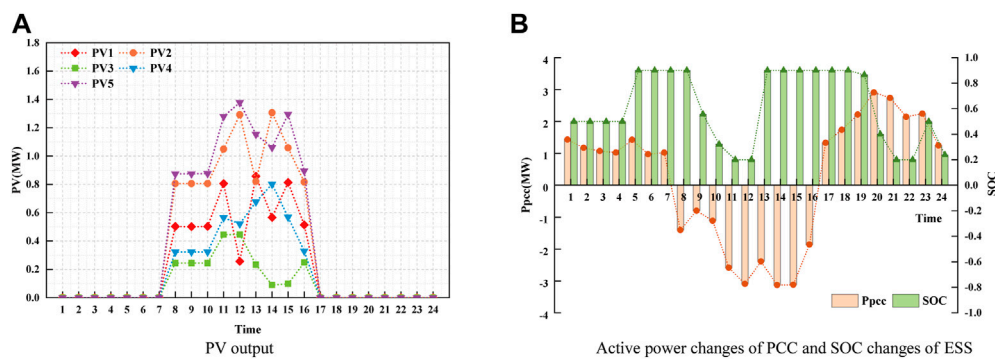
FIGURE 7
Partial-component-change curves for Case A. **(A)** PV output, **(B)** Active power changes of PCC and SOC changes of ESS.

To verify the significance of considering the time-varying characteristic of the PV-output spatial correlation, the numerical tests were mainly conducted in the following two cases:

Case A. Robust dispatching model for the ADN without considering the time-varying characteristics of PV-output spatial correlation.

Case B. Robust dispatching model for the ADN with time-varying characteristic consideration of PV-output spatial correlation.

4.3 Dispatching results for case A

When the time-varying characteristic of PV-output spatial correlation is not considered, the correlation coefficients among the five PVs can easily be derived from the Pearson coefficient. In this case, the ellipsoidal uncertainty set is static, as shown in Eq.

64. The objective function and related parameters can be determined as follow:

Figure 7A depicts the PV output curves, and Figure 7B illustrates the active power changes of PCC and the SOC curves of ESS for Case A. It can be observed that when the time-varying spatial correlation is ignored, the PV-output curves are jagged. Some PV-power valleys occur around midday, which leads to the apparent fluctuations of the PCC active power in Figure 7B. To secure the balance of power supply for the entire system, the SOC state of ESS begins charging immediately at 12:00 when the PV output is low and reaches full power at 13:00. The full power condition lasts for nearly 7 h to guarantee that the load is supplied throughout the night so that the objective function is minimized to the greatest extent.

The maximum number of OLTC changes within the dispatching period was set to no more than two. Three CBs were connected to nodes 9, 27, and 44. The maximum number of access CB groups was set to five, and the maximum number of changes was two. As shown in Supplementary Figure S1, the

TABLE 4 Dispatching results of MILP.

Objective function (yuan)	Total PV output (MW)	PV absorption rate (%)	Transmission losses (MW)
103101.694	30.499	73.0	0.461

TABLE 5 Results of robust dispatching.

Confidence coefficient (%)	Objective function (yuan)	Total PV output (MW)	PV absorption rate (%)	Transmission losses (MW)
99	43663.394	31.603	75.6	0.451
95	54631.883	31.343	75.0	0.448
90	67956.374	31.055	74.3	0.448
85	76864.216	30.892	73.9	0.486
80	92331.939	30.681	73.4	0.440
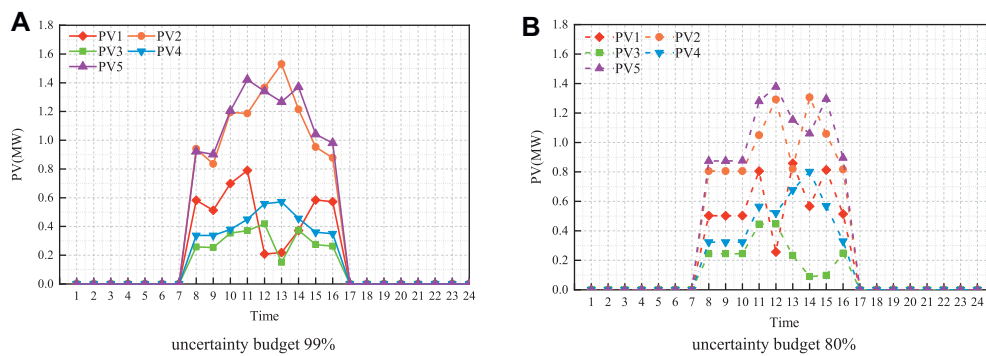
FIGURE 8
PV output under different uncertainty budget for Case B. **(A)** uncertainty budget 99%, **(B)** uncertainty budget 80%.
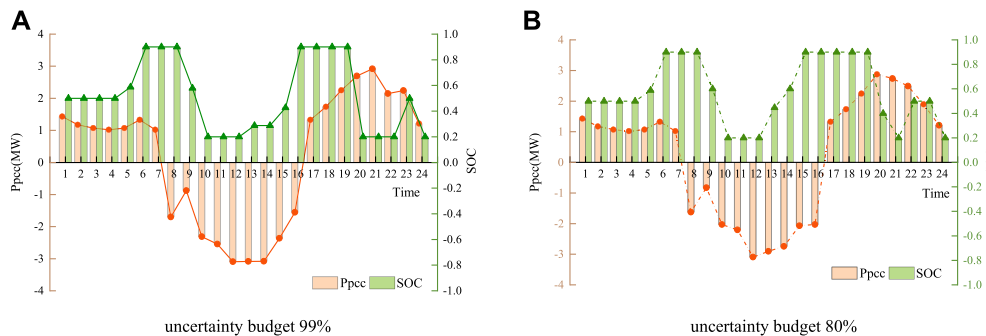
FIGURE 9
Active power changes of PCC and SOC changes of ESS for Case B. **(A)** uncertainty budget 99%, **(B)** uncertainty budget 80%.

variations in OLTC and CB both satisfied the limits. The maximum number of access CB groups during the dispatching period was five. This means that a high proportion of PV in the ADN will cause reactive power shortages and other problems, requiring timely action of reactive-power compensation equipment to ensure stable system operation. In the proposed coordinated dispatching model of ADN, OLTC and CB operate together with the ESS to achieve active management of the ADN and always ensure the voltage quality of the entire system supply.

4.4 Dispatching results for case B

Considering the dynamic trait of PV-output spatial correlation, the covariance matrix Q_t, interconnected with the DCC by Eq. 11, can be used in the uncertainty set, where the

time-varying ellipsoidal uncertainty set is obtained, as shown in Eq. 65. In addition, because the dispatching interval is 1 h, the PV output time was set as 8:00–16:00, according to the actual situation. The covariances between PVs are shown in Supplementary Figure S2, which indicates the spatial correlation variation. The covariance curves for different PVs share a similar trend: a strong correlation at noon and a weak correlation in the morning and evening, which is caused by the illumination intensity and temperature.

Subsequently, a model for the robust dispatching of ADN that considers time-varying spatial correlation was developed. Considering the influence of different uncertainty budgets on the ellipsoidal uncertainty set, the objective function and related parameters were obtained under different uncertainty budgets, as listed in Table 5, where the PV consumption rate is the ratio of the actual output to the ideal output.

First, the effect of time-varying spatial correlation is considered. Comparing Table 5 with Table 4, without time-varying spatial correlation, it can be observed that the total cost of operation increases owing to the reduction in PV output, which increases the cost of power purchase from the upper grid. On the other hand, the decrease in PV output affects the charging and discharging status of the ESS, thus reducing the ESS benefits.

Figure 8 illustrates the PV output, and Figure 9 reveals the active power changes at the point of common coupling (PCC) at node 1 and the SOC tendencies of the ESS. Compared with Figure 7, under any uncertainty budget, the curves of the PV output and PCC output are smoother, and the value of the PV output at each node is higher when the time-varying spatial correlation is considered. In Figure 8, the PCC output is in the trend of the morning and evening peaks and noon trough. Because most of the loads are residential loads, the peak period of electricity consumption is from 20:00 to 22:00. During this period, the PCC output reaches its peak, and the ESS is in a discharged state to ensure the load supply. The SOC curves indicate that the ESS is releasing energy during the morning peak of electricity consumption after 7 a.m. and charges during the peak of the PV generation. In conclusion, considering the time-varying spatial correlation of PVs is helpful for comprehensively evaluating the output characteristics of PV and optimizing the dispatching results.

Secondly, we consider the influence of the uncertainty budget. As can be observed from Table 5, as the uncertainty budget increases, the overall operating cost decreases, and the PV consumption rate increases progressively. This is caused by the selection of the uncertainty budget influencing the robustness of the system operation: the greater the uncertainty budget is, the more points are included in the ellipsoidal uncertainty set, and similarly, the more conservative are the results (Wu et al., 2022). Because the total cost of operation only includes the cost of power purchase and energy storage operation, not the cost of PV operation, to minimize the objective function, a high PV output caused by the high uncertainty budget will become the main power supply of the grid, which will reduce the cost of power purchase from the upper grid and the total cost of operation. Under different circumstances, the network loss varies based on the dispatching status of the PV output and the upper-grid supply.

Under uncertainty budgets of 99% and 80%, Figures 8, 9 shows quite different curves. When the uncertain budget is 99%, the output value of the PV at each moment is slightly larger than that under the 80% budget, and the output curve of the PCC is smoother. Because the total operating cost considers the lifespan

loss cost of the ESS, to minimize the objective function as much as possible, the charging and discharging times of the ESS are reduced under an uncertainty budget of 99% with higher conservatism.

Because the case is a rural distribution network, a low load demand is accompanied by high PV penetration. In the high PV output period, combining the peak–valley spread revenue of the ESS, surplus power will be sold to the upper grid at the purchase price. This approach can improve the PV consumption rate and result in PCC power for negative values from 8:00 to 16:00. In the entire dispatching process with an uncertainty budget of 99%, the ESS benefit is 649.108 yuan, which appropriately reduces the total operation cost.

In the daytime, the voltage of each node connected to the PV system increases significantly, as shown in Supplementary Figure S3. Owing to the PV power cut-in at 8:00 and cut-out at 16:00, all five node voltages exhibited considerable fluctuations. Additionally, more PVs with larger capacities were connected to Line I, resulting in a higher overall node voltage than that of Line III.

5 Conclusion

In this study, a robust dispatching model for an ADN was proposed, which considers PV-output spatial correlation and uncertainty. A dynamic spatial correlation model was proposed to characterize the time-varying characteristics of PV output spatial correlation. Based on this, a time-varying ellipsoidal uncertain set was constructed and applied to the ADN dispatching model, which improved the robustness of PV-output model. Case studies on a rural distribution network in China demonstrated the validity and rationality of the proposed methods. The results indicated that:

(1) The DCC derived using the DCC-GARCH model correctly characterized the spatial correlation of PV output and reflected the time-varying properties of the spatial correlation.

(2) The value of DCC is related to the weather conditions and temperature difference in the area where the PV is located: When the temperature difference swings more consistently, the DCC changes more smoothly; When the weather is favorable, the DCC is greater. When the temperature difference varies dramatically, which is generally accompanied by severe weather, the DCC also changes.

(3) The time-varying ellipsoidal uncertainty set constructed using the DCC can be well applied to the optimal

dispatching model of ADN. Considering the time-varying characteristics of the spatial correlation, it is advantageous to build a complete PV output model and optimize the dispatching results.

Data availability statement

The original contributions presented in the study are included in the article/Supplementary Material, further inquiries can be directed to the corresponding author.

Author contributions

XM: Methodology, analysis, and writing. HW: Conceptualization, software, review, and editing. YY: supervision, review, and editing.

Funding

This work is supported by the Major Basic Research Project of the Natural Science Foundation of the

Jiangsu Higher Education Institutions of China (22KJD470003).

Conflict of interest

The authors declare that the research was conducted in the absence of any commercial or financial relationships that could be construed as a potential conflict of interest.

Publisher's note

All claims expressed in this article are solely those of the authors and do not necessarily represent those of their affiliated organizations, or those of the publisher, the editors and the reviewers. Any product that may be evaluated in this article, or claim that may be made by its manufacturer, is not guaranteed or endorsed by the publisher.

Supplementary material

The Supplementary Material for this article can be found online at: https://www.frontiersin.org/articles/10.3389/fenrg.2022. 1012581/full#supplementary-material

References

Aghamohamadi, M., Mahmoudi, A., and Haque, M. H. (2021). Two-stage robust sizing and operation co-optimization for residential PV–battery systems considering the uncertainty of PV generation and load. *IEEE Trans. Ind. Inf.* 17, 1005–1017. doi:10.1109/TII.2020.2990682

Aharon, B.-T., and Laurent El, G. (2009). *Robust optimization*. Princeton: Princeton University Press.

Antoniadou-Plytaria, K. E., Kouveliotis-Lysikatos, I. N., Georgilakis, P. S., and Hatziargyriou, N. D. (2017). Distributed and decentralized voltage control of smart distribution networks: Models, methods, and future research. *IEEE Trans. Smart Grid* 8, 2999–3008. doi:10.1109/TSG.2017.2679238

Calcabrini, A., Ziar, H., Isabella, O., and Zeman, M. (2019). A simplified skyline-based method for estimating the annual solar energy potential in urban environments. *Nat. Energy* 4, 206–215. doi:10.1038/s41560-018-0318-6

Chassein, A., and Goerigk, M. (2016). *Min-max regret problems with ellipsoidal uncertainty sets*. arXiv: Optimization and Control. doi:10.48550/arXiv.1606.01180

Choi, J., Lee, J.-I., Lee, I.-W., and Cha, S.-W. (2022). Robust PV-BESS scheduling for a grid with incentive for forecast accuracy. *IEEE Trans. Sustain. Energy* 13, 567–578. doi:10.1109/TSTE.2021.3120451

Ding, F., and Mather, B. (2017). On distributed PV hosting capacity estimation, sensitivity study, and improvement. *IEEE Trans. Sustain. Energy* 8, 1010–1020. doi:10.1109/TSTE.2016.2640239

El-Meligy, M. A., El-Sherbeeny, A. M., and Anvari-Moghaddam, A. (2022). Transmission expansion planning considering resistance variations of overhead lines using minimum-volume covering ellipsoid. *IEEE Trans. Power Syst.* 37, 1916–1926. doi:10.1109/TPWRS.2021.3110738

Engle, R., and Sheppard, K. (2001). *Theoretical and empirical properties of dynamic conditional correlation multivariate GARCH*. Cambridge, MA: National Bureau of Economic Research.

Golestaneh, F., Pinson, P., Azizipanah-Abarghooee, R., and Gooi, H. B. (2018). Ellipsoidal prediction regions for multivariate uncertainty characterization. *IEEE Trans. Power Syst.* 33, 4519–4530. doi:10.1109/TPWRS.2018.2791975

Haque, M. M., and Wolfs, P. (2016). A review of high PV penetrations in LV distribution networks: present status, impacts and mitigation measures. *Renew. Sustain. Energy Rev.* 62, 1195–1208. doi:10.1016/j.rser.2016.04.025

Hu, R., Wang, W., Wu, X., Chen, Z., Jing, L., Ma, W., et al. (2022). Coordinated active and reactive power control for distribution networks with high penetrations of photovoltaic systems. *Sol. Energy* 231, 809–827. doi:10.1016/j.solener.2021. 12.025

Ji, H., Wang, C., Li, P., Ding, F., and Wu, J. (2019). Robust operation of soft open points in active distribution networks with high penetration of photovoltaic integration. *IEEE Trans. Sustain. Energy* 10, 280–289. doi:10.1109/TSTE.2018. 2833545

Liu, H., Zhang, Y., Ge, S., Gu, C., and Li, F. (2019). Day-ahead scheduling for an electric vehicle PV-based battery swapping station considering the dual uncertainties. *IEEE Access* 7, 115625–115636. doi:10.1109/ACCESS.2019. 2935774

Luo, Y., Yang, D., Yin, Z., Zhou, B., and Sun, Q. (2020). Optimal configuration of hybrid-energy microgrid considering the correlation and randomness of the wind power and photovoltaic power. *IET Renew. Power Gener.* 14, 616–627. doi:10.1049/ iet-rpg.2019.0752

Pan, C., Wang, C., Zhao, Z., Wang, J., and Bie, Z. (2019). A copula function based monte Carlo simulation method of multivariate wind speed and PV power spatio-temporal series. *Energy Procedia* 159, 213–218. doi:10.1016/j.egypro.2018. 12.053

Sun, X., Qiu, J., Tao, Y., Ma, Y., and Zhao, J. (2022). Coordinated real-time voltage control in active distribution networks: An incentive-based fairness approach. *IEEE Trans. Smart Grid* 13, 2650–2663. doi:10.1109/TSG.2022.3162909

Vilaça Gomes, P., Saraiva, J. T., Carvalho, L., Dias, B., and Oliveira, L. W. (2019). Impact of decision-making models in transmission expansion planning considering large shares of renewable energy sources. *Electr. Power Syst. Res.* 174, 105852. doi:10.1016/j.epsr.2019.04.030

Wang, Y., Zhou, Z., Botterud, A., Zhang, K., and Ding, Q. (2016). Stochastic coordinated operation of wind and battery energy storage system considering

battery degradation. *J. Mod. Power Syst. Clean. Energy* 4, 581–592. doi:10.1007/s40565-016-0238-z

Wu, H., Yuan, Y., Zhang, X., Miao, A., and Zhu, J. (2022). Robust comprehensive PV hosting capacity assessment model for active distribution networks with spatiotemporal correlation. *Appl. Energy* 323, 119558. doi:10.1016/j.apenergy.2022.119558

Wu, H., Yuan, Y., Zhu, J., Qian, K., and Xu, Y. (2021). Potential assessment of spatial correlation to improve maximum distributed PV hosting capacity of distribution networks. *J. Mod. Power Syst. Clean Energy* 9, 800–810. doi:10.35833/MPCE.2020.000886

Xu, S., Sun, H., Zhao, B., Yi, J., Hayat, T., Alsaedi, A., et al. (2020). The integrated design of a novel secondary control and robust optimal energy management for photovoltaic-storage system considering generation uncertainty. *Electronics* 9, 69. doi:10.3390/electronics9010069

Yang, Z., Bose, A., Zhong, H., Zhang, N., Xia, Q., and Kang, C. (2017). Optimal reactive power dispatch with accurately modeled discrete control devices: A successive linear approximation approach. *IEEE Trans. Power Syst.* 32, 2435–2444. doi:10.1109/TPWRS.2016.2608178

Yang, Z., Zhong, H., Xia, Q., Bose, A., and Kang, C. (2016). Optimal power flow based on successive linear approximation of power flow equations. *IET Gener. Transm. Distrib.* 10, 3654–3662. doi:10.1049/iet-gtd.2016.0547

Yu, Y., Konstantinou, G., Hredzak, B., and Agelidis, V. G. (2015). Operation of cascaded H-Bridge multilevel converters for large-scale photovoltaic power plants under bridge failures. *IEEE Trans. Ind. Electron.* 62, 7228–7236. doi:10.1109/TIE.2015.2434995

Zamee, M. A., and Won, D. (2020). Novel mode adaptive artificial neural network for dynamic learning: Application in renewable energy sources power generation prediction. *Energies* 13, 6405. doi:10.3390/en13236405

Nomenclature

A. Sets

B^{Node} set of all nodes

T set of dispatching time

B^{OLTC} set of OLTC nodes

B^{ESS} set of ESS nodes

B^{CB} set of CB nodes

B^{SVG} set of SVG nodes

B^{PV} set of PV nodes

B. Parameters

$S_{ij,max}$ maximum capacity of branch ij

$\overline{P_i^{Esschar}}, \underline{P_i^{Esschar}}$ maximum and minimum of charge power of ith ESS at time t

$\overline{P_i^{Essdis}}, \underline{P_i^{Essdis}}$ maximum and minimum of discharge power of ith ESS at time t

$SOC_{i,0}$, $SOC_{i,set}$, $SOC_{i,end}$ the initial value, the set initial value, and the end value of SOC during the dispatch cycle

$\overline{SOC_i}, \underline{SOC_i}$ maximum and minimum state of charge at node i

$Q_i^{CB,stepi}$ compensation capacity of OLTC per grade

$\overline{Y_i^{CB}}$ maximum capacitor number connected to the grid

$\overline{P_{i,t}^{PV}}$ maximum active power of ith PV at time t

S_i^{PV} maximum capacity of ith PV

C. Variables

$P_{i,t}^{Load}$ Actual active power demand on the load side

$P_{i,t}^{CL}$ Demand-side response power at node i at time t

$P_{ij,t}, Q_{ij,t}$ Active power and reactive power of branch ij at time t

$u_{i,t}$ Node voltage at node i at time t

$P_{i,t}, Q_{i,t}$ Injected active and reactive power at node i at time t.

$P_{i,t}^{Essdis}, P_{i,t}^{Esschar}$ ESS discharging and charging power at node i at time t

$Q_{i,t}^{CB}$ $Q_{i,t}^{SVG}$ Reactive power of CB and SVG at node i at time t

$Q_{i,t}^{Ess}$ Reactive power of ESS inverter at node i at time t

$u_{i,t}^{char}$ $u_{i,t}^{dis}$ Binary status of charging or discharging of ith ESS at time t

$SOC_{i,t}$ State of charge at node i at time t

$y_{i,t}^{CB}$ The number of capacitor groups in operation, which is integer

frontiers | Frontiers in Energy Research

Check for updates

Adaptive robust economic dispatch and real-time control of distribution system considering controllable inverter air-conditioner clusters

Guanhong Chen and Dong Liu*

Department of Electrical Engineering, Shanghai Jiao Tong University, Shanghai, China

With a tremendous number of renewable energy sources (RES) integrated into the distribution system, the inherent uncertainty of RES power generation brings about significant challenges in distribution and power balance within the distribution system. This article proposes an adaptive robust economic dispatch (ARED) model and a real-time control strategy for distribution systems as countermeasures, which make full use of the adjustable capabilities of controllable inverter air-conditioner (IAC) clusters. Firstly, the concept of the adjustable capacity curve (ACC) is developed to accurately quantify the adjustable capacity of an IAC cluster. Afterward, a two-stage adaptive robust optimization is formulated for ARED, which comprehensively takes the adjustable capacity of the IAC cluster and the uncertainty of RES into consideration. Meanwhile, the solution methodology of ARED is also designed based on the column and constraint generation (C&CG) algorithm, where the master problem is quadratic programming with quadratic constraints (QCQP), and the max-min sub-problem is reformulated to a mixed integer linear programming (MILP) form by taking advantage of linear duality theory and big-M method. Finally, a novel real-time decentralized control strategy for IAC clusters is also proposed for purpose of hedging against stochastic RES power fluctuation after every round of ARED decisions. The results of the case study validate the effectiveness of ARED model and real-time control strategy under different uncertainty scenarios of RES power generation.

1 Introduction

In recent years, in order to suppress fossil energy depletion and extreme climate change, innovative technologies and applications of energy and power in industry are going through a highly active period (Dai et al., 2017). Clean and low-carbon energy

utilization technologies have attracted broad attention from all countries, emphasizing the dominant position of renewable energy sources (RES) in future power system (Lu et al., 2017).

However, with the growing proportion of RES engaging in distribution system operation, significant challenges are brought about to distribution system operators (DSOs). On the one hand, during the power dispatching stage, traditional prediction value-based deterministic economic dispatch may suffer from suboptimality (Li et al., 2015) due to the inevitable prediction errors for RES power generation. Therefore, an uncertainty-based economic dispatch model is required, aiming to determine a relatively cost-efficient reference point for all dispatchable units. Stochastic optimization (SO) (Chen et al., 2018; Ye et al., 2018; Roldán et al., 2019; Shuai et al., 2019), chance-constrained programming (Zhou et al., 2018; Yang et al., 2021) and robust optimization (RO) (Gao et al., 2018; Liu et al., 2018; Chen et al., 2021) are three leading paradigms adopted widely in previous studies (Ning and You, 2018). Among these paradigms, SO is mainly formulated based on finite typical scenarios and corresponding discrete probability distribution after scenario generation and reduction. In the work of Ye et al. (2018), authors propose an optimal dispatch method for a power system with high penetration of wind power. Typical scenarios are generated by assuming the prediction error obeys the Gaussian probability density function. In the work of Chen et al. (2018), a generative adversarial network based data-driven approach is adopted to generate typical scenarios of RES power generation. A SO-based optimization model usually contains a relatively large number of constraints, and the applicability of the solution depends on the accuracy of the probability distribution. Distinct from SO, the two-stage adaptive RO does not require accurate probability distribution of uncertainty variables, thus is more practicable for systems with limited knowledge of stochastic RES characteristics (Zhang et al., 2019). Liu et al. (2018) develop a two-stage RO model to minimize the operation cost of the microgrid, in which uncertainties of RES and load are modeled by box constraints. In the study of Chen et al. (2021), a robust dynamic economic dispatching model of integrated transmission and distribution system is established, in which uncertainty set is decided according to conditional value-at-risk rather than manually assigned. Gao et al. (2018) explore the coordinated energy management among distribution systems and networked microgrids, in which a tractable typical budget set is adopted. To improve the conservativeness of RO's solution, in these works, different uncertainty sets with adjustable uncertainty budgets are employed, such as polyhedron uncertainty set (Gao et al., 2018; Liu et al., 2018; Chen et al., 2021), ellipsoid uncertainty set (Roldán et al., 2019). In addition, drawing advantages of both RO and SO, distributionally robust optimization (DRO) also attracts growing attention in recent years, which builds an ambiguity set of uncertainty variables based on statistical moments information and optimizes the

system's expected cost under the worst distribution. In the work of Ruan et al. (2019), the ambiguity set is developed by 1-norm and ∞-norm constraints of the distance between stochastic probability distribution and historical statistical distribution. Zhou et al. (2018) develop a distributionally robust dispatch model considering generalized moments uncertainty of wind power and equivalently transform it to deterministic quadratically constrained quadratic programming (QCQP) problem.

On the other hand, during the real-time operation stage, actual RES power generation deviates from the predicted value with stochastic amplitude and high variation frequency, which may lead to fierce fluctuation of exchange power between the distribution system and transmission system. Due to this reason, more ancillary resources are required for the transmission system to ensure real-time power balance (Kalantar-Neyestanaki et al., 2020). However, under severe operation scenarios such as a contingency state, the regulatable capacity of the transmission system may become extremely limited to meet the requirements, which greatly stimulates the need for ancillary resources from the distribution system side (Tan et al., 2020). To release the power balance burden of the transmission system, demand-side controllable load clusters have been considered to be important regulatory resources with great potential. Among different types of controllable loads, a thermostatically controllable load such as heat pumps and inverter air-conditioners (IAC) are the most characteristic types, due to their large scale, low cost, and fast response speed (Yao and Zhang, 2018). In the work of Wei et al. (2016), a hierarchical and distributed control strategy of heat pumps is proposed to balance the fluctuations caused by RES, in which each pump's target power is determined by solving the optimal setting temperature. Ding et al. (2021) also propose a game-theoretic demand side management strategy, which is capable of guiding users to make optimal power consumption schedules and smooth the tie-line power of microgrids simultaneously. Hui et al. (2019) propose equivalent modeling of IAC to provide frequency regulation service and verify the aggregation of IACs can be controlled in a similar way to traditional generators. Based on networked information interaction between each IAC aggregator, Jiang and Wei (2018) presents a distributed cooperation model and optimal control strategy for an IAC cluster and the power grid to avoid the occurrence of a new load peak. Based on a transactive control framework, Yao and Zhang (2018) propose a decentralized control strategy of the IAC cluster to provide peak shaving service, and furtherly explore the coordination of heterogeneous thermostatically controlled loads to provide real-time ancillary services in their follow-up study (Yao and Zhang, 2020).

Actually, the power-adjustable capability of thermostatic load and user's comfort experience is highly related to its temperature state, hence very sensitive to power adjustment instructions of

both economic dispatch stage and real-time control stage. In most of the previous studies of economic dispatch, controllable loads are scheduled like normal generators according to their power-adjustable capacity, without exploring the effect on users' comfort experience and variation of adjustable capability. In addition, the issues of how to reduce communication costs and protect users' private information should also be subtly considered when aggregating large-scale controllable loads. To address these issues, this paper first develops the concept of an adjustable capacity curve, which is capable of quantifying the exact adjustable capacity of each IAC cluster within a certain time period. Then, for the power dispatch stage, we propose an adaptive robust economic dispatch (ARED) model to achieve cost-efficient dispatching of all generation units by taking IAC clusters' adjustable capability and RES uncertainty into consideration. Afterward, for the real-time operation stage, a real-time control strategy is designed, where IAC clusters function as ancillary resources to hedge against the actual power fluctuation of RES based on decentralized control. Variation of power exchange between the transmission system and distribution system is effectively eliminated. The main contributions of this paper are summarized by the following aspects:

1) Sophisticated IAC model is first proposed in this paper, which not only contains common operation constraints in existing works (Yao and Zhang, 2018; Hui et al., 2019) but also takes the nonlinear relationship of IAC's compressor operation frequency and IAC's electrical/cooling power into consideration. More accurate quantification of IAC's power adjustable capacity and tractable decentralized control can be realized based on this model.

2) A two-stage adaptive robust optimization model is formulated for ARED in this paper by drawing the advantages of RO, where the uncertainty of RES is addressed by adjustable box constraints rather than by discrete scenarios in the work of Ye et al. (2018). ARED model also considers the IAC cluster as a dispatchable unit whose adjustable capability is dynamically updated along with real-time control processes of the IAC cluster. In addition, different from most literature such as Chen et al. (2021); Gao et al. (2018) where upward and downward power adjustment are modeled by two independent positive-define variables, we propose an equivalent formation by only one variable, which can simplify the expressions of objective function and constraints.

3) A decentralized real-time control strategy capable of aggregating and cooperatively controlling IACs is proposed for the purpose of compensating power deviation caused by stochastic RES power fluctuation. IAC clusters' power adjustable capacity can be quantified and updated rapidly during real-time control, which also functions as a constraints boundary in ARED model. Most of the computation is conducted locally, and less remote communication cost

is required compared with the work of Wei et al. (2016); Ding et al. (2021). Privacy protection of IACs' parameters and users' preference information can also be guaranteed under the designed strategy.

The remaining content of this paper is organized as follows. Section 2 introduces the model of IAC and the quantification method of the IAC cluster's adjustable capability. In Section 3, a two-stage adaptive robust optimization model for ARED considering IAC adjustable capacity is formulated and a C&CG algorithm-based solution methodology of ARED is elaborated as well. In Section 4, the real-time control strategy of the IAC cluster is proposed to hedge against RES power fluctuation during the real-time operation stage of the distribution system. In Section 5, a case study is explored to verify the effectiveness of ARED model and real-time control strategy of the IAC cluster. Section 6 concludes this paper.

2 Inverter air-conditioner modeling and adjustable capability quantification

2.1 IAC model

For a room equipped with an IAC, the first-order equivalent thermal parameter (ETP) dynamic model of room temperature T_a in continuous form can be expressed by (1):

$$\frac{dT_a}{dt} = -\frac{U_{oa}A_{room} + c_a\rho_a V_{room}\xi}{c_a\rho_a V_{room}}(T_a - T_{out}) - \frac{1}{c_a\rho_a V_{room}}q_{ac} \quad (1)$$

In (1), c_a and ρ_a stand for heat capacity and density of air; A_{room} and V_{room} stand for area and volume of the room; U_{oa} is heat transfer coefficient of the room; ξ is the number of air exchange times per hour; T_{out} is outdoor ambient temperature; q_{ac} is cooling power of IAC. For specific sampling and control period τ, the discrete-time formulation of (1) is derived and applied in this paper, where we introduce equivalent heat dissipation coefficient $\sigma = (U_{oa}A_{room} + c_a\rho_a V\xi)/c_a\rho_a V$ for simplicity of expression. The room temperature at discrete time point $k\tau = 0, \tau, 2\tau, \ldots$ can be calculated by:

$$T_a(k+1) = e^{-\sigma\tau}T_a(k) + \frac{e^{-\sigma\tau}-1}{c_a\rho_a V\sigma}q_{ac}(k) + (1 - e^{-\sigma\tau})T_{out} \quad (2)$$

For one IAC, the consumed electrical power p_{ac} and produced cooling power q_{ac} are actually adjusted by operation frequency f_{ac} of IAC compressor. However, the relationship between p_{ac}, q_{ac} and frequency f_{ac} are usually nonlinear, which means the adjustment sensitivity $\partial p_{ac}/\partial f_{ac}, \partial q_{ac}/\partial f_{ac}$ are diverse at different operation frequency point. In this paper, we adopt piecewise linearization technology to approximate the original nonlinear functions, as shown in Figure 1. Suppose the operation frequency f_{ac} is segmented into N intervals according to
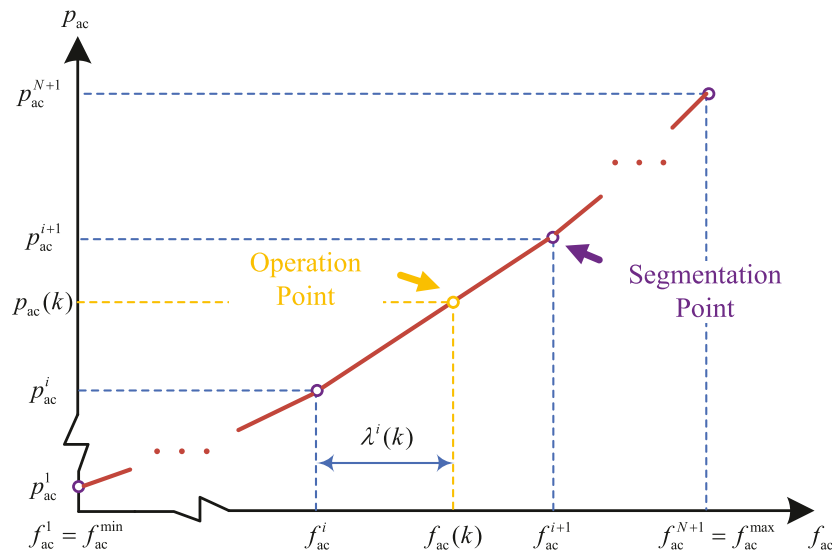
FIGURE 1
Piecewise linearization of nonlinear $p_{ac}-f_{ac}$ function.

(N+1) segmentation points $(f^1, \ldots, f^{N+1})$, and so are p_{ac} and q_{ac}. Then, the slope vectors $\mathbf{k}_{pseg} = (k_p^i)_{N\times1}, \mathbf{k}_{qseg} = (k_q^i)_{N\times1}$ concerning segment i can be calculated. Meanwhile, let $\mathbf{f}_{segF} = (f_{ac}^1, \ldots, f_{ac}^N)^T$ be the vector of the forward N segmentation points of f_{ac}, and $\mathbf{f}_{segB} = (f_{ac}^2, \ldots, f_{ac}^{N+1})^T$ be the backward N segmentation points. In a similar way, we can as well define $\mathbf{p}_{segF}$ and $\mathbf{q}_{segF}$. Drawing support from these definition of necessary coefficient vectors, the relationship between p_{ac}, q_{ac} and f_{ac} can be formulated in a compact form by a set of equalities and inequalities:

$$q_{ac}(k) = \mathbf{q}_{segF}^T \omega(k) + \mathbf{k}_{qseg}^T \lambda(k) \tag{3}$$

$$p_{ac}(k) = \mathbf{p}_{segF}^T \omega(k) + \mathbf{k}_{pseg}^T \lambda(k) \tag{4}$$

$$0 \leq \lambda(k) \leq (\mathbf{\Lambda}_B - \mathbf{\Lambda}_F)\omega(k) \tag{5}$$

$$\mathbf{1}^T \omega(k) = 1 \tag{6}$$

$$f_{ac}(k) = \mathbf{f}_{segF}^T \omega(k) + \mathbf{1}^T \lambda(k) \tag{7}$$

$$f_{ac}^{min} \leq f_{ac}(k) \leq f_{ac}^{max} \tag{8}$$

$$|f_{ac}(k+1) - f_{ac}(k)| \leq r \tag{9}$$

In (3)-(7), binary vector $\omega(k) = (\omega_i(k))_{N\times1}$ and continuous auxiliary vector $\lambda(k) = (\lambda^i(k))_{N\times1}$ are introduced to transform nonlinear equalities $p_{ac} = g_p(f_{ac}), q_{ac} = g_q(f_{ac})$ to mixed integer linear equalities and inequalities. $\omega(k)$ contains only one element 1, whose position indicates the segment where the operation frequency $f_{ac}(k)$ locates. $\mathbf{\Lambda}_F = \text{diag}(\mathbf{f}_{segF})$ and $\mathbf{\Lambda}_B = \text{diag}(\mathbf{f}_{segB})$ are two diagonal matrix, and $(\mathbf{\Lambda}_B - \mathbf{\Lambda}_F)\omega(k)$ determines the upper bound of auxiliary vector $\lambda(k)$. Constraint (8) represents the upper and lower bound of $f_{ac}(k)$, and constraint (9) represents frequency regulation limitations during discrete control interval.
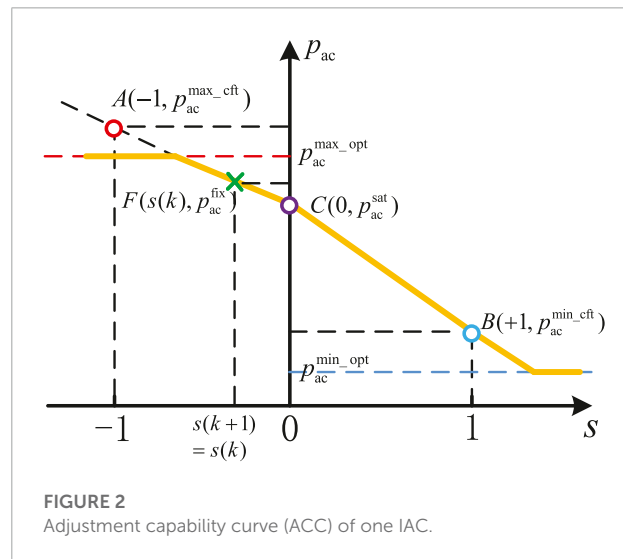
FIGURE 2
Adjustment capability curve (ACC) of one IAC.

2.2 Adjustable capability of one IAC

For each room equipped with an IAC, suppose there always exists an acceptable room temperature range $[T_{min}, T_{max}]$ and a most satisfactory temperature T_{fit} according to user's personal preference. So, electrical power p_{ac} of IAC can be regulated within a certain range without violating the user's comfort limitations, which provides substantial flexible power adjustment capability to the distribution system after aggregating.

To evaluate the power adjustment capability of one IAC and an IACs cluster, we firstly introduce a piecewise linear mapping

$\varphi : \mathbb{R} \mapsto \mathbb{R}$ of room temperature T_a:

$$\varphi(T_a) = \begin{cases} (T_a - T_{fit})/(T_{max} - T_{fit}), & if \quad T_a \geq T_{fit} \\ (T_a - T_{fit})/(T_{fit} - T_{min}), & if \quad T_a < T_{fit} \end{cases} \quad (10)$$

Thus, the mapping result $s = \varphi(T_a)$ will be a scalar within the range of $[-1, 1]$, which will be positive if room temperature T_a is above T_{fit}, and be negative if T_a is below T_{fit}. Meanwhile, smaller absolute value of s indicates that T_a is closer to T_{fit}, hence $|s|$ can be regarded as an index to quantify user's "unsatisfactory degree" [15] of current room temperature T_a.

Then, we define a monotonically decreasing function $p_{ac} = d_{ac}(s)$ termed adjustment capability curve (ACC) of one IAC according to user's preference information, which is illustrated in **Figure 2**. The horizontal axis represents the target "unsatisfactory degree" $s(k+1)$ after current round of control, and vertical axis represents the electrical power p_{ac} required to transfer $s(k)$ to $s(k+1)$. Intuitively, image of ACC is uniquely determined according to 4 characteristic points (F, A, B, C) and 2 horizontal power boundary values $p_{ac}^{max\_opt}, p_{ac}^{min\_opt}$. For point F, its abscissa value indicates target "unsatisfactory degree" $s(k+1)$ is fixed to current $s(k)$, and its ordinate value p_{ac}^{fix} represents the required electrical power to guarantee $s(k+1) = s(k)$ after control period τ. Similarly, for point A, it indicates the electrical power $p_{ac}^{max\_cft}$ required to ensure $s(k+1) = -1$; for point B, it indicates the electrical power $p_{ac}^{min\_cft}$ to satisfy $s(k+1) = +1$; for point C, it indicates the electrical power p_{ac}^{sat} to guarantee $s(k+1) = 0$. Except for these 4 characteristic electrical power values $\{p_{ac}^{fix}, p_{ac}^{max\_cft}, p_{ac}^{min\_cft}, p_{ac}^{sat}\}$, p_{ac} is also restricted by IAC's upper and lower bound of electrical power $\{p_{ac}^{max\_opt}, p_{ac}^{min\_opt}\}$ due to physical operation limitations. Consequently, $p_{ac} = d_{ac}(s)$ presents to be a monotonically decreasing piecewise linear function.

To obtain adjustable capacity of one IAC, firstly we should calculate corresponding characteristic cooling power values $\{q_{ac}^{fix}, q_{ac}^{max\_cft}, q_{ac}^{min\_cft}, q_{ac}^{sat}\}$ according to discrete ETP **Equation 2**:

$$q_{ac}^{fix}(k) = c_a \rho_a V_{room} \sigma(T_{out} - T_a(k)) \quad (11)$$

$$q_{ac}^{max\_cft}(k) = c_a \rho_a V_{room} \sigma\left(T_{out} - \frac{T^{min} - e^{-\sigma\tau}T_a(k)}{1 - e^{-\sigma\tau}}\right) \quad (12)$$

$$q_{ac}^{min\_cft}(k) = c_a \rho_a V_{room} \sigma\left(T_{out} - \frac{T^{max} - e^{-\sigma\tau}T_a(k)}{1 - e^{-\sigma\tau}}\right) \quad (13)$$

$$q_{ac}^{sat}(k) = c_a \rho_a V_{room} \sigma\left(T_{out} - \frac{T^{fit} - e^{-\sigma\tau}T_a(k)}{1 - e^{-\sigma\tau}}\right) \quad (14)$$

Then, by referring to aforementioned segmentation of IAC power and operation frequency, binary vector $\omega(k)$ and continuous auxiliary vector $\lambda(k)$ can be determined according to current cooling power $q_{ac}(k)$ *via* constraints (3)–(7). Afterward, characteristic power $p_{ac}^{\bullet}(k)$ (• stands for $\{fix, max\_cft, min\_cft, sat\}$) can be calculated:

$$p_{ac}^{\bullet}(k) = \mathbf{p}_{segF}^T \omega(k) + \frac{\mathbf{k}_{pseg}^T \omega(k)}{\mathbf{k}_{qseg}^T \omega(k)}\left[q_{ac}^{\bullet}(k) - \mathbf{q}_{segF}^T \omega(k)\right] \quad (15)$$

Finally, adjustable electrical power $p_{ac}^{\Delta}(k)$ of one IAC is quantified by:

$$\begin{cases} p_{ac}^{\Delta}(k) \geq \max\left\{p_{ac}^{min\_cft}(k), p_{ac}^{min\_opt}(k)\right\} - p_{ac}(k) \\ p_{ac}^{\Delta}(k) \leq \min\left\{p_{ac}^{max\_cft}(k), p_{ac}^{max\_opt}(k)\right\} - p_{ac}(k) \end{cases} \quad (16)$$

2.3 Adjustable capability of IAC cluster

During system-level dynamic economic dispatching and real-time control processes, the IAC cluster is the basic unit participating in power balance. So, an IAC cluster is working like a virtual power plant (VPP) to some extent, which is ought to provide its power-adjustable capacity and current operation power to DSO.

To achieve this goal, in this paper, we require all IACs belonging to the same cluster to follow a unified control signal $s^*(k+1)$. The advantages are twofold: (1) Unified "unsatisfactory degree" ensures fairness of different users' comfort experience without violating their personal preference, because $s^*(k+1) \in [-1, 1]$; (2) This requirement is sufficiently simple and tractable, which brings great convenience to decision-making process even if the number of IACs in one cluster is very large. Once the requirement is satisfied, the adjustment capability of the IAC cluster can be easily computed by simply aggregating (adding up) each IAC's ACC as an equivalent ACC of the IAC cluster:

$$p_{cluster} = d_{cluster}(s) \overset{\Delta}{=} \sum_{i \in cluster} d_{ac,i}(s) \quad (17)$$

So, (17) indicates that $p_{cluster}$ is also a monotonically decreasing piecewise linear function concerning cluster's unified control signal s. Suppose $p_{cluster} \in [p_{cluster}^{min}, p_{cluster}^{max}]$, the adjustable capacity $p_{cluster}^{\Delta}$ of IAC cluster can be quantified similarly with **(16)**:

$$\begin{cases} p_{cluster}^{\Delta,min} \leq p_{cluster}^{\Delta} \leq p_{cluster}^{\Delta,max} \\ p_{cluster}^{\Delta,min} = \min\left\{0, p_{cluster}^{min} - p_{cluster}(k)\right\} \\ p_{cluster}^{\Delta,max} = \max\left\{0, p_{cluster}^{max} - p_{cluster}(k)\right\} \end{cases} \quad (18)$$

where $p_{cluster}(k) = \sum_i p_{ac,i}(k)$ is the electrical power demand of IAC cluster at current time point $k\tau$. That's to say, once $p_{cluster}(k)$ and cluster's ACC are determined, adjustable capacity $[p_{cluster}^{\Delta,min}, p_{cluster}^{\Delta,max}]$ of IAC cluster can be quickly determined according to (17) (18).

3 Adaptive robust economic dispatch optimization and solution methodology

Due to the lack of uncertainty modeling of RES, under some extreme operation scenarios, the decision results of a traditional

deterministic economic dispatching model based on predicted values may lead to high adjustment costs during real-time power balance. To remedy this defect, in this section, we propose a two-stage adaptive robust economic dispatch optimization model ARED in (19), which takes both uncertainty of RES and adjustable capability of IAC clusters into consideration:

$$\min_{y^f} Q^f + \max_u \min_{y^s} Q^s \tag{19}$$

The object function of ARED is composed of two parts: normal-state operation cost Q^f (first stage decision) and re-dispatch cost Q^s under worst operation scenario (second stage decision). The decision variables of these two stages are defined by y^f, y^s respectively, and u denotes uncertainty variables, which is modeled within an adjustable uncertainty set.

3.1 First stage decision

3.1.1 Decision variables definition

In the first stage decision, the decision variables are:

$$y^f = \begin{cases} v_j | \forall j \in V \\ p_{ij}; q_{ij}; l_{ij} | \forall (i,j) \in \xi \\ p_{g,j}; q_{g,j} | \forall j \in G \end{cases} \tag{20}$$

where V stands for the set of all busbars, ξ stands for the set of all distribution lines, and G represents the set of all power generation units (generators and wind plants); Decision variable v is the square of busbar voltage, $\{p_{ij}; q_{ij}; l_{ij}\}$ stands for active power, reactive power and square of current magnitude of directed distribution line (i,j), and p_g is active power generation of power generation unit.

3.1.2 Objective function

The object of the first stage decision is to minimize power generation cost and wind curtailment punishment according to predicted power generation of wind plants w_g^e:

$$\min Q^f = \sum_{j \in \{G \setminus W\}} \left(c_{2,j} p_{g,j}^2 + c_{1,j} p_{g,j} + c_{0,j} \right) + \sum_{j \in W} \rho_{cr} \left(w_{g,j}^e - p_{g,j} \right) \tag{21}$$

where c_2, c_1, c_0 are coefficient of generator's quadratic generation cost function; ρ_{cr} is punishment coefficient of wind curtailment; W is the set of wind plants, which is a subset of G.

FIGURE 3
Local rolling MPC of IAC controller.
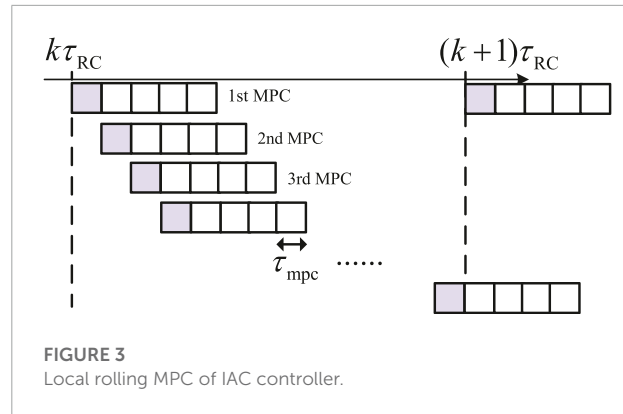
3.1.3 Constraints

$$p_{g,j} - p_{d,j} + \sum_{(i,j)\in\xi} \left(p_{ij} - r_{ij}l_{ij} \right) = \sum_{(j,k)\in\xi} p_{jk} + g_j v_j \tag{22}$$

$$q_{g,j} - q_{d,j} + \sum_{(i,j)\in\xi} \left(q_{ij} - x_{ij}l_{ij} \right) = \sum_{(j,k)\in\xi} q_{jk} + b_j v_j \tag{23}$$

$$v_j = v_i + \left(r_{ij}^2 + x_{ij}^2 \right) l_{ij} - 2 \left(r_{ij}p_{ij} + x_{ij}q_{ij} \right) \tag{24}$$

$$\left\| 2p_{ij}; 2q_{ij}; l_{ij} - v_i \right\|_2 \le l_{ij} + v_i \tag{25}$$

$$\left(V_j^{\min} \right)^2 \le v_j \le \left(V_j^{\max} \right)^2 \tag{26}$$

$$\begin{cases} p_{g,j}^{\min} \le p_{g,j} \le p_{g,j}^{\max} \\ q_{g,j}^{\min} \le q_{g,j} \le q_{g,j}^{\max} \end{cases} \quad j \in G \\ \begin{cases} 0 \le p_{g,j} \le w_{g,j}^e \\ p_{g,j}\tan\phi^{\min} \le q_{g,j} \le p_{g,j}\tan\phi^{\max} \end{cases} \quad j \in W \tag{27}$$

$$\begin{cases} -p_{ij}^{\max} \le p_{ij} \le p_{ij}^{\max} \\ -p_{ij}^{\max} \le p_{ij} - l_{ij}r_{ij} \le p_{ij}^{\max} \\ -q_{ij}^{\max} \le q_{ij} \le q_{ij}^{\max} \\ -q_{ij}^{\max} \le q_{ij} - l_{ij}x_{ij} \le q_{ij}^{\max} \\ l_{ij} \ge 0 \end{cases} \tag{28}$$

For $\forall j \in V$, constraints (22) (23) stand for nodal active power and reactive power balance equations respectively; For $\forall (i,j) \in \xi$, we specially use second-order cone relaxation (SOCR) inequality (25) to substitute original quadratic equation $v_i l_{ij} = (p_{ij})^2 + (q_{ij})^2$, which is widely used in modeling radial distribution network (Farivar and Low, 2013); Constraint (26) restricts upper and lower bound of busbar voltage; Boundary constraints of all power generation units and power factor constraints of wind plants are presented in (27), where $\phi \in [\phi^{\min}, \phi^{\max}]$ is allowable power factor angle. Constraints (28) represents bidirectional power flow limitations.

FIGURE 4
Schematic of ARED and real-time control processes.

FIGURE 5
Case study: a modified IEEE 33-busbar system.

3.2 Second stage decision

3.2.1 Decision variables definition

In the second stage decision, to ensure power balance, re-dispatch of all generation units, controllable load clusters (i.e., IAC clusters in this paper), wind power curtailment, and load shedding are deployed according to actual RES power generation during real-time operation. This stage is regarded as a "corrective stage" based on the first stage decision results. The decision

variables are listed in (29), where we use superscript Δ to indicate the variation of the corresponding decision variable, which can be positive or negative. In addition, two non-negative variables $p_{g,j}^{\Delta,abs}$ and $p_{d,j}^{\Delta,abs}$ are introduced, which equal the absolute values of $p_{g,j}^{\Delta}$ and $p_{d,j}^{\Delta}$.

$$y^s = \begin{cases} v_j^{\Delta}; \ |\forall j \in V \\ P_{ij}^{\Delta}; q_{ij}^{\Delta}; l_{ij}^{\Delta} \ |\forall (i,j) \in \xi \\ p_{g,j}^{\Delta}; q_{g,j}^{\Delta}; p_{g,j}^{\Delta,abs} \ |\forall j \in G \\ w_{g,j}^{cr} \ |\forall j \in W \\ p_{d,j}^{\Delta}; q_{d,j}^{\Delta}; p_{d,j}^{\Delta,abs} |\forall j \in L \end{cases} \quad (29)$$

3.2.2 Objective function

$$\max_{u} \min_{y^s} Q^s = \sum_{j \in \{G \backslash W\}} \rho_{ad,j} p_{g,j}^{\Delta,abs} + \sum_{j \in W} \rho_{cr,j} w_{g,j}^{cr}$$
$$+ \sum_{k \in CL} \rho_{d,j} p_{d,k}^{\Delta,abs} + \sum_{k \in \{L \backslash CL\}} \rho_{ls,j} p_{d,k}^{\Delta,abs} \quad (30)$$

The object function is to minimize the total cost of corrective actions under the worst uncertainty scenario $u \in U$, where U is the adjustable uncertainty set. CL stands for the set of all controllable IAC clusters. Coefficient $\{\rho_{ad}, \rho_{cr}, \rho_d, \rho_{ls}\}$ represents power adjustment cost of generation units, curtailment cost of wind plants, power adjustment cost of controllable IAC clusters and load shedding cost of normal loads.

3.2.3 Constraints

$$p_{\mathrm{g},j}^{\Delta} + p_{\mathrm{d},j}^{\Delta} + \sum_{(i,j)\in\xi}\left(p_{ij}^{\Delta} - r_{ij}l_{ij}^{\Delta}\right) = \sum_{(j,k)\in\xi} p_{jk}^{\Delta} + g_j v_j^{\Delta} \tag{31}$$

$$q_{\mathrm{g},j}^{\Delta} + q_{\mathrm{d},j}^{\Delta} + \sum_{(i,j)\in\xi}\left(q_{ij}^{\Delta} - x_{ij}l_{ij}^{\Delta}\right) = \sum_{(j,k)\in\xi} q_{jk}^{\Delta} + b_j v_j^{\Delta} \tag{32}$$

$$v_j^{\Delta} = v_i^{\Delta} + \left(r_{ij}^2 + x_{ij}^2\right)l_{ij}^{\Delta} - 2\left(r_{ij}p_{ij}^{\Delta} + x_{ij}q_{ij}^{\Delta}\right) \tag{33}$$

$$2p_{ij}p_{ij}^{\Delta} + 2q_{ij}q_{ij}^{\Delta} - l_{ij}v_i^{\Delta} - v_i l_{ij}^{\Delta} = 0 \tag{34}$$

$$\begin{cases} p_{\mathrm{g},j}^{\min} \le p_{\mathrm{g},j} + p_{\mathrm{g},j}^{\Delta} \le p_{\mathrm{g},j}^{\max} \\ q_{\mathrm{g},j}^{\min} \le q_{\mathrm{g},j} + q_{\mathrm{g},j}^{\Delta} \le q_{\mathrm{g},j}^{\max} \end{cases} \quad j \in G$$

$$\begin{cases} p_{\mathrm{g},j} + p_{\mathrm{g},j}^{\Delta} = w_{\mathrm{g},j}^{\mathrm{g}} - w_{\mathrm{g},j}^{\mathrm{cr}} \\ w_{\mathrm{g},j}^{\mathrm{cr}} \ge 0 \\ \left(p_{\mathrm{g},j} + p_{\mathrm{g},j}^{\Delta}\right)\tan\phi^{\min} \le q_{\mathrm{g},j} + q_{\mathrm{g},j}^{\Delta} \\ q_{\mathrm{g},j} + q_{\mathrm{g},j}^{\Delta} \le \left(p_{\mathrm{g},j} + p_{\mathrm{g},j}^{\Delta}\right)\tan\phi^{\max} \end{cases} \quad j \in W \tag{35}$$

$$\left(V_j^{\min}\right)^2 \le v_j + v_j^{\Delta} \le \left(V_j^{\max}\right)^2 \; j \in V$$

$$\begin{cases} -p_{ij}^{\max} \le \left(p_{ij} + p_{ij}^{\Delta}\right) \le p_{ij}^{\max} \\ -p_{ij}^{\max} \le \left(p_{ij} + p_{ij}^{\Delta}\right) - \left(l_{ij} + l_{ij}^{\Delta}\right)r_{ij} \le p_{ij}^{\max} \\ -q_{ij}^{\max} \le \left(q_{ij} + q_{ij}^{\Delta}\right) \le q_{ij}^{\max} \\ -q_{ij}^{\max} \le \left(q_{ij} + q_{ij}^{\Delta}\right) - \left(l_{ij} + l_{ij}^{\Delta}\right)x_{ij} \le q_{ij}^{\max} \\ l_{ij} + l_{ij}^{\Delta} \ge 0 \end{cases} \quad (i,j) \in \xi \tag{36}$$

$$\begin{cases} \beta^{\min} p_{\mathrm{d},j} \le p_{\mathrm{d},j}^{\Delta} \le \beta^{\max} p_{\mathrm{d},j} \\ \beta^{\min} q_{\mathrm{d},j} \le q_{\mathrm{d},j}^{\Delta} \le \beta^{\max} q_{\mathrm{d},j} \end{cases} \tag{37}$$

$$\begin{cases} w_{\mathrm{g},j}^{\mathrm{g}} = w_{\mathrm{g},j}^{\mathrm{e}} + \left(\theta_{\mathrm{g},j}^+ - \theta_{\mathrm{g},j}^-\right)\Delta w_{\mathrm{g},j} \\ 0 \le \theta_{\mathrm{g},j}^+, \theta_{\mathrm{g},j}^- \le 1 \end{cases} \tag{38}$$

$$\begin{cases} -p_{\mathrm{d},j}^{\Delta,\mathrm{abs}} \le p_{\mathrm{d},j}^{\Delta} \le p_{\mathrm{d},j}^{\Delta,\mathrm{abs}} \\ -p_{\mathrm{g},j}^{\Delta,\mathrm{abs}} \le p_{\mathrm{g},j}^{\Delta} \le p_{\mathrm{g},j}^{\Delta,\mathrm{abs}} \end{cases} \tag{39}$$

In these constraints, $\{p_{\mathrm{g}}, q_{\mathrm{g}}, p_{ij}, q_{ij}, l_{ij}, v\}$ are derived by the solutions of first stage decision model, and should be considered as constant known values during second stage decision. Constraints (31)–(36) basically inherit first stage constraints (22)–(28), but are presented in form of incremental expressions. (34) is derived through deploying first-order Taylor expansion on original constraints $v_i l_{ij} = (p_{ij})^2 + (q_{ij})^2$ at the operation point determined by first stage decision, which becomes a linear equation. (37) represents the adjustable capacity of IAC clusters or load shedding capacity of normal loads, where $\beta^{\min}, \beta^{\max}$ are two scale factors representing adjustable capacity (18) with their absolute value smaller than 1. For IAC clusters, they can not only reduce power demand, but also increase power demand, so $\beta^{\min} \le 0, \beta^{\max} \ge 0$; For normal loads, they can only reduce power demand (load shedding), hence $\beta^{\min} = 0, \beta^{\max} \ge 0$. (38) establishes a box-style uncertainty set to depict the relationship between actual power generation of wind plant $w_{\mathrm{g}}^{\mathrm{g}}$ and predicted value $w_{\mathrm{g}}^{\mathrm{e}}$. The maximum deviation Δw_{g} is adjustable, which can be used to obtain and compare solutions under different conservative levels. Auxiliary constraint (39) implicitly establishes non-negative restriction of variables $p_{\mathrm{g},j}^{\Delta,\mathrm{abs}}$, $p_{\mathrm{d},j}^{\Delta,\mathrm{abs}}$, and guarantees $p_{\mathrm{g},j}^{\Delta} = p_{\mathrm{g},j}^{\Delta,\mathrm{abs}}, p_{\mathrm{d},j}^{\Delta} = p_{\mathrm{d},j}^{\Delta,\mathrm{abs}}$ at optimal solution.

Different from the model formulation in previous work (Gao et al., 2018), the model in this paper not only requires fewer decision variables but also eliminates integer variables indicating upward or downward power adjustment states, which contributes to the simplification of ARED solution.

3.3 C&CG algorithm based ARED solution method

In our two-stage ARED optimization problem, the first stage decision is a QCQP problem due to SOCR of branch power flow equations. The second stage decision is a max-min problem, which can be regarded as a linear programming problem (LP) concerning decision variable y^{s} for given y^{f} and uncertainty scenario u. Considering the problem structure of ARED, we draw experience from column and constraints generation (C&CG) algorithm (Zeng and Zhao, 2013) to solve it, which iteratively solves the master problem (MP) and sub-problem (SP) to approximate the optimal solution. The compact form of MP and SP are:

$$\mathrm{MP}: \min_{y^{\mathrm{f}}, \eta, y^{\mathrm{s},l}} Q^{\mathrm{f}} + \eta$$
$$\mathrm{s.t.} \begin{cases} \eta \ge b^{\mathrm{T}} y^{\mathrm{s},l} \\ E_{\mathrm{ie}} y^{\mathrm{f}} + G_{\mathrm{ie}} y^{\mathrm{s},l} \le h_{\mathrm{ie}} - M_{\mathrm{ie}} u^l \quad , l = 1, \ldots, k \\ E_{\mathrm{e}} y^{\mathrm{f}} + G_{\mathrm{e}} y^{\mathrm{s},l} = h_{\mathrm{e}} - M_{\mathrm{e}} u^l \\ y^{\mathrm{f}} \in \Omega^{\mathrm{f}} \end{cases} \tag{40}$$

$$\mathrm{SP}: \max_u \min_{y^{\mathrm{s}}} Q^{\mathrm{s}} = b^{\mathrm{T}} y^{\mathrm{s}}$$
$$\mathrm{s.t.} \begin{cases} Qu \le q \\ G_{\mathrm{ie}} y^{\mathrm{s}} \le h_{\mathrm{ie}} - E_{\mathrm{ie}} y^{\mathrm{f}} - M_{\mathrm{ie}} u \\ G_{\mathrm{e}} y^{\mathrm{s}} = h_{\mathrm{e}} - E_{\mathrm{e}} y^{\mathrm{f}} - M_{\mathrm{e}} u \end{cases} \tag{41}$$

In MP, $y^{\mathrm{f}} \in \Omega^{\mathrm{f}}$ stands for feasible region of y^{f} generated by constraints (22)–(28); The first three constraints are gradually appended to MP after solving SP during each iteration, and k is current iteration times. In SP, $u \overset{\Delta}{=} ((\theta^+)^{\mathrm{T}}, (\theta^+)^{\mathrm{T}})^{\mathrm{T}}$, and constraint $Qu \le q$ stands for adjustable uncertainty set (38), and two remained equality and inequality correspond to constraints (31)–(37), (39).

To solve max-min problem SP, we firstly reformulate it to a single max-problem by deriving the dual problem of inner min-problem, which is named by DSP1:

$$\mathrm{DSP1}: \max_{u, \pi, \mu}$$
$$J = \left(h_{\mathrm{ie}} - E_{\mathrm{ie}} y^{\mathrm{f}} - M_{\mathrm{ie}} u\right)^{\mathrm{T}} \pi + \left(h_{\mathrm{e}} - E_{\mathrm{e}} y^{\mathrm{f}} - M_{\mathrm{e}} u\right)^{\mathrm{T}} \mu$$
$$\mathrm{s.t.} \begin{cases} Qu \le q, \; \pi \le 0 \\ \begin{bmatrix} G_{\mathrm{ie}} \\ G_{\mathrm{e}} \end{bmatrix}^{\mathrm{T}} \begin{pmatrix} \pi \\ \mu \end{pmatrix} = b \end{cases} \tag{42}$$

where π, μ are Lagrange multiplicators corresponding to inequality and equality constraints in (41). Notice that bilinear terms $u^{\mathrm{T}} M_{\mathrm{e}}^{\mathrm{T}} \mu$ and $u^{\mathrm{T}} M_{\mathrm{ie}}^{\mathrm{T}} \pi$ are incorporated in objective function of DSP1, which hinder DSP1 from being directly solved due to nonconvexity. Fortunately, by checking ARED model, it

can be deduced that:

$$u^{\mathrm{T}} M_{\mathrm{e}}{}^{\mathrm{T}} \mu = \left((\theta^+)^{\mathrm{T}} \quad (\theta^-)^{\mathrm{T}} \right) \begin{pmatrix} O & -\Lambda_{\mathrm{wg}} \\ O & \Lambda_{\mathrm{wg}} \end{pmatrix} \begin{pmatrix} \mu_{\neg\mathrm{wg}} \\ \mu_{\mathrm{wg}} \end{pmatrix}$$

$$= -(\theta^+)^{\mathrm{T}} \Lambda_{\mathrm{wg}} \mu_{\mathrm{wg}} + (\theta^-)^{\mathrm{T}} \Lambda_{\mathrm{wg}} \mu_{\mathrm{wg}} \qquad (43)$$

$$u^{\mathrm{T}} M_{\mathrm{ie}}{}^{\mathrm{T}} \pi = 0 \qquad (44)$$

where $\Lambda_{\mathrm{wg}} = \mathrm{diag}(\Delta w_{\mathrm{g}})$, μ_{wg} is the multiplicator related with equality constraint (45) synthetized from equations in (35) and 38 by eliminating intermediate variable $w_{\mathrm{g}}^{\mathrm{g}}$, and $\mu_{\neg\mathrm{wg}}$ is the rest multiplicator of μ.

$$p_{\mathrm{g},j} + p_{\mathrm{g},j}^{\Delta} = w_{\mathrm{g},j}^{\mathrm{e}} + \left(\theta_{\mathrm{g},j}^+ - \theta_{\mathrm{g},j}^- \right) \Delta w_{\mathrm{g},j} - w_{\mathrm{g},j}^{\mathrm{cr}} \, j \in W \qquad (45)$$

According to the work of Shao et al. (2017), max-min RO always derives its optimal solution at one vertex of the uncertainty set, so u can be regarded as a binary vector without loss of optimality. Considering this, we can furthermore eliminate bilinear terms in (43) by introducing auxiliary variable $z^+ = \theta^+ \circ \mu_{\mathrm{wg}}$, $z^- = \theta^- \circ \mu_{\mathrm{wg}}$ and applying big-M method:

$$\begin{cases} u^{\mathrm{T}} M_{\mathrm{e}}{}^{\mathrm{T}} \mu = -1^{\mathrm{T}} \Lambda_{\mathrm{wg}} z^+ + 1^{\mathrm{T}} \Lambda_{\mathrm{wg}} z^- \\ \mu_{\mathrm{wg}} + M(\theta^+ - 1) \le z^+ \le M\theta^+ \\ -M\theta^+ \le z^+ \le \mu_{\mathrm{wg}} - M(\theta^+ - 1) \\ \mu_{\mathrm{wg}} + M(\theta^- - 1) \le z^- \le M\theta^- \\ -M\theta^- \le z^- \le \mu_{\mathrm{wg}} - M(\theta^- - 1) \end{cases} \qquad (46)$$

where M is a big constant, $\circ$ stands for the Schur-Hadamard product of two matrices sharing the same size. Finally, DSP1 can be exactly linearized to an equivalent mixed integer linear programming (MILP) problem DSP2, which can be directly solved by commercial solvers:

$$\mathrm{DSP2}: \max_{u, \pi, \mu, z^+, z^-} J =$$
$$\left(h_{\mathrm{ie}} - E_{\mathrm{ie}} y^{\mathrm{f}} \right)^{\mathrm{T}} \pi + \left(h_{\mathrm{e}} - E_{\mathrm{e}} y^{\mathrm{f}} \right)^{\mathrm{T}} \mu - 1^{\mathrm{T}} \Lambda_{\mathrm{wg}} z^+ + 1^{\mathrm{T}} \Lambda_{\mathrm{wg}} z^-$$

$$\mathrm{s.t.} \begin{cases} Qu \le q, \pi \le 0 \\ \begin{bmatrix} G_{\mathrm{ie}} \\ G_{\mathrm{e}} \end{bmatrix}^{\mathrm{T}} \begin{pmatrix} \pi \\ \mu \end{pmatrix} = b \\ \mu_{\mathrm{wg}} + M(\theta^+ - 1) \le z^+ \le M\theta^+ \\ -M\theta^+ \le z^+ \le \mu_{\mathrm{wg}} - M(\theta^+ - 1) \\ \mu_{\mathrm{wg}} + M(\theta^- - 1) \le z^- \le M\theta^- \\ -M\theta^- \le z^- \le \mu_{\mathrm{wg}} - M(\theta^- - 1) \end{cases} \qquad (47)$$

To sum up, we use pseudo code to demonstrate the detailed solution process of ARED based on the C&CG algorithm.

4 Real-time control for compensation of res power fluctuation

The actual power generation of RES is revealed during real-time operation, which is very likely to deviate from the

```
Initialization:
   Set LB(0) = -inf, UB(0) = +inf, tolerance ε,
   iteration counter k = 1.
Iteration:
   1) Solve MP (40) and obtain yᶠ(k), η(k) and
      Qᶠ(k).
   2) Update LB(k) = max{LB(k-1),Qᶠ(k)}.
   3) Solve DSP2 (47) and obtain Qˢ(k) and
      worst scenario uᵏ = u(k).
   4) Update UB(k) = min{UB(k-1),LB(k)-η(k) +
      Qˢ(k)}.
Stopping Criteria:
   If:|[UB(k)-LB(k)]/LB(k)| ≤ε,stop;
   Else:append first three constraints in (40)
        to MP, and set k = k+1, go back to
        Iteration part.
```

Algorithm 1. C&CG Algorithm for Solving ARED.

predicted value due to RES power fluctuation. Hence, DSO distributes the power deviation to each generation unit and IAC cluster according to a proportion of their adjustable capacity. However, unlike distributed generators, the IAC cluster is unable to constantly generate and regulate a certain amount of power by itself, and it can only provide power adjustment by affecting the user's comfort experience (namely, by changing room temperature). Therefore, in this section, we propose a novel control strategy for IAC clusters to achieve power adjustment for compensation of RES power fluctuation without violating IAC users' comfort preferences.

4.1 Real-time control of IAC cluster

Suppose one IAC cluster's target power adjustment is $p_{\mathrm{cluster}}^{\Delta,*}(k)$. Hence, the immediate work of IAC cluster is to decompose $p_{\mathrm{cluster}}^{\Delta,*}(k)$ to every IAC, which turns out to find out the unified target $s^*(k+1)$ for all IACs to follow. Firstly, we calculate the target (reference) power of the IAC cluster by:

$$p_{\mathrm{cluster}}^*(k+1) = p_{\mathrm{cluster}}^{\Delta,*} + p_{\mathrm{cluster}}(k) \qquad (48)$$

Next, according to IAC cluster's ACC, the unified control target $s^*(k+1)$ can be determined by:

$$s^*(k+1) = d_{\mathrm{cluster}}^{-1} \left(p_{\mathrm{cluster}}^*(k+1) \right) \qquad (49)$$

where $d_{\mathrm{cluster}}^{-1}$ is the inverse function of d_{cluster}. Intuitively, $s^*(k+1)$ can derived by the intersection point of function curve $p_{\mathrm{cluster}} = d_{\mathrm{cluster}}(s)$ and horizontal line $p_{\mathrm{cluster}} = p_{\mathrm{cluster}}^*(k+1)$.

Finally, each IAC local controller conduct autonomous control of IAC to follow the target signal $s^*(k+1)$. Thus, this process can be carried out in a decentralized style. It is

TABLE 1 Parameters of power generation units.

Bus ID	Active Power Range (MW)	Reactive Power Range (MVar)	Cost Coefficient		
			c_2	c_1	c_0
1	[0, 10]	[−10,10]	0	25	0
9	[0, 0.8]	[−0.8, 0.8]	0	20	0
	0.5 Predicted	$\phi \in [0.1\pi, 0.2\pi]$			
19	[0, 0.8]	[−0.8, 0.8]	0	20	0
	0.45 Predicted	$\phi \in [0.1\pi, 0.2\pi]$			
24	[0, 0.8]	[−0.8, 0.8]	8	11.5	240
27	[0, 0.8]	[-0.8, 0.8]	5	12.1	220

TABLE 2 Random initialization of iac operation condition and user preference parameters.

Parameters		Distribution
IAC Operation Conditions	T_{out}(°C)	$U(31.5, 32.5)$
	$T_a(0)$(°C)	$N(25.0, 2.0)$
	$f_{ac}(0)$(Hz)	$U(30.0, 90.0)$
User Preference	T_{fit}(°C)	$N(25.4, 0.3)$
	T_{min}(°C)	$T_{fit} − U(1.0, 2.0)$
	T_{max}(°C)	$T_{fit} + U(1.0, 2.0)$

noteworthy that during local IAC control, to ensure accuracy and exactness of control, the sampling and control period is usually chosen to be smaller than that of determining the target signal. Therefore, a local model predictive control (MPC) optimization is developed to model and optimize the local process of tracking $s^*(k+1)$ with discrete time micro step $\tau = \tau_{mpc}$:

$$\min J_{ac} = \left(\mathbf{T}_a - \mathbf{T}_a^*\right)^T \Lambda_T \left(\mathbf{T}_a - \mathbf{T}_a^*\right)$$
$$+ \left(\mathbf{p}_{ac} - \mathbf{p}_{ac}^*\right)^T \Lambda_p \left(\mathbf{p}_{ac} - \mathbf{p}_{ac}^*\right)$$
$$s.t. \begin{cases} \mathbf{T}_a^* = \varphi^{-1}\left(s^*(k+1)\right) \times 1_{N_{mpc} \times 1} \\ \mathbf{p}_{ac}^* = d_{ac}\left(s^*(k+1)\right) \times 1_{N_{mpc} \times 1} \\ \text{constraints } (2) - (9) \text{ hold} \end{cases} \quad (50)$$

where N_{mpc} is the number of micro steps when applying MPC, which is also termed "prediction horizon" in some existed literature; $\mathbf{T}_a = [T_a(1), T_a(2),..T_a(N_{mpc})]^T \in \mathbb{R}^{N_{mpc}}$ is the room temperature at the end of each MPC micro step, and similarly $\mathbf{p}_{ac} \in \mathbb{R}^{N_{mpc}}$ is IAC electrical power of each micro step; Λ_T and Λ_p are two diagonal coefficient matrix; Constraints (2)–(9) are also required to be satisfied for each micro step. During the time period before receiving the next target signal, each IAC will repeatedly execute local MPC in a rolling manner, as shown in Figure 3. After each round of MPC, only the first micro step's control variable (namely, $f_{ac}(1)$) result is adopted by IAC controller (Chen and Liu, 2021).

4.2 Overall processes of ARED and real-time control

Now, we integrate ARED and real-time control together. The entire processes of conducting ARED and real-time control of IAC clusters are illustrated in Figure 4. The processes colored green, gray, and yellow are carried out by local IAC controllers, IAC load aggregators, and DSO respectively.

Firstly, each IAC aggregator computes the ACC of the IAC cluster and uploads its adjustable capacity to DSO every $\tau_{ARED} = 5$ min, which determines the lower and upper bound of load power adjustment in constraint (37). Based on IAC cluster adjustable capacity and predicted power generation of RES, DSO solves ARED optimization model and determines the optimal setting point for each power generation unit, which minimizes the total operation cost under the worst uncertainty scenario.

Afterward, real-time control processes are executed with a time cycle of $\tau_{RC} = 1$ min to ensure the minute-level power balance of the distribution system against RES power fluctuation. Concretely speaking, IAC aggregator determine its target "unsatisfactory degree" signal s^* according to (49), and broadcast s^* to its downstream IACs.

Finally, to track the target power indicated by s^*, each IAC will then execute rolling MPC locally and autonomously, which is conducted every $\tau_{mpc} = 15$ s with coefficient Λ_T set to zero matrix and Λ_p set to identity matrix. Therefore, to minimize cost function of MPC model (50), p_{ac} is forced to approach target value p_{ac}^* as quickly as possible during investigated prediction horizon, which ensures the accuracy of tracking target value. Although temperature T_a is not explicitly forced to track the target value T_a^* in objective function, its value is still located in the range of $[T_{min}, T_{max}]$ due to $s \in [-1, 1]$, which guarantees good comfort experience of IAC user.

TABLE 3 Results of ared's first and second stage decision.

Dispatchable Units	First Stage Decision		Second Stage Decision	
	p_g(MW)	q_g(MVar)	p^Δ(MW)	q^Δ(MVar)
S1	1.605	0.464	0.00	-0.071
W9	0.500	0.329	-0.200	-0.111
W19	0.400	0.291	-0.200	-0.145
G24	0.524	0.654	0.274	0.093
G27	0.745	0.606	0.055	0.110
IACs	–	–	0.066	0.065

TABLE 4 Per-hour cost comparison of ed and ared.

Method	1st Stage Cost ($)	2nd Stage Cost ($)	Total Cost ($)
ED	536.82	16.78	553.60
ARED	538.14	13.84	551.98

TABLE 5 Cost under different uncertainty magnitude.

Δw_g(MW)	0	0.05	0.1	0.15	0.2	0.25	0.3
1st Stage Cost ($)	536.82	536.92	537.16	537.57	538.14	538.78	539.48
2nd Stage Cost ($)	0	3.31	6.83	10.34	13.84	17.35	21.08
Overall Cost ($)	536.82	540.23	543.99	547.92	551.98	556.12	560.57
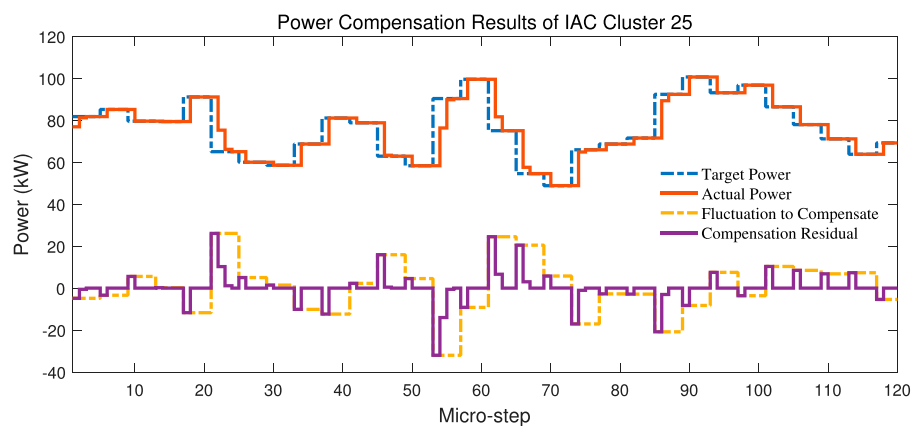
FIGURE 6
Compensation of wind power fluctuation.

5 Study case

5.1 Case description

A modified IEEE 33-busbar distribution network is adopted in this paper, the topology of which is shown in **Figure 5**. Two distributed generators and two wind plants are added to busbars 9, 19, 24, 27, and four IAC clusters with 15, 15, 30, and 15 IACs individually are also integrated into busbars 7, 8, 25, and 30. In this study case, wind plants account for 50% of the total installed capacity of the explored distribution system, and can undertake 43% of the total load at maximum power generation.
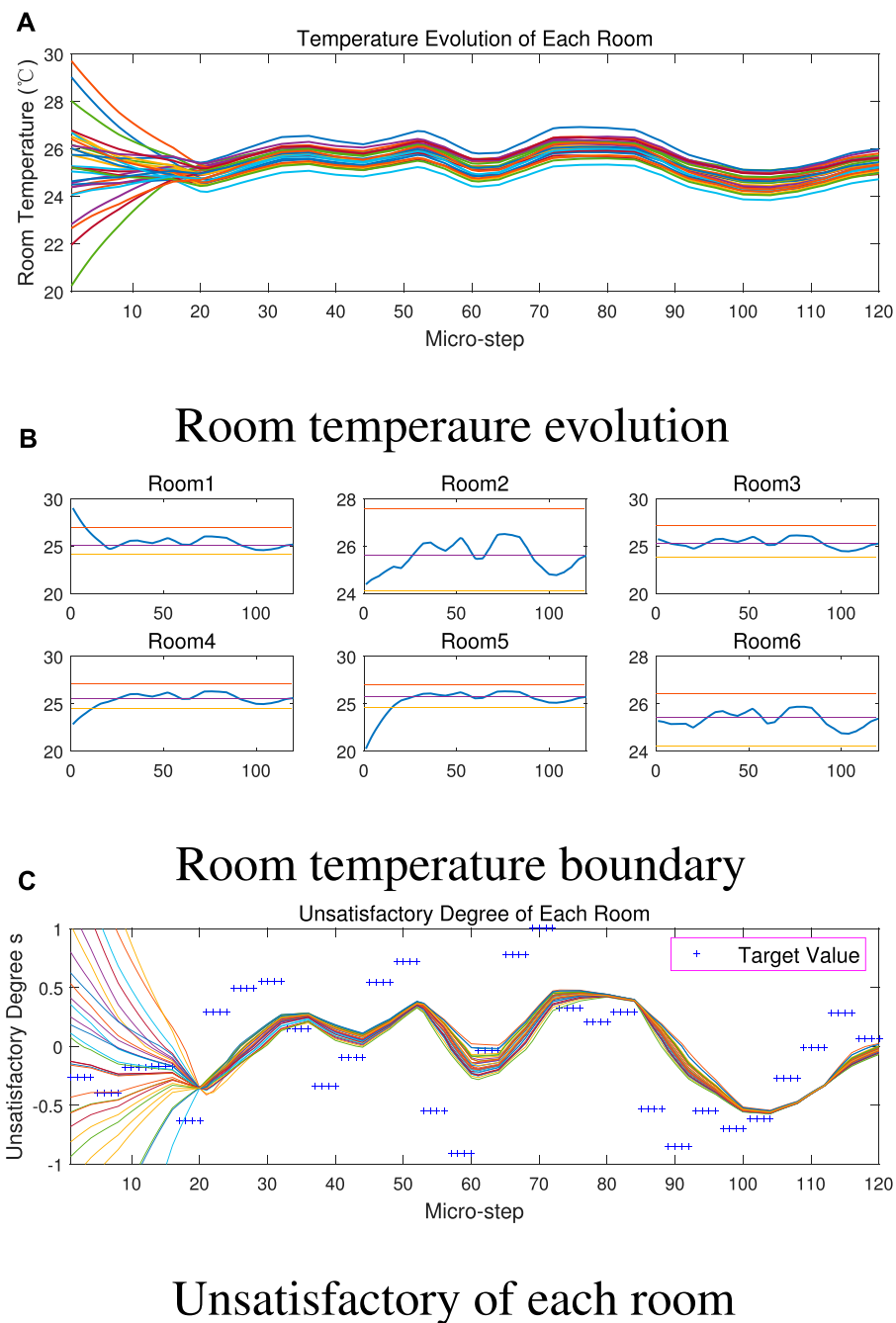
FIGURE 7
Evoluton of **(A)**, **(B)** room temperature and **(C)** unsatisfactory degree.

For the first stage decision of ARED, parameters of all dispatchable power generation units are listed in **Table 1**. For second stage decision of ARED, cost coefficients of wind curtailment and load shedding $\{\rho_{cr}, \rho_{ls}\}$ are set to 40, 60$/MW respectively. Power adjustment cost coefficient ρ_{ad} of the transmission system is set to 45$/MW, and that of distributed

generators is set to 35$/MW. IAC clusters in this paper are assumed to participate in power adjustment by incentive contracts, and the contract price (i.e., cost coefficient ρ_d) is set to 35$/MW.

The parameters of IAC are inherited from the literature [18], and for each room equipped with IAC, the initial
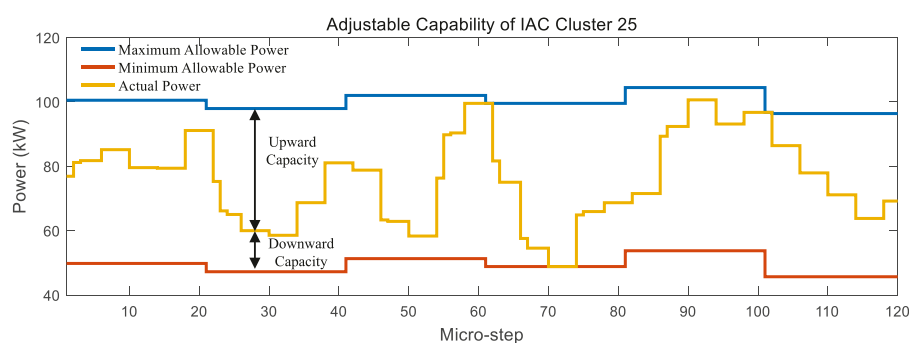
FIGURE 8
Adjustable capability of IAC cluster.

room temperature, initial IAC compressor operation frequency, and ambient temperature are randomly generated according to distributions in **Table 2** where N, U stands for Gaussian distribution and uniform distribution. We also simplify each room's structure to be a cuboid with length 12.5m, width 8m, and height 2.5 m.

5.2 Anaysis of ARED results

5.2.1 Results of ARED

Without losing generality, we firstly demonstrate ARED results with uncertainty budget set to $\Delta w_{g,j} = 0.2$ MW, which are listed in **Table 3**. For the results of the first stage decision, the operation power of wind plants at busbar 9 and 19 are scheduled to the same values as the predicted ones, which maximize the use of wind power. The second stage decision reveals the worst uncertainty scenario: the power generation of wind plants 9 and 19 simultaneously deviate -0.2 MW from predicted values, which causes an 0.4 MW power deficiency in total. To compensate for this deviation, distributed generators 24 and 27 increase their power generation by 0.274 and 0.055 MW, and controllable IAC clusters at busbar 7, 8, 25, and 30 decrease their power demand by 0.066 MW in total as well, which undertakes 16.5% of required power adjustment capacity. Meanwhile, the 0 MW power adjustment of the substation indicates that uncertain power fluctuation of RES is completely compensated within the distribution system itself, which stabilized power exchange between the distribution system and transmission system.

5.2.2 Comparison of ARED and traditional ED

In traditional ED, only the first stage decision is carried out to minimize total operation cost under predicted RES power generation, which is a deterministic optimization problem. As shown in **Table 4**. The cost of the first stage decision ($536.82/h) is lower than that of ARED ($538.14/h). However, under the

worst uncertainty scenario, ED's cost of corrective regulation in the second stage ($16.78/h) is contrarily higher than ARED ($13.84/h), which simultaneously causes a higher total cost ($553.60/h). The results also demonstrate the mechanism of ARED: by deviating the solution of the first stage decision from that of a deterministic model (which actually causes a suboptimal solution of the first stage), a smaller cost of the second stage under the worst operation scenario can be achieved, which leads to a lower total cost as well.

5.2.3 Influence of uncertainty budget

By adjusting uncertainty budget $\Delta w_{g,j}$ from 0 to 0.3 MW (interval 0.05 MW), ARED with different uncertainty budget are also solved to derive different robust optimal solutions under distinct conservative level. The results are shown in **Table 5**.

When $\Delta w_{g,j} = 0$, two-stage ARED model becomes a deterministic one with optimal first stage cost and 0 s stage cost. It is noteworthy that the optimal solution of the deterministic ARED model must be a feasible solution to other general ARED models with nonzero. Therefore, the optimal values of the objective function of other general ARED models are sure to be no less than that of the deterministic ARED model. Additionally, with the increase in the uncertainty budget, the cost of both two stages tends to increase simultaneously. This indicates that the more conservative the ARED model is, the less cost-effectiveness the results will be. So, the tradeoff between cost-effectiveness and robustness of ARED should be considered in practical situations by selecting an appropriate uncertainty budget.

5.3 Analysis of real-time control results

During real-time control, the deviation between RES actual and predicted power are distributed to dispatchable units for
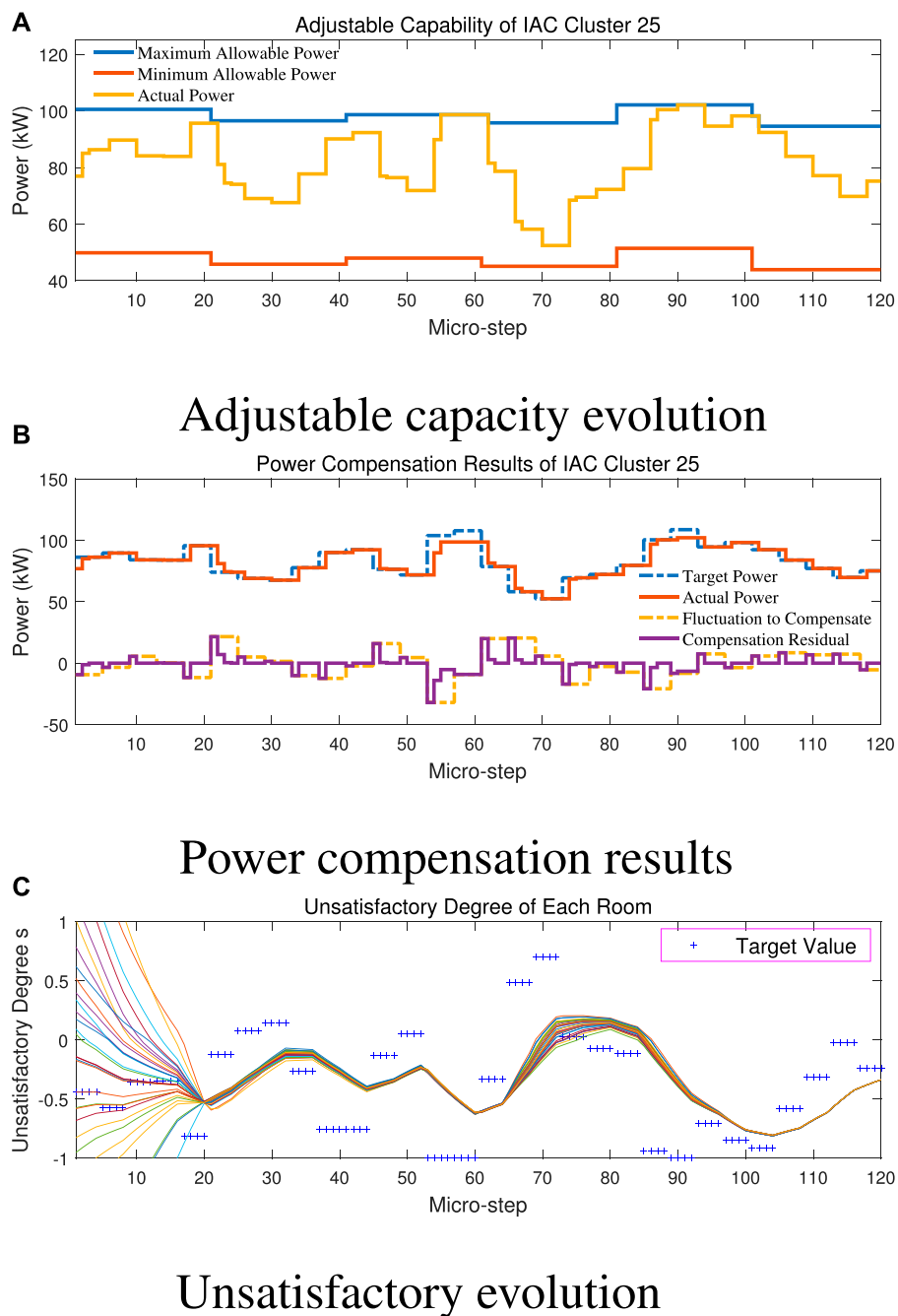
FIGURE 9
Results of real-time control with negative biased RES prediction error. **(A)** Adjustable capacity evolution. **(B)** Power compensation results. **(C)** Unsatisfactory evolution.

power compensation. Within these units, the IAC cluster is the most distinct because it works more like energy storage that is incapable of constantly generating and regulating a certain amount of power by itself. Hence, in this part, we focus on making an analysis of real-time control of IAC clusters.

5.3.1 Compensation of wind power fluctuation

Figure 6 demonstrates the power compensation effect of controllable IAC cluster at busbar 25 under the aforementioned control strategy. The yellow dotted line illustrates the fluctuation of the actual power of RES, which is sampled every 4 micro
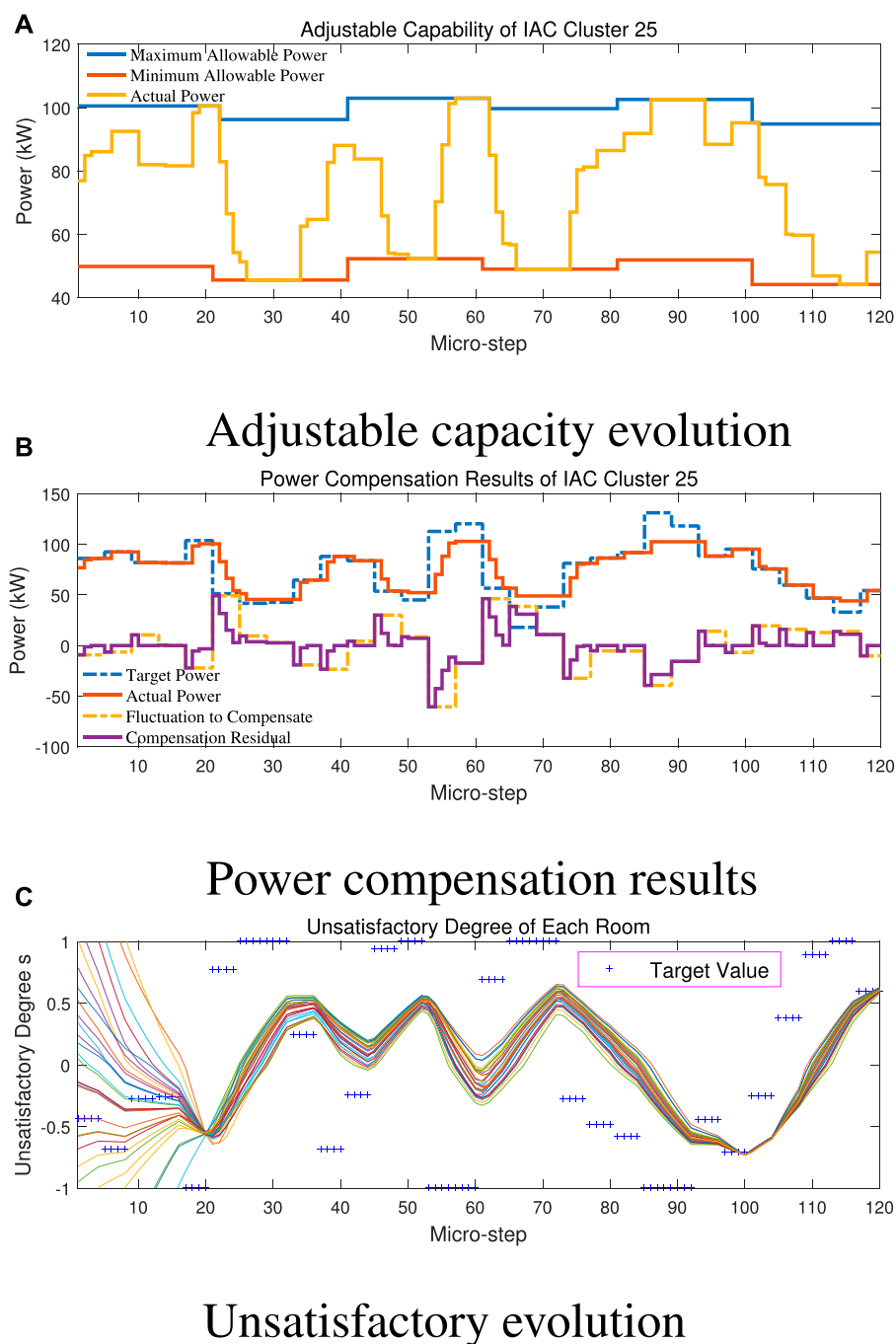
FIGURE 10
Results of real-time control with large power adjustment signal. **(A)** Adjustable capacity evolution. **(B)** Power compensation results. **(C)** Unsatisfactory evolution.

steps (τ_{RC} = 1 min), and indicates the latest power adjustment IAC cluster should undertake. By applying our control strategy, the target power of the IAC cluster is correspondingly calculated according to (48), as shown by the blue dotted line. Then, IACs

execute autonomous and local MPC control to track a unified target "unsatisfactory degree" signal translated from target power according to (49). The actual power response of IACs is shown by red line, which is updated every micro step (τ_{mpc} = 15 s).

It is clearly shown that the actual power of the IAC cluster perfectly follows the target power. Once the target power is updated, the actual power will start to vary towards the target value.

For a more intuitive presentation, we define the residual between target power and actual power by "compensation residual", which is presented by the purple line. The residual signal actually indicates the "unrealized" power adjustment to be undertaken by the transmission system. It can be found that the residual is a nonzero value at the beginning 1 micro-step of each τ_{RC} control interval (4 micro steps) due to updating of target power, but is gradually eliminated during the sequential 3 micro steps. This means power compensation can be fully achieved within the distribution system, and no more ancillary power adjustment is required in the transmission system.

5.3.2 Evolution of room temperature

The scaled adjustable capability of the IAC cluster is based on each IAC's minor contribution of power adjustment, which changes the temperature of a room. **Figure 7** demonstrates room temperature evolution of the 30 controllable IACs at busbar 25. In **Figure 7A**, we can find that initial values of room temperature are scattered in a wide range due to our random initialization. But these temperature values gradually converge to a narrow range after around 20 micro-steps and evolve following a similar tendency. This is the effect of adopting a unified target signal $s*$, as shown in **Figure 7C**. It can be found that the "unsatisfied degree" of each room gradually converges to the same value. Thus, high similarity can be observed concerning the evolution of different rooms' target temperature and actual temperature.

As real-time control proceeds, the room temperature is still within the range determined by each user's preference. For ease of explanation, we randomly choose 6 rooms and plot their individual temperature curve together with preference temperature levels in **Figure 7B**. It is clearly shown that after the initial 20 micro-steps, all rooms' temperature gradually locate within their individual allowable interval indicated by T_{max} (red horizontal line) and T_{min} (yellow horizontal line), and varies around T_{fit} (purple horizontal line). In fact, target signal $s*$ is bounded to [-1,1], as shown in **Figure 7C**, so room temperature will not violate user's preference constraints.

5.3.3 Adjustable capacity of IAC cluster

ACC of IAC cluster is updated for calculation of IAC cluster's adjustable capacity before conducting ARED, so its updating period is $\tau_{ARED} = 5$ min, which equals 20 micro-steps. **Figure 8** demonstrates adjustable capacity evolution of the IAC cluster at busbar 25. The upward adjustable capacity of the IAC cluster can be intuitively comprehended by the gap between maximum allowable power and actual power of IAC, and so is downward adjustable capacity similarly.

It can be observed that the maximum and minimum allowable power of IAC are time-variant, and this is the most prominent feature that distinguishes controllable IAC clusters from other dispatchable units such as distributed generators. The mechanism of this feature can be explained through ACC we proposed in **Section 2**: Firstly, higher room temperature will lead to larger maximum and minimum allowable power of IAC according to (12) and (13), which can be comprehended by shifting ACC curve upward along the vertical p_{ac} -axis; Meanwhile, "unsatisfactory degree" s is also monotonically increasing with respect to room temperature according to (10). Consequently, we can deduce that a bigger s corresponds to a higher value of the maximum and minimum allowable power of the IAC cluster. Referring to evolution of "unsatisfactory degree" s in **Figure 7C**, $s = -0.354, 0.116. -0.163, -0.421, -0.535$ at the 20th, 40th, 60th, 80th, and 100th micro-steps. Hence, the variation rule of the IAC cluster's maximum and minimum allowable power can be explained.

5.4 Influencing factors of real-time control performance

In this part, we discuss influencing factors of real-time control from two aspects: bias of prediction error and fluctuation amplitude of RES stochastic deviation from the predicted value.

5.4.1 Bias of prediction deviation

Under normal circumstances, the deviation between the predicted value and actual value of RES power generation obeys Gaussian distribution with a mean value of 0. The aforementioned results of real-time control are all obtained based on this assumption. However, positive-definite or negative-definite deviation may occur due to incorrect RES power prediction algorithm or other system failures, which is termed "bias" in this part.

Figure 9 demonstrates real-time control results of the IAC cluster at busbar 25 with a negative-definite bias of -4.5 kW superposed to its power adjustment signal, which requires the IAC cluster to increase power demand by an extra 4.5 kW. It can be noticed that curves of "unsatisfactory degree" are shifted downwards compared with those in **Figure 7C**. This means the power adjustment is achieved with lower room temperature, which affects the user's comfort experience. Meanwhile, the actual power of the IAC cluster is shifted upward and reaches the maximum allowable power boundary more frequently. On this occasion, the upward capacity of the IAC cluster is squeezed to 0, and the power adjustment signal may not be fully compensated, as shown at 60th and 90th micro-step in **Figure 9B**.

Consequently, the bias of prediction deviation will lead to orientated increasing or decreasing of IAC cluster power, which also shifts the variation range of room temperature.

The bias should be avoided as far as possible by improving the RES power prediction algorithm or eliminating system faults.

5.4.2 Amplitude of fluctuation

In this part, we amplify the power adjustment signal by 1.88 times to simulate violent RES power fluctuation. The results are calculated and shown in **Figure 10**.

Comparing **Figure 10A** with **Figure 8**, we can find that the actual power of IAC will reach maximum or minimum allowable boundary much more frequently under large fluctuation. When this happens, the upward capacity or downward capacity of the IAC cluster will be alternately squeezed to 0, and the power adjustment signal may not be fully compensated, as shown at the 55th, 70th, and 90th micro-steps in **Figure 10B**. For room temperature or "unsatisfactory degree" in **Figure 10C**, it is not shifted like the results under the biased situation of RES prediction, but the variation range becomes relatively wider compared with **Figure 7C**.

In fact, the actual power fluctuation of RES is usually bounded within a maximum range of 20% deviation from the predicted value. Therefore, the power adjustment signal can be fully compensated by the IAC cluster by aggregating a sufficient number of IACs or selecting the appropriate coefficient of distribution proportion.

6 Conclusion

This work proposes an adaptive robust economic dispatch (ARED) and real-time control scheme of the distribution system, which comprehensively takes the uncertainty of RES and flexibility of controllable IAC clusters into consideration. Firstly, the concept of the adjustable capacity curve (ACC) is developed to quantify the exact adjustable capacity of the IAC cluster within a certain time period and guide each IAC to carry out decentralized local model predictive control. Afterward, ARED model for the power dispatch stage is formulated, which incorporates the adjustable capacity of IAC and uncertainty set of RES power generation in the constraints. An iterative solution methodology of ARED is also designed by drawing the experience of the C&CG algorithm, of which the master problem is formulated as a QCQP and the max-min sub-problem is reformulated to a MILP *via* linear duality theory and big-M method. Finally, to hedge against stochastic RES power fluctuation, a real-time control strategy is also proposed, where IAC clusters provide ancillary power adjustment service based on decentralized control.

A case study on a modified IEEE 33-bus system verifies that ARED model can better guarantee the economic efficiency of the distribution system against the worst uncertainty scenario under different uncertainty budgets. Meanwhile, the real-time control strategy of the IAC cluster is also proved to be effective in eliminating RES power fluctuation without violating the comfort preferences of IAC users. In addition, the influence of biased prediction error and fluctuation amplitude is also analyzed in detail, which can provide a reference for enhancing the operation stability of the IAC cluster under our control strategy. In the future, we will furtherly investigate adjustable capability quantification and real-time control of IAC clusters based on price-based demand response.

Data availability statement

The original contributions presented in the study are included in the article/supplementary material, further inquiries can be directed to the corresponding author.

Author contributions

GC: modeling, simulation, and paper writing; DL: conceptualization and draft-reviewing.

Conflict of interest

The authors declare that the research was conducted in the absence of any commercial or financial relationships that could be construed as a potential conflict of interest.

Publisher's note

All claims expressed in this article are solely those of the authors and do not necessarily represent those of their affiliated organizations, or those of the publisher, the editors and the reviewers. Any product that may be evaluated in this article, or claim that may be made by its manufacturer, is not guaranteed or endorsed by the publisher.

References

Chen, G., and Liu, D. (2021). Hybrid flow model of cyber physical distribution network and an instantiated decentralized control application. *CSEE J. Power Energy Syst.* (Early Access). doi:10.17775/CSEEJPES.2020.05770

Chen, Y., Wang, Y., Kirschen, D., and Zhang, B. (2018). Model-free renewable scenario generation using generative adversarial networks. *IEEE Trans. Power Syst.* 33, 3265–3275. doi:10.1109/TPWRS.2018.2794541

Chen, Z., Guo, C., Dong, S., Ding, Y., and Mao, H. (2021). Distributed robust dynamic economic dispatch of integrated transmission and distribution systems. *IEEE Trans. Ind. Appl.* 57, 4500–4512. doi:10.1109/TIA.2021.3091663

Dai, Y., Kang, Y., and Xiong, X. (2017). *Energy development and carbon emission scenarios towards 2050 energy transition and low carbon development roadmap for China*. Beijing: China Environmental Publishing House.

Ding, Y., Xie, D., Hui, H., Xu, Y., and Siano, P. (2021). Game-theoretic demand side management of thermostatically controlled loads for smoothing tie-line power of microgrids. *IEEE Trans. Power Syst.* 36, 4089–4101. doi:10.1109/TPWRS.2021.3065097

Farivar, M., and Low, S. H. (2013). Branch flow model: Relaxations and convexification—Part i. *IEEE Trans. Power Syst.* 28, 2554–2564. doi:10.1109/TPWRS.2013.2255317

Gao, H., Liu, J., Wang, L., and Wei, Z. (2018). Decentralized energy management for networked microgrids in future distribution systems. *IEEE Trans. Power Syst.* 33, 3599–3610. doi:10.1109/TPWRS.2017.2773070

Hui, H. X., Ding, Y., and Zheng, M. L. (2019). Equivalent modeling of inverter air conditioners for providing frequency regulation service. *IEEE Trans. Ind. Electron.* 66, 1413–1423. doi:10.1109/tie.2018.2831192

Jiang, A., and Wei, H. (2018). Distributed cooperation model and optimal control strategy for interaction between large-scale air conditioning and power grid based on communication. *Proc. Chin. Soc. Electr. Eng.* 38, 6276–6283. doi:10.13334/j.0258-8013.pcsee.172036

Kalantar-Neyestanaki, M., Sossan, F., Bozorg, M., and Cherkaoui, R. (2020). Characterizing the reserve provision capability area of active distribution networks: A linear robust optimization method. *IEEE Trans. Smart Grid* 11, 2464–2475. doi:10.1109/TSG.2019.2956152

Li, Z., Shahidehpour, M., Wu, W., Zeng, B., Zhang, B., and Zheng, W. (2015). Decentralized multiarea robust generation unit and tie-line scheduling under wind power uncertainty. *IEEE Trans. Sustain. Energy* 6, 1377–1388. doi:10.1109/TSTE.2015.2437273

Liu, Y., Guo, L., and Wang, C. (2018). Economic dispatch of microgrid based on two stage robust optimization. *Proc. CSEE* 38, 4013–4022. doi:10.13334/j.0258-8013.pcsee.170500

Lu, Z., Huang, H., Shan, B., Wang, Y., Du, S., and Li, J. (2017). Morphological evolution model and power forecasting prospect of future electric power systems with high proportion of renewable energy. *Automation Electr. Power Syst.* 41, 12–18. doi:10.7500/AEPS20170109001

Ning, C., and You, F. (2018). Data-driven stochastic robust optimization: General computational framework and algorithm leveraging machine learning for optimization under uncertainty in the big data era. *Comput. Chem. Eng.* 111, 115–133. doi:10.1016/j.compchemeng.2017.12.015

Roldán, C., Mínguez, R., García-Bertrand, R., and Arroyo, J. M. (2019). Robust transmission network expansion planning under correlated uncertainty. *IEEE Trans. Power Syst.* 34, 2071–2082. doi:10.1109/TPWRS.2018.2889032

Ruan, H., Gao, H., Liu, J., and Huang, Z. (2019). A distributionally robust reactive power optimization model for active distribution network considering reactive power support of dg and switch reconfiguration. *Proceedings Chin. Soc. Electr. Eng.* 39, 685–695. doi:10.13334/j.0258-8013.pcsee.180241

Shao, C., Wang, X., Shahidehpour, M., Wang, X., and Wang, B. (2017). Security-constrained unit commitment with flexible uncertainty set for variable wind power. *IEEE Trans. Sustain. Energy* 8, 1237–1246. doi:10.1109/TSTE.2017.2673120

Shuai, H., Fang, J., Ai, X., Tang, Y., Wen, J., and He, H. (2019). Stochastic optimization of economic dispatch for microgrid based on approximate dynamic programming. *IEEE Trans. Smart Grid* 10, 2440–2452. doi:10.1109/TSG.2018.2798039

Tan, Z., Zhong, H., Xia, Q., Kang, C., Wang, X. S., and Tang, H. (2020). Estimating the robust p-q capability of a technical virtual power plant under uncertainties. *IEEE Trans. Power Syst.* 35, 4285–4296. doi:10.1109/TPWRS.2020.2988069

Wei, W., Wang, D., Jia, H., Wang, R., Guo, B., Qu, B., et al. (2016). A hierarchical and distributed control strategy of thermostatically controlled appliances for city park based on load model prediction. *Proc. Chin. Soc. Electr. Eng.* 36, 2049–2056. doi:10.13334/j.0258-8013.pcsee.2016.08.003

Yang, Y., Wu, W., Wang, B., and Li, M. (2021). Chance-constrained economic dispatch considering curtailment strategy of renewable energy. *IEEE Trans. Power Syst.* 36, 5792–5802. doi:10.1109/TPWRS.2021.3081120

Yao, Y., and Zhang, P. (2018). Coordinated control method for ancillary services of power system with participation of large-scale inverter air-conditioner. *Automation Electr. Power Syst.* 42, 127–134. doi:10.7500/AEPS20180131001

Yao, Y., and Zhang, P. (2020). Unified control strategy of heterogeneous thermostatically controlled loads with market-based mechanism. *J. Mod. Power Syst. Clean Energy* 8, 1231–1239. doi:10.35833/MPCE.2018.000828

Ye, L., Li, Z., Sun, B., Tang, Y., Lan, H., Wu, L., et al. (2018). Optimal dispatch of system integrated wind farm clusters based on stochastic model predictive control considering temporal correlation of wind power. *Proc. Chin. Soc. Electr. Eng.* 38, 3172–3183. doi:10.13334/j.0258-8013.pcsee.171162

Zeng, B., and Zhao, L. (2013). Solving two-stage robust optimization problems using a column-and-constraint generation method. *Operations Res. Lett.* 41, 457–461. doi:10.1016/j.orl.2013.05.003

Zhang, Z., Chen, Y., Liu, X., and Wang, W. (2019). Two-stage robust security-constrained unit commitment model considering time autocorrelation of wind/load prediction error and outage contingency probability of units. *IEEE Access* 7, 25398–25408. doi:10.1109/ACCESS.2019.2900254

Zhou, A., Yang, M., Zhai, H., Zhao, Y., Zhang, C., and Wei, S. (2018). Distributionally robust real-time dispatch considering moment uncertainty of wind generation. *Proc. Chin. Soc. Electr. Eng.* 38, 5937–5946. doi:10.13334/j.0258-8013.pcsee.180735

Improved unscented Kalman filter based interval dynamic state estimation of active distribution network considering uncertainty of photovoltaic and load

Jiawei Wu, Keman Lin, Feng Wu*, Zizhao Wang, Linjun Shi and Yang Li

College of Energy and Electrical Engineering, Hohai University, Nanjing, China

State estimation of active distribution network (ADN) plays an important role in distribution energy management system. The increase penetration of distributed generations, especially the distributed photovoltaic (PV), in ADN leads to high uncertainty of ADN's operation and the state of the ADN varies with the variation of the PV output power. For the uncertainty of PV power output, an interval dynamic state estimation (IDSE) method, which estimates the interval of ADN state variables is proposed in this paper. Firstly, considering the slow computation speed of the Unscented Kalman Filter (UKF), the square root UKF is used to predict the real-time operating level of the state variables. Secondly, since the power output of PV has features of the variation randomly, the neural network-based prediction intervals is employed to predict the power output interval of PV. Finally, the normal fluctuation range of ADN state is modelled as a bilevel non-linear programming problem to perform IDSE, which in turn monitors the operating state of ADN. The proposed method is evaluated on the IEEE 33-node and IEEE 123-node systems, respectively. The test results demonstrate that the dynamic status of the ADN can be tracked accurately using the proposed method.

KEYWORDS

interval dynamic state estimation, unscented Kalman filter, active distribution network, uncertainty, prediction interval

1 Introduction

State estimation (SE) is the basis for operation and control of active distribution network (ADN), providing a reliable foundation for advanced applications such as voltage control, security assessment, reactive power optimization, etc. The weighted least squares (WLS) method is the most used algorithm for traditional static state estimation (SSE). However, the large number of distributed generators (DG) such as photovoltaics (PV) connected to ADN highlights the non-linearity problem in ADN. Traditional SSE cannot satisfy real-time requirements, especially in capturing dynamic characteristics, the

dynamic state estimation (DSE) needs to be studied to support the efficient operation of ADN (Zhao et al., 2019).

The DSE could not only estimate the current state but also predict the state of the near future (Zhao et al., 2021), which is benefit for the timely problem detection and control of ADN, such as voltage exceeding limits. The traditional DSE method mainly includes Kalman Filter (KF) (Julier and Uhlmann, 2004, 2004; Valverde and Terzija, 2011; Karimipour and Dinavahi, 2015; Massignan et al., 2020). The Kalman-based DSE method, such as Extended Kalman Filter (EKF), is implemented on the assumption that the noise follows Gaussian distribution (Massignan et al., 2020). Unscented Kalman Filter (UKF) achieves higher accuracy than EKF due to unscented transformation, it propagates the mean and covariance through unscented transformation while capturing their nature to third order [6]. However, the accuracy of the UKF is dependent on the selection of initial values and the algorithm is too time consuming (Zhao et al., 2017), so it needs further improvement. Meanwhile, the large-scale grid integration of PV to ADN makes the results of SE need to consider more uncertainty factors, and how to consider the impact of uncertainty on SE is an urgent problem (Sihag and Tajer, 2018).

In general, the main methods of modelling uncertainty variables in ADN are probabilistic models (Valverde et al., 2013; Aien et al., 2014), fuzzy number models (AL-Othman, 2009) and interval number models (Rakpenthai et al., 2012). In (Valverde et al., 2013), the Gaussian mixture models are used to obtain the probability density function of DG and load, the result of Gaussian mixture models is introduced as input variables in state estimation of ADN. In (Aien et al., 2014), an analytical probabilistic-possibilistic tool based on the evidence theory and joint propagation of possibilistic and probabilistic uncertainties is proposed for the power flow uncertainty assessment. In (AL-Othman, 2009), the affiliation functions for loads and different DG outputs are established based on plausibility measures, and linear SE is performed by means of fuzzy analysis methods. The above methods can achieve good results, but the DSE methods based on probabilistic models and fuzzy number models need to obtain *a priori* probability density functions of uncertain variables in advance, which leads to an increase in the complexity of algorithm. In addition, the probability distribution of conventional electrical loads can be obtained from historical data in a real ADN, while the complete probability density function of PV power output is difficult to obtain. In most cases, only the upper and lower boundaries of its PV power fluctuations are known (Quan et al., 2014).

In contrast, the use of interval number model to describe uncertainty problems in SE is of greater application. Interval number model does not need to obtain specific distributions of variables, it only focuses on information about the upper and lower bounds of each uncertain variable (Khosravi et al., 2011).

At present, interval state estimator (ISE) has been initially investigated in ADN. In (Al-Othman and Irving, 2005), an optimization model is proposed for the interval SE that the measurement function is linearized as constrained formulations to estimate the upper and lower bounds on the states. In (Wang et al., 2018), an optimal solution method for interval SE is proposed to detect abnormal measurements. In (Huang et al., 2019), an optimization model of interval SE is combined with bad data identification to enhance the robustness of interval SE. In (Ngo and Wu, 2021), nonlinear measurement equation is transformed into dual inequality linear equations by mean value theorem to ensure the reliability of estimated intervals. However, the current ISE methods focus on interval static SE and there is little research on interval dynamic state estimator (IDSE).

In addition to the influence of uncertainty factors, the lack of real-time measurements limits the effective application of SE. Establishing accurate pseudo-measurement models can improve data redundancy and make the SE results of ADN more accurate (Schlösser et al., 2014). The data-driven method can mine the features of high-dimensional complex data and is highly superior in improving the accuracy of pseudo-measurement models (Massaoudi et al., 2021). In (Manitsas et al., 2012; Abdel-Majeed et al., 2014), the artificial neural networks are used for pseudo-measurement modelling, but to determine the model weights, the error distribution needs to be obtained in advance. In (Zhang et al., 2019), a deep recurrent neural network based pseudo-measurement postulating module is used to learn complex nonlinear functions to improve the accuracy of measurements. However, the modelling of pseudo-measurements is also subject to uncertainty factors that leads to reduced accuracy. Inspired by (Khosravi et al., 2011; Quan et al., 2014), pseudo-measurements can be modelled using interval models.

To deal with the uncertainty factors and lack of real-time measurements in ADN, an IDSE method is proposed for ADN integrated with PVs in this paper.

(1) In order to increase the calculation speed of the UKF without reducing accuracy, the square root of the covariance matrix is used instead of the covariance matrix in UKF and the improved UKF is used to determine the operating median values of all state variables.
(2) Neural network based prediction interval method is used to model the uncertainty of both pseudo-measurement of node injected power and real-time measurement in the system.
(3) The normal fluctuation range of ADN state is modelled as a bilevel non-linear programming problem to obtain the upper and lower bounds.

The simulations are carried out on IEEE 33-node and IEEE 123-node systems to evaluate the effectiveness of the proposed DSE method.

2 Dynamic state estimation based on square root unscented Kalman filter

2.1 Dynamic state estimation model

The state and measurement model of the nonlinear ADN can be written as follows (Zhao, 2018):

$$\begin{cases} x_k = f(x_{k-1}) + q_{k-1} \\ z_k = h(x_k) + r_k, \end{cases} \tag{1}$$

$$\begin{cases} q \sim N(0, Q) \\ r \sim N(0, R), \end{cases} \tag{2}$$

where, x_k is the n-dimensional state vector, sate variables are chosen as the voltage magnitude and phase angle for each bus, $x_k = [v_1^k, v_2^k, \ldots, v_n^k, \varphi_1^k, \varphi_2^k, \ldots, \varphi_n^k]$; z_k is the m-dimensional measurement vector, measurement variables are chosen as active and reactive power injections for each bus, $z_k = [P_1^k, P_2^k, \ldots, P_n^k, Q_1^k, Q_2^k, \ldots, Q_n^k]$; $f(\cdot)$ is the state transition function at k-1 time interval; $h(\cdot)$ is the measurement function; q_k is the system error; r_k is the measurement error, which is usually assumed to be uncorrelated Gaussian noise as Eq. 2; Q and R are system noise variance and measurement noise variance, respectively.

2.2 Square root unscented Kalman filter

2.2.1 Unscented Kalman filter

UKF is based on the basic steps of the Kalman filter, introducing the unscented transform as a sampling method to approximate the nonlinearity. The basic principle of UKF is to construct the Sigma point set with variance as the variance of the state variable around the mean point of the state variable, then perform a nonlinear transformation on each point in this point set, and finally weight the sum to obtain the state variable and variance after the nonlinear transformation, this method can achieve at least second order accuracy.

Unscented transform process: x is a random variable with mean $\bar{x}$ and covariance Px. Construct a Sigma point set $\{\chi_i\}$ that satisfies:

$$\bar{x} = \sum_{i=1}^{L} W_i^m \chi_i, \tag{3}$$

$$P_x = \sum_{i=1}^{L} W_i^c (\chi_i - \bar{x})(\chi_i - \bar{x})^T. \tag{4}$$

Perform a nonlinear transformation $y = f(x)$ on all Sigma points to obtain the transformed point set $\{\xi_i\}$. Once UKF has determined the sampling strategy, it also determines the number of sampling points L and weights W^m and W^c for mean and variance.

UKF consists of two main steps: time update and measurement update.

Step 1: time update

x_k is state variable at time k, P_k is the covariance of state variable at time k, the Sigma point set $\{\chi_k^i\}$ can be used to predict the state variable and variance in one step:

$$\chi_{k+1|k}^i = f(\chi_k^i) + q_k, \tag{5}$$

$$x_{k+1} = \sum_{i=1}^{L} W_i^m \chi_{k+1|k}^i \tag{6}$$

$$P_{k+1} = \sum_{i=1}^{L} W_i^c (\chi_{k+1|k}^i - x_{k+1})(\chi_{k+1|k}^i - x_{k+1})^T + Q_k, \tag{7}$$

$$\gamma_{k+1}^i = h(\chi_{k+1|k}^i) + r_k, \tag{8}$$

$$y_{k+1} = \sum_{i=1}^{L} W_i^m \gamma_{k+1}^i, \tag{9}$$

Step 2: measurement update

$$P_{y_{k+1}, y_{k+1}} = \sum_{i=1}^{L} W_i^c (\gamma_{k+1}^i - y_{k+1})(\gamma_{k+1}^i - y_{k+1})^T + R_{k+1}, \tag{10}$$

$$P_{x_{k+1}, y_{k+1}} = \sum_{i=1}^{L} W_i^c (\chi_{k+1|k}^i - x_{k+1})(\gamma_{k+1}^i - y_{k+1})^T, \tag{11}$$

$$K_{k+1} = \frac{P_{x_{k+1}, y_{k+1}}}{P_{y_{k+1}, y_{k+1}}}, \tag{12}$$

$$\hat{x}_{k+1} = x_{k+1} + K_{k+1}(z_{k+1} - \bar{y}_{k+1}), \tag{13}$$

$$P_{k+1} = P_{k+1} - K_{k+1} P_{y_{k+1}, y_{k+1}} K_{k+1}^T. \tag{14}$$

The detailed steps and derivation process of UKF can be found in [6]. The traditional UKF algorithm needs to perform a non-linear transformation on each sampling point, which is a quite complex calculation and has obvious numerical errors. As a result, it will affect the non-negative characterization and symmetry of error covariance, which will affect convergence speed and stability. To improve the efficiency and accuracy of filtering algorithm, the square root of covariance matrix can be used instead of covariance matrix in traditional UKF algorithm during recursive operation process.

2.2.2 Steps of square root unscented Kalman filter

The basic idea of square root UKF (SR-UKF) is to perform a QR decomposition of state variance matrix Pk in the UKF process, so that it satisfies $P_k = A_k * A_k^T = \bar{R}_k^T * \bar{R}_k$, where $\bar{R}_k$ is the upper triangular part of R in $A^T = QR$. The UKF filtering process is implemented by updating $\bar{R}_k$ instead of Pk.

Thus, Eq. 7 in time update step is modified as follows:

$$S_{k+1}^- = qr\left\{\left[\sqrt{W_1^c}(\chi_{k+1|k}^i - x_{k+1}), \sqrt{Q}\right]\right\}, \tag{15}$$

$$S_{k+1}^- = cholupdate\left\{S_{k+1}^-, \chi_{k+1|k}^0 - x_{k+1}, W_0^c\right\}. \tag{16}$$

Eq. 10 in measurement update step is modified as follows:

$$S_{y_{k+1}, y_{k+1}} = qr\left\{\left[\sqrt{W_1^c}(\gamma_{k+1}^i - y_{k+1}), \sqrt{R}\right]\right\}, \tag{17}$$

$$S_{y_{k+1}, y_{k+1}} = cholupdate\left\{S_{y_{k+1}, y_{k+1}}, \gamma_{k+1}^i - y_{k+1}, W_0^c\right\}, \tag{18}$$

Eq. 12 and Eq. 14 are modified as follows respectively:

FIGURE 1
The overall structure of Interval dynamic state estimator.

FIGURE 2
Prediction Interval model based on LUBE.
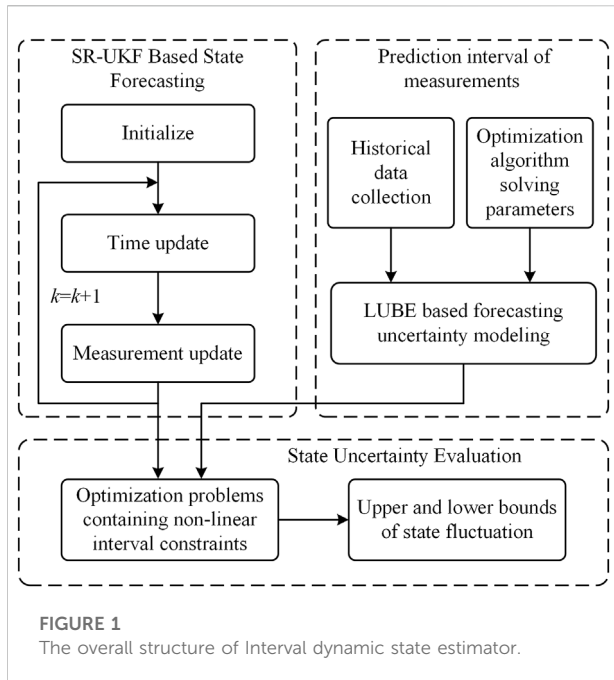
$$K_{k+1} = \frac{\left(P_{x_{k+1},y_{k+1}} \middle/ S_{y_{k+1},y_{k+1}}^T\right)}{S_{y_{k+1},y_{k+1}}}, \tag{19}$$

$$S_{k+1} = cholupdate\left\{S_{k+1}^-, K_{k+1}S_{y_{k+1},y_{k+1}}, -1\right\}, \tag{20}$$

where, $qr(\cdot)$ is QR decomposition, cholupdate$(\cdot)$ is Cholesky first-order update (Jafarzadeh et al., 2011). $\hat{x}_{k+1}$ represents the estimated optimal values for all state variables, including bus voltage magnitudes and phase angles. These values will be later used as inputs for IDSE in ADN.

3 Interval dynamic state estimator

In this section, a new generalized interval state estimator is proposed for ADN. It consists of three parts: SR-UKF, neural network (NN) and state uncertainty evaluation. SR-UKF is applied to obtain the operating states x^{k+1} of ADN (in Section 2). NN is mainly used for modeling the forecasting uncertainties of PV and load to obtain the upper and lower bounds of power. The purpose of state uncertainty evaluation is to quantify the upper and lower bounds of state fluctuation in ADN, the normal fluctuation range of ADN state is modelled as a bilevel non-linear programming problem to perform IDSE. The output parameters of the proposed state estimator are the normal fluctuation intervals for all state variables, The overall framework of IDSE is shown in Figure 1. The details of each part of the IDSE are given as follows.
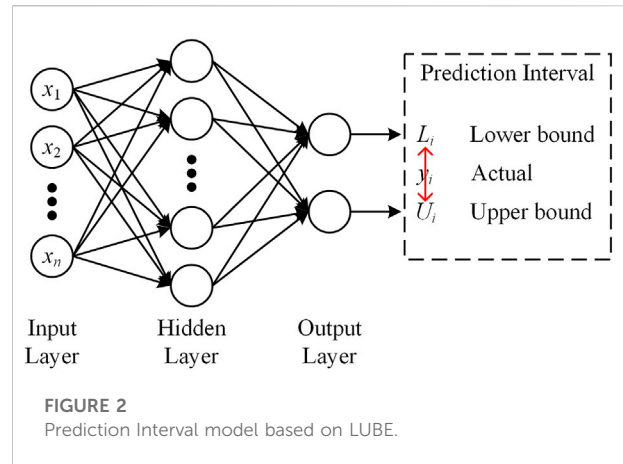
3.1 Prediction interval of measurements

Commonly used indicators for prediction interval assessment are prediction interval coverage probability (PICP), prediction interval normalized average width (PINAW) and prediction interval normalized root-mean-square width (PINRW):

$$PICP = \frac{1}{n}\sum_{i=1}^{n} \varepsilon_i, \tag{21}$$

where, n is the number of samples, $\varepsilon_i = 1$ if target value $y_i \in [L_i, U_i]$, otherwise $\varepsilon_i = 0$. L_i and U_i are the lower and upper bounds of the i-th prediction interval. PICP represents the probability that target value will fall within a prediction interval.

$$PINAW = \frac{1}{nR}\sum_{i=1}^{n} (U_i - L_i), \tag{22}$$

where, R is the range of the underlying target (maximum minus minimum), which ensures that PINAW is normalized to the interval [0,1]. Too wide interval leads to increased uncertainty in prediction results, reducing the predictability of the results for system scheduling. PINRW gives greater weight to wider intervals than PINAW, and practical results show that PINRW is more beneficial than PINAW for obtaining high quality intervals predictions [13].

$$PINRW = \frac{1}{R}\sqrt{\frac{1}{n}\sum_{i=1}^{n} (U_i - L_i)^2}. \tag{23}$$

The lower and upper boundary estimation (LUBE) theory [14] is based on a multi-layer perceptron neural network structure, which tunes the single node structure of the output layer of the back propagation neural network into a dual output node structure with lower and upper boundary values of prediction interval. Compared with traditional prediction interval schemes, LUBE avoids the limitations of data

distribution assumptions and complex calculations. The prediction interval model based on LUBE is shown in Figure 2, the number of layers and the number of nodes in each layer of neural network in LUBE can be adjusted according to actual situation.

For PV, the factors affecting the PV power output include solar radiation S, temperature T and humidity H. The inputs to the model at time i is:

$$X_i = \begin{bmatrix} S_i & T_i & H_i \end{bmatrix}^T \quad (24)$$

The output after forward propagation is:

$$\begin{aligned} Y_i &= \begin{bmatrix} L_i & U_i \end{bmatrix}^T \\ &= g(WX_i), \end{aligned} \quad (25)$$

where, $g(\cdot)$ is activation function. As the output prediction interval of PV is related to several influencing factors, an optimization function needs to be constructed by comprehensively evaluating the interval coverage and interval width, thus transforming multi-objective optimization into single-objective optimization. The integrated evaluation function for prediction interval (loss function) selected in this paper is as follows:

$$J = \begin{cases} f = PINRW\left(1 + \gamma(PICP)e^{-\eta(PICP-\mu)}\right) \\ \gamma = \begin{cases} 0, & PICP \geq \mu \\ 1, & PICP < \mu \end{cases} \end{cases}, \quad (26)$$

where, μ is confidence level and can be set to $1 - \alpha$, η is the parameter for f and usually $\eta \in [50, 100]$. Unlike traditional back propagation (BP) neural networks which use BP to obtain network parameters, LUBE can not use BP due to the lack of targets (observations of lower and upper bound). Therefore, optimization algorithms such as particle swarm optimization (PSO) can be used to obtain the parameters of LUBE model. Load can also be modelled using LUBE method.

3.2 Operating state uncertainty evaluation

To better reflect the influence of system uncertainties on ADN state estimation results, all bus measurements in the IDSE model established in this paper are objectively quantified and described as interval numbers, resulting in the solved system state variables are also interval numbers, which can provide effective system state boundary information for dispatchers.

The interval number [a] is defined as a non-empty real number set satisfying $[a] = \{a | \underline{a} \leq a \leq \bar{a}\}$ where $\bar{a}$ and $\underline{a}$ represent the upper and lower boundaries of the interval number [a], specifically, when $\underline{a} = \bar{a}$, interval number degenerates to real number. Thus, the measurement vector z and state vector x can be expressed as:
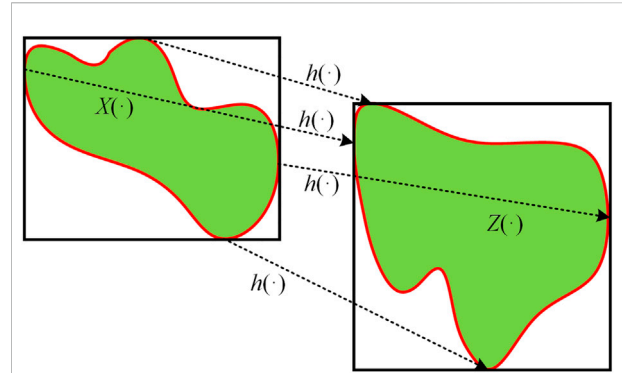
FIGURE 3
The relationship between the uncertainty sets $X(\ )$ and $Z(\ )$.

$$\begin{cases} [z] = \{[P_i], [Q_i], [P_{ik}], [Q_{ik}]\}^T & i, k = 1, 2, \ldots, n, \\ [x] = \{[U_i], [\theta_i]\}^T \end{cases} \quad (28)$$

where, n is the number of buses, active power P and reactive power Q are measurements, voltage magnitude U and phase angle θ are the state variables.

IDSE is to determine the state variable information of ADN based on the upper and lower bound information of measurement vector and non-linear mapping equation $z = h(x)$, which can be expressed as:

$$X(M, \underline{z}, \bar{z}) := \{x \in R^n : h(x) \in Z(M, \underline{z}, \bar{z})\}, \quad (29)$$

where, $X(\cdot)$ is the uncertainty set of system state variables, M is the set of system measurement, $Z(\cdot)$ is the uncertainty set of system measurement vector:

$$Z(M, \underline{z}, \bar{z}) := \left\{\hat{z} \in R^m : \underline{z_j} \leq z_j \leq \overline{z_j}, j = 1, 2, 3, \ldots, m\right\}, \quad (30)$$

where, $\hat{z}$ is an actual measurement vector, m is the cardinality of the system measurements set M. As the measurement vector has more dimensions than the state variable, and there is a nonlinear mapping relationship $h(\cdot)$, the geometry of the state set $X(\cdot)$ is complex, as shown in Figure 3.

It is difficult to establish uniform analytical expressions and standard analytical methods (Wang et al., 2013). However, based on the theory of unknown-but-bounded error (UBBE), the original problem can be transformed into two optimization problems containing non-linear interval constraints, where the upper and lower bounds on the variables to be solved are obtained separately (Bargiela et al., 2003). Thus, the interval state estimation model developed in this paper is expressed as follows:

Objectives:

$$\begin{aligned} \underline{x_i} &= \min x_i, \\ \bar{x}_i &= \max x_i. \end{aligned} \quad (31)$$

TABLE 1 Capacity and location of PV units.

PV location	PV capacity (MVA)
15, 46, 114	0.6
61, 88, 105	0.8
25, 68, 80	1.0
35, 98, 121	1.2

s.t.

$$P_i + \Delta P_i^G = V_i \sum_{j=1}^{n} V_j \left(G_{ij} \cos \theta_{ij} + B_{ij} \sin \theta_{ij} \right), \qquad (32)$$

$$Q_i + \Delta Q_i = V_i \sum_{j=1}^{n} V_j \left(G_{ij} \sin \theta_{ij} - B_{ij} \cos \theta_{ij} \right), \qquad (33)$$

$$\Delta P_i^G = \begin{cases} \Delta P_i^{RE}, & i \in \Omega_{RE}, \\ \Delta P_i^L, & i \in \Omega_L, \end{cases} \qquad (34)$$

$$\Delta P_{i,low}^{\tau,RE} \leq \Delta P_i^{RE} \leq \Delta P_{i,up}^{\tau,RE}, \qquad (35)$$

$$\Delta P_{i,low}^{\tau} \leq \Delta P_i^L \leq \Delta P_{i,up}^{\tau}, \qquad (36)$$

$$\Delta Q_{i,low}^{\tau} \leq \Delta Q_i \leq \Delta Q_{i,up}^{\tau}, \qquad (37)$$

where, $[\underline{x}_i, \bar{x}_i]$ is the interval value of state variable of node i, including voltage magnitude V and phase angle θ, P_i and Q_i are the active and reactive power of node i, G_{ij} and B_{ij} are admittance of branch ij, ΔP_i^{RE} is PV forecasting power output interval with lower bounds $\Delta P_{i,low}^{\tau,RE}$ and upper bounds $\Delta P_{i,up}^{\tau,RE}$, ΔP_i^L and ΔQ_i are load forecasting active and reactive power interval.

The estimation of individual state variable is independent of each other, as shown in Eq. 32, subject to the same equality and inequality constraints. The equality constraint contains active and reactive power balance constraints Eqs 33–35. Inequality constraints include PV forecasting uncertainty constraints Eq. 36 and load forecasting uncertainty constraints Eqs 37, 38. The upper and lower bounds of the forecasting uncertainty are updated in real time according to NN based LUBE.

4 Case study

In order to further verify the effectiveness and feasibility of the proposed IDSE method, a simulation study on IEEE 123-bus distribution system is carried out. The test system has a rated voltage of 4.16 kV and a total load of $3620 + j1324$ kVA, with individual load capacities and network branch parameters detailed in (Chai et al., 2018). 12 PV units are installed at 12 nodes, whose capabilities and locations are listed in Table 1. In addition, some nodes are selected to arrange real-time measurement devices, whose real-time measured power value is obtained from the power flow calculation of IEEE 123-bus system, and measurement error of ± 0.5% is superimposed on the rated value, the extended IEEE 123-bus distribution system is shown in Figure 4.

4.1 Prediction interval of measurements

(1) For PV power output, the ambient temperature, direct radiation, scattered radiation, and total radiation around the PV plant at various time sections during a week in a certain region are used as a source for PV power output prediction interval. The parameters of the LUBE are listed in Table 2. The resulting PV power output prediction interval based on LUBE estimates the PV power output curve at different time sections on a typical day is shown in Figure 5.

(2) For load, historical load data from AEMO (2006–2010) in New South Wales, Australia (Qiu et al., 2018) was used as a sample for load prediction interval. The resulting load prediction interval estimates the load curve at different times sections on a typical day is shown in Figure 6.

4.2 Interval dynamic state estimation

In order to make comparison of the results of IDSE for ADN, the PV power output interval [0, 0.1] kW at 01:00 a.m. and [302, 345] kW at 13:00 p.m. are selected for the test, based on which the EKF and UKF are used for the IDSE analysis with SR-UKF proposed in this paper. Figures 7, 8 show the results of IDSE in ADN based on these three methods.

As can be seen from the IDSE results shown in Figures 7, 8, the interval fluctuations in injected power of node cause the voltage magnitude and phase angle to fluctuate within a certain range, and the access to PV in ADN will increase the voltage level of the system. The comparison analysis shows that at any node of the ADN, the result interval of the IDSE method used in this paper is smaller than that of the EKF and closer to the result interval of the UKF, demonstrating that the conservativeness of the uncertain DSE solution can be effectively reduced by using the DSE algorithm with high accuracy. The EKF linearizes the system through Jacobian matrix calculation, which ignore higher order terms, making the state estimation of EKF less accurate and therefore the interval range obtained through the EKF is larger. The UKF approximates the non-linear system by unscented transformation, which can be approximated to at least second order for non-Gaussian inputs. Therefore, the UKF is more accurate than the EKF and has a smaller interval range than EKF. SR-UKF reduces computational errors and improves computational efficiency by propagating the SR of matrix instead of the matrix itself, its accuracy is slightly better than that of the UKF. SR-UKF has almost the same interval range as UKF.

In order to compare the conservativeness of the above three methods more intuitively, a comparative analysis of the interval width of IDSE for node voltage magnitude and phase angle is carried out, using two indicators to assess the conservativeness:
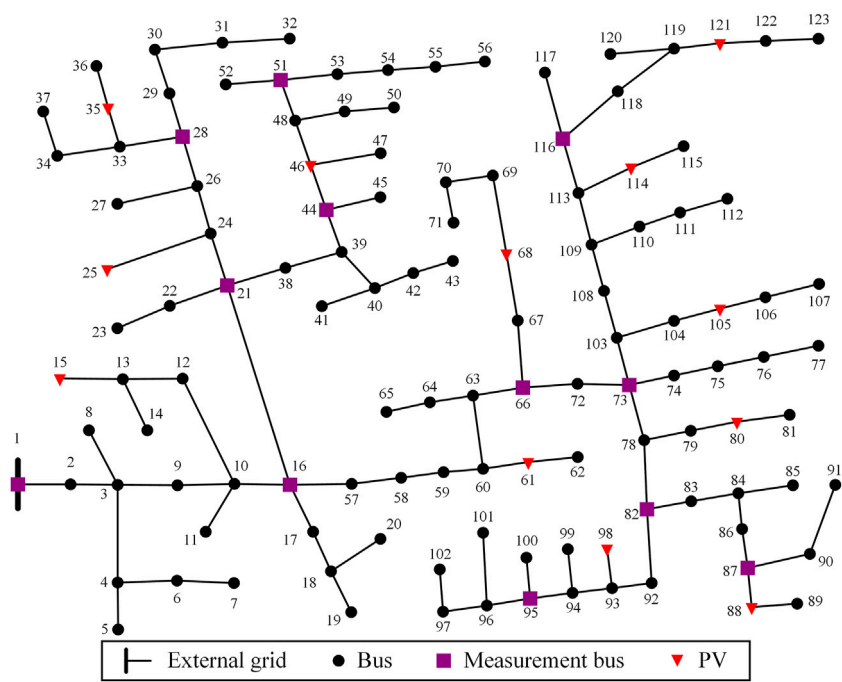
FIGURE 4
Topology of the extended IEEE-123 bus distribution system.

TABLE 2 LUBE parameters setting.

Number of net layers	Number of neurons per layer	η	μ
2	64	70	0.7

FIGURE 6
Prediction interval curve of load on a typical day.

FIGURE 5
Prediction interval curve of PV power output on a typical day.
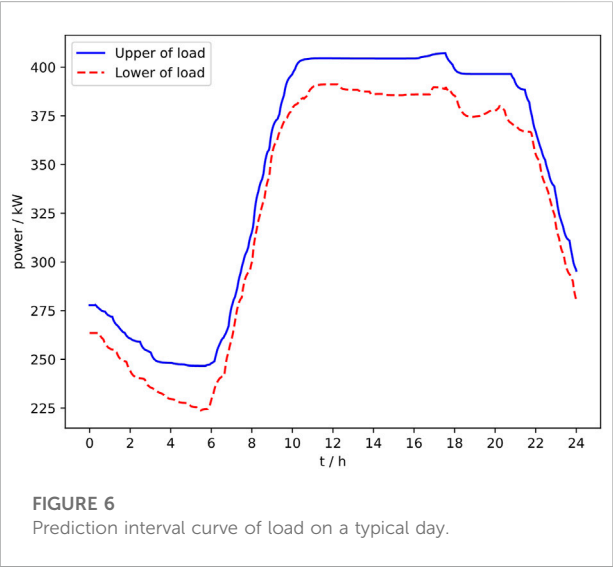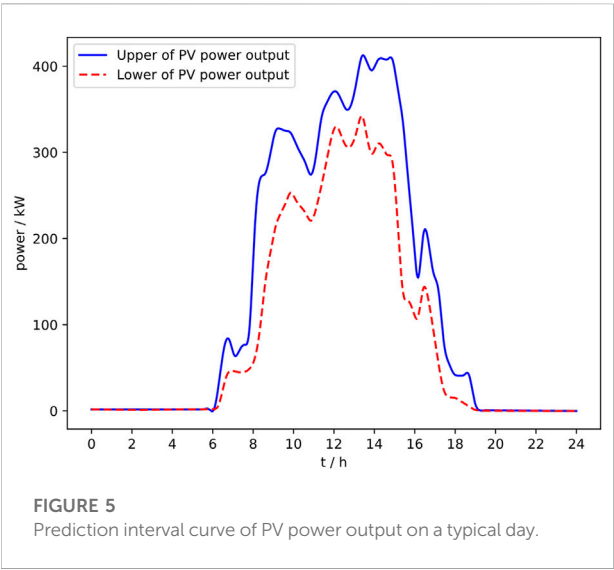
$$\begin{cases} \omega_1 = \dfrac{1}{n}\sum_{i=1}^{n}(\bar{x}_i - \underline{x}_i), \ \ i = 1, 2, \ldots, n, \\ \omega_2 = \max(\bar{x}_i - \underline{x}_i) \end{cases} \tag{38}$$

FIGURE 7
Estimation of node voltage amplitude and phase angle at t = 1 h.

FIGURE 8
Estimation of node voltage amplitude and phase angle at t = 13 h.
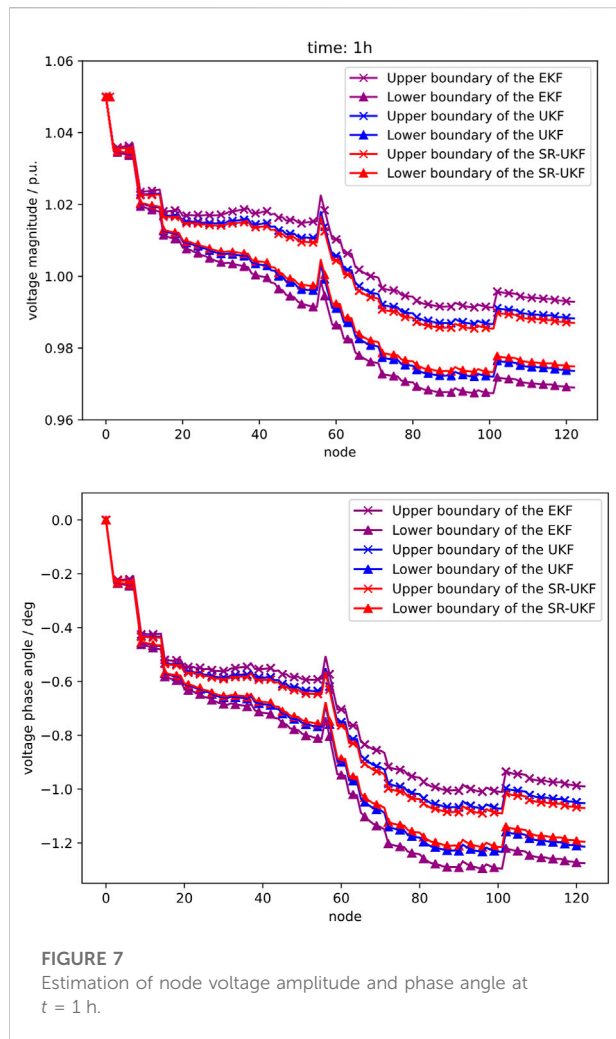
TABLE 3 Comparison bounds of node at t = 1 h

Method	Voltage magnitude		Phase angle	
	ω_1	ω_2	ω_1	ω_2
EKF	0.0185	0.0239	0.0050	0.0071
UKF	0.0115	0.0147	0.0034	0.0046
SR-UKF	0.0110	0.0131	0.0030	0.0041

TABLE 4 Comparison bounds of node at t = 13 h

Method	Voltage magnitude		Phase angle	
	ω_1	ω_2	ω_1	ω_2
EKF	0.0215	0.0284	0.0079	0.0113
UKF	0.0168	0.0221	0.0051	0.0072
SR-UKF	0.0162	0.0202	0.0044	0.0061

where, ω_1 is the average interval width, ω_2 is the maximum interval width. Larger ω_1 and ω_2 means higher conservativeness, the results are shown in Tables 3, 4.

The above results show that the SR-UKF method used for IDSE in this paper has a narrower solution interval width compared to EKF and UKF, is less comparative and has a higher

reliability of the estimation results. Meanwhile, comparing the results for t = 1 h and t = 13 h shows that the PV output increases as the light intensity becomes stronger, making the uncertainty also increasing, so that the interval width at t = 13 h is wider than that at t = 1 h.

TABLE 5 Comparison results of computing efficiency between different algorithms.

Method	Time consuming (s)
EKF	1.2121
UKF	0.4252
SR-UKF	0.1096

Next, the computing efficiency of the three methods is compared and analyzed, are shown in Table 5. From the comparison results, it can be seen that the SR-UKF method used in this paper has much better computing efficiency than EKF and UKF, and it is suitable for large-scale networks, thus making it suitable for online applications.

5 Conclusion

An interval dynamic state estimation considering the uncertainty of PV and load has been proposed in this paper.

(1) SR-UKF is used to determine the operating median values of all state variables to improve computing efficiency.
(2) The interval is used to analyze the measurement uncertainty of ADN, the NN based LUBE theory is used to predict the PV power output interval and the active and reactive power interval of unmeasured load.
(3) The interval state estimation is modelled as a bilevel nonlinear programming problem to obtain the upper and lower bounds. The modified test case demonstrates the feasibility and effectiveness of the proposed IDSE method.

The next step of the research will be to study the analysis of system measurement outliers (bad data), zero injection power node constraints and other factors to improve the online application of IDSE method for ADN.

References

Abdel-Majeed, A., Kattmann, C., Tenbohlen, S., and Saur, R. (2014). "Usage of Artificial Neural Networks for pseudo measurement modeling in low voltage distribution systems," in Proceedings of the IEEE PES General Meeting| Conference Expo, National Harbor, MD, USA, 1–5. doi:10.1109/PESGM.2014.6938843

Aien, M., Rashidinejad, M., and Fotuhi-Firuzabad, M. (2014). On possibilistic and probabilistic uncertainty assessment of power flow problem: A review and a new approach. Renew. Sustain. Energy Rev 37, 883–895. doi:10.1016/j.rser.2014.05.063

AL-Othman, A. K. (2009). A fuzzy state estimator based on uncertain measurements. Measurement 42, 628–637. doi:10.1016/j.measurement.2008.10.007

Al-Othman, A. K., and Irving, M. R. (2005). A comparative study of two methods for uncertainty analysis in power system State estimation. IEEE Trans. Power Syst. 20, 1181–1182. doi:10.1109/TPWRS.2005.846163

Data availability statement

The original contributions presented in the study are included in the article/supplementary material, further inquiries can be directed to the corresponding author.

Author contributions

JW, KL, and FW contributed to the conception and design of the study. ZW are responsible for providing experimental design and data analysis. LS and YL are responsible for providing code implementation. All authors contributed to the manuscript writing revision, read, and approved the submitted version.

Funding

Conflict of interest

The authors declare that the research was conducted in the absence of any commercial or financial relationships that could be construed as a potential conflict of interest.

Publisher's note

All claims expressed in this article are solely those of the authors and do not necessarily represent those of their affiliated organizations, or those of the publisher, the editors and the reviewers. Any product that may be evaluated in this article, or claim that may be made by its manufacturer, is not guaranteed or endorsed by the publisher.

Bargiela, A., Pedrycz, W., and Tanaka, M. (2003). A study of uncertain state estimation. IEEE Trans. Syst. Man. Cybern. A 33, 288–301. doi:10.1109/TSMCA.2002.806500

Chai, Y., Guo, L., Wang, C., Zhao, Z., Du, X., and Pan, J. (2018). Network partition and voltage coordination control for distribution networks with high penetration of distributed PV units. IEEE Trans. Power Syst. 33, 3396–3407. doi:10.1109/TPWRS.2018.2813400

Huang, M., Wei, Z., Pau, M., Ponci, F., and Sun, G. (2019). Interval state estimation for low-voltage distribution systems based on Smart meter data. IEEE Trans. Instrum. Meas. 68, 3090–3099. doi:10.1109/TIM.2018.2877549

Jafarzadeh, S., Lascu, C., and Fadali, M. S. (2011). "Square Root Unscented Kalman Filters for state estimation of induction motor drives," in Proceedings of the IEEE Energy Convers. Congr. Expo, Phoenix, AZ, USA, 75–82. doi:10.1109/ECCE.2011.6063751

Julier, S. J., and Uhlmann, J. K. (2004). Unscented filtering and nonlinear estimation. *Proc. IEEE* 92, 401–422. doi:10.1109/JPROC.2003.823141

Karimipour, H., and Dinavahi, V. (2015). Extended kalman filter-based parallel dynamic state estimation. *IEEE Trans. Smart Grid* 6, 1539–1549. doi:10.1109/TSG.2014.2387169

Khosravi, A., Nahavandi, S., Creighton, D., and Atiya, A. F. (2011). Lower upper bound estimation method for construction of neural network-based prediction intervals. *IEEE Trans. Neural Netw.* 22, 337–346. doi:10.1109/TNN.2010.2096824

Manitsas, E., Singh, R., Pal, B. C., and Strbac, G. (2012). Distribution system state estimation using an artificial neural network approach for pseudo measurement modeling. *IEEE Trans. Power Syst.* 27, 1888–1896. doi:10.1109/TPWRS.2012.2187804

Massaoudi, M., Abu-Rub, H., Refaat, S. S., Chihi, I., and Oueslati, F. S. (2021). Deep learning in Smart grid Technology: A review of recent advancements and future prospects. *IEEE Access* 9, 54558–54578. doi:10.1109/ACCESS.2021.3071269

Massignan, J. A. D., London, J. B. A., and Miranda, V. (2020). Tracking power system state evolution with maximum-correntropy-based extended kalman filter. *J. Mod. Power Syst. Clean. Energy* 8, 616–626. doi:10.35833/MPCE.2020.000122

Ngo, V., and Wu, W. (2021). Linear programming contractor for interval distribution state estimation using RDM arithmetic. *IEEE Trans. Power Syst.* 36, 2114–2126. doi:10.1109/TPWRS.2020.3033065

Qiu, X., Suganthan, P. N., and Amaratunga, G. A. J. (2018). Ensemble incremental learning Random Vector Functional Link network for short-term electric load forecasting. *Knowl. Based. Syst* 145, 182–196. doi:10.1016/j.knosys.2018.01.015

Quan, H., Srinivasan, D., and Khosravi, A. (2014). Short-Term load and wind power forecasting using neural network-based prediction intervals. *IEEE Trans. Neural Netw. Learn. Syst* 25, 303–315. doi:10.1109/TNNLS.2013.2276053

Rakpenthai, C., Uatrongjit, S., and Premrudeepreechacharn, S. (2012). State estimation of power system considering network parameter uncertainty based on parametric interval linear systems. *IEEE Trans. Power Syst* 27, 305–313. doi:10.1109/TPWRS.2011.2162859

Schlösser, T., Angioni, A., Ponci, F., and Monti, A. (2014). "Impact of pseudo-measurements from new load profiles on state estimation in distribution grids," in Proceedings of the IEEE Int. Instrum. Meas. Technol. Conf. (I2MTC), Montevideo, Uruguay, 625–630. doi:10.1109/I2MTC.2014.6860819

Sihag, S., and Tajer, A. (2018). Power system state estimation under model uncertainty. *IEEE J. Sel. Top. Signal Process.* 12, 593–606. doi:10.1109/JSTSP.2018.2827322

Valverde, G., Saric, A. T., and Terzija, V. (2013). Stochastic monitoring of distribution networks including correlated input variables. *IEEE Trans. Power Syst.* 28, 246–255. doi:10.1109/TPWRS.2012.2201178

Valverde, G., and Terzija, V. (2011). Unscented Kalman filter for power system dynamic state estimation. *IET Gener. Transm. Distrib.* 5, 29. doi:10.1049/iet-gtd.2010.0210

Wang, B., He, G., Liu, K., Lv, H., Yin, W., and Mei, S. (2013). Guaranteed state estimation of power system via interval constraints propagation. *IET Gener. Transm. & Distrib.* 7, 138–144. doi:10.1049/iet-gtd.2012.0333

Wang, H., Ruan, J., Wang, G., Zhou, B., Liu, Y., and Fu, X. (2018). Deep learning-based interval state estimation of AC Smart grids against sparse cyber attacks. *IEEE Trans. Ind. Inf.* 14, 4766–4778. doi:10.1109/TII.2018.2804669

Zhang, L., Wang, G., and Giannakis, G. B. (2019). "Distribution system state estimation via data-driven and physics-aware deep neural networks," in Proceedings of the IEEE Data Sci. Workshop (DSW), Minneapolis, MN, USA, 258–262. doi:10.1109/DSW.2019.8755581

Zhao, J. (2018). Dynamic state estimation with model uncertainties using H_∞ extended kalman filter. *IEEE Trans. Power Syst.* 33, 1099–1100. doi:10.1109/TPWRS.2017.2688131

Zhao, J., Netto, M., Huang, Z., Yu, S. S., Gomez-Exposito, A., Wang, S., Kamwa, I., Akhlaghi, S., Mili, L., Terzija, V., and Meliopoulos, A.S. (2021). Roles of dynamic state estimation in power system modeling, monitoring and operation. *IEEE Trans. Power Syst.* 36, 2462–2472. doi:10.1109/TPWRS.2020.3028047

Zhao, J., Netto, M., and Mili, L. (2017). A robust iterated extended kalman filter for power system dynamic state estimation. *IEEE Trans. Power Syst.* 32, 3205–3216. doi:10.1109/TPWRS.2016.2628344

Zhao, J., Qi, J., Huang, Z., Meliopoulos, A. P. S., Gomez-Exposito, A., Netto, M., Mili, L., Abur, A., Terzija, V., Kamwa, I., Pal, B., and Singh, A.K. (2019). Power system dynamic state estimation: Motivations, definitions, methodologies, and future work. *IEEE Trans. Power Syst.* 34, 3188–3198. doi:10.1109/TPWRS.2019.2894769

Check for updates

Transactive energy system: Concept, configuration, and mechanism

Hai Zhou[1], Biao Li[2]*, Xingchen Zong[2] and Dawei Chen[3]

[1]China Electric Power Research Institute Co., Ltd., Nanjing, China, [2]College of Electrical Engineering, Zhejiang University, Hangzhou, China, [3]State Grid Fujian Electric Power Research Institute, Fuzhou, China

Transactive energy systems (TESs) combine both economical and control mechanisms, and have become promising solutions to integrate distributed energy resources (DERs) in modern power systems. This article will introduce the basic concept of a TES, including its definition, process, time scale, and benefits. The configuration of the TES is then described in detail from the perspectives of the physical system, information system, transaction system, and regulatory system. The transaction mechanism allows participants (e.g., customer, generator, transmission operator, marketer, etc.) to conduct various transactions with any other party to the extent that regulatory policy permits. Transactive control is regarded as one of the most advanced approaches to realize the full response potential of flexible devices and respect the end user's privacy, preference, and free will. Finally, some challenges to the development of TESs that arise from the limitations of current equipment level and methodological concepts will be discussed. In summary, TESs provide a more efficient, fair, and transparent environment for participants to promote DERs utilization, improve market efficiency, and increase economic benefits.

1 Introduction

The energy industry is currently at a critical juncture of transition. Many changes are taking place in the power system—such as, increasing complexity of power grids, growing penetration of renewable generations, and proliferating distributed energy resources (DERs)—, which lead to an increased requirement for efficiency, reliability, security, economic, and environmentally sustainable (Moslehi and Kumar, 2010; Barrager and Cazalet, 2014; Lezama et al., 2019). Consequently, the operation and regulatory models in generation-based power systems find it difficult to deal with these issues at both bulk-power and distribution levels (Rahimi et al., 2016).

Demand side management (DSM) refers to the energy management of the demand side, using effective incentives or other suitable measures to improve the efficiency of terminal electricity consumption, both for economic profits and grid reliability. DSM was at first utility driven but more attention has been paid to the customer driven approach in

recent years (Mohsenian-Rad et al., 2010; Palensky and Dietrich, 2011; Yan et al., 2021). Demand response (DR) describes the changes in electricity usage by end users from their normal consumption patterns in response to changes in the price of electricity over time and was first classified into two main types: incentive-based and price-based (Albadi and El-Saadany, 2008). The incentive-based method is a centralized mechanism that provides users with an incentive (or compensation) from top to bottom. In the price-based method, users respond to the market price in a one-way communication. In addition, the price-based approach is the basis for the development of the market-based mechanism. Hence, the electricity market has developed rapidly due to the excess of power, and therefore, a third type called the transaction-based or market-based approach has emerged in the last few years.

As an expansion form of DR, transactive energy manages both supply and demand sides simultaneously (Chen and Liu, 2017). Transactive energy (TE) is a new market-based energy management approach to cope with the increasing demand for DERs and smart devices (Chang et al., 2017), which is a decentralized mechanism. In addition, unlike the price-based mechanism, transactive energy systems (TESs) pay more attention to the two-way interaction between the market and users, and the combination of the market mechanism and control mechanism. The term "transactive energy" was first proposed by the GridWise Architecture Council (GWAC), which was established by the US Department of Energy (DOE) in May 2004 to realize the combination of economic and control mechanisms improving grid efficiency and reliability (Melton, 2015). TES is a more efficient, fair, and transparent version, which proposes innovative and disruptive technologies to facilitate energy efficiency, storage, DERs, and renewable resources.

TE research pays attention to intelligent agent-based innovation in smart building equipment and local demonstrations involving operators, energy suppliers, consumers, prosumers, marketers, and regulators (Melton, 2015). Implementations in the United States and Europe have shown that TESs are feasible and high-potential mechanisms, particularly in three major demonstration projects that were performed by the US DOE partnered with several organizations. The first project of TES conceptual implementation was the GridWise Olympic Peninsula Demonstration (2005–2007), which was located in Washington state (Ambrosio, 2016). Its initial purpose was to test the potential for taking advantage of DERs to postpone or reduce the need for a transmission upgrade. The market mechanism used 5-min double auctions to coordinate over 100 homes, a marine science laboratory, and four large water pumps. This project established multiple objectives, such as reducing system peak load, managing distribution operations, and saving energy costs to explain the viability of TE (Kok and

Widergren, 2016). In support of the American Reinvestment and Recovery Act (ARRA) of 2009, a group of smart grid field demonstrations was built across the United States (Hammerstrom et al., 2016a). Based on the Olympic Peninsula project, the AEP Ohio Real-Time Pricing gridSMART demonstration project (2010–2014) used a double-auction market mechanism in a real-time price (RTP) model to dispatch participating responsive loads (Pratt, 2012; Kok and Widergren, 2016). The results showed that the bills of wholesale buyers were reduced by around 5%, and its data were used to calibrate simulated DR models that searched for participants in higher penetration levels. The Pacific Northwest Smart Grid Demonstration (PNWSGD, 2010–2015) involved several states and electric utilities, comprising around 60,000 end users (Ambrosio, 2016), (Huang et al., 2010; Jin et al., 2012). A TES was implemented to coordinate the operation of DERs and regional objectives across 11 utilities to mitigate the intermittency of renewable generations and flatten system load, and showed the viability of DERs that were dynamically integrated on a large scale (Kok and Widergren, 2016).

TE is becoming one of the more novel and interesting approaches to the grid of the future (Olken, 2016). TESs provide an effective and healthy transaction environment for participants who wish to buy and sell energy using automated control. As a solution to deal with the growing penetration of highly uncertain renewable energy, TES has great potential in mobilizing demand response to integrating DERs in more effective, fair, and transparent ways.

2 Basic concept

2.1 Definition

A TES is defined by the GWAC as "a system of economic and control mechanisms that allows the dynamic balance of supply and demand across the entire electrical infrastructure using value as a key operational parameter" (Melton, 2015). This definition seems to be broad, given that it considers both the existing use of current techniques and the potential use of new techniques.

The following 11 attributes (shown in Table 1) are defined for two reasons: to present a broader view of TE and to provide common approaches to implement TES (Melton, 2015).

The necessity to define the principles of TES was discussed during the GWAC workshop in Philadelphia (February 2014). Six principles were defined, as follows (Transactive Energy Principles (V1.0), 2022):

1) Implement some form of highly coordinated self-optimization. This principle explains the efficient operation of TE.

TABLE 1 Attributes of TE.

Attributes
1. Architecture 2. Extent 3. Transacting parties 4. Transaction 5. Transacted commodities 6. Temporal variability 7. Interoperability 8. Value discovery mechanism 9. Assignment of value 10. Alignment of objectives 11. Assuring stability

2) Maintain system reliability and control while enabling optimal integration of renewables and DERs. This shows the high consumption capacity of renewables and DERs.

3) Provide for non-discriminatory participation by qualified participants. TE is committed to constructing a fair transaction milieu.

4) Observable and auditable at interfaces. Transparency and supervision are the sources of trust for TE customers.

5) Scalable, adaptable, and extensible across several devices, participants, and geographic extents. The high degree of extensibility is a strong boost to TE's sustainable development.

6) Transacting parties are accountable for standards of performance. Rich information can be sought in this principle, including the hint of distributed operation, the respect for personal privacy, and the improvement of system efficiency.

In short, these six principles demonstrate that TE operates in an efficient, fair, and transparent manner, realizing the efficient market and the full potential of demand response.

2.2 Process and time scale

Three actors in TES are related to the transaction process: energy buyers, energy sellers, and marketers. Based on the market price, buyers submit bids to purchase energy considering their costs and preference, while sellers make tenders to sell energy by maximizing their profits. A transaction will be established when their requirements are matched. The bids and transactions can be made either in exchanges or bilaterally. In addition, transaction platforms are virtualized as software applications on the "cloud". Marketers are responsible for managing transactions and reducing the imbalance between energy demand and supply. With large-scale, frequent, and efficient transactions, the market price will gradually stabilize, and balance supply and demand.

The process in TES is dynamic. A buyer has a position after being transacted in the market. If something better happens or their energy needs to change, then the process will repeat until a better position is found for the buyer. The same process is used for sellers. The transaction can continue until delivery time.

The key objective of system operators is to provide reliable and secure power to loads, thereby avoiding power outages. Actions will take place in the period from milliseconds to

years to guarantee power reliability. With the development of emerging trends, operations will gradually shift to shorter periods. This means that human control may not be sustainable, and therefore, automated and intelligent control with manual supervision will be needed.

The system will also become harder to operate by manual control because of the growing number of data sources, communication spots, and control points. The time frame of TE may have a large period from minutes (real-time transaction) to a day (day-ahead transaction), or even years (forward transaction). A span from minutes to a few hours is regarded as the most critical timeframe where demand response works effectively.

3 System configuration

As was performed for the topic of grid interoperability with the publication of the "GridWise Interoperability Context Setting Framework," the GWAC created the TE framework to provide a common ground and facilitate further development of TESs (Forfia et al., 2016). This is defined as a shared tool to spread and serve smart communities (e.g., smart grid).

There are four main systems in the TE model: physical system, information system, transaction system, and regulatory system. The physical system includes energy generation, storage, transmission, and distribution, together with the end user's smart devices. The information system is built to collect, process, organize, and transmit information, both in the power system and energy markets. The transaction system manages various types of energy transactions to establish an effective energy market. The regulatory system safeguards against economic abuse and rule violation. It also maintains market safety and reliability. TES offers a method to ensure the reliability and security of the power system while improving efficiency by coordinating a growing number of DERs. A brief configuration of TES is shown in Figure 1.

3.1 Physical system

3.1.1 Inherit and develop current systems

TES can be implemented with a few modifications (depending on the size and complexity) of the current physical systems. Communication and information technology

FIGURE 1
Transaction energy system configuration.
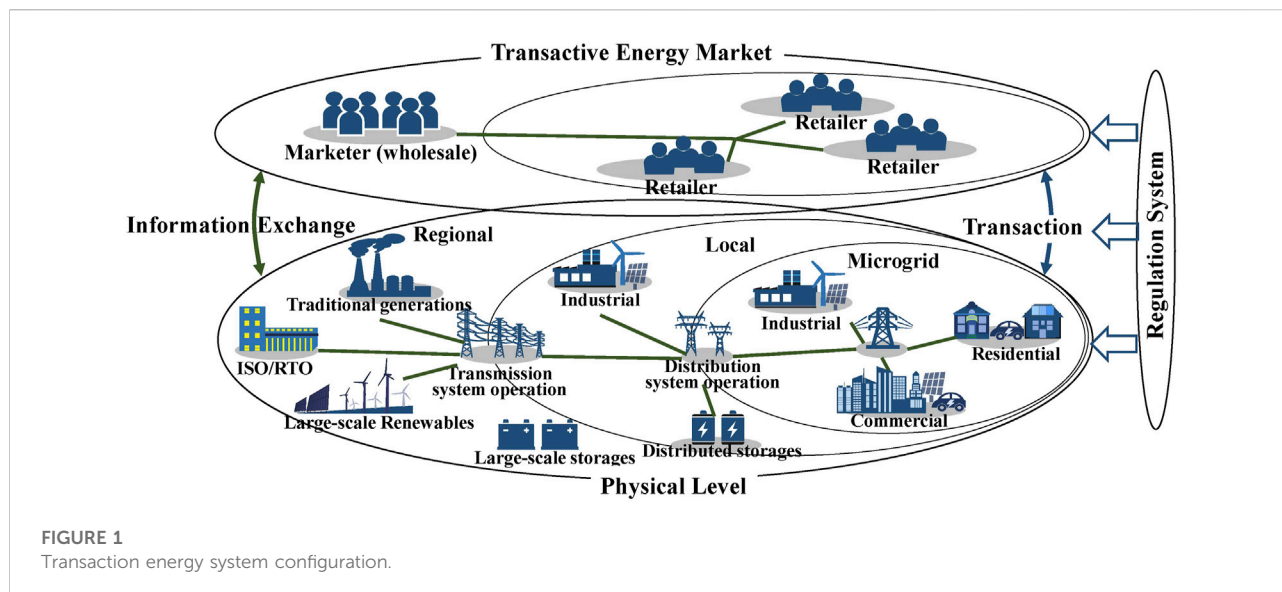
(CIT) is needed to build the physical system of TES. The cyber-physical elements of the grid also need to be developed for further support of TES with new sensors, actuators, and control elements. The current physical systems and devices need to be developed to realize information collection and automation more flexibly than required for operating the traditional grid. Features such as information exchange, data dealing, system decoupling, and interactions are needed to enhance flexibility.

3.1.2 Smart connections

The connection and communication technology required for TE is in place due to the fast, universal, and wireless Internet. The Internet enables two-way communication between all entities connected to the TE Platform. All devices can get decision-related information on the Internet, such as weather, emergency warnings, and market signals. Wireless Internet or Wi-Fi enables different devices to communicate with each other. Humans, data, and devices can be connected to various places with access to the Internet. In addition, Wi-Fi completes the link from the TE Platform to EMS to smart appliances. TES communicates over the Internet and connects the TE platforms with different parties through TE Interface and EMS, which can be a device in a building or an application in the cloud.

3.1.3 Smart devices

Devices are becoming smarter thanks to the fast development of automation technology and artificial intelligence technology. In addition, more devices related to renewables are being deployed, driven by the growing demand for clean energy. Many appliances equipped with Wi-Fi capability are available nowadays. For example, smart clothes dryers can be closed at a high electricity price (or by the EMS instruction), and smart water heaters can adjust heat power depending on the price

signals (Barrager and Cazalet, 2014). The control strategy of devices aims to coordinate the end-user's comfort and energy cost. Smart devices apply advanced technologies, including the ability of wireless communication with other devices throughout the building and the Internet. Devices such as heating, ventilation, air conditioning (HVAC), and electric vehicles can access the TES directly. EVs can make decisions considering the current and predicted charging or discharging price send in the charging/discharging market of EVs.

Smart meters, EMS, Wi-Fi, and smart devices are in place to build TES. In addition, smart buildings (e.g., commercial buildings, smart homes, and factories) are also prepared for TES implementation. Consequently, smart energy and the smart city will become a reality in the near future.

3.2 Information system

Information interoperability is an important element of TES. It not only needs to clear the valuation and process of transactions but also needs to understand operation mechanisms and the control approaches both in the TES and the grid. Therefore, the concept of information interoperability is directly related to both the transaction and operation models.

3.2.1 Information models

The Transactive Energy Market Information Exchange (TeMIX) is a framework and protocol for spot and forward transactions, which are based on standards. Transactions can then be made automatically on a large scale and at high speed with smart meters, Internet communications, smart applications, and TeMIX protocols (TeMIX, 2010). TeMIX supports decentralized control or decision-making at the edges of the

TABLE 2 Elements of the four information models (Cazalet, 2022).

Model	Elements
Energy transaction	Extended price, rate of delivery, delivery period, buyer, seller, transaction execution time, location, meter ID, currency, and units
Energy offer	Price, rate of delivery, delivery period, buyer/seller flag, offering party, counterparty, offer availability interval, location, meter ID, currency, and units
Energy option transaction	Extended price, strike price, rate of delivery, delivery period, buyer, seller, put/call flag, transaction execution time, exercise period, location, meter ID, currency, and units
Energy option offer	Option price, strike price, rate of delivery, delivery period, offering party, counterparty, exercise party, put/call flag, offer availability interval, exercise period, location, meter ID, currency, and units

grid. End-user applications (e.g., HVAC, EVs, distributed photovoltaic generation, and storage) are automatically transactive with distribution grid devices. Therefore, TeMIX implements a smart grid, quickly adapting to the high penetration of renewables, EVs, and distributed storage.

Four information models have been defined for the transactional energy model (Cazalet, 2022): energy transaction, energy offer, energy option transaction, and energy options offer. Energy transaction or energy offer is easy to understand. Energy option transaction means that there is an option for an energy transaction and energy options offer, which refers to an offer for an energy option transaction. The information model is mainly used for the effective exchange of energy transaction information. In addition to spot transactions, customers can make forward transactions at high or low prices using energy option transactions, which are similar to capacity and ancillary services. Energy options can also be energy contracts such as demand response contracts. The elements of the four information models are described in Table 2.

3.2.2 Information security

The integration of ICT with the traditional transmission infrastructure may lead to new vulnerabilities. Although the standards and technologies of information security have improved dramatically over the past decades, they still need to be adjusted to meet the unique requirements of the power system and the continued evolving capabilities of hackers. Information disruption can be costly because a great number of services on the grid may be destroyed by exploiting security weaknesses.

3.3 Transaction system

3.3.1 Transaction parties

The transaction parties contain energy suppliers, consumers, energy transmission owners, and intermediaries (Barrager and Cazalet, 2014). Both energy suppliers and consumers are energy service parties, including power producers, consumers, prosumers, and storage owners. Marketers, retailers, exchangers, and system operators are all intermediary entities

to provide transaction services and energy management. Transmission and distribution owners are also encouraged to participate in the transactive platform.

3.3.2 Transaction platform

As shown in Figure 2, the transaction platforms aggregate four transaction parties to build transactions and provide energy services. The exchanges are associated with the transactive platform, which is associated with the EMS of the grid. The intermediaries also connect with their customers and the exchanges through the platform. The intermediaries support a more active market to small-scale customers making transactions, as well as taking transaction risks for others. For example, some intermediaries may purchase long-term forward positions and sell them closer to delivery time.

3.3.3 Transaction activities

Marketers play an important role in market mobility by adjusting the market price. First, several small forward bids will be posted by marketers with small price differences. The tenders will then expire after a short period. If counterparties accept larger amounts of buy bids than sell bids during this time, then the marketer will reduce the prices of the next bids to lower net positive positions (or raise the prices in net negative positions). The energy markets will be driven toward equilibrium through the iterative process. Some activities of the transaction process in TES are shown in Table 3.

In addition to providing market mobility, marketers also reduce transaction costs and facilitate trade through price differentials in markets. The marketers should be independent parties that are licensed and regulated. They are not allowed to manipulate the market, either for their own profit or for others' profits.

3.4 Regulation system

Regulators will always play an important role in maintaining power system security, competition fairness, and protecting the health of the markets. Regulators are also responsible for ensuring rules in TES and fighting against economic abuses.
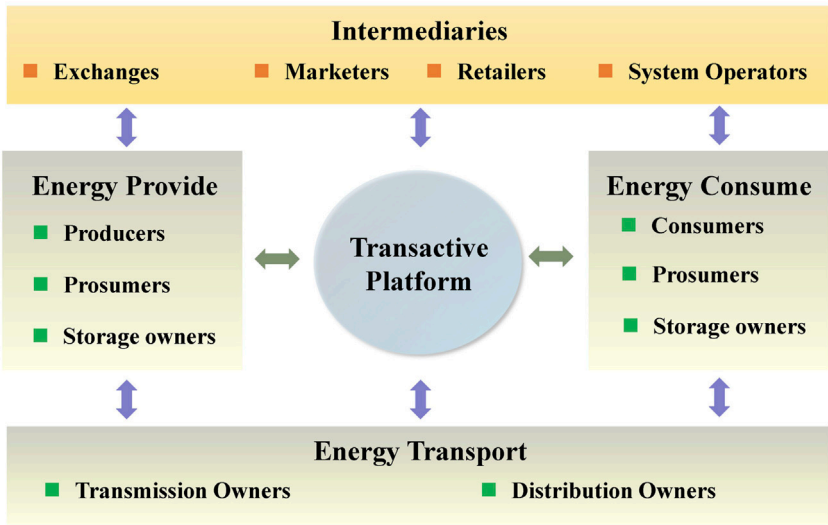
FIGURE 2
Transactive platform diagram (Barrager and Cazalet, 2014).

TABLE 3 Activities in the transactive platform (Barrager and Cazalet, 2014).

Platform and activity	Function
Transactive platform	Places where buyers and sellers go to tender and accept tenders to form transactions
Exchanges	Facilitates anonymous matching of buyers and sellers
Market making	Provides liquidity to the market
Clearing	Activities between transaction and settlement (including credit and collateral management, reporting and monitoring, tax handling, and failure handling)
Arbitraging	Closes differences in prices for energy at two different locations and the price of transport between the two locations
Hedging	Risk management where forward transactions are used in place of uncertain prices of further spot transactions

TES can reduce the workload of economic regulators and the requirement for oversight on price setting. Market prices for customers are impartial thanks to forward and spot transaction processes under the supervision of a regulation system. Consequently, regulation ensures that TES is essentially fair and transparent.

The regulation system of TES requires three regulatory framework elements (Kristov et al., 2016). The first key element is to ensure open access and TES principles that are applied to the interconnection process, infrastructure projects, operating procedures, and market transactions. Second, states should be allowed to manage markets for distribution system operators (DSOs) and DSO operations within their jurisdiction. The purpose of this element is to regulate energy markets by each state, thereby facilitating widespread adoption across the country. The last key element is the establishment of reliable shared responsibilities between the transmission system operator (TSO) and DSO. The regulation for

DSO needs to assign responsibility and accountability for reliable service to end users in ways that go beyond reliable distribution services (which may vary from state to state).

3.5 Operation modes and value realization

3.5.1 Operation modes

In TES, different operation parties can operate in four modes as transactive agents (Rahimi et al., 2016), as follows: 1) operating autonomously based on the preferences of customers, 2) responding to bilateral transactive bids and offers, 3) responding to market price signals made by marketers, and 4) responding to operator instructions. The first two modes have the least constraint on prosumers but may influence the reliability of the power system. The schedule is not needed to be known before the operation

FIGURE 3
Transactive parties and their interactions.
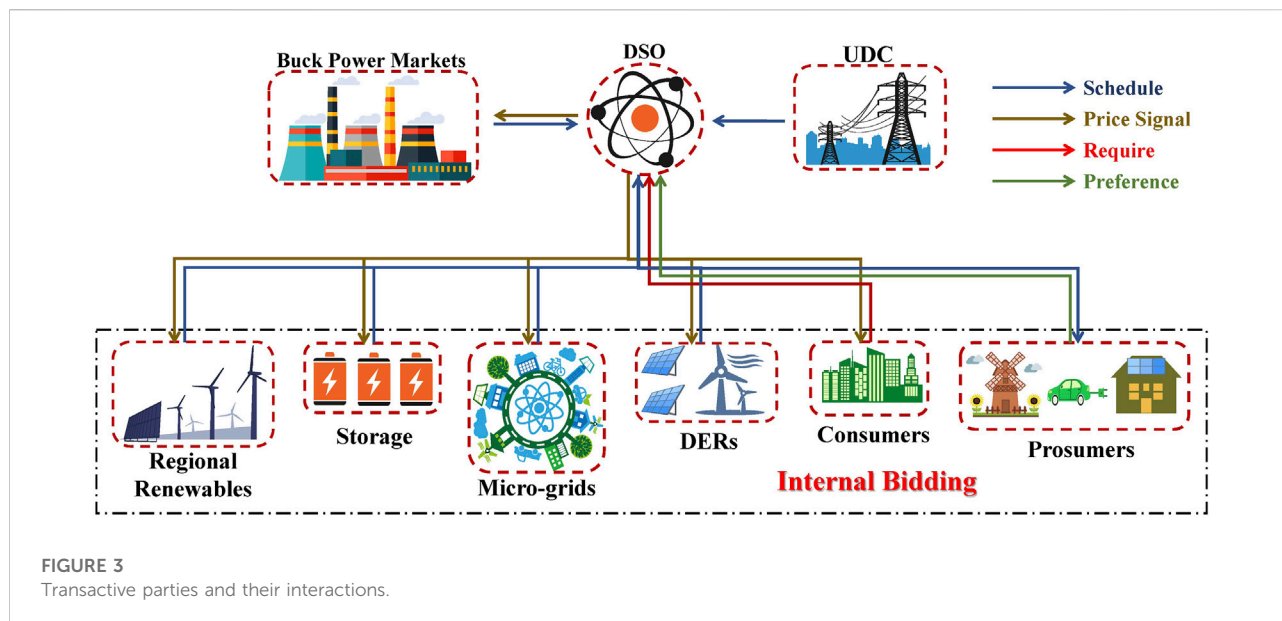
in the first mode, while it is determined in other modes. The operation mode can be transformed from one to another depending on the situation of entity status, time, environment, or system conditions. The autonomous operation, bilateral transactive response, and market price response would prevail in the TES configuration.

In the DSO-based operation, the DSO will finalize a bilateral transaction as an operational schedule to be conveyed to the transacting parties. The DSO's instructions may replace the operation mode of some devices in some emergency conditions (e.g., priority plans established through the electronic tag). Sometimes, the DSO dispatches operation license signals to a subset of registered transactive agents, depending on the state of the grid or the electricity price (Moazeni and Defourny, 2017). Whether the ability of the prosumer to transition from one mode to another will be restricted or not depends on the TES protocols that are made by relevant local, state, or other regulatory entities. The interactions among different agents— including the DSO, consumers, prosumers, storages, utility distribution companies (UDCs), microgrids, DER providers, regional renewable providers, and the bulk-power markets—are shown in Figure 3.

3.5.2 Value realization
3.5.2.1 Value streams

With growing access to information, customers have higher requirements for reliability and quality of energy service, as well as eco-friendly choices and lower costs. In addition, customers can gain new revenue opportunities and value streams by providing services to the grid through innovative market design and regulatory policies. Sometimes, TE also can be seen as valve-based energy management (Makhmalbaf et al., 2017). Melton (2015) shows that 30 value

streams (which include both buck-power and distribution systems) can be considered by different parties to provide energy services and make their own objections.

3.5.2.2 Alignment of value streams

TES proposes an opportunity for utilities and third parties to offer value-added services to energy customers, and also extend them beyond regulatory coverage. However, viable transactive approaches need to introduce opportunities to build and target value streams for all of the participants. In addition, the value achieved by the grid or customer utility should not be at the cost of end users, TSOs, or generators. The alignment of value streams makes a great contribution to establishing multi-objective optimization models that combine both operational and economic factors. Although they may not support the value creation and alignment by current business models, they can be adjusted when necessary and new business models may emerge during the process.

4 Transaction mechanism

Transactive markets allow different entities to transact with each other, as far as the regulatory policy allows. Both generators and customers can take the double role of energy selling and consumption compared to a simple buyer or seller role in the past.

4.1 Transaction classification

4.1.1 Forward transaction and spot transaction

Two kinds of decisions are made in the electricity ecosystem: investment and operation. Forward transactions, which can be

made by bilateral contracts or on exchanges, are used to coordinate investment decisions and manage risk. Spot transactions, which can be built on an ISO/DSO platform, are used to coordinate operating decisions and mitigate risk.

Forward transactions in TES are used to coordinate investments throughout the electricity ecosystem. Consumers, prosumers, and DERs owners use transactive platforms to develop forward transactions in a fair competitive environment. Investors can manage price and cost risk using forward transactions. Long-term contracts (a form of forwarding transactions) are used by power producers to reduce their current risk. Customers in retail markets may install assets such as PV panels or other efficient appliances to manage the risks of investments.

Spot transactions in TES are employed to coordinate operating decisions. All of the parties have access to the same spot transaction exchanges in the same game rules. However, in the current electricity market, spot transactions are often developed by large wholesale or industrial customers to coordinate system operations, and few are used by small customers. Investment and operation are autonomous in spot transactions. Participants decide what to invest in and how to operate it, and their autonomous decisions are coordinated on the same transactive platforms.

4.1.2 Wholesale transaction and retail transaction

The wholesale market relies on bids and offers to issue delivery orders. When the system constraint is not satisfied by economic bids and offers, then administrative measures will be taken to reject certain transactions or arrange resources outside the market to deal with system constraints (Rahimi and Albuyeh, 2016). The TES paradigm extends the current wholesale market to retail markets, including consumers, prosumers, DERs owners, and various smart devices.

DSO is created (not only) for the following two motivations: the first is to integrate DERs in a market environment to obtain economic benefits, and the second is to establish a market environment to incentivize customers, utilities, and third parties to invest in DERs. In both cases, it is necessary to organize markets and manage system reliability, in addition to transactive with wholesale markets. The presentations on motivation for DSOs specify a significant difference between the wholesale markets (at the ISO level) and the retail markets (at the DSO level) (Masiello and Aguero, 2016).

The retail market is not a new concept, and has been demonstrated and applied in many countries, such as Europe and the United States (Nair and Nair, 2016). There is a tendency to deregulate the electricity markets in many countries. However, the lesson learned from organizational insolvency in California shows that over-deregulation of the retail market may lead to higher electricity costs for customers and improper commercial intervention by competing service operators. TES proposes and

encourages distributed control approaches rather than traditional centralized optimized control. TES is an effective correction for the deregulated market. The energy is extended to be traded by the retail market on account of the distributed control mechanism in TES. As a result, small-scale energy resources in DSM can be effectively used and uncertain renewables can be greatly consumed. The relationships between the wholesale market and the retail market are shown in Figure 4 (supported by TeMIX).

4.1.3 Bilateral auction

To make a bilateral auction, buyers submit their bids while sellers send their offers at the same time. They then each compete to get the best price. In this kind of auction, the ideal transaction price is the equilibrium price corresponding to the value at the intersection point of the supply curve and the demand curve (Xavier et al., 2017). The bilateral auction is one of the most popular models studied in the electricity market. It is also widely used in day-ahead and hourly auctions, which can be seen in the UK or the US electricity markets.

A bilateral auction is a feasible solution to handle resource distribution problems in different regions. In addition, an auction can be seen as a fair, effective, and eco-driven scheme. Consequently, several research efforts have been devoted to considering auction behaviors in the resource distribution of the grids (Li et al., 2017). By taking advantage of the potentialities of blockchain technologies, energy exchanges and auctions can be operated automatically in the transactive market (Kounelis et al., 2017).

4.2 Local market designs

This section introduces two local market designs: the first is the direct peer-to-peer (P2P) market and the second is the closed-order book market. The closed-order book market is slow in transaction speed and takes a long time to confirm the order, which is suitable for larger time scales. In comparison, transactions in the P2Pmarket are faster and more flexible, and therefore, the P2P market can be used in shorter time scales.

4.2.1 Order book market

The order book market is designed as a double-auction market with discrete market closing times (Mengelkamp et al., 2017). An energy order book is an electronic list of buying and selling orders for energy transactions, and is dynamic and continually updated. In the order book market, the clearing price is the uniform settlement price for each trading period. The bid and offer bills of customers are gathered and ordered. The bids are sorted by descending order and the offers are sorted by ascending order. When the energy supply is given, the clearing price in the market is influenced by all of the bid/offer prices, even the lowest bid price. In an order book market, customers
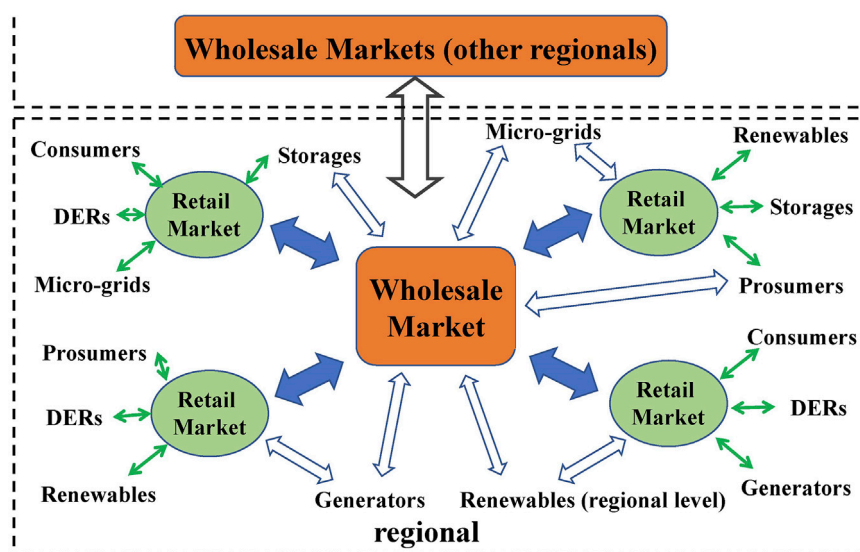
FIGURE 4
Interaction between wholesale markets and retail markets.

who successfully booked their energy orders pay the bills for the procured electricity at the market clearing price.

4.2.2 Peer-to-peer market

The P2P network uses a decentralized and distributed network architecture. The individual nodes in the P2P network perform as both suppliers and consumers of energy resources. In contrast to the centralized client-server model, client nodes request access to resources provided by central servers (Barrager and Cazalet, 2014). P2P trading represents direct energy transactions between peers; for example, a direct transaction between consumers and/or prosumers is a simple example of a P2P transaction (Zhang et al., 2018). In the P2P market, customers transact with each other in a randomized based on a payment order. At each session, each buyer is paired with sellers randomly and iteratively until all of the electricity is procured or all of the potential sellers have been matched. A prosumer is paired with the consumer when the bid price of the consumer is higher or equal to the offer price. The matching amount is determined to be the minimum amount offered by the seller and the buyer. The P2P market with intelligent agents may seem to be the best market mechanism because it has the lowest average electricity price of all transactions and the highest participation enthusiasm of end users (Mengelkamp et al., 2017).

4.3 Price mechanism

There are two types of market price: the first is the local marginal price (LMP) and the second is the uniform market price

(UMP) (Albadi and El-Saadany, 2008). In a TE environment, distribution locational marginal price (DLMP) is the basis for energy pricing among transactive market participants (Sajjadi et al., 2016). Long-term DLMPs are mainly used to stimulate investments, while short-term DLMPs are used for market clearing and energy balancing in real-time markets or day-ahead markets (Rahimi et al., 2016). The communication mechanism that sends market price signals to smart devices of end users can help to transfer wholesale LMPs to DLMPs considering the transmission losses and operation costs. In a transactive market, the market signals are sent to end users through software nodes, and each node is responded with a prospective energy requirement based on the market signal (Chandler et al., 2014).

4.4 Stakeholder responsibilities

The clear definition of the stakeholder responsibilities is one of the key elements to realize the bulk-power recombination in the past (Rahimi et al., 2016). It is also an indispensable step to establish a novel structural framework for all of the transaction and operation parties to clear the responsibilities of each stakeholder. For instance, the system operators are responsible for balancing energy between supply and demand, managing transmission congestion, and reducing (or stopping) transactions in urgent situations. They also have the right to get transmission and scheduling information in their jurisdiction. The main responsibility of marketers/retailers is to manage energy transactions. Marketers or retailers make suitable market

TABLE 4 Four main categories of energy management.

Category	Decision made	Communication
Top-down switching	Centrally	One-way
Centralized optimization	Centrally	Two-way
Price reaction	Locally	One-way
Transactive control	Locally	Two-way

prices, both for forward transactions and spot transactions, and send market signals to the end users' devices (or show them on the Internet). Together with the regulators, they are responsible to enable a healthy and effective market ambience. The customers should be responsible for the transactions that they made and obey the transaction formal process and rules (a breach of contract may be punished).

4.5 Transactive control

4.5.1 Category of EMS

As shown in Table 4, energy management approaches can be classified into four main categories (Kok and Widergren, 2016): top-down switching, centralized optimization, price reaction, and transactive control in a distribution-level energy management system.

Top-down switching, like direct load control (DLC) (Xie et al., 2018), is the earliest and most straightforward energy management approach of DR. Although recently implemented in different countries, it does not take full advantage of the end users' responses. Price reaction (PR) uses price signals that are sent by marketers to change the end users' electricity consumption. However, the customers are not allowed to send their preferences to marketers or system operators because it is one-way communication. Although the centralized optimization (CO) approach is also a centralized control approach, it takes a large amount of information (both power system and energy customers) into account through two-way communications. However, the communication and optimization times grow nonlinearly as the number of end users increases. Price reaction and centralized optimization can realize the full use of demand response potential. However, the two approaches also have some constraints. For the former, the consumer's reaction to each price signal is uncertain due to the lack of user's preferences and the state of the device. The latter one has privacy issues because the exchanged information involves the details of devices and individual behaviors of the end users.

Transactive control (TC) is a distributed control strategy that uses self-interested responsive loads to provide energy services to the grid based on market mechanisms (Hao et al., 2017). The energy quantities and market price signals are the entire information need to be exchanged. Therefore, compared to

PR, TC is much more efficient in market mechanisms with no privacy problems. Moreover, TC displays much higher scalability than the CO approach, due to its distributed structure. In short, the TE approach realizes the full use of the potential of flexible devices, provides greater certainty about the instantaneous system response, gives appropriate incentives to achieve effective markets, and respects the end users' privacy, preference, and free will.

4.5.2 Transactive control strategies

Transactive control will provide a means to coordinate the response of smart devices at all levels of the power system (Melton and Hammerstrom, 2012). Based on TC, each stakeholder is allowed to have their own set of optimal control strategies based on the market mechanism and are accountable for their standards of performance. The application of TE has been studied in renewables integration, EV management and integration, efficient and intelligent management for microgrids, commercial buildings and smart houses, and other aspects. These TC strategies and modeling may look unique on different occasions but in fact the difference primly lies in the diversification of objective function and constraint—the core is still the optimization control strategy under the market mechanism using price and energy quantities as key parameters.

4.5.2.1 Renewables

The use of renewable energy resources is increasing, due to the strong support of many governments. For example, the European Union has a renewable portfolio standard (RPS) of 20% by 2020 and the United States 20% by 2030 (Sahin and Shereck, 2014). As the proportion of renewable energy generation grows, which replaces more traditional energy resources, concerns about the reliability and security of the grid increase. More approaches are needed to properly account for integrating renewables on the grid—and TC is a suitable solution. Kiani and Annaswamy (2012) and Kiani Bejestani et al. (2014) present a hierarchical TC architecture, which considers market transactions at both the lower levels (unit-level control) and the higher levels (inter-area control). A hierarchical control framework is described in Hansen et al. (2017), which is used to coordinate DERs and demand response.

4.5.2.2 Electric vehicles and storage

The use of EVs has become more popular over the past few years because they are environmentally friendly, cost effective, and highly efficient. However, the reliability of the power system is greatly challenged by large-scale access of EVs, especially in power distribution systems (Galvan et al., 2016). This issue can be subtly solved by transactive control, which is an advanced control approach that is supported by an increasing amount of smart devices that use ICT (Lopes et al., 2011; Hu et al., 2015; Behboodi et al., 2016; Hu et al., 2017a; Divshali et al., 2017). Although

storage cost has been reduced considerably, storage technology is still expensive. Therefore, there are still risks in investing in storage equipment (Parandehgheibi et al., 2017). Building distributed, small-scale energy storage is one way to reduce investment risk. Therefore, approaches and mechanisms to aggregate small energy storage need to be studied.

4.5.2.3 Microgrids

In the past few decades, extensive research has been conducted to develop energy efficient operation strategies for microgrids, which can be classified into two categories: the first is individual microgrid operation (Amin et al., 2016; Patterson and Geary, 2016; Prinsloo et al., 2016; Prinsloo et al., 2017; Yao and Zhang, 2017) and the second is multiple interconnected microgrid operation (as microgrid clusters) (Chen and Hu, 2016; Baron-Prada et al., 2017; Nunna and Srinivasan, 2017; EduardoCeseña et al., 2018). Microgrid clusters and individual operation both have advantages and constraints. Microgrid clusters can significantly reduce energy costs and improve resilience ability. However, most of the existing operation models for microgrid clusters have difficulty ensuring individual interests because they focus on collective interests (Yang, 2018).

4.5.2.4 Smart buildings

The energy consumption of buildings has accounted for more than 40% of whole consumption in the United States since 2010, which is higher than the transportation industry and industrial sector by 44% and 36%, respectively (Chen and Hu, 2016). Recently, the growth of smart building development has provided an opportunity for transactive systems to provide grid services. In addition, the potential value of TES for smart buildings extends beyond the grid services (and may include other energy services, not only electricity services) (Hammerstrom et al., 2016b). The transactive behavior of buildings can be classified into the following categories: interior of the building, different buildings, and building to the grid. Aggregation and coordination of commercial buildings loads (Rahimi and Ipakchi, 2016; Ramdaspalli et al., 2016; Hao et al., 2017) and smart house (residential) loads (Mohsenian-Rad and Leon-Garcia, 2010; Widergren et al., 2014; Dai et al., 2015; Adhikari et al., 2016; Pratt et al., 2016; Siano and Sarno, 2016; Zhou et al., 2016; Ji and Zhang, 2017; Yue et al., 2017; Rayati and Ranjbar, 2018) for TC have drawn attention, and modeling and control strategies have started to emerge.

4.5.2.5 Distributed multi-energy system

Distributed multi-energy systems can flexibly provide a broad range of energy services (EduardoCeseña et al., 2018). A multi-energy system is commonly designed with one or more forms of energy utilization (except electricity), such as gas boilers, combined heat and power (CHP) units, thermal

energy storages, and battery energy storages (BES). Oikonomou et al. (2018) presents a comprehensive architecture to improve the participation of water distribution system operators (W-DSOs) in DR and frequency services to gain profit opportunities. A transactive approach has been proposed to the optimal scheduling for prosumers in coupled energy systems (Qiu et al., 2018), where DERs are operated in coordination in the form of a virtual power plant (VPP) (Qiu et al., 2017), which actively take part in the electricity market and the wholesale gas market. Hu et al. (2017b) proposed a network-constrained transactive energy method to schedule EVs and heat pumps in a retailer's aggregation.

5 Impacts and future directions

5.1 Benefits

5.1.1 Power system benefits

First, TES uses advanced automation and control, which increases the flexibility of microgrids and enhances the local and regional resilience of electric networks (Transactive Energy Infographics, 2022). Second, TES increases interoperability between regional and local markets that coordinates the use of energy resources to improve efficiency and reliability. Third, the strength of the TES lies in the innovative mechanisms that combine the economics of managing buck-power systems with the objectives of coordinated control (Nair and Nair, 2016). Finally, the high cost of system operation, which requires a considerable amount of reserve generation to safeguard against fluctuations caused by intermittent renewable generations (O'Connell et al., 2014), can be significantly reduced by TES through load curtailment and shifting.

5.1.2 Customer benefits

First, customers are offered more choices in the TES. They can freely produce and sell energy and services, as well as purchase energy from multiple sources. Second, opportunities for new services to customers are unlocked by wider information exchange in TES. Therefore, customers are free to choose and enjoy their favorite services. Finally, TES will save customers' costs over time and reduce the volatility of their bills, which will increase their economic benefits.

5.1.3 Market benefits

First, TES is conducive to attracting market investment. It has significant efficiency profits, both in the forward markets and in the spot markets. Second, market impartiality is regulated and guaranteed by the TES, which provides an efficient, fair, and transparent platform for all participants. Finally, by having more active participation in the market, a significant enhancement in market efficiency may be realized (Siano, 2014). A further benefit

is that it may reduce average wholesale prices, as well as the volatility of peak prices.

5.2 Challenges

TES is a complex system that can provide functional and extendible ways to integrate the self-directed resources of participants to achieve the objective of coordinating the interests of the single-user and region. A reasonable solution requires the following issues to be addressed (Kok and Widergren, 2016): 1) privacy and security; 2) standards-formulating; 3) feasible transition; and 4) reliable, stable, and automatic operation.

In addition to these concerns, one of the most challenging for grid related control systems is the shift from a highly centralized control system to a more distributed control system under the TES configuration. The demand side will take a more important role in the power system and diversified distributed control strategies may emerge, both for energy suppliers and energy consumers. As a result, the coordination between the distributed control of end users and the centralized control of the grid is a critical issue that urgently needs to be addressed. There are currently many control methods for communication speed and distributed control. For example, the distributed consensus control algorithm is a high-speed communication method, which is oriented to fully distributed control (Sun et al., 2015; Wang et al., 2015; Qin et al., 2019). In addition, the effectiveness of distributed control algorithm based on the back-and-forth communication framework has also been verified (Yu et al., 2021).

Realizing effective and high-speed communications is a significant challenge for smart meters. This issue may be difficult considering the varying environments and locations of smart meters, especially in remote areas. This situation may be very different between rural areas and urban areas. So far, there are a large number of solutions, such as the use of cell and pager networks, satellite, radios, power line communication, and Internet-related networks (e.g., fixed wireless, mesh network, and Wi-Fi). However, no single solution seems to be optimal for all applications.

5.3 Future directions

New market structures will need to be developed to deal with the uncertainty and intermittent of renewable energy resources, both on a large-scale and distributed level. A cost-effective, high-efficient, fair, and transparent market operation mechanism will need to be built for customers to make their transactions more free, safe, and trusting. In addition, an active supplier community (or technology ecosystem) will need to emerge to provide a healthy supply

of transactional energy products and services for customers. Meanwhile, new business and regulatory models should be established in the TES configuration, which will guarantee a fair and transparent transaction environment for all of the participants.

Considering the periodicity of the users' energy consumption and the uncertainty of new energy output, future research should include a combined multi-time scale transaction control mechanism. This will help to explore the potential of the TES in the construction and development of power market and distributed trading market, and promote the consumption of renewable energy. The emergence of prosumers and distributed renewable energy will bring a large amount of controllable distributed energy to the demand side. Therefore, future research in TES should focus on improving the interaction between flexible resources. In addition, the development of smart cities and smart energy has improved the level of intelligent control of equipment, which will provide a foundation for TES to build a clean, efficient, interactive, and intelligent energy trading community.

TESs may also contain more energy forms, turning into integrated energy systems. The new energy system is dominated by electric energy and supplemented by other energy, including natural gas energy, chilling water resources, and thermal energy resources. The Internet of Things (IoT) will be further developed by implementing TES. Finally, an Energy Internet may emerge in the future.

6 Conclusion

TES, combined with both economic and control mechanisms, provides an effective transactive platform for all transacting parties to transact and communicate with each other. This study introduces the basic concepts, system configuration, and transaction mechanism of TES, which can integrate DERs into the transactive market. By using a TES configuration, an optimal control mechanism for integrated energy systems can be established that considers flexible coupling and the complementarity of multi-energy at the end users' or regional level. In addition, the benign competition mechanism in the TE market improves the efficiency of the market and establishes a reasonable market price. In the future, TE will play an increasingly important role in energy management and service, promote the establishment of new energy system structures, and will also build new business and regulatory models.

Author contributions

HZ conceptualized the study and wrote part of the originaldraft. BL contributed to the construction of the

theoretical research framework, manuscript writing—review and editing. XZ and DC contributed to the revision of the manuscript. All authors have read and agreed to the published version of the manuscript.

Conflict of interest

HZ was employed by China Electric Power Research Institute Co., Ltd.

The remaining authors declare that the research was conducted in the absence of any commercial or financial

relationships that could be construed as a potential conflict of interest.

Publisher's note

All claims expressed in this article are solely those of the authors and do not necessarily represent those of their affiliated organizations, or those of the publisher, the editors, and the reviewers. Any product that may be evaluated in this article, or claim that may be made by its manufacturer, is not guaranteed or endorsed by the publisher.

References

Adhikari, R., Pipattanasomporn, M., Kuzlu, M., and Rahman, S. (2016). "Simulation study of transactive control strategies for residential HVAC systems," in *2016 IEEE PES innovative smart grid technologies conference Europe (ISGT-Europe)* (Ljubljana), 1–5.

Albadi, M. H., and El-Saadany, E. F. (2008). A summary of demand response in electricity markets. *Electr. Power Syst. Res.* 78 (11), 1989–1996. doi:10.1016/j.epsr.2008.04.002

Ambrosio, R. (2016). Transactive energy systems [viewpoint]. *IEEE Electrific. Mag.* 4 (4), 4–7. doi:10.1109/mele.2016.2614234

Amin, U., Hossain, M. J., Lu, J., and Mahmud, M. A. (2016). "Cost-benefit analysis for proactive consumers in a microgrid for transactive energy management systems," in *2016 australasian universities power engineering conference (AUPEC)* (Brisbane, QLD), 1–6.

Baron-Prada, E., Osorio, E., and Mojica-Nava, E. (2017). "Resilient transactive control in microgrids under dynamic load altering attacks," in *2017 IEEE 3rd Colombian conference on automatic control (CCAC)* (Cartagena, Colombia, 1–5).

Barrager, S., and Cazalet, E. (2014). *Transactive energy: A sustainable business and regulatory model for electricity*. Francisco: Baker Street Publishing.

Behboodi, S., Chassin, D. P., Crawford, C., and Djilali, N. (2016). "Electric vehicle participation in transactive power systems using real-time retail prices," in *2016 49th Hawaii international conference on system sciences (HICSS)* (Koloa, HI), 2400–2407.

Cazalet, E. G. (2022). *An official white paper of the OASIS EMIX Technical Committee*. Available at: http://www.oasis-open.org/committees/download.php/37954/TeMIX-20100523.pdf.

Chandler, S. A., Rinaldi, J. H., Bass, R. B., and Beckett, L. (2014). "Smart grid dispatch optimization control techniques for transactive energy systems," in *2014 IEEE conference on technologies for sustainability (SusTech), Portland, OR* (Portland: OR), 51–54.

Chang, L., Wang, X., and Mao, M. (2017). "Transactive energy scheme based on multi-factor evaluation and contract net protocol for distribution network with high penetration of DERs," in *2017 Chinese Automation Congress (CAC), Jinan, China, October 20–22, 2017 (IEEE)*, 7139–7144.

Chen, S., and Liu, C. C. (2017). From demand response to transactive energy: State of the art. *J. Mod. Power Syst. Clean. Energy* 5 (1), 10–19. doi:10.1007/s40565-016-0256-x

Chen, Y., and Hu, M. (2016). Balancing collective and individual interests in transactive energy management of interconnected micro-grid clusters. *Energy* 108, 1075–1085. doi:10.1016/j.energy.2016.05.052

Dai, Rui, Hu, Mengqi, Dong, Yang, and Chen, Yang (2015). A collaborative operation decision model for distributed building clusters. *Energy* 84, 759–773. doi:10.1016/j.energy.2015.03.042

Divshali, P. H., Choi, B. J., and Liang, H. (2017). Multi-agent transactive energy management system considering high levels of renewable energy source and electric vehicles *IET Gener. Transm. Distrib.* 11, 3713–3721. doi:10.1049/iet-gtd.2016.1916

EduardoCeseña, A. Martínez, Good, Nicholas, Syrri, A. L., and Mancarella, P. (2018). Techno-economic and business case assessment of multi-energy microgrids with co-optimization of energy, reserve and reliability services. *Appl. Energy* 210, 896–913. doi:10.1016/j.apenergy.2017.08.131

Forfia, D., Knight, M., and Melton, R. (2016). The view from the top of the mountain: Building a community of practice with the GridWise transactive energy framework. *IEEE Power Energy Mag.* 14 (3), 25–33. doi:10.1109/mpe.2016.2524961

Galvan, E., Mandal, P., Velez-Reyes, M., and Kamalasadan, S. (2016). "Transactive control mechanism for efficient management of EVs charging in transactive energy environment," in *2016 north American power symposium (NAPS)* (Denver, CO), 1–6.

Hammerstrom, D. J., Corbin, C. D., Fernandez, N., Homer, J. S., Makhmalbaf, A., Pratt, R. G., et al. (2016). *Valuation of transactive systems*. Richland, WA: Pacific Northwest National Laboratory.

Hammerstrom, D. J., Widergren, S. E., and Irwin, C. (2016). Evaluating transactive systems: Historical and current U.S. DOE research and development activities. *IEEE Electrific. Mag.* 4 (4), 30–36. doi:10.1109/mele.2016.2614182

Hansen, J., Edgar, T., Daily, J., and Wu, D. (2017). "Evaluating transactive controls of integrated transmission and distribution systems using the Framework for Network Co-Simulation," in *2017 American control conference (ACC)* (Seattle, WA), 4010–4017.

Hao, H., Corbin, C. D., Kalsi, K., and Pratt, R. G. (2017). Transactive control of commercial buildings for demand response. *IEEE Trans. Power Syst.* 32 (1), 774–783. doi:10.1109/tpwrs.2016.2559485

Hu, J., Yang, G., and Xue, Y. (2017). Economic assessment of network-constrained transactive energy for managing flexible demand in distribution systems. *Energies* 10, 711. doi:10.3390/en10050711

Hu, J., Yang, G., and Bindner, H. W. (2015). "Network constrained transactive control for electric vehicles integration," in *2015 IEEE power & energy society general meeting, Denver, CO*, 1–5.

Hu, J., Yang, G., Bindner, H. W., and Xue, Y. (2017). Application of network-constrained transactive control to electric vehicle charging for secure grid operation. *IEEE Trans. Sustain. Energy* 8 (2), 505–515. doi:10.1109/tste.2016.2608840

Huang, P., Kalagnanam, J., Natarajan, R., Sharma, M., Ambrosio, R., Hammerstrom, D., et al. (2010). "Analytics and transactive control design for the Pacific Northwest smart grid demonstration project," in *2010 first IEEE international conference on smart grid communications, Gaithersburg, MD*, 449–454.

Ji, M., and Zhang, P. (2017). "Transactive control and coordination of multiple integrated energy systems," in *2017 IEEE conference on energy Internet and energy system integration (EI2)* (Beijing, 1–6).

Jin, D., Zhang, X., and Ghosh, S. (2012). "Simulation models for evaluation of network design and hierarchical transactive control mechanisms in Smart Grids," in *2012 IEEE PES Innovative Smart Grid Technologies (ISGT), Washington, DC, January 16–20, 2012 (IEEE)*, 1–8.

Kiani, A., and Annaswamy, A. (2012). "A hierarchical transactive control architecture for renewables integration in Smart Grids," in *2012 IEEE 51st IEEE conference on decision and control (CDC)* (Maui, HI, 4985–4990).

Kiani Bejestani, A., Annaswamy, A., and Samad, T. (2014). A hierarchical transactive control architecture for renewables integration in smart grids: Analytical modeling and stability. *IEEE Trans. Smart Grid* 5 (4), 2054–2065. doi:10.1109/tsg.2014.2325575

Kok, K., and Widergren, S. (2016). A society of devices: Integrating intelligent distributed resources with transactive energy. *IEEE Power Energy Mag.* 14 (3), 34–45. doi:10.1109/mpe.2016.2524962

Kounelis, I., Steri, G., Giuliani, R., Geneiatakis, D., Neisse, R., and Nai-Fovino, I. (2017). "Fostering consumers' energy market through smart contracts," in *2017 international conference in energy and sustainability in small developing economies (ES2DE)* (New York, NY: IEEE), 1–6.

Kristov, L., De Martini, P., and Taft, J. D. (2016). A tale of two visions: Designing a decentralized transactive electric system. *IEEE Power Energy Mag.* 14 (3), 63–69. doi:10.1109/mpe.2016.2524964

Lezama, F., Soares, J., Hernandez-Leal, P., Kaisers, M., Pinto, T., and Vale, Z. (2019). Local energy markets: Paving the path toward fully transactive energy systems. *IEEE Trans. Power Syst.* 34 (5), 4081–4088. doi:10.1109/tpwrs.2018.2833959

Li, D., Yang, Q., Yu, W., An, D., Yang, X., and Zhao, W. (2017). "A strategy-proof privacy-preserving double auction mechanism for electrical vehicles demand response in microgrids," in *2017 IEEE 36th international performance computing and communications conference (IPCCC)* (San Diego, CA, USA, 1–8).

Lopes, J. A. P., Soares, F. J., and Almeida, P. M. R. (2011). Integration of electric vehicles in the electric power system. *Proc. IEEE* 99 (1), 168–183. doi:10.1109/jproc.2010.2066250

Makhmalbaf, A., Hammerstrom, D. J., Huang, Q., and Tang, Y. (2017). "Valuation diagramming and accounting of transactive energy systems," in 2017 IEEE conference on technologies for sustainability (Phoenix, AZ: SusTech), 1–7.

Masiello, R., and Aguero, J. R. (2016). Sharing the ride of power: Understanding transactive energy in the ecosystem of energy economics. *IEEE Power Energy Mag.* 14 (3), 70–78. doi:10.1109/mpe.2016.2524965

Melton, R. B., and Hammerstrom, D. J. (2012). "Transactive control: A technique for widespread coordination of responsive smart grid assetsin *2012 IEEE PES innovative smart grid technologies (ISGT)*, (Washington, DC), 1.

Melton, R. B. (2015). *"Gridwise transactive energy framework version 1,"* Grid-Wise Archit. Council. Richland, WA, USA: Tech. Rep. PNNL-22946.

Mengelkamp, E., Staudt, P., Garttner, J., and Weinhardt, C. (2017). "Trading on local energy markets: A comparison of market designs and bidding strategies," in *2017 14th international conference on the European energy market (EEM)* (Dresden, 1–6).

Moazeni, S., and Defourny, B. (2017). "Distribution system controls assessment in a nonbinding transactive energy market," in *2017 north American power symposium*, Morgantown, WV, 1–6.

Mohsenian-Rad, A. H., and Leon-Garcia, A. (2010). Optimal residential load control with price prediction in real-time electricity pricing environments. *IEEE Trans. Smart Grid* 1 (2), 120–133. doi:10.1109/tsg.2010.2055903

Mohsenian-Rad, A. H., Wong, V. W. S., Jatskevich, J., Schober, R., and Leon-Garcia, A. (2010). Autonomous demand-side management based on game-theoretic energy consumption scheduling for the future smart grid. *IEEE Trans. Smart Grid* 1 (3), 320–331. doi:10.1109/tsg.2010.2089069

Moslehi, K., and Kumar, R. (2010). A reliability perspective of the smart grid. *IEEE Trans. Smart Grid* 1 (1), 57–64. doi:10.1109/tsg.2010.2046346

Nair, V. V., and Nair, U. (2016). "Distributed energy integration and transactive energy framework for a developing economy," in 2016 IEEE International Symposium on Technology and Society (ISTAS), Trivandrum, India, October 20–22, 2016 (IEEE).

Nunna, H. S. V. S. K., and Srinivasan, D. (2017). Multiagent-based transactive energy framework for distribution systems with smart microgrids. *IEEE Trans. Ind. Inf.* 13 (5), 2241–2250. Oct. doi:10.1109/tii.2017.2679808

O'Connell, N., Pierre, P., Madsen, H., and O'Malley, M. (2014). Benefits and challenges of electrical demand response: A critical review. *Renew. Sustain. Energy Rev.* 39, 686–699. doi:10.1016/j.rser.2014.07.098

Oikonomou, K., Parvania, M., and Khatami, R. (2018). Optimal demand response scheduling for water distribution systems. *IEEE Trans. Ind. Inf.* 14 (11), 5112–5122, Nov. doi:10.1109/tii.2018.2801334

Olken, M. (2016). Transactive energy: Providing an enabling environment [from the editor]. *IEEE Power Energy Mag.* 14 (3), 4. doi:10.1109/mpe.2016.2525878

Palensky, P., and Dietrich, D. (2011). Demand side management: Demand response, intelligent energy systems, and smart loads. *IEEE Trans. Ind. Inf.* 7 (3), 381–388. doi:10.1109/tii.2011.2158841

Parandehgheibi, M., Pourmousavi, S. A., Nakayama, K., and Sharma, R. K. (2017). *A two-layer incentive-based controller for aggregating BTM storage devices based on transactive energy framework*. Chicago, IL, USA: IEEE Power & Energy Society General Meeting, 1–5.

Patterson, B. T., and Geary, D. E. (2016). "Real-Time transactional power management in a microgrid mesh network: The enernet," in *2016 IEEE international telecommunications energy conference (INTELEC)* (Austin, TX, 1–7).

Pratt, A., Krishnamurthy, D., Ruth, M., Wu, H., Lunacek, M., and Vaynshenk, P. (2016). Transactive home energy management systems: The impact of their proliferation on the electric grid. *IEEE Electrific. Mag.* 4 (4), 8–14. doi:10.1109/mele.2016.2614188

Pratt, R. (2012). Transactive control with real-time prices and a double-auction feeder market. In *2012 IEEE PES innovative smart grid technologies (ISGT)* (Washington, DC, 1).

Prinsloo, Gerro, Mammoli, Andrea, and Dobson, Robert (2017). Customer domain supply and load coordination: A case for smart villages and transactive control in rural off-grid microgrids. *Energy* 135, 430–441. doi:10.1016/j.energy.2017.06.106

Prinsloo, G., Mammoli, A., and Dobson, R. (2016). "Participatory smartgrid control and transactive energy management in community shared solar cogeneration systems for isolated rural villages," in *2016 IEEE global humanitarian technology conference (GHTC)* (Seattle, WA, 352–359).

Qin, J., Wan, Y., Yu, X., Li, F., and Li, C. (2019). Consensus-based distributed coordination between economic dispatch and demand response. *IEEE Trans. Smart Grid* 10 (4), 3709–3719. doi:10.1109/tsg.2018.2834368

Qiu, J., Meng, K., Zheng, Y., and Dong, Z. Y. (2017). Optimal scheduling of distributed energy resources as a virtual power plant in a transactive energy framework. *IET Gener. Transm. & Distrib.* 11 (13), 3417–3427. doi:10.1049/iet-gtd.2017.0268,

Qiu, J., Zhao, J., Yang, H., and Dong, Z. Y. (2018). Optimal scheduling for prosumers in coupled transactive power and gas systems. *IEEE Trans. Power Syst.* 33 (2), 1970–1980. doi:10.1109/tpwrs.2017.2715983

Rahimi, F., and Albuyeh, F. (2016). "Applying lessons learned from transmission open access to distribution and grid-edge Transactive Energy systems," in 2016 IEEE Power & Energy Society Innovative Smart Grid Technologies Conference (ISGT), (Minneapolis, MN), 1–5.

Rahimi, F., Ipakchi, A., and Fletcher, F. (2016). The changing electrical landscape: End-to-End power system operation under the transactive energy paradigm. *IEEE Power Energy Mag.* 14 (3), 52–62. doi:10.1109/mpe.2016.2524966

Rahimi, F., and Ipakchi, A. (2016). Using a transactive energy framework: Providing grid services from smart buildings. *IEEE Electrific. Mag.* 4 (4), 23–29. doi:10.1109/mele.2016.2614181

Ramdaspalli, S., Pipattanasomporn, M., Kuzlu, M., and Rahman, S. (2016). "Transactive control for efficient operation of commercial buildings," in *2016 IEEE PES innovative smart grid technologies conference Europe (ISGT-Europe)*, Ljubljana, 1–5.

Rayati, M., and Ranjbar, A. M. (2018). Resilient transactive control for systems with high wind penetration based on Cloud computing. *IEEE Trans. Ind. Inf.* 14 (3), 1286–1296. doi:10.1109/tii.2017.2759223

Sahin, T., and Shereck, D. (2014). "Renewable energy sources in a transactive energy market," in *The 2014 2nd international conference on systems and informatics (ICSAI 2014)*, Shanghai, 202–208.

Sajjadi, S. M., Mandal, P., Tseng, T. L. B., and Velez-Reyes, M. (2016). "Transactive energy market in distribution systems: A case study of energy trading between transactive nodes," in *2016 north American power symposium (NAPS)* (Denver, CO, 1–6).

Siano, P. (2014). Demand response and smart grids - a survey. *Renew. Sustain. Energy Rev.* 30, 461–478. doi:10.1016/j.rser.2013.10.022

Siano, Pierluigi, and Sarno, Debora (2016). Assessing the benefits of residential demand response in a real time distribution energy market. *Appl. Energy* 161, 533–551. doi:10.1016/j.apenergy.2015.10.017

Sun, Q., Han, R., Zhang, H., Zhou, J., and Guerrero, J. M. (2015). A multiagent-based consensus algorithm for distributed coordinated control of distributed generators in the energy Internet. *IEEE Trans. Smart Grid* 6 (6), 3006–3019, Nov. doi:10.1109/tsg.2015.2412779

TeMIX, E. G. C. (2010). A foundation for transactive energy in a smart grid world. *Grid-Interop Forum*.

Transactive Energy Infographics (2022). *The grid-wise architecture Council*. Washington, DC, USA: US Department of Energy. Available at: http://www.gridwiseac.org.

Transactive Energy Principles (V1.0) (2022). *The grid-wise architecture Council*. Washington, DC, USA: US Department of Energy. Available at: http://www.gridwiseac.org.

Wang, Y., Yemula, P., and Bose, A. (2015). Decentralized communication and control systems for power system operation. *IEEE Trans. Smart Grid* 6 (2), 885–893. doi:10.1109/tsg.2014.2363192

Widergren, S., Fuller, J., Marinovici, C., and Somani, A. (2014). *Residential transactive control demonstration*. Washington, DC: ISGT 2014, 1–5.

Xavier, E. B., Goncalves, D. A. V., Dias, B. H., and Borba, B. S. M. C. (2017). Electricity auction simulation platform for learning competitive

energy markets. *IEEE Potentials* 36 (5), 32–36. doi:10.1109/mpot.2016.2563179

Xie, D. J., Hui, H. X., Ding, Y., and Lin, Z. Z. (2018). Operating reserve capacity evaluation of aggregated heterogeneous TCLs with price signals. *Appl. Energy* 216, 338–347. doi:10.1016/j.apenergy.2018.02.010

Yan, M., Shahidehpour, M., Paaso, A., Zhang, L., Alabdulwahab, A., and Abusorrah, A. (2021). Distribution network-constrained optimization of peer-to-peer transactive energy trading among multi-microgrids. *IEEE Trans. Smart Grid* 12 (2), 1033–1047. doi:10.1109/tsg.2020.3032889

Yang, C. (2018). *Uncertainty-aware transactive operation decisions for grid-friendly building clusters*. Chicago, IL: University of Illinois at Chicago.

Yao, Y., and Zhang, P. (2017). "Transactive control of air conditioning loads for mitigating microgrid tie-line power fluctuations," in *2017 IEEE power & energy society general meeting* (Chicago, IL, USA, 1–5).

Yu, P., Wan, C., Song, Y., and Jiang, Y. (2021). Distributed control of multi-energy storage systems for voltage regulation in distribution networks: A back-and-forth communication framework. *IEEE Trans. Smart Grid* 12 (3), 1964–1977. doi:10.1109/tsg.2020.3026930

Yue, J., Hu, Z., Li, C., Vasquez, J. C., and Guerrero, J. M. (2017). Economic power schedule and transactive energy through an intelligent centralized energy management system for a DC residential distribution system. *Energies* 10, 916–945. doi:10.3390/en10070916

Zhang, Chenghua, Wu, Jianzhong, Zhou, Yue, Cheng, Meng, and Long, Chao (2018). Peer-to-Peer energy trading in a Microgrid. *Appl. Energy* 220, pp1–12. doi:10.1016/j.apenergy.2018.03.010

Zhou, Bin, Li, Wentao, Chan, KaWing, Cao, Y., Kuang, Y., Liu, X., et al. (2016). Smart home energy management systems: Concept, configurations, and scheduling strategies. *Renew. Sustain. Energy Rev.* 61, 30–40. doi:10.1016/j.rser.2016.03.047

frontiers | Frontiers in Energy Research

Deep learning model-transformer based wind power forecasting approach

Sheng Huang, Chang Yan and Yinpeng Qu*

College of Electrical and Information Engineering, Hunan University, Changsha, China

The uncertainty and fluctuation are the major challenges casted by the large penetration of wind power (WP). As one of the most important solutions for tackling these issues, accurate forecasting is able to enhance the wind energy consumption and improve the penetration rate of WP. In this paper, we propose a deep learning model-transformer based wind power forecasting (WPF) model. The transformer is a neural network architecture based on the attention mechanism, which is clearly different from other deep learning models such as CNN or RNN. The basic unit of the transformer network consists of residual structure, self-attention mechanism and feedforward network. The overall multilayer encoder to decoder structure enables the network to complete modeling of sequential data. By comparing the forecasting results with other four deep learning models, such as LSTM, the accuracy and efficiency of transformer have been validated. Furthermore, the migration learning experiments show that transformer can also provide good migration performance.

1 Introduction

Wind energy is an economical, efficient and environment friendly renewable energy source that plays an important role in reducing global carbon emissions (Lin and Liu, 2020). According to Global Wind Report 2022, total installed WP capacity had reached 837 GW by the end of 2021 (Council, 2022). As the proportion of installed wind turbines (WTs) increases year by year, the strong randomness, volatility and intermittency of WP lead to the contradiction between the safe operation of the power grid and the efficient consumption of WP (Yang et al., 2022). Accurate forecasting can reduce the uncertainty and increase the penetration rate of WP.

The WPF mentioned in this paper refers to the forecasting of specific point values of future wind speed or WP. It is called the deterministic forecasting model, which mainly includes physical forecasting models, statistical forecasting models and hybrid forecasting models (Hanifi et al., 2020; Sun et al., 2021).

Physical forecasting modeling obtains wind speed forecasting information based on numerical weather forecast data with mathematical models, and then predicts WP with the help of relevant WP curves using the wind speed forecasts (Li et al., 2013). Therefore

improving the accuracy of the NWP model directly affects the forecasting accuracy of the physical model (Cassola and Burlando, 2012).

Statistical forecasting modeling is establishing a mapping relationship between historical data and forecasted data. Statistical models can be classified into traditional statistical models, time series models, traditional machine learning models and deep learning models. The persistence method, known as the most classical traditional statistical method, uses the wind power at the current moment as the forecasted value. This method is simple but limited to the use of ultra-short-term forecasting (Wu and Hong, 2007). Commonly used time series models include AutoreGressive (AR) (Poggi et al., 2003), Auto Regression Moving Average (ARMA) (Huang et al., 2012), Autoregressive Integrated Moving Average (ARIMA) (Hodge et al., 2011), etc. Time series models are difficult to explore the non-linear relationship in the data. So such models are only suitable for static data analysis. Traditional machine learning models can predict future wind power value adaptively based on historical WP data. Machine learning models are widely used in wind power forecasting and related fields. The popular methods include artificial neuro network (ANN) (Hu et al., 2016), support vector machine (SVM) (Li et al., 2020), Piecewise support vector machine (PSVM) (Liu et al., 2009), Least Square support vector machine (LSSVM) (Chen et al., 2016), Random Forest (RF) (Lahouar and Slama, 2017), Bayesian Additive RegressionTrees (Alipour et al., 2019), K-Nearest-Neighbors (KNN) (Yesilbudak et al., 2017), etc. These machine learning models require additional time to extract features from multidimensional data with good accuracy and relevance. Optimization algorithms can effectively solve this problem (Shahid et al., 2021). Li et al. (2021) proposed a hybrid improved cuckoo search algorithm to optimize the hyperparameters of support vector machines for short-term wind power forecasting.

In recent years, deep learning models have provided promising performance in natural language processing (NLP), computer vision and other fields, while related techniques are also applied to wind power forecasting. Among them, two recurrent neural networks (RNN), Long Short Term Memory (LSTM) and Gated Recurrent Unit (GRU), are mainly utilized for wind power forecasting research (Lu et al., 2018; Deng et al., 2020; Wang et al., 2020). used wavelet decomposition to reduce the volatility of the original series. They transformed non-stationary time series into stable and predictable series to forecast by LSTM Liu et al. (2020). enhanced the effect of forgetting gate in LSTM, optimized the convergence speed, and filtered the feature data within a certain distance based on correlation. The forecasting permance was futher improved by clustering Yu et al. (2019). used variable mode decomposition to stratify wind power sequences according to different frequencies. Then similar fluctuating patterns were identified in each

layer by K-means clustering algorithm. Furthermore, the unstable features were captured in each set by LSTM Sun et al. (2019). To address the overfitting problem, employed multi-level residual networks and DenseNet to improve the overall performance Ko et al. (2020). introduced the attention mechanism into the GRU to obtain a novel sequence-to-sequence model Niu et al. (2020). The combination of multiple deep learning models can also improve the accuracy of WPF. proposed a novel spatio-temporal correlation model (STCM) for ultra-short-term wind power forecasting Wu et al. (2021). proposed a hybrid deep learning algorithm, which consists of GRU, LSTM, and fully connected neural networks, to accurately predict ultra-short-term wind power generation at the Boco Rock wind farm in Australia, Hossain et al. (2020). The RNN model is unable to capture the long periods temporal correlation due to the gradient disappearance problem. To address this problem, Lai et al. (2018) developed an RNN-skip structure with time-hopping connections to extend the time span of the information flow. RNN also suffers from the inability of recursive computation to parallelize problem. The transformer is the first sequence transcription model based solely on the attention mechanism, which has been proved that it can solve the aforementioned problems (Vaswani et al., 2017). The transformer was first proposed in NLP. BERT (Devlin et al., 2018), GPT-2 (Radford et al., 2019), RoBERTa (Liu et al., 2019), T5 (Raffel et al., 2020) and BART (Lewis et al., 2019) based on transformer have made a huge impact in the NLP field. Recently, almost all advanced NLP models have been adapted from one of above basic models (Bommasani et al., 2021). Transformer made a big splash in the field of computer visiona along with the publication of the VIT (Dosovitskiy et al., 2020), CvT (Wu et al., 2021), CaiT (Touvron et al., 2021), DETR (Carion et al., 2020), and Swin Transformer (Liu et al., 2021). Transformer was also applied to the field of power system time series forecasting. Lin et al. employed the Spring DWT attention layer to measure the similarity of query-key pairs of sequences (Lin et al., 2020). Santos et al. and Phan et al. employed the transformer-based time series forecasting model to predict the PV power generation for each hour (López Santos et al., 2022; Phan et al., 2022). L'Heureux et al. proposed a transformer-based architecture for load forecasting (L'Heureux et al., 2022).

Transformer architecture has become a mainstream technology in NLP which performs better than RNN or Seq2Seq algorithms. For this reason, this paper used the transformer as the basic model for wind power forecasting research.

The remainder of the paper is organized as follows. Section 2 presents the forecasting problem. Section 3 introduces Data-driven model of wind power forecasting. Section 4 shows the analysis and discussion of the numerical simulation results. Section 5 concludes this paper.

FIGURE 1
Encoder to decoder structure.
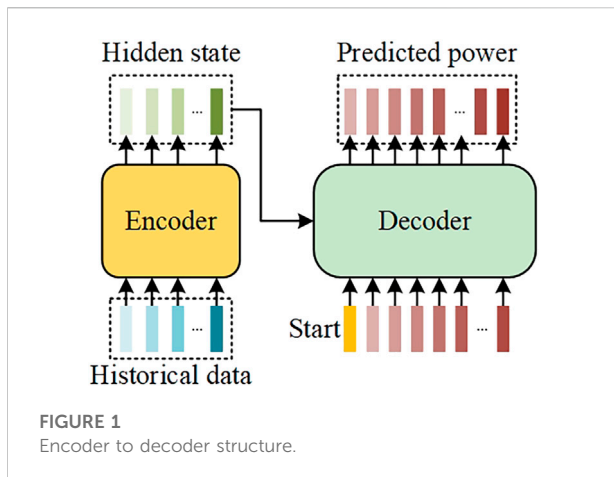
2 Problem description

In this paper, wind power forecasting refers to making speculations about the possible levels of wind power in several future periods.

Suppose $D = \{D_1, D_2, \cdots, D_n\}$ is the historical information collected from WPAPs, where n is the number of WPAPs. $D_i = \{P_i, F_i\}$ is the historical information of i th WPAP, where P_i. is the power output of the i th WPAP and F_i is other characteristic information of the i th WPAP. For each P_i^t in $P_i = \{P_i^1, P_i^2, \cdots, P_i^t\}$ is the power outputs of the i th WPAP at timestamp t. For each $F_{i,j}^t$ in $F_i = \left\{F_{i,1}^1, F_{i,1}^2, \cdots, F_{i,1}^t, F_{i,2}^1, F_{i,2}^2, \cdots, F_{i,2}^t, \cdots, F_{i,j}^1, F_{i,j}^2, \cdots, F_{i,j}^t\right\}$ is the j th feature data of the i th WPAP at timestamp t. Common characteristics are wind speed and WPAP ambient temperature, etc. The one-step ahead wind power sequence forecasting model f can be denoted as:

$$P_i^{pre} = f(D_i), \quad i \in [0, n]$$

Where P_i^{pre} denotes the power forecasting sequence of the i th WPAP.

3 Deep learning model for wind power forecasting

In this paper, the transformer is chosen as the basic deep learning model for wind power forecasting because it is considered to use a broader inductive bias compared to RNN, allowing it to handle more generalized information. The inductive bias of a learning algorithm is the set of assumptions that the learner uses to predict outputs of given inputs that it has not encountered. For example, the loop structure and gate structure are the inductive bias of RNNs. The transformer model mainly includes self-attentive mechanisms, position-wise feed-forward networks and

residual connections. These three neural network structures do not rely on strong assumptions on the objective function. Furthermore, they do not have the inductive bias as translation invariance or the time invariance. So, a much more general form makes the transformer model applicable to more subjects. In this section, we introduce the structure of the transformer.

3.1 Encoder to decoder structure

Numerous wind power sequence forecasting models follow the encoder to decoder structure (Lu et al., 2018; Niu et al., 2020; Li and Armandpour, 2022), which is illustrated in Figure 1. The encoder maps the WPAP historical sequence data $D = \{D_1, D_2, \cdots, D_n\}$ to the hidden state $H = \{H_1, H_2, \cdots, H_n\}$. The decoder then outputs the forecasted power sequence $P^{pre} = \left\{P_1^{pre}, P_2^{pre}, \cdots, P_n^{pre}\right\}$ based on the hidden state H. As shown in Figure 2, transformer architecture also follows this architecture and uses stacked self-attentive mechanisms, pointwise fully connected layers and the RetNet structure (He et al., 2016) to build the decoder and encoder. Encoder consist of a self-defined number of identical encoder layers stacked on top of each other. Each encoder layer has two sub-layers: multi-head self-attention mechanism and position-wise fully connected feed-forward network. Each sub-layer uses a residual structure and then the output data is layer-normalized which can be expressed as:

$$O_{sub} = LN(x + SL(x))$$

Where O_{sub} is the output of sub-layer, x is the input of the sub-layer, LN is the layer normalization function, SL is the function employed in the sub-layer.

To facilitate residual connectivity, outputs produced from all sublayers in the model as well as the embedding layer have the same self-defined dimension d_{model}.

The decoder has the same number of stack layers as the encoder. each decoder layer consists of three sub-layers. The first sublayer is the Masked Multi-head attention layer, whose main function is to ensure that the forecasting of position i only depends on the known outputs of positions smaller than i. The last two layers use the same sub-layers as the encoder layer. Each sub-layer has a residual architecture and layer normalization of the output.

3.2 Self-attentive mechanism

The attention mechanism (AM) is a resource allocation scheme that allocates computational resources to more important tasks while solving the information overload problem in the presence

FIGURE 2
Encoder and decoder stacks of transformer.

FIGURE 3
Self-attention with masking function.
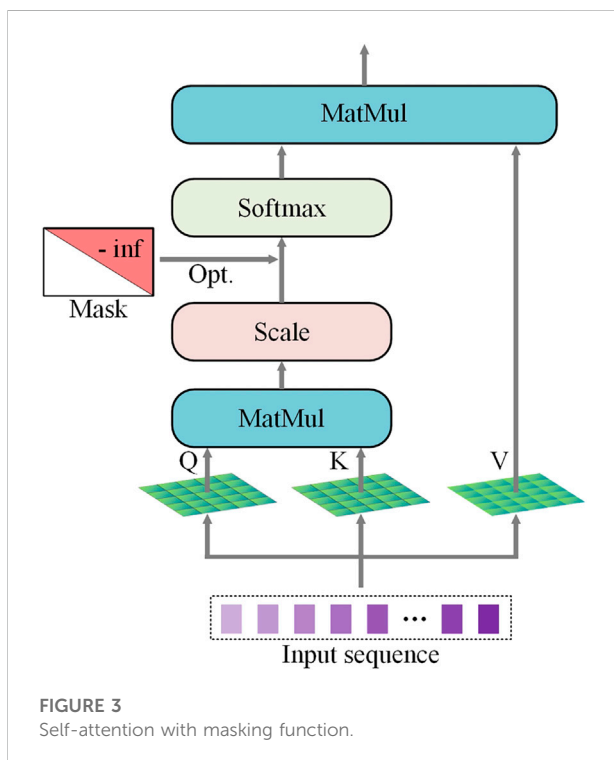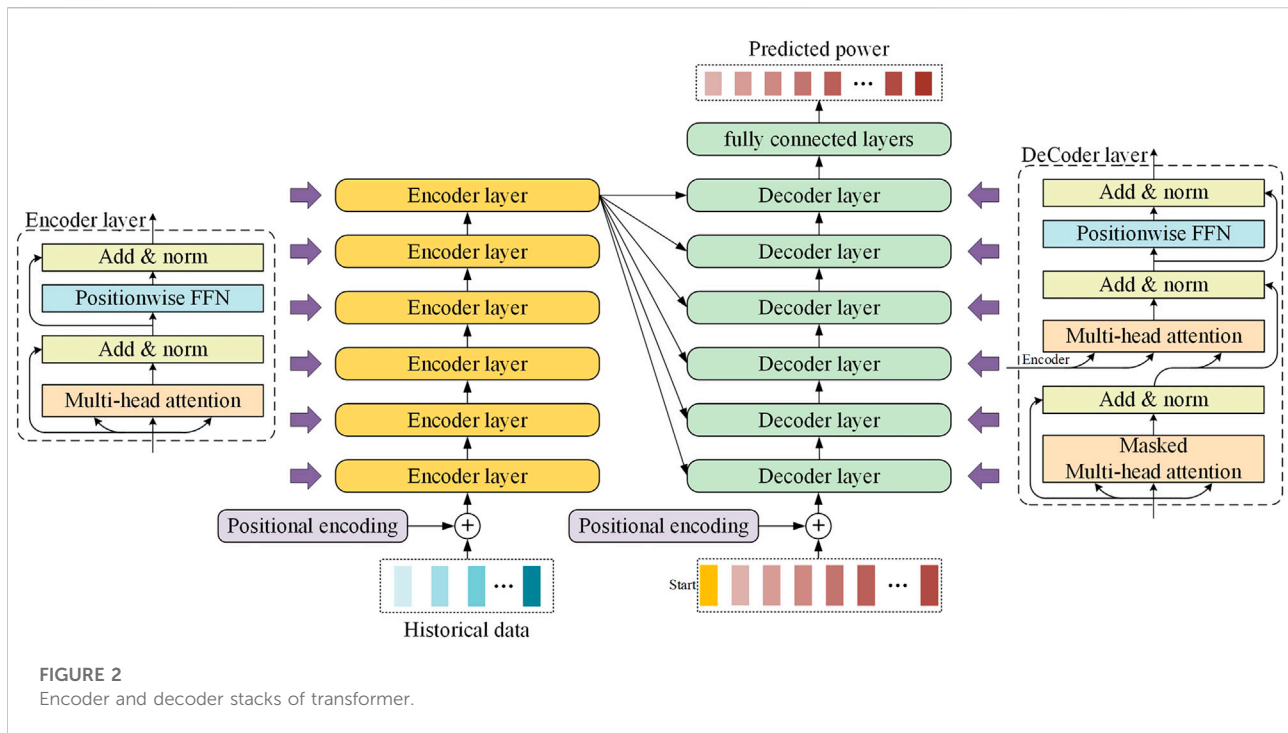
of limited computational power. The input information of AM can be represented by key vector -value vector pairs $[(k_1, v_1), (k_2, v_2), \ldots, (k_m, v_m)]$. The target value information

can be represented by query vector. The weight of the value vectors are calculated based on the similarity of query vector and key vector. And then, the final attention value can be obtained by weighted summation of value vector. The core idea of the attention mechanism can be expressed as the following equation.

$$S_{att} = W \times V$$
$$W = func(Q, K)$$

Where S_{att} is the attention value, V is the value vector of key-value pairs, K is the key vector of key-value pairs, Q is the query vector, W is the corresponding weight of V and func is the weight transformation function.

The self-attentive mechanism (SAM) uses three learnable parameter matrices W_q, W_k and W_v to transform the input sequence X into the query vector Q_s, key vector K_s and value vector V_s. The model uses a SoftMax function as the weight transformation function. The weights of the V_s are obtained by calculating the dot product of Q_s and K_s divided by $\sqrt{d_k}$. The output of SAM is obtained by weighted summation of V_s, as depicted in Figure 3.

$$Q_s = W_Q X \in \mathbb{R}^{d_k \times N}$$

$$K_s = W_K X \in \mathbb{R}^{d_k \times N}$$

$$V_s = W_V X \in \mathbb{R}^{d_v \times N}$$

$$\text{Attention}(Q, K, V) = \text{softmax}\left(\frac{QK^T}{\sqrt{d_k}}\right)V$$

Where d_k is the dimension of K_s.

FIGURE 4
Multi-head attention.

FIGURE 5
Data input.

FIGURE 6
Data subset allocation ratio.
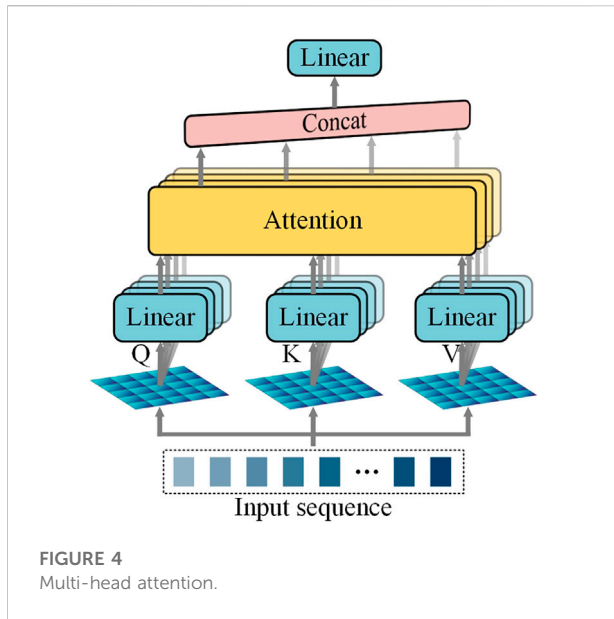
3.3 Multi-head attention and masked multi-head attention

Multi-head attention mechanism uses different weight matrices to project the single attention head input sequence into different subspaces, which allows the model to focus on different aspects of information. The different weight matrices W_i^Q, W_i^K and W_i^V transform the vectors Q, K and V of dimension d_{model} into h vectors Q_i, K_i and V_i of dimension d_{model}/h and input them into the corresponding parallel attention layers, where h is the number of parallel layers. Then the outputs of each layer are concatenated and the results output *via* the linear layer, as depicted in Figure 4.

$$\text{MultiHead}(Q, K, V) = \text{Concat}(\text{head}_1, \ldots, \text{head}_h)W^O$$
$$\text{where } head_i = \text{Attention}(Q_i, K_i, V_i)$$
$$Q_i = QW_i^Q \qquad i = 1, 2, \ldots, h$$
$$K_i = KW_i^K$$
$$V_i = VW_i^V$$

Where $W_i^Q \in \mathbb{R}^{d_{\text{model}} \times d_k}$, $W_i^K \in \mathbb{R}^{d_{\text{model}} \times d_k}$, $W_i^V \in \mathbb{R}^{d_{\text{model}} \times d_v}$, $W^O \in \mathbb{R}^{hd_v \times d_{\text{model}}}$, and $d_k = d_v = d_{model}/h$

Masked multi-head attention mechanism is proposed to prevent the decoder from seeing future information. An upper triangular matrix with all values of "-inf" is added to the dot product matrix before it is softmaxed, as depicted in Figure 3.

3.4 Position-wise feed-forward networks and positional encoding

Each encoder and decoder layer contains a position-wise feed-forward networks, which is composed of two linear transformations and uses the ReLu function as the activation function. Due to the existence of two linear transformations, the inner layer dimension can be adjusted while the input and output dimensions are guaranteed to be equal to d_{model}. The formula is as follows.
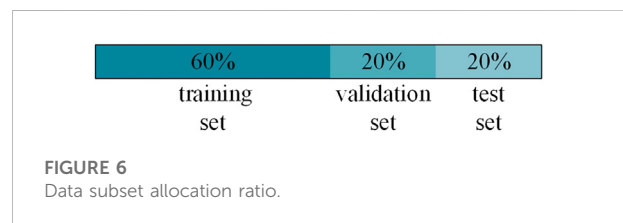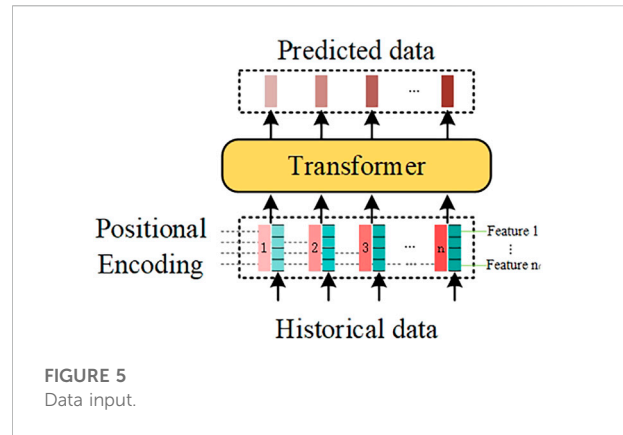
$$\text{FFN}(x) = ReLu(xW_1 + b_1)W_2 + b_2$$
$$\text{where } ReLu(x) = max(0, x)$$

where W_1 and W_2 are the two linear transformation matrixes, b_1 and b_2 are biases of the two linear transformations and x is the input data.

Since transformer architecture does not contain recursion and there is no relative or absolute position information of each value in the inputs of the transformer, it is necessary to there is no relative or absolute position information of each value in the inputs of the transformer so that the model can make use of the sequential information. Transformer uses sine and cosine functions of different frequencies.

$$PE_{(pos, 2id)} = \sin\left(pos / 10000^{2id/d_{\text{model}}}\right)$$
$$PE_{(pos, 2id+1)} = \cos\left(pos / 10000^{2id/d_{\text{model}}}\right)$$

where *pos* is the position and *id* is the dimension.

FIGURE 7
One-step power forecasting experimental results of NO.1-NO.8 WPAP.
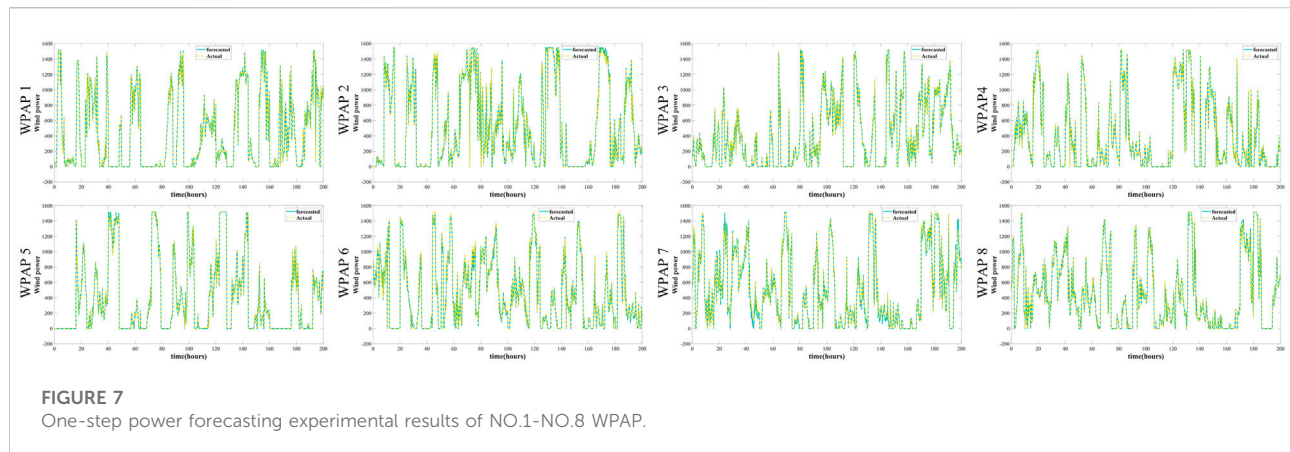
3.5 Power forecasting and model migration

In this paper, transformer is used as the power prediction model. The historical feature data needs to be processed before it can be input into transformer. The transformation of historical data into feature vectors and positional encoding are shown in the Figure 5. The feature vector at each timestamp consists of different WPAP feature values in the specified order. Each encoder layer extracts features from the input data using the multi-head attention mechanism, position-wise feed-forward networks, normalization layer and residual structure. The last encoder layer passes the feature information to each decoder layer. The first sub-layer of each decoder layer extracts the sequence feature information from the predicted data. Finally, the predicted data of the specified length is processed by the fully-connected layer and output.

Migrating the trained model parameters to another model for a related task can effectively speed up the model convergence and reduce the overfitting problem. The data between different WPAPs has some similarity. This paper proposes to train untrained WPAP prediction models which we migrate the trained WPAP power prediction model parameters to.

4 Experimental results and discussion

To verify the effectiveness of transformer for wind power forecasting, we conducted a case study using areal-world wind farm operation dataset.

4.1 Dataset preparation

In this paper, experiments are conducted by using the Spatial Dynamic Wind Power Forecasting (SDWPF) dataset, which is constructed based on real-world wind farm data from Longyuan Power Group Corp. Ltd. (Zhou et al., 2022). SDWPF contains 134 WPAPs output power, wind speed, ambient temperature and other characteristic information, which is sampled at 10-min intervals and covers 245 days of data. From them, we selected the power, wind speed and ambient temperature of eight WPAPs data as the feature information used for single turbine one-step ahead wind power prediction. Three data subsets are used in the evaluation: training set, validation set, and test set, and the three subsets are assigned in the ratio of 6:2:2 as shown in Figure 6. The training set is used to update the model parameters. First, the results of the forward calculation are stored for each parameter. Then, the partial derivatives of each parameter can be calculated through loss function based on the chain rule subsequently. At last, the partial derivatives are multiplied with the learning rate to obtain the optimized values of the parameters. The validation set is used for hyperparameter tuning during the model training, and the test set is used to evaluate the generalization ability of the model.

4.2 Data processing

The input variables used in this study are normalized in order to speed up the gradient descent for optimal solutions and to improve the accuracy of the model after training. The feature information is scaled to the range (0, 1) by min-max normalization, and the model output is denormalized.

TABLE 1 Each prediction model corresponds to the performance index of each WPAP.

Model	Number	*MSE*	*MAE*	*RMSE*	r2score
Transformer	WPAP 1	17.85	2.79	4.22	0.9927
	WPAP 2	81.79	5.28	9.04	0.9873
	WPAP 3	22.18	3.11	4.71	0.9916
	WPAP 4	31.35	3.11	5.60	0.9917
	WPAP 5	34.81	3.56	5.90	0.9907
	WPAP 6	349.80	10.96	18.70	0.9708
	WPAP 7	1854.07	12.75	43.06	0.9659
	WPAP 8	43.18	3.82	6.57	0.9888
LSTM	WPAP 1	30,054.43	102.95	173.36	0.7670
	WPAP 2	19,369.12	80.15	139.17	0.7914
	WPAP 3	24,852.67	95.47	157.65	0.7419
	WPAP 4	33,919.56	110.45	184.17	0.7033
	WPAP 5	41,330.30	122.23	203.30	0.6806
	WPAP 6	22,473.57	86.20	149.91	0.7702
	WPAP 7	38,449.08	118.99	196.08	0.6815
	WPAP 8	19,042.41	79.31	138.00	0.7676
LSTM (encoder-decoder)	WPAP 1	25,685.14	92.67	160.27	0.7762
	WPAP 2	26,958.49	99.14	164.19	0.7135
	WPAP 3	24,751.02	93.21	157.32	0.7166
	WPAP 4	24,181.57	93.14	155.50	0.7207
	WPAP 5	25,359.76	94.54	159.25	0.7282
	WPAP 6	25,101.07	94.25	158.43	0.7171
	WPAP 7	30,025.81	105.08	173.28	0.6911
	WPAP 8	31,325.91	105.32	176.99	0.6667
GRU	WPAP 1	19,987.32	85.33	141.38	0.8069
	WPAP 2	21,242.36	86.55	145.75	0.7747
	WPAP 3	19,528.68	85.69	139.75	0.7684
	WPAP 4	20,628.77	85.88	143.63	0.7693
	WPAP 5	19,067.65	80.58	138.09	0.7894
	WPAP 6	28,290.43	99.28	168.20	0.7353
	WPAP 7	25,172.07	95.83	158.66	0.7435
	WPAP 8	17,800.28	77.21	133.42	0.7737
GRU (encoder-decoder)	WPAP 1	27,126.60	92.52	164.70	0.7766
	WPAP 2	22,599.75	85.18	150.33	0.7538
	WPAP 3	23,005.86	89.85	151.68	0.7268
	WPAP 4	21,207.50	80.54	145.63	0.7585
	WPAP 5	21,693.08	82.02	147.29	0.7642
	WPAP 6	25,015.56	88.84	158.16	0.7334
	WPAP 7	24,351.19	93.96	156.05	0.7238
	WPAP 8	27,082.16	94.26	164.57	0.7017

$$x'_{inp} = \mathrm{normal}(x_{inp})$$

$$\mathrm{normal}(x_{inp}) = \frac{x_{inp} - max(x_{inp})}{max(x_{inp}) - min(x_{inp})}$$

Where x'_{inp} is the normalized output of the model input data x_{inp}

$$x'_{out} = de\mathrm{normal}(x_{out})$$

$$\mathrm{denormal}(x_{out}) = \frac{x_{out} - max(x_{in})}{max(x_{in}) - min(x_{in})}$$

Where x'_{out} is the denormalized output of the model output data x_{out}

FIGURE 8
Transformer model migration based one-step power forecasting experimental results of NO.9-NO.20 WPAP.
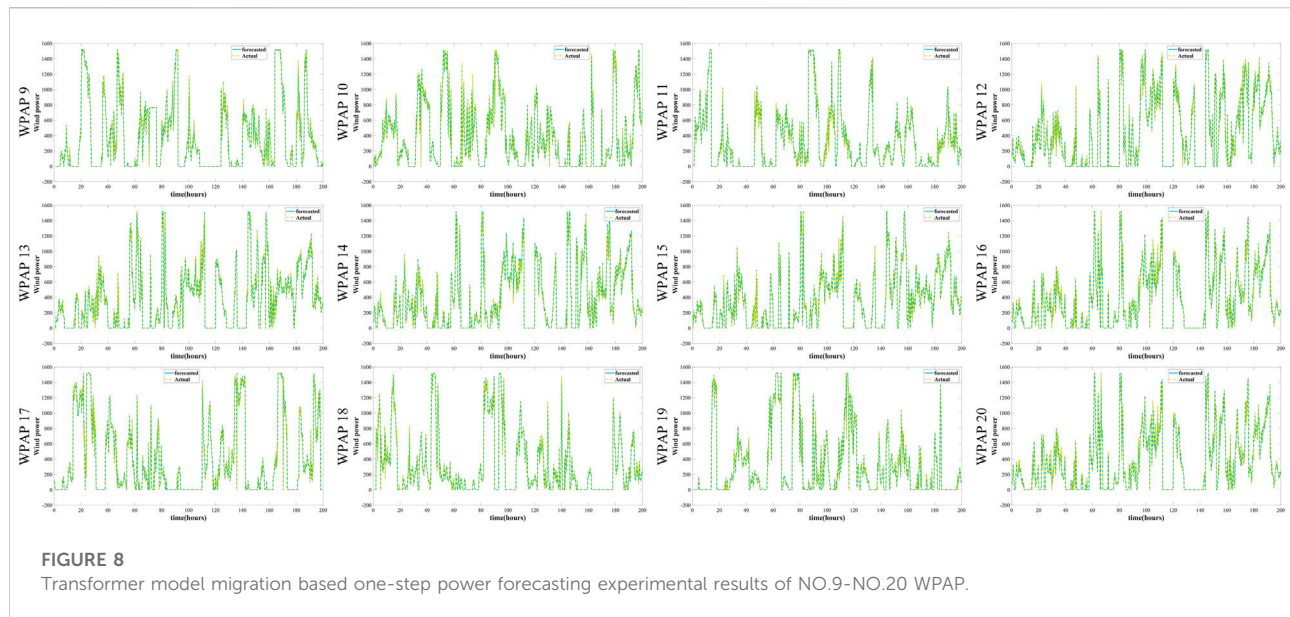
4.3 Performance evaluation

In this paper, we use four metrics to evaluate the prediction performance of transformer, namely mean squared error (MSE), mean absolute error (MAE), mean square root error (RMSE), r2score, and explained variance (EV). They can be expressed mathematically as:

$$MSE = \frac{1}{l} \sum_{i=1}^{l} (p - \hat{p})^2$$

$$MAE = \frac{1}{l} \sum_{i=1}^{l} |p - \hat{p}|$$

$$RMSE = \sqrt{\frac{1}{l} \sum_{i=1}^{l} (p - \hat{p})^2}$$

$$\text{r2score} = 1 - \frac{\sum |p - \hat{p}|}{\sum |p - p'|}$$

Where p denotes the original power, $\hat{p}$ denotes the forecasted power, l denotes the length of the forecast series and p' denotes the mean value of original power.

The better the fit between the prediction structure and the actual results, the better *MSE*, *MAE* and *RMSE* tend to 0 and r2score tend to one

4.4 Experimental numerical results

In this paper, the experiments performed by all the models use the historical wind power data of the 40 h to predict the wind power value of the next 8 h.

TABLE 2 Performance indicators of WPAPs 9 to 20 and the distance of relative location between each WPAP and WPAP one.

Number	Distance	*MSE*	*MAE*	*RMSE*	r2score
WPAP 9	476.91	31.52	3.27	5.61	0.9914
WPAP 10	949.88	37.13	3.91	6.09	0.9895
WPAP 11	1448.69	49.21	3.99	7.01	0.9896
WPAP 12	2,373.70	38.76	4.77	6.23	0.9869
WPAP 13	3,251.40	29.15	3.61	5.40	0.9891
WPAP 14	3,863.73	107.50	5.00	10.37	0.9850
WPAP 15	4,162.78	23.67	3.23	4.87	0.9895
WPAP 16	4,326.15	23.61	3.10	4.86	0.9906
WPAP 17	5,228.90	14.42	2.22	3.80	0.9941
WPAP 18	5,697.92	6.04	1.39	2.46	0.9961
WPAP 19	6,173.15	46.62	3.63	6.83	0.9899
WPAP 20	6,648.17	10.76	2.04	3.28	0.9942

First, we use transformer to perform a one-step power forecasting on eight WPAPs datasets. A comparison of the predicted and actual power curves for each WPAP is shown in Figure 7. It can be seen that the predicted power of each WPAP can match the actual power well, and the two curves have similar trends. This power comparison graph shows that transformer has good prediction capability. Also, we perform the same experiments using LSTM, GRU models and LSTM and GRU models with encoder-decoder structure. The performance indexes for each WPAP power forecasting using the five models are shown in Table 1. It can be seen that the forecasting performance of transformer on this dataset is much better than the four models. The mean MSE, MAE and RMSE of transformer prediction results are 304.38, 5.67 and

12.23 respectively. They are small compared to the mean power output value of 393.47 and the maximum value of 1552.76. The mean r2score of transformer forecasting results is 0.9849, which is 33.47%, 37.50%, 27.88% and 32.66% improvement compared to 0.7379, 0.7163, 0.7702 and 0.7424 of the other four models. It can be seen that transformer forecasts very accurately, thanks to the structure of encoder-decoder, the design of multi-headed self-attentiveness, the ability of masked multi-headed self-attentiveness to extract sequence information and the structure of residuals, etc.

Transformer has certain generalization performance, and we randomly selected 12 WPAPs datasets, using the model parameters already trained by WPAP 1, to train the model and complete the prediction task. The experimental results are shown in Figure 8, and the prediction performance indexes of transformer migration learning on each t WPAP dataset and the distance of relative location between each WPAP and WPAP1 are shown in Table 2. The MSE, MAE and RMSE of forecasting results are 34.87, 3.35 and 5.57, which are also small. The r2score of 0.9904 is likewise very close to 1. Transformer has a better model migration effect due to its minimal inductive bias. It can be seen that other WPAPs within the same area can use the trained transformer model parameters for model training and achieve good prediction accuracy.

5 Conclusion

In this paper, we illustrate the principle of transformer with powerful sequence modeling capabilities such as encoder to decoder architecture, self-attentive mechanism, multi-headed attention, and sequence modeling using masks, and use it for WPAP power forecasting. We use 40 h of historical power data, wind speed data and ambient temperature data to predict the output power of WPAPs for the next 8 h. The mean values of MSE, MAE and RMSE of the transformer model prediction results are 304.38, 5.67 and 12.23, respectively, which are relative small compared to the mean power output value and the maximum value. The r2score is 0.9849 which is very close to 1. We then use the 12 WPAPs dataset for transformer's migration learning experiment. The predicted results show that the MSE, MAE and RMSE are also small and the r2score is also very close to

1. The transformer can have good migration performance within the same area.

Data availability statement

The original contributions presented in the study are included in the article/supplementary material; further inquiries can bedirected to the corresponding author.

Author contributions

SH proposed the concept of the study and reviewed the manuscript. YQ designed the project and revised the manuscript. CY completed the experiments and wrote the original draft.

Funding

Conflict of interest

The authors declare that the research was conducted in the absence of any commercial or financial relationships that could be construed as a potential conflict of interest.

Publisher's note

All claims expressed in this article are solely those of the authors and do not necessarily represent those of their affiliated organizations, or those of the publisher, the editors and the reviewers. Any product that may be evaluated in this article, or claim that may be made by its manufacturer, is not guaranteed or endorsed by the publisher.

References

Alipour, P., Mukherjee, S., and Nateghi, R. (2019). Assessing climate sensitivity of peak electricity load for resilient power systems planning and operation: A study applied to the Texas region. *Energy* 185, 1143–1153. doi:10.1016/j.energy.2019.07.074

Bommasani, R., Hudson, D. A., Adeli, E., Altman, R., Arora, S., von Arx, S., et al. (2021). *On the opportunities and risks of foundation models. arXiv* https://arxiv.org/abs/2108.07258.

Carion, N., Massa, F., Synnaeve, G., Usunier, N., Kirillov, A., and Zagoruyko, S. (2020)., 12346. Springer, 213–229. End-to-end object detection with transformers*Eur. Conf. Comput. Vis.*

Cassola, F., and Burlando, M. (2012). Wind speed and wind energy forecast through Kalman filtering of Numerical Weather Prediction model output. *Appl. energy* 99, 154–166. doi:10.1016/j.apenergy.2012.03.054

Chen, T., Lehr, J., Lavrova, O., and Martinez-Ramonz, M. (2016). "Distribution-level peak load prediction based on bayesian additive regression trees," in Proceedings of the 2016 IEEE Power and Energy Society General Meeting (PESGM): IEEE), Boston, MA, USA, 1–5.

Council, G. W. E. (2022). *GWEC global wind Report 2022*. Bonn, Germany: Global Wind Energy Council.

Deng, X., Shao, H., Hu, C., Jiang, D., and Jiang, Y. (2020). Wind power forecasting methods based on deep learning: A survey. *Comput. Model. Eng. Sci.* 122 (1), 273–301. doi:10.32604/cmes.2020.08768

Devlin, J., Chang, M.-W., Lee, K., and Toutanova, K. (2018). *Bert: Pre-training of deep bidirectional transformers for language understanding*. arXiv https://arxiv.org/abs/1810.04805.

Dosovitskiy, A., Beyer, L., Kolesnikov, A., Weissenborn, D., Zhai, X., Unterthiner, T., et al. (2020). *An image is worth 16x16 words: Transformers for image recognition at scale*. https://arxiv.org/abs/2010.11929.

Hanifi, S., Liu, X., Lin, Z., and Lotfian, S. (2020). A critical review of wind power forecasting methods—Past, present and future. *Energies* 13 (15), 3764. doi:10.3390/en13153764

He, K., Zhang, X., Ren, S., and Sun, J. (2002). "Deep residual learning for image recognition," in Proceedings of the IEEE conference on computer vision and pattern recognition, San Juan, PR, USA, 770–778.

Hodge, B.-M., Zeiler, A., Brooks, D., Blau, G., Pekny, J., and Reklatis, G. (2011)., 29. Elsevier, 1789–1793. Improved wind power forecasting with ARIMA models*Comput. Aided Chem. Eng.*

Hossain, M. A., Chakrabortty, R. K., Elsawah, S., and Ryan, M. J. (2020). "Hybrid deep learning model for ultra-short-term wind power forecasting," in Proceedings of the 2020 IEEE International Conference on Applied Superconductivity and Electromagnetic Devices (ASEMD): IEEE, Tianjin, China, 1–2.

Hu, Q., Zhang, R., and Zhou, Y. (2016). Transfer learning for short-term wind speed prediction with deep neural networks. *Renew. Energy* 85, 83–95. doi:10.1016/j.renene.2015.06.034

Huang, R., Huang, T., Gadh, R., and Li, N. (2012). "Solar generation prediction using the ARMA model in a laboratory-level micro-grid," in Proceedings of the 2012 IEEE third international conference on smart grid communications (SmartGridComm): IEEE, Tainan, Taiwan, 528–533.

Ko, M.-S., Lee, K., Kim, J.-K., Hong, C. W., Dong, Z. Y., and Hur, K. (2020). Deep concatenated residual network with bidirectional LSTM for one-hour-ahead wind power forecasting. *IEEE Trans. Sustain. Energy* 12 (2), 1321–1335. doi:10.1109/tste.2020.3043884

Lahouar, A., and Slama, J. B. H. (2017). Hour-ahead wind power forecast based on random forests. *Renew. energy* 109, 529–541. doi:10.1016/j.renene.2017.03.064

Lai, G., Chang, W.-C., Yang, Y., and Liu, H. (2018). "Modeling long-and short-term temporal patterns with deep neural networks," in Proceedings of the The 41st international ACM SIGIR conference on research & development in information retrieval), Ann Arbor MI USA, 95–104.

Lewis, M., Liu, Y., Goyal, N., Ghazvininejad, M., Mohamed, A., Levy, O., et al. (2019). *Bart: Denoising sequence-to-sequence pre-training for natural language generation, translation, and comprehension*. arXiv https://arxiv.org/abs/1910.13461.

L'Heureux, A., Grolinger, K., and Capretz, M. A. (2022). Transformer-based model for electrical load forecasting. *Energies* 15 (14), 4993. doi:10.3390/en15144993

Li, J., and Armandpour, M. (2022). "Deep spatio-temporal wind power forecasting," in Proceedings of the ICASSP 2022-2022 IEEE International Conference on Acoustics, Speech and Signal Processing (ICASSP): IEEE), Singapore, 4138–4142.

Li, L.-l., Cen, Z.-Y., Tseng, M.-L., Shen, Q., and Ali, M. H. (2021). Improving short-term wind power prediction using hybrid improved cuckoo search arithmetic-Support vector regression machine. *J. Clean. Prod.* 279, 123739. doi:10.1016/j.jclepro.2020.123739

Li, L.-L., Zhao, X., Tseng, M.-L., and Tan, R. R. (2020). Short-term wind power forecasting based on support vector machine with improved dragonfly algorithm. *J. Clean. Prod.* 242, 118447. doi:10.1016/j.jclepro.2019.118447

Li, L., Liu, Y.-q., Yang, Y.-p., Shuang, H., and Wang, Y.-m. (2013). A physical approach of the short-term wind power prediction based on CFD pre-calculated flow fields. *J. Hydrodyn.* 25 (1), 56–61. doi:10.1016/s1001-6058(13)60338-8

Lin, Y., Koprinska, I., and Rana, M. (2020)., 12534. Springer, 616–628.SpringNet: Transformer and Spring DTW for time series forecasting*Int. Conf. Neural Inf. Process.*

Lin, Z., and Liu, X. (2020). Assessment of wind turbine aero-hydro-servo-elastic modelling on the effects of mooring line tension via deep learning. *Energies* 13 (9), 2264. doi:10.3390/en13092264

Liu, B., Zhao, S., Yu, X., Zhang, L., and Wang, Q. (2020). A novel deep learning approach for wind power forecasting based on WD-LSTM model. *Energies* 13 (18), 4964. doi:10.3390/en13184964

Liu, Y., Ott, M., Goyal, N., Du, J., Joshi, M., Chen, D., et al. (2019). *Roberta: A robustly optimized bert pretraining approach*. arXiv https://arxiv.org/abs/1907.11692.

Liu, Y., Shi, J., Yang, Y., and Han, S. (2009). Piecewise support vector machine model for short-term wind-power prediction. *Int. J. Green Energy* 6 (5), 479–489. doi:10.1080/15435070903228050

Liu, Z., Lin, Y., Cao, Y., Hu, H., Wei, Y., Zhang, Z., et al. (2021). "Swin transformer: Hierarchical vision transformer using shifted windows," in Proceedings of the IEEE/CVF International Conference on Computer Vision), Montreal, BC, Canada, 10012–10022.

López Santos, M., García-Santiago, X., Echevarría Camarero, F., Blázquez Gil, G., and Carrasco Ortega, P. (2022). Application of temporal fusion transformer for day-ahead PV power forecasting. *Energies* 15 (14), 5232. doi:10.3390/en15145232

Lu, K., Sun, W. X., Wang, X., Meng, X. R., Zhai, Y., Li, H. H., et al. (2018)., 186. IOP Publishing, 012020.Short-term wind power prediction model based on encoder-decoder LSTM, *IOP Conf. Ser. Earth Environ. Sci.*

Niu, Z., Yu, Z., Tang, W., Wu, Q., and Reformat, M. (2020). Wind power forecasting using attention-based gated recurrent unit network. *Energy* 196, 117081. doi:10.1016/j.energy.2020.117081

Phan, Q.-T., Wu, Y.-K., and Phan, Q.-D. (2022). "An approach using transformer-based model for short-term PV generation forecasting," in Proceedings of the 2022 8th International Conference on Applied System Innovation (ICASI): IEEE, Nantou, Taiwan, 17–20.

Poggi, P., Muselli, M., Notton, G., Cristofari, C., and Louche, A. (2003). Forecasting and simulating wind speed in Corsica by using an autoregressive model. *Energy Convers. Manag.* 44 (20), 3177–3196. doi:10.1016/s0196-8904(03)00108-0

Radford, A., Wu, J., Child, R., Luan, D., Amodei, D., and Sutskever, I. (2019). Language models are unsupervised multitask learners. *OpenAI blog* 1 (8), 9.

Raffel, C., Shazeer, N., Roberts, A., Lee, K., Narang, S., Matena, M., et al. (2020). Exploring the limits of transfer learning with a unified text-to-text transformer. *J. Mach. Learn. Res.* 21 (140), 1–67.

Shahid, F., Zameer, A., and Muneeb, M. (2021). A novel genetic LSTM model for wind power forecast. *Energy* 223, 120069. doi:10.1016/j.energy.2021.120069

Sun, R., Zhang, T., He, Q., and Xu, H. (2021). Review on key technologies and applications in wind power forecasting. *High. Volt. Eng.* 47, 1129–1143.

Sun, Z., Zhao, S., and Zhang, J. (2019). Short-term wind power forecasting on multiple scales using VMD decomposition, K-means clustering and LSTM principal computing. *IEEE Access* 7, 166917–166929. doi:10.1109/access.2019.2942040

Touvron, H., Cord, M., Sablayrolles, A., Synnaeve, G., and Jégou, H. (2021). "Going deeper with image transformers," in Proceedings of the IEEE/CVF International Conference on Computer Vision), Montreal, BC, Canada, 32–42.

Vaswani, A., Shazeer, N., Parmar, N., Uszkoreit, J., Jones, L., Gomez, A. N., et al. (2017). Attention is all you need. *Adv. neural Inf. Process. Syst.* 30.

Wang, Y., Gao, J., Xu, Z., and Li, L. (2020). A short-term output power prediction model of wind power based on deep learning of grouped time series. *Eur. J. Electr. Eng.* 22 (1), 29–38. doi:10.18280/ejee.220104

Wu, H., Xiao, B., Codella, N., Liu, M., Dai, X., Yuan, L., et al. (2021). "Cvt: Introducing convolutions to vision transformers," in Proceedings of the IEEE/CVF International Conference on Computer Vision), Montreal, BC, Canada, 22–31.

Wu, Q., Guan, F., Lv, C., and Huang, Y. (2021). Ultra-short-term multi-step wind power forecasting based on CNN-LSTM. *IET Renew. Power Gen.* 15 (5), 1019–1029. doi:10.1049/rpg2.12085

Wu, Y.-K., and Hong, J.-S. (2007). A literature review of wind forecasting technology in the world. *IEEE Lausanne Power Tech.* 2007, 504–509.

Yesilbudak, M., Sagiroglu, S., and Colak, I. (2017). A novel implementation of kNN classifier based on multi-tupled meteorological input data for wind power prediction. *Energy Convers. Manag.* 135, 434–444. doi:10.1016/j.enconman.2016.12.094

Yu, R., Gao, J., Yu, M., Lu, W., Xu, T., Zhao, M., et al. (2019). LSTM-EFG for wind power forecasting based on sequential correlation features. *Future Gener. Comput. Syst.* 93, 33–42. doi:10.1016/j.future.2018.09.054

Zhou, J., Lu, X., Xiao, Y., Su, J., Lyu, J., Ma, Y., et al. (2022). *Sdwpf: A dataset for spatial dynamic wind power forecasting challenge at kdd cup 2022*. arXiv https://arxiv.org/abs/2208.04360.

Check for updates

Accommodation capacity evaluation of renewable energy in power systems considering peak and frequency regulation

Yi Yu[1], Hongsheng Zhao[1], Yang Zeng[2]*, Feng Chen[1], Dongjun Yang[1], Bo Wang[1], Qiushi Xu[1] and Binxian Li[2]

[1]Economics and Technology Research Institute, State Grid Hubei Electric Power Co, Ltd., Wuhan, China, [2]College of Electrical and Information Engineering, Hunan University, Changsha, China

With the fast growth of renewable energy, the modern power systems are transitioning to the renewable energy dominated energy systems. However, the intrinsic intermittence and volatility of renewable energy also impose considerable challenges on the power system operation. Hence, it is of great significance to accurately evaluate the renewable energy accommodation capacity (REAC) in power system so as to effectively instruct the sustainable development of renewable energy and to alleviate the ongoing operational burdens. This paper proposes a novel evaluation method of REAC in power system comprehensively considering peak and frequency regulation. First, the mechanism and cost of deep peak regulation of thermal power units are deeply analyzed, and then the frequency dynamics response is modeled explicitly and simplified effectively. Next, a synthetic interaction model of "source-network-storage" is developed with diversified generation units, network and energy storage constraints. Furthermore, a multi-objective optimization model is established considering both economic and technical issues, and a REAC evaluation method is developed by integrating an incremental capacity augment approach with the proposed multi-objective model. Finally, the proposed REAC evaluation method is tested on the modified IEEE 39-bus system, and the numerical results verify the effectiveness of the proposed method.

KEYWORDS

renewable energy accommodation capacity, deep peak regulation, frequency dynamics response, "source-network-storage" interaction, multi-objective optimization model

1 Introduction

Driven by the promotion of the clean and sustainable development of energy system, there has been a proliferation of various renewable energy units, e.g. wind turbines (WT) and photovoltaic (PV) panels, in the power systems over the past years, leading to the transition of the power system structure and operating features to be increasingly complex (Khalkho et al., 2022; Majeed et al., 2022). Due to the significant inconsistency between

the generation pattern of renewable energy and the consumption pattern of load demand, the increasing integration of renewable energy exacerbates the difficulty for the peak shaving and valley filling of load, posing a substantial challenge to the peak regulation of the net load (You et al., 2022). Moreover, the replacement of conventional synchronous generation by the electronic-interfaced renewable energy generation will inevitably result in the continuous decline of power system inertia (Alves et al., 2021), which in turn weakens the frequency response ability to the emergencies and poses a serious threat to the power system stability. It has been reported that the present scale of renewable energy installation in some places of China has exceeded the accommodation capacity of its local power system, resulting in the substantial curtailment of wind power and photovoltaic power (Guo et al., 2020). Therefore, it is necessary to develop an effective evaluation method for accurate estimation of renewable energy accommodation capacity in order to provide a clear guidance for the progressive development and utilization of renewable energy.

Some efforts have been devoted to the investigation of renewable energy accommodation capacity (REAC) evaluation. To name it, the authors in (Lin et al., 2020) proposes a REAC evaluation method by simply considering the transmission line capacities in a power system simulation tool. In (He et al., 2018), peak load regulation and power equipment capacity limits have been identified as the key influencing factors of the REAC and based on this finding, an evaluation method is developed. In (Wang et al., 2016), an evaluation algorithm is proposed for the REAC based on sequential Monte Carlo simulation. Ref. (Zhang et al., 2019) uses the maximum flow model of network to study the REAC of power grid. Ref. (Chen et al., 2014) develops an assessment method for the renewable energy carrying capacity based on a stochastic long-term security constrained unit commitment model. However, the aforementioned research works oversimplify the various operating constraints of different devices, and also fail to account for the impact of deep peak regulation and frequency response on the evaluation outcome.

The interaction among power sources, network operator, load demand and energy storage exerts considerable influence on the REAC. Previously, most researchers merely focus on one simple aspect of the source-network-storage interaction. For instance, ref. (Xie et al., 2016) studies wind power accommodation capability from the perspective of network security. Ref. (Li et al., 2021) focuses on the correlation between wind power volatility and consumption capacity to evaluate the wind power consumption capacity. Ref. (Wang et al., 2018) investigates the power output model of WT and PV based on Copula theory to construct the REAC evaluation method. In (Xu et al., 2014), a probabilistic method is developed to determine the wind power accommodation capacity considering wind power and load scenarios. These works mainly focus on analyzing the influencing factors of renewable energy, and fail to account for the interaction among source, network, load and

storage as a whole. Therefore, to overcome this drawback, the interaction of "source-network-storage" is accurately modeled in detail and is seamlessly integrated in the REAC evaluation method.

In a word, most existing studies fail to account for the impact of peak regulation and frequency response requirements on the REAC, and also do not fully consider the interaction among "source-network-storage." To fill this research gap, this paper proposes an evaluation method of REAC considering peak regulation and frequency response requirements. First, the mechanism and cost of deep peak regulation of thermal power units is analyzed and then the frequency response dynamics is modeled explicitly and further simplified effectively. Subsequently, a comprehensive interaction model of "source-network-storage" is established with various generation, network and energy storage constraints. Finally, a novel REAC evaluation method is developed based on a proposed multi-objective optimization model considering both economic and technical issues. The contributions of this paper are three-fold as follows.

1) The peak regulation and frequency response requirements of power system are comprehensively incorporated in the proposed REAC evaluation method and explicitly modeled. Furthermore, to reduce computational complexity, the original complex peak regulation mechanism and frequency response dynamic are converted equivalently into several mathematically tractable mixed integer linear equations.

2) A multi-objective optimization model is established considering both the economic and technical issues in accommodating renewable energy, where the interaction among "source-network-storage" is fully considered to account for the realistic situation.

3) A novel REAC evaluation method is developed by integrating the above multi-objective optimization model with an incremental capacity augment approach. Consequently, the actual REAC which yields the lowest overall cost can be obtained efficiently and accurately.

The rest of this paper is arranged as follows. **Section 2** analyzes the peak regulation mechanism and frequency response requirement of the power system. **Section 3** constructs and analyzes a power system model considering "source-network-storage" interaction. **Section 4** presents a multi-objective optimization model of power system and a method to evaluate the accommodation capacity of renewable energy. In **Section 5**, the simulation is carried out and the numerical results are discussed. **Section 6** concludes the paper.

2 Peak and frequency regulation requirements

As is widely recognized, the high penetration of renewable energy in power system will aggravate the variation of net-load and thus increasing burden on peak load regulation.
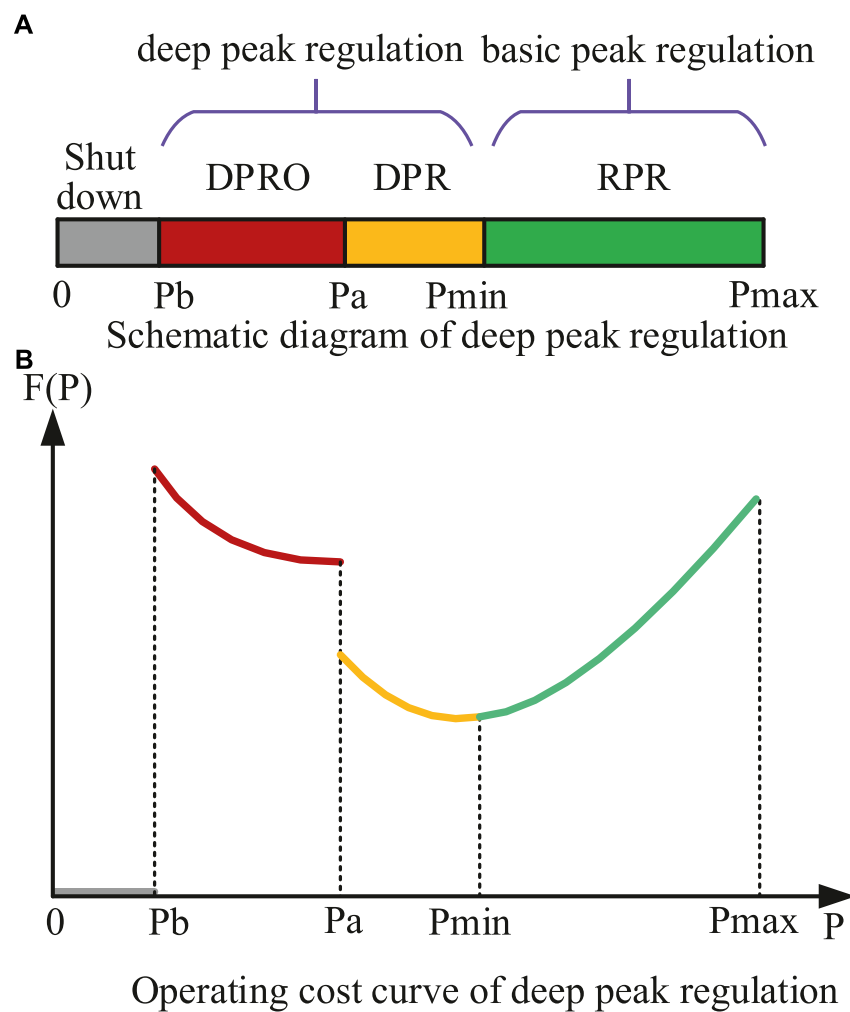
FIGURE 1
Deep peak regulation of thermal power unit. **(A)** Three states of peak regulation. **(B)** Overall operation cost curve in the deep peak regulation stage.

Furthermore, the replacement of conventional thermal generation by the electronic-interfaced renewable energy generation causes the significant decline of power system inertia, which places considerable stress on the frequency regulation. Therefore, it is necessary to deeply analyze the peak and frequency regulation requirements when evaluating the REAC.

2.1 Deep peak regulation mechanism

As conventional power generation units, e.g., thermal power units (TPU) and hydro units, are relatively more flexible in terms of regulation capacity compared with the renewable energy generation, they are the fundamental sources of peak regulation (Gao et al., 2020; Guan et al., 2022). The power output of the hydro units can be dropped to zero rapidly, while the thermal

power units are subject to the lower limits of the power output in order to maintain the on-state operation. When the thermal power units are invoked for the deep peak regulation, their minimum level of power outputs can be further lowered to achieve higher regulation capacity. However, the deep peak regulation by the thermal power units will cause additional cost and highly complex. In the following, we will thoroughly analyze the deep peak regulation mechanism and its cost composition.

2.1.1 Deep peak regulation mechanism of thermal power unit

The peak regulation process of TPU consists of three states, namely the regular peak regulation (RPR), the deep peak regulation without oil (DPR), and the deep peak regulation with oil (DPRO), as shown in **Figure 1A**, where P_{max} is the upper limit of the unit power output; P_{min} is the minimum technical power

output of the RPR state; P_a is the minimum stable power output of the DPR state; P_b is the minimum power output of the DPRO state. The operation costs of the thermal power unit during the deep peak regulation is composed of the coal consumption cost, tear-and-wear cost, oil input cost, and environmental pollution cost. The curve overall operation cost of thermal power unit considering deep peak regulation is shown in **Figure 1B**.

2.1.2 Deep peak regulation cost of thermal power unit

As can be seen from **Figure 1**, the operation cost of thermal power units is highly related to the deep peak regulation states. If the TPU is in the RPR state, its operation cost only consists of coal consumption cost. When the TPU is in the DPR and DPRO states, its power output deviates from the normal range leading to the accelerated aging of mechanical parts and shortening of its life cycle. Thus, in addition to the coal consumption cost, the TPU operation cost in the DPR and DPRO states also includes the tear-and-wear cost. When a TPU is operated in DRRO state, additional oil input is required to maintain the steady operation of the units, which will further cause environmental pollution. Hence, the costs of oil fuel and environment pollution should be taken into account. Therefore, the TPU operation cost in deep peak regulation state consists of coal consumption cost $C_{i,t}^{coal}$, tear-and-wear cost $C_{i,t}^{abr}$, fuel cost $C_{i,t}^{oil}$ and additional environment pollution cost $C_{i,t}^{ev}$, as illustrated by the following equations.

$$C_{i,t}^{coal} = a_i\left(P_{i,t}^g\right)^2 + b_i P_{i,t}^g + c_i \qquad \forall i \in N_g, \forall t \in T \qquad (1a)$$

$$C_{i,t}^{abr} \approx \frac{\beta S_i^g}{\left[2 N_f\left(P_{i,t}^g\right)\right]} \qquad \forall i \in N_g, \forall t \in T \qquad (1b)$$

$$N_f\left(P_{i,t}^g\right) = 0.005778\left(P_{i,t}^g\right)^3 - 2.682\left(P_{i,t}^g\right)^2$$
$$+ 484.8 P_{i,t}^g - 8411 \qquad \forall i \in N_g, \forall t \in T \qquad (1c)$$

$$C_{i,t}^{oil} = \gamma_{oil} Q_i^{oil} \qquad \forall i \in N_g, \forall t \in T \qquad (1d)$$

$$C_{i,t}^{ev} = \Delta\mu_{env,i} \omega_{env} \qquad \forall i \in N_g, \forall t \in T \qquad (1e)$$

Eq. 1a is the quadratic coal consumption cost of TPU i at the time t, where $P_{i,t}^g$ is the power output; a_i, b_i, and c_i are the cost coefficients. **Eq. 1b** approximates the tear-and-wear cost of TPU based on the commonly used Manson-Coffin formula, where β is a cost conversion coefficient; S_i^g is the overall investment cost of TPU i, and $N_f(P_{i,t}^g)$ is the number of rotor cracking cycles. **Eq. 1c** is the calculation formula of rotor cracking cycles number, which is a cubic equation of power output. **Eq. 1d** shows that the oil consumption cost, where Q_i^{oil} is the amount of oil fuel consumption and γ_{oil} is the price of oil fuel. **Eq. 1e** shows additional environment pollution surcharge during

DRPO, where $\Delta\mu_{env,i}$ and ω_{env} are the amount of additional emission caused by DPRO and the unit penalty for environment pollution, respectively.

Based on the discussed above, the overall operation cost of TPU in deep peak regulation can be expressed as **Eq. 2**.

$$F_{i,t}^g = \begin{cases} C_{i,t}^{coal} & \text{if } \underline{P}_i^g < P_{i,t}^g < \overline{P}_i^g \\ C_{i,t}^{coal} + C_{i,t}^{abr} & \text{if } P_i^{ga} < P_{i,t}^g < \underline{P}_i^g \\ C_{i,t}^{coal} + C_{i,t}^{abr} + C_{i,t}^{oil} + C_{i,t}^{env} & \text{if } P_i^{gb} < P_{i,t}^g < P_i^{ga} \end{cases} \qquad \forall i \in N_g, \forall t \in T$$

$$(2)$$

where $F_{i,t}^g$ is the overall operation cost of TPU i at the time t; $\overline{P}_i^g$ and $\underline{P}_i^g$ are the upper and lower power limit of TPU i in the RPR state; P_i^{ga} is the lower power limit of TPU i in the DPR state; P_i^{gb} is the lower power limit of TPU i in the DPRO stage.

2.1.3 The linearization of deep peak regulation cost

It can be seen from (1) and (2) the coal consumption cost $C_{i,t}^{coal}$, tear-and-wear cost $C_{i,t}^{abr}$, and the overall operation cost $F_{i,t}^g$ are nonlinear, which results in the significant computational complexity. Hence, those terms need to be linearized for computational simplicity.

Both $C_{i,t}^{coal}$ and $C_{i,t}^{abr}$ are nonlinear functions of the single variable (the active power output $P_{i,t}^g$), which can be linearized using piecewise linearization (PWL) technology (Carrión and Arroyo, 2006). For brevity, $C_{i,t}^{coal}$ and $C_{i,t}^{abr}$ are first generalized as a nonlinear function of a single variable $F(a)$ and then $F(a)$ is further linearized as follows,

$$F(a) \approx F(a_1) + \sum_{k=1}^K \left[F(a_{k+1}) - F(a_k)\right]\delta_k \qquad (3a)$$

$$a = a_1 + \sum_{k=1}^K \left(a_{k+1} - a_k\right)\delta_k \qquad (3b)$$

$$\delta_{k+1} \le \sigma_k \le \delta_k \qquad k \in \{1, \ldots, K-1\} \qquad (3c)$$

$$0 \le \delta_k \le 1 \qquad k \in \{1, \ldots, K\} \qquad (3d)$$

where a is the input single variable of the function $F(a)$ and its range is divided into K segments; a_k and a_{k+1} are the two endpoints of the kth segment; δ_k is a continuous variable that represents the portion of the kth segment; σ_{k-1} is an auxiliary binary variable that indicates whether a lies on the right-side of the kth segment.

The overall operation cost $F_{i,t}^g$ is not only related to the active power output $P_{i,t}^g$, but also related to the deep peak regulation state. Hence, the cost $F_{i,t}^g$ can be reformulated as **Eqs 4a, 4b** by introducing several binary variables $U_{i,t}^{g1}$, $U_{i,t}^{g2}$, $U_{i,t}^{g3}$ and $X_{i,t}^g$.

$$F_{i,t}^g = X_{i,t}^g C_{i,t}^{coal} + \left(U_{i,t}^{g2} + U_{i,t}^{g3}\right) C_{i,t}^{abr}$$
$$+ U_{i,t}^{g3} C_{i,t}^{oil} + U_{i,t}^{g3} C_{i,t}^{env} \qquad \forall i \in N_g, \forall t \in T \qquad (4a)$$
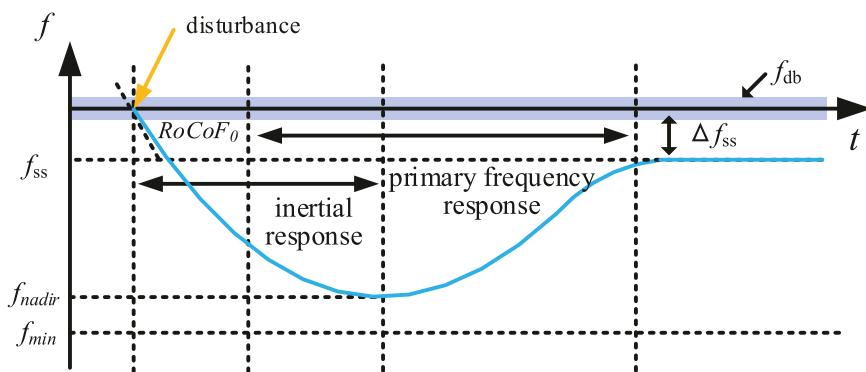
FIGURE 2
Schematic diagram of primary frequency dynamic response in power system.

$$U_{i,t}^{g1} + U_{i,t}^{g2} + U_{i,t}^{g3} = X_{i,t}^{g} \qquad \forall i \in N_g, \forall t \in T \qquad (4b)$$

where $U_{i,t}^{g1}$, $U_{i,t}^{g2}$ and $U_{i,t}^{g3}$ indicate the different peak regulation states; $X_{i,t}^{g}$ denotes the on or off state. If the TPU i has been turned on at time t, $X_{i,t}^{g}$ is equal to 1; otherwise it is equal to 0. If the unit i is in the RPR state, $U_{i,t}^{g1} = 1$, otherwise it is equal to 0; if the unit i is in the DPR state, $U_{i,t}^{g2} = 1$, otherwise it is equal to 0; if the unit i is in the DPRO state, $U_{i,t}^{g3} = 1$, otherwise it is equal to 0. If the TPU i has been turned off at time t, $U_{i,t}^{g1}$, $U_{i,t}^{g2}$ and $U_{i,t}^{g3}$ are enforced to be 0 due to **Eq. 4b**.

The first two terms of **Eq. 4a** are nonlinear, which can be linearized using big M method. **Eq. 4a** can be reformulated as mixed integer linear equation as follows,

$$F_{i,t}^{g} = C_{i,t}^{Xcoal} + C_{i,t}^{Xabr} + U_{i,t}^{g3}C_{i,t}^{oil} + U_{i,t}^{g3}C_{i,t}^{env} \qquad \forall i \in N_g, \forall t \in T$$
$$(5a)$$

$$\begin{cases} X_{i,t}^{g}C_{i,min}^{coal} \le C_{i,t}^{Xcoal} \le X_{i,t}^{g}C_{i,max}^{coal} \\ C_{i,t}^{coal} - \left(1 - X_{i,t}^{g}\right)M \le C_{i,t}^{Xcoal} \le C_{i,t}^{coal} + \left(1 - X_{i,t}^{g}\right)M \end{cases} \qquad \forall i \in N_g, \forall t \in T$$
$$(5b)$$

$$\begin{cases} \left(U_{i,t}^{g2} + U_{i,t}^{g3}\right)C_{i,min}^{abr} \le C_{i,t}^{Xabr} \le \left(U_{i,t}^{g2} + U_{i,t}^{g3}\right)C_{i,max}^{abr} \\ C_{i,t}^{abr} - \left(1 - \left(U_{i,t}^{g2} + U_{i,t}^{g3}\right)\right)M \le C_{i,t}^{Xabr} \le C_{i,t}^{abr} + \left(1 - \left(U_{i,t}^{g2} + U_{i,t}^{g3}\right)\right)M \end{cases} \qquad \forall i \in N_g, \forall t \in T$$
$$(5c)$$

where $C_{i,t}^{Xcoal}$, $C_{i,t}^{Xabr}$ are new variables representing $X_{i,t}^{g}C_{i,t}^{coal}$ and $(U_{i,t}^{g1} + U_{i,t}^{g2})C_{i,t}^{abr}$, respectively; M is a large number.

2.2 Frequency response requirements

The frequency response dynamic reflects the instantaneous power balance. When a large power disturbance occurs, the frequency may fall too fast or deviate too far from the nominal value if the frequency response requirement is not appropriated considered, which will further trigger the action of under frequency load shedding (UFLS) relay resulting in serious power

accidents. In order to make the system have sufficient inertia support and maintain the frequency dynamic stability, the frequency dynamic response should be taken into account during REAC evaluation (Kushwaha et al., 2018).

2.2.1 Primary frequency response constraints

The frequency response process includes inertial response, primary frequency response (PFR), secondary and tertiary responses (Teng and Strbac, 2016). Since three key performance indices of frequency response, including rate of change of frequency $RoCoF$, frequency level at nadir f_{nadir}, and frequency deviation level at quasi-steady state Δf_{ss}, are only related to the inertial response and PFR as shown in **Figure 2**, secondary and tertiary responses are not considered in this paper. Specifically, $RoCoF$ reflects the rate of change in the frequency, f_{nadir} reflects the largest frequency deviation during frequency response dynamic, and Δf_{ss} reflects the regulation effect of PFR at the stead state.

The frequency response dynamic is affected by multiple factors, including system inertia, load variation, generator governor response, which results in a highly complex process. In order to reduce the computational complexity, the load damping rate is ignored. The frequency dynamics of the simplified system can be expressed by **Eq. 6**.

$$2\frac{H_t^{sys}}{f_0}\frac{d\Delta f}{dt} = \frac{\Delta P_m - \Delta P_e}{S_b} \qquad (6)$$

where Δf is the frequency deviation; f_0 is the rated frequency, S_b is the system capacity base; H_t^{sys} is the system inertia constant at the time t; ΔP_m and ΔP_e are the mechanical power output and electrical power output of the system, respectively. In this paper, thermal power unit, hydro-power unit and pumped storage unit with inherent inertia are considered to participate in the primary frequency response.

2.2.1.1 RoCoF limits

When an disturbance occurs, the power imbalance - ΔP_L will arise which is equal to the difference between the change of system mechanical power output and electrical power output ΔP_m - ΔP_e. The RoCoF reaches the maximum at the occurrence of the interference according to (6), which is related to the system inertia and power imbalance (Wen et al., 2016). In order to prevent the triggering of UFLS relay caused by the too fast change of frequency, $RoCoF$ should be maintained below a certain level $RoCoF_{\max}$, as illustrated by the following equations.

$$RoCoF_0 = \frac{d\Delta f}{dt} = -\frac{\Delta P_L f_0}{2H_t^{sys} S_b} \tag{7a}$$

$$|RoCoF| \leq RoCoF_{max} \tag{7b}$$

Since H_t^{sys} is the total inertia of all remaining online units in the system, the operation status of the units needs to be optimized to ensure that the system has sufficient units to provide inertia support after disturbance. Therefore, constraints (7) can be converted into the following linear constraint with respect to the unit status.

$$H_t^{sys} = \frac{\sum_{i=1}^{N_k} H_i^{gen} P_i^{genmax} X_i^{genN}}{S_b} \geq \frac{\Delta P_L f_0}{2S_b RoCoF_{max}} \tag{8}$$

where H_i^{gen} and P_i^{genmax} denote the inertia constant and the maximum power output of the generator unit i, respectively; X_i^{genN} is the operation status of the generator unit i; N_k is the set of generator units that have rotational inertia.

2.2.1.2 Frequency nadir limits

The frequency level at nadir f_{nadir} is related to factors such as system inertia, governor response, and governor dead zone. In order to ensure the frequency does not fall below the minimum frequency requirement $f_{\min}$ or exceed the maximum frequency requirement $f_{\max}$ specified by the UFLS relay, the generator units involved in PFR should reserve sufficient frequency regulation capacity (Chávez et al., 2014). Meanwhile, the reserves of each unit participating in PFR should be delivered at or before the frequency level at nadir f_{nadir}. Therefore, the reserve of each unit should not exceed an upper limit, so that the governor of each unit can respond rapidly and counteract the frequency deviation before the frequency exceeds the limit of the UFLS relay (Zhang et al., 2018). The constraints of the downward and upward reserves ($RU_{i,t}$ and $RU_{i,t}$) of each unit after reformulation are demonstrated as follows,

$$RU_{i,t} \leq 2c_i^R \frac{2H_t^{sys} S_b \left(f_0 - f_{min} - f_{db}\right)}{f_0 \Delta P_L} \tag{9a}$$

$$RD_{i,t} \leq 2c_i^R \frac{2H_t^{sys} S_b \left(-f_0 + f_{max} - f_{db}\right)}{f_0 \Delta P_L} \tag{9b}$$

where f_{db} is the frequency response dead-band of the governor, and c_i^R is the maximum ramping rate of the unit i's governor.

2.2.1.3 Frequency level limits at quasi steady state

After the generation units deliver the reserves, the system frequency will gradually recover, and then enter the quasi-steady state, so that the primary frequency response stage ends. The quasi-stable state frequency Δf_{ss} of the power system is related to the system droop coefficient K_s and interference power ΔP_L.

$$\left|\Delta f_{ss} = -\frac{\Delta P_L}{K_s}\right| \leq \Delta f_{ss}^{max} \tag{10a}$$

$$K_s = K_G + K_D = \frac{\sum_{i=1}^{N_k} K_{G,i}^{\star} P_i^{genN} X_{i,t}^{genN}}{f_0} + \frac{K_D^{\star} P_t^D}{f_0} \tag{10b}$$

where Δf_{ss}^{max} is the maximum allowable frequency deviation of quasi-steady state; K_G and $K_G^{\star}$ are the actual value and per-unit value of the droop coefficient of unit i, respectively; K_D and $K_D^{\star}$ are the actual value and per-unit value of the load damping constant, respectively; P_i^{genN} and $X_{i,t}^{genN}$ are the rated active power and on/off state of unit i, respectively; P_t^D is the total load at time t.

3 Interaction modeling of "source-network-storage"

As previously discussed, in order to improve the REAC, it is necessary to take into account the interaction among various power sources, network and energy storage. To this end, detailed models of multiple types of power generation including TPU, hydro-power plant (HPP), wind farm and PV farm, energy storage systems including battery energy storage station (BES) and pumped storage power station (PSP) as well as transmission network are established in the following. **Figure 3** demonstrates a graphical representation of modern power system with various power sources and energy storage systems, where the interaction of "source-network-storage" is achieved through power system scheduling.

3.1 Modeling of various power sources

3.1.1 Thermal power unit

With the increasing penetration of renewable energy, the role of TPU is changing from conventional energy supplier to the flexibility provider in order to accommodate renewable energy in power systems. The operational constraints of TPU are formulated as follows,

$$U_{i,t}^{g1} \underline{P}_i^g + U_{i,t}^{g2} P_i^{ga} + U_{i,t}^{g3} P_i^{gb} \leq P_{i,t}^g \leq X_{i,t}^g \overline{P}_i^g \qquad \forall i \in N_g, \forall t \in T \tag{11a}$$

$$X_{i,t}^g - X_{i,t-1}^g \leq X_{i,\tau}^g \qquad \forall i \in N_g, \tau \in [t+1, min\{t + MinUp_i - 1, T\}], t \in [2, T] \tag{11b}$$

FIGURE 3
A modern power system with various power sources and energy storage systems.
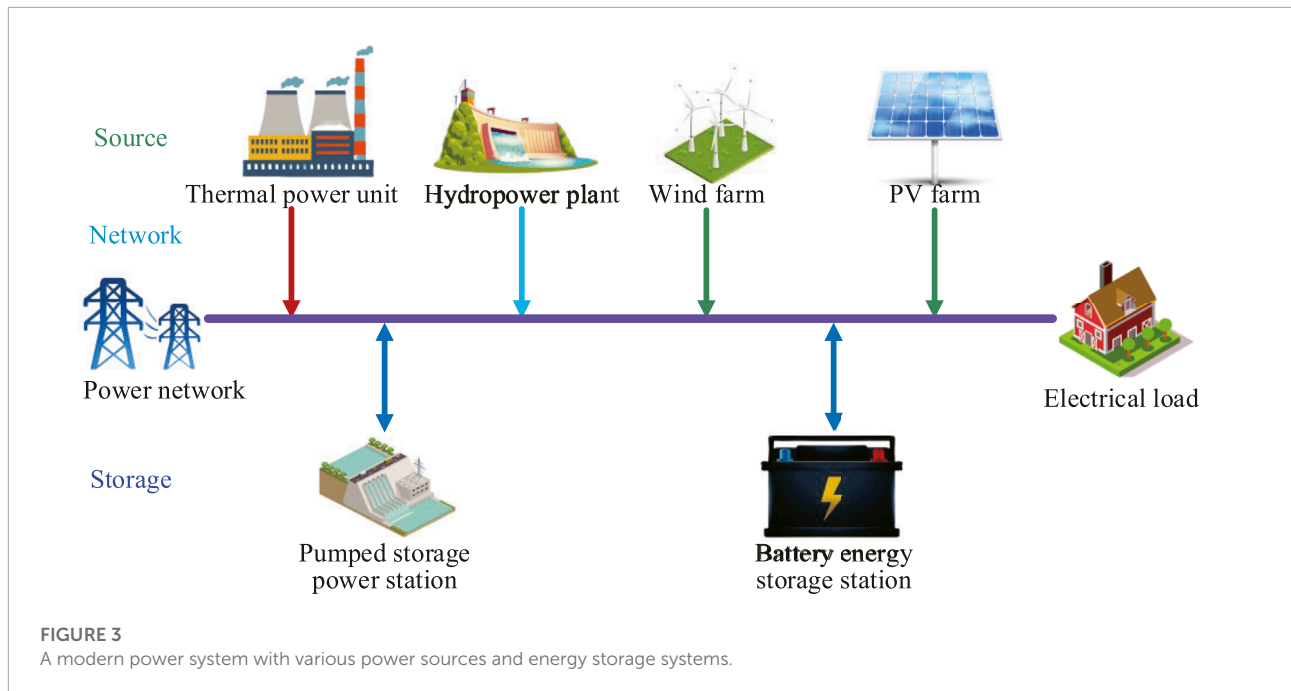
$$X_{i,t-1}^g - X_{i,t}^g \leq 1 - X_{i,\tau}^g \quad \forall i \in N_g, \tau \in [t+1, min\{t + MinDw_i - 1, T\}], t \in [2,T]$$
(11c)

$$P_{i,t}^g - P_{i,t-1}^g <= Y_{i,t}^g P_i^{gsu} + X_{i,t-1}^g R_i^{up} \qquad \forall i \in N_g, \forall t \in T \quad (11d)$$

$$P_{i,t-1}^g - P_{i,t}^g <= Z_{i,t}^g P_i^{gsd} + X_{i,t}^g R_i^{dw} \qquad \forall i \in N_g, \forall t \in T \quad (11e)$$

$$X_{i,t}^g - X_{i,t-1}^g = Y_{i,t}^g - Z_{i,t}^g \qquad \forall i \in N_g, \forall t \in T \qquad (11f)$$

$$Y_{i,t}^g + Z_{i,t}^g \leq 1 \qquad \forall i \in N_g, \forall t \in T \qquad (11g)$$

$$RU_{i,t}^g \leq min\left\{X_{i,t}^g \overline{P}_i^g - P_{i,t}^g, R_i^{up}\right\} \qquad \forall i \in N_g, \forall t \in T \qquad (11h)$$

$$RD_{i,t}^g \leq min\left\{P_{i,t}^g - \left(U_{i,t}^{g1}\underline{P}_i^g + U_{i,t}^{g2}P_i^{ga} + U_{i,t}^{g3}P_i^{gb}\right), R_i^{dw}\right\} \qquad \forall i \in N_g, \forall t \in T$$
(11i)

Constraint (11a) imposes the power output limits on TPU considering the deep peak regulation. Constraints (11b) and (11c) enforce the minimum on time limits and minimum off time limits, where $MinUp_i$ and $MinDw_i$ are the minimum on time limit and minimum off time limit, respectively; T denotes the operation horizon, which is divided into T time intervals with the duration of each time interval being 1 h. Constraints (11d) and (11e) describe the ramp rate limit of TPU, where R_i^{up}, R_i^{dw} are the ramp-up and ramp-down rate limits, respectively; P_i^{gsu}, P_i^{gsd} are the minimum startup and shutdown power limit, respectively; $Y_{i,t}^g$ and $Z_{i,t}^g$ are the startup and shutdown indicator variables at time t, respectively. The

logical relationship between startup/shutdown indicators and on/off state variables is represented by constraints (11f) and (11g). When the TPU i starts up at time t, $Y_{i,t}^g = 1$, otherwise it is 0; when the TPU i shuts down at time t, $Z_{i,t}^g = 1$, otherwise it is 0. Constraints (11h) and (11i) show the limits of the upward and downward reserves, where $RU_{i,t}^g$ and $RD_{i,t}^g$ are the upward and downward reserves at time t, respectively.

3.1.2 Hydro-power plant

As one of major power sources, HPP can be flexibly dispatched to meet the peak and frequency regulation requirements. The HPP mainly includes the following operational constraints.

$$\underline{V}_h \leq V_{h,t} \leq \overline{V}_h \qquad \forall h \in N_h, \forall t \in T$$
(12a)

$$V_{h,0} = v_{h,0}, V_{h,T} = v_{h,T} \qquad \forall h \in N_h, \forall t \in T$$
(12b)

$$V_{h,t} = V_{h,t-1} + Qn_{h,t} - Q_{h,t} - SQ_{h,t} \qquad \forall h \in N_h, \forall t \in T$$
(12c)

$$u_{h,t}^{hy}\underline{Qb}_h \leq Q_{h,t} + SQ_{h,t} \leq u_{h,t}^{hy}\overline{Qb}_h \qquad \forall h \in N_h, \forall t \in T$$
(12d)

$$u_{h,t}^{hy}\underline{P}_h \leq P_{h,t} \leq u_{h,t}^{hy}\overline{P}_h \qquad \forall h \in N_h, \forall t \in T$$
(12e)

$$P_{h,t}^h = g\eta_h Q_{h,t} H_{h,t} \qquad\qquad \forall h \in N_h, \forall t \in T \tag{12f}$$

$$H_{h,t} = Hd_{h,0} + \alpha_h V_{h,t} \qquad\qquad \forall h \in N_h, \forall t \in T \tag{12g}$$

$$RU_{h,t}^{hy} \le u_{h,t}^{hy} \overline{P}_h - P_{h,t} \qquad\qquad \forall h \in N_h, \forall t \in T \tag{12h}$$

$$RD_{h,t}^{hy} \le P_{h,t} - u_{h,t}^{hy}\underline{P}_h \qquad\qquad \forall h \in N_h, \forall t \in T \tag{12i}$$

$$u_{h,t}^{hy} - u_{h,t-1}^{hy} = Y_{h,t}^{hy} - Z_{h,t}^{hy} \qquad\qquad \forall h \in N_h, \forall t \in T \tag{12j}$$

$$Y_{h,t}^{hy} + Z_{h,t}^{hy} \le 1 \qquad\qquad \forall h \in N_h, \forall t \in T \tag{12k}$$

Constraints (12a) and (12b) impose the limits of reservoir capacity, where $V_{h,t}$ is the reservoir storage capacity at time t; $\overline{V}_h$ and $\underline{V}_h$ are the upper and lower limits of reservoir capacity, respectively; $v_{h,0}$ and $v_{h,T}$ represent the initial and final reservoir capacity of the entire operation horizon, respectively. Constraint (12c) describes the conservation law of water mass, where $Qn_{h,t}$ and $SQ_{h,t}$ are the natural flow into the reservoir and the spillage of HPP h, respectively; $Q_{h,t}$ is the water flow for generation. Constraint (12d) enforces the limits on the water discharge, where $\overline{Qb}_h$ and $\underline{Qb}_h$ are the upper and lower limits of discharge water flow, respectively; $u_{h,t}$ is the on/off state variable of HPP. Constraint (12e) shows the power output limits of HPP, where $P_{h,t}$ is power output; $\overline{P}_h$ and $\underline{P}_h$ are the upper and lower limits of power output, respectively; Constraint (12f) is the hydraulic conversion function of HPP, which describes the relationship between power generation, water head and water flow, where $H_{h,t}$ is the water head of HPP h at time t; g is the gravity coefficient, η_h is the energy conversion efficiency. Constraint (12g) shows the short-term relationship between water head and reservoir capacity, where $Hd_{h,0}$ and α_h are the correlation coefficients between water head and reservoir capacity. Constraints (12h) and (12i) illustrates the upward and downward reserves capacity of HPP, where $RU_{h,t}^{hy}$ and $RD_{h,t}^{hy}$ are the upward and downward reserves at time t, respectively. The logical relationship between startup/shutdown indicator variables and on/off state variable of HPP is represented by constraints (12j) and (12k), where $Y_{h,t}^{hy}$ and $Z_{h,t}^{hy}$ are the startup and shutdown indicators of the HPP h at time t, respectively.

Since constraint (Eq. 12f) is nonlinear, in order to reduce computational complexity, the linearization method in (Babayev, 1997; Wu et al., 2008) is adopted. For HPP, constraint (Eq. 12g) is incorporated into constraint (Eq. 12f) to obtain the

hydraulic conversion formula as $P_{h,t}^h = g\eta_h Q_{h,t}(Hd_{h,0} + \alpha_h V_{h,t})$. By dividing $Q_{h,t}$ and $V_{h,t}$ into subintervals $[Q_i, Q_{i+1}]$ and $[V_j, V_{j+1}]$, the hydraulic conversion equation is split into a grid of $(m-1)$ () $(n-1)$ in which each point corresponding to the original function is $P_{i,j} = g\eta_h Q_i (Hd_{h,0} + \alpha_h V_j)$, where $i = 1,\dots,m-1$, $j = 1,\dots,n-1$. Consequently, the constraint (Eq. 12f) is transformed into linear Equation 13 by introducing several auxiliary variables.

$$Q_{h,t} = \sum_{i=1}^m \sum_{j=1}^n Q_i \cdot \phi_{i,j}, \quad V_{h,t} = \sum_{i=1}^m \sum_{j=1}^n V_j \cdot \phi_{i,j} \tag{13a}$$

$$\sum_{i=1}^m \sum_{j=1}^n \left(\zeta_{i,j} + \xi_{i,j}\right) = 1 \qquad \zeta_{i,j}, \xi_{i,j} \in \{0,1\} \tag{13b}$$

$$\sum_{i=1}^m \sum_{j=1}^n \phi_{i,j} = 1 \qquad\qquad \phi_{i,j} \ge 0 \tag{13c}$$

$$\phi_{i,j} \le \zeta_{i,j-1} + \zeta_{i,j} + \zeta_{i,j+1} + \xi_{i-1,j} + \xi_{i,j} + \xi_{i+1,j} \tag{13d}$$

$$P_{h,t}^h = \sum_{i=1}^m \sum_{j=1}^n P_{i,j} \cdot \phi_{i,j} \tag{13e}$$

3.1.3 Renewable energy generation

The renewable energy is less flexible in power output adjustment. When it is required by the system operator, the renewable energy like PV and WT can be curtailed to maintain the power balance. The operational constraints of WT and PV mainly include:

$$0 \le \Delta P_{m,t}^{wt} \le P_m^{wt} \qquad\qquad \forall m \in N_{wt}, \forall t \in T \tag{14a}$$

$$0 \le \Delta P_{n,t}^{pv} \le P_n^{pv} \qquad\qquad \forall n \in N_{pv}, \forall t \in T \tag{14b}$$

constraints (14a) and (14b) illustrate the curtailment of wind power and PV power should not exceed their predicted output, where $\Delta P_{m,t}^{wt}$ and $\Delta P_{n,t}^{pv}$ are the curtailments of wind power and PV power, respectively; $P_{m,t}^{wt}$, $P_{n,t}^{pv}$ are the predicted WT output and PV output at time t, respectively.

3.2 Modeling of energy storage systems

The rapid development energy storage technology especially the battery energy storage provides a promising solution for the renewable energy accommodation problem. In this subsection, the operational models of both battery energy storage systems and pumped storage power station are established.

3.2.1 Battery energy storage

The flexible and rapid adjustment capability of BES can be deployed to provide peak regulation and frequency regulation support (Tan and Zhang, 2017; Carrión et al., 2018). The operational model of BES mainly includes the following constraints.

$$0 \le P_{s,t}^{ch} \le W_{s,t}^{BES} \overline{P}_s^{ch} \qquad \forall s \in N_{BES}, \forall t \in T \qquad (15a)$$

$$0 \le P_{s,t}^{dis} \le \left(1 - W_{s,t}^{BES}\right) \overline{P}_s^{dis} \qquad \forall s \in N_{BES}, \forall t \in T \qquad (15b)$$

$$SOC_{s,t} = SOC_{s,t-1} + \left(\eta^{ch} P_{s,t}^{ch} - \frac{P_{s,t}^{dis}}{\eta^{dis}}\right)/C_s^{BES} \Delta T \qquad \forall s \in N_{BES}, \forall t \in T \qquad (15c)$$

$$\underline{SOC}_s \le SOC_{s,t} \le \overline{SOC}_s \qquad \forall s \in N_{BES}, \forall t \in T \qquad (15d)$$

Constraints (15d) and (15b) describe the charge and discharge power limits of BES, where $P_{s,t}^{ch}$ and $P_{s,t}^{dis}$ are charging, discharging power at time t, respectively; $\overline{P}_s^{ch}$ and $\overline{P}_s^{dis}$ are the upper limits of charging and discharging power, respectively; $W_{s,t}^{BES}$ is the logical variable that indicates the charging and discharging state of BES s at the time t; $W_{s,t}^{BES} = 1$ indicates that it is in the charge state; $W_{s,t}^{BES} = 0$ indicates that it is in the discharge state. Note that the simultaneous charging and discharging is forbidden by Eqs 15a, 15b. Constraint (15c) describes the variation of state of charge (SOC), where $SOC_{s,t}$ is the SOC of BES s at time t; C_s^{BES} is the energy storage capacity of BES s; η^{ch} and η^{dis} are the charging and discharging efficiency of BES s, respectively. Constraint (15d) indicates that SOC of BES needs to be maintained within the allowable range, where $\underline{SOC}_s$ and $\overline{SOC}_s$ are the upper and lower limit of SOC, respectively; ΔT denotes the time interval of the operation horizon T with a duration of 1 h.

3.2.2 Pumped storage power station

The PSP can be operated in either generating mode or pumping mode (Xia et al., 2019; Liu et al., 2021). Different operation modes can be switched smoothly. Thus, it is effective device for the peak shaving and valley filling of power system. The operational model of PSP consists of the following constraints. For brevity, we will define the subscriptions, superscriptions and several commonly used notations first and no longer illustrate those afterwards. Specifically, subscriptions p and g denote the indices of the pumped storage power station and pumped generation units with a PSP, respectively; Superscriptions pg and ph denote the generating mode and pumping mode, respectively; u denotes the operation state of the PSP or the unit; Y and Z represent the startup and shutdown indicators of the PSP unit, respectively.

$$u_{p,t}^{pg} + u_{p,t}^{ph} \le 1 \qquad \forall p \in N_{PS}, \forall t \in T \qquad (16a)$$

$$u_{p,g,t}^{pg} \le u_{p,t}^{pg}, u_{p,g,t}^{ph} \le u_{p,t}^{ph} \qquad \forall p \in N_{PS}, \forall g \in N_p^{gu}, \forall t \in T \qquad (16b)$$

$$u_{p,g,t}^{pg} \underline{P}_{p,g}^{pg} \le P_{p,g,t}^{pg} \le u_{p,g,t}^{pg} \overline{P}_{p,g}^{pg} \qquad \forall p \in N_{PS}, \forall g \in N_p^{gu}, \forall t \in T \qquad (16c)$$

$$u_{p,g,t}^{ph} \underline{P}_{p,g}^{ph} \le P_{p,g,t}^{ph} \le u_{p,g,t}^{ph} \overline{P}_{p,g}^{ph} \qquad \forall p \in N_{PS}, \forall g \in N_p^{gu}, \forall t \in T \qquad (16d)$$

$$RC_{p,t} = RC_{p,t-1} + \left(\sum_{g=1}^{N_p^{gu}} \eta_{ph} P_{p,g,t}^{ph} - \sum_{g=1}^{N_p^{gu}} \eta_{pg} P_{p,g,t}^{pg}\right)\Delta T \qquad \forall p \in N_{PS}, \forall t \in T \qquad (16e)$$

$$\underline{RC}_p \le RC_{p,t} \le \overline{RC}_p \qquad \forall p \in N_{PS}, \forall t \in T \qquad (16f)$$

$$RC_{p,T} = RC_{p,0} \qquad \forall p \in N_{PS} \qquad (16g)$$

$$u_{p,g,t}^{pg} - u_{p,g,t-1}^{pg} = Y_{p,g,t}^{pg} - Z_{p,g,t}^{pg} \qquad \forall p \in N_{PS}, \forall g \in N_p^{gu}, \forall t \in T \qquad (16h)$$

$$Y_{p,g,t}^{pg} + Z_{p,g,t}^{pg} \le 1 \qquad \forall p \in N_{PS}, \forall g \in N_p^{gu}, \forall t \in T \qquad (16i)$$

$$u_{p,g,t}^{ph} - u_{p,g,t-1}^{ph} = Y_{p,g,t}^{ph} - Z_{p,g,t}^{ph} \qquad \forall p \in N_{PS}, \forall g \in N_p^{gu}, \forall t \in T \qquad (16j)$$

$$Y_{p,g,t}^{ph} + Z_{p,g,t}^{ph} \le 1 \qquad \forall p \in N_{PS}, \forall g \in N_p^{gu}, \forall t \in T \qquad (16k)$$

$$RU_{p,g,t}^{PS} \le u_{p,g,t}^{pg} \overline{P}_{p,g}^{pg} - P_{p,g,t}^{pg} + P_{p,g,t}^{ph} - u_{p,g,t}^{ph}\underline{P}_{p,g}^{ph} \qquad \forall p \in N_{PS}, \forall g \in N_p^{gu}, \forall t \in T \qquad (16l)$$

$$RD_{p,g,t}^{PS} \le u_{p,g,t}^{ph} \overline{P}_{p,g}^{ph} - P_{p,g,t}^{ph} + P_{p,g,t}^{pg} - u_{p,g,t}^{pg}\underline{P}_{p,g}^{pg} \qquad \forall p \in N_{PS}, \forall g \in N_p^{gu}, \forall t \in T \qquad (16m)$$

Constraint (16a) ensures the simultaneous pumping and generating states of PSP is avoided. Constraint (16b) illustrates the operation states of internal units of PSP are consistent with operation state of the station. Constraints (16c) and (16d) impose the power generation limits and pumping power limits on individual PSP units, respectively, where $\underline{P}^{pg}/\overline{P}^{pg}$ is the minimum/maximum generating power of the unit; $\underline{P}^{ph}/\overline{P}^{ph}$ is the minimum/maximum pumping power of the unit; P^{pg}/P^{ph} is the generating/pumping power of the unit. The variation of the PSP reservoir capacity is represented by constraint (16e), where RC is the storage capacity of upper reservoir; η_{ph} and η_{pg} are water-volume-electricity conversion coefficients during pumping and generating, respectively. Constraints (16f) enforces the upper and lower limits of the PSP reservoir capacity, where $\overline{RC}$ and $\underline{RC}$ are the upper and lower limits of the capacity of the upper reservoir. Constraint (16g) shows that at the end of the operation horizon the capacity of PSP reservoir should be equal to the capacity at the beginning. Constraints (16h–k) represent the logic relationship between the startup/shutdown indicators and the on/off state variables of the PSP units. Constraints (16l) and (16m) enforce upper limits of the upward and downward reserves of the PSP units, respectively, where RU^{PS} and RD^{PS} are the upward and downward reserves, respectively.

3.3 Modeling of power network

The DC power flow model is used to represent the power flow in transmission network (Li, 2014). The related constraints are formulated as follows.

$$
\begin{aligned}
P_{i,t}^g + P_{i,t}^h + \left(P_{i,t}^{pv} - \Delta P_{i,t}^{pv}\right) + \left(P_{i,t}^{wt} - \Delta P_{i,t}^{wt}\right) \\
+ \left(P_{i,t}^{dis} - P_{i,t}^{ch}\right) + \left(P_{i,t}^{pg} - P_{i,t}^{ph}\right) - P_{i,t}^L = P_{i,t} \quad \forall i \in N_d, \forall t \in T
\end{aligned}
\tag{17a}
$$

$$
P_{ij,t} = \frac{\theta_{i,t} - \theta_{j,t}}{x_{ij,t}} \qquad \forall i,j \in N_d, \forall t \in T \tag{17b}
$$

$$
P_{i,t} = \sum_{j \in \Phi_i} P_{ij,t} \qquad \forall i,j \in N_d, \forall t \in T \tag{17c}
$$

$$
-\overline{P}_{ij} \le P_{ij,t} \le \overline{P}_{ij} \qquad \forall i,j \in N_d, \forall t \in T \tag{17d}
$$

$$
\sum_{i=1}^{N_g} RU_{i,t} + \sum_{h=1}^{N_h} RU_{h,t} + \sum_{p=1}^{N_{PS}} \sum_{g=1}^{N_p^{gu}} RU_{p,g,t} \ge \Delta P_L \qquad \forall t \in T \tag{17e}
$$

$$
\sum_{i=1}^{N_g} RD_{i,t} + \sum_{h=1}^{N_h} RD_{h,t} + \sum_{p=1}^{N_{PS}} \sum_{p=1}^{N_{PS}} RD_{p,g,t} \ge \Delta P_L \qquad \forall t \in T \tag{17f}
$$

Constraint (17a) describes the nodal active power balance of the network, where $P_{i,t}$ and $P_{i,t}^L$ are the active power injection and load of bus i at time t, respectively. Constraints (17b) and (17c) represent the DC power flow model of the transmission network, where x_{ij} is the reactance of branch between buses i and j; $\theta_{i,t}$ is the voltage angle of bus i at time t; $P_{ij,t}$ is active power flow on the branch between buses i and j at time t; Φ_i is the set of buses directly connected with bus i. Constraint (17d) imposes the power flow capacity on branches, where $\overline{P}_{ij}$ is the active power flow capacity of branch between buses i and j. Constraints (17e) and (17f) ensure that the upward and downward reserves of power system are sufficient to handle the pre-specified power disturbance.

4 Multi-objective optimization-based renewable energy accommodation capacity evaluation method

Accommodating renewable energy not only needs to resolve the technical issues as previously illustrated but also needs to tackle the economic issues since it does not necessary mean the higher penetration of the renewable brings about the lower overall operational cost of the entire power system. The relationship between overall operational cost and the penetration

FIGURE 4
The relationship between the overall cost and penetration of renewable energy.
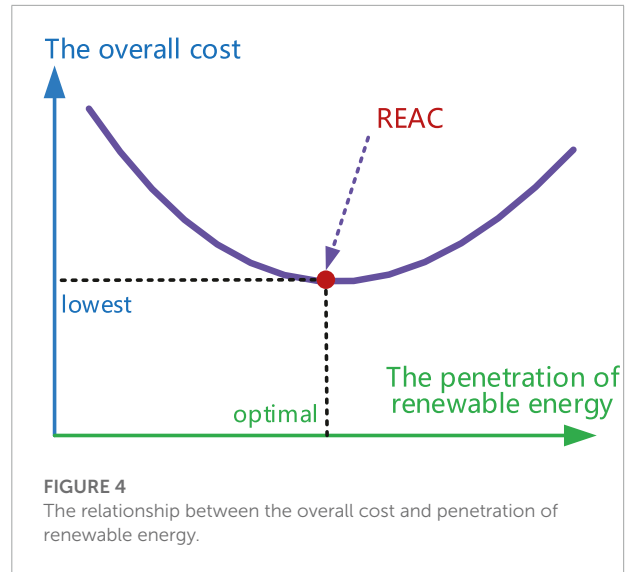
of renewable energy is illustrated in **Figure 4**. Intuitively, when the penetration of renewable energy is relatively low, increasing renewable energy installation will contribute to the reduction of overall operational cost as the costly thermal power is replaced by the free renewable energy generation. However, there exists a turning point where further improving renewable energy penetration no longer leads to the decline of the overall operational cost when the increment accommodation cost surpasses the extra energy cost saving. Thus, at this turning point the overall operational cost is lowest and mathematically it can be interpreted as the renewable energy accommodation capacity of the power system. To find the REAC accurately, it is necessary to establish a multi-objective optimization model considering both economic and technical issues.

4.1 Multi-objective optimization model

Multiple objectives need to be considered when optimizing the power system operation, including renewable energy curtailment penalty f_1, renewable energy units daily maintenance cost f_2, thermal power unit operation cost f_3, battery energy system degradation cost f_4, hydro-power plant startup/shutdown cost f_5, pumped storage power station startup/shutdown cost f_6, and the upward and downward reserve acquirement cost f_7, which are formulated as follows.

$$
min \quad f = f_1 + f_2 + f_3 + f_4 + f_5 + f_6 + f_7 \tag{18a}
$$

$$
f_1 = \sum_{t=1}^{T} \sum_{m=1}^{N_{wt}} K_{wt}^{ctl} \Delta P_{m,t}^{wt} + \sum_{t=1}^{T} \sum_{m=1}^{N_{pv}} K_{pv}^{ctl} \Delta P_{n,t}^{pv} \tag{18b}
$$

$$
f_2 = \sum_{t=1}^{T} \sum_{m=1}^{N_{wt}} K_{wt} P_{m,t}^{wt} + \sum_{t=1}^{T} \sum_{m=1}^{N_{pv}} K_{pv} P_{m,t}^{pv} \tag{18c}
$$
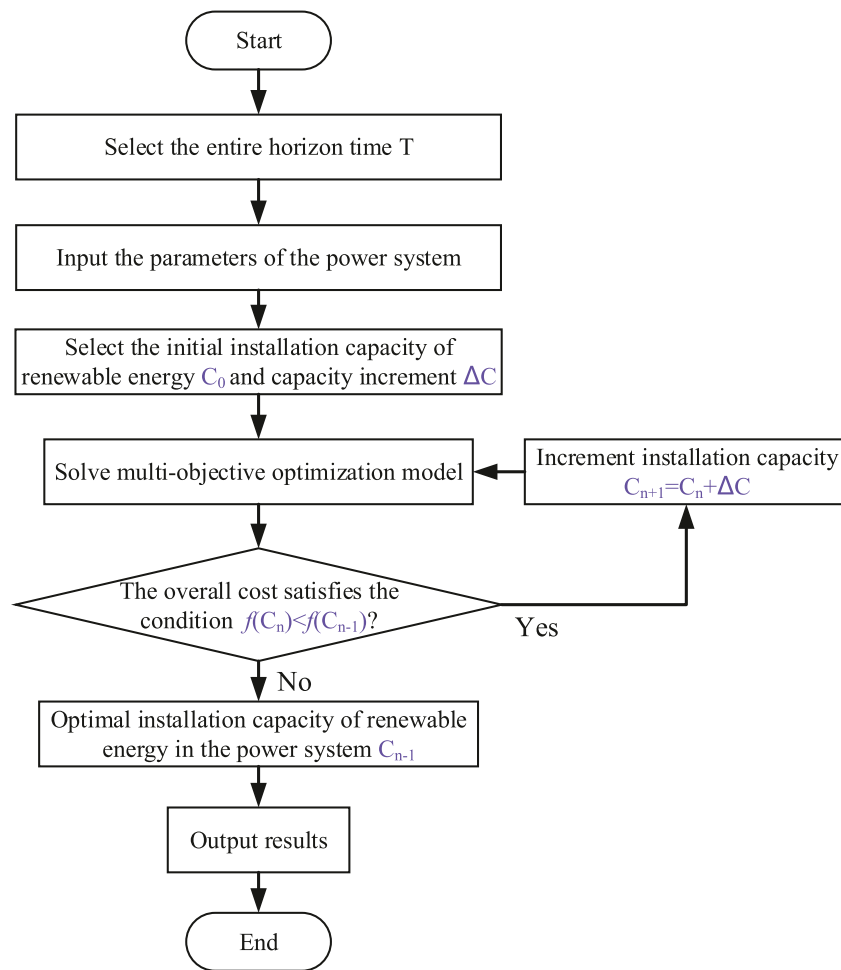
FIGURE 5
Flowchart of the proposed REAC evaluation method.

$$f_3 = \sum_{t=1}^{T}\sum_{i=1}^{N_g} F_{i,t}^g + \sum_{t=1}^{T}\sum_{m=1}^{N_g}\left(Y_{i,t}^g C_i^{SU} + Z_{i,t}^g C_i^{SD}\right) \quad (18d)$$

$$f_4 = \sum_{s=1}^{N_{BES}}\sum_{t=1}^{T} K_{s,t}^{BES}\left(P_{s,t}^{ch} + P_{s,t}^{dis}\right) \quad (18e)$$

$$f_5 = \sum_{t=1}^{T}\sum_{h=1}^{N_h}\left(Y_{h,t}^{hy} C_h^{UH} + Z_{h,t}^{hy} C_h^{DH}\right) \quad (18f)$$

$$f_6 = \sum_{t=1}^{T}\sum_{p=1}^{N_{PS}}\sum_{p=1}^{N_p^{gu}}\left(\left(Y_{p,g,t}^{pg} + Y_{p,g,t}^{ph}\right) C_{p,g}^{on} + \left(Z_{p,g,t}^{pg} + Z_{p,g,t}^{ph}\right) C_{p,g}^{off}\right) \quad (18g)$$

$$f_7 = \sum_{t=1}^{T}\left\{\sum_{i=1}^{N_g}\left(C_i^{RU} RU_{i,t}^g + C_i^{RD} RD_{i,t}^g\right)\right.$$
$$+ \sum_{h=1}^{N_h}\left(C_h^{RU} RU_{h,t}^{hy} + C_h^{RD} RD_{h,t}^{hy}\right)$$
$$\left. + \sum_{p=1}^{N_{PS}}\sum_{g=1}^{N_p^{gu}}\left(C_p^{RU} RU_{p,g,t}^{PS} + C_p^{RD} RD_{p,g,t}^{PS}\right)\right\} \quad (18h)$$

where K_{wt}^{ctl} and K_{pv}^{ctl} are the unit penalty costs for the curtailment of WT and PV power, respectively; K_{wt} and K_{pv} are the maintenance cost coefficients of WT and PV, respectively; f_3 includes the operating cost and startup/shutdown cost considering deep peak regulation, where C_i^{SU} and C_i^{SD} are the unit startup and shutdown costs of TPU i, respectively; $K_{s,t}^{BES}$ is the unit degradation cost of BES; C_h^{UH} and C_h^{DH} are the unit startup and shutdown costs, respectively; $C_{p,g}^{on}$ and $C_{p,g}^{off}$ are the unit startup and shutdown costs of the unit g in PSP p, respectively; C^{RU} and C^{RD} are the unit upward and downward reserves acquirement
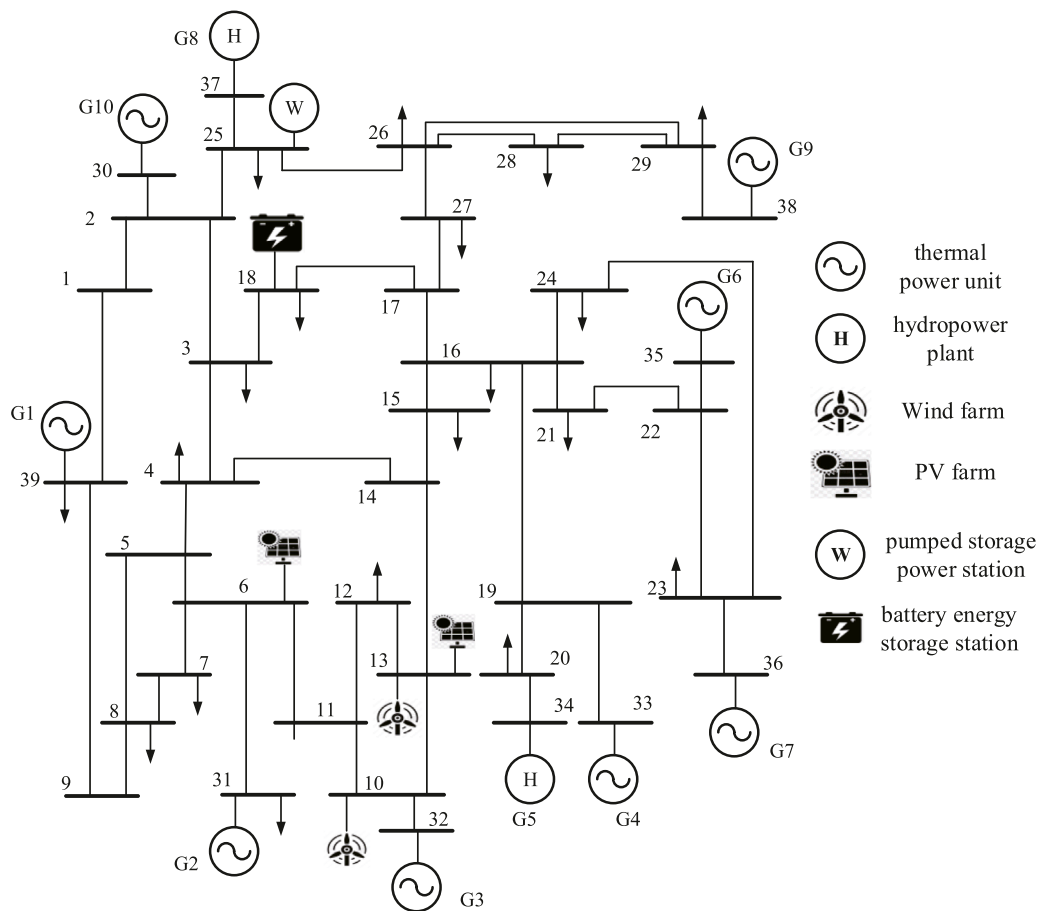
FIGURE 6
The network topology of the modified IEEE 39-bus transmission system.

cost, respectively; N_{wp}, N_{pv}, N_g, N_h, N_{BES}, N_{PS} are the set of wind farm, PV farm, TPU, HPP, BES and PSP, respectively; N_p^{gu} is the set of the pumped generator units in PSP p.

Three categories of system security and operation constraints are considered as follows,

1) Constraints derived from the deep peak regulation requirement (4b), (5).
2) Constraints derive from the primary frequency response requirement (8), (9), (10).
3) Interaction model of "source-network-storage", including constraints (11), (12), (14), (15), (16), (17).

4.2 Incremental capacity augmentation-based renewable energy accommodation capacity evaluation

Based on the established multi-objective optimization model, we develop an novel evaluation method of REAC in

power system based on an incremental capacity augmentation approach. The flowchart of the proposed REAC method is demonstrated in **Figure 5**.

The proposed evaluation method of the REAC in power system consists of seven steps illustrated as follows,

***Step* (*B*1)** Select the entire horizon time T;

***Step* (*B*2)** Input the relevant parameters of the power system;

***Step* (*B*3)** Select the initial installation capacity of renewable energy C_0 and installation capacity increment ΔC;

***Step* (*B*4)** Solve the established multi-objective optimization model by integrating the interaction of "source-network-storage" and the requirements of peak and frequency regulation.

***Step* (*B*5)** Compare the solved optimal operational cost $f(C_n)$ of this iteration with that $f(C_{n-1})$ of the last iteration. If the operation cost still declines, i.e., $f(C_n) < f(C_{n-1})$, increment the installation capacity of renewable energy by ΔC and return to ***Step* (*B*4)**; otherwise, the installation capacity of renewable energy C_{n-1} is recognized as the REAC of the power system.

***Step* (*B*6)** Output the REAC result.

TABLE 1 The parameters of thermal power units.

unit	P_i^{gN}(MW)	H_i^{gen}(s)	a_i($/(MW)^2)	b_i($/MW)	c_i($)	S_i^g($)	R_i^{Up}/R_i^{Dw}(MW/h)
1	1,050	5.0	0.000158*900	0.18*900	4.0*900	3633000	400
2	650	4.3	0.000182*900	0.25*900	5.0*900	2249000	300
3	750	4.5	0.000183*900	0.26*900	4.5*900	2595000	250
4	650	4.3	0.000178*900	0.25*900	5.0*900	2249000	200
5	700	4.5	0.000178*900	0.26*900	5.0*900	2422000	250
6	600	4.2	0.000185*900	0.30*900	4.5*900	2076000	200
7	850	4.8	0.000175*900	0.26*900	5.0*900	2941000	350
8	1,000	5.0	0.000180*900	0.27*900	6.0*900	3460000	400

TABLE 2 Parameters of hydropower plants, battery energy storage station and pumped storage power station.
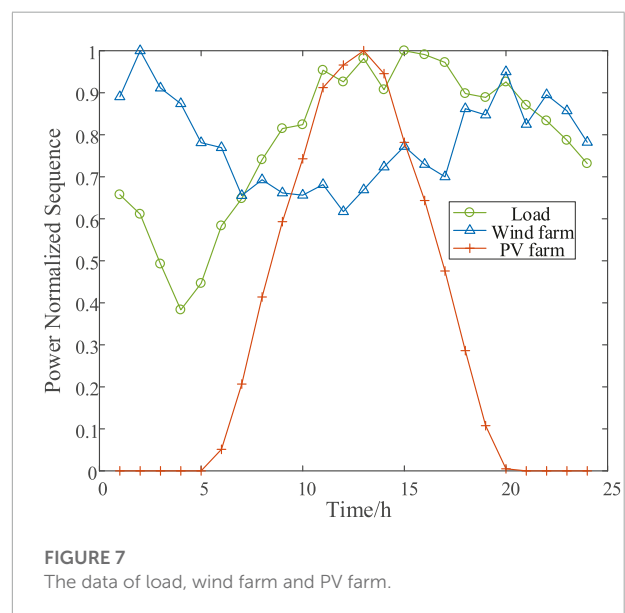
Battery storage power station		Pumped storage power station		Hydropower plant			
para	value	para	value	para	value	para	value
$\overline{SOC_s}$	0.9	$\overline{RC_p}$(m^3)	1332740	$\overline{V_h}$(Hm^3)	500	η_h	6.465
$\underline{SOC_s}$	0.1	$\underline{RC_p}$(m^3)	75640	$\underline{V_h}$(Hm^3)	100	$Hd_{h,0}$	0.58434
C_s^{BES}(MVA)	600	$\overline{P_s^{pg}}$(MW)	4 × 200	$\overline{Qb_h}$(Hm^3/h)	40	α_h	0.00115
$\overline{P_s^{ch}}$(MW)	10	$\overline{P_s^{pw}}$(MW)	4 × 200	$\underline{Qb_h}$(Hm^3/h)	0	H_i^{gen}(s)	8.0
$\overline{P_i^{dis}}$(MW)	10	H_i^{gen}(s)	3.2	$\overline{P_h}$(MW)	500	$K_{G,i}^{\star}$	40
η^{ch}/η^{dis}	0.9	$K_{G,i}^{\star}$	28.57	$\underline{P_h}$(MW)	7	$v_{h,0}$(Hm^3)	300
K_s^{BES}($/MW·h)	10	η^{pw}/η^{pg}	74.9/99.8	$Qn_{h,t}$(Hm^3/h)	5.0	$v_{h,T}$(Hm^3)	300
—	—	$C_{p,g}^{on}/C_{p,g}^{off}$($)	20	C_h^{Uh}/C_h^{Dh}($)	20	—	—

5 Numerical results

The proposed REAC evaluation method is tested on the modified IEEE 39-bus system to verify its effectiveness. All case studies are carried out on MATLAB platform using CPLEX as the MILP solver. The modified IEEE 39-bus system includes 8 TPUs, 2 HPPs, 2 wind farms, 2 PV farms, a BES and a PSP, as shown in Figure 6. The installation capacity of WT is set equal with that of PV, and the parameters of 2 HPPs are identical.

In the test cases, all TPUs, HPPs and PSP are enabled to provide primary frequency regulation, and all TPUs are able to provide deep peak regulation. The maximum power outputs of TPUs are their rated capacities P_i^{gN}. Without loss of generality, the normal minimum power output without deep peak regulation is assumed to be 0.5 times of the rated capacity, i.e., $0.5P_i^{gN}$; The minimum technical power outputs in DPR and DPRO states are assumed to be 0.4 and 0.3 times of the rated capacity, i.e., $0.4P_i^{gN}$, $0.3P_i^{gN}$, respectively. The minimum on and off times of TPUs are assumed 2h. The per-unit values of the droop coefficients are randomly generated from 20∼ 25 with respect to the rated capacities of the TPUs. The unit penalty cost for wind power and PV power curtailment is set as 20 $/(MW·h).

The rated frequency of the test system is 50 Hz, and the upper limit of RoCoF is chosen as 1 Hz/s. The maximum allowable frequency deviation of UFLS relay is set as ± 0.8 Hz. The quasi-steady frequency deviation limit is set as ± 0.2 Hz. Other parameters of TPUs are listed in Table 1, and the parameters of

FIGURE 7
The data of load, wind farm and PV farm.

HPPs, battery energy storage power station and PSP are listed in Table 2. The typical daily load profile, wind and PV power output profiles are depicted in Figure 7.

It is known that both the tripping of the conventional generator and the realization of the forecast error of renewable energy can lead to the great power disturbance. Hence, in this paper we chose the disturbance as the larger one between the loss
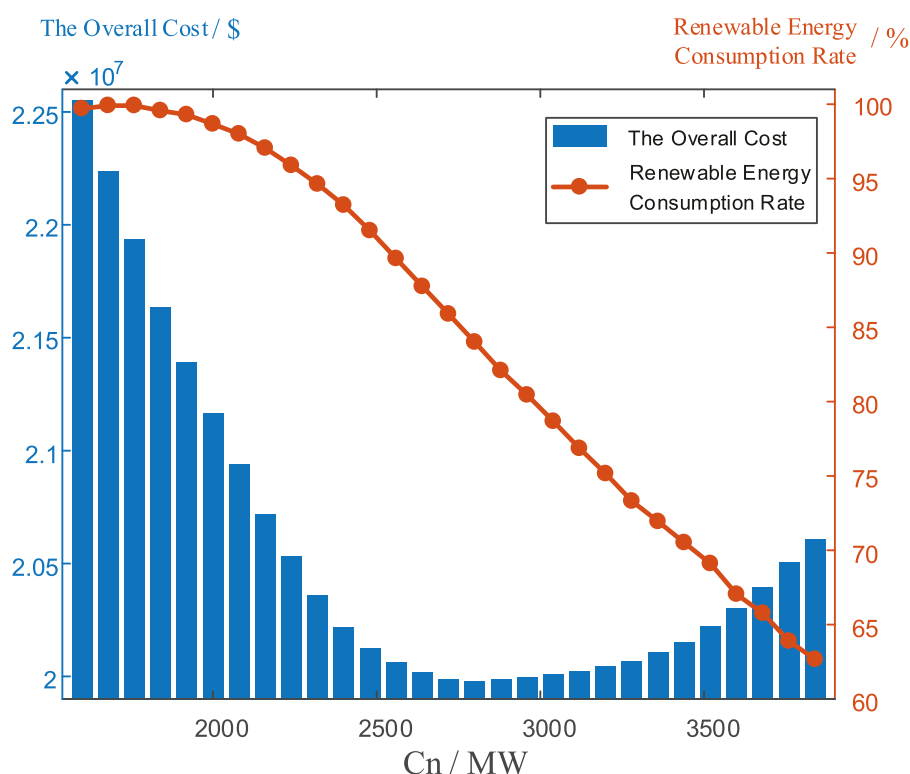
FIGURE 8
The overall operational cost and renewable energy consumption rate with different total renewable energy installation capacities.

of the largest generation unit and the conservative estimation of the total renewable energy forecast error which is set as ± 30% of the total predicated renewable energy output.

5.1 Effectiveness of the proposed evaluation method

In this subsection, the effectiveness of the proposed REAC evaluation method is verified on the modified IEEE 39-bus test system. Here, the initial installation capacity of renewable energy C_0 is equal to 1600 MW and installation capacity increment ΔC is equal to 80 MW. **Figure 8** depicts the relationship between the overall operational cost of the system and the total renewable energy installation capacity as well as the relationship between the renewable energy accommodation rates of the system and the total renewable energy installation capacity. **Figure 9** demonstrates the accommodated wind/PV energy and generated energy of TPUs under different total renewable energy installation capacities.

It can be observed from **Figure 8**, with the growth of total renewable energy installation capacity, the overall operational cost declines first as a portion of TPU power output is replaced by the renewable energy output as demonstrated

in **Figure 9**. The overall operational cost reaches the lowest value given $Cn = 2800\ MW$ and then starts to augment with further growth of the total renewable energy installation capacity as the REAC become saturated. The reason is that the system requires sufficient conventional generators to provide frequency response regulation support and thus the further expanding the total renewable energy capacity only results in the increased curtailment rather than the replacement of TPU as show in **Figures 8**, **9**. Therefore, $Cn = 2800\ MW$ is considered as the renewable energy accommodation capacity of the test system since at this point the overall operational cost is lowest, which verifies the effectiveness of the proposed method.

5.2 Performance comparison

In this subsection, the superiority of the proposed REAC evaluation method considering both peak and frequency regulation, is validated through the comparison with three benchmark schemes. The first benchmark scheme considers neither peak regulation nor frequency regulation, denoted as S1. The second benchmark scheme only considers peak regulation, denoted as S2, and the last benchmark scheme only considers
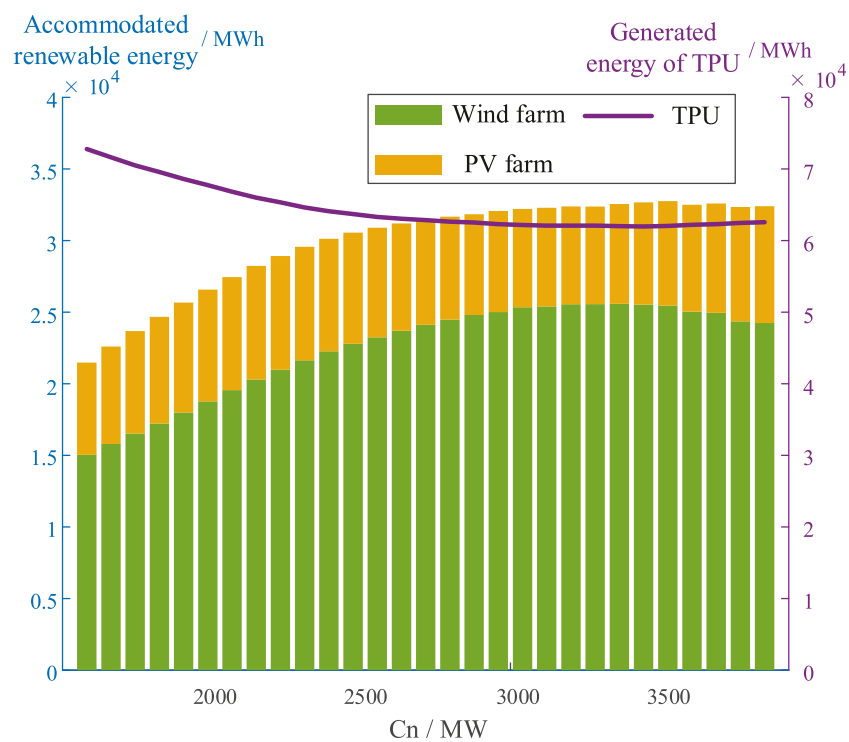
FIGURE 9
The accommodated PV/Wind energy and generated energy of TPU with different total renewable energy installation capacities.
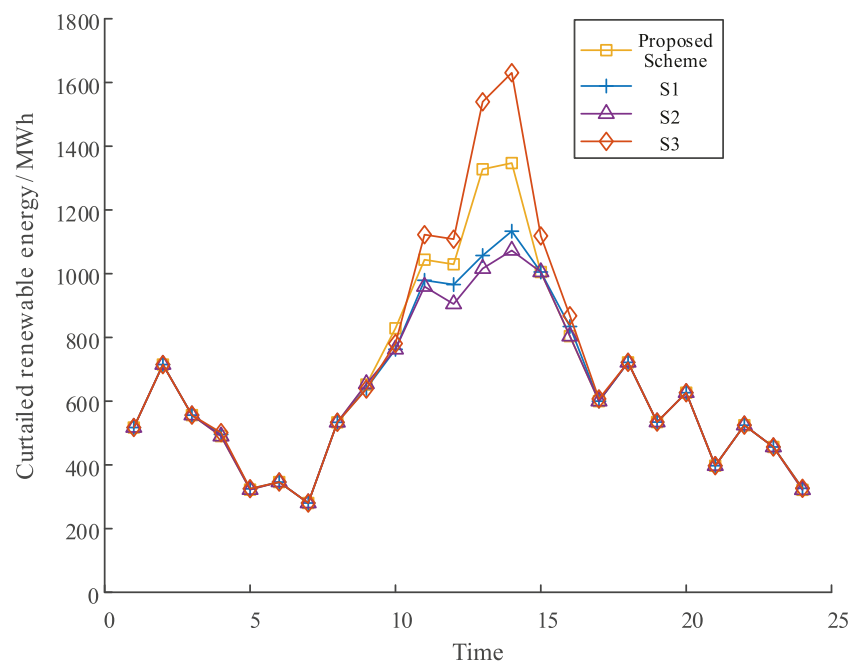

FIGURE 10
The curtailment of renewable energy with different schemes.

TABLE 3 The operation cost and renewable energy accommodation rate using different schemes.

Scheme	Overall operational cost f($)	Curtailment cost f_1($)	Other costs $\sum_{i=2}^{7} f_i$($)	Renewable energy accommodation rate
Proposed	2.0302×10^7	319610.3693	1.9982×10^7	67.0397%
S1	2.0105×10^7	306652.7749	1.9798×10^7	68.3760%
S2	1.9866×10^7	302428.6012	1.9564×10^7	68.8116%
S3	2.0902×10^7	335478.5843	2.0566×10^7	65.4033%

frequency regulation, denoted as S3. The installation capacity of each wind farm and PV farm is set as 900 MW in all schemes.

Table 3 summarizes the comparison of the operation cost and renewable energy accommodation rate of different schemes. As shown in the table, the overall cost of scheme S3 is largest, which is followed by the proposed scheme and S1, and S2 yields the lowest overall cost. The ranking order of the renewable energy accommodation rate of the four schemes is exactly reversed, which means the higher accommodation rate gives rise to the lower overall cost. Figure 10 shows the renewable energy curtailment profiles using different schemes. It is shown that the curtailment is highest during the period of the renewable energy peak generation. Moreover, S3 has the highest curtailment and S2 yields the lowest curtailment, which is consistent with the results in Table 3. Hence, we can conclude from the above results the considering deep peak regulation is beneficial for the renewable energy accommodation and incorporating the frequency regulation inhibits the renewable energy accommodation. The reason is that when deep peak regulation is considered, the minimum power output of TPUs can be further lowered leading the improvement of the power system flexibility and hence promoting the renewable energy accommodation. When the frequency response requirement is taken into account, the system requires sufficient generators online to maintain the required inertia level and to provide sufficient reserve to handle power disturbance, which squeezes the renewable energy hosting capacity of the power system and thus causing higher wind and PV power curtailment. Therefore, it is necessary to consider both the peak regulation and frequency regulation in order to obtain the accurate outcome of the REAC evaluation since both regulations are the fundamental part of the power system operation and have considerable impact on the renewable energy accommodation.

6 Conclusion

In this paper, a novel REAC evaluation method is developed for power systems considering peak and frequency regulation as well as the "source-network-storage" interaction. First, the peak and frequency regulation response model is established and simplified to reduce the computational complexity. Then, according to the interaction of "source-network-storage", a daily

power system operational model is constructed. Furthermore, a multi-objective optimization model is proposed considering both economic and technical issues, and an novel evaluation REAC method is developed based on the incremental capacity augmentation technique. Finally, the numerical tests on the modified IEEE 39-bus system verify the effectiveness of the proposed method.

Data availability statement

The data analyzed in this study is subject to the following licenses/restrictions: The dataset involve commercial privacy. Requests to access these datasets should be directed to zycy@hnu.edu.cn.

Author contributions

YY conceptualized the study, contributed to the study methodology, and wrote the original draft. HZ contributed to the writing-review and editing, data curation and investigation. YZ contributed to study methodology, data analysis, wrote the original draft and writing-review. DY contributed to software and data analysis. BW contributed to investigation and writing-original draft. QX contributed to supervision and writing-review and editing. BL contributed to software and paper revision. All authors have read and agreed to the published version of the manuscript.

Funding

Conflict of interest

Authors YY, HZ, FC, DY, BW, and QX were employed by State Grid Hubei Electric Power Co., Ltd.

The authors declare that this study received funding from science and technology project of State Grid

Hubei Electric Power Company Limited. The funder had the following involvement in the study: data curation, investigation, the study methodology, software and data analysis, writing the original draft and the writing-review & editing.

The remaining authors declare that the research was conducted in the absence of any commercial or financial relationships that could be construed as a potential conflict of interest.

Publisher's note

All claims expressed in this article are solely those of the authors and do not necessarily represent those of their affiliated organizations, or those of the publisher, the editors and the reviewers. Any product that may be evaluated in this article, or claim that may be made by its manufacturer, is not guaranteed or endorsed by the publisher.

References

Alves, E. F., Mota, D. d. S., and Tedeschi, E. (2021). Sizing of hybrid energy storage systems for inertial and primary frequency control. *Front. Energy Res.* 206, 649200. doi:10.3389/fenrg.2021.649200

Babayev, D. A. (1997). Piece-wise linear approximation of functions of two variables. *J. Heuristics* 2, 313–320. doi:10.1007/bf00132502

Carrión, M., and Arroyo, J. M. (2006). A computationally efficient mixed-integer linear formulation for the thermal unit commitment problem. *IEEE Trans. Power Syst.* 21, 1371–1378. doi:10.1109/tpwrs.2006.876672

Carrión, M., Dvorkin, Y., and Pandžić, H. (2018). Primary frequency response in capacity expansion with energy storage. *IEEE Trans. Power Syst.* 33, 1824–1835. doi:10.1109/TPWRS.2017.2735807

Chávez, H., Baldick, R., and Sharma, S. (2014). Governor rate-constrained opf for primary frequency control adequacy. *IEEE Trans. Power Syst.* 29, 1473–1480. doi:10.1109/tpwrs.2014.2298838

Chen, Z., Wu, L., and Shahidehpour, M. (2014). Effective load carrying capability evaluation of renewable energy via stochastic long-term hourly based scuc. *IEEE Trans. Sustain. Energy* 6, 188–197. doi:10.1109/tste.2014.2362291

Gao, Y., Zeng, D., Zhang, L., Hu, Y., and Xie, Z. (2020). Research on modeling and deep peak regulation control of a combined heat and power unit. *IEEE Access* 8, 91546–91557. doi:10.1109/ACCESS.2020.2993279

Guan, H., Feng, Y., Yang, X., Du, Y., Feng, D., and Zhou, Y. (2022). Optimization strategy of combined thermal-storage-photovoltaic economic operation considering deep peak load regulation demand. *Energy Rep.* 8, 112–120. doi:10.1016/j.egyr.2022.03.050

Guo, Z., Zhang, X., Feng, S., and Zhang, H. (2020). The impacts of reducing renewable energy subsidies on China's energy transition by using a hybrid dynamic computable general equilibrium model. *Front. Energy Res.* 8, 25. doi:10.3389/fenrg.2020.00025

He, W., Gao, Q., and Chen, Y. (2018). "Evaluation on renewable energy accommodation ability based on peak load regulation and capacity constraint," in 2018 International Conference on Power System Technology (POWERCON), Guangzhou, China, November 6–8, 2018, (IEEE), 905–910.

Khalkho, A. M., Rapada, B., Majumder, G., Cherukuri, M., and Mohanta, D. K. (2022). Impact assessment of solar power generation uncertainty on smart grid reliability and carbon neutrality. *Front. Energy Res.* 10, 220. doi:10.3389/fenrg.2022.851449

Kushwaha, P., Prakash, V., Bhakar, R., Yaragatti, U. R., Jain, A., and Sumanth, Y. (2018). Assessment of energy storage potential for primary frequency response adequacy in future grids," in 2018 8th IEEE India International Conference on Power Electronics (IICPE), Jaipur, India, December 13–15, 2018, (IEEE), 1–6.

Li, H., Wang, Y., Zhang, X., and Fu, G. (2021). Evaluation method of wind power consumption capacity based on multi-fractal theory. *Front. Energy Res.* 9, 634551. doi:10.3389/fenrg.2021.634551

Li, W. (2014). *Risk assessment of power systems: Models, methods, and applications*. Vancouver, Canada: John Wiley & Sons.

Lin, K., Lu, X., Wu, F., and Shi, L. (2020). "Evaluation of the renewable energy accommodation capacity in the regional power grid," in 2020 12th IEEE PES Asia-Pacific Power and Energy Engineering

Conference (APPEEC), Nanjing, China, September 20–23, 2020 (IEEE), 1–4.

Liu, Y., Wu, L., Yang, Y., Chen, Y., Baldick, R., and Bo, R. (2021). Secured reserve scheduling of pumped-storage hydropower plants in iso day-ahead market. *IEEE Trans. Power Syst.* 36, 5722–5733. doi:10.1109/tpwrs.2021.3077588

Majeed, A., Ahmad, M., Rasheed, M. F., Khan, M. K., Popp, J., and Oláh, J. (2022). The dynamic impact of financial globalization, environmental innovations and energy productivity on renewable energy consumption: Evidence from advanced panel techniques. *Front. Environ. Sci.* 447, 894857. doi:10.3389/fenvs.2022.894857

Tan, J., and Zhang, Y. (2017). Coordinated control strategy of a battery energy storage system to support a wind power plant providing multi-timescale frequency ancillary services. *IEEE Trans. Sustain. Energy* 8, 1140–1153. doi:10.1109/tste.2017.2663334

Teng, F., and Strbac, G. (2016). Assessment of the role and value of frequency response support from wind plants. *IEEE Trans. Sustain. Energy* 7, 586–595. doi:10.1109/tste.2015.2505085

Wang, C., Bie, Z., Yan, C., Li, Z., Liu, F., Ding, K., et al. (2016). Evaluation of power grids' renewable energy accommodation capacity considering wind power and photovoltaic power. *IEEE PES Asia-Pacific Power Energy Eng. Conf.*, 1518–1522. doi:10.1109/APPEEC.2016.7779744

Wang, C., Liu, S., Bie, Z., and Wang, J. (2018). Renewable energy accommodation capability evaluation of power system with wind power and photovoltaic integration. *IFAC-PapersOnLine* 51, 55–60. doi:10.1016/j.ifacol.2018.11.677

Wen, Y., Li, W., Huang, G., and Liu, X. (2016). Frequency dynamics constrained unit commitment with battery energy storage. *IEEE Trans. Power Syst.* 31, 5115–5125. doi:10.1109/tpwrs.2016.2521882

Wu, L., Shahidehpour, M., and Li, Z. (2008). Genco's risk-constrained hydrothermal scheduling. *IEEE Trans. Power Syst.* 23, 1847–1858. doi:10.1109/tpwrs.2008.2004748

Xia, P., Deng, C., Chen, Y., and Yao, W. (2019). Milp based robust short-term scheduling for wind–thermal–hydro power system with pumped hydro energy storage. *IEEE Access* 7, 30261–30275. doi:10.1109/access.2019.2895090

Xie, J., Wang, K., Feng, D., Zeng, D., Li, Y., and Yue, D. (2016). A security-constrained flexible demand scheduling strategy for wind power accommodation. *Int. Trans. Electr. Energy Syst.* 26, 1171–1183. doi:10.1002/etep.2123

Xu, Q., Kang, C., Zhang, N., Ding, Y., Xia, Q., Sun, R., et al. (2014). A probabilistic method for determining grid-accommodable wind power capacity based on multiscenario system operation simulation. *IEEE Trans. Smart Grid* 7, 400–409. doi:10.1109/tsg.2014.2381271

You, F., Si, X., Dong, R., Lin, D., Xu, Y., and Xu, Y. (2022). A state-of-charge-based flexible synthetic inertial control strategy of battery energy storage systems. *Front. Energy Res.* 603, 908361. doi:10.3389/fenrg.2022.908361

Zhang, G., Ela, E., and Wang, Q. (2018). Market scheduling and pricing for primary and secondary frequency reserve. *IEEE Trans. Power Syst.* 34, 2914–2924. doi:10.1109/tpwrs.2018.2889067

Zhang, X., Wang, J., Wang, Y., Zou, M., and Ning, Y. (2019). "Consumption capability of renewable energy based on network maximum flow model," in Proceedings of the 2nd International Conference on Information Technologies and Electrical Engineering, Zhuzhou, China, December 6–7, 2019, 1–6.

A data-driven hybrid interval reactive power optimization based on the security limits method and improved particle swarm optimization

Dawen Chen[1], Shaoqing Qu[1], Qian Liu[2]*, Wei Xiao[1], Xiao Liu[1], Yufeng Luo[2], Huaizhi Yang[2] and Na Kuang[3]

[1]Changsha Power Supply Branch, State Grid Hunan Electric Power Co., Ltd, Changsha, China, [2]College of Electrical and Information Engineering, Hunan University, Changsha, China, [3]School of Educational Science, Hunan Normal University, Changsha, China

The integration of renewable power generation introduces randomness and uncertainties in power systems, and the reactive power optimization with interval uncertainty (RPOIU) problem has been constructed to acquire the voltage control strategy. However, the large amount of uncertain data and the coexistence of discrete and continuous control variables increase the difficulty of solving the RPOIU problem. This paper proposes a data-driven hybrid interval reactive power optimization based on the security limits method (SLM) and the improved particle swarm optimization (IPSO) to solve the RPOIU problem. In this method, the large amount of historical uncertain data is processed by data-driven to obtain the boundary of optimal uncertainty set. The control variable optimization is decomposed into continuous variable optimization and discrete variable optimization. The continuous variables are optimized by applying the SLM with the discrete variables fixed, and the discrete variables are optimized by the IPSO with the continuous variables fixed. The two processes are applied alternately, and the values of the control variables obtained by each method are used as the fixed variables of the other method. Based on simulations carried out for the IEEE 30-bus system with three optimization methods, we verified that the voltage control strategy obtained by the data-driven hybrid optimization could ensure that the state variable intervals satisfied the constraints. Meanwhile, the values of the real power losses obtained by the proposed method were smaller than those obtained by the SLM and IPSO. The simulation results demonstrated the effectiveness and value of the proposed method.

KEYWORDS

renewable power generation, data-driven hybrid optimization, interval reactive power optimization, security limits method, particle swarm optimization

1 Introduction

Reactive power optimization is directly related to the security and economy of a power system. There is inherent randomness and volatility with renewable energy resources (RESs), including wind and photovoltaic power, so that the data of the RES output and the power load demand are generally uncertain in the power system. There will be voltage security problems under the effects of these uncertainties. Therefore, it is necessary to construct an uncertain reactive power optimization (URPO) strategy to realize voltage security control while handling the uncertainties. The URPO model incorporates the general reactive power flow (RPF) model with uncertain data, aiming at improving the voltage profile and reducing the loss.

Some approaches have been proposed to solve the URPO model, which is non-convex and non-linear. These approaches mainly include probabilistic programming, robust programming, and interval programming. The probabilistic approach acquires the specific probability distribution of the uncertain data, because it considers them to be random variables. This process represents the RPO model as an expectation model or chance-constrained programming model and obtains the results under a stated confidence level (Arefifar and Mohamed, 2014; Liu et al., 2016). Probabilistic programming requires a large amount of historical data, while the amount of data is generally limited, causing a bias of the empirical distribution. A data-driven modeling approach is introduced to address the issue, and the model is formulated as a two-stage problem, where the first-stage variables find the optimal control for discrete reactive power compensation equipment and the second-stage variables are adjusted to an uncertain probability distribution (Ding et al., 2018). A scenario-based two-stage stochastic optimization framework is also developed in (Saraswat et al., 2020) to minimize the total real power losses in the transmission network. To solve the URPO issue of two conflicting objective functions, the active power loss and voltage deviation are minimized simultaneously, and appropriate probability distribution functions are considered to model the stochastic behavior of wind and solar power generation with the Monte Carlo simulation (MCS) technique (Keerio et al., 2020). These probabilistic processes are quite time-consuming, and the probability distribution of uncertainties is rough due to the limited data.

In contrast, robust programming considers the uncertainties to be from various sets, such as box, cone, or ellipsoid sets, without assuming the probability distribution functions. A two-stage distributed robust optimization model for optimal operation is formulated considering wind-power-uncertainty-based data-driven methods, where the polyhedra-based linearization method is introduced to approximate the second-order cone power flow constraints with a series of linear constraints (Gao et al., 2021). To improve the computational performance, a second-order cone relaxation and decomposition algorithm is proposed to solve the multi-period reactive power

optimization problem (Liu et al., 2017). The processes obtain the results with good robustness, while the accuracy of the robust programming model is low due to the linearization. Furthermore, there will be infeasible solutions sometimes because robust optimization is only applicable to convex models, while the general URPO model is non-convex.

The development of interval programming has addressed the issues of probabilistic and robust approaches. This approach expresses the uncertain data as intervals and therefore establishes the RPOIU problem in which the state variables are regarded as intervals. Notably, the control variables include both continuous (generator voltage) and discrete (transformer ratio and reactive power compensation) variables. Interval programming can ensure that the ranges of the state variables are completely confined within the security constraints. The methods for solving the RPOIU problem mainly include intelligent algorithms and mathematical processing. To solve the RPOIU model, the genetic algorithm (GA) is employed as the solution algorithm, where the reliable power flow calculation is used to judge the constraints of the model (Zhang et al., 2017). The improved genetic algorithm (IGA) is proposed to solve the problem that the simple GA is inefficient in the application of power system reactive power optimization, where the coding method, fitness function, initial population generation, and crossover and mutation strategy are modified (Chang and Zhang, 2017; Liu et al., 2022). Particle swarm optimization (PSO) is also widely applied to solve this problem (Li et al., 2017; Khan et al., 2020; Shri et al., 2021). An improved particle swarm optimization and Pareto archive algorithm are combined to solve the multi-objective reactive power optimization problem, and it outperforms the non-dominated sorting genetic algorithm II (NSGA-II) (Liu et al., 2021).

For the application of mathematical processing, the linear approximation method is formulated using the interval Taylor extension to help solve the RPOIU model (Jiang et al., 2014; Zhang et al., 2018b). In order to improve the accuracy of the approximation, the interval sequential quadratic programming method (ISQPM), which employs a second-order interval Taylor expansion, is proposed (Zhang et al., 2019). In addition, the security limits method (SLM) is defined to solve the RPOIU problem, and the model is switched to two deterministic reactive power optimization models (Zhang et al., 2018a).

It is noted again that the coexistence of discrete and continuous variables increases the difficulty of solving the RPOIU problem, and the accuracy when solving the problem by applying a single algorithm is generally low. Considering the above interval approaches, mathematical processing can deal with the continuous variables well, and intelligent algorithms are better at handling discrete variables. Therefore, the problem of mixed-variable processing can be addressed by a co-evolution method, which adopts a mathematical method to deal with continuous variables and an intelligent algorithm to deal with discrete variables to solve the RPOIU problem.

The present work establishes a hybrid interval reactive power optimization algorithm considering the uncertainty of RESs. The algorithm uses interval programming to deal with uncertainties and decomposes the control variable optimization into two subproblems: continuous variable optimization and discrete variable optimization. Since the SLM can reduce the conservation of the interval reactive power optimization algorithm and has a better performance in searching for the optimal solution than other mathematical methods, the SLM is applied for continuous variable optimization. Since the PSO has faster convergence rate and simpler processes, the improved PSO (IPSO) is applied for discrete variable optimization. There are the algorithm alternations between these processes.

The construction of the RPOIU problem is presented in Section 2, followed by the hybrid optimization of the SLM and IPSO for solving the RPOIU problem in Section 3. The simulations employed to demonstrate the performance of the proposed method are presented in Section 4. The conclusions and contributions of this paper are given in Section 5.

2 Modeling of reactive power optimization with interval uncertainty (RPOIU) based on data-driven

As mentioned above, the large amount of historical uncertain data is processed by data-driven to obtain the boundary value of the uncertainties, and the input data of the power grid associated with uncertainties can be described as intervals, including power generation $\hat{P}_{Gi}$, active load demand $\hat{P}_{Li}$, and reactive load demand $\hat{Q}_{Li}$, which are expressed as $[P_{Gi}^{\min}, P_{Gi}^{\max}]$, $[P_{Li}^{\min}, P_{Li}^{\max}]$, and $[Q_{Li}^{\min}, Q_{Li}^{\max}]$, respectively. The RPOIU problem is modeled with the real power losses P_{loss} as the objective function and power flow equations, security, and operational limits as constraints:

$$\min P_{\text{loss}} = \sum_{i \in S} \sum_{j \in S} V_i V_j G_{ij} \cos \theta_{ij} \tag{1}$$

s.t.

$$\begin{cases} \hat{P}_{Gi} - P_{Li} - P_i = 0, & i \in S'_G \\ Q_{Gi} - Q_{Li} - Q_i = 0, & i \in S'_G \end{cases} \tag{2}$$

$$\begin{cases} -\hat{P}_{Li} - P_i = 0, & i \in S_L \\ Q_{Ci} - \hat{Q}_{Li} - Q_i = 0, & i \in S_L \end{cases} \tag{3}$$

$$\begin{cases} P_{Gi} - P_{Li} - P_i = 0, & i \in S_{Gs} \\ Q_{Gi} - Q_{Li} - Q_i = 0, & i \in S_{Gs} \end{cases} \tag{4}$$

$$Q_{Gi}^{\min} \leq Q_{Gi} \leq Q_{Gi}^{\max}, \quad i \in S_G \tag{5}$$

$$Q_{Ci}^{\min} \leq Q_{Ci} \leq Q_{Ci}^{\max}, \quad i \in S_C \tag{6}$$

$$V_i^{\min} \leq V_i \leq V_i^{\max}, \quad i \in S_G \cup S_L \tag{7}$$

$$P_{Gi}^{\min} \leq P_{Gi} \leq P_{Gi}^{\max}, \quad i \in S_{Gs} \tag{8}$$

$$T_l^{\min} \leq T_l \leq T_l^{\max}, \quad l \in S_T \tag{9}$$

Here

$$P_i = V_i \sum_{j \in S} V_j \left(G_{ij} \cos \theta_{ij} + B_{ij} \sin \theta_{ij} \right) \tag{10}$$

$$Q_i = V_i \sum_{j \in S} V_j \left(G_{ij} \sin \theta_{ij} - B_{ij} \cos \theta_{ij} \right) \tag{11}$$

Moreover, S is the subset of whole system buses, S_G is the set of all generator buses, S'_G is the set of renewable power generator buses (except the slack bus), S_{Gs} is the slack bus, where there is generally only one, S_L is the set of load buses, S_C is the index set of load buses with compensators, and S_T is the index set of transformer branches. Eq. 1 is the objective function, where V_i and θ_i are the voltage magnitude and bus angle at bus i, respectively, $\theta_{ij} = \theta_i - \theta_j$, and G_{ij} and B_{ij} are the real and imaginary parts of the admittance matrix, respectively. Eqs 2–4 are the power flow equations with interval uncertainties, where P_{Li} is the active load generation, P_{Gi} is the active power generation of slack bus, Q_{Gi} is the reactive power generation, Q_{Li} is the reactive load generation, Q_{Ci} is the reactive power compensation of the capacitor, P_i (Eq 10) and Q_i (Eq 11) are the injected active and reactive power at bus i, respectively. Eqs 5–9 are the security and operational constraints, where T_l is the tap position of the transformer. The lower and upper limits of the variables are identified with the superscripts "min" and "max," respectively.

All the variables in the RPOIU model can be divided into state variables and control variables. The state variables include the voltage magnitudes of the load buses, bus angle, and reactive power generation. The control variables include the generator voltage, transformer ratio, and reactive power compensation. Therefore, the formulation of the RPOIU model can be simplified by expressing the vector of state variables as X and the set of control variables as μ:

$$\min f(X, u) = [f^L, f^U]$$
$$s.t. \begin{cases} h(X, u) = [h^L, h^U] \\ g^{\min} \leq g(X, u) \leq g^{\max} \end{cases} \tag{12}$$

where $f(X, u)$ represents the real power losses of the RES power system, which is an interval and can be expressed as $[f^L, f^U]$, $[h^L, h^U]$ is the variation vector of the power input data in Eqs 2–4, and $h^L = h^U$ represent the deterministic input data. $g(X, u)$ represents all security and operational constraints, $g^{\min}$ and $g^{\max}$ are the lower and upper limits, respectively.

To express the model more conveniently, the bus order of the system is adjusted. Assuming that the slack bus is denoted by index 1, the number of all system buses is n, the number of generator buses is m (including the slack bus), the number of buses with the reactive power capacitor is r, and the number of transformers is k. The generator buses are denoted by index numbers in the range from two to m, the load buses are denoted by index numbers from $m+1$ to n, and the load buses with the reactive power capacitor are denoted by index numbers from

$m+1$ to $m + r$. Therefore, the vectors of state and control variables are expressed as $X = [P_{G1}Q_{G1}\cdots Q_{Gm}V_{m+1}\cdots V_n\theta_2\cdots\theta_n]^{\mathrm{T}}$ and $u = [V_2\cdots V_mQ_{Cm+1}\cdots Q_{Cm+r}T_1\cdots T_k]^{\mathrm{T}}$, respectively.

It is noted that the output of the reactive power compensator $Q_{Cm+1}\cdots Q_{Cm+r}$ and transformer ratios $T_1\cdots T_k$ are discrete, and the voltages of the generators $V_2\cdots V_m$ are continuous for the control variable vector u. There are interval variables within the state variable vector X. Accordingly, the RPOIU problem is a non-linear model that requires the hybrid processing of continuous and discrete variables.

3 Hybrid optimization for solving the RPOIU problem based on security limits method (SLM) and improved particle swarm optimization (IPSO)

The hybrid interval reactive power optimization algorithm adopts the SLM and IPSO to process the RPOIU problem alternately. The SLM is applied to deal with the continuous variables in the model to improve the efficiency and optimization effect of the model and ensure that the load voltage is not off-limit in all scenarios. The IPSO is applied to deal with the discrete variables in the model to avoid the problem that the continuous rounding of discrete quantities may lead to inaccurate or even infeasible solutions. It is noted that the power flow equations with interval uncertainties are solved by the optimizing-scenarios method (OSM) (Zhang et al., 2018c).

3.1 SLM-based continuous variable processing

The RPOIU model is solved by the SLM under the condition that the discrete variables Q_{Ci} and T_l are fixed at stable values to obtain the optimal continuous variables $V_i(i \in S'_G)$. The specific process of the SLM is to define the determined security limits, and the interior point method (IPM) is used to solve the deterministic RPO model, which is modified by the security limits. Then, the optimal continuous variable is acquired.

Since the inequality constraints (5)–(9) in the RPOIU model are all univariate, the model can be expressed as follows:

$$\min\ f(X,u) = \left[f^{\mathrm{L}}, f^{\mathrm{U}}\right]$$
$$s.t.\begin{cases} h(X,u) = \left[h^{\mathrm{L}}, h^{\mathrm{U}}\right] \\ X_{(1)}^{\min} \le X_{(1)} \le X_{(1)}^{\max} \\ u^{\min} \le u \le u^{\max} \end{cases} \tag{13}$$

where $X_{(1)}$ is a vector composed of the load bus voltage magnitudes and reactive power generation of the generator buses, and $X_{(1)}^{\max}$ and $X_{(1)}^{\min}$ are the upper and lower bounds,

respectively. The vector composed of bus angles and real power generation of the slack bus is denoted as $X_{(2)}$. Then, the vector of state variables is $X = [X_{(1)}^{\mathrm{T}}, X_{(2)}^{\mathrm{T}}]^{\mathrm{T}}$. $u^{\max}$ and $u^{\min}$ are the upper and lower bounds of the vector of control variables u, respectively.

To obtain the maximum radii of the interval variables, a vector consisting of the maximum radii of the state variables is defined as $\overline{\Delta X_{(1)}}$, which is formulated as follows and can be computed through the OSM and MCS (Zhang et al., 2018a):

$$\overline{\Delta X_{(1),i}} = \max_{u^{\min} \le u \le u^{\max}} \left\{ \Delta X_{(1),i} \,\middle|\, h(X,u) = \left[h^L, h^U\right] \right\} \tag{14}$$

where $\Delta X_{(1),i}$ is the radius of the ith variable in $X_{(1)}$.

According to $\overline{\Delta X_{(1)}}$, the security limits of the RPOIU model are defined as follows:

$$\begin{cases} AX_{(1)}^{\min} = X_{(1)}^{\min} + 2\overline{\Delta X_{(1)}} \\ AX_{(1)}^{\max} = X_{(2)}^{\max} - 2\overline{\Delta X_{(1)}} \end{cases} \tag{15}$$

Apparently, (15) represents the worst-case security bounds, while the difference between the security limit $AX_{(1)}^{\min}$ (or $X_{(1)}^{\max}$) and the original limit $X_{(1)}^{\max}$ (or $X_{(1)}^{\min}$) is close to $\Delta X_{(1)}$. In order to reduce the conservation of the proposed security limits, the interval ratio k^I is introduced to modify the definition of the security limits, and it is expressed as follows assuming that the control variables u are fixed at $u_0 = (u^{\min} + u^{\max})/2$:

$$k^I = \frac{x_0 - \underline{X_0}}{\overline{X_0} - \underline{X_0}} \tag{16}$$

where x_0 represents the state variables acquired by solving the equations $h(x,u_0) = (h^L + h^U)/2$, and $\underline{X_0}$ and $\overline{X_0}$ are the lower and upper bounds of the state variable intervals obtained by solving the equations $h(X,u_0) = [h^L, h^U]$.

Assuming that the interval ratio corresponding to $X_{(1)}$ is $k^I_{(1)}$, the security limits are modified as follows:

$$\begin{cases} SX_{(1)}^{\min} = X_{(1)}^{\min} + 2k^I_{(1)}\overline{\Delta X_{(1)}} \\ SX_{(1)}^{\max} = X_{(1)}^{\max} - 2\left(1 - k^I_{(1)}\right)\overline{\Delta X_{(1)}} \end{cases} \tag{17}$$

where $0 \le k^I \le 1$. It should be noted that there may be a violation when applying the modified security limits (17), because the interval ratio k^I is defined at the midpoint of the control variables, while the state variables are not usually obtained at x_0. Accordingly, the correction coefficients δ_u and δ_l are introduced to avoid the violation, and the corrected security limits are expressed as follows:

$$\begin{cases} S'X_{(1)}^{\min} = SX_{(1)}^{\min} + \delta_l X_{(1)} \\ S'X_{(1)}^{\max} = SX_{(1)}^{\max} - \delta_u X_{(1)} \end{cases} \tag{18}$$

where $\delta_l X_{(1)}$ is the extent that $X_{(1)}$ exceeds $X_{(1)}^{\min}$, and $\delta_u X_{(1)}$ is the extent that $X_{(1)}$ exceeds $X_{(1)}^{\max}$. If there is no violation, $\delta_u X_{(1),i} = 0$ or $\delta_l X_{(1),i} = 0$.

Therefore, the RPOIU model can be transformed to a deterministic RPO model through Eqs 15–18, expressed as follows:

$$\min\ f(\boldsymbol{x}, \boldsymbol{u})$$

$$s.t. \begin{cases} \boldsymbol{h}(\boldsymbol{x}, \boldsymbol{u}) = \boldsymbol{\xi} \\ S' \boldsymbol{X}_{(1)}^{\min} \le \boldsymbol{x}_{(1)} \le S' \boldsymbol{X}_{(1)}^{\max} \\ \boldsymbol{u}^{\min} \le \boldsymbol{u} \le \boldsymbol{u}^{\max} \end{cases} \quad (19)$$

where $\boldsymbol{\xi}$ is any vector in the interval $[\boldsymbol{h}^L, \boldsymbol{h}^U]$, and $f(\boldsymbol{x}, \boldsymbol{u})$ is the predictive value of the real power losses at the midpoint $(\boldsymbol{h}^L + \boldsymbol{h}^U)/2$. It is noted that if the state variables of deterministic model (16) are restricted within the security limits, the state variable intervals of the RPOIU model must be within their limits.

3.2 IPSO-based discrete variable processing

PSO is applied to deal with the discrete variables Q_{Ci} and T_l when solving the RPOIU model, and the continuous variables $V_i (i \in S'_G)$ are fixed. Each variable in the population is regarded as a particle in the PSO, and the position and speed of each particle can be obtained. It should be noted that the values of the state variables corresponding to the particles should satisfy the constraint condition. Accordingly, the fitness value corresponding to each particle can be acquired. The fitness value is the midpoint of the real power losses, and the corresponding fitness function has a penalty term.

The position of each particle in the search space is represented as $X_i = (x_1, x_2, \ldots, x_n)$, and the speed is represented as $V_i = (v_1, v_2, \ldots, v_n)$. The speed and position updating rules are expressed respectively as follows:

$$V_i = \omega \times V_i + c1 \times rand() \times (pBest_i - X_i) \\ + c2 \times rand() \times (gBest - X_i) \quad (20)$$

$$X_i = X_i + V_i \quad (21)$$

where $c1$ and $c2$ are the learning parameters, which are usually taken as 2, $rand()$ is a random number within $[0, 1]$, $pBest_i$ is the best solution of the ith particle, and $gBest$ is the global best solution of the whole population. ω is the inertia factor, which is formulated as follows by the linearly decreasing weight (LDW) strategy:

$$\omega(t) = (\omega_{ini} - \omega_{end})(Gk - t)/Gk + \omega_{end} \quad (22)$$

where ω_{ini} is the initial inertia weight, ω_{end} is the inertial weight at the maximum iteration number, Gk is the maximum number of iterations, and t is the current iteration time.

PSO is a global optimization method with a strong global search ability. However, it cannot make full use of the feedback information in the population, resulting in a poor local optimization ability, and the optimal value in the neighborhood of the $pBest_i$ is often ignored. In order to address this issue, a local search around $pBest_i$ is added in the PSO. The improvement of $pBest_i$ is determined as follows:
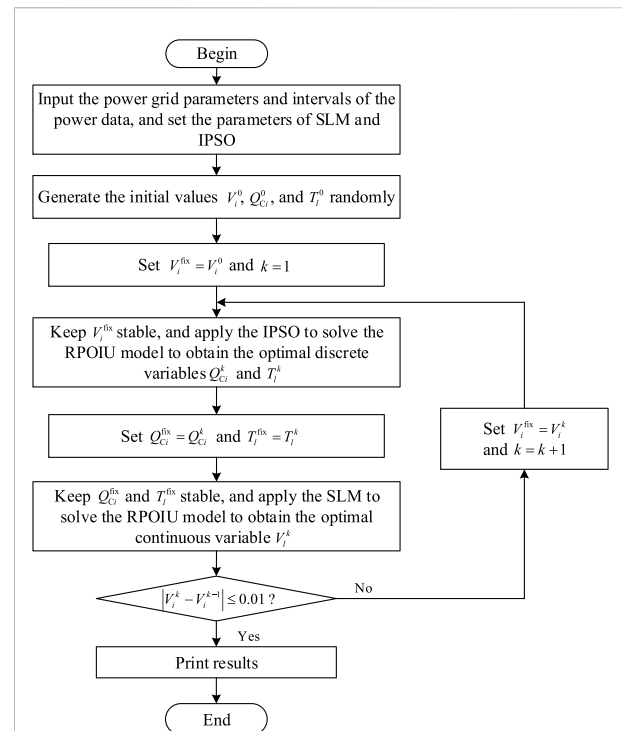
FIGURE 1
Procedure of the hybrid processing based on security limits method (SLM) and improved particle swarm optimization (IPSO) for solving the reactive power optimization with interval uncertainty (RPOIU) problem.

$$pbest_i = \begin{cases} pbest_i + \omega \cdot step \cdot rand(), rand < 0.5 \\ pbest_i - \omega \cdot step \cdot rand(), \text{else} \end{cases} \quad (23)$$

where $step$ is the initial step length of the local search. The relationship between the global and local optima is well balanced through the improvement of $pBest_i$, allowing the algorithm to avoid falling into local optima and improving the accuracy of the PSO.

The discrete variables are processed by a crossover operation in the IPSO, including the crossover between the particle and itself and the crossover between the particle and optimal individuals. The crossover process can be expressed as follows:

$$u_i = \begin{cases} cu_i^{\max} \\ cu_i + (1 - c)u_j \end{cases} \quad (24)$$

where u_i represents the discrete variables that require the crossover operation, c is a random number in $[0,1]$, $u_i^{\max}$ is the maximum of the transformer ratio and reactive power compensation, and u_j represents the optimal individuals including $pBest$ and $gBest$.

3.3 Hybrid optimization based on SLM and IPSO

The RPOIU problem is solved through the hybrid optimization of SLM and IPSO. The values of the continuous variables obtained by SLM are applied as fixed continuous variable values in the IPSO, and the values of the discrete variables obtained by the IPSO are applied as fixed discrete variable values in the SLM. The two methods are applied to solve the RPOIU model alternately, and the values of the control variables are interactive. The final solution of the control variables when solving the RPOIU problem is obtained when the control variable values obtained by the two methods are consistent. Because the discrete variable values obtained by the IPSO are directly used by the SLM, the values of the continuous variables are used for the termination criterion. For convenience, in the example below, when the difference of the continuous variable values between the two methods was less than 0.01, the control variables values were considered to be approximately consistent. Accordingly, the detailed procedure of the hybrid optimization based on the SLM and IPSO is described as follows. It is noted again that the intervals of the state variables are obtained by using the OSM, and they should satisfy the constraints. The flow chart of the proposed method is presented in Figure 1.

The steps of the proposed algorithm are as follows:

Step (1) Input the power grid parameters and intervals of the power data and set the parameters of SLM and IPSO.

Step (2) Generate the initial values V_i^0, Q_{Ci}^0, and T_l^0 randomly in the feasible region of the control variables.

Step (3) Set $V_i^{fix} = V_i^0$ and $k = 1$. Here, V_i^{fix} is the fixed value in the IPSO and k is the time of circulation.

Step (4) Keep V_i^{fix} stable and apply the IPSO to solve the RPOIU model to obtain the optimal discrete variables Q_{Ci}^k and T_l^k.

Step (5) Set $Q_{Ci}^{fix} = Q_{Ci}^k$ and $T_l^{fix} = T_l^k$, where Q_{Ci}^{fix} and T_l^{fix} are the fixed values in the SLM, respectively.

Step (6) Keep Q_{Ci}^{fix} and T_l^{fix} stable and apply the SLM to solve the RPOIU model to obtain the optimal continuous variable V_i^k.

Step (7) Determine whether the difference between V_i^k and V_i^{k-1} is less than 0.01. If it is, stop the iteration process and print results. Otherwise, set $V_i^{fix} = V_i^k$ and $k = k + 1$, then return to Step (4).

4 Simulation results

In this section, the simulations conducted for an IEEE 30-bus system are discussed to demonstrate the effectiveness and superiority of the hybrid optimization based on the SLM and IPSO in solving the RPOIU model problem. The results obtained by the proposed method are compared with those obtained by the SLM and IPSO. All parameters in the simulations were assigned values in a per-unit system, with 100 MV•A set as

FIGURE 2
Topology of IEEE 30-bus system.
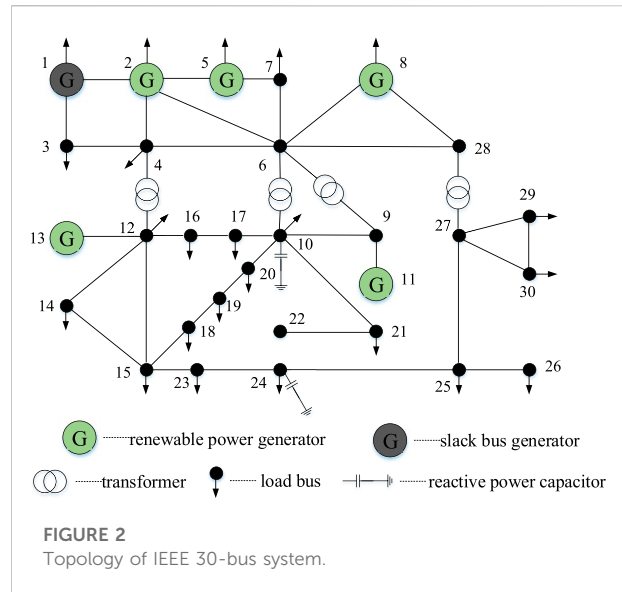
the base power. All calculations were conducted using MATLAB with a 2.9-GHz CPU and 8 GB of RAM.

The IEEE-30 bus system included six generators (five renewable power generators), four transformers, and two capacitors. The topology of IEEE 30-bus system is shown in Figure 2. The active power generation and related variable ranges of the generators are shown in Table 1. The settings of the capacitors are shown in Table 2. The voltage magnitudes of the load buses were limited to the range of [0.95, 1.05]. The transformer ratios were limited to the range of [0.9, 1.1] with a step of 0.05. The parameters of SLM and IPSO are set as follows. The iteration precision $\varepsilon = 10^{-4}$ in SLM. The number of iterations Size = 100, the population size M = 50, the learning factors c1 = c2 = 2, the initial inertia weight $\omega_{ini} = 0.9$, and the final inertia weight $\omega_{end} = 0.1$ in IPSO.

According to the settings specified in Tables 1, 2, the proposed hybrid optimization strategy based on the SLM and IPSO was used to solve the RPOIU model problem for the IEEE 30-bus system, and the results were compared with those obtained by the SLM and IPSO. The results obtained by the hybrid optimization, SLM, and IPSO for the IEEE 30-bus system are presented in Figures 3, 4. Figure 3A; Figure 4A show the voltage magnitude intervals acquired by the hybrid optimization, SLM, and IPSO. The interval bounds were all within the voltage limits. The boundary of state variable intervals obtained by the SLM was closer to the security limits than the hybrid optimization and IPSO. The intervals obtained by the hybrid optimization were close to that obtained by IPSO. Figure 3B; Figure 4B present the reactive power generation intervals acquired by the hybrid optimization, SLM, and IPSO. The interval bounds also were within the limits of the reactive power generation and the interval results obtained by the three methods were close for most of the buses. The results

TABLE 1 Active power generation and related variable ranges of generators in IEEE 30-bus system (p.u.).

Bus number	Active power generation	Reactive power output		Voltage magnitude	
		Lower bounds	Upper bounds	Lower bounds	Upper bounds
1	—	−0.2	1.5	0.9	1.1
2	0.8	−0.2	0.6	0.9	1.1
5	0.5	−0.15	0.63	0.9	1.1
8	0.2	−0.15	0.5	0.9	1.1
11	0.2	−0.1	0.4	0.9	1.1
13	0.2	−0.15	0.45	0.9	1.1

TABLE 2 Settings of capacitors in IEEE 30-bus system (p.u.).

Bus number	Lower bounds	Upper bounds	Variation step
10	0	0.5	0.1
24	0	0.1	0.02
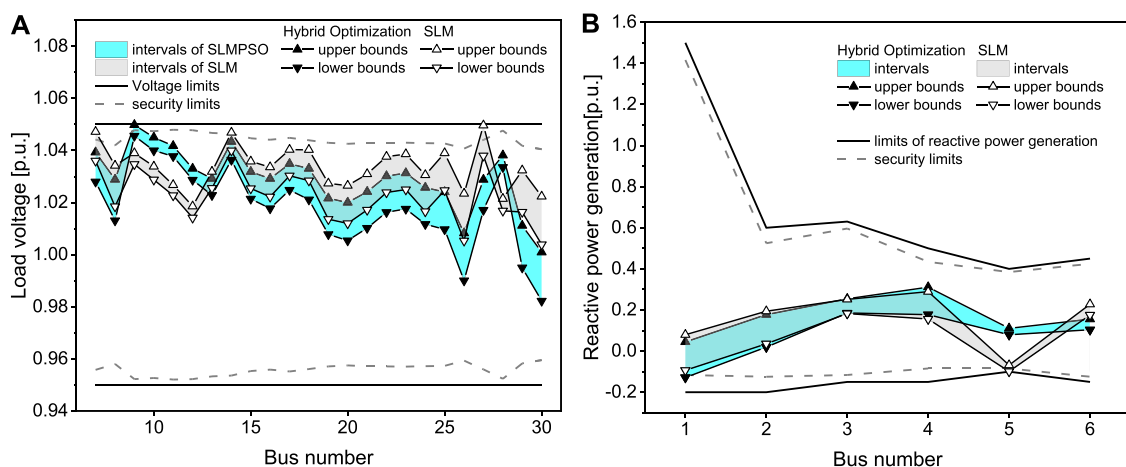
FIGURE 3
Results obtained by the hybrid optimization and SLM for the IEEE 30-bus system: **(A)** voltage magnitude and **(B)** reactive power generation.

verified the effectiveness of the proposed method for solving the RPOIU problems. The reasons for ensuring the interval results within voltage limits or reactive power generation limits were that the hybrid optimization and SLM both used the security limits to ensure the feasibility of the control variables, and the IPSO determined the feasibility of the control variables by judging whether the state variable intervals satisfied the constraints of the RPOIU model. Figure 5 presents the iterative convergence process of the three algorithms, and the

results are shown in Table 3. The hybrid optimization achieved the minimum real power loss, and the IPSO had a relatively large loss of active power compared to the other algorithms. This was because the hybrid optimization could obtain better solutions for the continuous and discrete variables, in contrast to the single optimization, which had difficulty dealing with mixed control variables. It demonstrated that the proposed method had higher accuracy than SLM and IPSO for solving RPOIU models.
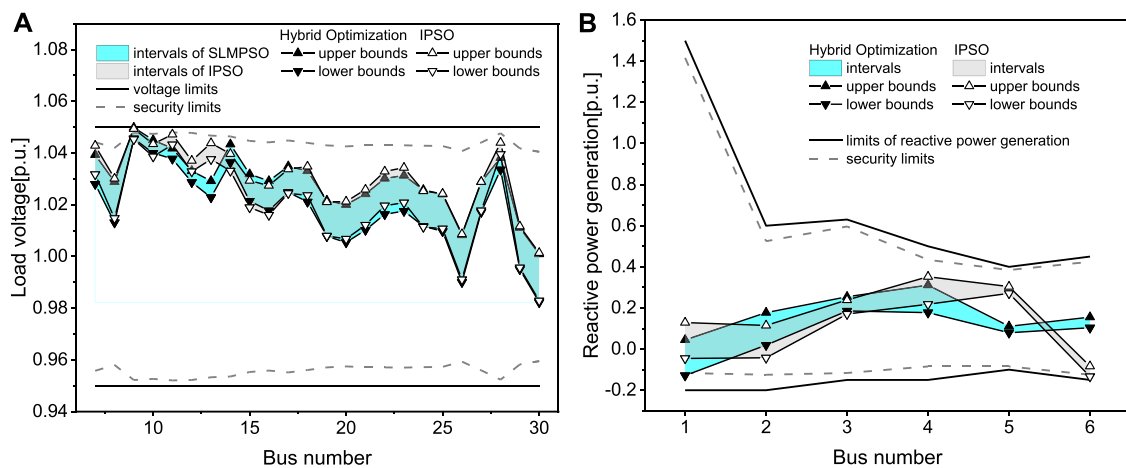
FIGURE 4
Results obtained by the hybrid optimization and IPSO for the IEEE 30-bus system: **(A)** voltage magnitude and **(B)** reactive power generation.
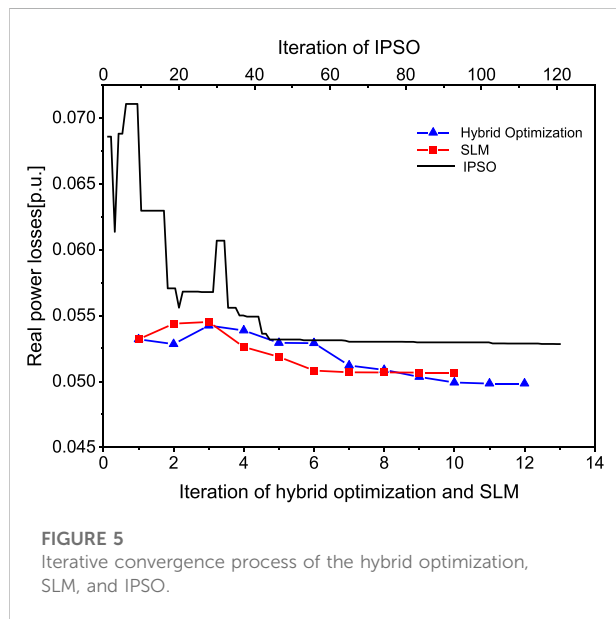
FIGURE 5
Iterative convergence process of the hybrid optimization, SLM, and IPSO.

TABLE 3 Values of real power losses optimized by the hybrid optimization, SLM, and IPSO.

	Hybrid Optimization	SLM	IPSO
Real power losses [p.u.]	0.0498	0.0507	0.0528

5 Conclusion

This paper proposed a data-driven hybrid interval reactive power optimization based on SLM and IPSO for solving the RPOIU problem to address the issue of dealing with mixed control variables. The large amount of uncertain data is expressed as intervals based on data-driven, and the control variable optimization is decomposed into continuous variable optimization and discrete variable optimization. For reducing the conservation of the interval algorithm, the SLM is applied for continuous variable optimization and the IPSO is applied for discrete variable optimization. The two processes are used to solve the RPOIU problem alternately and iteratively until the control variables optimized by the two processes are consistent.

The simulation results obtained by the proposed data-driven hybrid interval reactive power optimization for the IEEE 30-bus system were compared with those obtained by the SLM and IPSO. The proposed data-driven hybrid interval reactive power optimization acquired smaller real power losses than the SLM and IPSO, and it ensured that the interval bounds of the state variables remained within the constraints. The simulation results verified the effectiveness and advantages of the proposed method.

Data availability statement

The original contributions presented in the study are included in the article/supplementary material, further inquiries can be directed to the corresponding author.

Author contributions

DC conceptualized the study, contributed to the study methodology, and wrote the original draft. SQ

contributed to the writing—review and editing, data curation and investigation. QL contributed to study methodology, data analysis, wrote the original draft and writing-review. WX contributed to software and paper revision. XL contributed to investigation and writing—original draft. YL contributed to supervision and writing—review and editing. HY contributed to the revision of the paper. NK contributed to editing of the paper. All authors have read and agreed to the published version of the manuscript.

Funding

Conflict of interest

Authors DC, SQ, WX and XL were employed by the State Grid Hunan Electric Power Co., Ltd.

The remaining authors declare that the research was conducted in the absence of any commercial or financial relationships that could be construed as a potential conflict of interest.

The authors declare that this study received funding from State Grid Hunan Electric Power Company Limited. The funder had the following involvement in the study: Data curation, investigation, the study methodology, data analysis, and the writing-review\editing.

Publisher's note

All claims expressed in this article are solely those of the authors and do not necessarily represent those of their affiliated organizations, or those of the publisher, the editors and the reviewers. Any product that may be evaluated in this article, or claim that may be made by its manufacturer, is not guaranteed or endorsed by the publisher.

References

Arefifar, S. A., and Mohamed, Y. (2014). Probabilistic optimal reactive power planning in distribution systems with renewable resources in grid-connected and islanded modes. *IEEE Trans. Ind. Electron.* 61 (11), 5830–5839. doi:10.1109/tie.2014.2308144

Chang, S. Y., and Zhang, S. W. (2017). "Research on reactive power optimization algorithm of power system based on improved genetic algorithm," in Proceedings of the International Conference on Industrial Informatics - Computing Technology, Intelligent Technology, Industrial Information Integration (ICIICII), Wuhan, China, 02-03 December 2017, 21–24.

Ding, T., Yang, Q. R., Yang, Y. H., Li, C., Bie, Z. H., and Blaabjerg, F. (2018). A data-driven stochastic reactive power optimization considering uncertainties in active distribution networks and decomposition method. *IEEE Trans. Smart Grid* 9 (5), 4994–5004. doi:10.1109/tsg.2017.2677481

Gao, H. J., Wang, J. Y., Liu, Y. B., Wang, L. F., and Liu, J. Y. (2021). An improved ADMM-based distributed optimal operation model of AC/DC hybrid distribution network considering wind power uncertainties. *IEEE Syst. J.* 15 (2), 2201–2211. doi:10.1109/jsyst.2020.2994336

Jiang, C., Zhang, Z. G., Zhang, Q. F., Han, X., Xie, H. C., and Liu, J. (2014). A new nonlinear interval programming method for uncertain problems with dependent interval variables. *Eur. J. Operational Res.* 238 (1), 245–253. doi:10.1016/j.ejor.2014.03.029

Keerio, M. U., Ali, A., Saleem, M., Hussain, N., and Hussain, R. (2020). "Multi-objective optimal reactive power dispatch considering probabilistic load demand along with wind and solar power integration," in Proceedings of the International Conference on Smart Power & Internet Energy Systems (SPIES), Bangkok, Thailand, 15-18 September 2020, 502–507.

Khan, N. H., Wang, Y., Tian, D., Raja, M., Jamal, R., and Muhammad, Y. (2020). Design of fractional particle swarm optimization gravitational search algorithm for optimal reactive power dispatch problems. *IEEE Access* 8, 146785–146806. doi:10.1109/access.2020.3014211

Li, H., Liu, S., Lu, S., Chen, L., Yuan, X., and Huang, J. (2017). "Reactive power optimization of distribution network including photovoltaic power and SVG considering harmonic factors," in Proceedings of the International Conference on High Voltage Engineering and Power Systems (ICHVEPS), Denpasar, Indonesia, 02-05 October 2017, 219–224.

Liu, K. Y., Jia, D. L., He, K. Y., Zhao, T. T., and Zhao, F. Z. (2016). "Research on probabilistic reactive power optimization considering the randomness of distribution network," in Proceedings of the International Conference on Probabilistic Methods Applied to Power Systems (PMAPS), Beijing, China, 16-20 October 2016, 1–6.

Liu, S. Y., Ding, T., Bie, Z. H., Berizzi, A., and Hong, Y. (2017). "A second order cone based relaxation and decomposition algorithm for multi-period reactive power

optimization considering uncertain PV integration in active distribution networks," in Proceedings of the IEEE International Conference on Environment and Electrical Engineering, Milan, Italy, 06-09 June 2017, 1–6.

Liu, X., Zhang, P., Fang, H., and Zhou, Y. (2021). Multi-objective reactive power optimization based on improved particle swarm optimization with ε-Greedy strategy and Pareto Archive algorithm. *IEEE Access* 9, 65650–65659. doi:10.1109/access.2021.3075777

Liu, Y., Li, L., Li, Y., Li, M., Huang, M., Yu, H., et al. (2022). "Distributed photovoltaic cluster partition and reactive power optimization strategy based on BAS-IGA algorithm," in Proceedings of the Asia Conference on Power and Electrical Engineering (ACPEE), Hangzhou, China, 15-17 April 2022, 2198–2203.

Saraswat, A., Ucheniya, R., and Gupta, Y. (2020). "Two-stage stochastic optimization for reactive power dispatch with wind power uncertainties," in Proceedings of the International Conference on Computation, Automation and Knowledge Management (ICCAKM), Dubai, United Arab Emirates, 09-10 January 2020, 332–337.

Shri, S. H., Essa, M. B., and Mijbas, A. F. (2021). "Solving reactive power optimization problem using weight improved PSO algorithm," in Proceedings of the International Conference on Electrical, Computer, Communications and Mechatronics Engineering (ICECCME), Mauritius, Mauritius, 07-08 October 2021, 1–5.

Zhang, C., Chen, H., Hua, D., Shi, K., Liu, Y., Wang, X., et al. (2018a). "Solution of interval reactive power optimization model through defining security limits," in Proceedings of the International Conference on Power System Technology (POWERCON), Guangzhou, China, 06-08 November 2018, 1384–1389.

Zhang, C., Chen, H. Y., Liang, Z. P., Guo, M. L., Hua, D., and Ngan, H. (2018c). Reactive power optimization under interval uncertainty by the linear approximation method and its modified method. *IEEE Trans. Smart Grid* 9 (5), 4587–4600. doi:10.1109/tsg.2017.2664816

Zhang, C., Chen, H. Y., Ngan, H. W., Liang, Z. P., Guo, M. L., and Hua, D. (2017). Solution of reactive power optimisation including interval uncertainty using genetic algorithm. *IET Gener. Transm. &amp. Distrib.* 11 (15), 3657–3664. doi:10.1049/iet-gtd.2016.1195

Zhang, C., Chen, H. Y., Shi, K., Liang, Z. P., Mo, W. K., and Hua, D. (2019). A multi-time reactive power optimization under interval uncertainty of renewable power generation by an interval sequential quadratic programming method. *IEEE Trans. Sustain. Energy* 10 (3), 1086–1097. doi:10.1109/tste.2018.2860901

Zhang, C., Chen, H. Y., Shi, K., Qiu, M., Hua, D., and Ngan, H. (2018b). An interval power flow analysis through optimizing-scenarios method. *IEEE Trans. Smart Grid* 9 (5), 5217–5226. doi:10.1109/tsg.2017.2684238

Online prediction and control of post-fault transient stability based on PMU measurements and multi-task learning

Tingjian Liu[1], Zhiyuan Tang[1]*, Yuan Huang[1], Lixiong Xu[1] and Yue Yang[2]

[1]College of Electrical Engineering, Sichuan University, Chengdu, China, [2]Electric Power Research Institute of Guangdong Power Grid Co. Ltd, Guangzhou, China

The combined usage of phasor measurement units and machine learning algorithms provides the opportunity for developing response-based wide-area system integrity protection scheme against transient instability in power systems. However, only the transient stability status is usually predicted in the literature, which is not enough for real-time decision-making for response-based emergency control. In this paper, an integrated approach is proposed. The GRU-based predictor is firstly proposed for post-disturbance transient stability prediction. On this basis, a multi-task learning framework is proposed for the identification of unstable machines and also the estimation of generation shedding. Case study on the IEEE 39-bus system demonstrates that, apart from the basic task of transient stability prediction, the proposed GRU-based multi-task predictor can predict the grouping of unstable machines correctly. Moreover, based on the estimated amount of generation shedding, the generated remedial control actions can retain the synchronism of the power system.

1 Introduction

Transient stability refers to the ability of power systems to maintain synchronism when subjected to large disturbances (Hatziargyriou et al., 2021). When a power system is at risk of losing the transient stability, if no proper actions are taken, it may cause cascading outages, uncontrolled network splitting, and eventually wide-spread disruption of electricity supply (Andersson et al., 2005). Therefore, maintaining the secure operation of power systems is of great concern to transmission system operators (TSOs). To protect power systems against transient instability, a considerate amount of research efforts has been spent on developing advanced approaches in the field of power engineering.

Online transient stability assessment (TSA) is the first and foremost step for instability prevention as it provides the TSOs with the ability of situation awareness. The

conventional method for TSA is the time-domain simulation (TDS) (Kundur et al., 1994). However, TDS is not capable for real-time stability assessment as solving the high-dimensional differential algebraic equations (DAEs) of an interconnected transmission system is computationally burdensome. Also, TDS cannot provide the information on the stability margin and the countermeasures against the unstable scenarios. To address these two drawbacks of the TDS method, transient energy function (TEF) methods (Pai, 1989), also known as direct methods, have been studied since 1980s. By comparing the kinetic energy at the fault clearing time with the critical energy, the stability status and the energy margin can be assessed without the need of simulating the post-fault trajectories by the TDS. While the critical energy is related with the controlling unstable equivalent point (CUEP) (Chiang, 2011), the CUEP of an ongoing fault contingency is usually hard to identify in real-time manner.

Both the TDS and the TEF are model-driven methods for TSA. With the development of phasor measurement units (PMUs), data-driven methods are considered as the prospective alternative to the model-driven methods. Emergency single machine equivalent (E-SIME) approach (Pavella et al., 2000) attempts to compute the energy margin based on the synchronized PMU measurements. But still, the critical unstable mode should be predicted correctly so as to ensure the accuracy of this approach. The maximal Lyapunov exponent (MLE) is proposed in (Dasgupta et al., 2015) to detect the divergence or convergence of the generator rotor angle trajectories. But the MLE may oscillate from positive and negative values before the disturbed power system settles down, which thus requires a sufficiently long monitoring window to avoid the misclassification of stability status. In recent years, encouraged by the success of artificial intelligence (AI) in the fields such as computer vision and nature language processing, AI-based approaches are gaining more attentions.

Machine learning (ML) algorithms including the decision trees (DTs) (Yang et al., 2017; Cremer et al., 2019), support vector machines (SVMs) (Wang et al., 2016; Hu et al., 2019), neural networks (NNs) (AL-Masri et al., 2013; Zheng et al., 2017), and ensemble predictors (Kamwa et al., 2010; Qiu et al., 2019) have been proposed for power system security assessment. The existing literature on this topic can be sorted into two categories, which are *Pre-disturbance Stability Assessment* and *Post-disturbance Stability Assessment*, depending on whether the post-disturbance measurement is used as the input features. In this paper, post-disturbance stability assessment is studied. At the early stage of the researches on post-disturbance stability assessment, swallow predictors, such as SVMs and single-layer NNs, are used. Considering that the natural characteristics of power system transient stability is highly nonlinear, feature extraction should be performed before developing the predictor for stability assessment. While some literature

adopts the wide-area severity indexes as the input features based on the expects' experience (Kamwa et al., 2010; Wang et al., 2016), voltage templates-based (Rajapakse et al., 2010) and Shapelet learning-based (Zhu et al., 2016; Zhu and Hill, 2022) feature extraction schemes are proposed to improve the performance of the stability predictors. The emerging deep learning algorithms can be used for representation learning without the need of feature engineering. In (Yu et al., 2018), the long short-term memory (LSTM)-based recurrent learning algorithm is proposed to develop a time-adaptive transient stability framework. In (Zhu et al., 2020), a convolution neural network (CNN)-based hierarchical learning machine is proposed to learn transient temporal correlations for online TSA.

When the impending instability status is detected, remedial actions, also termed as system integrity protection scheme (SIPS), should be implemented to retore the synchronism of the power system. In (Bhui and Senroy, 2017), a look-up table of modes of disturbance is proposed to assist the online computation of the CUEP and the critical energy for TEF methods. Following the E-SIME framework, the pair-wise relative energy function is proposed in (Gou et al., 2017) to identify the critical unstable mode and to design the emergency generation shedding scheme for transient instability prevention. Although AI-based pre-disturbance stability predictors have been widely studied and employed to develop the integrated preventive control schemes, such as (Xu et al., 2012; Liu et al., 2014; Liu et al., 2020), AI-based approaches for emergency control against post-disturbance transient instability are rarely reported to the best of the authors knowledge. The decision trees are used to trigger the controlled islanding (Senroy, 2006) and the power regulation of HVDC intertie (Gao and Rovnyak, 2011). But these control actions are determined by offline analysis. In (Paul et al., 2020), the LSTM network is also used as the instability detector and then the remedial actions are determined by the continual monitoring of the out-of-step generators based on the individual machine transient energy function.

With the ever-increasing penetration of renewable energies, TSOs are facing with greater challenges in protecting power system. On one hand, it is more difficult to implement preventive control due to the inadequate resources for operating condition regulation. On the other hand, the intermittency of renewable energies will inevitably increase the variation of the real-time operating condition, which also make it more difficult to design the fixed system integrity protection scheme, that is, effective for different scenarios. Therefore, response-based SIPS should be developed to address the above-mentioned challenges. This paper attempts to fill the gap between PMU-based post-disturbance transient stability prediction and AI-driven real-time decision making of emergency generation shedding in order to develop an integrated wide-area protection and control scheme. The gated recurrent unit (GRU)-based RNN is proposed as the base predictor. As is discussed, the decision-making for post-disturbance transient stability includes the
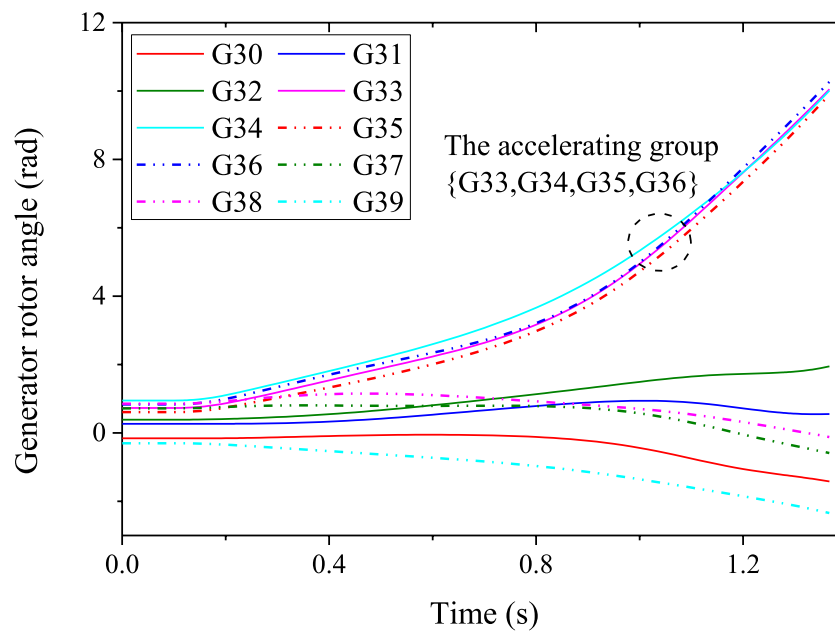
FIGURE 1
The generator rotor angle trajectories under the fault contingency.

prediction of the stability status, the unstable mode and the needed amount of generation shedding. Considering that these three predictive targets are basically correlated tasks, a multi-task learning (MTL) framework is proposed. Case studies on the IEEE 39-bus system is presented to demonstrate the effectiveness of the proposed approach.

The rest of this paper is organized as follows. Problem description is provided in Section 2. The gated recurrent units-based recurrent neural network is introduced in Section 3. The multi-task learning scheme for integrated real-time decision-making of transient stability protection is proposed in Section 4. Case studies on the IEEE 39-bus system is presented to illustrate the effectiveness of the proposed scheme in Section 5. Finally, conclusions are drawn in Section 6.

2 Problem description

As is discussed, transient stability relates to whether the power system can maintain synchronism when subjected to a large disturbance. The disturbance, such as a short-circuit fault, will lead to the imbalance of the mechanical torque and the electrical torque of each of the generators. Then some of the generators will increase their rotor speed with respect to the others, which forms the accelerating group and the decelerating group of generators. The generator rotor angle trajectories under a fault contingency in the IEEE 39-bus system is shown in Figure 1. As can be seen from Figure 1, the generators {G33,

G34, G35, G36} together form the accelerating group, while the rest of generators form the decelerating group.

Based on the idea of center of inertia (COI), the accelerating group and the decelerating group of generators can be reduced to two equivalent machines by Eq. 1:

$$
\begin{cases}
\delta_S = \dfrac{\left(\sum_{i \in S} M_i \delta_i\right)}{M_S, M_S} = \sum_{i \in S} M_i \\[3mm]
\delta_A = \dfrac{\left(\sum_{j \in A} M_j \delta_j\right)}{M_A, M_A} = \sum_{j \in A} M_j.
\end{cases}
\tag{1}
$$

After the grouping of the generators, the SIngle Machine Equivalent (SIME) can be further determined by Eq. 2:

$$
\begin{cases}
\delta \quad = \delta_S - \delta_A \\[2mm]
M \quad = \dfrac{M_S M_A}{(M_S + M_A)} \\[3mm]
\dfrac{d^2 \delta}{dt^2} = M^{-1} (P_m - P_e),
\end{cases}
\tag{2}
$$

where

$$
P_m = (M_S + M_A)^{-1} \left(M_A \sum_{i \in S} P_{mi} - M_S \sum_{j \in A} P_{mj} \right), \tag{3}
$$

$$
P_e = (M_S + M_A)^{-1} \left(M_A \sum_{i \in S} P_{ei} - M_S \sum_{j \in A} P_{ej} \right). \tag{4}
$$

After computing the SIME of the multi-machine power system, the conventional equal-area criterion (EAC) can be used to compute the energy margin-based transient stability index (TSI) and to estimate the necessary amount of

FIGURE 2
Demonstration of generation shedding control based on the EAC criterion.

FIGURE 3
The structure of the GRU.
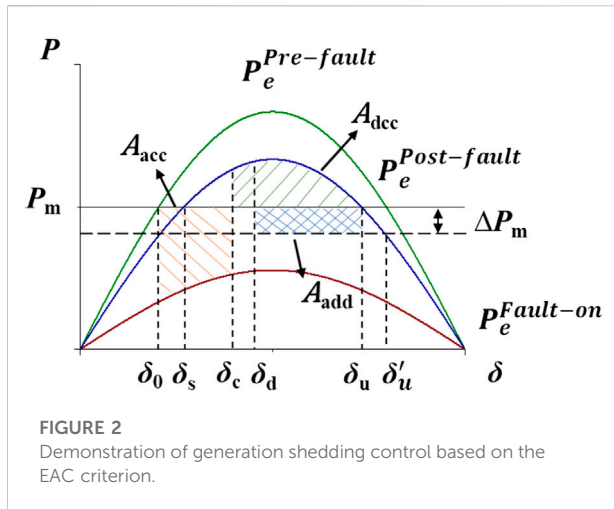
generation shedding for instability prevention when the system is about to lose synchronism. Figure 2 depicts the EAC criterion (Kundur et al., 1994; Gou et al., 2017). If the decelerating area A_{dec} is smaller than the accelerating area A_{acc}, the system will lose synchronism when the operating point travels through the unstable equivalent point (UEP), which refers to the operating point with the equivalent rotor angle to be δ_u.

In Figure 2, δ_0 denotes the rotor angle of the SIME at pre-fault condition, δ_s is the rotor angle relating with the stable equilibrium point of the post-fault condition, while δ_u is the one relating with the unstable equilibrium point of the post-fault condition without generation shedding. δ_c is the rotor angle of the SIME at fault clearing time and δ_d is the rotor angle of the SIME when generation shedding is implemented. Accordingly, δ_u' is the rotor angle relating with the unstable equilibrium point after generation shedding. Respectively, $P_e^{\text{Pre-fault}}$, $P_e^{\text{Fault-on}}$, and $P_e^{\text{Post-fault}}$ denote the mechanical power output of the SIME for pre-fault condition, fault-on condition and post-fault condition. $\triangle P_{\text{shed}}$ denotes the amount of generation shedding and A_{add} is the increased decelerating area caused by generation shedding.

For unstable cases, generation shedding should be implemented to make the SIME decelerates before travelling through the unstable equivalent point. Based on the EAC, the necessary amount of generation shedding P_{shed} can be computed by Eq. 5 (Pavella et al., 2000; Gou et al., 2017):

$$P_{\text{shed}} = \frac{A_{\text{acc}} - A_{\text{dec}}}{\delta_u' - \delta_d} \approx \frac{E_{KE}(\delta_u)}{\delta_u - \delta_d} = \frac{(1/2)M[\omega(t_u)]^2}{\delta_u - \delta_d}, \qquad (5)$$

where $E_{KE}(\delta_u)$ denotes the kinetic energy of the SIME at the UEP. ω is the rotor speed of the SMIE and $\omega(t_u)$ denotes the value at the UEP.

The earlier the control decision is made; the less generation shedding is needed. However, for E-SIME method and its derivatives, it is usually difficult to identify the critical
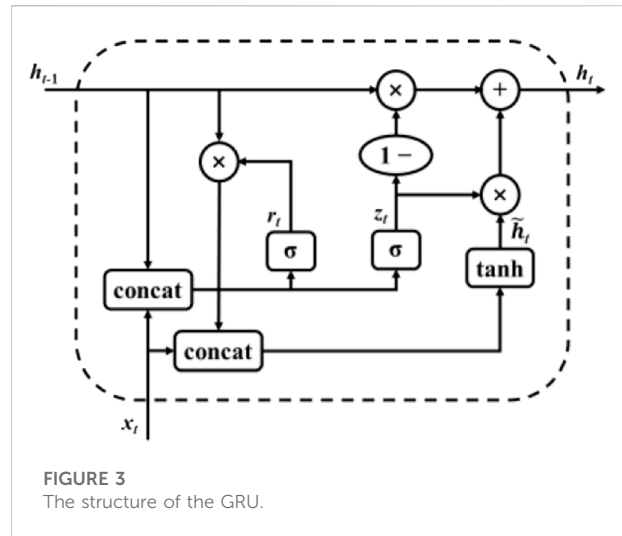
unstable mode and the relative UEP. To tackle this problem, this paper tries to make the best of deep learning algorithms, which have the attractive capability of nonlinear representation and real-time decision-making. By learning from the offline generated knowledge base, the deep learning-based predictor not only predict the stability status, but further address the problems including the grouping of unstable generators and the estimation of the amount of generation shedding.

3 GRU-based RNN for post-fault transient stability prediction

3.1 Brief introduction of gated recurrent unit

As the PMU measurements have the form as temporal sequential data, recurrent neural networks (RNNs) can be used as the predictor for post-fault transient stability assessment. The gated recurrent units (GRU)-based RNN is used in this paper as the base predictor. The structure of the GRU is shown in Figure 3.

GRU consists of the reset gate, the update gate and the state unit. The reset gate $\mathbf{r}_t$ decides whether the previous hidden state $\mathbf{h}_{t-1}$ is ignored and is computed by Eq. 6:

$$\mathbf{r}_t = \sigma\left(\mathbf{W}^{(r)}\mathbf{x}_t + \mathbf{U}^{(r)}\mathbf{h}_{t-1}\right). \qquad (6)$$

The update gate $\mathbf{z}_t$ selects whether the hidden state is to be updated and is computed by Eq. 7:

$$\mathbf{z}_t = \sigma\left(\mathbf{W}^{(z)}\mathbf{x}_t + \mathbf{U}^{(z)}\mathbf{h}_{t-1}\right). \qquad (7)$$

The actual activation of the state unit $\mathbf{h}_t$ is then computed by Eq. 8:

FIGURE 4
The proposed GRU-based transient stability predictor.

FIGURE 5
The hard parameter sharing structure for transient stability prediction and control.
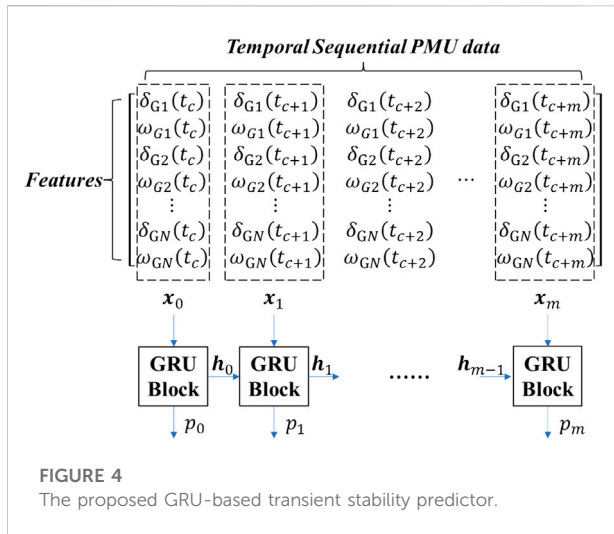
$$\mathbf{h}_t = \mathbf{z}_t \odot \mathbf{h}_{t-1} + (1 - \mathbf{z}_t) \odot \mathbf{h}_t', \quad (8)$$

where

$$\mathbf{h}_t' = \tanh\left(\mathbf{W}^{(o)}\mathbf{x}_t + \mathbf{r}_t \odot \mathbf{U}^{(o)}\mathbf{h}_{t-1}\right). \quad (9)$$

In Eqs 6–9, $\mathbf{x}_t$ is the input at current stage. $\odot$ denotes the element-wise product. $\sigma(\cdot)$ and $\tanh(\cdot)$ respectively denote the *sigmoid* activation function and the *tanh* activation function.

3.2 GRU-based post-fault transient stability prediction

The proposed GRU-based transient stability predictor is demonstrated in Figure 4. Assuming that PMUs are equipped at all the generator buses, the rotor angle and the rotor speed of all the generators can be measured by PMUs and then are used as the sequential input for the predictor. Considering the complexity and the nonlinearity of transient stability problem, multi-layer GRU block is used as the predictor. Also, the one-hot encoding is used as the label for post-disturbance transient stability status classification. $y_s = [1, 0]$ indicates that the sample is stable, otherwise, $y_s = [0, 1]$ is referred to as unstable. In this case, the output of the GRU-based predictor is set to be two-dimensional and is preprocessed by *softmax* activation function. With the output of the GRU-based predictor to be $p_s = [p_s(0), p_s(1)]$, following the idea of time-adaptive prediction as in (Yu et al., 2018), decision of transient stability classification is made by Eq. 10:

$$prediction = \begin{cases} Stable, \ p_s(0) - p_s(1) \geq 0.9 \\ Unstable, \ p_s(1) - p_s(0) \geq 0.9, \\ No\ decision, otherwise \end{cases} \quad (10)$$
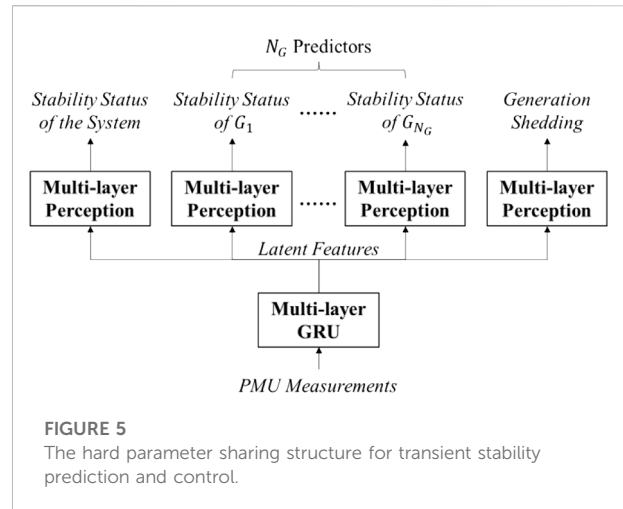
4 Multi-task learning-based framework for transient stability prediction and control

In Section 3, the GRU-based predictor is proposed for post-disturbance transient stability classification. In this section, the predictor is extended for the integrated prediction and control against transient instability by multi-task learning (MTL).

There are a handful of examples of multi-task learning, such as natural language processing (Collobert and Jason, 2008) and computer vision (Girshick, 2015). Although one can handle these tasks in the separated way, i.e., a specific neural network is developed for each task, multi-task learning aims to improve the generalization by leveraging domain-specific information contain in the training signals of related tasks (Ruder, 2017). In practical power systems, there are some transmission interfaces that are correlated in terms of the dominated stability mode. In (Huang et al., 2019), multi-task learning is proposed to train a compact model to evaluate the total transfer capacity (TTC) of these correlated interfaces in the united manner.

The prediction of post-fault stability status, the identification of critical unstable machines, and the estimation of generation shedding are related tasks. Therefore, multi-task learning is used to fulfill the above-mentioned tasks in order to develop the adaptive PMU-based system integrity protection scheme against transient instability. The structure of the multi-task deep neural network is demonstrated in Figure 5. The GRU-based RNN is used to extract the latent features following the basic MTL structure of hard parameter sharing. After extracting the latent features, task-oriented multi-layer perception model are developed to fulfill different tasks. To train the parameters of the multi-task deep neural network, the loss function is defined as is in (11):

$$\mathcal{L} = \mathcal{L}_{TSA} + \sum_{i=1}^{N_G} \mathcal{L}_{Gi} + \mathcal{L}_{GS}, \qquad (11)$$

where

$$\mathcal{L}_{TSA} = \frac{1}{N_S} \sum_s -\left[y_s^{TSA} \log p_s^{TSA} + (1 - y_s^{TSA}) \log p_s^{TSA} \right], \qquad (12)$$

$$\mathcal{L}_{Gi} = \frac{1}{N_S} \sum_s -\left[y_s^{Gi} \log p_s^{Gi} + (1 - y_s^{Gi}) \log p_s^{Gi} \right], \qquad (13)$$

$$\mathcal{L}_{GS} = \frac{1}{N_S} \sum_s \left[y_s^{GS} - p_s^{GS} \right]^2. \qquad (14)$$

The subscript s denotes the serial number of a training sample and N_S is the total number of training samples. $\mathcal{L}_{TSA}$ denotes the cross-entropy loss function for transient stability classification. y_s^{TSA} is the label of stability status for the sth sample, while p_s^{TSA} is the related prediction. $\mathcal{L}_{Gi}$ denotes the cross-entropy loss function for the ith generator. y_s^{Gi} is the label that indicates whether the ith generator belongs to the accelerating group for the sth sample, while p_s^{Gi} is the related prediction. $\mathcal{L}_{GS}$ denotes the mean square error (MSE) for generation shedding estimation. y_s^{GS} denotes the amount of generation shedding and is computed by offline SMIE analysis, while p_s^{GS} is the related prediction.

The pseudo-code of the training procedure is demonstrated in Algorithm I.

5 Implementation of the proposed method

The proposed scheme includes two stages, namely the offline model training stage and the online decision-making stage.

5.1 Offline data generation and model training

During the offline stage, data generation is firstly performed. Historical operating conditions (OCs) and stochastic OCs that are simulated by Monte-Carlo sampling of supply and demand are collected to form the database of OCs. For each OC, contingency screening is performed to generate the knowledge base of transient stability. Credible contingencies, including but not limited to N-1 and N-2 fault contingencies, are considered during the generation of knowledge base. The simulated post-disturbance generator rotor angle trajectories are used to simulate the PMU measurements. The stability status is labeled according to whether the maximum separation of rotor angle exceeds 360°. For those unstable instances, the SIME method is used to determine the grouping of unstable generators and the amount of generation shedding. With the generated knowledge base, the multi-task deep neural network is trained and stored for online application.

FIGURE 6
The network structure of the testing system.

5.2 Online instability prediction and emergency control

During the online stage, when a fault signal is received, the PMU measurements are collected and are used as the input of the well-trained predictor. The output of transient stability status is checked firstly. If the prediction of stability status is stable, wait for the input of next time step. If the monitoring duration exceed the maximum monitoring window, the protection scheme will disarm and wait for next fault signal. If the prediction of stability status is unstable, the outputs of generator-wise stability status are collected to determine the grouping of accelerating generators. If the unstable mode is multi-machine unstable mode, these unstable generators are ranked according to the output p_s^{Gi}. Then according to the output of generation shedding, the unstable generators are added to the control actions one-by-one until the necessary amount of generation shedding is met by this control action. If the necessary amount of generation shedding is higher than a pre-set threshold, emergency generation shedding may not be the proper countermeasure for transient stability protection. In this case, other measures, such as controlled islanding and load shedding, should be used instead. Otherwise, the generation shedding actions are implemented to retain the synchronism of the disturbed power system.

6 Case studies

The proposed scheme is illustrated by case study on the IEEE 10-machine 39-bus system (Pai, 1989). The network structure of

the testing system is shown in Figure 6. Power flow and time-domain simulation are implemented by using PSD-BPA, which is the power system analysis package developed by the China Electric Power Research Institute (CEPRI). It is assumed that all the generator buses are equipped with PMUs so as to enable post-fault transient stability prediction and real-time decision-making for emergency generation shedding control. Also, all the power plants are assumed to be formed by five identical units that operate in parallel. The maximum number of units that allow to be shed is four so that at least one unit should be connected to the power grid.

6.1 Data generation

Operating conditions of different loading scenarios, which varies from 80% to 120% of base condition with the increment of 5%, are firstly generated. On this basis, the *N*-1 operating scenarios are simulated by randomly selecting one of the transmission lines to be out of service. These normal OCs and *N*-1 OCs are combined to form the database of OCs. Three-phase short-circuit faults, which are isolated by opening the relative transmission line, are considered as credible contingencies. Fault location is randomly chosen at 0%, 50% and 100% of the length of the transmission line, while the fault clearing time is randomly set between 6 cycles and 9 cycles. 5000 samples are generated. For performance evaluation, the samples are separated by 60:20:20, which are then used as the training set, the validation set, and the testing set of samples.

6.2 Development of GRU-based predictor

After knowledge base generation, the GRU-based predictor is trained based on the MTL-based framework proposed in Section 4. As is proposed, the post-disturbance PMU measurements of generator rotor angles and rotor speeds are used as the input features. The hyperparameters of the predictor is determined by trial and error. In this case study, the GRU block consists of two layers and the number of hidden states is set to be 1024. The MLP blocks for all the predicting tasks consists of two hidden layers and the number of hidden states is also set to be 1024. The training epoch is set to be 200, while early stopping is enabled by using the validation data.

6.3 Performance on post-disturbance transient stability assessment

The performance of the well-trained predictor on post-disturbance transient stability assessment is evaluated by

using the testing data. The maximum monitoring window is set as six cycles after fault clearing. Two cases, which are fixed-time prediction and time-adaptive prediction, are studied.

1) Fixed-time prediction

In the first case, the post-disturbance PMU measurements from the fault clearing time to the end of the maximum monitoring window are collected and used as the input of the predictor. Numerical results of the confusion matrix in transient stability classification are shown in Table 1. The overall classification accuracy is 99.4%.

2) Time-adaptive prediction

In the second case, the performance of the time-adaptive prediction scheme proposed in Section 3.2 is validated. The testing results of time-adaptive prediction is shown in Table 2. The overall classification accuracy is 99.6%, which is comparable to fixed-time prediction. However, 29.8% of unstable instances can be assessed in three cycles after fault clearing, which helps to enable faster response for remedial control against the impending instability of the power system.

3) Comparison with the task-separated predictor

To demonstrate the effectiveness of the proposed MTL framework, the comparison between the MTL-based predictor and the task-separated predictor is studied. The numerical results are shown in Table 3. False alarm (FA) refers to the ratio of stable cases that are misclassified as unstable, while false dismissal (FD) refers to the ratio of unstable cases that are misclassified as stable. As can be seen from Table 3, the proposed MTL-based predictor achieves higher accuracy in transient stability classification comparing with the separated predictor, that is, trained without the consideration of related tasks. As transient instability will lead to catastrophic blackout, lower value of false dismissal is preferred. In this regard, the proposed MTL-based predictor also performs better that the task-separated predictor.

Apart from post-disturbance transient stability classification, the MTL-based predictor is used for real-time decision-making for mitigation of the impending transient instability. A thorough test on the performance on instability mitigation is investigated. Numerical results are shown in Table 4. There are 357 unstable testing instances. All these unstable instances are correctly classified as unstable. Based on the decision-making scheme proposed in Section 5.2, 337 instances are stabilized by implementing the generated

TABLE 1 The confusion matrix in transient stability classification for fixed-time (6 cycles) prediction.

		Prediction of the testing data	
		Classified as Stable	*Classified as Unstable*
Stability Status of the Testing data	*Stable*	638/643 (99.22%)	5/643 (0.78%)
	Unstable	1/357 (0.28%)	356/357 (99.72%)

TABLE 2 The testing results of time-adaptive prediction in transient stability classification.

Decision-making time (cycles)	Instances to be classified	Instances with classification decision	Correct	Incorrect
3	1000	298	298	0
4	702	22	22	0
5	680	11	11	0
6	669	669	665	4

TABLE 3 Comparison between the MTL-based predictor and the task-separated predictor.

Metrics	MTL-based predictor (%)	Task-separated predictor (%)
Accuracy	99.6	98.8
False Alarm	0.62	0.16
False Dismissal	0.00	3.18

Performance on Real-time Decision-making for Instability Mitigation.

TABLE 4 Numerical results on real-time decision-making for instability mitigation.

Number of unstable testing instances	Instances that are correctly predicted	Instances that are stabilized
357	357(100.0%)	337 (94.4%)

remedial actions. So, the overall percentage of success decision-making is 94.40%.

The procedure of decision-making against transient instability is demonstrated by an unstable testing instance. The rotor angle trajectories without any control actions are shown previously in Figure 1. In this case, the unstable status is predicted at three cycles. After stability prediction, unstable machine identification is enabled by the outputs p_s^{Gi} of the MTL-based predictor. Numerical results are shown in Figure 7 and accordingly the generators (G33, G34, G35, G36) are identified as unstable machines. Then the estimated amount of generation shedding is 558.96 MW. To meet this requirement of generation shedding, 4 units at Bus-36 and 1 unit at Bus-35 are disconnected from the power grid. The power angle trajectories after the control actions are shown in Figure 8. As can be seen from Figure 8, after disconnecting the above-mentioned units, the rest of generators can restore synchronism and the impending instability is mitigated.
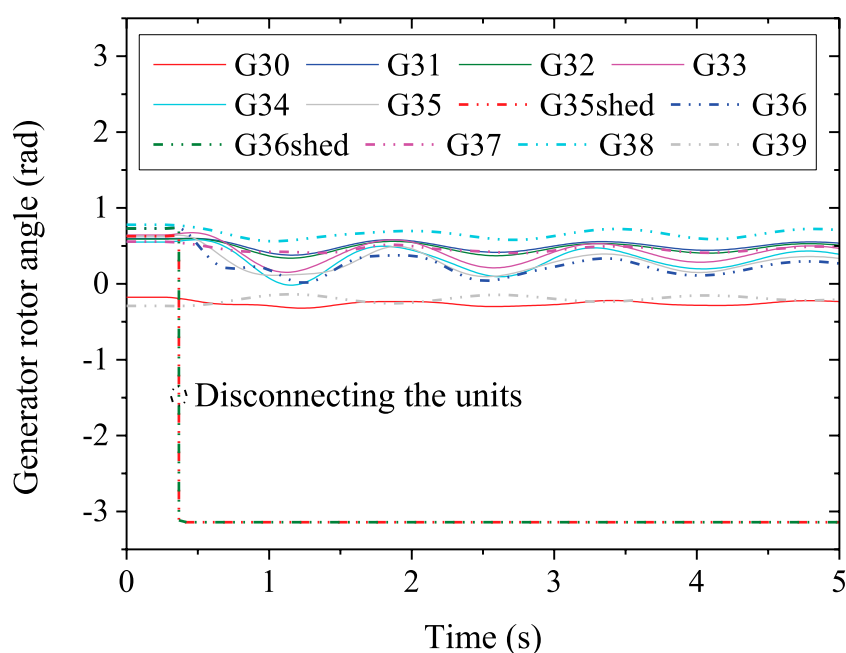

FIGURE 7
Indicator of critical unstable machine based on the output of the MTL predictor.
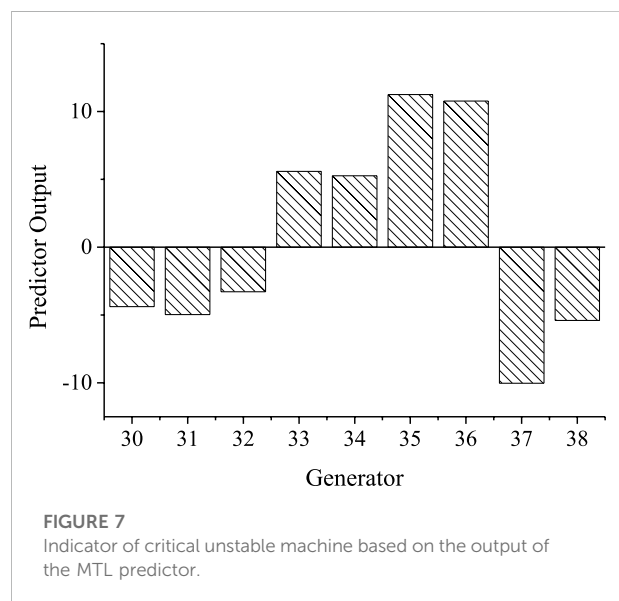
FIGURE 8
The generator rotor angle trajectories after generation shedding control.

7 Conclusion

To protect power systems from transient instability and the subsequent catastrophic blackouts, an integrated scheme is proposed by using post-disturbance PMU measurements and multi-task deep learning. The GRU-based predictor is firstly proposed for post-disturbance transient stability prediction. On this basis, considering that the prediction of the impending instability, the identification of the unstable mode, and the estimation of generation shedding are essentially related tasks, a multi-task learning framework is proposed to develop the PMU-based system integrity protection scheme for transient stability. Case study on the IEEE 39-bus system demonstrates that, apart from the basic task of transient stability prediction, the proposed multi-task predictor can predict the grouping of generators correctly. Moreover, based on the estimated amount of generation shedding, the generated remedial control actions can retain the synchronism of the power system.

Future research involves two aspects:

1) The proposed scheme is an open-loop SIPS and the overall percentage of success decision-making is 94.40% in the case study on the IEEE 39-bus system. In this regard, future research focuses on developing the close-loop SIPS following this paper so as to further enhance the percentage of success decision-making.

2) In this paper, generation shedding of synchronous generators is used as remedial actions. With the increasing penetration of renewables, how to coordinate the conventional generation shedding with the fast regulation of inverter-based renewables is another topic for future work.

Data availability statement

The original contributions presented in the study are included in the article/supplementary material, further inquiries can be directed to the corresponding author.

Author contributions

TL: Methodology, Writing. ZT: Conceptualization, Supervision. YH: Investigation. LX: Software, Validation. YY: Software, Validation.

Funding

Conflict of interest

Publisher's note

References

Al-Masri, A. N., Ab Kadir, M. Z. A., Hizam, H., and Mariun, N. (2013). A novel implementation for generator rotor angle stability prediction using an adaptive artificial neural network application for dynamic security assessment. *IEEE Trans. Power Syst* 28 (3), 2516–2525. doi:10.1109/TPWRS.2013.2247069

Andersson, G., Donalek, P., Farmer, R., Hatziargyriou, N., Kamwa, I., and Kundur, P., (2005). Causes of the 2003 major grid blackouts in North America and Europe, and recommended means to improve system dynamic performance. *IEEE Trans. Power Syst* 20 (4), 1922–1928, Nov. doi:10.1109/TPWRS.2005.857942

Bhui, P., and Senroy, N. (2017). Real-time prediction and control of transient stability using transient energy function. *IEEE Trans. Power Syst* 32 (2), 1–934. doi:10.1109/TPWRS.2016.2564444

Chiang, H.-D. (2011). "Controlling UEP method: Theory," in *Direct methods for stability analysis of electric power systems: Theoretical foundation, BCU methodologies, and applications* (IEEE), New York, NY, USA, 177–195. doi:10.1002/9780470872130.ch11

Collobert, R., and Jason, W. (2008). A unified architecture for natural language processing: Deep neural networks with multitask learning. Proceedings of the 25th international conference on Machine learning, Helsinki, Finland, 160–167.

Cremer, J. L., Konstantelos, I., and Strbac, G. (2019). From optimization-based machine learning to interpretable security rules for operation. *IEEE Trans. Power Syst* 34 (5), 3826–3836. doi:10.1109/TPWRS.2019.2911598

Dasgupta, S., Paramasivam, M., Vaidya, U., and Ajjarapu, V. (2015). PMU-based model-free approach for real-time rotor angle monitoring. *IEEE Trans. Power Syst* 30 (5), 2818–2819. doi:10.1109/TPWRS.2014.2357212

Gao, Q., and Rovnyak, S. M. (2011). Decision trees using synchronized phasor measurements for wide-area response-based control. *IEEE Trans. Power Syst* 26 (2), 855–861. doi:10.1109/TPWRS.2010.2067229

Girshick, R. (2015). Fast R-CNN. Proceedings of the IEEE international conference on computer vision, Washington, DC, USA, 1440–1448.

Gou, J., Liu, Y., Liu, J., Taylor, G. A., and Alamuti, M. M. (2017). Novel pair-wise relative energy function for transient stability analysis and real-time emergency control. *IET Gener. Transm. &amp. Distrib* 11 (18), 4565–4575. doi:10.1049/iet-gtd.2016.1671

Hatziargyriou, N., Milanovic, J., Rahmann, C., Ajjarapu, V., Canizares, C., and Erlich, I., (2021). Definition and classification of power system stability – revisited & extended. *IEEE Trans. Power Syst* 36 (4), 3271–3281. doi:10.1109/TPWRS.2020.3041774

Hu, W., Lu, Z., Wu, S., Zhang, W., Dong, Y., and Yu, R., (2019). Real-time transient stability assessment in power system based on improved SVM. *J. Mod. Power Syst. Clean. Energy* 7 (1), 26–37. doi:10.1007/s40565-018-0453-x

Huang, T., Guo, Q., Sun, H., Tan, C.-W., and Hu, T. (2019). A deep learning approach for power system knowledge discovery based on multitask learning. *IET Gener. Transm. &amp. Distrib* 13 (5), 733–740. doi:10.1049/iet-gtd.2018.5078

Kamwa, I., Samantaray, S. R., and Joos, G. (2010). Catastrophe predictors from ensemble decision-tree learning of wide-area severity indices. *IEEE Trans. Smart Grid* 1 (2), 144–158. doi:10.1109/TSG.2010.2052935

Kundur, P., Balu, N. J., and Lauby, M. G. (1994). *Power System Stability And Control*. New York, NY, USA: McGraw-Hill.

Liu, C., Sun, K., Rather, Z. H., Chen, Z., Bak, C. L., and Thogersen, P., (2014). A systematic approach for dynamic security assessment and the corresponding preventive control scheme based on decision trees. *IEEE Trans. Power Syst* 29 (2), 717–730. doi:10.1109/TPWRS.2013.2283064

Liu, T., Liu, Y., Liu, J., Wang, L., Xu, L., and Qiu, G., (2020). A bayesian learning based scheme for online dynamic security assessment and preventive control. *IEEE Trans. Power Syst* 35 (5), 4088–4099. doi:10.1109/TPWRS.2020.2983477

Pai, M. A. (1989). *Energy Function Analysis For Power System Stability*. Boston, MA: Kluwer.

Paul, A., Kamwa, I., and Joos, G. (2020). PMU signals responses-based RAS for instability mitigation through on-the fly identification and shedding of the run-away generators. *IEEE Trans. Power Syst* 35 (3), 1707–1717. doi:10.1109/TPWRS.2019.2926243

Pavella, M., Ernst, D., and Ruiz-Vega, D. (2000). *Transient Stability Of Power Systems: A Unified Approach To Assessment And Control*. Norwell, MA, USA: Kluwer.

Qiu, G., Liu, J., Liu, Y., Liu, T., and Mu, G. (2019). Ensemble learning for power systems TTC prediction with wind farms. *IEEE Access* 7, 16572–16583. doi:10.1109/ACCESS.2019.2896198

Rajapakse, A. D., Gomez, F., Nanayakkara, K., Crossley, P. A., and Terzija, V. V. (2010). Rotor angle instability prediction using post-disturbance voltage trajectories. *IEEE Trans. Power Syst* 25 (2), 947–956. doi:10.1109/TPWRS.2009.2036265

Ruder, S. "An overview of multi-task learning in deep neural networks." arXiv preprint arXiv:1706.05098 (2017).

Senroy, N., and (2006). Decision tree assisted controlled islanding. *IEEE Trans. Power Syst.* 21 (4), 1790–1797, Nov. doi:10.1109/TPWRS.2006.882470

Wang, B., Fang, B., Wang, Y., Liu, H., and Liu, Y. (2016). Power system transient stability assessment based on big data and the core vector machine. *IEEE Trans. Smart Grid* 7 (5), 2561–2570. doi:10.1109/TSG.2016.2549063

Xu, Y., Dong, Z. Y., Guan, L., Zhang, R., Wong, K. P., and Luo, F. (2012). Preventive dynamic security control of power systems based on pattern discovery technique. *IEEE Trans. Power Syst* 27 (3), 1236–1244. doi:10.1109/TPWRS.2012.2183898

Yang, Y., Huang, Y., Liu, J., Liu, Y., Liu, T., and Xiang, Y. (2017). Measurement-based cell-DT method for power system transient stability classification. *CSEE J. Power Energy Syst* 3 (3), 278–285. doi:10.17775/CSEEJPES.2015.01230

Yu, J. J. Q., Hill, D. J., Lam, A. Y. S., Gu, J., and Li, V. O. K. (2018). Intelligent time-adaptive transient stability assessment system. *IEEE Trans. Power Syst* 33 (1), 1049–1058. doi:10.1109/TPWRS.2017.2707501

Zheng, L., Hu, W., Zhou, Y., Min, Y., Xu, X., Wang, C., et al. (2017). *Deep Belief Network Based Nonlinear Representation Learning For Transient Stability Assessment*. Chicago, IL, USA: IEEE Power & Energy Society General Meeting, 1–5. doi:10.1109/PESGM.2017.8274126

Zhu, L., Hill, D. J., and Lu, C. (2020). Hierarchical deep learning machine for power system online transient stability prediction. *IEEE Trans. Power Syst* 35 (3), 2399–2411. doi:10.1109/TPWRS.2019.2957377

Zhu, L., and Hill, D. J. (2022). Networked time series shapelet learning for power system transient stability assessment. *IEEE Trans. Power Syst* 37 (1), 416–428. doi:10.1109/TPWRS.2021.3093423

Zhu, L., Lu, C., and Sun, Y. (2016). Time series shapelet classification based online short-term voltage stability assessment. *IEEE Trans. Power Syst* 31 (2), 1430–1439. doi:10.1109/TPWRS.2015.2413895

Enhancing transient stability of power systems using a resistive superconducting fault current limiter

Mohamed Alashqar[1,2,3], Conghuan Yang[1]*, Ying Xue[4], Zhaoxi Liu[4], Weiye Zheng[4] and Xiao-Ping Zhang[2]

[1]Department of Electrical Engineering, School of Naval Architecture and Ocean Engineering, Guangzhou Maritime University, Guangzhou, China, [2]Department of Electronic, Electrical and Systems Engineering, School of Engineering, University of Birmingham, Birmingham, England, United Kingdom, [3]Qatar General Electricity & Water Corporation (KAHRAMAA), Doha, Qatar, [4]School of Electric Power Engineering, South China University of Technology, Guangzhou, China

The electricity demand keeps increasing with development and time, which leads to the need to install more generating units in the grid. Therefore, the fault current levels will rise above the limits of the electrical equipment, particularly when the electric grid becomes meshed and interconnected with neighboring networks. Consequently, the electrical equipment needs to be replaced or use a method that will decrease the fault current to be within the permissible boundaries. The existing solutions such as neutral impedance, current limiting reactor (CLR), and bus splitting have negative impacts on the electric grid. The superconducting fault current limiter (SFCL) appears to be a promising solution. In this paper, the resistive SFCL is proposed to enhance the stability of the interconnected power system. The two-area system is used as a case study for the interconnected power system. Also, the optimal value and locations of the resistive SFCL are analyzed. The results show that the system will remain stable without tuning the power system stabilizer (PSS).

1 Introduction

One of the unique properties of the power system operation is that the electrical speed of all generating units must be the same (Padiyar, 2004). This is known as the synchronous operation of the power system. However, any disturbance to the power system operation can affect the rotating speeds of rotors, i.e., the network frequency (Kundur, 1994; Anderson and Fouad, 2003; Kundur et al., 2004; Padiyar, 2004; Grigsby, 2012). The transient stability (*large-disturbance rotor angle stability)* is defined as "the ability of the power system to maintain synchronism when subjected to a severe disturbance, such as a short circuit on transmission facilities, loss of generation, or loss of a large load" where the small-signal stability is defined as "the ability of the power system to maintain

synchronism when subjected to small disturbances, such as switching of small loads, generators or transmission line tripping, for which the equations that describe the dynamics of the power system may be linearized for analytical purposes." (Kundur, 1994), (Kundur et al., 2004; Das, 2007; Machowski et al., 2008). It is essential to note that the transient stability is dependent on the operating condition and the perturbation, which makes the analysis of the transient stability more complicated. Also, the linearization analysis does not apply to transient stability analysis (Padiyar, 2004). Under a transient event, the system response involves large excursions of generator rotor angles, power flows, bus voltages, and other system variables. If the resulting angular separation between the machines in the power system remains within certain bounds, the system maintains synchronism. Loss of synchronism because of transient instability, if it occurs, will usually be evident within 2–3 s of the initial disturbance (Kundur, 1994).

The fault levels in the power system drastically increased due to various reasons. For example, the integration of multiple energy sectors (Zheng et al., 2020), the continuous increase in electricity demands, the massive scale of the power plants either conventional or renewable generation, and the expansion of power grid (Koyama and Yanabu, 2009; Sung et al., 2009; Li et al., 2014). Therefore, the stresses caused by excessive fault currents led to high mechanical, electrical, and thermal instabilities of electric networks (Lee et al., 2008). Consequently, the electrical apparatus might be damaged and cause a partial blackout or even a major blackout if the existing switch gears are not upgraded (Anderson and Fouad, 2003), (Grigsby, 2012), (Miyashita et al., 2005; Kodle et al., 2016; Glover et al., 2017). These changes are the main concerns for the transmission system operators because an increase in the fault levels negatively impacts the power system in terms of security and reliability (Ravindranath and Chander, 1977). Therefore, fault-limiting techniques are required. Many effective methods were used, for instance, bus splitting, current limiting reactors, and others. However, each of these has its own limiting factors. For example, using bus splitting will reduce the reliability of the interconnected system. Also, series reactors have drawbacks such as constant high reactive losses, bulky, and contributing to grid voltage drops. Therefore, a new technique should be utilized to overcome the disadvantages (Blair et al., 2012; Son et al., 2012; Jain et al., 2016). Different methods were used to mitigate the transient instability, such as flexible AC transmission system (FACTS) controller, which includes static VAR Compensator (SVC), thyristor-controlled series capacitor (TCSC), static synchronous series compensator (STATCOM) and unified power flow controller (UPFC) (Kamarposhti et al., 2021), (Wang et al., 2020).

Superconducting fault current limiters are superconducting power equipment whose impedance is small in steady-state condition and large in a fault condition. Therefore, SFCLs do not deteriorate power system stability in steady-state conditions

and effectively limit the short-circuit currents in a fault condition (Sjostrom et al., 1999). Different types of SFCL are available in the market; resistive SFCLs, shielded Core FCL, SFCL bridge, and saturated iron core FCL. The Resistive SFCLs have been the primary choice for SFCL field experiments. Its popularity due to its simple concept, compact size and weight, and resistant nature (Blair, 2013). The shielded iron core SCFCL, or often called inductive SCFCL advantageous is that there is no current lead to cryogenic temperatures and that the superconductor is exhibited to large currents but low voltages. Like resistive SCFCLs, a quench takes place in the superconductor and therefore a recovery time of several seconds is needed. However, A major drawback of this type is the large volume and weight which is similar to a transformer of the same power rating (Noe and Steurer, 2007). SCFCL bridge rectifiers are made up of diodes or thyristors arranged in a complete bridge configuration. This SFCL type is undesirable because it no longer controls short-circuit current if, for example, one of the semiconductors fails and causes a short circuit. Furthermore, the total losses are rather substantial.

SFCLs are used to minimize the short circuit current to a definite value and have the ability to decrease the levels of fault current within the electricity grid by factors of 3–10 times (Baldan et al., 2007), (Egorova et al., 2013). Under normal circumstances, SFCL is quenched to a temperature of approximately −200°C, which can be accomplished in a cost-efficient way by using liquid nitrogen (Blair et al., 2012), (Sjostrom et al., 1999), (Lee, 2011), (Vojenčiak et al., 2016). This will minimize the material's resistivity, which means that it will not have any influence on the network under normal conditions (Matsumoto et al., 2010), (Yonemura et al., 2015). However, if the current goes above the nominal, the materials instantaneously lose their properties of superconductivity and work as a typical resistor. During that situation, the current will be reduced to a predefined value (Lee et al., 2008), (Wang et al., 2014). These properties make superconductors work as a self-triggered current limiter. Moreover, significant features introduced by the superconductors, such as negligible voltage drop and energy losses during steady-state operating conditions, enable higher grid loads without upgrading the equipment in the power system (Kovalsky et al., 2005; Zhang et al., 2015; Kumar et al., 2016).

The normalized non-linear relationship between current flow in a superconductor and its resistance is demonstrated in Figure 1. It can be seen from Figure 1 that when a fault develops, the current rises, causing the superconductor to quench and exponentially increase its resistance. Most SFCL designs consider the above behavior to limit the fault current in the first cycle [Electric Power Research Institute (EPRI), 2009], (Khatibi and Bigdeli, 2014). Under normal grid operation, resistive SFCLs use superconducting material as the main current-carrying conductor. The principle of operation is shown in the single-line diagram in the upper half of
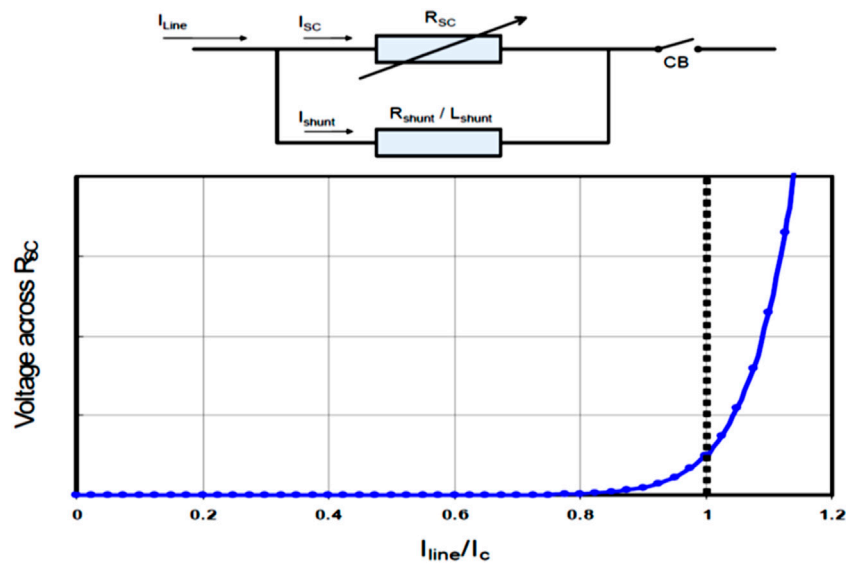
FIGURE 1
Resistive Type SFCL with Shunt Element and a normalized plot of voltage and current in a superconductor at a constant temperature and magnetic field. [Electric Power Research Institute (EPRI), 2009], (Pawar and Chavan, 2017).
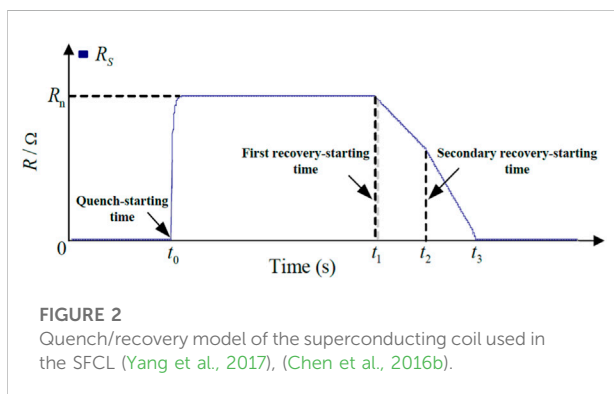

FIGURE 2
Quench/recovery model of the superconducting coil used in the SFCL (Yang et al., 2017), (Chen et al., 2016b).
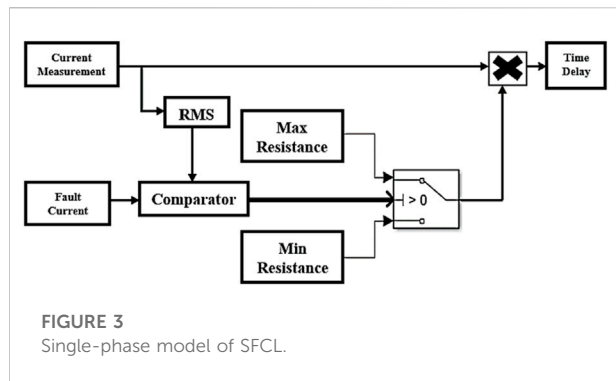
Figure 1. As mentioned before, the lower plot is a normalized performance of the voltage across R_{sc} as a function of the ratio of the current through the SFCL device (I_{Line})to the critical current (I_c) of the superconducting element. The level of the current at which the quench happens is identified by the operating temperature, the size, and the category of the superconductor. The quick rise in resistance produces a voltage across the superconductor and leads the current to convey to a shunt, a combination of resistor and inductor. The shunt's role is to limit the voltage increase across the superconductor in the quench situation. In essence, the superconductor works like a switch with a millisecond response that stimulates the transition of the load current to the shunt impedance. Theoretically, the initial fault current is restricted to less than one cycle [Electric Power Research Institute (EPRI), 2009].

Eq. 1 describes the characteristics of the resistive type of SFCL behavior (Chen et al., 2016a), (Moon et al., 2011).

$$
R(t) = \begin{cases} 0 & (t < t_0) \\ R_n \left[1 - e^{\left(-\frac{t-t_0}{T} \right)} \right]^{1/2} & (t_0 \le t < t_1) \\ C_1 (t - t_1) + D_1 & (t_1 \le t < t_2) \\ C_2 (t - t_2) + D_2 & (t_2 \le t < t_3) \end{cases} \tag{1}
$$

R_n denotes the SFCL's normal-state resistance; T is the time constant. The SFCL's time-domain characteristics of $t0$, $t1$, and $t2$ indicate the quench-starting time, the first recovery-starting time, and the secondary recovery-starting time, respectively, as shown in Figure 2. The function coefficients are C1, D1, C2, and D2, as stated in Eq. 1 (Sung et al., 2009), (Chen et al., 2016a), (Elshiekh et al., 2013), (Lim et al., 2009).

In this paper, the resistive SCFL is used to verify that the fault current can be minimized significantly. Also, the transient stability of the power system can be enhanced without tuning the PSS. There are difficulties in tuning the PSS because the technique used, simulation study, field implementation, and the number of standard tests to be undertaken for its evaluation differ from utility to utility and vendor to vendor. As a result, the power system planner and the operator must examine and evaluate the efficiency of PSS tuning following the stated criteria for the specific power system. Nevertheless, many power plants have been reported to have tuned their PSS at unit commissioning, during automatic voltage regulator (AVR)

FIGURE 3
Single-phase model of SFCL.

TABLE 1 Parameters used in the SFCL.

Parameters	Value
System voltage (3-phase)	230 kV
Maximum resistance	10Ω
Minimum resistance	0.01Ω
Trigger current	850 A
Time delay (recovery time)	1 s

modernization, or based on system operator observation/feedback (Wang et al., 2019).

It should be noted that refs (Miyashita et al., 2005), (Pawar and Chavan, 2017), (Mohamed, 2012), and (Wang et al., 2018a) used a single-machine infinite bus (SMIB) to study the improvement of the transient stability by using SCFL. However, each area contributes to the short circuit within the interconnected network in the interconnected power system. Therefore, this paper uses a two-area system with four synchronous machines to analyze the impact of resistive SCFL on angle stability. Different fault locations and fault types are considered in the analysis. Also, the optimal location and value of the resistive SFCL were analyzed.

2 Superconductor fault current limiter

To design a resistive SCFL, five parameters need to be defined (Sung et al., 2009), (Zhang et al., 2015), (Alaraifi et al., 2013), (Wang et al., 2018a):

1 The triggering current (the value at which the SFCL will be stimulated).
2 The quenching resistance (Maximum resistance).
3 The quenching time is the time that the SFCL will be activated.
4 The minimum resistance of 0.01Ω, which is the SFCL's normal operation resistance.
5 The recovery time of 1 s.

All these parameters have been taken into consideration in designing SFCL. The design of the single phase of the step resistance SFCL model is shown in Figure 3. The principle of operation can be described as follows: firstly, the current measurement is used to measure the current of each phase to compute the absolute and RMS values of the phase line current by RMS block. If the RMS current is less than the triggering

current, then the model will consider the SFCL in the normal operating state (superconductivity situation), and the SFCL will take a resistive value of 0.0 L Ω (the minimum resistance). Otherwise, if the RMS value of the line current is higher than the triggering current, then the model will lose the superconductivity state and increase rapidly to the maximum predefined value. Lastly, the fault current drops below the triggering current because the fault was cleared, and the SFCL restores the superconducting condition after recovery. The transport delay block is installed to implement the maximum resistance for 1 s from the moment the fault occurs. The resistive SFCL is connected in series with the transmission line in the event of a short circuit. According to the above-mentioned, the summary of the parameters used in the SFCL modeling can be represented in Table 1.

3 Power system model

The interconnected two-area system is shown in Figure 4. The system consists of two similar areas connected *via* a weak tie line (230 kV lines of 220 km length (Kundur, 1994)). Each area has two synchronous generators, and there are 967 MW, and 1767 MW loads at area 1 and area 2, respectively, and the system operates with area 1 exporting 400 MW to area 2; detailed parameters in the Appendix A1. Figure 4 shows the proposed locations of the resistive type SFCL in the interconnected power system, case 1 in Figure 4A, and case 2 in Figure 4B. The power system has been modeled in MATLAB and SIMULINK software to perform different scenarios. In the simulation studies, different types of faults are applied in different locations on line one to demonstrate the performance of SFCLs.

The short circuit current at bus i can be calculated as follows

$$I_{sc} = \frac{E^i}{Z_{ii}} \qquad (2)$$

where is Z_{ii} bus impedance from i, which includes the SFCL impedance as well, and E^i is the pre-fault voltage of bus i.

Increasing the critical clearing time or angle typically improves angular stability. Critical clearance time for a machine can be
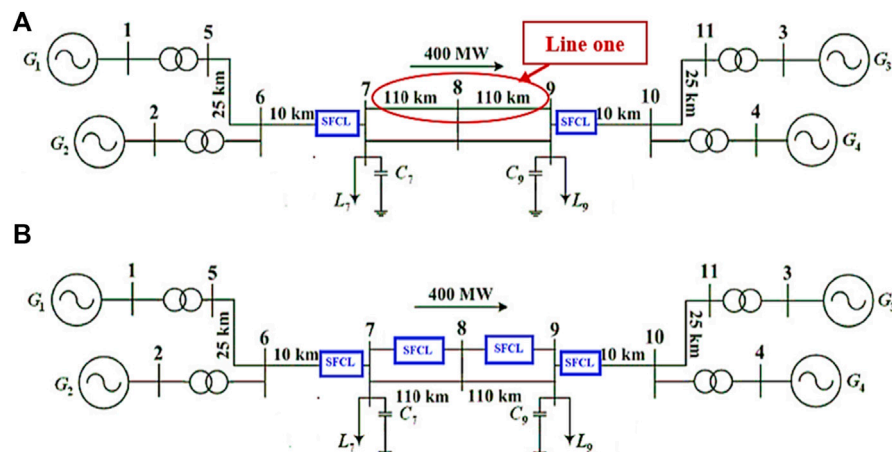
FIGURE 4
Two area system **(A)** case 1. **(B)** Case (2).

improved by avoiding active power changes during faults, according to the swing equation for a synchronous machine.

$$\frac{d\omega_k}{dt} = \frac{1}{M_k}\left(P_m^k - P_e^k\right) \qquad (3)$$

$$\omega_k = \frac{d\delta_k}{dt} \qquad (4)$$

$$H = \frac{\omega_0}{2M_k} \qquad (5)$$

Where M_k is the inertia consatant of machine k, ω_k is the rotor speed of machine k, δ_k is the rotor angle of machine k, P_m^k is the mechanical power of machine k, and P_e^k is the electrical power delevied machine k. Hence, By substituting Eqs 4, 5 into Eq. 3, the swing equation will be formulated in Eq. 6

$$\frac{2H_k}{\omega_0}\frac{d^2\delta_k}{dt^2} = \left(P_m^k - P_e^k\right) \qquad (6)$$

4 Simulation results and observations

In this section, the system will be tested under different scenarios to verify that the SFCL can not only limit the fault current but also improve the power system's transient stability without tuning PSSs. Two kinds of PSS have been used: simplified PSS and conventional PSS. The simplified PSS is MB-PSS designed to introduce intermediate phase advance at all oscillation frequencies of interest, compensating for the inherent lag between field excitation and electrical torque (Zheng et al., 2020), (Leiva Roca et al., 2022). Therefore, only six parameters are required to be tuned. In contrast, the conventional PSS uses the measured electrical power and its
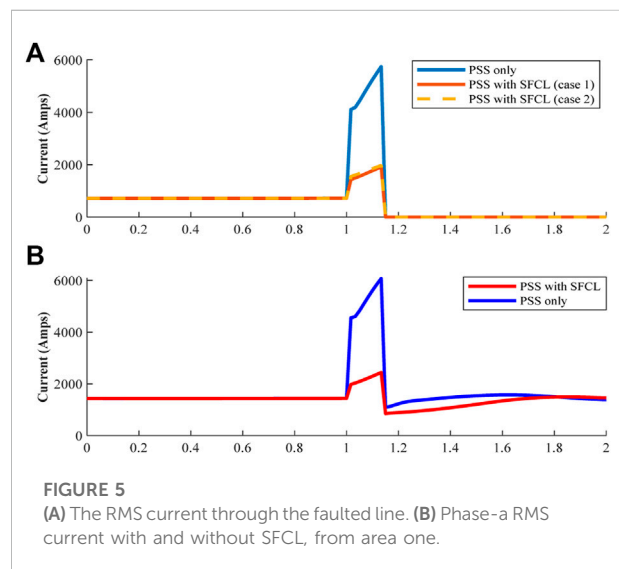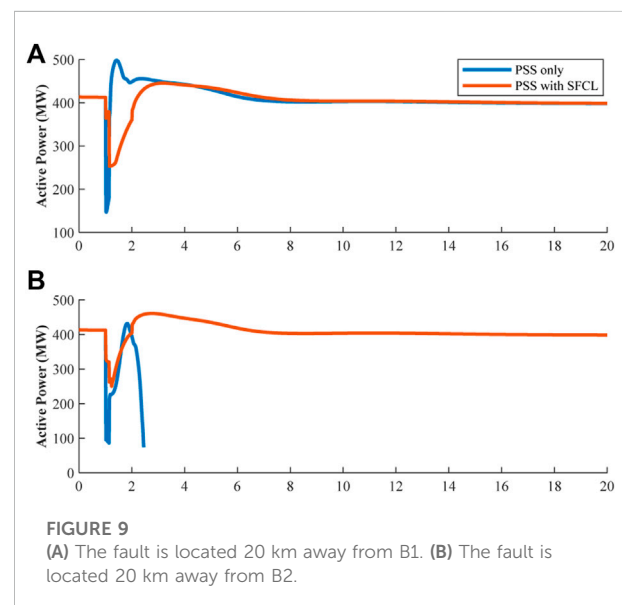

FIGURE 5
(A) The RMS current through the faulted line. **(B)** Phase-a RMS current with and without SFCL, from area one.

relationship to shaft speed as an input signal (Leiva Roca et al., 2022), (Wang et al., 2018b).

4.1 Simplified PSS with SFCL

As mentioned in the previous section, the main objective of using SFCL is to minimize the fault current. As shown in Figures 5A, B, using the SFCL help reduce the fault current through the faulted line by 58%, and the fault current shared from area 1 is reduced by more than 50%.

FIGURE 6
(A) Active power transferred from B1 and B2 when a three-phase fault is applied at the middle of line one. **(B)** Single line to ground fault applied in the middle of line one. **(C)** Different values of resistance of SFCLs in case 1.

FIGURE 8
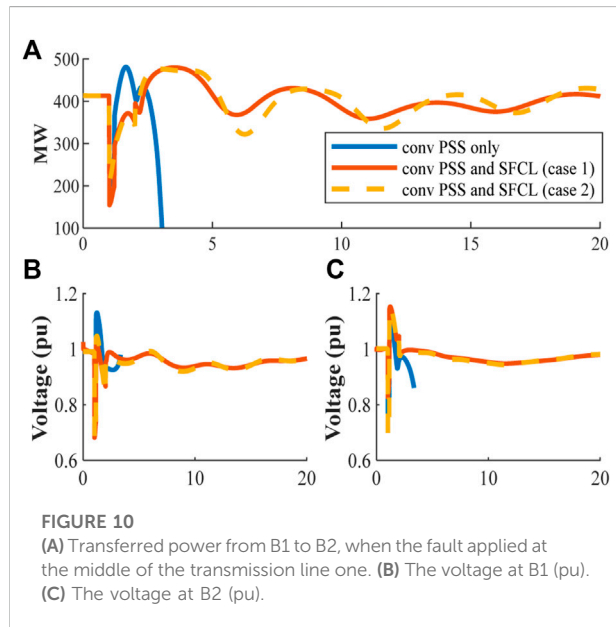**(A)** G1 rotor speed (pu). **(B)** Electrical power output from G1 (pu). **(C)** The system performance when the fault resistance is 80Ω. **(D)** The system performance when the fault resistance is 10Ω.

FIGURE 7
(A) The voltage at B1 (pu). **(B)** The voltage at B2 (pu). **(C)** G1 terminal voltage (pu).

FIGURE 9
(A) The fault is located 20 km away from B1. **(B)** The fault is located 20 km away from B2.

It is well known that PSS is one of the robust solutions to maintain system stability, if it is perfectly tuned, which can be seen in Figures 6–8. However, if the SFCLs are installed in specific locations, the behavior of the power system will be enhanced. For example, Figure 6 shows the active power transferred from B1 to B2 when a severe fault (three phase fault) occurs in the middle of line one. During the fault, the active power drops 210 MW when PSS is only used and when the SFCL installed at the end of each

area (case 1) as shown in Figure 4A. However, if the SFCL added also at the end of the faulted line (case 2) as shown in Figure 4B, the active power drops will be less with 160 MW.

For single phase fault in the middle of line one, the active power drops with 130 MW in the case of PSS only used as shown in Figure 6A. While in cases 1 and 2, the active power drops further with 150 MW. In all cases, the system reaches the same steady state as shown in Figure 6B.

FIGURE 10
(A) Transferred power from B1 to B2, when the fault applied at
the middle of the transmission line one. **(B)** The voltage at B1 (pu).
(C) The voltage at B2 (pu).

FIGURE 11
(A) G1 rotor speed (pu). **(B)** The terminal voltage of G1. **(C)**
Electrical power output from G1.

The resistance value of the SFCL is important. For instance,
Figure 6C illustrates the performance of the active power flow
from B1 to B2 when the resistance of the SFCLs changes. It can be
seen that when the resistance value increases, there is a further
drop in the active power in the event of a three-phase short circuit
due to the power loss increasing during the quenching time of the
SFCL. Also, increasing the resistance of the SFCL will increase the
voltage drop in the grid.

The voltage stability is essential, which needs to be maintained
at certain limits before, during, and after the fault. Figures 7A, B
show the voltage at B1 and B2, while Figure 7C illustrates the
terminal voltage of the G1. From these figures, it can be noticed that
voltages drop to new steady-state conditions but are still within ±5%
of the nominal. During the fault, the voltage dip is more because the
system impedance increases during the disturbance with SFCLs.
Nevertheless, once the fault is cleared, the SFCL returns to normal
operation, and all buses' voltages return to a stable state.

During the fault, the impact on the rotor speed of G1 is less
when SFCLs are installed in both areas. Non-etheless, after the
disturbance is cleared the rotor speed decreases by 0.002 pu lower
than the system with only PSSs installed at all units. Then this
increases gradually to a new operating point, which is exemplified in
Figure 8A. When the disturbance occurs, the frequency rose to
60.18 Hz because the active power is dropped sharply. Once the fault
is cleared, the frequency drops to 59.82 Hz, which is the minimum
frequency. After that, the system returns to a steady state with a
frequency of around 60.18 Hz. Moreover, Figure 8B demonstrates
the electrical output power from generator one, which is located in
area one, and the impact of using SFCL in desired locations.

The fault resistance can affect the system's transient
performance. The following figures show the system
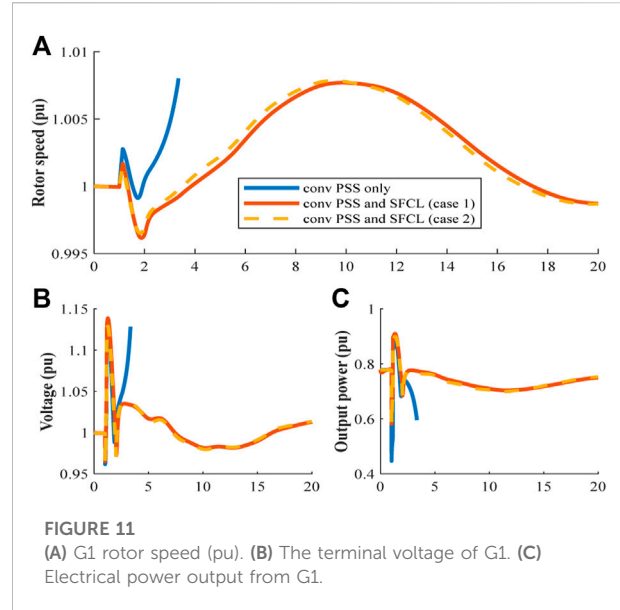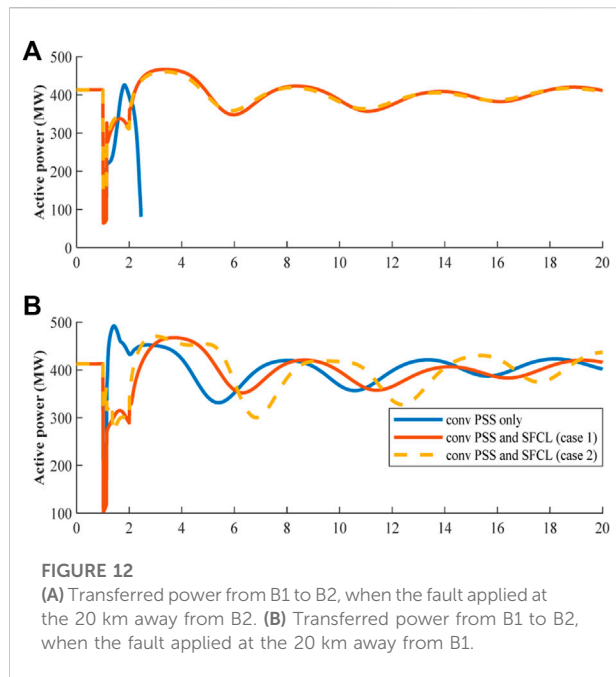performance when the value of the fault resistance is changed.

Figure 8C displays the active power transferred from B1 to
B2 when the three-phase fault is applied at 1s for eight cycles. The
fault resistance is 80Ω. Without installing SFCLs, the active
power transfer from area1 to area2 increases to 600 MW
compared to Figure 6A when the fault resistance is small
(0.001Ω). However, if the SFCLs are installed at the proposed
locations, as shown in Figure 4, the transient active power will be
reduced by 100 MW, which means the stress on the generating
units will be decreased. Additionally, if the fault resistance is 10Ω,
the active power flow will reach the pre-fault value steadily with
the proposed locations as shown in Figure 8D.

The fault location is also crucial in the power system
stability study. When the three-phase fault occurs at 20 km
away from B2, the system losses synchronism as shown in
Figure 9B and without SFCL. Hence, by using SFCLs, the power
system's synchronism can be maintained without any tuning of
the PSS. Similarly, when the fault happens 20 km away from B1,
the system performance without SFCLs was influenced severely
during and after the fault, with a maximum of 500 MW and a
minimum of 150 MW. Notably, when the SFCLs are used in
both areas, the difference will be reduced to 450 MW at the
maximum and 250 MW at the minimum, as shown in
Figure 9A. Consequently, the stress on the generators will be
restricted.

4.2 Conventional PSS with SFCL

The most crucial point is maintaining the continuity of
power flow from B1 to B2. This depends on the severity of the
short circuit and the system condition at the time of the fault. In
this case, a three-phase fault has been applied in different

FIGURE 12

(A) Transferred power from B1 to B2, when the fault applied at the 20 km away from B2. **(B)** Transferred power from B1 to B2, when the fault applied at the 20 km away from B1.

locations on line 1. Before the fault incident, both transmission lines carried the same active power. However, once line 1 is tripped, the other line must carry the full transferred power from area-1 to area-2. Figure 10A shows the power flow from B1 to B2 when a three-phase short circuit occurs in the middle of line one. The system with only conventional acceleration power delta power system stabilizer (Delta Pa) goes to instability, which means that the synchronism

of the grid has been lost. Synchronization failure happens because Delta Pa PSS uses an open loop system. The conventional acceleration power-based- (Delta Pa) PSS is used for damping the small-signal oscillation and is unsuitable for large disturbances. However, with resistive SFCL the system is stable.

Figures 10C show the voltages at B1 and B2. It can be seen from the figure that the voltages go into instability after the disturbance. However, if the SFCL is used, the voltages are stable and within the operational limits of ±5% of the nominal value.

Figure 11A demonstrates the rotor speed of generator 1 in area 1. The frequency drops to 59.76 Hz, with a peak value of 60.48 Hz. Finally, the system reaches a steady state at 59.94 Hz. That change in frequency is related to the change in electrical power output from generator 1, which is shown in Figure 11C. While Figure 11B shows the terminal voltage of machine 1 in area 1 as an example, and it is observed that the simulation stopped running for a few seconds after the short circuit happens. This is because the terminal voltage keeps increasing and the active power decreases. Nevertheless, the voltage is closer to the nominal value when the SFCLs were installed (either case 1 or 2).

Figure 12A shows that when the disturbance occurs near the receiving end bus, the system will collapse because the Delta Pa PSS uses an open loop system which is unable to maintain the system synchronism under a new highly stressed operating point. However, if the SFCLs are installed in association with the conventional PSS the system will remain synchronized and stable. Figure 12B emphasizes that the SFCLs would improve the power system stability under any condition.

TABLE 2 Resistive SFCL Demonstration Projects [Electric Power Research Institute (EPRI), 2009], (Martini et al., 2014).

Projects	England	Germany	A2A
Location	Lancashire, United Kingdom	Boxberg, Germany	North Italy
Site	Bamber Bridge	Local Power Plant	San Dionigi Substation (MI)
Status	Operating	Operating	Fabrication of the first prototype
Utility/Host	Consortium	Vattenfall Europe Generation AG	A2A Reti Elettriche Spa Group
In-Grid Start	Fall 2009	Fall 2009	Early 2010
Rated Current	100 A	800 A	250 A
Expected Max Fault Current	55 kA	63 kA	30 kA
Current-Limiting Capability	55 kA → 7 kA	63 kA → 30 kA	$2 < I_{SC}/I_{Lim} < 2.2$
Max Limiting Duration	0.12 s	0.12 s	300–400 m
HTS Material	BSSCO-2212 bulk tubes	BSSCO-2212 bulk tubes	BSCCO 1G
HTS Conductor Supplier/Fabricator	Nexans	Nexans	SEI
Cryogen	LN2	LN2	LN2
Nominal Operating Temperature	75 K	65 K	65 K

FIGURE 13
Total tripping in the transmission network in 2020 and 2021.
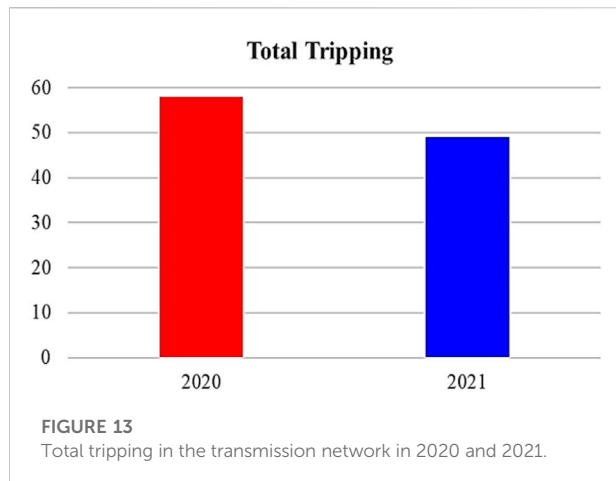
5 SFCL practical application issues

There are still obstacles to the large-scale application of resistive-type SFCL. Although it is compact in structure, simple to implement (directly connected to the transmission line), has no control required, is rapid in response, and has minimal impact on the power grid, it requires a significant number of superconducting tapes (high in cost). In addition, it has higher AC loss generated during the current limiting period. There are still other issues, such as the costly material
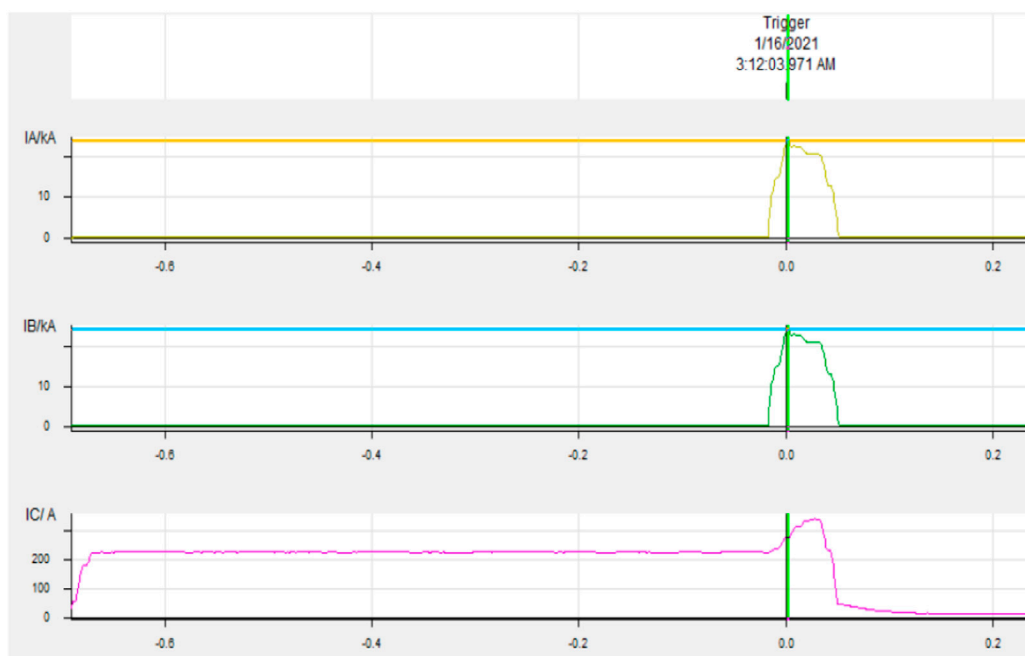
and production costs, the high cost of low-temperature operation and maintenance, and the operation's dependability not yet shown. Furthermore, the cryogenic system's capacity will rise with the number of superconductors. Therefore, the cryogenic system must be inspected and replaced regularly. As a result, cryogenic system stability and extended life expectancy should be necessary for the stable and safe operation of SFCLs.

From a protection point of view, when SFCLs were added to existing electric networks, the amount of the maximum fault current might change, affecting the protection coordination system between protective relays. To examine protection coordination with fault current limiters, the triggering level of the fault current limiters, the installation site, and the amount of impedance caused by the fault current limiter should also be considered.
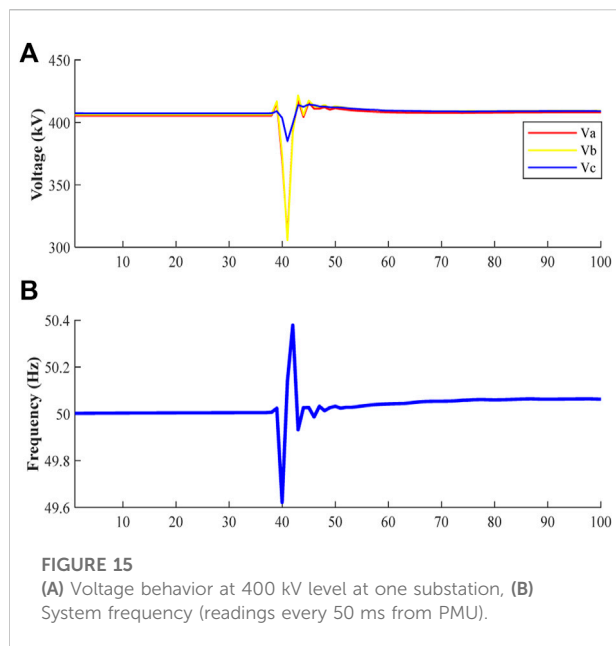
Despite the superior current limiting capabilities achieved by SFCLs, commercialization and installation of superconducting fault limiters have been delayed due to technical and economic concerns as mentioned above. Table 2 shows three resistive SFCL implemented in England, Germany and Italy.

6 Fault current techniques within Qatar national grid

The transmission network in Qatar consists of 8 power plants that use natural gas and one PV power plant, and above

FIGURE 14
Three phase current after phase–to–phase fault occurred.

FIGURE 15
(A) Voltage behavior at 400 kV level at one substation, **(B)** System frequency (readings every 50 ms from PMU).

400 substations with different voltage levels (400 kV, 220 kV, 132 kV, 66 kV, 33 kV, 22 kV, and 11 kV) (Alashqar et al., 2022). As a result, the transmission and distribution expansion meshed the national grid, and the fault level increased. Figure 13 shows the comparison between 2020 and 2021 subject to the total number of tripping the transmission network, and these tripping due to several reasons such as joint cable failure, protection maloperation, fault in the OHL, third-party damage, *etc.,*

Figures 14, 15 show a real measurement for the system behavior after a phase-phase fault occurred in the 400 kV OHL circuit. The fault happened during the minimum time on 16th January 2021 when the number of running machines was less than the peak in summer. As a result, the system peak on the day of incidence is 50% less compared to the system peak in summer. Figure 14 illustrates that the fault current reached around 23 kA in both phase a and phase b. Also, Figure 15A shows the voltage behavior, and it can be seen clearly that a voltage dip occurred, and the voltage reached 308 kV and normalized within 71 m. Furthermore, as shown in Figure 15B, the system frequency fluctuated to reach around 50.4 Hz maximum and approximately 49.6 Hz minimum.

Traditional techniques are used to limit the fault current, such as splitting busbars, restricting generations in some locations, opening circuits (cable, OHL, and transformers), installing series reactors, and for future generations, high-impedance transformers are required. The SFCL is not preferable from a planning perspective due to the high cost compared to the other solution. For example, the cost of a series reactor in the 400 kV level costs

3.2 M\$ (excluding the modification cost in the line), whereas a SFCL unit costs three times the series reactor. However, the SFCL is still developing, and the cost will decline with time.

6 Conclusion

Stability is a great concern of the power system operations, which needs to be maintained under any operating condition. However, the growth in the electricity supply and the sophistication in the electrical networks leads to an increase in fault current levels, threatening the power system stability. Therefore, a SFCL becomes a promising solution to overcome these challenges. This paper shows a comprehensive analysis of the influence of the SFCL in an interconnected power system. The key findings are:

1) The resistive value of the SFCL needs to be adjusted to avoid voltage drop during normal and abnormal operation conditions.
2) The best location for installing SFCL in the interconnected power system is at the end of each area before the tie line.
3) The fault current is reduced, avoiding the upgrade of the electric equipment.
4) The results show that deploying resistive SFCL enhances the system stability without tuning the power system stabilizer (PSS).

Data availability statement

The original contributions presented in the study are included in the article/Supplementary Material, further inquiries can be directed to the corresponding author.

Author contributions

MA, CY, and YX developed the original ideas and prepared the manuscript; ZL, WZ, and X-PZ helped revise the paper.

Conflict of interest

MA was empoyed by the Qatar General Electricity & Water Corporation (KAHRAMAA).

The remaining authors declare that the research was conducted in the absence of any commercial or financial relationships that could be construed as a potential conflict of interest.

Publisher's note

All claims expressed in this article are solely those of the authors and do not necessarily represent those of their affiliated organizations, or those of the publisher, the editors and the reviewers. Any product that may be evaluated in this article, or claim that may be made by its manufacturer, is not guaranteed or endorsed by the publisher.

References

Alaraifi, S., Moursi, M. S. E., and Zeineldin, H. H. (2013). Optimal allocation of HTS-FCL for power system security and stability Enhancement. *IEEE Trans. Power Syst.* 28 (4), 4701–4711. doi:10.1109/TPWRS.2013.2273539

Alashqar, M., Xue, Y., Yang, C., and Zhang, X.-P. (2022). Comprehensive economic analysis of PV farm -A case study of Alkarsaah PV farm in Qatar. *Front. Energy Res.* 10. 987773. doi:10.3389/fenrg.2022.987773

Anderson, P. M., and Fouad, A. A. (2003). *Power system control and stability*. Second edition. Piscataway, NJ: IEEE Press: Wiley-Interscience.

Baldan, C. A., Shigue, C. Y., Lamas, J. S., and Filho, E. R. (2007). Test results of a superconducting fault current limiter using YBCO Coated conductor. *IEEE Trans. Appl. Supercond.* 17 (2), 1903–1906. doi:10.1109/TASC.2007.897771

Blair, S. M., Booth, C. D., and Burt, G. M. (2012). Current–time characteristics of resistive superconducting fault current limiters. *IEEE Trans. Appl. Supercond.* 22 (2), 5600205. doi:10.1109/TASC.2012.2187291

Blair, S. M. (2013). *The analysis and application of resistive superconducting fault current limiters in present and future power systems*. Glasgow, Scotland: University of Strathclyde, 192.

Chen, L., Chen, H., Yang, J., Shu, Z., He, H., and Shu, X. (2016). Conceptual design of a high-speed electromagnetic switch for a modified flux-coupling-type SFCL and its application in renewable energy system. *SpringerPlus* 5, 771. doi:10.1186/s40064-016-2347-6

Chen, L., Tu, X., Chen, H., Yang, J., Wu, Y., Shu, X., et al. (2016). Technical evaluation of superconducting fault current limiters used in a Micro-grid by considering the Fault characteristics of distributed generation, energy Storage and power loads. *Energies* 9 (10), 769. doi:10.3390/en9100769

Das, D. (2007). *Electrical power systems*. New Delhi,India: New Age International.

Egorova, E., Bahirat, H., Mork, D. B. A., Perger, D. W. F., and Holcomb, D. M. (2013). EMTP-ATP modeling of a resistive superconducting fault current limiter. Available at: https://www.ipstconf.org/papers/Proc_IPST2013/13IPST071.pdf.

Electric Power Research Institute (Epri) (2009). *Superconducting Fault current limiters, technology watch 2009*. Palo Alto, CA: EPRI, 1017793. http://assets.fiercemarkets.net/public/smartgridnews/000000000001017793.pdf (accessed 20, 08, 2019).

Elshiekh, M. E., Mansour, D. A., and Azmy, A. M. (2013). Improving Fault Ride-through capability of DFIG-based Wind Turbine using superconducting fault current limiter. *IEEE Trans. Appl. Supercond.* 23 (3), 5601204. doi:10.1109/TASC.2012.2235132

Glover, J. D., Overbye, T. J., and Sarma, M. S. (2017). *Power system analysis & design*. Sixth edition. Boston, MA: Cengage Learning.

Grigsby, L. L. (2012). *Power system stability and control [electronic resource]*. 3rd ed. (Boca Raton, Fla: CRC Press).

Jain, A., Dubey, V. K., Jawale, G., Mangalvedekar, H. A., and Kanakgiri, K. (2016). "Limiting fault current in a power system network by SFCL: A step input approach," in 2016 IEEE 6th International Conference on Power Systems (ICPS), New Delhi, India, March 2016 (IEEE), 1–5. doi:10.1109/ICPES.2016.7584095

Kamarposhti, M. A., Shokouhandeh, H., Colak, I., Band, S. S., and Eguchi, K. (2021). Optimal location of FACTS devices in Order to Simultaneously improving transmission losses and stability Margin using artificial Bee Colony algorithm. *IEEE Access* 9, 125920–125929. doi:10.1109/ACCESS.2021.3108687

Khatibi, M., and Bigdeli, M. (2014). Transient stability improvement of power systems by optimal sizing and allocation of resistive superconducting fault current limiters using Particle. *Swarm Optim.* 1 (3), 17.

Kodle, S., Padmini, V., Bahirat, H. J., Khaparde, S. A., Lubicki, P., and Dabeer, V. (2016). "Application of Super Conducting fault current limiter in Indian grid," in 2016 IEEE 6th International Conference on Power Systems (ICPS), New Delhi, India, March 2016 (IEEE), 1–6. doi:10.1109/ICPES.2016.7584226

Kovalsky, L., Xing, Y., Tekletsadik, K., Keri, A., Bock, J., and Breuer, F. (2005). Applications of superconducting fault current limiters in electric power transmission systems. *IEEE Trans. Appl. Supercond.* 15 (2), 2130–2133. doi:10.1109/TASC.2005.849471

Koyama, T., and Yanabu, S. (2009). Study and development of superconducting fault current limiter with high speed Reclosing. *IEEE Trans. Appl. Supercond.* 19 (3), 1868–1871. doi:10.1109/TASC.2009.2018783

Kumar, A., Verma, N., and Kumari, S. K. (2016). Application of superconducting fault current limiter in single phase system using Simulink. *Imperial J. Interdiscip. Res.* 2 (8). Available at: http://www.imperialjournals.com/index.php/IJIR/article/view/1563 (Accessed 25, 06, 2019).

Kundur, P., Paserba, J., Ajjarapu, V., Andersson, G., Bose, A., Canizares, C., et al. (2004). Definition and classification of power system stability IEEE/CIGRE joint task force on stability terms and definitions. *IEEE Trans. Power Syst.* 19 (3), 1387–1401. doi:10.1109/TPWRS.2004.825981

Kundur, P. (1994). *Power system stability and control*. New York ; London: McGraw-Hill.

Lee, B. W., Sim, J., Park, K. B., and Oh, I. S. (2008). Practical application issues of superconducting fault current limiters for electric power systems. *IEEE Trans. Appl. Supercond.* 18 (2), 620–623. doi:10.1109/TASC.2008.920784

Lee, G.-J. (2011). "Superconductivity application in power system," in *Applications of high-Tc superconductivity* (London: IntechOpen). doi:10.5772/16334

Leiva Roca, D. A., Mercado, P., and Suvire, G. (2022). System frequency response model considering the influence of power system stabilizers. *IEEE Lat. Am. Trans.* 20 (6), 912–920. doi:10.1109/TLA.2022.9757373

Li, B., Li, C., Guo, F., and Xin, Y. (2014). Overcurrent protection coordination in a power distribution network with the active superconductive fault current limiter. *IEEE Trans. Appl. Supercond.* 24 (5), 1–4. doi:10.1109/TASC.2014.2333811

Lim, S., Kim, J.-S., Moon, J. F., Kim, J.-C., Rhee, S.-B., Kim, C.-H., et al. (2009). Quench and recovery characteristics of a SFCL applied into neutral line of a three-phase power system. *IEEE Trans. Appl. Supercond.* 19 (3), 1835–1838. doi:10.1109/TASC.2009.2017754

Machowski, J., Bialek, J., and Bumby, D. J. (2008). *Power system dynamics: Stability and control*. 2nd edition. Chichester, U.K: Wiley-Blackwell.

Martini, L., Bocchi, M., Ascade, M., Valzasina, A., Rossi, V., Ravetta, C., et al. (2014). The first Italian Superconducting Fault Current Limiter: Results of the field testing experience after one year operation. *J. Phys. Conf. Ser.* 507 (3), 032003. doi:10.1088/1742-6596/507/3/032003

Matsumoto, K. (2010). "General theory of high-Tc superconductors," in *High temperature superconductors*. Editors R. Bhattacharya and M. P. Paranthaman (Weinheim, Germany: Wiley-VCH Verlag GmbH & Co. KGaA), 1–47. doi:10.1002/9783527631049.ch1

Miyashita, M., Umeda, S., Nagao, S., Amemiya, N., Kubota, H., Kudo, Y., et al. (2005). Measurement of lateral current redistribution of fault current limiter using YBCO thin film. *IEEE Trans. Appl. Supercond.* 15 (2), 2023–2026. doi:10.1109/TASC.2005.849442

Mohamed, E. (2012). "Enhancement of power system transient stability using superconducting fault current limiters with YBCO and Bi-2212," in The Middle East Power Systems Conference (MEPCON'2012), December 2012 (MEPCON).

Moon, J., Lim, S., Kim, J., and Yun, S. (2011). Assessment of the impact of SFCL on voltage Sags in power distribution system. *IEEE Trans. Appl. Supercond.* 21 (3), 2161–2164. doi:10.1109/TASC.2010.2093592

Noe, M., and Steurer, M. (2007). High-temperature superconductor fault current limiters: Concepts, applications, and development status. *Supercond. Sci. Technol.* 20 (3), R15–R29. doi:10.1088/0953-2048/20/3/R01

Padiyar, K. R. (2004). *Power system dynamics: Stability and control*. Anshan, China: Wiley.

Pawar, R., and Chavan, P. (2017). Minimizing of fault current using SFCL Technology. *Int. J. of Eng. Dev. Res.* 5, 1261–1267.

Ravindranath, B., and Chander, M. (1977). *Power system protection and switchgear*. New Delhi,India: New Age.

Sjostrom, M., Cherkaoui, R., and Dutoit, B. (1999). Enhancement of power system transient stability using superconducting fault current limiters. *IEEE Trans. Appl. Supercond.* 9 (2), 1328–1330. doi:10.1109/77.783547

Son, G. T., Lee, H., Lee, S., and Park, J. (2012). A study on the Direct stability analysis of Multi-machine power system with resistive SFCL. *IEEE Trans. Appl. Supercond.* 22 (3), 5602304. doi:10.1109/TASC.2011.2177626

Sung, B. C., Park, D. K., Park, J., and Ko, T. K. (2009). Study on a series resistive SFCL to improve power system transient stability: Modeling, simulation, and Experimental Verification. *IEEE Trans. Industrial Electron.* 56 (7), 2412–2419. doi:10.1109/TIE.2009.2018432

Vojenčiak, M., Dutoit, B., Šouc, J., and Gömöry, F. (2016). Can resistive-type fault current limiter operate in Cryogen-Free Environment? *IEEE Trans. Appl. Supercond.* 26 (3), 1–4. doi:10.1109/TASC.2016.2535175

Wang, H., Zhang, J., Niu, X., Tian, B., Hong, H., and Xin, Y. (2014). Electrical Insulation of HTS coils in saturated iron core superconducting fault current limiter. *IEEE Trans. Appl. Supercond.* 24 (3), 1–4. doi:10.1109/TASC.2013.2290944

Wang, M. H., He, Y. F., Yang, T. B., Jia, Y., and Xu, Z. (2020). Cascaded voltage control for electric Springs with DC-Link film capacitors. *IEEE J. Emerg. Sel. Top. Power Electron.* 8 (4), 3982–3994. doi:10.1109/jestpe.2019.2962238

Wang, M. H., Mok, K. T., Tan, S. C., and Hui, S. Y. R. (2018). Multifunctional DC electric Springs for improving voltage Quality of DC grids. *IEEE Trans. Smart Grid* 9 (3), 2248–2258.

Wang, M. H., Yan, S., Tan, S. C., and Hui, S. Y. R. (2018). Hybrid-DC electric Springs for DC voltage regulation and Harmonic Cancellation in DC Microgrids. *IEEE Trans. Power Electron.* 33 (2), 1167–1177. doi:10.1109/tpel.2017.2681120

Wang, M. H., Yang, T. B., Tan, S. C., and Hui, S. Y. R. (2019). Hybrid electric Springs for grid-tied power control and Storage Reduction in AC Microgrids. *IEEE Trans. Power Electron.* 34 (4), 3214–3225. doi:10.1109/tpel.2018.2854569

Yang, Q., Blond, S. L., Liang, F., Yuan, W., Zhang, M., and Li, J. (2017). Design and application of superconducting fault current limiter in a Multiterminal HVDC system. *IEEE Trans. Appl. Supercond.* 27 (4), 1–5. doi:10.1109/TASC.2017.2669152

Yonemura, N., Yamabe, K., Shirai, Y., Kobayashi, S., Nagaishi, T., and Konishi, M. (2015). Current limiting performance of transformer-type superconducting fault current limiter made of BSCCO and REBCO Wires. *IEEE Trans. Appl. Supercond.* 25 (3), 1–4. doi:10.1109/TASC.2014.2377126

Zhang, X., Ruiz, H. S., Zhong, Z., and Coombs, T. A. (2015). Implementation of resistive type superconducting fault current limiters in electrical grids: Performance analysis and measuring of optimal locations. Available at: http://arxiv.org/abs/1508.01162 (Accessed 18, 06, 2019).

Zheng, W., Zhu, J., and Luo, Q. (2022). Distributed Dispatch of Integrated Electricity-Heat Systems with Variable Mass Flow. *IEEE Transactions Smart Grid*. doi:10.1109/TSG.2022.3210014

Appendix A1:

The generator parameters used in Figure 4 (the studied system) in per unit are as follows:

$X_d = 1.8$	$X_q = 1.7$	$X_l = 0.2$	$X_d' = 0.3$	$X_q' = 0.55$
$X_d'' = 0.25$	$X_q'' = 0.25$	$R_a = 0.0025$	$T_{d0}' = 8s$	$T_{q0}' = 0.4s$
$T_{d0}'' = 0.03s$	$T_{q0}'' = 0.05s$	$A_{Sat} = 0.015$	$B_{Sat} = 9.6$	$\Psi_{T1} = 0.9$
$H = 6.5$ (for G1 and G2)		$H = 6.175$ (for G3 and G4)		$K_D = 0$

Each step-up transformer has an impedance of $0 + j0.15\ pu$, and the lines parameters in per unit.

$r = 0.0001\ pu/km$	$x_L = 0.001\ pu/km$	$b_c = 0.00175\ pu/km$

The generating units loaded as follows:

G1:	$P = 700\ MW$	$Q = 185\ MVar$	$E_t = 1.03\angle 20.2^o$
G2:	$P = 700MW$	$Q = 235\ MVar$	$E_t = 1.01\angle 10.5^o$
G3:	$P = 719MW$	$Q = 176\ MVar$	$E_t = 1.03\angle - 6.8^o$
G4:	$P = 700MW$	$Q = 202\ MVar$	$E_t = 1.01\angle - 17^o$

Loads and reactive power supplied by shunt capacitor at bus 7 and bus 9 are as follows:

Bus 7:	$P_L = 967MW$	$Q_L = 100\ MVar$	$Q_C = 200\ MVar$
Bus 9:	$P_L = 1767MW$	$Q_L = 100\ MVar$	$Q_C = 350\ MVar$

Virtual inertia based hierarchical control scheme for distributed generations considering communication delay

Chang Zhou[1,2], Yingqi Liao[3], Kaifeng Zhang[1]*, Xiaohui Xu[2] and Jiaqi Liao[2]

[1]Key Laboratory of Measurement and Control of CSE, School of Automation, Southeast University, Nanjing, Jiangsu, China, [2]Renewable Energy Research Center, State Key Laboratory of Operation and Control of Renewable Energy and Storage Systems, China Electric Power Research Institute, Nanjing, Jiangsu, China, [3]State Grid Nanjing Power Supply Company, Nanjing, Jiangsu, China

The virtual inertia technology of DGs (Distributed Generations) can provide inertia and damping support for the power system by imitating the traditional synchronous machine. However, the inherent delay problems around the communication and process links of the virtual inertia control will make an impact on the fast support effect. In this paper, the virtual inertia based hierarchical control scheme considering communication delay for distributed generations integration systems is proposed. The hierarchical control architecture including the PQ primary control and the virtual inertia based secondary control method which can realize the optimal power utilization and certain frequency support under the situation of communication signal delay at the same time. Firstly, the basic hierarchical control scheme for distributed generations and corresponding small signal modeling considering communication delay are presented. Then to enhance the inertia support ability of the distributed generation integration system, an improved hierarchical control strategy considering communication delay is designed based on the robust passivity method to compensate the equivalent delay disturbance. Finally, the effectiveness verification of the proposed control is carried out with the simulation cases in PSCAD platform.

1 Introduction

With the rapid development of distributed generations (DGs) such as wind and photovoltaic, the inertia level of power system is greatly reduced, which seriously weakens the inertia support and frequency stabilization ability of the system. Nevertheless, the frequency stability of power system with high proportion DG integration can be significantly improved by making full use of the flexible adjustment ability of large-scale DGs (Liu et al., 2019; Razavi et al., 2019; Quan et al., 2020). As the energy storage system has the characteristics of stable performance, flexible control and fast response, some studies have used the energy storage system to assist the frequency regulation process, but the high cost and low life of the energy storage system are its main shortcomings (Guan, 2022; Guo et al., 2023). Besides, the DGs can participate in the

frequency modulation of power grid through the direct control of the DG output power (Zhang et al., 2021), which directly controls the DGs to respond when the frequency is adjusted. This method makes the DGs unable to work at its optimal power point, which is equivalent to increasing the investment of distributed power supply.

In order to improve the stability of DG integration system, researchers are trying to find a suitable control method of power electronic converter to improve the stability of power system. It is a promising method to control the power electronic converter to have the dynamic characteristics of the traditional synchronous machine, which is called the virtual inertia technology (Beck and Hesse, 2007; Zhong and Weiss, 2011). The virtual inertia technology uses the mathematical model of the traditional synchronous machine to calculate the reference value of the inverter current and then controls the output current. The DG integration system under this control method can provide virtual inertia and damping for the power system by imitating the traditional synchronous machine. In (Kheshti et al., 2022), a novel Gaussian distribution-based inertial control scheme that can improve the frequency nadir without rotor speed over-deceleration is proposed. In (Guo et al., 2022), an inertial phase-locked loop is proposed for grid-connected converter to achieve fast frequency support which is analogous to the motion equation of synchronous generator. In (Yang et al., 2022), a fast frequency response strategy of a DFIG is proposed based on variable power point tracking control to boost the frequency support capability with grid-friendly rotor speed recovery. In (Xiong et al., 2021), a frequency trajectory planning based strategy is developed to improve frequency stability of droop-controlled inverter-based standalone power systems. To remain the basic structure of the DG control system, the power tracking scheme is adopted in this paper, which introduces the rate of change of frequency to the active power control loop of DG to provide inertia support by adjusting the active power command when the system frequency changes (Meng et al., 2019; Sun et al., 2020).

However, the virtual inertia control technology is realized by using digital control technology which includes the instruction generation and control realization processes. Hence the inherent delay problems around the communication and process links will make an impact on the fast frequency support effect (Liu et al., 2015; Yuan et al., 2022). According to (Vafamand et al., 2019; Lian et al., 2021), the time delays in digital signal may compromise the integrity and timeliness of the inertial support of the DGs and can be up to hundreds of milliseconds. From the point of view of synchronizing machine simulation, the time delay in the virtual inertia control is expected to be as small as possible. And too much large control delay may even make the system becomes unstable in severe cases (Nan et al., 2018). To handle this problem, the Rekasius substitution is used in (Suud et al., 2022) to compute the stability delay margin of an islanded micro-grid with virtual inertia and constant communication delay. Reference (Yang et al., 2019a) intends to reveal that the effects of delay, which are caused by frequency measurements and DC-link voltage regulation during the inertia emulation, are non-negligible in small-scale low inertia power systems with virtual inertia control implementations. In (Yang et al., 2019b), a detailed analysis of the effect of time-delays on virtual inertia control is presented which reveals that instability will happen when the virtual inertia is greater than the existing power system inertia regardless of time-delays. In (Haldar et al., 2022), a

delay based control strategy for emulation of virtual inertia in inverters operating in islanded operation mode is presented. Most of the existing literature relies on classical control theory to analyze the delay problem of a certain part of the control system, but there is a lack of delay modeling and suppression techniques including the control link of the system. Since the virtual inertia control requires fast frequency recovery ability, this paper focuses on the control system modeling and time delay compensation to eliminate the communication signal time-delay influence.
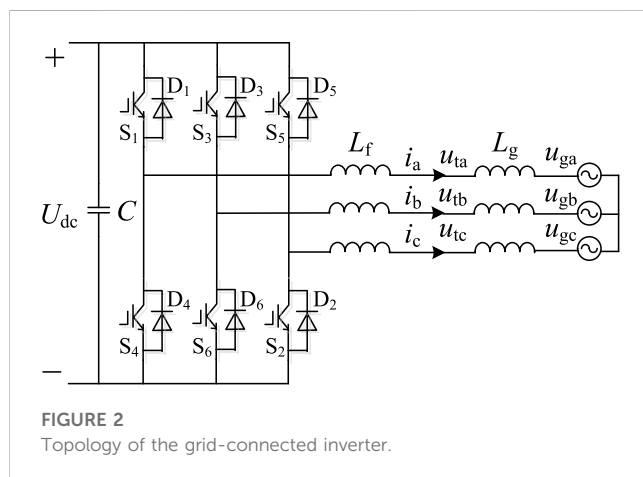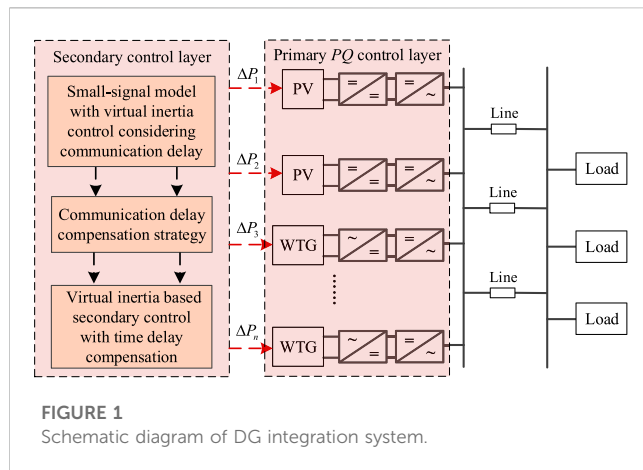
In this paper, the virtual inertia based hierarchical control scheme considering communication delay for DGs integration systems is proposed. The main contributions of the paper can be given as following:

(1) The hierarchical control architecture including the PQ primary control and the virtual inertia based secondary control method is presented which can realize the optimal power utilization and certain frequency support under the situation of communication signal delay at the same time.

(2) To enhance the inertia support ability of the DG integration system with communication delay, the small signal modeling for DGs considering communication delay is presented. Then an improved hierarchical control strategy is designed based on the robust passivity method, which can compensate the equivalent delay disturbance with fast response speed and superior robustness.

The effectiveness verification of the proposed control is carried out with the simulation cases in PSCAD platform, which shows that the proposed virtual inertia control can track the equivalent disturbance caused by time delay and compensate for the delay with superior dynamic response.

2 System structure and hierarchical control architecture for DGs

The systems structure and hierarchical control architecture for DGs are shown in Figure 1. The hierarchical control architecture including the *PQ* primary control and the virtual inertia based secondary control method is proposed in this paper for DGs. For the DGs, the *PQ* control mode is adopted in the primary control layer for the optimal utilization efficiency of DGs. In order to make full use of the flexible regulation ability of DGs, the additional virtual inertia control is implemented in the secondary control layer for frequency support of the utility grid. According to the rate of change of frequency, the additional control command can be generated and attached to the active power control loop of DG in the primary *PQ* control layer to provide inertia support. In the practical operation, due to the communication transmission from the secondary control layer to the controller of each DG unit, the time delay in the hierarchical control scheme is inevitable. Since the secondary virtual inertia control is implemented for fast frequency recovery of the utility grid, the control performance would be significantly impacted by the communication delay, which may bring serious disturbance and reduce the system stability. To eliminate the communication signal time-delay influence, the improved hierarchical control

FIGURE 1
Schematic diagram of DG integration system.

FIGURE 2
Topology of the grid-connected inverter.

FIGURE 3
The vector control based on grid voltage orientation of the inverter.

FIGURE 4
The PLL control strategy.

FIGURE 5
The virtual inertia based secondary control method for DGs.

strategy based on virtual inertial considering communication delay is proposed in the following section.

3 Hierarchical control strategy for DGs

3.1 Primary PQ control layer

The topology structure of the grid-connected inverter is shown in Figure 2 where C is the DC filter capacitor, U_{dc} is the DC voltage, L_f is the filter inductance of inverter, L_g is the grid inductance, U_t and U_g are rms values of the grid voltages.

From Figure 2, the mathematical model is shown in Eq. 1

$$
\begin{cases}
L\dfrac{di_d}{dt} = U_d - U_{td} + \omega L i_q \\[2mm]
L\dfrac{di_q}{dt} = U_q - U_{tq} - \omega L i_d \\[2mm]
U_{dc} \cdot C \dfrac{dU_{dc}}{dt} = i_{PV} \cdot U_{dc} - U_{td} \cdot i_d
\end{cases}
\tag{1}
$$

The inverter generally adopts the vector control strategy based on grid voltage orientation, as shown in Figure 3. The power outer loop control generates d axis and q axis current
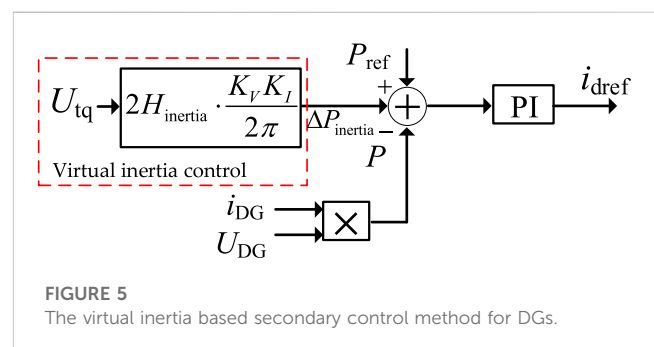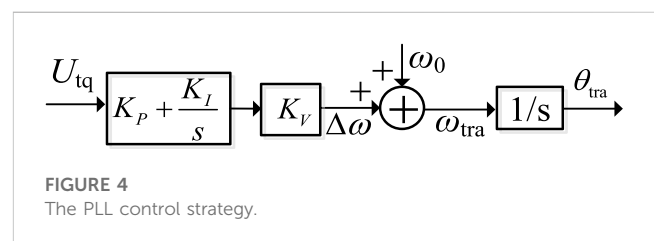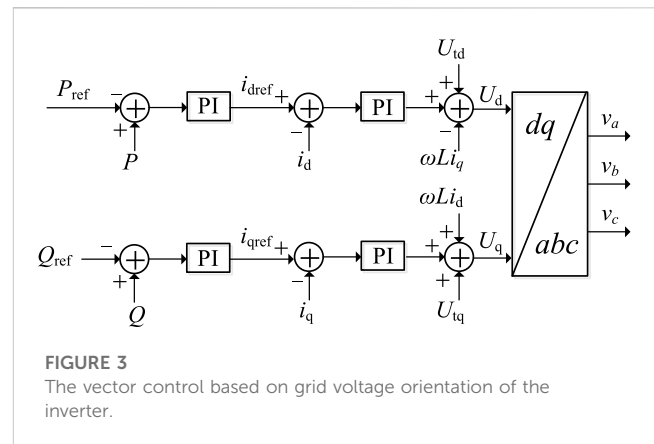
command values respectively according to the demand of active and reactive power, and regulates the active and reactive power injected into the grid by adjusting the current values of d axis and q axis. In Figure 3, P_{ref} and P are the reference and actual values of the active power respectively; Q_{ref} and Q are the reference value and actual value of reactive power respectively; i_{dref} and i_{qref} are the reference values of d axis current and q axis current, respectively; i_d and i_q are the d axis and q axis components of the inverter output current, respectively; U_d and U_q are the d axis and q axis components of the modulated voltage output by the current controller.

3.2 Virtual inertia based secondary control method of DGs

In the DG grid connection inverter, the phase-locked loop (PLL) is needed to generate the reference phase of the power grid.
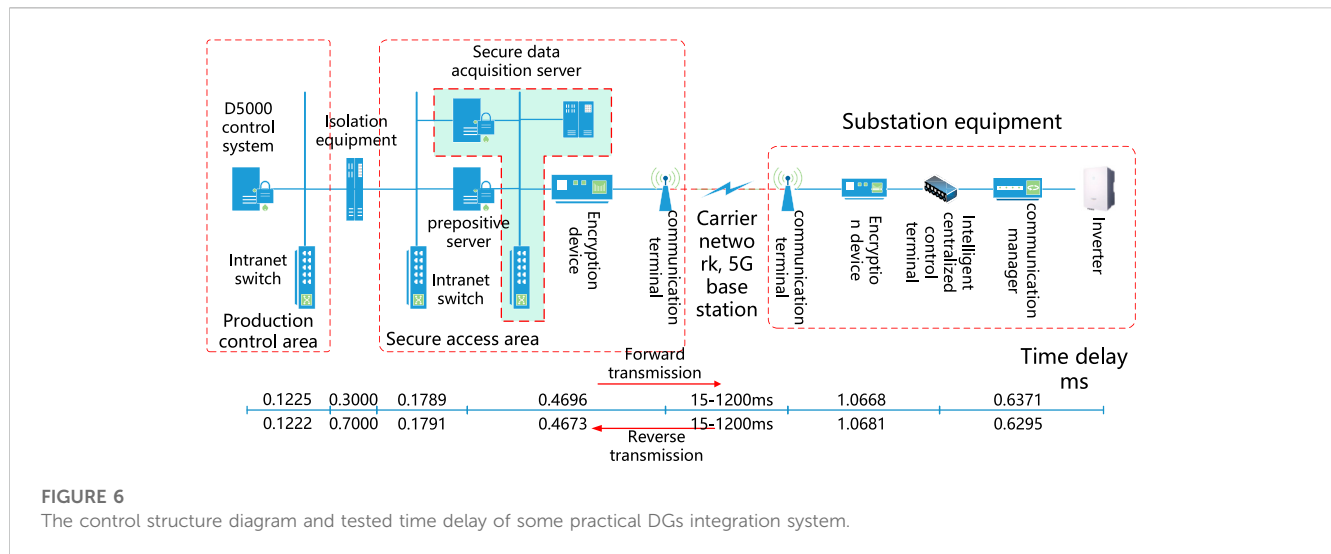
FIGURE 6
The control structure diagram and tested time delay of some practical DGs integration system.
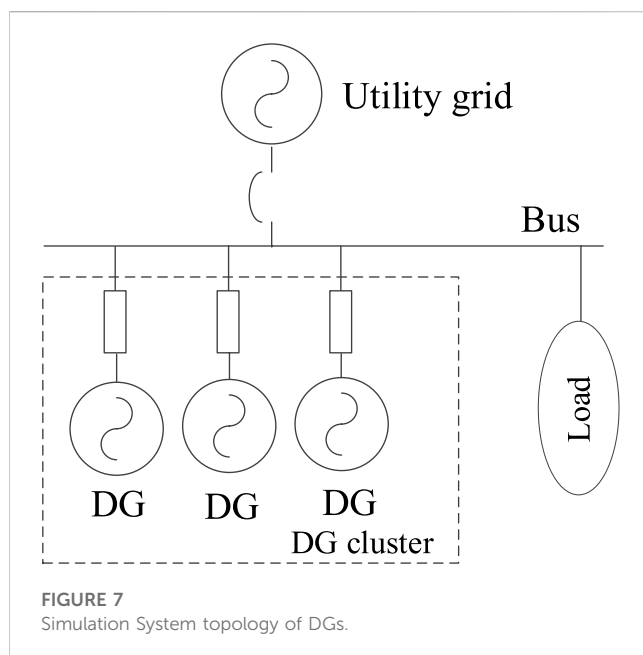

FIGURE 7
Simulation System topology of DGs.

The PLL usually uses the q-axis component generated by coordinate transformation and obtains the reference phase by controlling the q-axis voltage to zero (Nabil et al., 2022). The PLL adopted in the grid-connected inverter is given in Figure 4 where U_{tq} is the q-axis component of the voltage vector at the grid-connection point. The working principle is that the instantaneous value of grid voltage is transformed to generate U_{tq}. Through the PI controller and coefficient K_V, the angular frequency difference $\Delta\omega$ can be obtained. Then the angular frequency ω_{tra} is obtained by adding $\Delta\omega$ to the rated angular frequency ω_0, and the measured value angle θ_{tra} of the phase is obtained by the integration process.

According to Figure 4, the power grid frequency f obtained from the PLL is given as

$$f = K_V \cdot \frac{U_{tq}}{2\pi} \cdot \left(K_P + \int K_I dt \right) + \frac{\omega_0}{2\pi} \tag{2}$$

where K_P and K_I are the proportional and integral coefficients; K_V is the gain coefficient. By taking the derivative of Eq. 2, the frequency change rate df/dt of the power grid is obtained as

$$\frac{df}{dt} = \frac{U_{tq} \cdot K_V K_I}{2\pi} \tag{3}$$

Then the active power increment $\Delta P_{inertia}$ is further obtained as

$$\Delta P_{inertia} = 2H_{inertia}\frac{df}{dt} = 2H_{inertia} \cdot \frac{U_{tq} \cdot K_V K_I}{2\pi} \tag{4}$$

where $H_{inertia}$ is the virtual inertia time constant. Therefore, the virtual inertia control of DGs based on the PLL control of the grid-side inverter is realized.

The above virtual inertia based secondary control method for DGs actively participating in power grid frequency regulation is shown in Figure 5.

4 Hierarchical control strategy for DGs considering communication delay

4.1 Small signal modeling of DGs with the hierarchical control strategy considering communication delay

The system small-signal model of hierarchical control scheme is firstly established in this part. The mathematical model of the grid-connected inverter in the synchronous rotating d-q reference frame is given as

$$\begin{cases} L\dfrac{di_d}{dt} = U_d - U_{td} + \omega L i_q \\[2mm] L\dfrac{di_q}{dt} = U_q - U_{tq} - \omega L i_d \end{cases} \tag{5}$$
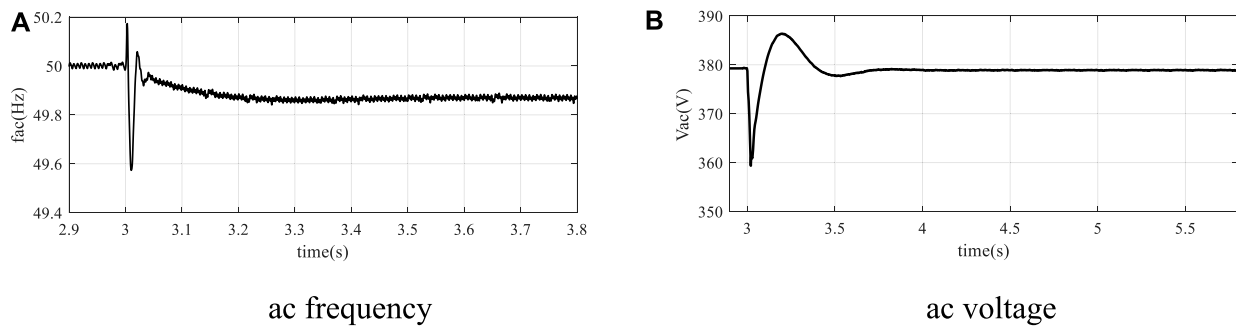
FIGURE 8
The simulation results with no time delay. **(A)** ac frequency, **(B)** ac voltage.

From the primary PQ control in Section 3.1, the inverter current i_d and i_q are controlled to follow the current references i_{dref} and i_{qref} through the PI controller, and it yields

$$\begin{cases} U_d = U_{td} - \omega L i_q + \left(K_{PId} + \dfrac{K_{IId}}{s}\right)(i_{dref} - i_d) \\ U_q = U_{tq} + \omega L i_d + \left(K_{PIq} + \dfrac{K_{IIq}}{s}\right)(i_{qref} - i_q) \end{cases} \quad (6)$$

where K_{PId} and K_{IId}, K_{PIq} and K_{IIq} are the proportional and integral parameters of the PI controllers. The outer power loop controls are also based on the PI controllers which has

$$\begin{cases} i_{dref} = (P_{ref} - P)\left(K_{PP} + \dfrac{K_{IP}}{s}\right) \\ i_{qref} = (Q_{ref} - Q)\left(K_{PQ} + \dfrac{K_{IQ}}{s}\right) \end{cases} \quad (7)$$

where K_{PP} and K_{IP}, K_{PQ} and K_{IQ} are the proportional and integral parameters of the power loop PI controllers. Then the following differential and algebraic equations can be obtained as

$$\begin{cases} \dfrac{dx_P}{dt} = P_{ref} - P, \dfrac{dx_Q}{dt} = Q_{ref} - Q \\ \dfrac{dx_{id}}{dt} = i_{dref} - i_d, \dfrac{dx_{iq}}{dt} = i_{qref} - i_d \end{cases} \quad (8)$$

and

$$\begin{cases} i_{dref} = K_{IP}x_P + (P_{ref} - P)K_{PP} \\ i_{qref} = K_{IQ}x_Q + (Q_{ref} - Q)K_{PQ} \\ U_d = U_{td} - \omega L i_q + K_{IId}x_{id} + K_{PId}(i_{dref} - i_d) \\ U_q = U_{tq} + \omega L i_d + K_{IIq}x_{iq} + K_{PIq}(i_{qref} - i_q) \end{cases} \quad (9)$$

where x_P, x_Q, x_{id} and x_{iq} are the intermediate state variables. Based on the above derivation, the small signal model of the grid-connected inverter with primary PQ control is formulated as

$$\Delta\dot{x} = \mathbf{A}\Delta x \quad (10)$$

where $x = [x_P, x_Q, x_{id}, x_{iq}, P, Q, i_d, i_q, i_{dref}, i_{qref}]^T$; here Δ stands for the small-signal components and $\mathbf{A}$ is the system matrix which can be obtained from Eqs 8, 9.

Besides the primary PQ control, the virtual inertia based secondary control method of DGs is carried out for the fast frequency enhancement. Once receiving the measurements sent from the inverters, the secondary controller generates the supplementary power signal for frequency regulation. According to (4), the power reference command with the virtual inertia based secondary control is given as

$$P_{ref} = P_n + \Delta P_{inertia} = P_n + \dfrac{H_{inertia}K_V K_I}{\pi}U_{tq} \quad (11)$$

where P_n is the power reference command from primary PQ control. Defining the control input as

$$u_{sec} = \dfrac{H_{inertia}K_V K_I}{\pi}U_{tq} \quad (12)$$

Then the Small signal modeling of DGs with the hierarchical control strategy is

$$\Delta\dot{x} = \mathbf{A}\Delta x + \mathbf{B}u \quad (13)$$

where the control input $u = u_{sec}$, and the matrix $\mathbf{B}$ is given as

$$\mathbf{B} = \left[\dfrac{H_{inertia}K_V K_I}{\pi} \quad \mathbf{0}_{1 \times 9} \right]^T \quad (14)$$

However, the unavoidable time delay in signal sampling, measurement and execution may reduce the fast control performance of the virtual inertia based secondary control. The control structure diagram and tested time delay of some practical DGs integration system can be seen in Figure 6, which shows that the total time delay in the signal communication can be up to tens to hundreds of milliseconds. That is to say, the problems caused by the time delay may make the virtual inertia based secondary controller not only unable to achieve the expected control objectives, but also may lead to the deterioration or even instability of the dynamic performance of the inverter systems.

Considering the time delay, the system model can be written as

$$\Delta\dot{x} = \mathbf{A}\Delta x(t - \tau_1) + \mathbf{B}u(t - \tau_2) \quad (15)$$

The equivalent delays τ_1 and τ_2 contain both transmission delays of state variables and control inputs and satisfy

$$\begin{cases} 0 \le \tau_1(t) \le \tau_{max} \\ 0 \le \tau_2(t) \le \tau_{max} \end{cases} \quad (16)$$

where τ_{max} is a positive constant. It can be seen from Eq. 13 that the system stability under the control input u can be guaranteed
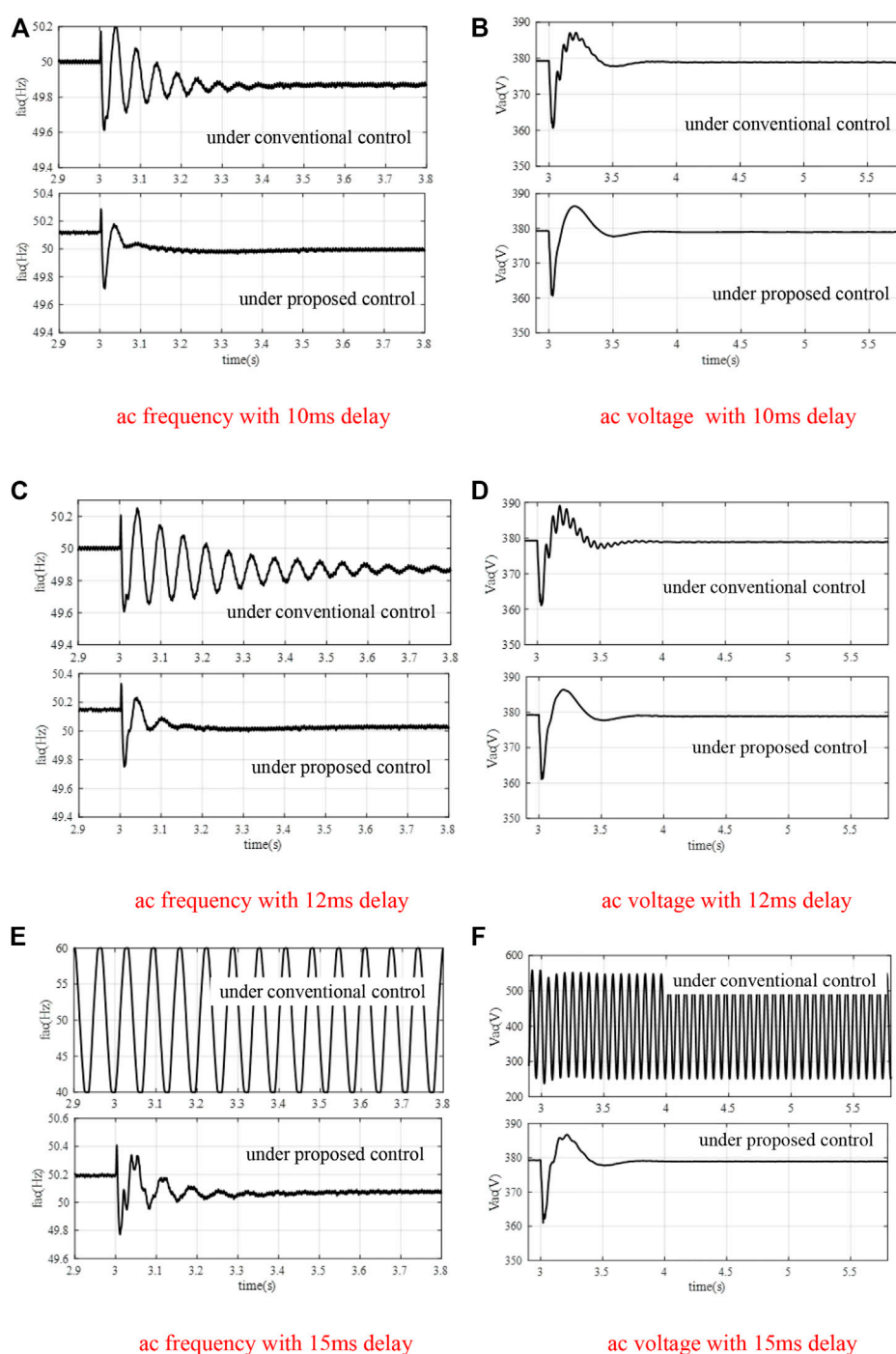
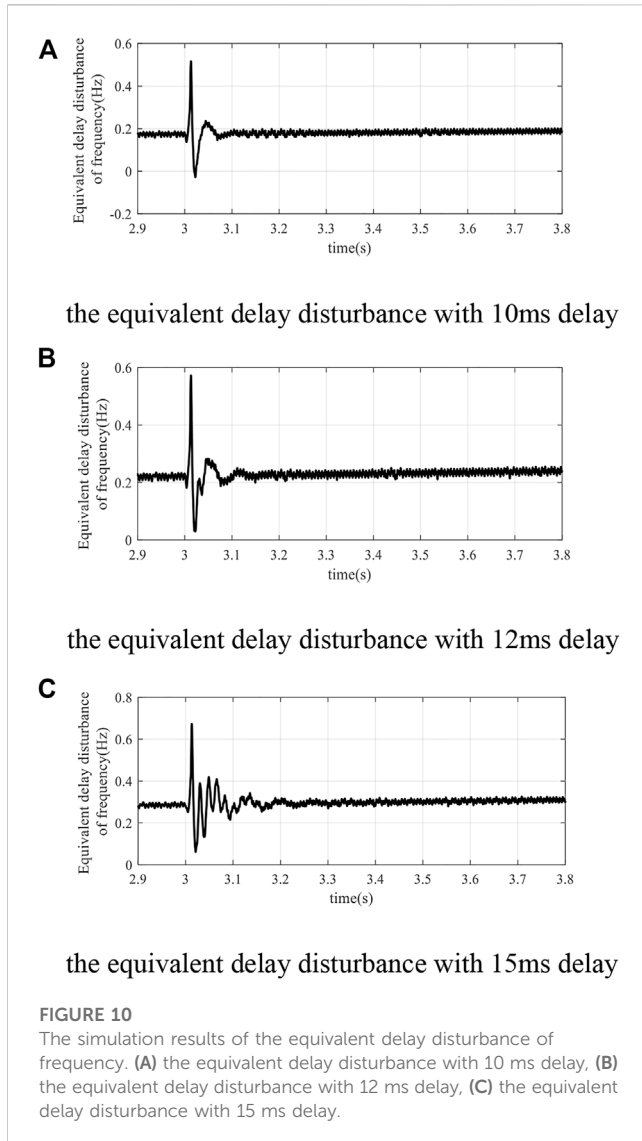**FIGURE 9**
The simulation results with different time delays. **(A)** ac frequency with 10 ms delay, **(B)** ac voltage with 10 ms delay, **(C)** ac frequency with 12 ms delay, **(D)** ac voltage with 12 ms delay, **(E)** ac frequency with 15 ms delay, **(F)** ac voltage with 15 ms delay.

with the small disturbance analysis method. However, the existing of delays τ_1 and τ_2 in Eq. 14 may destroy the system stability and make the stability condition no longer satisfied. Therefore, the effects of time delays in system state transmission and control inputs are simultaneously considered in the model and corresponding improved control is proposed in the next section.

4.2 Improved hierarchical control strategy based on virtual inertial considering communication delay

In this section, an improved hierarchical control strategy considering communication delay is designed based on the robust passivity method to compensate the equivalent delay

FIGURE 10
The simulation results of the equivalent delay disturbance of frequency. **(A)** the equivalent delay disturbance with 10 ms delay, **(B)** the equivalent delay disturbance with 12 ms delay, **(C)** the equivalent delay disturbance with 15 ms delay.

disturbance. The main problem to design the improved control is how to deal with the time delay term both in state variable and control input properly. To handle this, the system dynamic equation is transformed in the following form.

$$\Delta \dot{\boldsymbol{x}} = \mathbf{A}\Delta \boldsymbol{x}(t) + \mathbf{B}\boldsymbol{u}(t) + \mathbf{D}(t) \tag{17}$$

where the equivalent delay disturbance is defined as $\mathbf{D}(t) = \mathbf{A}\Delta \boldsymbol{x}(t - \tau_1) - \mathbf{A}\Delta \boldsymbol{x}(t) + \mathbf{B}\boldsymbol{u}(t - \tau_2) - \mathbf{B}\boldsymbol{u}(t)$. In this part, the robust passivity method is proposed to compensate the equivalent delay disturbance $\mathbf{D}(t)$. For the equivalent delay disturbance $\mathbf{D}(t)$, the expansion expression can be given according to Taylor's formula

$$\mathbf{D}(t) = \underbrace{-\tau_1 \mathbf{A}\Delta \boldsymbol{x}'(t) + \frac{\tau_1^2}{2!}\mathbf{A}\Delta \boldsymbol{x}''(t) - \cdots}_{\text{Taylor expansion of } \tau_1 \text{ in } \Delta \boldsymbol{x}(t)} \underbrace{-\tau_2 \mathbf{B}\boldsymbol{u}'(t) + \frac{\tau_2^2}{2!}\mathbf{B}\boldsymbol{u}''(t) - \cdots}_{\text{Taylor expansion of } \tau_2 \text{ in } \boldsymbol{u}(t)} \tag{18}$$

Since the equivalent delay time τ_1 and τ_2 are time-varying, the high-order polynomial with respect to time t can be used to express the equivalent delay disturbance $\mathbf{D}(t)$, which is given as

$$\mathbf{D}(t) = \sum_{i=0}^{\infty} \boldsymbol{a}_i t^i \tag{19}$$

where a_i ($i = 0,\ldots$) is the constant coefficient of the polynomial. Considering that the noise becomes serious and the structure becomes complicated in the controller design, the high order dynamic behavior of the delay disturbance is ignored and it has

$$\frac{\mathrm{d}}{\mathrm{dt}}\mathbf{D}(t) = 0 \tag{20}$$

Then the robust passivity method to compensate the equivalent delay disturbance is proposed in this paper. For the system dynamic model (15), take the following variable transformation

$$\Delta \boldsymbol{x}(t) = \Delta \boldsymbol{x}^\star(t) + \Delta \tilde{\boldsymbol{x}}(t) \tag{21}$$

where $\Delta \boldsymbol{x}^\star(t)$ and $\Delta \tilde{\boldsymbol{x}}(t)$ are the ideal value at the equilibrium point and the corresponding error. By taking (19) into (15), it has

$$\frac{\mathrm{d}}{\mathrm{dt}}\Delta \boldsymbol{x}^\star(t) - \mathbf{A}\Delta \boldsymbol{x}^\star(t) - \mathbf{B}\boldsymbol{u}(t) - \hat{\mathbf{D}}(t) = -\frac{\mathrm{d}}{\mathrm{dt}}\Delta \tilde{\boldsymbol{x}}(t) + \mathbf{A}\Delta \tilde{\boldsymbol{x}}(t) + \tilde{\mathbf{D}}(t) \tag{22}$$

where $\hat{\mathbf{D}}(t)$ and $\tilde{\mathbf{D}}(t)$ are the dynamic estimate and estimate error of the unknown equivalent delay $\mathbf{D}(t)$, which means $\tilde{\mathbf{D}}(t) = \mathbf{D}(t) - \hat{\mathbf{D}}(t)$. To stabilize the system with the existence of communication delay, the virtual damping matrix $\mathbf{R}(t)$ is introduced in Eq. 20 to compensate the equivalent delay disturbance, which has

$$\frac{\mathrm{d}}{\mathrm{dt}}\Delta \boldsymbol{x}^\star(t) - \mathbf{A}\Delta \boldsymbol{x}^\star(t) - \mathbf{B}\boldsymbol{u}(t) - \hat{\mathbf{D}}(t) + \mathbf{R}(t)\Delta \tilde{\boldsymbol{x}}(t)$$
$$= -\frac{\mathrm{d}}{\mathrm{dt}}\Delta \tilde{\boldsymbol{x}}(t) + \mathbf{A}\Delta \tilde{\boldsymbol{x}}(t) + \tilde{\mathbf{D}}(t) + \mathbf{R}(t)\Delta \tilde{\boldsymbol{x}}(t) \tag{23}$$

If the actual control law $\boldsymbol{u}(t)$ is taken as

$$\boldsymbol{u}(t) = \mathbf{B}^+\left(\frac{\mathrm{d}}{\mathrm{dt}}\Delta \boldsymbol{x}^\star(t) - \mathbf{A}\Delta \boldsymbol{x}^\star(t) - \hat{\mathbf{D}}(t) + \mathbf{R}(t)\Delta \tilde{\boldsymbol{x}}(t)\right) \tag{24}$$

where $\mathbf{B}^+$ is the inverse matrix of $\mathbf{B}$, it has

$$-\frac{\mathrm{d}}{\mathrm{dt}}\Delta \tilde{\boldsymbol{x}}(t) + \mathbf{A}\Delta \tilde{\boldsymbol{x}}(t) + \tilde{\mathbf{D}}(t) + \mathbf{R}(t)\Delta \tilde{\boldsymbol{x}}(t) = \mathbf{0} \tag{25}$$

Then the system Lyapunov function with equivalent time delay is chosen as

$$H(\Delta \tilde{\boldsymbol{x}}) = \frac{1}{2}\Delta \tilde{\boldsymbol{x}}(t)^T \boldsymbol{Q}_x \Delta \tilde{\boldsymbol{x}}(t) + \frac{1}{2}\tilde{\mathbf{D}}(t)^T \boldsymbol{Q}_D \tilde{\mathbf{D}}(t) \tag{26}$$

where $\boldsymbol{Q}_x$ and $\boldsymbol{Q}_D$ are the positive coefficient matrix. Together with Eq. 23, the derivative of the Lyapunov function $H(\Delta \tilde{\boldsymbol{x}})$ is

$$\frac{\mathrm{d}}{\mathrm{dt}}H(\Delta \tilde{\boldsymbol{x}}) = \Delta \tilde{\boldsymbol{x}}(t)^T \boldsymbol{Q}_x\left(\mathbf{A}\Delta \tilde{\boldsymbol{x}}(t) + \tilde{\mathbf{D}}(t) + \mathbf{R}(t)\Delta \tilde{\boldsymbol{x}}(t)\right)$$
$$+ \tilde{\mathbf{D}}(t)^T \boldsymbol{Q}_D \dot{\tilde{\mathbf{D}}}(t) \tag{27}$$

From Eq. 18 it is seen that the equivalent delay disturbance is assumed to be first-order. Thus it yields

$$\frac{\mathrm{d}}{\mathrm{dt}}H(\Delta \tilde{\boldsymbol{x}}) = \Delta \tilde{\boldsymbol{x}}(t)^T (\boldsymbol{Q}_x\mathbf{A} + \boldsymbol{Q}_x\mathbf{R}(t))\Delta \tilde{\boldsymbol{x}}(t) + \Delta \tilde{\boldsymbol{x}}(t)^T \boldsymbol{Q}_x\tilde{\mathbf{D}}(t)$$
$$- \tilde{\mathbf{D}}(t)^T \boldsymbol{Q}_D \dot{\hat{\mathbf{D}}}(t) \tag{28}$$
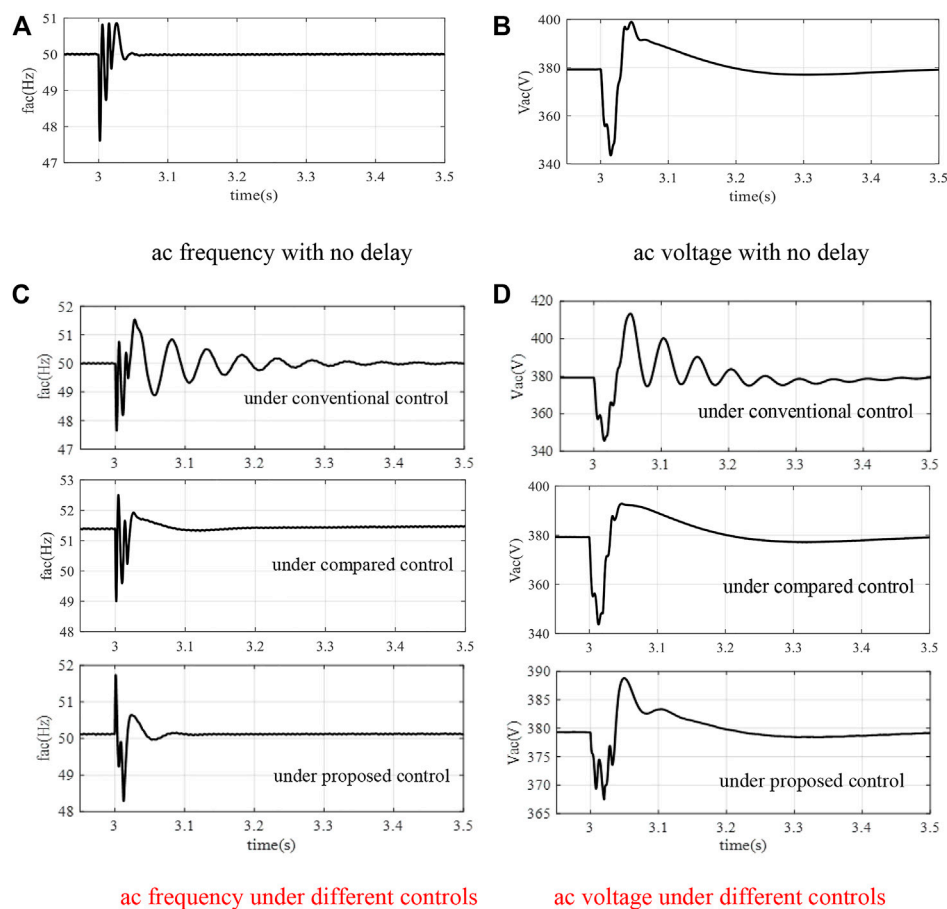
FIGURE 11
The simulation results with 10 ms delay of case 2. **(A)** ac frequency with no delay, **(B)** ac voltage with no delay, **(C)** ac frequency under different controls, **(D)** ac voltage under different controls.

If the adaptive law is designed as

$$\dot{\hat{\mathbf{D}}}(t) = \mathbf{Q}_D^{-1}\left(\tilde{\mathbf{D}}(t)^T\right)^{-1}\Delta\tilde{\mathbf{x}}(t)^T\mathbf{Q}_x\tilde{\mathbf{D}}(t) \qquad (29)$$

then the derivative of the Lyapunov function $H(\Delta\tilde{\mathbf{x}})$ can be written as

$$\frac{\mathrm{d}}{\mathrm{dt}}H(\Delta\tilde{\mathbf{x}}) = \Delta\tilde{\mathbf{x}}(t)^T\left(\mathbf{Q}_x\mathbf{A} + \mathbf{Q}_x\mathbf{R}(t)\right)\Delta\tilde{\mathbf{x}}(t) \qquad (30)$$

To ensure the system Lyapunov function $H(\Delta\tilde{\mathbf{x}})$ with the virtual damping matrix $\mathbf{R}(t)$ can be convergent, the virtual damping matrix $\mathbf{R}(t)$ should be determined to ensure that the term $\mathbf{Q}_x\mathbf{A} + \mathbf{Q}_x\mathbf{R}(t) < \mathbf{0}$ is satisfied. Then the Lyapunov function $H(\Delta\tilde{\mathbf{x}})$ satisfy the system asymptotic stability condition and the asymptotic stability of the system can be guaranteed, which means the improved hierarchical control strategy based on virtual inertial considering communication delay is realized with the robust passivity control law (22) and the equivalent delay disturbance compensation law (27).

5 Case study

To verify the validation of the proposed control strategy, the DG integration system shown in Figure 7 is established in PSCAD platform. The capacity of each DG unit in the simulation model is 40 kW and use the hierarchical scheme based on virtual inertia control strategy proposed in this paper. The rated ac frequency is 50 Hz and the ac voltage is 380 V. Two cases including the load power fluctuation and the single-phase ground fault are conducted in this section to verify the validation of the proposed control strategy under common disturbances.

5.1 Case 1

In this case, the initial active load in the system is 40 kW. At time 3 s, the load power increases to 60 kW. Besides, there exists time delay in the communication of the virtual inertia based secondary controller. The system simulation results with and without the proposed improved control are shown in Figures 8–10.

The system simulation results in Figures 8, 9 show the ac frequency and voltage response of the DG integration system during the load fluctuation in different situations. In Figure 8, the conventional virtual inertia control without any time delay compensation is adopted with no time delay in the signal communication. It can be seen that the system frequency and voltage can transition to a new steady state after the load increase at 3 s. However, when there exists time delay in the signal communication of the virtual inertia based secondary controller, the system response gets worse and even becomes unstable. From the system response under conventional control in Figure 9, it is seen that when the time delay is 10 ms, the system frequency is oscillating and the oscillation continues to 3.4 s. When the time delay increases to 12 ms, the dynamic response of system frequency and voltage gets larger oscillation with the conventional virtual inertia control. More serious is that the system loses stability when the time delay is 15 ms from Figures 9E, F with the conventional virtual inertial control. The simulation results under proposed robust passivity control method in Figure 9 show the ac frequency and voltage with different time delays to compensate the equivalent delay disturbance. It is seen that the ac frequency and voltage all respond satisfactorily no matter how much the communication time delay is. Figure 10 gives the simulation results of the equivalent delay disturbance of frequency, which indicates that the proposed control can track the equivalent disturbance caused by time delay and then compensate for the delay.

5.2 Case 2

In this case, the active load in the system is still 40 kW. At time 3 s, a single-phase ground fault occurs and lasts for 10 ms. It is also assumed that there exists different time delay in the communication of the virtual inertia based secondary controller. The system simulation results with and without the proposed control are shown in Figure 11. Besides, the system performance is also compared with the time delay compensation control in the existing literature (Natoriand and Ohnishi, 2008).

The simulation results show that during the single-phase ground fault, the transient process is deteriorated when there exist time delays in the signal communication with the conventional virtual inertia control. However, when the proposed robust passivity method works to compensate the equivalent delay disturbance, the oscillations of ac frequency and voltage can still be decreased and the impact of time delay can be well suppressed. The system response is also compared with the time delay compensation control in (Natoriand and Ohnishi, 2008), which shows that although the oscillations can be suppressed, large overshoots still exist. It can be concluded from the above cases that even the system suffers large disturbances, the improved hierarchical control strategy based on the robust passivity method can significantly enhance the robustness of the DG integration system for superior dynamic response when there exists time delay in the communication channel.

6 Conclusion

As the rapid development of DGs and the development of virtual inertia control, the inherent communication delay problems around the control link makes an impact on the fast support effect which cannot be ignored. This paper proposes the virtual inertia based hierarchical control scheme for DGs considering communication delay, which includes the PQ primary control and the virtual inertia based secondary control method. To enhance the inertia support ability of the DG integration system, an improved hierarchical control strategy considering communication delay is designed based on the robust passivity method to compensate the equivalent delay disturbance. The effectiveness verification of the proposed control is then carried out with the simulation cases in PSCAD platform. In further research, it is necessary to conduct the inertia enhancement method study of multiply distribution systems with DGs on a broader level to comprehensively improve the stability of the distribution power system.

Data availability statement

The raw data supporting the conclusion of this article will be made available by the authors, without undue reservation.

Author contributions

CZ: Conceptualization, methodology, validation, writing–original draft. YL: Data curation, writing–original draft. KZ: Methodology, conceptualization, writing–review and editing. XX: Methodology, validation. JL: Writing–review and editing.

Funding

Conflict of interest

Author YL was employed by State Grid Nanjing Power Supply Company.

The remaining authors declare that the research was conducted in the absence of any commercial or financial relationships that could be construed as a potential conflict of interest.

Publisher's note

References

Beck, H. P., and Hesse, R. (2007). *Virtual synchronous machine[C]//2007 9th international conference on electrical power quality and utilization(EPQU)*. Spain: IEEE, 1–6.

Guan, M. Y. (2022). Scheduled power control and autonomous energy control of grid-connected energy storage system (ESS) with virtual synchronous generator and primary frequency regulation capabilities. *IEEE Trans. Power Syst.* 37 (2), 942–954. doi:10.1109/tpwrs.2021.3105940

Guo, M. L., Zheng, J. Y., Mei, F., Sha, H., Gao, A., and Xie, Y. (2023). Double-layer AGC frequency regulation control method considering operating economic cost and energy storage SOC consistency. *Int. J. Electr. Power and Energy Syst.* 145, 108704. doi:10.1016/j.ijepes.2022.108704

Guo, X., Zhu, D., and Hu, J. (2022). Inertial PLL of grid-connected converter for fast frequency support[J]. *CSEE J. Power Energy Syst.* early access.

Haldar, A., Khatua, R., and Malkhandi, A. (2022). *Delay based virtual inertia emulation for a grid forming system[C]//2022 IEEE Power and Energy Conference at Illinois (PECI)*. IL, USA: Champaign, 10–11.

Kheshti, M., Lin, S., Zhao, X., Ding, L., Yin, M., and Terzija, V. (2022). Gaussian distribution-based inertial control of wind turbine generators for fast frequency response in low inertia systems. *IEEE Trans. Sustain. Energy* 13 (3), 1641–1653. doi:10.1109/tste.2022.3168778

Lian, Z., Deng, C., Wen, C., Guo, F., Lin, P., and Jiang, W. (2021). Distributed event-triggered control for frequency restoration and active power allocation in microgrids with varying communication time delays. *IEEE Trans. Industrial Electron.* 68 (9), 8367–8378. doi:10.1109/tie.2020.3016272

Liu, S. C., Wang, X. Y., and Liu, P. X. (2015). Impact of communication delays on secondary frequency control in an islanded microgrid. *IEEE Trans. Industrial Electron.* 62 (4), 2021–2031. doi:10.1109/tie.2014.2367456

Liu, Z. W., Miao, S. H., Fan, Z. H., Liu, J., and Tu, Q. (2019). Improved power flow control strategy of the hybrid AC/DC microgrid based on VSM. *Transm. Distribution* 13 (1), 81–91. doi:10.1049/iet-gtd.2018.5839

Meng, X., Liu, J., and Liu, Z. (2019). A generalized droop control for grid-supporting inverter based on comparison between traditional droop control and virtual synchronous generator control. *IEEE Trans. Power Electron.* 34 (6), 5416–5438. doi:10.1109/tpel.2018.2868722

Nabil, M., Zhou, W., and Behrooz, B. (2022). Comparison of PLL-based and PLL-less control strategies for grid-following inverters considering time and frequency domain analysis. *IEEE Access* 10, 80518–80538. doi:10.1109/access.2022.3195494

Nan, C., Tingcun, W., Ke, S., and Wang, R. (2018). Digital controller based on delta operator for high-frequency DC–DC switching converters. *IET Power Electron.* 11 (7), 1224–1230. doi:10.1049/iet-pel.2017.0556

Natoriand, K., and Ohnishi, K. (2008). A design method of communication disturbance observer for time-delay compensation, taking the dynamic property of network disturbance into account. *IEEE Trans. Industrial Electron.* 55 (5), 2152–2168. doi:10.1109/tie.2008.918635

Quan, X., Yu, R., Zhao, X., Lei, Y., Chen, T., Li, C., et al. (2020). Photovoltaic synchronous generator: Architecture and control strategy for a grid-forming PV energy system. *J]. IEEE J. Emerg. Sel. Top. Power Electron.* 08 (2), 936–948. doi:10.1109/jestpe.2019.2953178

Razavi, S. E., Rahimi, E., Javadi, M. S., Nezhad, A. E., Lotfi, M., Shafie-khah, M., et al. (2019). Impact of distributed generation on protection and voltage regulation of distribution systems: A review. *Renew. Sustain. Energy Rev.* 105, 157–167. doi:10.1016/j.rser.2019.01.050

Sun, D., Liu, H., Gao, S., Wu, L., Song, P., and Wang, X. (2020). Comparison of different virtual inertia control methods for inverter-based generators. *J. Mod. Power Syst. Clean Energy* 8 (4), 768–777. doi:10.35833/mpce.2019.000330

Suud, A. H., Şahin, S., and Saffet, A. (2022). *Impact of virtual inertia on stability delay margins of micro grids with communication time delay[C]//2022 4th Global Power, Energy and Communication Conference (GPECOM)*. Turkey: Nevsehir, 14–17.

Vafamand, N., Khooban, M. H., Dragičević, T., Boudjadar, J., and Asemani, M. H. (2019). Time-delayed stabilizing secondary load frequency control of shipboard microgrids. *IEEE Syst. J.* 13 (3), 3233–3241. doi:10.1109/jsyst.2019.2892528

Xiong, L., Liu, L., Liu, X., and Liu, Y. (2021). Frequency trajectory planning based strategy for improving frequency stability of droop-controlled inverter based standalone power systems. *IEEE J. Emerg. Sel. Top. Circuits Syst.* 11 (1), 176–187. doi:10.1109/jetcas.2021.3052006

Yang, D., Yan, G., Zheng, T., Zhang, X., and Hua, L. (2022). Fast frequency response of a DFIG based on variable power point tracking control. *IEEE Trans. Industry Appl.* 58 (4), 5127–5135. doi:10.1109/tia.2022.3177590

Yang, H. X., Fang, J. Y., and Tang, Y. (2019). *Exploration of time-delay effect on the stability of grid-connected power converters with virtual inertia[C]//2019 10th International Conference on Power Electronics and ECCE Asia (ICPE 2019 - ECCE Asia)*. Busan, Korea (South), 27–30.

Yang, H. X., Fang, J. Y., and Yi, T. (2019). *On the stability of virtual inertia control implemented by grid-connected power converters with delay effects [C]// 2019 IEEE Energy Conversion Congress and Exposition (ECCE)*. MD, USA: Baltimore.

Yuan, Z-L., Zhang, C-K., Shangguan, X-C., Jin, L., Xu, D., and He, Y. (2022). Stability analysis of load frequency control for shipboard microgrids with occasional large delays. *IEEE Trans. Circuits Syst. II Express Briefs* 69 (4), 2161–2165. doi:10.1109/tcsii.2021.3135962

Zhang, H., Xiang, W., Lin, W., and Wen, J. (2021). Grid forming converters in renewable energy sources dominated power grid: Control strategy, stability, application, and challenges. *J. Mod. Power Syst. Clean Energy* 09 (6), 1239–1256. doi:10.35833/mpce.2021.000257

Zhong, Q., and Weiss, G. (2011). Synchronverters: Inverters that mimic synchronous generators. *IEEE Trans. Industrial Electron.* 58 (4), 1259–1267. doi:10.1109/tie.2010.2048839

Online correction of the transient voltage security region boundary based on load parameter variations in power systems

Zhenyu Zhang[1], Yuan Zeng[1]*, Junlong Ma[1], Chao Qin[1], Dezhuang Meng[2], Qichao Chen[3] and Wei Chen[4]

[1]Key Laboratory of Smart Grid of Ministry of Education, Tianjin University, Tianjin, China, [2]State Grid Jibei Electric Power Company Limited, Beijing, China, [3]State Grid Economic and Technological Research Institute Co., Ltd., Beijing, China, [4]State Grid Sichuan Economic Research Institute, Chengdu, China

The transient voltage security region (TVSR) is an essential part of the dynamic safety region of a power system, which represents the safe operating region of the transient voltage where there is no loss in stability. The power system load significantly affects the transient voltage stability. However, the load model in the existing power systems, which considers the security region of the dynamic process, is too simple to comprehensively characterize the load characteristics of the dynamic process. Furthermore, it neglects the influence of the load model parameters on the dynamic process security region. In this study, a composite load model with distributed photovoltaic power is used as the research object. The main load parameters affecting the voltage stability and the generator nodes that are sensitive to the load parameters are calculated using the trajectory sensitivity method. The TVSR of the system is constructed based on the load and generator's active powers. The correlations between different load-leading parameter combination scenarios and TVSR boundary points are mined using the CatBoost learning framework. Thus, the TVSR boundary can be promptly corrected online based on the changes in the load parameters, and the system security boundary can be described more accurately. The proposed method is verified using the IEEE39 and IEEE118 node systems. It is observed that the proposed method can correct the TVSR boundary online with high precision corresponding to real-time changes in the load model parameters. This provides a more accurate TVSR boundary for the power system operation scheduler, which helps in guiding it to control the system more accurately.

1 Introduction

The power load is the core of power consumption and significantly affects the design, analysis, and control of power systems (Arif et al., 2018). The complexity, time variability, and randomness of power system loads are constantly increasing with the development of the social economy, and the load exhibits more diverse dynamic characteristics. Therefore, it is essential to establish a load model that is as close as possible to the actual load characteristics for simulation calculation and to perform a more accurate simulation analysis of a power system. In load modeling at high-voltage levels, the load models are

primarily divided into two categories: static and dynamic load models. The static load model includes the constant impedance, constant current, and constant power load models (IEEE Standards Association, 2020). The dynamic load model includes an induction motor (Arif et al., 2018). In recent years, an increasing number of distributed power sources have been connected to the grid, owing to the development of emerging smart grid technologies, such as distributed generators. Access to distributed power significantly affects the load characteristics (Song and Blaabjerg, 2017). Mather (2012) established a distributed photovoltaic cell model with grid-connected inverters to simulate the characteristics of distributed photovoltaics similar to a constant power load. Soliman et al. (1997) proposed an AND dynamic equivalent model, which considers static load, dynamic load, and distributed generation. In this paper, we comprehensively analyze the applicability of a load model and adopt the composite load model with distributed photovoltaic power as the research object. Following the selection of the appropriate load model, the parameters of the load model must be determined according to the actual regional load operation characteristics. Two main types of load model parameter identification methods are commonly used: component-based modeling (Gaikwad et al., 2016; Zhu et al., 2012) and measurement-based modeling (Hu et al., 2016; Visconti et al., 2014). The component-based modeling method has limitations due to the requirement of acquiring massive amounts of data. Therefore, modeling methods based on measurement data are preferable and widely implemented. Consequently, extensive research has been conducted on the application of modeling methods based on measurement data. In Han et al. (2009), Rodríguez-García et al. (2020), and Avila et al. (2020), an equivalent load model was established based on the measured data on the load under a large disturbance of the system, and the model parameters were identified. In Wang et al. (2022), the load model parameters online were identified based on the measurement data on the load during routine operation.

The power system security region is an area that ensures the safe and stable operation of the power system. Any operating point within the security region of the power system is considered safe. Conversely, any operating point outside the security region of a power system is considered unsafe (Yixin et al., 2020). The power system security region includes the power flow, static, small disturbances, and dynamic security region (Yixin et al., 2020). Here, the dynamic security region is the region in the power injection space before an expected accident, which ensures the transient stability of the system after the accident, and its boundary can be fitted by using one or more hyperplanes (Yixin et al., 2020). This region primarily focuses on the generator power angle and bus voltage during the dynamic process of the power system. The dynamic security theory of a power system overcomes the limitations to the running state of the system. It corresponds only to the system network structure and parameters before and after an expected accident (Yuan and Yu, 2002). The dynamic security theory has been implemented in several fields of power systems. In the study by Zeng et al. (2006), the effective application of the dynamic security theory in power systems is described. Zhang et al. (2017) presented a practical solution for dynamic security regions based on the coupling correlation of the system power flow. Maihemuti et al. (2021) solved the problem of a dynamic security

region of an integrated energy system with natural gas access through high renewable energy permeability. In the study by Zhou et al. (2018), the transient stability of the access nodes on wind farms was analyzed by constructing a dynamic security region. Finally, Xiran et al. (2013) proposed a power system emergency control strategy based on a dynamic security region.

The load is the most variable component of the power system; it has the most significant effect on the safety and stability of the system and largely determines the process of voltage collapse (Li et al., 2006; Meng et al., 2014; Monteiro Pereira et al., 2008). However, several accidents have occurred in recent years involving power system stability problems caused by changes in load characteristics. For example, the power-grid voltage collapse incident in Tokyo, Japan (July 1987), was caused by the dynamic characteristics of a sudden and substantial increase in temperature control loads. Therefore, an accurate load model is crucial for analyzing power system security and stability (Taylor, 1994). With the development of load modeling technology, particularly online load identification technology, it has become possible to analyze load characteristics in real-time. Changes in the power system network parameters caused by variations in the load model or load parameters lead to a change in the dynamic security region of the power system. Therefore, it is necessary to closely monitor changes in the dynamic security region under the load model, load parameters, and load power changes. It is complicated and computationally expensive to analyze the safety and stability of each running state using the point-by-point method for load power that fluctuates frequently. However, using the security region to describe the safe operating boundary of the load significantly reduces the number of calculations and presents considerable potential for engineering applications. Therefore, the influence of real-time load changes on the dynamic security-region boundary must be comprehensively analyzed. Furthermore, the dynamic security-region boundary can be modified in real time to more accurately represent the dynamic security-region changes of the system and provide a valuable reference for power system schedulers.

In previous studies, a constant power load model was used in the calculation for the construction and analysis of the dynamic security region of a power system, with the dynamic characteristics of the load ignored. Therefore, we have considered a composite load model with distributed photovoltaic power as the research object in this study to overcome the existing issues. The load-dominant parameters that significantly affect the system voltage in the load model were calculated through sensitivity analysis. The key generator nodes were sensitive to the load parameters, with the load power changes calculated through a trajectory sensitivity analysis. The transient voltage security region (TVSR) was constructed using the active generator and load powers, and the TVSR boundary characteristics under different load–voltage-dominant parameters were analyzed. A fast TVSR boundary correction method under load-parameter changes was proposed based on the CatBoost learning framework. The online modification of the TVSR boundary can be realized based on changes in the load parameters through offline training of the TVSR boundary points in the scenario of multiple load parameters. The proposed method was verified using the IEEE39 and IEEE118 node systems.

FIGURE 1
The composite load model with distributed photovoltaic power.
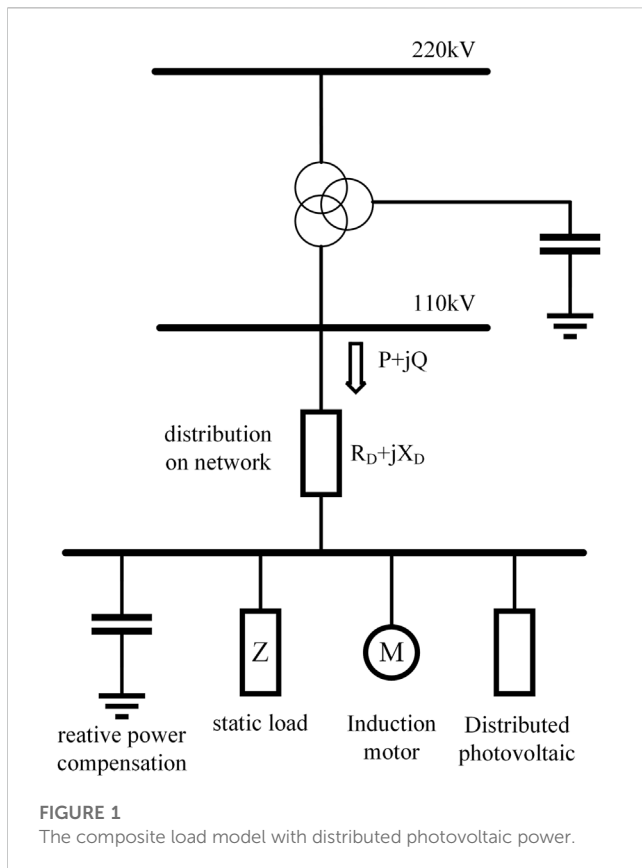
Based on the increasing proportion of distributed power supply units in power systems, the proposed TVSR online correction method can realize real-time correction of the TVSR boundary due to changes in the load model parameters containing the distributed power supply. This provides a more accurate TVSR boundary for the operation scheduler to guide the operation scheduler in conducting more precise system operation regulations.

2 Transient voltage security region of power systems

2.1 Correlation between the transient voltage stability and injected power of system nodes

Transient voltage instability is primarily attributed to the transient failure or misoperation of the system, which causes a voltage drop in the system node and leads to a voltage collapse of the entire system. When a transient fault occurs in the system, the voltage at the short-circuit point is zero, and the other nodes in the system exhibit corresponding voltage drops based on the strength of the connection to the short-circuit point. A part of the electromagnetic power is lost due to the transient failure of the system, and the mechanical power of the prime mover surpasses the electromagnetic power. Thus, the prime mover continues to accelerate, leading to a further decline in the system voltage, causing transient voltage instability.

The node injection active power and reactive power significantly affect the transient process of the power system (Yu et al., 2006). The active power injected into the nodes mutates due to the occurrence of transient faults, leading to a system power imbalance and fluctuations in the dynamic components of the system, which further results in transient fluctuations in the system voltage and frequency. Conversely, the reactive power injected by the nodes causes the voltage of the power system to fluctuate temporarily when a transient fault occurs. The nodes with reactive power support ability adjust their reactive power to stabilize the node voltage to suppress these voltage fluctuations. For example, a generator excitation system adjusts the excitation current to stabilize the generator node voltage when it experiences a transient fault.

In the dispatching operation of an actual power system, the operation controller controls the output of the active power of the generator and the power consumption of the active power of the load. Essentially, the operation controller controls the active power injected by the node. Therefore, we focus primarily on the active power injection of the system nodes for power system operation and dispatching controllers. Furthermore, in high-voltage power networks, it is assumed that the reactive power of the nodes can be balanced locally. Therefore, in this study, we analyzed the effect of node active power injection on the transient process of the system, particularly on the transient voltage. In future studies, a sufficient reactive power reserve will be provided for the generator nodes of the system, and an analysis will be conducted on the correlation between the active power injection of the nodes and the transient voltage stability.

When the system load increases and more power is required from the generator, the node injection power increases along with the output of the generator excitation system. Accordingly, the dynamic response ability of the system decreases, which leads to the weakening of the voltage maintenance ability of the system when the transient fault occurs. Thus, increasing the node-injected power decreases the transient voltage stability of the system, making it essential to analyze the stability of the transient voltage of a power system based on the node-injection power.

2.2 Definition of the transient voltage security region

The power system security region of the dynamic process was defined in the node power injection space before the accident. This is the set of all the operating points that can maintain the transient stability after experiencing a large disturbance. For a specific accident, the structure of the power system goes through three stages, that is, before, during, and after the accident, and the corresponding equation of state is given as follows:

$$\dot{x} = \begin{cases} f_i(x) & -\infty < t < 0, \\ f_F(x) & 0 \le t < \tau, \\ f_j(x) & \tau \le t < +\infty, \end{cases} \tag{1}$$

where x denotes the state variable of the system and τ denotes the duration of the accident. $f_i, f_F,$ and f_j represent the equations of the state of the system before, during, and after an accident, respectively.
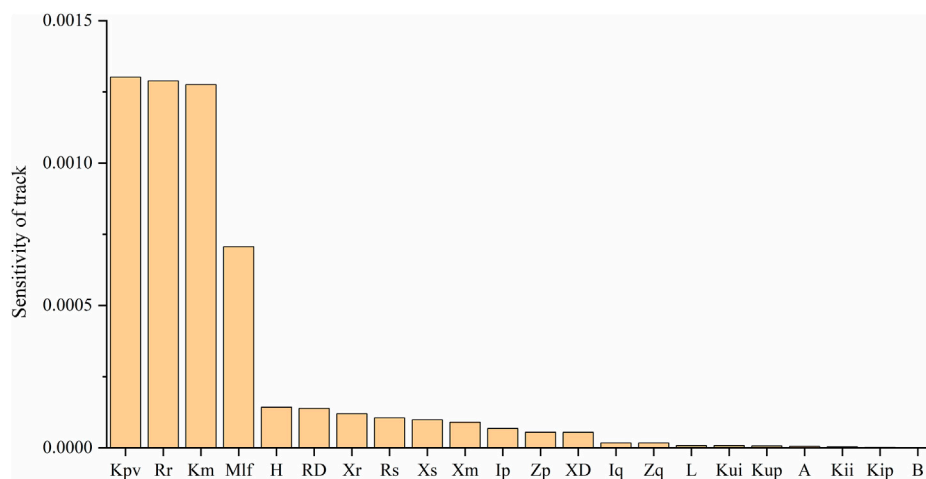
FIGURE 2
Calculation of trajectory sensitivity of load parameters.

The dynamic security region in the injection space can be expressed as follows:

$$\Omega_d\left(i, j, \tau\right) = \left\{ y \mid x_d\left(y\right) \in A\left(y\right) \right\}, \quad (2)$$

where y denotes the node power injection vector of the system, $x_d\left(y\right)$ denotes the state of the system at the time of accident clearing, and $A\left(y\right)$ denotes the stable region of the stable equilibrium point in the state space of the system after failure, which is determined by the injection, y. The boundary of the dynamic security domain can be represented by $\partial\Omega_d\left(i, j, \tau\right)$.

In the studies conducted on security regions, the node power injection space that the power system can actively control is often used to construct and analyze security regions. The common node-controlled injection space typically includes the active and reactive powers of the system nodes. However, from the perspective of the physical characteristics of a high-voltage AC system, the reactive power can be assumed to be in local balance, with only the active power injected by the nodes considered for constructing a security region. When the hyperplane approximation is used to describe the boundary of the dynamic security region, the expression of the dynamic security region in the active power-injection space is given as follows:

$$\Omega_d := \left\{ P \in R^n \,\middle|\, \sum_{i=1}^{n}\alpha_i P_i \leq 1 \quad P_i^m \leq P_i \leq P_i^M, i = 1, 2, \cdots, n \right\}, \quad (3)$$

where n denotes the total number of buses in the system excluding the equilibrium bus, P denotes the active power injection vector of the node, and P_i denotes the active power injection at the $i-th$ node. P_i^m and P_i^M represent the lower and upper limits of the active power injection at the node, respectively, α_i denotes the hyperplane coefficient corresponding to node i, and R^n denotes the n-dimensional real number space.

In the security region of the power system dynamic process, system security problems primarily comprise generator power angle stability, voltage stability, and small disturbance stability. In previous studies, the generator power angle stability in the

transient process was the primary concern in the dynamic security region of the power system. However, the effect of load characteristics on the safety and stability of the power system was primarily reflected in the transient voltage stability. Therefore, this study focuses on the occurrence of voltage instability during the transient process. The security region of the power system, considering the transient process voltage stability, is the TVSR, which is the main research objective of this study.

2.3 Solution method

The solution methods of the security region can generally be divided into the fitting and analytical methods: 1) the fitting method requires a large number of numerical simulations to obtain multiple critical points. The security region boundary obtained exhibits high accuracy but requires a large amount of calculation. 2) Conversely, the analytical method generally requires less computation but can exhibit lower accuracy in some cases. For security regions having unknown boundary characteristics, the fitting method is typically used to search the boundaries point-by-point.

3 Load model

The load parameter is one of the most random and time-varying components of a power system and considerably affects the voltage stability of the power system. Furthermore, the load characteristics significantly affect the transient process of the power system, and different load models and load model parameters exhibit different load characteristics. Therefore, the selection of the load model is a critical process. There are a large number of model parameters in the load model; however, not all of them significantly affect the dynamic characteristics of the load voltage. As a result, it is essential to screen the load model
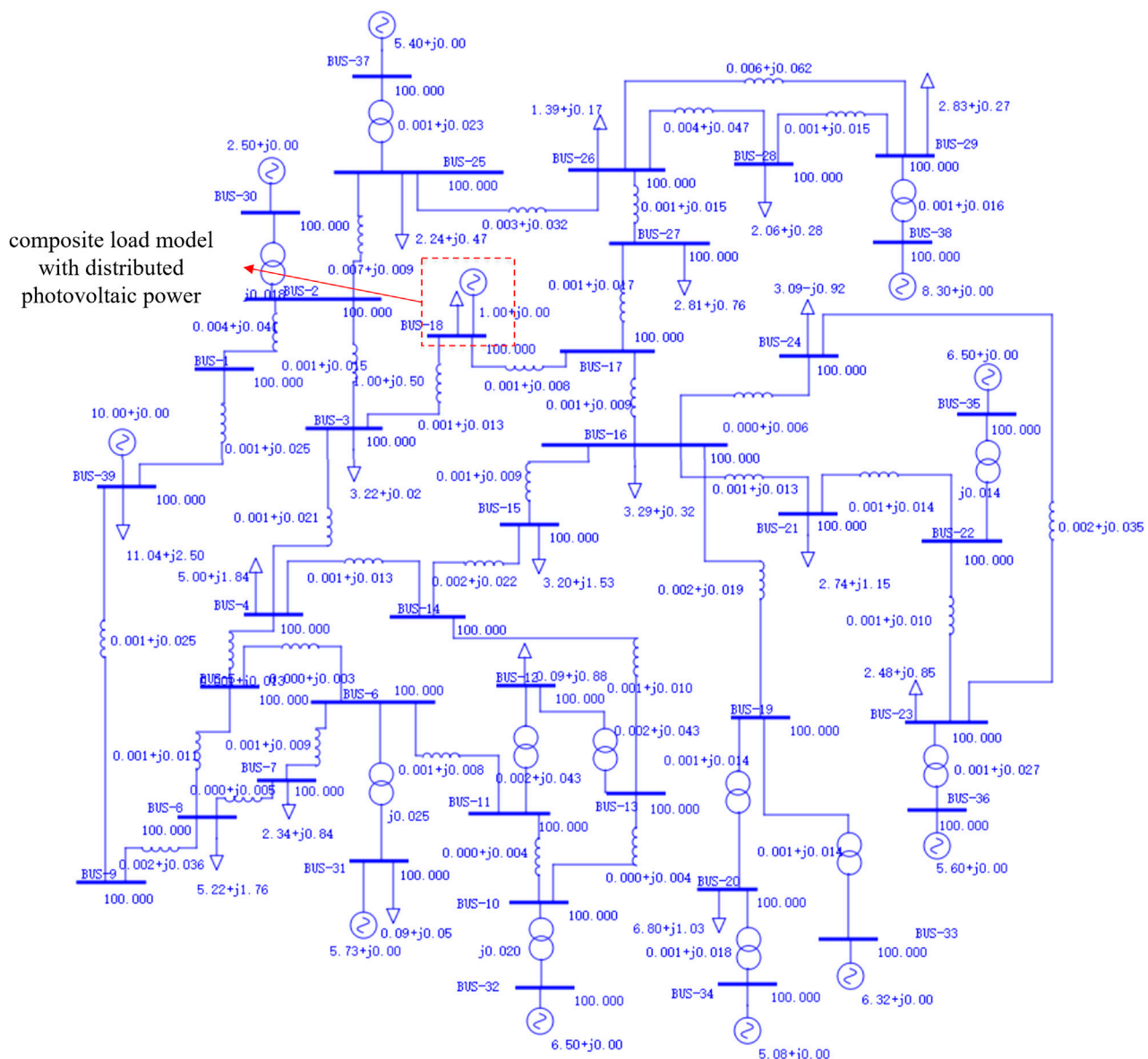
FIGURE 3
Wiring diagram of the IEEE39 node system.

parameters and select those that considerably affect the dynamic voltage response of the system for subsequent research.

3.1 Structure of the load model

In this study, we employed a composite load model with distributed photovoltaic power. It comprises a distribution network model, static load model, dynamic load model, and distributed photovoltaic power generation model. Figure 1 shows the structure of the model.

The distribution network model was composed of the distribution network impedance, the static load model was a constant impedance model, the dynamic load model was a third-order induction motor model, and the distributed photovoltaic

power generation module was a double-loop controlled photovoltaic inverter model. Nomenclature presents the model parameters and a description of the composite load model with distributed photovoltaic power.

3.2 Main parameter set of the load model

In this study, multiple load model parameters were considered. When selecting the load parameters, the parameters that significantly impact the output response of the load were generally selected, while typical values were used for the remaining parameters. This concept is also used to analyze the effect of load parameters on dynamic security-region boundaries. The parameter changes that have a greater

FIGURE 4
Transient voltage trace sensitivity of generator nodes in the IEEE39 node system.
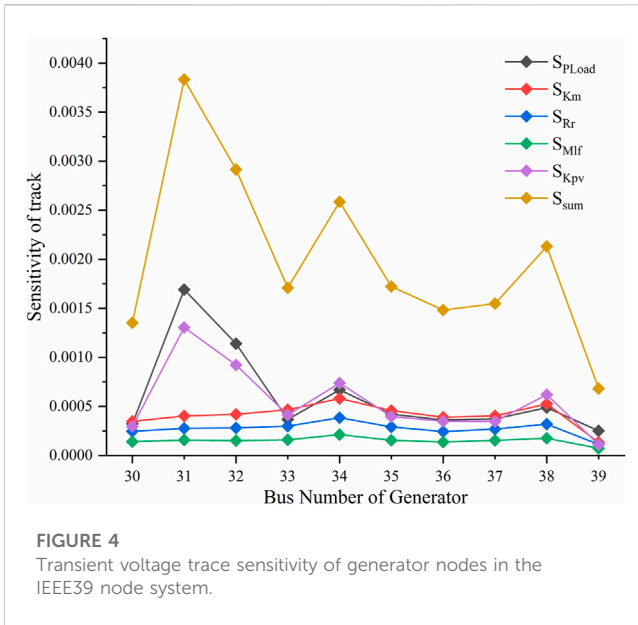
impact on the load output also have a greater influence on the transient stability of the system. Conversely, parameters having a smaller impact on the load output also have a smaller impact on the transient stability of the system. Based on the analysis of the TVSR, the transient voltage response of the load bus was selected as the reference basis to determine the effect of the load parameters on the output.

The trajectory sensitivity method was used to calculate the sensitivity of the load parameters and to determine the parameter set that significantly affects the load voltage response. The calculation formula for the trajectory sensitivity is as follows:

$$
\begin{aligned}
S_{ij}(t) &= \frac{\partial y_i(t)/y_i(t)}{\partial \theta_j / \theta_j} \\
&= \lim_{\Delta \theta_j \to 0} \frac{\left[y_i(\theta_{j0} + \Delta \theta_j, t) - y_i(\theta_{j0}, t) \right]/y_i(\theta_{j0}, t)}{\Delta \theta_j / \theta_{j0}}.
\end{aligned}
\tag{4}
$$

Here, θ_j denotes the $j-th$ parameter, θ_{j0} and $\Delta \theta_j$ represent the initial value and variation in the parameter θ_j, respectively, and y_i denotes the trajectory of the $i-th$ output variable, which represents the bus voltage response of the transient process load. In this paper, the variable $\Delta \theta_j / \theta_{j0}$ of the parameter is set to be 10%. The load model described in this study was built into the simulation software application, and a transient fault was set up for the transient simulation. First, the initial value of the load model was set as a typical value, and each parameter in the load was then increased by 10%, corresponding to the initial value. The voltage-response data on the load bus within 3 s of the occurrence of a transient fault were selected as valid data for the calculation. Figure 2 presents the calculation results for the trajectory sensitivity for each load parameter.

The analysis in Figure 2 shows that the sensitivity of the four parameters, K_M, K_{PV}, R_r, and M_{If}, is high, whereas the sensitivity of the other parameters was low. The low-sensitivity parameters do not significantly affect the system stability; therefore, they were not analyzed in this study. The load parameters set for this study were as follows:

$$
p = \{ K_M, K_{PV}, R_r, M_{If} \},
\tag{5}
$$

where K_M denotes the ratio of the active power of the dynamic load to the active power of the total load, K_{PV} denotes the ratio of the active power of the distributed photovoltaic generation to the active power of the total load, R_r denotes the stator resistance of the dynamic load, and M_{If} denotes the initial slip of the dynamic load.

4 The concept of the online TVSR boundary correction

4.1 Building the TVSR

The controllable variables of key nodes are often selected when constructing a power system security region. In selecting the critical nodes, different types of power system security regions are considered with different priorities. In this paper, we analyzed the construction of the TVSR; therefore, we focused more on the transient stability of the system, particularly the system voltage stability caused by load power fluctuation.

A composite load model with distributed photovoltaic power was built at BUS18 of the IEEE39 node system. Figure 3 presents a diagram of the system structure. Depending on the load used in this study, the active power of the load is considered one of the node injection quantities for constructing the TVSR. For practical engineering applications, based on the node voltage sensitivity under the change of load parameters, we determine the generator node with the greatest influence from the change of load parameters and use the active power of the generator node as another injection amount for constructing the TVSR.

The sensitivity of the transient voltage response of the generator node is calculated using the trajectory sensitivity method. Eq. 4 presents the calculation formula for trajectory sensitivity. The calculation process and method are approximately identical to those in the analysis of the sensitivity of the load parameters in Section 2.2. The trace sensitivity values of the four parameters in the load parameter set are defined as S_{Km}, S_{Rr}, S_{Mlf}, and S_{Kpv}. The locus sensitivity of the transient voltage response of the system bus corresponding to the load active power is defined as S_{PLoad}. The total track sensitivity, S_{sum}, of the ith bus in the system is expressed as follows:

$$
S_{sum,i} = S_{Km,i} + S_{Rr,i} + S_{Mlf,i} + S_{Kpv,i} + S_{PLoad,i}.
\tag{6}
$$

Figure 4 presents the calculation results for the load power and node voltage sensitivity of the four load parameters.

According to the analysis in Figure 4, the generator nodes had the highest trajectory sensitivity, except for the equilibrium nodes BUS31, BUS32, and BUS34. Therefore, the two-dimensional (2D) and three-dimensional (3D) TVSR were constructed using the three-node controllable injection quantities of the active generator power of the BUS32 and BUS34 nodes and the active load power of the BUS18 nodes. For the construction of a 2D TVSR, a combination of the active power and load active power of any generator was selected. Conversely, the construction of a 3D TVSR involved selecting a combination of the active power and load active power of the two generators. The fluctuation range of the load power during
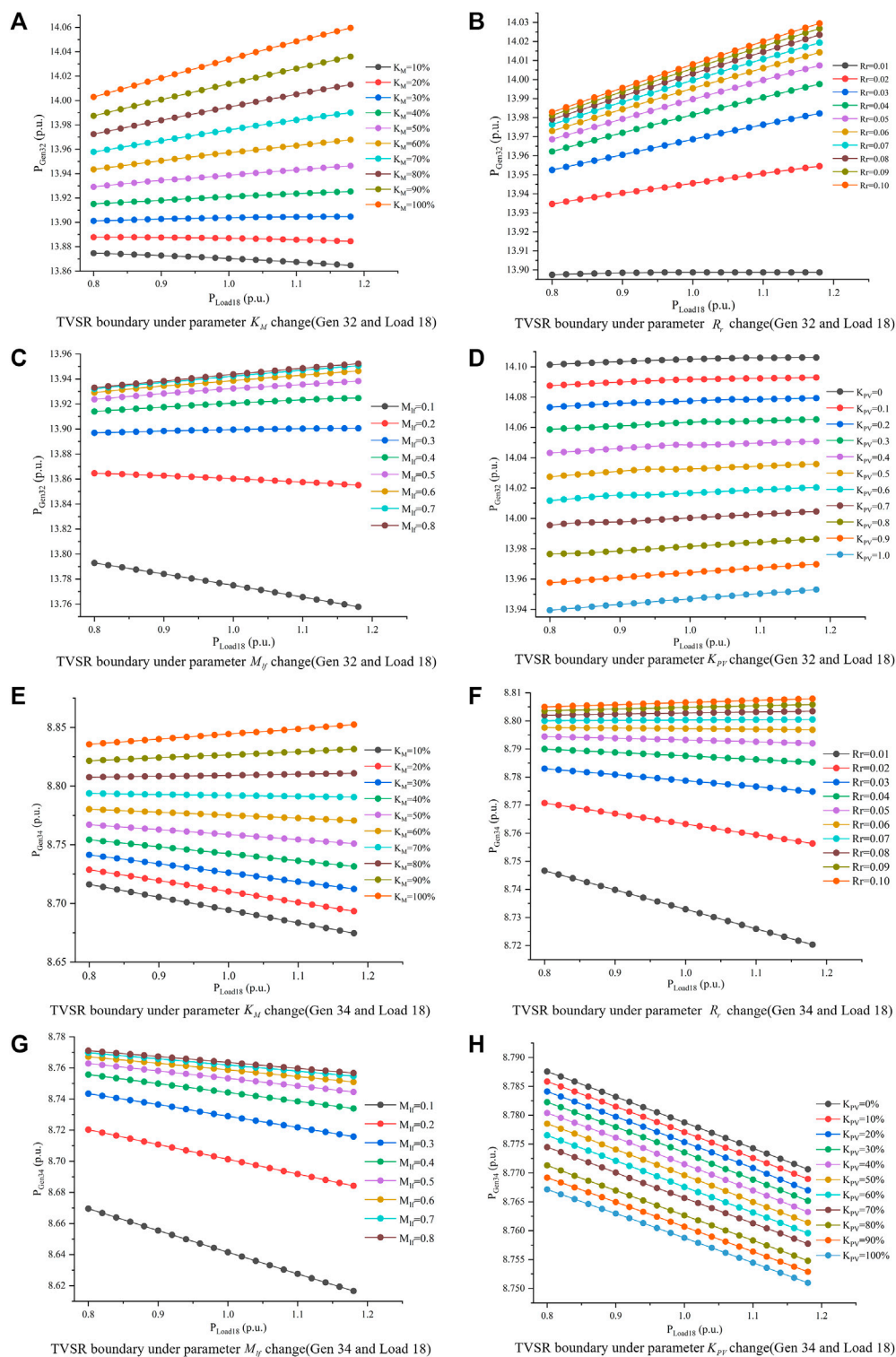
the operation of the transmission network was approximately 40%. Therefore, the TVSR was constructed in the range of 80%–120% of the initial active power of the load. A point-by-point method was used to explore the TVSR boundary to determine the unknown TVSR boundary characteristics.

The three-phase short circuit was set at 50% of the line between buses BUS18 and BUS17 of the system load, with the short-circuit time set to 0.1 s. The voltage stability of the system bus was considered the criterion. In other words, when the transient process causes the voltage of the system bus to be lower than
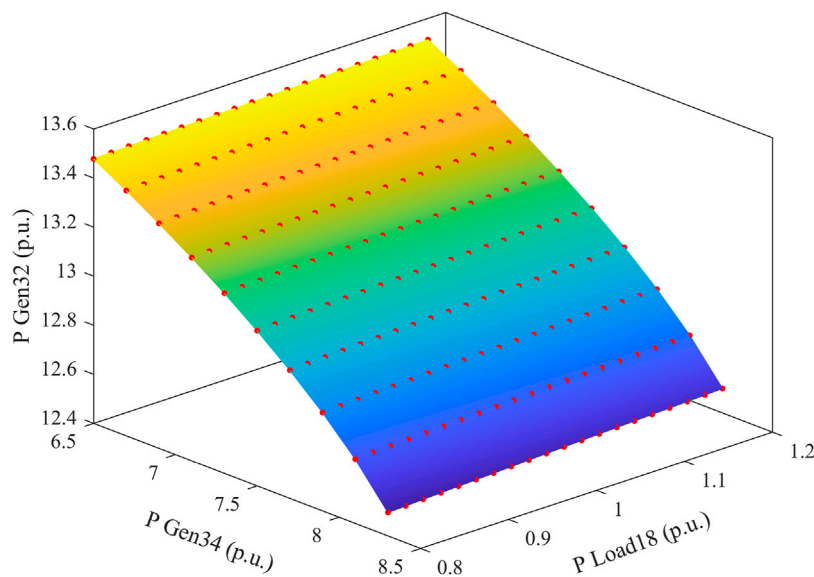
FIGURE 6
IEEE39 node system 3D TVSR boundary.

0.7 p.u. for more than 1 s, the voltage instability of the system is determined. The critical instability points of the TVSR boundary were identified point-by-point using the fitting method.

4.2 Analysis of boundary characteristics

The changes in the TVSR boundary characteristics caused by the changes in the four parameters in the load parameter set p were analyzed. According to the recommended IEEE parameters and the load model structure built in this study, the range of the load parameter changes is as follows: 1) K_M is 0%–100%, 2) K_{PV} is 0–1, 3) R_r is 0.01 p.u. to 0.1 p.u., and 4) M_{lf} is 0.1 p.u. to 0.8 p.u. Considering generators No. 32 and 34 (with the highest trajectory sensitivity) as examples, this study analyzed the characteristics of two 2D DSR boundaries comprising the active load power and active power of two generators, respectively, when the load parameters at BUS18 changed. Figure 5 shows the 2D TVSR boundaries under the changes in the four load parameters.

When a single load parameter is represented by each subgraph in Figure 5, the other load parameters adopt typical values. Notably, the variation in the load parameters significantly affects the TVSR boundary in the figure, which was linearly fitted. The sum of squared errors (SSE), R^2, and the root mean squared error (RMSE) were calculated as 4.4366E-8, 0.9990, and 4.1959E-5, respectively. Through verification, it was determined that the 2D TVSR boundary analyzed in this study presented good linear characteristics within the scope of the engineering applications and that the linear fitting error was minimal.

The 3D TVSR boundary, comprising the generator at BUS32 and BUS34, and the load at BUS18 can be represented by multiple sets of 2D linear TVSR boundaries. Figure 6 shows the 3D TVSR boundary when typical load parameters are adopted.
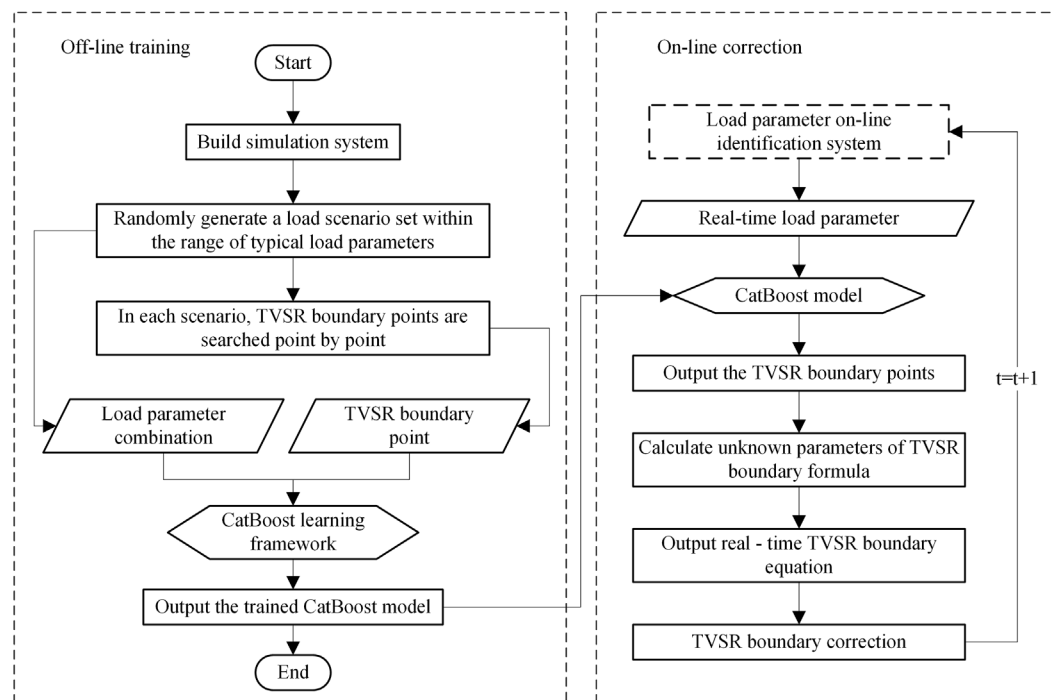
4.3 Online correction of the TVSR boundary

Based on the analysis of the TVSR boundary characteristics in the previous section, it can be observed that the 2D TVSR boundary exhibited good linear characteristics. The TVSR boundary in a 2D plane can be represented by the set $l_{n,i,j}$, which is given as follows:

$$l_{n,i,j} = \left\{ (P_{Gen,i,n}, P_{Load,j,n}) \middle| P_{Gen,i,n} - k_{1,n} P_{Load,j,n} - k_{2,n} = 0, \\ P_{Load,j,n} \in \left[P_{Load,j,min}, P_{Load,j,max} \right] \right\}, \quad (7)$$

where n represents the $n - th$ scenario under different load parameter combinations, i represents the generator node number, j represents the load node number, P_{Gen} represents the active power of the generator under the critical instability state of TVSR, P_{Load} represents the active power of the load under the critical instability state of TVSR, k_1 and k_2 represent the linear characteristics of the TVSR boundary, and $P_{Load,j,min}$ and $P_{Load,j,max}$ represent the maximum and minimum values of active power when the $j - th$ load runs, respectively.

To determine the 2D TVSR boundary in scenario n comprising any combination of load parameters, the values of coefficients k_1 and k_2 must be determined. Therefore, two equations must be constructed and solved. This requires the knowledge of two critical points on the TVSR boundary in each scenario. Eq. 7 requires two equations to be constructed by obtaining two pairs of values of P_{Gen} and P_{Load} in scenario n. However, there are infinite permutations and combinations of the four load parameter values. Therefore, two running points on the new TVSR boundary must be calculated each time a new load parameter combination scenario appears. Nonetheless, using the point-by-point method to identify the boundary points is very time-consuming and cannot adapt to the rapidly changing load parameters.

FIGURE 7
Overall process of TVSR boundary online correction.

TABLE 1 IEEE39 node example of CatBoost learning framework verification indicators.

Case	MSE (E)	RMSE	MAE	R^2
Point 1	2.40657−6	5.79162E−12	7.64397E−11	0.999,419
Point 2	3.41859−6	1.16867E−11	3.09445E−10	0.999,341

Therefore, this study uses a combination of load parameters as the input and the critical point of the TVSR as the output. A machine learning algorithm was then used to explore the correlation between different load parameter combinations and the critical instability point of the TVSR boundary. Thus, the online calculation of the TVSR boundary under different load parameter combinations can be realized. In this study, we use the CatBoost algorithm as a framework for machine learning.

During the calculation and analysis of the leading parameters of the load model, the extracted leading parameters were essentially identical when calculating the trajectory sensitivity of the leading parameters since the same models were used. When selecting key generator nodes for power systems with different structures, the key nodes of different systems vary due to the considerable differences in the system structure and parameters. Therefore, when TVSR boundary correction is performed, the key generator nodes must be rescreened based on the different systems and faults. Figure 7 shows the overall process of the rapid boundary correction of 2D TVSR.

The 3D TVSR boundary surface is obtained by fitting the linear boundaries of multiple 2D TVSR. The 3D TVSR boundary can be represented by the set $\alpha_{n,i,i',j}$, which is given as follows:
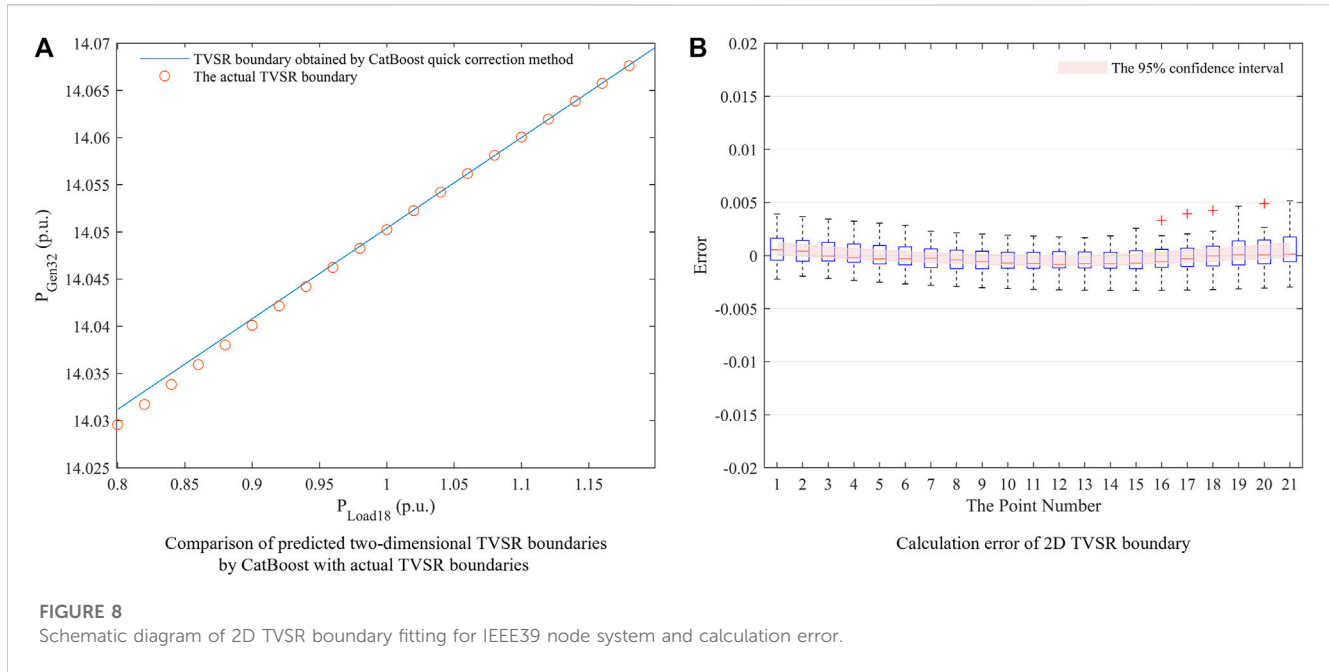
$$\alpha_{n,i,i',j} = \left\{ \left(P_{Gen,i,n}, P_{Gen,i',n}, P_{Load,j,n} \right) \middle| P_{Gen,i,n} - k_{1,n} P_{Load,j,n} - k_{2,n} = 0, \right.$$
$$\left. P_{Load,j,n} \in \left[P_{Load,j,\,min}, P_{Load,j,\,max} \right] \right\}, \tag{8}$$

where i' represents the node number of the second generator that constitutes the 3D TVSR plane. The other parameters in the formula have the same meanings, as those in Eq. 7. Therefore, after establishing the CatBoost training models under different $P_{Gen,i',n}$, a 3D TVSR plane can be fitted by calculating multiple sets of TVSR boundaries. Similarly, a high-dimensional TVSR boundary comprising more node generator active powers and load active powers was calculated.

5 Introduction to the algorithm

CatBoost is a gradient-boosting decision tree (GBDT) framework based on a symmetric decision tree that has fewer parameters, supports class-type variables, and exhibits high accuracy. The structure of a symmetric oblivious tree presents fewer super-parameters and faster training speed. CatBoost solves the problem of gradient bias and prediction shift by using the sorting promotion method to reduce the occurrence of overfitting and improve the accuracy and generalization ability of the algorithm. CatBoost displays superiority in processing missing values and noisy data and exhibits a certain tolerance for outliers and noise when compared to XGBoost and LightBoost, the two other mainstream algorithms of GBDT. Furthermore, the risk of overfitting can be reduced via the random arrangement and sampling of the training samples.

FIGURE 8
Schematic diagram of 2D TVSR boundary fitting for IEEE39 node system and calculation error.

5.1 CatBoost iteration process

During model training, each iteration generates a weak learner and minimizes the loss function of the current iteration. Assuming that the loss function is $L[y, f(x)]$, the objective function h^t of each iteration can be defined as follows:

$$h^t = \underset{h \in H}{\arg \min} EL[y, F^{t-1}(x) + h(x)], \qquad (9)$$

where h^t denotes the tree selected from a series of H functions, E denotes the expected function, and $F^{t-1}(x)$ denotes the strong learner obtained in the last iteration.

The negative gradient, $-g^t(x, y) = -\partial L[y, F^{t-1}(x)]/\partial F^{t-1}(x)$, of the loss function is the direction in which the error decreases the fastest. It is used to fit the loss approximation of each iteration, and the objective function h^t can be expressed as follows:

$$h^t = \underset{h \in H}{\arg \min} E[-g^t(x, y) - h(x)]^2. \qquad (10)$$

Subsequently, the strong learner of this iteration is obtained as follows:

$$F(x)^t = F(x)^{t-1} + \alpha h^t, \qquad (11)$$

where α denotes the learning rate of the model.

5.2 Sort promotion

In the iteration process, the GBDT algorithm uses the same training samples to calculate the iteration gradient in each round. Eq. 10 can then be expressed as follows:

$$h^t = \underset{h \in H}{\arg \min} \frac{1}{n} \sum_{k-1}^{n} [-g^t(x_k, y_k) - h(x_k)]^2, \qquad (12)$$

where n denotes the number of training samples and $\{x_k, y_k\}$ denotes the k training samples, where $y_k \in \{0, 1\}$.

This leads to a deviation between the gradient distribution $g^t(x_k, y_k)|x_k$ obtained from the training sample and the real gradient distribution $g^t(x, y)|x$ o in the data space (Yu et al., 2006; Dorogush et al., 2018). The objective function determined using Eq. 12 deviates from the objective function in Eq. 9, which affects the accuracy and generalization ability of the model $F(x)$.

The CatBoost algorithm adopts the sorting and lifting method to perform the unbiased calculation of the gradient, which is based on the following principle. For each sample x_i, the training set excluding x_i is used to train a model, M_i, separately, and M_i is used to calculate the gradient on x_i. Dorogush et al. (2018) and Prokhorenkova et al. (2017) demonstrated the effectiveness of the sorting promotion method.
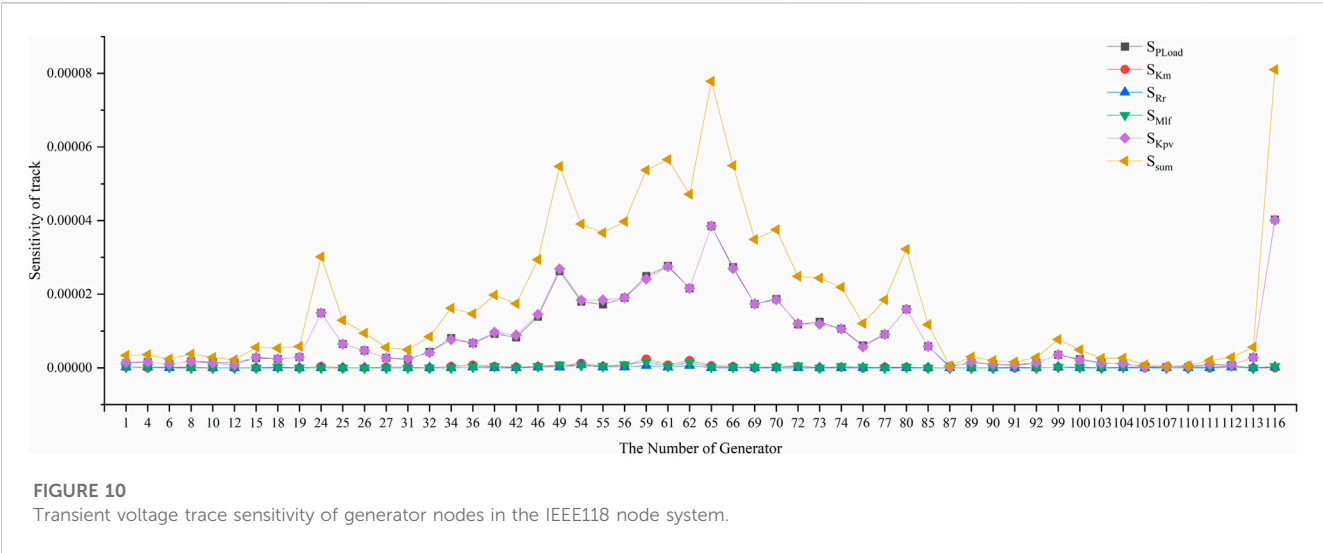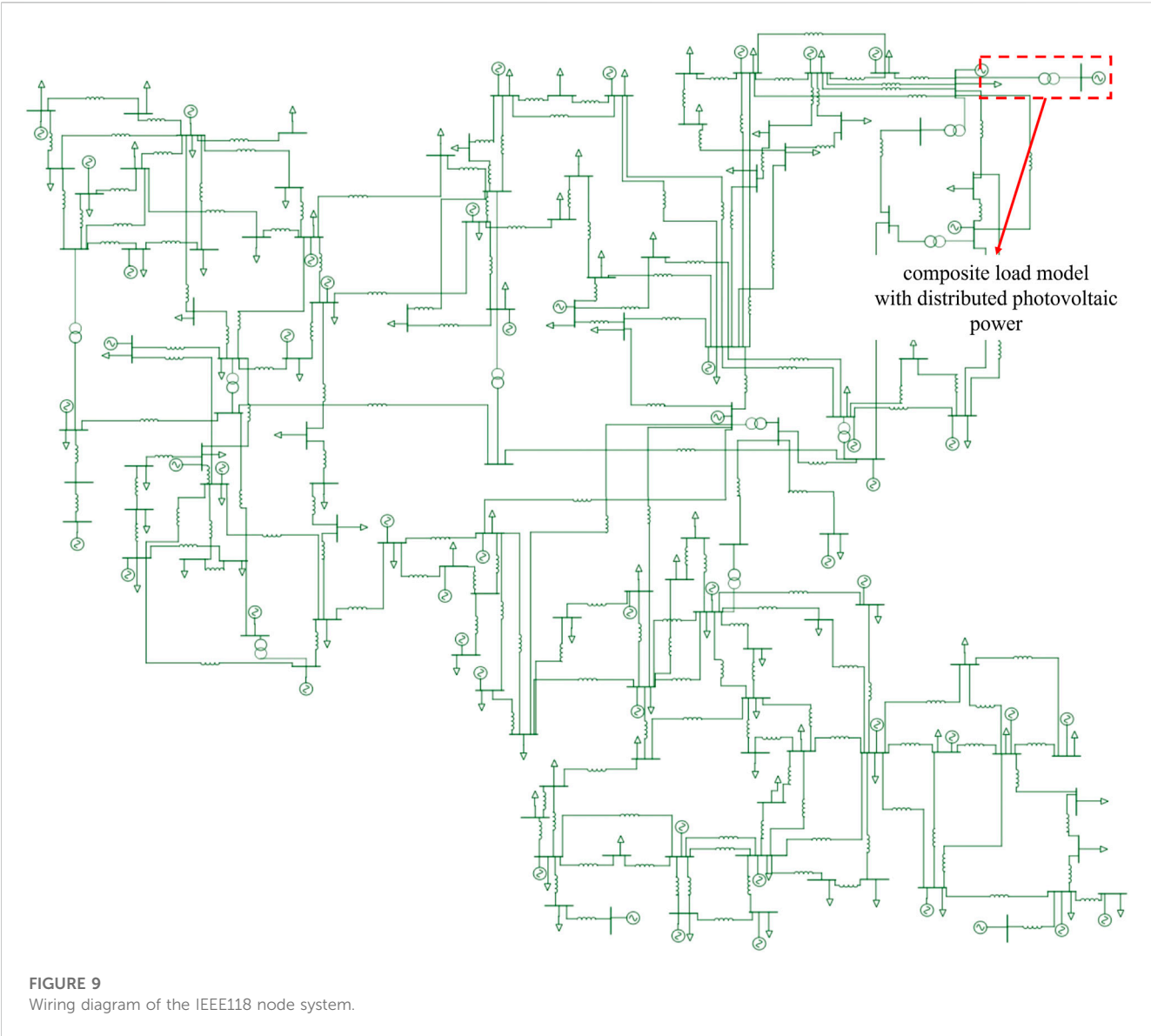
5.3 Algorithm hyperparameter settings

Owing to the ability of CatBoost to achieve high model quality without tuning parameters, most CatBoost hyperparameters were set to default values in this study. The main self-set parameters and their values were set as follows: iterations to 8,000, learning rate to 0.1, and depth to 3. The default values of the other parameters were retained.

6 Case study and result

6.1 Calculation and analysis of the IEEE39 node system

In this study, an IEEE39 node was used as an example to verify the proposed method. The composite load model with
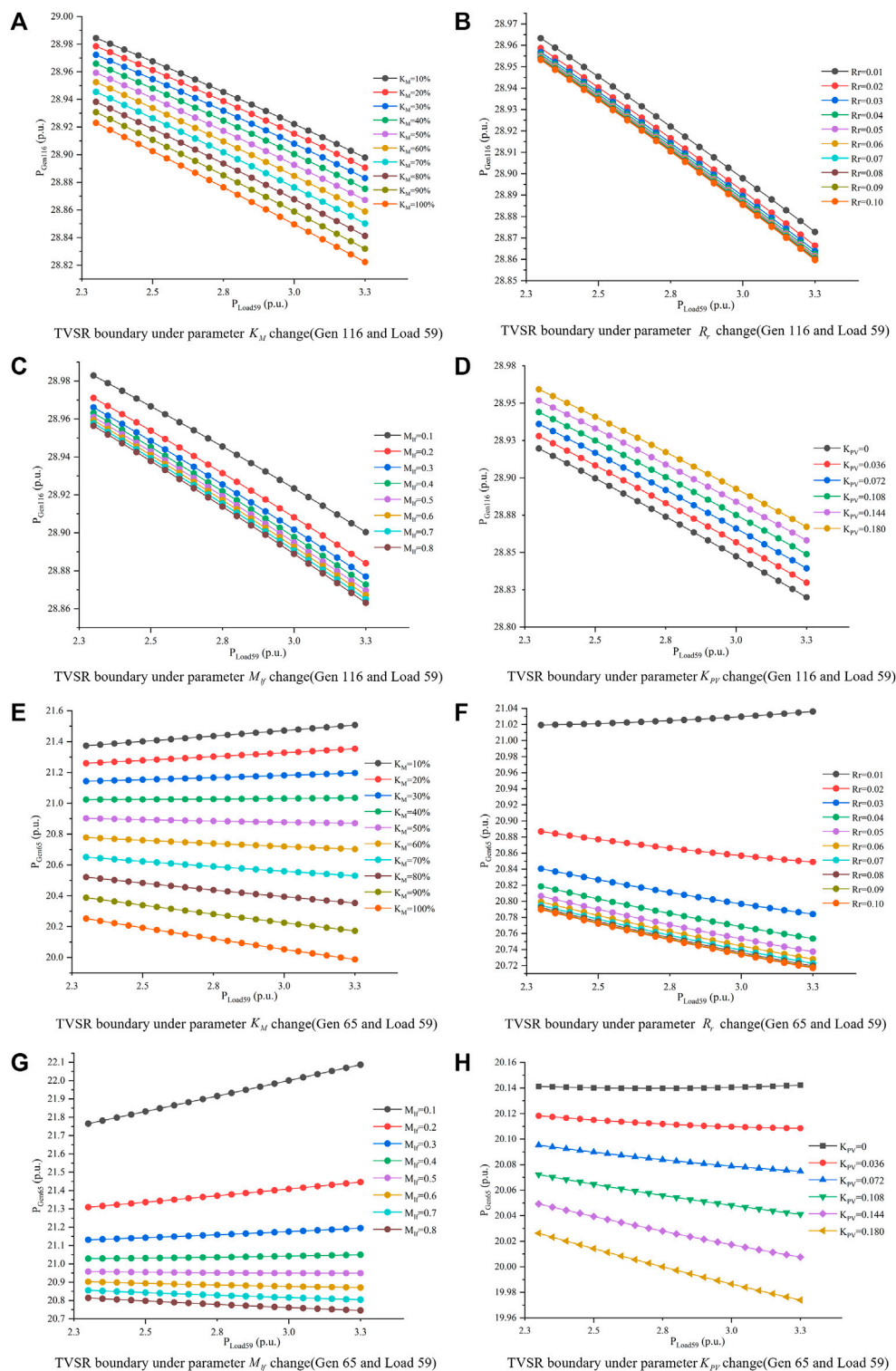
FIGURE 9
Wiring diagram of the IEEE118 node system.

FIGURE 10
Transient voltage trace sensitivity of generator nodes in the IEEE118 node system.

FIGURE 11
Two-dimensional TVSR boundary of IEEE118 node system influenced by load parameters.

distributed photovoltaic power is built at BUS18. Based on the analysis in Section 3, the active power of the load being analyzed and that of the generator at BUS32 were selected as the injection quantities to construct the 2D TVSR. In total, 5,000 groups of parameter combinations were generated

uniformly and randomly within the range of the load parameters listed in Table 1 to construct 5,000 different types of system operation scenarios. When the active power consumed by BUS18 load was 0.9 and 1.1 p.u., the fitting method was used to search the critical active power running
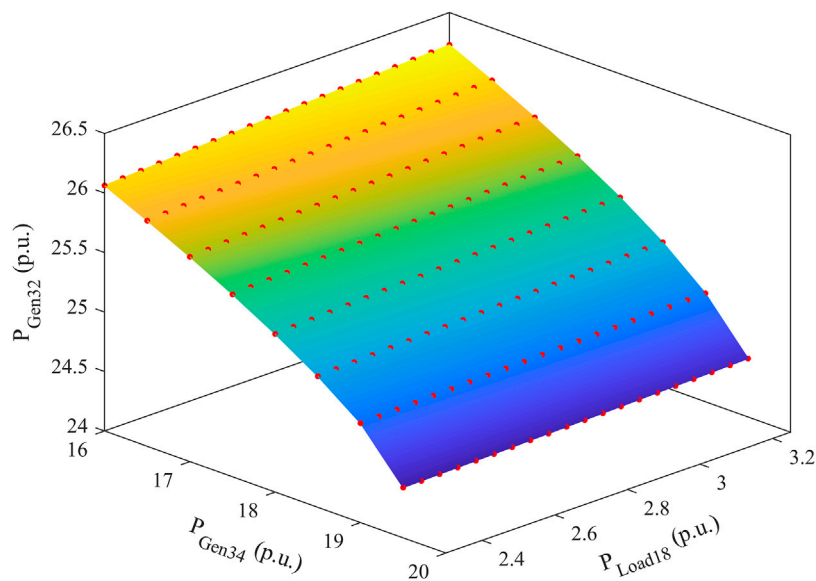
FIGURE 12
IEEE118 node system 3D TVSR boundary.

TABLE 2 IEEE118 node example of CatBoost learning framework verification indicators.

Case	MSE (E)	RMSE	MAE	R^2
Point 1	6.33416–8	4.01215E–15	1.87086E–14	0.99991
Point 2	1.05895–7	1.12138E–14	9.95759E–14	0.99989

points of BUS32 point-by-point, and 5,000 training samples were constructed.

Two CatBoost learning frameworks were constructed and trained for two TVSR boundary points in each load–parameter combination scenario. The parameter combination in the constructed training sample was used as the input for the CatBoost learning framework, and the TVSR boundary point corresponding to the parameter combination was used as the output. To train and verify the model, we selected 80% of the data for the training set and 20% for the verification set.

The model training hyperparameters were automatically selected using CatBoost based on the number of training sets and their feature structure. The mean value of 100 iterations for the CatBoost-independent training and calculation results was used to calculate the regression validation indicators, such as the MSE, RMSE, the mean absolute error (MAE), and R^2 of the validation sets, as shown in Table 1.

We selected an untrained load parameter combination scenario and fed the load parameter combination into the trained CatBoost framework as an input. The TVSR boundary expression is calculated based on the outputs of the two TVSR boundary points. The calculated TVSR boundary is compared with the actual TVSR boundary, as shown in Figure 8A.
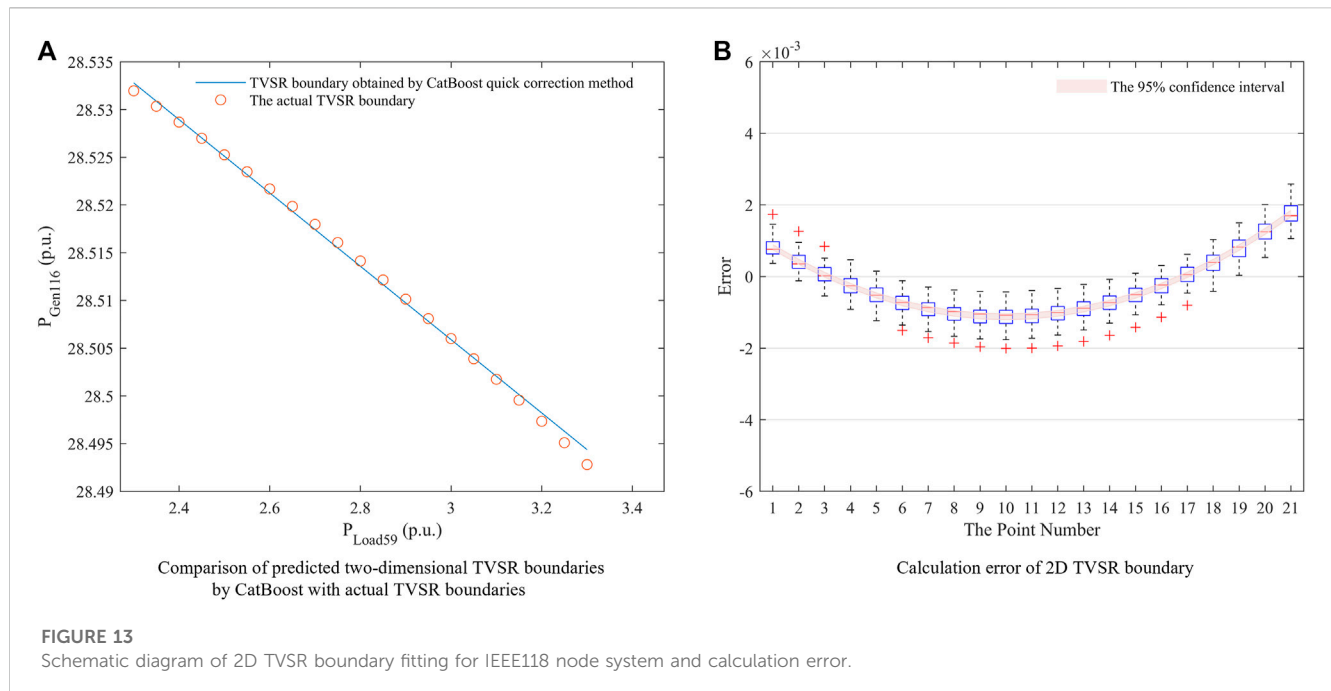
An error analysis of the 2D TVSR boundary calculated by CatBoost was then performed as follows. The TVSR boundary point was ascertained using the verification set based on Eq. 7. A

total of 21 boundary points were uniformly identified on the P load axis of the 2D TVSR space, with the error between the 21 and the real boundary points of the system calculated. The error distribution between the TVSR boundary obtained using the proposed method and the actual TVSR boundary was also determined. Figure 8B shows the error bars and 95% confidence intervals of the errors.

According to the analysis in Table 1, the CatBoost calculation method presents better prediction performance for the TVSR boundary points in scenarios with different load parameters, and a small number of training sets can be used to obtain higher prediction accuracy. Based on the analysis shown in Figure 8, the fast TVSR boundary correction method based on load parameter changes in the IEEE39 standard example system presents a high boundary fitting accuracy, and the calculated results are relatively reliable.

6.2 Calculation and analysis of the IEEE118 node system

The proposed method was verified in the case of IEEE118 nodes. Load 59, with high power on BUS59, was selected as the research object, with its model changed to a composite load model with distributed photovoltaic power. The active and reactive power of the load remained unchanged, and the added distributed PV active power was 50 MW. Figure 9 shows the wiring diagram of the modified example. The load model parameters were set to typical values, and a three-phase short circuit was set at 50% of the transmission line between BUS59 and BUS61 with a short circuit time of 0.1 s. The trajectory sensitivity of the bus voltage of each generator was calculated corresponding to the load parameters and load active power under transient fault conditions.

FIGURE 13
Schematic diagram of 2D TVSR boundary fitting for IEEE118 node system and calculation error.

The transient voltage locus sensitivities of the BUS116 and BUS65 nodes were relatively high, as shown in Figure 10. Therefore, the active power of the Gen116 and Gen65 generators and the active power of Load 59 were selected as the node injection quantities to construct 2D and 3D TVSR. The effects of different load parameters on the TVSR boundary in two 2D spaces constructed using the load active power and the active power of the two generators were calculated, as shown in Figure 11. Figure 12 shows the TVSR boundary in 3D space with typical parameter values for the load.

The TVSR boundary shown in the figure was linearly fitted. The SSE, R^2, and RMSE values were calculated as 5.2956E-6, 0.9997, and 5.3940E-4, respectively.

The range of the load parameter changes is as follows: 1) K_M is 0%–100%, 2) K_{PV} is 0–0.18, 3) R_r is 0.01–0.1 p.u., and 4) M_{lf} is 0.1–0.8 p.u. A total of 5,000 groups of parameter combinations were generated uniformly and randomly within the range of the load parameters to construct 5,000 system operation scenarios. When the unit value of active power consumed by the BUS59 load is 2.4 and 3.1 p.u. respectively, the fitting method is used to search for the critical active power running point of BUS116 point-by-point, and 5,000 training samples are constructed.

Similar to the calculation of the IEEE39 nodes, two CatBoost learning frameworks were constructed and trained, respectively. Furthermore, 80% of the data were selected as the training set and 20% as the verification set. Table 2 lists the averaged verification results of 100 independent CatBoost training sessions.

Any group of the calculated TVSR boundaries was selected and compared with the real TVSR boundaries, as shown in Figure 13A.

The error distribution between the TVSR boundary obtained using the proposed method and the actual TVSR boundary was calculated. Figure 13B shows the error bars and 95% confidence intervals of the errors.

The data in Table 2 show CatBoost exhibits high calculation accuracy and produces reliable results in the calculation examples of the IEEE118 nodes. The analysis presented in Figure 13 highlights that the TVSR boundary calculated using the proposed method exhibits a good fitting effect with high fitting accuracy. The load parameter change of the IEEE39 node system exerts a lesser effect on the TVSR boundary than that of the IEEE118 node system, and the range of the boundary change is smaller. This results in the variance in the error distribution of the IEEE118 node system from that of the IEEE39 node system. Therefore, the TVSR boundary fitting error of the IEEE118 nodes was smaller than that of the IEEE39 nodes, and the error distribution was more compact.

The proposed TVSR online correction method trains the CatBoost network offline, inputs the CatBoost network online based on the change in the load parameters, and outputs the TVSR boundary online without delay. Therefore, it only requires time to train the model and does not perform complex calculations in online applications. The results are directly output by the model, which satisfies the demand for fast online applications.

Based on the calculation and verification of the IEEE39 and IEEE118 node systems, the proposed method can complete the training of the CatBoost network in the offline state to realize fast correction of the TVSR boundary of the power system online and satisfy the demands of the rapidly changing load. This capability addresses the requirements of dynamically changing loads, which is crucial for network regulation and security of power systems.

7 Conclusion

In this study, we used a composite load model with distributed photovoltaic power as the research object to comprehensively analyze the influence of the load model parameters on the TVSR of a smart grid. The trajectory sensitivity method was employed to determine the main voltage stability parameters of the load model

that significantly affect the transient response of the node voltage. Furthermore, the trajectory sensitivity method was employed to determine the main generator node sensitive to the load parameters and load power changes. The main generator node and node active power of the load are used as the injection amounts to construct the TVSR in this project. Considering the 2D and 3D TVSR space as an example, it was observed that the boundary characteristics of the TVSR present a good linear effect within the range of the normal variation in the load active power, which helps in deriving the TVSR boundary expression. We proposed a fast TVSR boundary correction method based on the CatBoost learning framework. The various combination scenarios of the dominant parameter set of voltage stability under different loads were constructed offline, and the parameter combinations were considered inputs, while the TVSR boundary points were considered outputs to train the CatBoost model offline. Based on the trained CatBoost model and the TVSR expression, the TVSR boundary can be modified online, corresponding to the real-time changes in the load parameters. The proposed TVSR boundary correction method was verified based on the IEEE39 and IEEE118 node systems. The calculated results exhibited a high degree of fitness to the TVSR boundary along with good engineering practicability. The proposed TVSR boundary online correction method can correct the TVSR boundary online with high precision based on real-time changes in the load model parameters. This can provide a more accurate TVSR boundary, aiding the power system operation scheduler in controlling the system more accurately.

Data availability statement

The original contributions presented in the study are included in the article/Supplementary Material; further inquiries can be directed to the corresponding author.

Author contributions

The paper was completed with the joint efforts of five authors; each of them has made their own contributions to the model, algorithm, data, and other aspects. ZZ: conceptualization and methodology. ZY: supervision. ZY: writing—original draft. QC: software. MJ: translation. MD: resources. All authors contributed to the article and approved the submitted version.

Funding

Conflict of interest

Author DM was employed by State Grid Jibei Electric Power Company Limited. Author QC was employed by State Grid Economic and Technological Research Institute Co., Ltd.

The remaining authors declare that the research was conducted in the absence of any commercial or financial relationships that could be construed as a potential conflict of interest.

Publisher's note

References

Arif, A., Wang, Z., Wang, J., Mather, B., Bashualdo, H., and Zhao, D. (2018). Load modeling—a review. *IEEE Trans. Smart Grid* 9 (6), 5986–5999. doi:10.1109/TSG.2017.2700436

Avila, N. F., Callegaro, L., and Fletcher, J. (2020). "Measurement-based parameter estimation for the WECC composite load model with distributed energy Resources," in Proccedings of the 2020 IEEE Power & Energy Society General Meeting (PESGM), Montreal, QC, Canada, August 2020, 1–5. doi:10.1109/PESGM41954.2020.9281843

Dorogush, A. V., Ershov, V., and Gulin, A. (2018). CatBoost: gradient boosting with categorical features support. Available at: https://arxiv.org/abs/1810.11363.

Gaikwad, A., Markham, P., and Pourbeik, P. (2016). "Implementation of the WECC Composite Load Model for utilities using the component-based modeling approach," in Proccedings of the 2016 IEEE/PES Transmission and Distribution Conference and Exposition (T&D), Dallas, TX, USA, May 2016, 1–5. doi:10.1109/TDC.2016.7520081

Han, D., Ma, J., He, R. -m., and Dong, Z. -y. (2009). A real application of measurement-based load modeling in large-scale power grids and its validation. *IEEE Trans. Power Syst.* 24 (4), 1756–1764. doi:10.1109/TPWRS.2009.2030298

Hu, F., Sun, K., Del Rosso, A., Farantatos, E., and Bhatt, N. B. (2016). "Measurement-based real-time voltage stability monitoring for load areas," in Proccedings of the 2016 IEEE Power and Energy Society General Meeting (PESGM), Boston, MA, USA, July 2016, 1. doi:10.1109/PESGM.2016.7741116

IEEE Standard Association (2020). "IEEE guide for load modeling and simulations for power systems," in Proccedings of the IEEE Std 2781-2022, September 2022, 1–88. doi:10.1109/IEEESTD.2022.9905546

Li, H., Fan, Y., and Wu, T. (2006). "Impact of load characteristics and low-voltage load shedding schedule on dynamic voltage stability," in Proccedings of the 2006 Canadian Conference on Electrical and Computer Engineering, Ottawa, ON, Canada, May 2006, 2249–2252. doi:10.1109/CCECE.2006.277553

Maihemuti, S., Wang, W., Wang, H., Wu, J., and Zhang, X. (2021). Dynamic security and stability region under different renewable energy permeability in IENGS system, in *IEEE Access*. 9 19800–19817. doi:10.1109/ACCESS.2021.3049236

Mather, B. A. (2012). "Quasi-static time-series test feeder for PV integration analysis on distribution systems," in Proccedings of the 2012 IEEE Power and Energy Society General Meeting, San Diego, CA, USA, July 2012, 1–8. doi:10.1109/PESGM.2012.6345414

Meng, Y., Yuquan, L., Wen, X., Xin, L., Ying, C., and Yuquan, L. (2014). "Voltage stability research of receiving-end network based on real-time classification load model," in Proccedings of the 2014 IEEE International Conference on Mechatronics and Automation, Tianjin, China, August 2014, 1866–1870. doi:10.1109/ICMA.2014.6885986

Monteiro Pereira, R. M., Pereira, A. J. C., Machado Ferreira, C. M., and Maciel Barbosa, F. P. (2008). "Dynamic voltage stability assessment of an electric power network using composite load models," in Proceedings of the 2008 43rd International Universities Power Engineering Conference, Padua, Italy, September 2008, 1–5. doi:10.1109/UPEC.2008.4651522

Prokhorenkova, L., Gusev, G., Vorobev, A., et al. (2017). *CatBoost: Unbiased boosting with categorical features.*

Rodríguez-García, L., Pérez-Londoño, S., and Mora-Florez, J. J. (2020). "Methodology for measurement-based load modeling considering integration of dynamic load models," in Proccedings of the 2020 IEEE International Autumn Meeting on Power, Electronics and Computing (ROPEC), Ixtapa, Mexico, November 2020, 1–6. doi:10.1109/ROPEC50909.2020.9258723

Soliman, S. A., Abbasy, N. H., and El-Hawary, M. E. (1997). Frequency domain modelling and identification of nonlinear loads using a least error squares algorithm. *Electr. Power Syst. Res.* 40 (1), 1–6. doi:10.1016/S0378-7796(96)01123-6

Song, Y., and Blaabjerg, F. (2017). Overview of DFIG-based wind power system resonances under weak networks. *IEEE Trans. Power Electron.* 32 (6), 4370–4394. doi:10.1109/TPEL.2016.2601643

Taylor, C. W. (1994). *Power system voltage stability (the EPRI power system engineering series)*. New York, NY, USA: McGraw-Hill.

Visconti, I. F., Lima, D. A., Costa, J. M. C. d. S., and Sobrinho, N. R. d. B. C. (2014). Measurement-based load modeling using transfer functions for dynamic simulations. *IEEE Trans. Power Syst.* 29 (1), 111–120. doi:10.1109/TPWRS.2013.2279759

Wang, Y., Lu, C., Wu, P., Zhang, X., Su, Y., Xiong, C., et al. (2022). Online realization of an ambient signal-based load modeling algorithm and its application in field measurement data. *IEEE Trans. Industrial Electron.* 69 (7), 7451–7460. doi:10.1109/TIE.2021.3102428

Xiran, W., Huaidong, L., Yanyang, F., and Wei, C. (2013). "Improved emergency control strategy with optimal control time based on dynamic security region," in Proccedings of the 2013 IEEE International Conference of IEEE Region 10 (TENCON 2013), Xi'an, China, October 2013, 1–4. doi:10.1109/TENCON.2013.6718824

Yixin, Yu., Yanli, Liu., Chao, Qin., and Tiankai, Yang. (2020). Theory and method of power system integrated security region irrelevant to operation states: an introduction. *Engineering* 6 (7), 754–777. doi:10.1016/j.eng.2019.11.016

Yu, Yixin, Dong, Cun, Lee, StephenT., and Zhang, Pei (2006). *Practical dynamic security region in complex power injection space*. Tianjin: Journal of Tianjin University, 129–134.

Yuan, Zeng, and Yu, Yixin (2002). A practical direct method for determining dynamic security regions of electrical power systems. *Proc. Int. Conf. Power Syst. Technol.* 2, 1270–1274. doi:10.1109/ICPST.2002.1047606

Zeng, Y., Zhang, P., Wang, M., Jia, H., Yu, Y., and Lee, S. T. (2006). "Development of a new tool for dynamic security assessment using dynamic security region," in Proccedings of the 2006 International Conference on Power System Technology, Chongqing, China, October 2006, 1–5. doi:10.1109/ICPST.2006.321756

Zhang, P., Hu, W., Liu, X., Xu, X., and Shao, G. (2017). "Study on practical dynamic security region of power system based on big data," in Proccedings of the 2017 12th IEEE Conference on Industrial Electronics and Applications (ICIEA), Siem Reap, Cambodia, June 2017, 1996–1999. doi:10.1109/ICIEA.2017.8283165

Zhou, B., Zeng, Y., Zhen, Q., Wang, A., Xie, Y., and Sun, F. (2018). "Research on the transient stability influenced by wind farm access nodes based on dynamic security region," in Proccedings of the 2018 China International Conference on Electricity Distribution (CICED), Tianjin, China, September 2018, 2044–2046. doi:10.1109/CICED.2018.8592528

Zhu, L., Li, X., Ouyang, H., Wang, Y., Liu, W., and Shao, K. (2012). "Research on component-based approach load modeling based on energy management system and load control system," in Proccedings of the IEEE PES Innovative Smart Grid Technologies, Tianjin, China, May 2012, 1–6. doi:10.1109/ISGT-Asia.2012.6303137

Nomenclature

X_s	Motor stator reactance
R_s	Motor stator resistance
X_r	Rotor reactance of the motor
R_r	Motor rotor resistance
X_M	Field reactance of the motor
X_D	Distribution network reactance
R_D	Distribution resistance
M_{lf}	Induction motor load rate
H	Inertia time constant of the induction motor
A	Torque coefficient of the induction motor
B	Torque coefficient of the induction motor
I_P	Constant current active load factor
Z_P	Constant impedance active load factor
I_Q	Constant current reactive load coefficient
Z_Q	Constant impedance reactive load factor
L	Distributed photovoltaic outlet inductance
K_{II}	Integrated coefficient of the distributed photovoltaic current
K_{IP}	Proportional coefficient of the distributed photovoltaic current
K_{UI}	Distributed photovoltaic voltage integration coefficient
K_{UP}	Distributed photovoltaic voltage ratio coefficient
K_M	Proportion of static load active power to load total active power
K_{PV}	Ratio of distributed PV active power to load active power

Frontiers in
Energy Research

Advances and innovation in sustainable, reliable and affordable energy

Explores sustainable and environmental developments in energy. It focuses on technological advances supporting Sustainable Development Goal 7: access to affordable, reliable, sustainable and modern energy for all.

Discover the latest Research Topics

See more →

Frontiers

Avenue du Tribunal-Fédéral 34
1005 Lausanne, Switzerland
frontiersin.org

Contact us

+41 (0)21 510 17 00
frontiersin.org/about/contact

frontiers

Frontiers in
Energy Research

frontiers | Research Topics